Continuum Modelling and Vibration Analysis of String-Harnessed Structures

by

Blake Martin

A thesis
presented to the University of Waterloo
in fulfillment of the
thesis requirement for the degree of
Doctor of Philosophy
in
Mechanical and Mechatronics Engineering

Waterloo, Ontario, Canada, 2017

Examining Committee Membership

The following served on the Examining Committee for this thesis. The decision of the Examining Committee is by majority vote.

External Examiner:	Dimitrios Konstantinidis Associate Professor Dept. of Civil Engineering McMaster University
Supervisor:	Armaghan Salehian Associate Professor Dept. of Mechanical and Mechatronics Engineering University of Waterloo
Internal Member:	John Medley Professor Dept. of Mechanical and Mechatronics Engineering University of Waterloo
Internal Member:	Clifford Butcher Assistant Professor Dept. of Mechanical and Mechatronics Engineering University of Waterloo
Internal-External Member:	Kirsten Morris Professor Dept. of Applied Mathematics University of Waterloo

I hereby declare that I am the sole author of this thesis. This is a true copy of the thesis, including any required final revisions, as accepted by my examiners.

I understand that my thesis may be made electronically available to the public.

Abstract

Power and signal cables in recent years have been observed to constitute a major component in the dynamic behaviour of space structures. In a typical system, the cables-to-payload mass ratio can be as high as 20%. Ignoring the effects of these space flight cables has led to model inaccuracies in the dynamic analysis of such structures. Obtaining simple analytical solutions that can predict the dynamic behaviour of these structures has numerous advantages for vibration suppression using active control system, structural design, and modelling before their launch. As a result, mission accuracy is less likely to be jittered to due disturbances in the space environment. The intention of the presented work is to develop low-order high-fidelity partial differential equation models for the transverse bending of harnessed structures. The focus is on string-harnessed beam structures as a way to study the mass and stiffness effects of the space flight cables. In this thesis, strings are assumed to not be able to have a varying stress distribution across the cross section, unlike a cable. A continuum modelling approach is developed for the string-harnessed system and a homogenization technique is applied to obtain the governing equation of motion. Two periodic wrapping patterns for the string are initially considered such that the homogenization technique may be applied. The results are compared with numerical simulations and experimental results and are shown to agree quite well.

Subsequently, non-periodic wrapping patterns are investigated and a perturbation theory approach is employed to determine the frequencies and mode shapes. The Lindstedt-Poincaré method is applied to an Euler-Bernoulli model for the transverse vibrations with non-constant coefficients and extended to include additional corrections to the frequencies and mode shapes than previously considered in the literature. Furthermore, various ways to choose the reference values from which the system is perturbed are considered and compared for their effect on the accuracy of the solution. Numerical and experimental results for the frequency response functions are shown to be in strong agreement for both the periodic and non-periodic wrapping pattern cases. Finally, a model approximation method is developed to determine an equivalent constant coefficient model for the transverse displacement of the string-harnessed system. The model approximation method uses the perturbation theory results to predict the frequencies and mode shapes of the system, then applies an inverse problem approach to determine the approximate model. Numerical simulations are performed and show that the approximate model is quite capable of predicting the frequencies and mode shapes of the system for both periodic and non-periodic wrapping patterns. Frequency response functions for the approximate model are also compared to previous experimental results and are shown to be in very good agreement.

Acknowledgements

First and foremost, I would like to express my highest level of appreciation and gratitude to my supervisor Dr. Armaghan Salehian. Her guidance over these last few years have helped me flourish into the researcher I have become. When I started graduate studies as a Master's student, her words of encouragement, motivation, support, and help solidified my decision to pursue my PhD under her supervision. Her knowledge and insight made sure that no stone was left unturned during my research and I am very thankful for this. I cannot begin to explain how fortunate I feel to have had such a great supervisor who cares so deeply about the success of her students.

I would also like to thank all the members of our research team, both past and present: Mohammed Ibrahim, Tim Pollock, Steven Lao, Hamza Edher, Egon Fernandes, Gary Chan, Karthik Yerrapragada, Dil Bath, and Pranav Agrawal. Everyone's support and kindness has been greatly appreciated and has made working in the lab incredibly enjoyable.

In addition, a special thanks to Dr. Kirsten Morris who insisted on a NSERC Undergraduate Student Research Award while I was completing my undergraduate degree. This first taste of research in 2011 was the catalyst for pursuing graduate studies.

Finally, I'd like to acknowledge the wonderful friends and family that are in my life. Thank you all for celebrating my successes with me and being supportive when in need. I could not have done all of this without each and every one's encouragement, support, and love. Thank you from the bottom of my heart.

Dedication

I would like to dedicate this thesis to my parents Lynne Larabie and Dean Martin, as well as my step-parents Louise Forget and Shane Lebrun. The love and support I have received from all of you has kept me motivated and determined all these years.

Table of Contents

List of Figures

List of Tables

List of Abbreviations

BAR	=	System with bar model assumption for string
CC	=	Clamped-Clamped
CF	=	Clamped-Free
Diff.	=	Norm of difference minimization for reference value selection
EB	=	Euler-Bernoulli
ECM	=	Equivalent Continuum Model
FEA	=	Finite Element Analysis
FF	=	Free-Free
FRF	=	Frequency Response Function
Grad.	=	Gradient norm minimization for reference value selection
HOM	=	Homogenized model for transverse vibration of string-harnessed system
MPF	=	Modal Participation Factor
ODE	=	Ordinary Differential Equation
Pert.	=	Norm of perturbation minimization for reference value selection
PDE	=	Partial Differential Equation
POD	=	Proper Orthogonal Decomposition
STR	=	Analytical model for transverse vibration of string-harnessed system

List of Symbols

A_b	=	bh, cross-sectional area of beam, m^2
A_n	=	normalization coefficient for mode shapes, $1/\sqrt{\mathrm{kg}}$
$A_{n1}^{(1)}$	=	normalization coefficient for mode shapes in perturbation theory
A_s	=	πr_s^2, cross-sectional area of string, m^2
$A_{s,i}$	=	$\pi r_{s,i}^2$, cross-sectional area of ith string, m^2
b	=	beam width, m
$\overline{b}$	=	$b/2 + r_s$
C_1, C_2, C_3, C_4	=	coefficients in strain energy using homogenization
c	=	ratio of change in beam thickness
d_1	=	objective function of metric minimization method
E_b	=	modulus of beam, $\mathrm{N/m}^2$
E_s	=	modulus of string, $\mathrm{N/m}^2$
$E_{s,i}$	=	modulus of ith string, $\mathrm{N/m}^2$
$EI(x)$	=	bending stiffness, Nm^2
EI^*	=	bending stiffness reference value, Nm^2
$\widehat{EI}$	=	equivalent bending stiffness of approximate model, Nm^2
$f(x)$	=	spatial function in separation of variables
$f_{n1}(X), f_{n2}(X)$	=	first-order mode shape corrections
G_b	=	shear modulus of beam, $\mathrm{N/m}^2$
g	=	acceleration due to gravity, $\mathrm{m/s}^2$
$g(t)$	=	temporal function in separation of variables
g_f	=	dimensionless gravitational acceleration factor
$H(x, \omega_s)$	=	frequency response function, $\mathrm{m/(m/s}^2)$
h	=	beam thickness, m
$\overline{h}$	=	$h/2 + r_s$
I_b	=	$bh^3/12$, second moment of area of beam about y axis, m^4
I_{xx}	=	$I_{yy} + I_{zz}$, polar moment of area of abeam about x axis, m^4

I_{yy}	=	$bh^3/12$, second moment of area of beam about y axis, m^4
I_{zz}	=	$b^3h/12$, second moment of area of beam about z axis, m^4
J	=	torsion constant, m^4
K_1	=	coefficient in kinetic energy using homogenization
k_n	=	nth mode shape coefficient
L	=	length of fundamental element, m
l	=	length of system, m
l_0	=	location of step in beam, m
$M(X)$	=	moment in dimensionless system
M_k	=	lumped mass located at $x = x_k$
(N_x, M_x, P_x)	=	stress resultants
P	=	$P_{EI} \cup P_{\rho A}$
$\widehat{P}$	=	P/l
P_{EI}	=	set of points where $EI(x)$ is not C^∞
$P_{\rho A}$	=	set of points where $\rho A(x)$ is not C^∞
p	=	integer value in norm minimization
$R(x,s)$	=	correlation function between two points in system, m^2
$r(x,t)$	=	function used to eliminate inhomogeneous boundary conditions, m
r_s	=	radius of string, m
$r_{s,i}$	=	radius of ith string, m
$S(X)$	=	shear in dimensionless system
S_{1n}, S_{2n}	=	integral values for metric and error minimization methods
T	=	dimensionless time
$\overline{T}$	=	sampling interval, s
$\widehat{T}(x)$	=	function in string-harnessed model due to string tension, Nm
T_s	=	tension in string, N
$T_{s,i}$	=	tension in ith string, N
T_e, T_{system}, T_{tot}	=	kinetic energy in fundamental element, system, and in total, Nm
t	=	time, s
U_{beam}, U_{string}	=	strain energy in beam and string, Nm
U_{system}, U_{tot}	=	strain energy in system and in total, Nm
$u(X)$	=	dimensionless spatial function in separation of variables
$u(x,t)$	=	longitudinal displacement, m
$(u_i, v_i, w_i, \theta_i)$	=	nodal parameters in FEA
u_x, u_y, u_z	=	displacement field in x, y, and z direction, m
$v(x,t)$	=	transverse displacement in y direction, m
$\overline{v}(x,t)$	=	transverse displacement in y direction about equilibrium position, m

$W(X,T)$	=	dimensionless transverse displacement in z direction
$w(x,t)$	=	transverse displacement in z direction, m
$\overline{w}(x,t)$	=	transverse displacement in z direction about equilibrium position, m
$\widehat{w}(x,t)$	=	transverse displacement in z direction of approximate model, m
$w_e(x)$	=	equilibrium solution, m
X	=	dimensionless position
X^*	=	0 or 1, location where dimensionless boundary conditions are applied
X_{P_i}	=	ith largest point in $\widehat{P}$
x^*	=	0 or l, location where boundary conditions are applied, m
(x,y,z)	=	Cartesian coordinates, m
$y(x,t)$	=	$w(x,t) - r(x,t)$
$y_s(x)$	=	y coordinate of centre of string, m
$y_{s,i}(x)$	=	y coordinate of centre of ith string, m
$z_s(x)$	=	z coordinate of centre of string, m
$x_{s,i}(x)$	=	z coordinate of centre of ith string, m
$\overline{\alpha}$	=	$\sqrt{(-C_2 + \sqrt{C_2^2 + 4C_1K_1\omega^2})/2C_1}$
α_{n1}, α_{n2}	=	first-order frequency corrections
β	=	$\sqrt[4]{K_1\omega^2/C_1}$
$\overline{\beta}$	=	$\sqrt{(C_2 + \sqrt{C_2^2 + 4C_1K_1\omega^2})/2C_1}$
$\beta_{n1}, \beta_{n2}, \beta_{n3}$	=	second-order frequency corrections
γ	=	mass per unit length on right side of beam, kg/m^3
Δ	=	objective function of error minimization method
Δ_m	=	change in length along midlines of beam, m
Δ_s	=	change in length of string, m
$\delta(x)$	=	Dirac delta
δ_{ij}	=	Kronecker delta
$\boldsymbol{\varepsilon^{(2)}}$	=	Green-Lagrange strain tensor
ε_s	=	strain along length of string
$\epsilon\widehat{EI}$	=	$(EI(X) - EI^*)/EI^*$
$\epsilon\widehat{M}_k$	=	$M_k/l\rho A^*$
$\epsilon\widehat{\rho A}$	=	$(\rho A(X) - \rho A^*)/\rho A^*$
(η,y,z)	=	local Cartesian coordinates, m
θ	=	periodic wrapping pattern angle, rad
$\overline{\theta}(x,t)$	=	torsional displacement about equilibrium position, rad
$\theta_x(x,t)$	=	torsional displacement, rad

$\lambda, \overline{\lambda}$	=	eigenvalues in POD method
μ_n	=	nth mode shape parameter
ρ_b	=	density of beam, kg/m^3
ρ_s	=	density of string, kg/m^3
$\rho_{s,i}$	=	density of ith string, kg/m^3
$\widehat{\rho A}$	=	equivalent mass per unit length of approximate model, kg/m^3
$\rho A(x)$	=	mass per unit length, kg/m^3
ρA^*	=	mass per unit length reference value, kg/m^3
σ_{xx}	=	longitudinal stress, N/m^2
τ	=	bending stiffness on right side of beam, Nm^2
$\phi(x), \overline{\phi}(x), \widehat{\phi}(x)$	=	mode shape
$\phi(X)$	=	dimensionless mode shape
$\overline{\phi}_i$	=	$K_1 \int_0^l \phi_i(x)\,\mathrm{d}x$
$\widetilde{\phi}_i$	=	$\int_0^l \rho A(x) \widehat{\phi}_i(x)\,\mathrm{d}x$
$\Psi_i(x)$	=	cosine of angle formed between ith string and x axis
$\Omega_n(EI^*, \rho A^*)$	=	total corrections to the frequency
$\omega, \overline{\omega}, \widehat{\omega}$	=	frequency, rad/s
ω_s	=	shaker driving frequency, rad/s

Chapter 1

Introduction

1.1 Motivation

The evolution of spacecraft and technological advances have generated exceptionally lightweight structural materials and an increase in the number of signal and power cables found aboard these structures. In modern spacecraft, the total mass of the power and signal cables typically accounts for approximately 6-7% of the total mass, and can be as high as 20%. It is quite common for these cables to be harnessed on structural elements and their presence plays a significant role in changing the dynamic behaviour of these structures. Obtaining simple analytical solutions that can predict the dynamic behaviour of these structures has numerous advantages for vibration suppression using active control system, structural design, and modelling before their launch. As a result, mission accuracy is less likely to be jittered to due disturbances in the space environment. Figure 1.1 shows an example of a cable-harnessed structure.

Figure 1.1: Example of power and signal cables on spacecraft, [8].

In 2003, the United States Air Force Research Laboratory, Space Vehicle Components Branch (AFRL/VSSV) launched a research program with the aim of developing a deeper understanding of the dynamic effects of harnessed cables on their host structure. Since this time, the AFRL/VSSV has been heavily invested in obtaining simple analytical models for cable-harnessed space structures that may be used in a joint design and vibrations analysis process. Obtaining a simple analytical model is particularly important in predicting the dynamic effect of cables in large systems that cannot be fully tested before launch. Furthermore, a simple analytical model is beneficial for vibrations control methods employed during the launch of spacecraft.

The cables used on spacecraft are typically composed of multiple helically twisted cables wrapped with Kapton tape, see Fig. 1.2. The complexity of these cables poses a significant challenge for the modelling process. Currently, the effects of harnessed cables on spacecraft dynamics are either ignored or the added mass is included using ad hoc models. In the latter case, a non-structural mass is commonly added to the model to include the cable effects. In certain scenarios the stiffening effect of the cables can be negligible and in these cases simply accounting for the additional mass will provide a reasonably accurate model. However this type of modelling omits the more complex dynamic behaviour introduced by these harnessed cables and, as structures become more lightweight, this becomes less accurate as the stiffening effect of the cables becomes more apparent.

Figure 1.2: Typical cable used in spacecraft, [142].

The motivation for the focus of the present research is twofold: The need for an accurate modelling technique that incorporates the full effects of harnessed cables on structural elements, and the need for simple analytical models to predict the dynamic behaviour of the harnessed systems. To make the problem tractable, and as a means to produce initial results into this new topic of research, a string model is employed for the cables. Analyzing string-harnessed structures provides an initial investigation into the mass and stiffening effects that occur when structures are harnessed. In order to obtain simple analytical models for the string-harnessed systems, homogenization theory, perturbation theory, and methods for model approximation are considered.

1.2 Literature Review

1.2.1 Cable-Harnessed Space Structures

Initial findings for the research program launched in 2003 by the AFRL/VSSV were reported in [8, 61, 50]. These initial studies indicated a paucity in relevant published materials for the area of research concerned with cable-harnessed space structures. Preliminary tests to investigate the dynamic effect of cable-harnessed structures were performed in [8, 61] on an aluminium alloy beam and truss structure harnessed with a cable. The cables were held in place using mounting tabs, as shown in Fig. 1.3. It was shown that even a single cable could significantly affect the dynamics. In [8] the authors developed experimental procedures to determine certain physical properties of cables that could be used in future modelling endeavours. Two simple mounting configurations were considered in [50] and testing was performed to determine the importance of mounting parameters and cable harness pattern on the dynamics of the system. It was observed that at low frequencies

the mass effect of the cables would dominate, while at higher frequencies there would be increased modal damping. The authors in [8, 61, 50] acknowledged that further research was required to fully understand space cables and the dynamics of cable-harnessed structures. In this research, it was shown once again that even a single cable could significantly affect the dynamics of a beam or truss structure. This will become a particularly important problem as structures are made increasingly more lightweight. These initial studies also addressed the modelling of cables and cable-harnessed structures for spacecraft as paramount for the aerospace industry.

Figure 1.3: Mounting tab used for cable restraint, [50].

Following these initial studies, the research on cable-harnessed space structures was focused mainly on the parameter estimation and dynamic characterization of the cables. Preliminary tests for parameter estimation and dynamic modelling of only the cables were outlined in [51, 48]. The focus in these works was using lateral excitation methods to obtain the experimental results. In [48] the focus of the work was on the frequency progression of the cable versus mode number and [51] outlined a signal processing and analysis method to obtain the cable parameters from experimental results. The cumulation of a three-year study at the AFRL was presented in [7] and includes every valuable result, dead end, rat hole, and tangent that was discovered and explored during the study. The significant contribution of the work in [7] is the development of a full test methodology for identifying cable parameters and tie-down stiffness identification shown in Fig. 1.4. Further investigation into methodologies for identifying cable structural parameters through testing, in particular the equivalent extensional modulus, damping ratios, area moment of inertia, and shear rigidity in cables, was performed in [49].

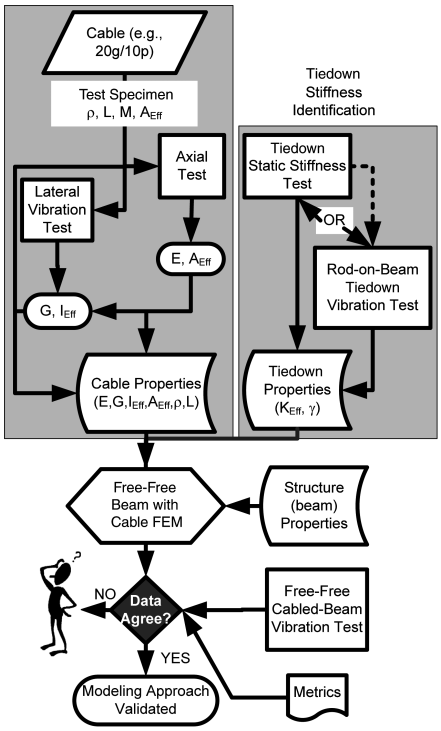

Figure 1.4: Process for cable modelling approach validation, [7].

With the cable property identification methods fully outlined in [51, 48, 7, 49], the research on cable-harnessed structures branched out into two main categories. The first main category was research investigating more closely the effects of damping and their inclusion in predictive models. Various possible models that include damping have been considered for spacecraft wiring harnesses. An Euler-Bernoulli (EB) beam with a 'geometric' viscous damping term was considered in [76, 77], damping for shear beam models was the focus of [68, 69], and the inclusion of damping in Timoshenko beams was examined in [67]. The 'geometric' damping that is considered in [76, 77] involves an internal shear force that is proportional to the time rate of change of slope. These works were mainly focused on the development of mathematical models for the cables used in aerospace applications.

Further work on modelling the typical aerospace cables involved characterization of damping. An experimental approach was undertaken to study the damping, along with the effect of various parameters on the dynamics, of aerospace cables in [142]. Parameters including tension, zip tie attachment method, excitation method, and length of the cable were considered and their effects on the dynamics of the cable were studied. A focus on

modelling the internal damping mechanisms was done in [140] and identifies the multitude of cable models available throughout the literature. The inclusion of viscous damping and time hysteresis to accurately model cables was investigated in [141]. A general approach for modelling stranded cables as structural beams by determining effective homogeneous parameters was done in [138, 137].

The second main branch of cable-harnessed structures research involves the use of simple beam models for the cables and subsequently modelling the harnessed structures, including tie-downs. Research on the modelling of cable-harnessed structures was continued from earlier work in [11, 33]. In [11, 33] the cable parameters were estimated using experimental techniques and then subsequently modelled using shear beams. The tie-downs holding the cable in place on the host structure were modelled as linear spring elements. Multiple cable families were considered and numerical results were computed using NASTRAN to compare and validate against experimental results. In [11] a cable running along the length of a free-free boundary condition beam is considered, Fig. 1.5, and in [33] a cable-loaded panel is considered, Fig. 1.6.

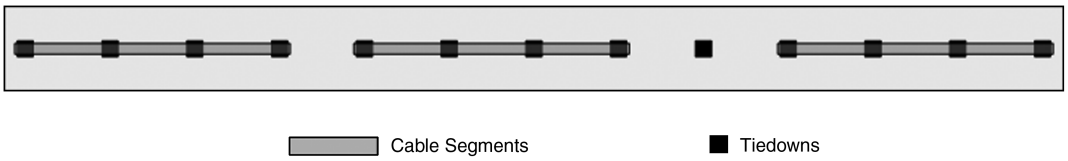

Figure 1.5: Cable-harnessed beam setup in [11].

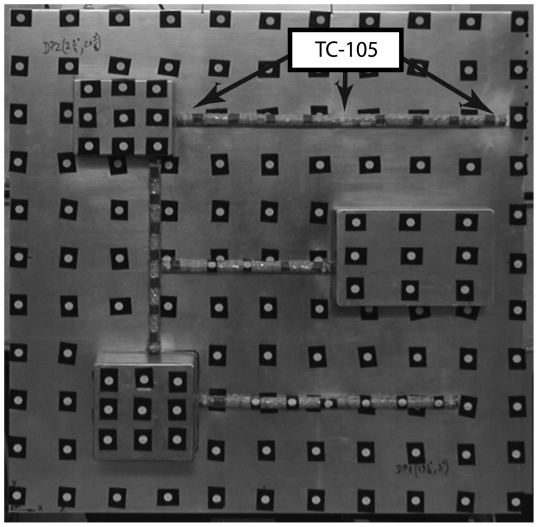

Figure 1.6: Cable-loaded panel setup in [33].

More recently [28, 29, 30] have investigated the use of a spectral element method (SEM) for the modelling of cable-harnessed systems with tie-downs. The cable was modelled as an EB beam and connected to the host structure with spring elements to represent the mounting tabs. They reported higher accuracies compared with a finite element analysis (FEA). Finally, a distributed transfer function method was developed in [139] for a system with a longitudinal cable.

In this thesis, the focus is on developing an analytical model for string harnessed-systems as a way to make the problem more tractable. This will also allow for a focus on the mass and stiffness effects without the complexities of tie-downs. A survey of the literature revealed that combinations of string and beam have not been largely studied. A common system that appears is that of a string that shares a finite number of attachment locations with the host structure, see [26, 63], or the endpoints of the string and the host structure are attached using rigid connectors, see [149, 55]. In these types of systems the string-beam system is coupled, and therefore a coupled set of partial differential equations (PDEs) must be solved. Another commonly seen string-harnessed system involves strings running along a designated path inside the host structure, such as along the midline of the beam. A typical scenario is structures embedded with shape memory alloy (SMA) wires, see [35, 34, 100]. By having a string inside the host structure the displacement of the string is known since it will move with the host structure and the need for coupled PDEs is overcome.

There is a significant gap in the literature that the presented research aims to fill. There currently does not exist a method to analytically model the effect of harnessed cables on a host beam. This will be approached by considering a string, for simplicity, and making preliminary steps to effectively model the stiffening and added mass effects. This will also provided additional work on string and beam systems that is lacking in the literature.

1.2.2 Homogenization of Periodic Structures

Continuum modelling is a fundamental component in the description and analysis of system behaviour. As systems became increasingly complex, researchers developed novel methods for deriving equivalent continuum models for periodic, lattice-like, and truss structures. Typically the equivalent continuum models are constant coefficient PDEs, which provide a simple and efficient manner for analyzing the complex structure. Additionally, equivalent continuum models are a practical approach for analyzing these structures and avoids the problem of computationally expensive simulations, such as FEA. The fundamental idea behind equivalent continuum modelling is schematically illustrated in Fig. 1.7.

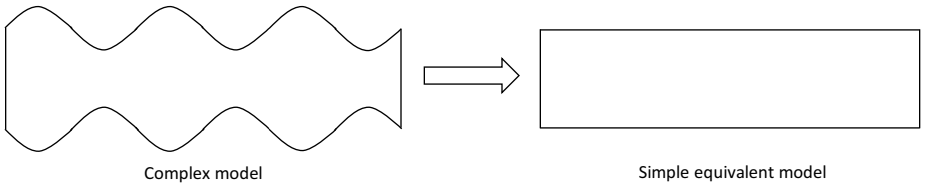

Figure 1.7: Fundamental idea of equivalent continuum modelling.

An excellent review on equivalent continuum modelling is found in [107] and three typical approaches for determining equivalent continuum models exist. They are using a discrete field to obtain difference equations, which are then either solved directly or converted to differential equations, applying a multi-scale asymptotic expansion, and an energy equivalence approach. These methods are commonly called homogenization techniques. Using a discrete field to determine the equivalent continuum model was done in [37, 118, 119, 146], with a focus on grids and trusses. The method of asymptotic expansions was applied in [109, 43, 23, 71, 79, 1] for periodic systems. In these cases small parameters are defined, typically the ratios of length of periodicity to total length as well as height to total length. The idea is that in the limit as these small parameters tend to zero will yield a homogenized model. The efficacy of this method is shown with regards to stiffness

parameter estimation in [23] by comparing the results of the homogenization to reference solutions for corrugated beams and a stranded rope.

The energy equivalence homogenization technique is widely used throughout the literature. This homogenization technique is found in modelling the dynamic behaviour of systems with lattice-like structure, where the system can be viewed as containing a large amount of discrete points over the domain. Notable examples stem from work in modelling a micropolar continuum, see [9], gridwork dynamics, see [144], as well as the modelling of net and cloth dynamics, see [74]. The process involves determining the strain energy and kinetic energy of an arbitrary discrete point in terms of continuous functions, typically displacement, evaluated at the spatial coordinates of the point in question. Summing the energies of all the discrete points in the domain can be approximated by an integral over the domain. To obtain the integral formulation, the integrand is determined by dividing the strain and kinetic energies by the lengths over which would constitute a single element in the continuum model to produce a strain energy density as well as a kinetic energy density. In generating the energy densities, the system is converted from containing continuous functions evaluated at discrete points to a system that only contains continuous functions. Applying Hamilton's principle then allows an equivalent homogenized continuum model for the system to be determined.

The energy equivalence homogenization technique has seen many application in the field of truss dynamics, see [107, 108, 143, 19, 127, 131, 129, 130, 125, 126, 128]. For modelling truss structures, the homogenization technique involves defining an equivalent continuum beam that, under the same deformation as the original system, exhibits the same amount of strain energy and kinetic energy. Using an exact representation for the displacement of the system, the strain and kinetic energy of each fundamental element can be determined. As with the homogenization in lattice theory, a corresponding strain and kinetic energy density is found and integrating the energy densities over the domain allows one to use Hamilton's principle. By using this approach, the truss system is modelled by an equivalent, homogenized, PDE that only depends on time and a single spatial variable. The homogenized model can readily be solved using well-known mathematical techniques. In [129], an experimental validation is provided for the homogenization method in the case of only a few truss elements and shows agreement for the first four vibratory frequencies.

The energy equivalence homogenization technique is adopted in the present work due to simplicity in the application and previous work in the literature demonstrating the accuracy of the technique, particularly when a large number of repeated elements are considered. Obtaining a homogenized model provides a simple manner in which the global behaviour of string-harnessed systems can be studied, thus providing preliminary insight into a new and novel problem.

1.2.3 Solution Methods for Spatially-Dependent Differential Equations

The second major component of the presented research considers a spatially dependent model for string-harnessed systems. Working with a spatially dependent model allows for an investigation into local effects, something that is not possible when applying homogenization as the local effects of bending stiffness and mass per unit length are averaged over the length of the system. Furthermore, a spatially dependent model is not only more accurate, but it is more representative of real-world applications. This makes determining the frequencies of vibration and the associated mode shapes of great interest. One of the difficulties, however, is that spatially dependent PDEs are not always readily solvable. A variety of solution methods have been explored in the literature.

One common method for obtaining frequency and mode shape results are through a FEA. The FEA is well known and is based on placing a fixed number of nodes along the system and using interpolating functions between the nodes. For an Euler-Bernoulli beam, the focus of the presented research, the interpolating functions are typically in the form of a polynomial of degree 3 and at each node the displacement and slope are recorded. An outline of the FEA approach can be found in [62], as well as in many other texts. A second common numerical method is the Rayleigh-Ritz, which provides an upper bound estimate for the frequencies. This has been done successfully in the literature for a host of different applications including graded microbeams [3], ocean towers [6], and tapered beams [10, 133]. One of the downfalls of the Rayleigh-Ritz method is the user must supply approximate mode shapes to obtain the estimates for the frequencies. In complex cases, it can be quite difficult to estimate the mode shapes of the system and this can cause large upper bound estimates for the frequencies. Hence in some cases it may not be desirable to use this approach.

It is always advantageous when it is possible to determine an analytical solution to a spatially varying PDE as the results will always output the exact frequencies and mode shapes. While this is not always possible, there are certain specific cases when this is achievable. In particular, the cases of exponential variations in the beam and polynomial expressions of varying degrees have received a lot of attention in the literature. Examples of each of these two main types of systems are presented in Figs. 1.8 and 1.9.

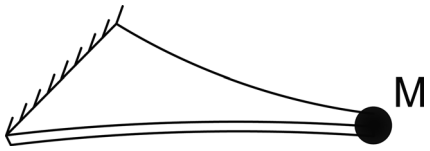

Figure 1.8: Exponentially tapered beam with tip mass in [147].

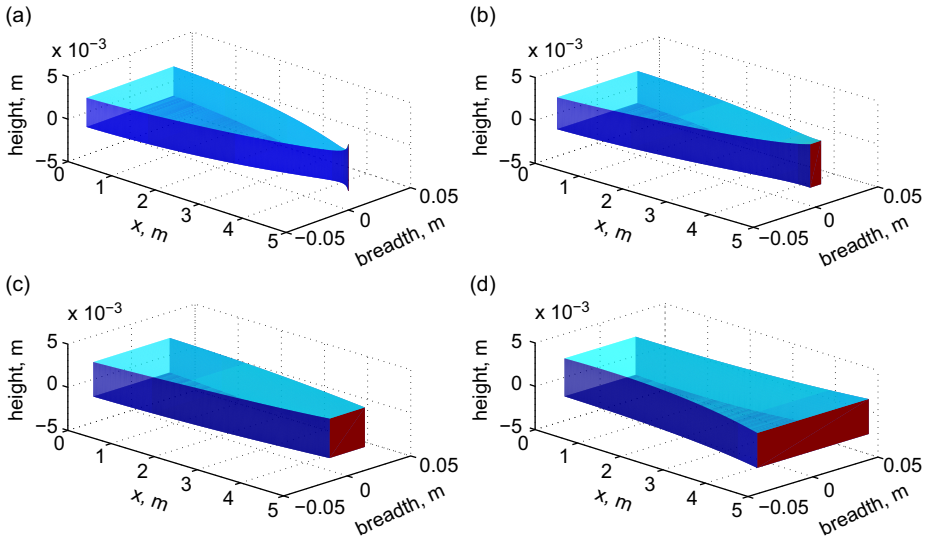

Figure 1.9: Multiple polynomial variations in [132].

Exponentially varying beams have been studied in such works as [147, 40, 145, 58] and the general expression for the bending stiffness and mass per unit length of the system are $EI(x) = EI_0 e^{\alpha x}$ and $\rho A(x) = \rho A_0 e^{\alpha x}$. When these specific forms are used in combination with separation of variables, it is found that the resulting spatially dependent ordinary differential equation (ODE) has constant coefficients due to the elimination of the exponential terms. From the constant coefficient ODE, the steps that are used for solving a homogeneous beam are then employed and analytical expressions for the frequencies and mode shapes are obtained. Polynomial variations have been studied in such works as [132, 2, 66, 47, 102, 121, 10]. A host of various solution methods are employed depending on the specific form of the polynomial variations, including applying transformation to obtain a homogeneous EB model, transformation to obtain the solution in terms of Bessel

functions, the Frobenius method, and Galerkin's method. Other types of spatial variations have also been considered such as cantilevers with parabolic thickness in [24] and wedge and cone beams in [103]. The clear limitation with the these particular cases of variations in the system is that a very specific form is required and therefore the techniques cannot be applied to the general case.

The most general approaches to solving spatially dependent systems that do not depend on a specific form come from perturbation theory and asymptotic analysis. An excellent, and often referenced, text on the subject is [104]. One such technique is the Wentzel-Kramers-Brillouin (WKB) approximation, which has been applied to a general equation of a spatially dependent system in [120, 106]. That is to say the form of the spatial variations has not been specified in the mathematical development. The WKB method is quite useful for obtaining a global approximation in cases where the highest derivative of the system is multiplied by a small parameter. Typically, the small parameter multiplying the highest order derivative is introduced by dividing the spatial ODE by the square of the frequency. The method of matched asymptotic expansion, which similarly to the WKB has a small parameter multiplying the highest derivative, was studied in [134]. The matched asymptotic expansion is applied when the solution to the ODE behaves on different scales in overlapping regions. In [134] a gravity loaded beam was considered when there is a great influence from gravity. Additionally in [134] regular perturbation theory is applied to the case when the effect of gravity is small. In addition to these common methods, many other perturbation theory approaches have been considered in the literature such as, to name a few, the method of varying amplitudes in [136], a generalized Senator-Bapat in [73], and the method of multiple time scales in [32].

The Lindstedt-Poincaré method is a perturbation method that has received very little attention when it comes to spatially dependent EB models. The Lindstedt-Poincaré method is applied to obtain periodic solutions when regular perturbation theory fails by removing terms that grow without bound, *i.e.* secular terms. Applying this method to system where the bending stiffness and mass per unit length are expressed as a constant value from which spatially dependent perturbations occur was first introduced in [75]. Since this work, the method of Lindstedt-Poincaré has not undergone any further developments for spatially dependent system given a linear equation of motion. There is an untapped potential for this method that has yet to be investigated. In the presented research, consideration is given to exploring various avenues. In particular, additional corrections are determined and multiple manners in which the solution can be found are compared for accuracy. Due to the relative simplicity in terms of mathematical details to other perturbation methods, the Lindstedt-Poincaré approach is of great interest to further develop.

1.2.4 Model Approximation for Non-Periodic Structures

The final component of the presented research concerns determining the coefficients for a PDE using a single spectrum, which is a set of natural frequencies. Typically, the forward problem is solved and involves knowing the coefficients of a PDE and determining the frequencies and mode shapes. When the problem is approached knowing the frequencies and the coefficients of the PDE are to be determined this falls under the broad category of inverse problems, which can also be referred to as parameter estimation.

As an example, a common ODE that is studied in the literature and in general by mathematicians is the Sturm-Liouville (SL) problem. The solution to specific forms of the SL problem yields such important quantities such as the Bessel and Legendre functions. In the most general sense, the SL problem can be described as

$$\frac{\mathrm{d}}{\mathrm{d}x}\left(p(x)\frac{\mathrm{d}y}{\mathrm{d}x}\right) + q(x)y + \lambda r(x)y = 0$$

The question of inverse problems associated with SL problem have been studied in [53, 59, 123, 56, 72, 4, 5, 122], to name only a handful of the available works in the literature. Commonly, a specific form for the SL problem is given and the focus is on determining whether or not the inverse problem will yield a unique solution. This was the main focus of the work in [53, 59, 56, 72, 4]. Uniqueness is an important question as it is crucial to know that the result of the inverse problem will yield the correct form of the unknown coefficients and that this is the only possible result. Other times, the focus is on determining a numerical implementation for obtaining the unknown coefficients, as was the case in [123, 5, 122]. Some of the numerical implementations that were studied are a finite difference method and an iterative method.

Another problem that has received a lot of attention in the literature is with respect to EB beam models and general fourth order differential equations. A static EB problem was considered in [82, 81], a constant coefficient EB model with spatial and temporal-dependent forcing in [60], the general form for a spatially dependent EB model in [110, 95, 16, 15, 112, 45, 46], and general fourth order ODEs in [94, 96, 13]. These works deal with the existence and uniqueness of the inverse problem. Specifically, it is determined that the spatially dependent coefficients can be uniquely determined when three spectra, each from different boundary conditions, are determined. In the more general case of higher order ODEs, it was shown in [14] that when the highest derivative is $2n$, then $n+1$ spectra from distinct boundary conditions are required to uniquely determine the unknown coefficients. It is seen from this general result that if an EB model is considered, $n = 2$, then indeed three unique spectra are required to obtain the bending stiffness and mass per unit length. An

excellent reference text for inverse problems, with a section dedicated to the EB models, is found in [46].

Inverse problems have also been used for real-world applications, in particular attention has been given to structural health monitoring and damage detection. These applications were considered for rods in [38, 99] and for beams in [22, 39]. Using the frequency results of a system before and after damage, the location of cracks were identified within the system. To date, inverse problems are mainly focused on exactly determining the spatially dependent coefficients of a system. While this is an important problem, it is not the focus of the presented research. In this work the expressions for the spatially dependent bending stiffness and mass per unit length are exactly known, and thus reconstructing these quantities from multiple spectra is not of great interest. The goal is to take the frequencies and mode shapes of the string-harnessed system and determine a constant coefficient model that can approximate these with minimal error.

After exhaustively searching through available literature, it appears as though the case of taking a spatially dependent model and using an inverse method to determine an approximate constant coefficient model has not yet been studied. The most relevant piece of research that was found involved a constant coefficient model whose frequencies were determined using ANSYS, and then the constant coefficients were obtained from a numerical optimization method that involved minimizing the sum of the square of the differences between the ANSYS and analytical results in [12]. The idea considered in the presented research is similar in concept to a homogenization procedure, in which an equivalent continuum model is determined, however differs significantly due to the intermediate steps implemented to determine the approximate model. The frequencies of the string-harnessed system will be obtained from a perturbation theory and these will be taken as the exact value for the frequencies that the constant coefficient model must approximate. The end goal is the ability to provide the information of $EI(x)$, $\rho A(x)$, and the boundary conditions and obtain as an output a set of equivalent coefficients $\widehat{EI}$ and $\widehat{\rho A}$ that approximate the system's dynamic behaviour.

1.3 Thesis Organization

The following outlines a summary of the presented research and its contributions.

Chapter 2 presents a continuum modelling approach for string-harnessed structures and the use of a homogenization technique for periodic wrapping patterns. Two periodic wrapping patterns are considered and the coordinates of vibration are assumed to be

decoupled. The PDEs governing the bending, longitudinal, and torsional vibrations are obtained. Numerical simulations are performed for varying system parameters and the results are compared to a fully coupled finite element analysis. Experimental results are also included to demonstrate the accuracy of the proposed model.

Chapter 3 develops the perturbation theory applied to an EB beam model with spatially varying coefficients. In applying the perturbation theory, second-order corrections are found for the natural frequencies and first-order corrections are found for the mode shapes. The problem statement is formulated by assuming there exist reference values from which the bending stiffness and mass per unit length of the system are perturbed. A major focus is on the appropriate choice of these reference values as they directly influence the accuracy of the perturbation theory results.

Chapter 4 applies the developed perturbation theory to string-harnessed systems. In particular, the perturbation theory is applied to determine how changes in non-periodic wrapping patterns affect the frequencies of the system. Multiple non-periodic wrapping patterns are considered and are extensions of the periodic wrapping patterns studied in Chapter 2. Experimental results for both periodic and non-periodic wrapping patterns are considered for validation.

Chapter 5 investigates the applicability of model approximation as a means for non-periodic structure homogenization. Using the perturbation theory results of Chapter 3 and 4, the goal is to produce simple analytical models that are accurate approximations to the original spatially dependent model. This constitutes an inverse problem since the natural frequencies and mode shapes of the system are assumed to be known and the coefficients of the model are to be determined. A constant coefficient EB model and multiple methods for determining the coefficients are considered.

Chapter 6 presents a summary and conclusion of the conducted research.

Chapter 2

Periodic Wrapping Patterns

In this chapter an energy equivalent continuum model is derived for string-harnessed systems with periodic wrapping patterns using a homogenization technique. To begin, multiple initial modelling attempts that were considered are presented and compared to a simple experimental test to verify accuracy. From the correct model, a detailed analysis of periodically wrapped string-harnessed systems is performed and validated experimentally. The contents of Section 2.3 and Appendix A consist of previous work by the author from [88]; reprinted by permission of the American Institute of Aeronautics and Astronautics, Inc. The contents of Sections 2.2.2, 2.2.3, and 2.4 consist of previous work by the author from [87]; reprinted by permission of the American Institute of Aeronautics and Astronautics, Inc.

2.1 Initial Modelling Approaches and Homogenization

Figure 2.1 shows the schematic of a beam structure and a periodically wrapped string. The complete system is composed of multiple fundamental elements, which are a single instance of the periodic wrapping pattern. The fundamental elements of a hybrid structure with the diagonal and zigzag wrapping patterns considered are shown in Fig. 2.2. Local Cartesian coordinates (η, y, x) are used for the fundamental element in the homogenization technique, whereas global Cartesian coordinates (x, y, z) are used the for the hybrid structure as a whole in the vibrations analysis.

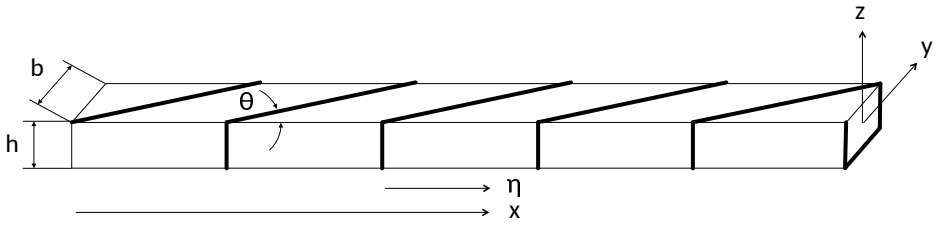

Figure 2.1: String-harnessed system composed of multiple fundamental elements.

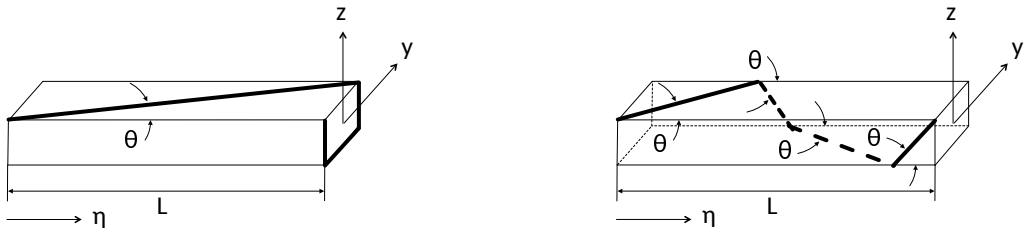

(a) Diagonal

(b) Zigzag

Figure 2.2: Fundamental elements for the diagonal and zigzag wrapping patterns.

Consider first the transverse vibrations for the zigzag wrapping pattern. Assume that the various coordinates of vibration are decoupled. This specific case is considered as the mass per unit length is constant throughout the system and reduces the amount of error introduced through the modelling process of the stiffening effect of the string. Furthermore, it is assumed that there is no slip between the string and the beam at their point of contact. Under the assumptions of small displacements this is a reasonable assumption and makes the problem more tractable. Euler-Bernoulli (EB) assumptions are employed for the host structure. Finally, it is assumed that the geometric properties and the shear modulus of the elasticity of the beam, as well as the pretension value, are such that any initial twisting behaviour caused by imposing the wrapping pattern is negligible.

The homogenization technique determines the global system parameters by considering a single fundamental element of the system. For the zigzag wrapping pattern, the length of a fundamental element is $L = \left(4\overline{b} + 4\overline{h}\right) / \tan(\theta)$. In the previous expression, θ is the string wrapping angle, $\overline{b} = b/2 + r_s$, and $\overline{h} = h/2 + r_s$, where b and h are the width and thickness of the beam, respectively, and r_s denotes the radius of the string. Using the local Cartesian coordinate system presented in Fig. 2.2b, the centre of the string in the zigzag

pattern is given by:

$$(\eta, y, z) = \begin{cases} \left(\eta, \tan(\theta)\eta - \overline{b}, \overline{h}\right), & 0 \leq \eta \leq \frac{2\overline{b}}{\tan(\theta)} \\ \left(\eta, \overline{b}, -\tan(\theta)\eta + 2\overline{b} + \overline{h}\right), & \frac{2\overline{b}}{\tan(\theta)} \leq \eta \leq \frac{2\overline{b}+2\overline{h}}{\tan(\theta)} \\ \left(\eta, -\tan(\theta)\eta + 3\overline{b} + 2\overline{h}, -\overline{h}\right), & \frac{2\overline{b}+2\overline{h}}{\tan(\theta)} \leq \eta \leq \frac{4\overline{b}+2\overline{h}}{\tan(\theta)} \\ \left(\eta, -\overline{b}, \tan(\theta)\eta - 4\overline{b} - 3\overline{h}\right), & \frac{4\overline{b}+2\overline{h}}{\tan(\theta)} \leq \eta \leq L \end{cases} \tag{2.1}$$

An important consideration in the modelling of the string-harnessed system is the accuracy of the displacement field, the strain calculations employed, and the manner in which the string effects are included in the model. To demonstrate this, the various methods for modelling the string-harnessed system which where considered for the presented research are presented. Clamped-free (CF) boundary conditions are considered as these can be imposed experimentally for model validation.

2.1.1 Proposed String-Harnessed System Models

Mass Updated Model

The first proposed model takes into account the added mass of the string and neglects any stiffening effect. As previously mentioned, for the zigzag wrapping pattern the mass per unit length of the system is a constant. Assuming an Euler-Bernoulli beam model and taking into account the added mass of the string, the partial differential equation (PDE) for the free transverse vibrations $w(x,t)$ is

$$E_b I_b \frac{\partial^4 w}{\partial x^4}(x,t) + \left(\rho_b A_b + \frac{\rho_s A_s}{\cos(\theta)}\right) \frac{\partial^2 w}{\partial t^2}(x,t) = 0 \tag{2.2}$$

and the boundary conditions are

$$w(0,t) = 0 \quad , \quad \frac{\partial w}{\partial x}(0,t) = 0 \quad , \quad E_b I_b \frac{\partial^2 w}{\partial x^2}(l,t) = 0 \quad , \quad E_b I_b \frac{\partial^3 w}{\partial x^3}(l,t) = 0 \tag{2.3}$$

In Eq. (2.2), E_b is the Young's modulus of the host structure, $I_b = bh^3/12$ is the second moment of area, and l is the total length. ρ_b and ρ_s are the densities of the beam and the string, respectively. $A_b = bh$ and $A_s = \pi r_s^2$ are the cross-sectional areas of the beam and the string, respectively. In Eq. (2.3), the boundary conditions represent zero displacement and zero slope at the clamped end ($x = 0$) and zero moment and zero shear at the free end ($x = l$). Lastly, $t > 0$ denotes time.

First-Order Displacement Field, Arc Length Strain Calculation, No String Compressive Force

Using EB assumptions for the host structure, assuming a small transverse displacement $w(x,t)$ along the midline of the beam leads to the first-order displacement field in Eqs. (2.4):

$$u_x(x,t) = -z\frac{\partial w}{\partial x}(x,t) \tag{2.4a}$$
$$u_y(x,t) = 0 \tag{2.4b}$$
$$u_z(x,t) = w(x,t) \tag{2.4c}$$

Consider a differential element of the string and calculate the strain energy. Following the work of [135] the change in length of the string during vibration must first be determined. Using the formula for arc length and the displacement field in Eqs. (2.4), the change in length of the string is calculated. Let $y_s(x)$ and $z_s(x)$ denote the y and z coordinates of the centre of the string.

$$\begin{aligned}
\mathrm{d}\Delta_s =& \mathrm{d}l_{\text{deformed}} - \mathrm{d}l_{\text{initial}} \\
=& \sqrt{\left(1 - \frac{\mathrm{d}z_s}{\mathrm{d}x}\frac{\partial w}{\partial x} - z_s\frac{\partial^2 w}{\partial x^2}\right)^2 + \left(\frac{\mathrm{d}y_s}{\mathrm{d}x}\right)^2 + \left(\frac{\mathrm{d}z_s}{\mathrm{d}x} + \frac{\partial w}{\partial x}\right)^2}\,\mathrm{d}x - \sqrt{1 + \left(\frac{\mathrm{d}y_s}{\mathrm{d}x}\right)^2 + \left(\frac{\mathrm{d}z_s}{\mathrm{d}x}\right)^2}\,\mathrm{d}x \\
=& \sqrt{1 + \left(\frac{\mathrm{d}y_s}{\mathrm{d}x}\right)^2 + \left(\frac{\mathrm{d}z_s}{\mathrm{d}x}\right)^2 + z_s^2\left(\frac{\partial^2 w}{\partial x^2}\right)^2 + \left(1 + \left(\frac{\mathrm{d}z_s}{\mathrm{d}x}\right)^2\right)\left(\frac{\partial w}{\partial x}\right)^2 + 2z_s\frac{\mathrm{d}z_s}{\mathrm{d}x}\frac{\partial w}{\partial x}\frac{\partial^2 w}{\partial x^2} - 2z_s\frac{\partial^2 w}{\partial x^2}}\,\mathrm{d}x \\
& - \sqrt{1 + \left(\frac{\mathrm{d}y_s}{\mathrm{d}x}\right)^2 + \left(\frac{\mathrm{d}z_s}{\mathrm{d}x}\right)^2}\,\mathrm{d}x
\end{aligned}$$

To simplify the expression, use a Taylor series for $\sqrt{1+x}$ centred about $x = \left(\frac{\mathrm{d}y_s}{\mathrm{d}x}\right)^2 + \left(\frac{\mathrm{d}z_s}{\mathrm{d}x}\right)^2$. Using the first two terms in the the Taylor series the approximation is

$$\sqrt{1+x} = \sqrt{1 + \left(\frac{\mathrm{d}y_s}{\mathrm{d}x}\right)^2 + \left(\frac{\mathrm{d}z_s}{\mathrm{d}x}\right)^2} + \frac{1}{2}\left(1 + \left(\frac{\mathrm{d}y_s}{\mathrm{d}x}\right)^2 + \left(\frac{\mathrm{d}z_s}{\mathrm{d}x}\right)^2\right)^{-1/2}\left(x - \left(\frac{\mathrm{d}y_s}{\mathrm{d}x}\right)^2 + \left(\frac{\mathrm{d}z_s}{\mathrm{d}x}\right)^2\right)$$

For the zigzag wrapping pattern in consideration, $\left(\frac{\mathrm{d}y_s}{\mathrm{d}x}\right)^2 + \left(\frac{\mathrm{d}z_s}{\mathrm{d}x}\right)^2 = \tan^2(\theta)$ for all x. Therefore the differential change in length of the string can be approximated as

$$\mathrm{d}\Delta_s = \left[\left(\frac{1}{2}z_s^2\left(\frac{\partial^2 w}{\partial x^2}\right)^2 + \frac{1}{2}\left(1 + \left(\frac{\mathrm{d}z_s}{\mathrm{d}x}\right)^2\right)\left(\frac{\partial w}{\partial x}\right)^2 + z_s\frac{\mathrm{d}z_s}{\mathrm{d}x}\frac{\partial w}{\partial x}\frac{\partial^2 w}{\partial x^2} - z_s\frac{\partial^2 w}{\partial x^2}\right)\cos^2(\theta)\right]\frac{\mathrm{d}x}{\cos(\theta)} \tag{2.5}$$

In Eq. (2.5), the non-bracketed term represents the differential length of undeformed string expressed in terms of $\mathrm{d}x$. As such, the bracketed term represents the strain along the length of the string, denoted ε_s. Letting T_s denote the pretension in the string and E_s the Young's modulus of the string, the differential strain energy is calculated.

$$\mathrm{d}U_{\text{string}} = \left(T_s + E_s A_s \varepsilon_s\right)\left(\varepsilon_s \mathrm{d}l\right) = \left(T_s\varepsilon_s + E_s A_s \varepsilon_s^2\right)\frac{\mathrm{d}x}{\cos(\theta)} \tag{2.6}$$

Next the differential strain energy in the beam is calculated. Since a first-order displacement field is considered for the EB beam, the differential strain in the beam due to bending is

$$\mathrm{d}U_{\text{beam,1}} = \frac{1}{2}E_b I_b \left(\frac{\partial^2 w}{\partial x^2}\right)^2 \mathrm{d}x \tag{2.7}$$

In addition to the strain energy from bending, the strain energy due to the change in length of the beam against the force of the string must be taken into account. Assume that the force of the string can be considered as acting only along the midline of the string-harnessed system. Using the arc length formula and the displacement field in Eqs. (2.4) evaluated at $z = 0$, the differential change in length of the midline of the beam can be determined.

$$\mathrm{d}\Delta_m = \sqrt{1 + \left(\frac{\partial w}{\partial x}\right)^2}\,\mathrm{d}x - \mathrm{d}x \approx \frac{1}{2}\left(\frac{\partial w}{\partial x}\right)^2 \tag{2.8}$$

In Eq. (2.8), the approximation is due to the truncation of the Taylor series of $\sqrt{1+x}$, centred about $x = 0$, after 2 terms. Using the expression for the differential stretch in the midline, the differential strain energy due to the change in length of the beam against the force of the string is

$$\mathrm{d}U_{\text{beam,2}} = -T_s\cos(\theta)\left(\frac{1}{2}\left(\frac{\partial w}{\partial x}\right)^2\right)\mathrm{d}x = -\frac{1}{2}T_s\cos(\theta)\left(\frac{\partial w}{\partial x}\right)^2\mathrm{d}x \tag{2.9}$$

Combining Eqs. (2.6), (2.7), and (2.9) the final expression for the differential strain is found.

$$\mathrm{d}U_{\text{system}} = \left\{\frac{1}{2}E_b I_b\left(\frac{\partial^2 w}{\partial x^2}\right)^2 + \frac{\left(T_s\varepsilon_s + E_s A_s \varepsilon_s^2\right)}{\cos(\theta)} - \frac{1}{2}T_s\cos(\theta)\left(\frac{\partial w}{\partial x}\right)^2\right\}\mathrm{d}x \tag{2.10}$$

Due to the complex final form of the strain energy, it is not immediately obvious if this will always be positive quantity. The strain energy being a positive quantity is an important quantity for analyzing the stability of the system.

Finally, the differential kinetic energy is determined. For the zigzag wrapping pattern, the mass per unit length is constant throughout the system. The rotary inertia effect is ignored. Therefore, the differential kinetic energy for the string-harnessed system can be written as

$$\mathrm{d}T_{\text{system}} = \frac{1}{2}\left(\rho_b A_b + \frac{\rho_s A_s}{\cos(\theta)}\right)\left(\frac{\partial w}{\partial t}\right)^2 \mathrm{d}x \tag{2.11}$$

Second-Order Displacement Field, Green-Lagrange Strain Tensor, No String Compressive Force

Imposing a small transverse displacement $z = w(x,t)$ to the midline of the beam and retaining up to second-order terms produces the following displacement field

$$u_x(x,t) = -z\frac{\partial w}{\partial x} \tag{2.12a}$$

$$u_y(x,t) = 0 \tag{2.12b}$$

$$u_z(x,t) = w - \frac{z}{2}\left(\frac{\partial w}{\partial x}\right)^2 \tag{2.12c}$$

The Green-Lagrange strain tensor is calculated and employed in the calculation of the differential strain energy. The Green-Lagrange strain tensor is an exact representation of strain and will provide additional terms, and hence accuracy, in contrast to using the infinitesimal strain tensor. The Green-Lagrange strain tensor is defined as

$$\varepsilon_{ij}^{(2)} = \frac{1}{2}\left(\frac{\partial u_i}{\partial j} + \frac{\partial u_j}{\partial i} + \sum_{k=\{x,y,z\}} \frac{\partial u_k}{\partial i}\frac{\partial u_k}{\partial j}\right), \quad i,j = \{x,y,z\} \tag{2.13}$$

The superscript indicates the highest order of terms in the displacement field. Substituting Eq. (2.12) into Eq. (2.13) we obtain the strain tensor shown in Eq. (2.14). In calculating the strain tensor we only keep up to second-order terms.

$$\boldsymbol{\varepsilon}^{(\mathbf{2})} = \begin{bmatrix} -z\frac{\partial^2 w}{\partial x^2} + \frac{z^2}{2}\left(\frac{\partial^2 w}{\partial x^2}\right)^2 + \frac{1}{2}\left(\frac{\partial w}{\partial x}\right)^2 & 0 & 0 \\ 0 & 0 & 0 \\ 0 & 0 & 0 \end{bmatrix} \tag{2.14}$$

Note that $\varepsilon_{xx}^{(2)}$ is the only non-zero term in the strain tensor. This is expected due to the assumption of using a one-dimensional element to model the hybrid structure.

The pre-strain in the string is equal to T_s/E_sA_s and this strain pertains to the case where the beam remains straight and there is no deformation. To determine the strain along the string during vibrations a tensor transformation is used on Eq. (2.14). Since the string wrapping angle is θ, the strain during vibrations is $\varepsilon_{xx}^{(2)}\cos^2(\theta)$. Consider now a differential element of the string and calculate the strain energy. Assume that the string obeys Hooke's law and that the strain at the centre of the string can be taken as the strain at all the points in the cross section for a given position x.

$$
\begin{aligned}
\mathrm{d}U_{\text{string}} &= \left\{ \iint_{\text{string}} \frac{1}{2} E_s \left(\frac{T_s}{E_s A_s} + \varepsilon_{xx}^{(2)}\big|_{z=z_s} \cos^2(\theta) \right)^2 \mathrm{d}A \right\} \mathrm{d}l \\
&= \left\{ \iint_{\text{string}} \frac{1}{2} E_s \left(\frac{T_s}{E_s A_s} - z_s \cos^2(\theta) \frac{\partial^2 w}{\partial x^2} + \frac{z_s^2 \cos^2(\theta)}{2} \left(\frac{\partial^2 w}{\partial x^2} \right)^2 \right. \right. \\
&\qquad \left. \left. + \frac{\cos^2(\theta)}{2} \left(\frac{\partial w}{\partial x} \right)^2 \right)^2 \mathrm{d}A \right\} \left(\frac{\mathrm{d}x}{\cos(\theta)} \right) \\
&\approx \left\{ \iint_{\text{string}} \frac{1}{2} E_s \left(\frac{T_s^2}{E_s^2 A_s^2} + z_s^2 \cos^4(\theta) \left(\frac{\partial^2 w}{\partial x^2} \right)^2 - \frac{2 T_s z_s \cos^2(\theta)}{E_s A_s} \frac{\partial^2 w}{\partial x^2} \right. \right. \\
&\qquad \left. \left. + \frac{T_s z_s^2 \cos^2(\theta)}{E_s A_s} \left(\frac{\partial^2 w}{\partial x^2} \right)^2 + \frac{T_s \cos^2(\theta)}{E_s A_s} \left(\frac{\partial w}{\partial x} \right)^2 \right) \mathrm{d}A \right\} \left(\frac{\mathrm{d}x}{\cos(\theta)} \right) \\
&= \left\{ \frac{1}{2} \left[E_s A_s z_s^2 \cos^3(\theta) + T_s z_s^2 \cos(\theta) \right] \left(\frac{\partial^2 w}{\partial x^2} \right)^2 - T_s z_s \cos(\theta) \frac{\partial^2 w}{\partial x^2} \right. \\
&\qquad \left. + \frac{1}{2} T_s \cos(\theta) \left(\frac{\partial w}{\partial x} \right)^2 + \frac{T_s^2}{2 E_s A_s \cos(\theta)} \right\} \mathrm{d}x
\end{aligned}
\tag{2.15}
$$

In Eq. (2.15) the approximation symbol is used since only terms up to second-order in $w(x,t)$ and its derivatives are kept. In the expression for the strain energy in the string it is seen that there is a term with a negative coefficient. Of interest is determining whether or not the strain energy in the string is always a positive quantity. Completing the square using the $\left(\frac{\partial^2 w}{\partial x^2}\right)^2$, $\frac{\partial^2 w}{\partial x^2}$, and constant terms, the strain energy in the string can be written

as

$$\mathrm{d}U_{\text{string}} = \left\{ \frac{1}{2}\left[E_s A_s z_s^2 \cos^3(\theta) + T_s z_s^2 \cos(\theta)\right] \left(\frac{\partial^2 w}{\partial x^2} - \frac{T_s}{E_s A_s z_s \cos^2(\theta) + T_s z_s}\right)^2 + \frac{1}{2} T_s \cos(\theta) \left(\frac{\partial w}{\partial x}\right)^2 + \frac{T_s^2}{2E_s^2 A_s^2 \cos^3(\theta) + 2E_s A_s T_s \cos(\theta)} \right\} \mathrm{d}x \tag{2.16}$$

Equation (2.16) clearly demonstrates that the strain energy in the string is always a positive quantity.

Next, the strain energy in the beam is calculated. Assume that the beam obeys Hooke's law and the strain in the beam due to vibrations is $\varepsilon_{xx}^{(2)}$. Consider now a differential element of the beam and calculate the strain energy.

$$\begin{aligned}
\mathrm{d}U_{\text{beam}} &= \left\{ \iint_{\text{beam}} \frac{1}{2} E_b \left(\varepsilon_{xx}^{(2)}\right)^2 \mathrm{d}A \right\} \mathrm{d}x \\
&= \left\{ \iint_{\text{beam}} \frac{1}{2} E_b \left(\frac{-T_s \cos(\theta)}{E_b A_b} - z\frac{\partial^2 w}{\partial x^2} + \frac{z^2}{2}\left(\frac{\partial^2 w}{\partial x^2}\right)^2 + \frac{1}{2}\left(\frac{\partial w}{\partial x}\right)^2 \right)^2 \mathrm{d}A \right\} \mathrm{d}x \\
&\approx \left\{ \iint_{\text{beam}} \frac{1}{2} E_b \left(z^2 \left(\frac{\partial^2 w}{\partial x^2}\right)^2 \right) \mathrm{d}A \right\} \mathrm{d}x \\
&= \left\{ \frac{1}{2} E_b I_b \left(\frac{\partial^2 w}{\partial x^2}\right)^2 \right\} \mathrm{d}x
\end{aligned} \tag{2.17}$$

In Eq. (2.50) the approximation symbol is used since only terms up to second-order in $w(x,t)$ and its derivatives are kept. The strain energy for the beam is always a positive quantity.

Summing Eqs. (2.15) and (2.50) the strain energy for a differential element of the hybrid system is found.

$$\mathrm{d}U_{\text{system}} = \left\{ \frac{1}{2}\left[E_b I_b + E_s A_s z_s^2 \cos^3(\theta) + T_s z_s^2 \cos(\theta)\right] \left(\frac{\partial^2 w}{\partial x^2}\right)^2 + \frac{1}{2} T_s \cos(\theta) \left(\frac{\partial w}{\partial x}\right)^2 - T_s z_s \cos(\theta) \frac{\partial^2 w}{\partial x^2} + \frac{T_s^2}{2E_s A_s \cos(\theta)} \right\} \mathrm{d}x \tag{2.18}$$

Since the strain energy in the string and beam were shown to be positive quantities, the total strain energy in the string-harnessed system is always positive. Since the strain

energy is always positive, the system will be positive definite and thus the frequencies will be positive. This indicates that for this modelling approach the system will be stable for all possible parameter values.

For the zigzag wrapping pattern, the mass per unit length is a constant throughout the entire system. As with the previous model, the differential kinetic energy is

$$\mathrm{d}T_{\text{system}} = \frac{1}{2}\left(\rho_b A_b + \frac{\rho_s A_s}{\cos(\theta)}\right)\left(\frac{\partial w}{\partial t}\right)^2 \mathrm{d}x \tag{2.19}$$

Second-Order Displacement Field, Green-Lagrange Strain Tensor, With Compressive Force

For the final model, the steps for determining the strain energy in the system are the same as the previous model with the exception that a compressive force due to the string is considered in the beam differential strain energy. As such, the differential strain energy in the string is the same as Eq. (2.15).

$$\begin{aligned}\mathrm{d}U_{\text{string}} = \Bigg\{ &\frac{1}{2}\left[E_s A_s z_s^2 \cos^3(\theta) + T_s z_s^2 \cos(\theta)\right]\left(\frac{\partial^2 w}{\partial x^2}\right)^2 - T_s z_s \cos(\theta)\frac{\partial^2 w}{\partial x^2} \\ &+\frac{1}{2}T_s \cos(\theta)\left(\frac{\partial w}{\partial x}\right)^2 + \frac{T_s^2}{2E_s A_s \cos(\theta)}\Bigg\}\,\mathrm{d}x\end{aligned} \tag{2.20}$$

Since the strain energy in the string is the same as in the previous model, it is known that the strain energy in the string is always a positive quantity.

Next consider the strain in the beam. Let the beam be pre-compressed with a force equal in magnitude to the pre-tension in the string and acting in the same direction as the string longitudinal axis. The initial compressive strain in the beam is therefore $-T_s \cos(\theta)/E_b A_b$. The strain energy in the beam due to vibrations is $\varepsilon_{xx}^{(2)}$, which is the non-zero component in Eq. (2.14) for the Green-Lagrange strain tensor assuming a second-order displacement

field. Consider now a differential element of the beam and calculate the strain energy.

$$\begin{aligned}
\mathrm{d}U_{\text{beam}} &= \left\{ \iint_{\text{beam}} \frac{1}{2} E_b \left(-\frac{T_s \cos(\theta)}{E_b A_b} + \varepsilon_{xx}^{(2)} \right)^2 \mathrm{d}A \right\} \mathrm{d}x \\
&= \left\{ \iint_{\text{beam}} \frac{1}{2} E_b \left(\frac{-T_s \cos(\theta)}{E_b A_b} - z\frac{\partial^2 w}{\partial x^2} + \frac{z^2}{2}\left(\frac{\partial^2 w}{\partial x^2}\right)^2 + \frac{1}{2}\left(\frac{\partial w}{\partial x}\right)^2 \right)^2 \mathrm{d}A \right\} \mathrm{d}x \\
&\approx \left\{ \iint_{\text{beam}} \frac{1}{2} E_b \left(\frac{T_s^2 \cos^2(\theta)}{E_b^2 A_b^2} + z^2 \left(\frac{\partial^2 w}{\partial x^2}\right)^2 + \frac{2T_s z \cos(\theta)}{E_b A_b}\frac{\partial^2 w}{\partial x^2} \right. \right. \\
&\quad \left. \left. -\frac{T_s z^2 \cos(\theta)}{E_b A_b}\left(\frac{\partial^2 w}{\partial x^2}\right)^2 - \frac{T_s \cos(\theta)}{E_b A_b}\left(\frac{\partial w}{\partial x}\right)^2 \right) \mathrm{d}A \right\} \mathrm{d}x \\
&= \left\{ \frac{1}{2}\left[E_b I_{yy} - \frac{T_s \cos(\theta) I_{yy}}{A_b} \right] \left(\frac{\partial^2 w}{\partial x^2}\right)^2 - \frac{1}{2} T_s \cos(\theta) \left(\frac{\partial w}{\partial x}\right)^2 + \frac{T_s^2 \cos^2(\theta)}{2E_b A_b} \right\} \mathrm{d}x
\end{aligned} \tag{2.21}$$

In Eq. (2.21) the approximation symbol is used since only terms up to second-order in $w(x,t)$ and its derivatives are kept. In the expression for the strain energy in the beam it is clearly seen that for certain choices of system parameters this quantity can be made negative. For example, the tension in the string can be made exceptionally large.

Summing Eqs. (2.20) and (2.21) the strain energy for a differential element of the hybrid system is found.

$$\begin{aligned}
\mathrm{d}U_{\text{system}} = \left\{ \frac{1}{2}\left[E_b I_{yy} + E_s A_s z_s^2 \cos^3(\theta) + T_s z_s^2 \cos(\theta) - \frac{T_s \cos(\theta) I_{yy}}{A_b} \right] \left(\frac{\partial^2 w}{\partial x^2}\right)^2 \right. \\
\left. -T_s z_s \cos(\theta)\frac{\partial^2 w}{\partial x^2} + \frac{T_s^2}{2E_s A_s \cos(\theta)} + \frac{T_s^2 \cos^2(\theta)}{2E_b A_b} \right\} \mathrm{d}x
\end{aligned} \tag{2.22}$$

The major difference between the system differential strain energy of Eqs. (2.18) and (2.22) is the presence of term $\frac{1}{2}T_s \cos(\theta)\left(\frac{\partial w}{\partial x}\right)^2 \mathrm{d}x$ in Eq. (2.18). When the compressive force of the string is considered in the beam differential strain energy, the term $\frac{1}{2}T_s \cos(\theta)\left(\frac{\partial w}{\partial x}\right)^2 \mathrm{d}x$ from Eq. (2.18) is cancelled out. Further, since the strain energy in the beam can potentially be a negative value, the total strain of the system must be analyzed to determine under which conditions the strain energy in the system will be positive or negative.

Using the results of completing the square for the string strain energy to obtain Eq. (2.16)

from Eq. (2.15), the total strain energy of the system in Eq. (2.22) can be written as

$$\begin{aligned}\mathrm{d}U_{\text{system}} = \Bigg\{ & \frac{1}{2}\left[E_s A_s z_s^2 \cos^3(\theta) + T_s z_s^2 \cos(\theta)\right]\left(\frac{\partial^2 w}{\partial x^2} - \frac{T_s}{E_s A_s z_s \cos^2(\theta) + T_s z_s}\right)^2 \\ & + \frac{1}{2}\left[E_b I_{yy} - \frac{T_s \cos(\theta) I_{yy}}{A_b}\right]\left(\frac{\partial^2 w}{\partial x^2}\right)^2 + \frac{T_s^2}{2E_s^2 A_s^2 \cos^3(\theta) + 2E_s A_s T_s \cos(\theta)} \\ & + \frac{T_s^2 \cos^2(\theta)}{2E_b A_b}\Bigg\}\,\mathrm{d}x \end{aligned} \tag{2.23}$$

In Eq. (2.23) it can be seen that if the coefficient of the $\left(\frac{\partial^2 w}{\partial x^2}\right)^2$ term is made positive, then the strain energy in the system will be positive at every point x. This is a stronger condition than requiring that the total strain energy be positive when integrating over the entire system. To achieve this positive strain at each point x, the value of the tension in the string must be $T_s \leq E_b A_b / \cos(\theta)$. Considering the upper limit for the value of tension, this would lead to the following strain along the longitudinal axis of the beam

$$\epsilon = \frac{\sigma}{E_b} = \frac{1}{E_b}\frac{T_s \cos(\theta)}{A_b} = \frac{1}{E_b}\frac{E_b A_b}{A_b} = 1$$

The result of $\epsilon = 1$ indicates that the beam has undergone a change in length equal to the total length of the beam. However, this is not possible physically and thus any real world test setup will always have a positive strain energy value. In the case of positive strain for all system parameter values, the frequencies of the system will be positive and thus stability is ensured.

Theoretically, the tension in the string can be made larger than $E_b A_b / \cos(\theta)$, in which case the strain energy in the system can potentially be made negative. Consider the case of a string with a constant height $z_s(x) = \overline{z}$. Completing the square for the total strain energy of the system in Eq. (2.22) leads to

$$\begin{aligned}\mathrm{d}U_{\text{system}} = \Bigg\{ & \frac{1}{2}\left[E_b I_{yy} + E_s A_s \overline{z}^2 \cos^3(\theta) + T_s \overline{z}^2 \cos(\theta) - \frac{T_s \cos(\theta) I_{yy}}{A_b}\right]\Bigg(\frac{\partial^2 w}{\partial x^2} \\ & - \frac{T_s \overline{z} \cos(\theta)}{E_b I_{yy} + E_s A_s \overline{z}^2 \cos^3(\theta) + T_s \overline{z}^2 \cos(\theta) - \frac{T_s \cos(\theta) I_{yy}}{A_b}}\Bigg)^2 + \frac{T_s^2}{2E_s A_s \cos(\theta)} \\ & + \frac{T_s^2 \cos^2(\theta)}{2E_b A_b} - \frac{T_s^2 \overline{z}^2 \cos^2(\theta)}{2\left[E_b I_{yy} + E_s A_s \overline{z}^2 \cos^3(\theta) + T_s \overline{z}^2 \cos(\theta) - \frac{T_s \cos(\theta) I_{yy}}{A_b}\right]}\Bigg\}\,\mathrm{d}x \end{aligned} \tag{2.24}$$

First consider the coefficient of the term containing $\frac{\partial^2 w}{\partial x^2}$. If $\overline{z}^2 \geq I_{yy}/A_b$, then the coefficient will always be positive for all possible system parameters. However, if $\overline{z}^2 < I_{yy}/A_b$, then for $T_s > \left(E_b I_{yy} + E_s A_s \overline{z}^2 \cos^3(\theta)\right) / \cos(\theta) \left(\frac{I_{yy}}{A_b} - \overline{z}^2\right)$ the coefficient will be negative. Next, consider the constant terms in Eq. (2.24). Algebraic manipulation to have a common denominator for these constant terms results in

$$\begin{aligned}
&\left\{ T_s^2 E_b A_b \left[E_b I_{yy} + T_s \cos(\theta) \left(\overline{z}^2 - \frac{I_{yy}}{A_b} \right) \right] \right. \\
&\left. + T_s^2 E_s A_s \cos^3(\theta) \left[E_b I_{yy} + E_s A_s \overline{z}^2 \cos^3(\theta) + T_s \cos(\theta) \left(\overline{z}^2 - \frac{I_{yy}}{A_b} \right) \right] \right\} \\
&\left\{ 2 \left[E_b I_{yy} + E_s A_s \overline{z}^2 \cos^3(\theta) + T_s \cos(\theta) \left(\overline{z}^2 - \frac{I_{yy}}{A_b} \right) \right] E_b A_b E_s A_s \cos(\theta) \right\}^{-1}
\end{aligned}$$

Above, it is seen that if $\overline{z}^2 \geq I_{yy}/A_b$ then the constant terms will produce a positive value. However, if $\overline{z}^2 < I_{yy}/A_b$, then the sum of the constant terms will be negative when

$$\frac{E_b I_{yy} + \frac{\left(E_s A_s \cos^3(\theta)\right)^2 \overline{z}^2}{E_b A_b + E_s A_s \cos^3(\theta)}}{\cos(\theta) \left(\frac{I_{yy}}{A_b} - \overline{z}^2 \right)} < T_s < \frac{E_b I_{yy} + E_s A_s \cos^3(\theta) \overline{z}^2}{\cos(\theta) \left(\frac{I_{yy}}{A_b} - \overline{z}^2 \right)}$$

and positive otherwise. Note the the lower bound above is larger than $E_b A_b / \cos(\theta)$, which was the condition for positivity in the strain energy previously determined.

To summarize the results, if $\overline{z}^2 \geq I_{yy}/A_b$ then the strain energy in the system will always be positive for all values of system parameters. If $\overline{z}^2 < I_{yy}/A_b$, then the value for T_s can potentially make either the coefficient of the term containing $\frac{\partial^2 w}{\partial x^2}$ or the sum of the constant terms negative. Having one of these being negative could result in the overall strain energy in the system being negative. This demonstrates that the wrapping pattern being applied to the system will influence whether the strain energy in the system will remain strictly positive for all system parameters or could become negative. However, to reiterate, this would only be possible in a theoretical situation as the values for tension required are larger than $E_b A_b / \cos(\theta)$, which is the value for which the strain in the beam is equal to its length.

For the zigzag wrapping pattern, the mass per unit length is a constant throughout the entire system. As with the previous model, the differential kinetic energy is

$$\mathrm{d}T_{\text{system}} = \frac{1}{2} \left(\rho_b A_b + \frac{\rho_s A_s}{\cos(\theta)} \right) \left(\frac{\partial w}{\partial t} \right)^2 \mathrm{d}x \tag{2.25}$$

2.1.2 Homogenization of Models

In working towards the equation of motion for the free transverse vibrations of the string-harnessed system, the total kinetic and strain energy are to be determined. For the zigzag wrapping pattern the mass per unit length is a constant throughout the system and thus the same differential kinetic energy is found in Eqs. (2.11), (2.19), and (2.25). Integrating these equations over the length of the system yields the kinetic energy for the entire structure

$$T_{\text{tot}} = \int_0^l \frac{1}{2} \left[\rho_b A_b + \frac{\rho_s A_s}{\cos(\theta)} \right] \left(\frac{\partial w}{\partial t} \right)^2 \, \mathrm{d}x \tag{2.26}$$

For the strain energy in the system a homogenization technique is employed. The homogenization technique used in this work follows an energy equivalence approach to determine a constant coefficient model for the string-harnessed system. This is achieved by considering a single fundamental element of the system, determining an equivalent strain energy per unit length, and then integrating to determine the total strain energy in the system.

A second-order Taylor series of $w(\eta, t)$ about the centre of a fundamental element is substituted into the expression for the differential strain energy in Eqs. (2.10), (2.18), and (2.22). Integration is then performed over the length of the fundamental element to determine a strain energy for the fundamental element U_{e}. The strain energy per unit length of the fundamental element is found by dividing U_{e} by the length of a fundamental element. Integrating the strain energy per unit length over the entire domain of the string-harnessed system gives the total strain energy. The general form for the total strain energy determined using the homogenization technique is

$$U_{\text{tot}} = \int_0^l \left(\frac{1}{2} C_1 \left(\frac{\partial^2 w}{\partial x^2} \right)^2 + C_2 \left(\frac{\partial w}{\partial x} \right)^2 + C_3 + C_4 \frac{\partial w}{\partial x} \frac{\partial^2 w}{\partial x^2} \right) \, \mathrm{d}x \tag{2.27}$$

The coefficients for the modelling approaches initially considered for the string-harnessed system are summarized.

Coefficients for First-Order Displacement Field, Arc Length Strain Calculation, No String Compressive Force

$$
\begin{aligned}
C_1 =& E_b I_b + \frac{2E_s A_s \left(3\overline{b}\overline{h}^2 + \overline{h}^3\right)\cos^3(\theta)}{3\left(\overline{b}+\overline{h}\right)} + \frac{T_s\left(6\overline{b}^2\overline{h} + 6\overline{b}\overline{h}^2 + 6\overline{h}^3 + \left(\overline{h}^3 + 3\overline{b}\overline{h}^2\right)\sin^2(\theta)\right)\cos(\theta)}{3\left(\overline{b}+\overline{h}\right)} \\
C_2 =& \frac{T_s\overline{h}\sin^2(\theta)}{\left(\overline{b}+\overline{h}\right)\cos(\theta)} \\
C_3 =& 0 \\
C_4 =& \frac{T_s\overline{b}\overline{h}\sin(\theta)}{\left(\overline{b}+\overline{h}\right)}
\end{aligned}
\tag{2.28}
$$

Coefficients for Second-Order Displacement Field, Green-Lagrange Strain Tensor, No String Compressive Force

$$
\begin{aligned}
C_1 =& E_b I_b + \frac{E_s A_s \overline{h}^2 \cos^3(\theta)\left(\overline{b}+\overline{h}/3\right)}{\overline{b}+\overline{h}} + T_s\cos(\theta)\frac{\overline{h}^2\left(\overline{b}+\overline{h}/3\right)}{\overline{b}+\overline{h}} \\
C_2 =& T_s\cos(\theta) \\
C_3 =& \frac{T_s^2}{2E_s A_s\cos(\theta)} \\
C_4 =& 0
\end{aligned}
\tag{2.29}
$$

Coefficients for Second-Order Displacement Field, Green-Lagrange Strain Tensor, With Compressive Force

$$
\begin{aligned}
C_1 =& E_b I_b + \frac{E_s A_s \overline{h}^2 \cos^3(\theta)\left(\overline{b}+\overline{h}/3\right)}{\overline{b}+\overline{h}} + T_s\cos(\theta)\left[\frac{\overline{h}^2\left(\overline{b}+\overline{h}/3\right)}{\overline{b}+\overline{h}} - \frac{I_b}{A_b}\right] \\
C_2 =& 0 \\
C_3 =& \frac{T_s^2}{2E_s A_s\cos(\theta)} + \frac{T_s^2\cos^2(\theta)}{2E_b A_b} \\
C_4 =& 0
\end{aligned}
\tag{2.30}
$$

In Eq. (2.30), it can be shown that $\overline{h}^2\left(\overline{b}+\overline{h}/3\right)/\left(\overline{b}+\overline{h}\right)-I_b/A_b>0$ always holds, and therefore C_1 will always be a positive constant.

Note, the homogenized strain energy with coefficients given in Eq. (2.30) is always a positive quantity. This indicates that likely the spatially dependent strain energy in Eq. (2.22) is also always a positive quantity, at least when integrated over the length of a fundamental element. For this reason, changing the system parameters, in particular T_s, does not cause the strain energy to become negative. It is expected that if the spatially dependent strain energy could be made negative through changing system parameters that this would also be captured in the homogenization process. This is clearly seen for a system with a constant position $z_s(x)=\overline{z}$, which results in the following homogenized strain energy

$$\mathrm{d}U_{\text{system, hom}}=\left\{\frac{1}{2}\left[E_bI_{yy}+E_sA_s\overline{z}^2\cos^3(\theta)+T_s\overline{z}^2\cos(\theta)-\frac{T_s\cos(\theta)I_{yy}}{A_b}\right]\left(\frac{\partial^2 w}{\partial x^2}\right)^2 -T_s\overline{z}\cos(\theta)\frac{\partial^2 w}{\partial x^2}+\frac{T_s^2}{2E_sA_s\cos(\theta)}+\frac{T_s^2\cos^2(\theta)}{2E_bA_b}\right\}\mathrm{d}x$$

It is seen that the homogenized differential strain energy and the exact strain energy from Eq. (2.24) are identical. This means that the possibility of obtaining a negative strain energy when $\overline{z}^2<I_{yy}/A_b$ in the spatially dependent model is also captured in the homogenized model. Thus for a simple case it is seen that the homogenized model predicts the mathematical possibility of instability in the system. However, it is possible that the process of homogenization would not predict the instabilities in the system as predicted in the exact spatially dependent strain due to the average of local effects.

2.1.3 Vibration Analysis

Denote the total kinetic energy of the system in Eq. (2.26) as $T_{\text{tot}}=\int_0^l\frac{1}{2}K_1\left(\frac{\partial w}{\partial t}\right)^2\mathrm{d}x$. Using this and the general form for the strain energy in Eq. (2.27), the Lagrangian for the string-harnessed system can be found. Hamilton's principle is then applied, and the partial differential equation for the free vibration of the transverse displacement $w(x,t)$ for the string-harnessed system is

$$C_1\frac{\partial^4 w}{\partial x^4}-C_2\frac{\partial^2 w}{\partial x^2}+K_1\frac{\partial^2 w}{\partial t^2}=0 \tag{2.31}$$

and the clamped-free boundary conditions are

$$w(0,t) = 0 \quad , \quad \frac{\partial w}{\partial x}(0,t) = 0 \quad , \quad C_1 \frac{\partial^3 w}{\partial x^3}(l,t) - C_2 \frac{\partial w}{\partial x}(l,t) = 0 \quad , \quad C_1 \frac{\partial^2 w}{\partial x^2}(l,t) + C_4 \frac{\partial w}{\partial x}(l,t) = 0 \tag{2.32}$$

In Eq. (2.31), the first and third terms in the PDE are those relating to the bending stiffness and mass per unit length of the system, respectively, as is typically seen in an EB beam model. The second term in the PDE is due to compressive forces along the longitudinal axis. C_2 is a positive quantity and is the magnitude of the compressive force obtained after homogenization. If the beam was under a tensile force, the C_2 would remain a positive quantity, since it is the magnitude, and the sign in the PDE would switch from a subtraction to an addition. A compressive force in the system has the effect of lowering the natural frequencies.

The free-end boundary conditions in Eq. (2.32) can be interpreted as zero shear and zero moment, respectively. With respect to the moment, the additional term in the boundary condition with coefficient C_4 is only present for the system model using the arc length calculation for the stretch in the string. This term is not given a physical interpretation since the arc length model is incorrect. With respect to the shear, the additional term in the boundary condition with coefficient C_2 is due to the axial compressive force. During vibrations, changes in the location of the midline and the compressive force always being in the x direction will introduce a shear force. Therefore the shear force at the free end of the system is a balance between the beam shear and the shear from the compressive force.

Using separation of variables, assume the solution to Eqs. (2.31) and (2.32) is $w(x,t) = f(x)e^{i\omega t}$. This lead to an ordinary differential equation (ODE) in terms of $f(x)$ and the general solution is given in Eqs. (2.33).

$$f(x) = A\cos(\overline{\alpha}x) + B\sin(\overline{\alpha}x) + C\cosh(\overline{\beta}x) + D\sinh(\overline{\beta}x) \tag{2.33a}$$

$$\overline{\alpha} = \sqrt{\frac{-C_2 + \sqrt{C_2^2 + 4C_1K_1\omega^2}}{2C_1}} \tag{2.33b}$$

$$\overline{\beta} = \sqrt{\frac{C_2 + \sqrt{C_2^2 + 4C_1K_1\omega^2}}{2C_1}} \tag{2.33c}$$

Applying the boundary conditions to the solution in Eqs. (2.33), the characteristic equation

of the string-harnessed system is

$$\begin{aligned}0 =&C_1\left(\overline{\alpha}^4+\overline{\beta}^4\right)+C_2\left(\overline{\alpha}^2-\overline{\beta}^2\right)+\left[2C_1\overline{\alpha}^2\overline{\beta}^2-C_2\left(\overline{\alpha}^2-\overline{\beta}^2\right)\right]\cos(\overline{\alpha}l)\cosh(\overline{\beta}l)\\&+\overline{\alpha}\overline{\beta}\left[2C_2+C_1\left(\overline{\alpha}^2-\overline{\beta}^2\right)\right]\sin(\overline{\alpha}l)\sinh(\overline{\beta}l)+C_4\overline{\beta}\left(\overline{\alpha}^2+\overline{\beta}^2\right)\cos(\overline{\alpha}l)\sinh(\overline{\beta}l)\\&+C_4\overline{\alpha}\left(\overline{\alpha}^2+\overline{\beta}^2\right)\sin(\overline{\alpha}l)\cosh(\overline{\beta}l)\end{aligned}\tag{2.34}$$

The mode shapes obtained after applying the boundary conditions are then mass normalized. For the n^{th} mode of the string-harnessed system the mode shape is

$$\phi_n(x) =A_n\left\{\cos(\overline{\alpha}_n x)-\cosh(\overline{\beta}_n x)-k_n\left[\sin(\overline{\alpha}_n x)-\frac{\overline{\alpha}_n}{\overline{\beta}_n}\sinh(\overline{\beta}_n x)\right]\right\}\tag{2.35a}$$

$$k_n =\frac{C_1\overline{\alpha}_n^2\cos(\overline{\alpha}_n l)+C_1\overline{\beta}_n^2\cosh(\overline{\beta}_n l)+C_4\overline{\alpha}_n\sin(\overline{\alpha}_n l)+C_4\overline{\beta}_n\sinh(\overline{\beta}_n l)}{C_1\overline{\alpha}_n^2\sin(\overline{\alpha}_n l)+C_1\overline{\alpha}_n\overline{\beta}_n\sinh(\overline{\beta}_n l)-C_4\overline{\alpha}_n\cos(\overline{\alpha}_n l)+C_4\overline{\alpha}_n\cosh(\overline{\beta}_n l)}\tag{2.35b}$$

$$A_n=\left(K_1\int_0^l\left(\cos(\overline{\alpha}_n x)-\cosh(\overline{\beta}_n x)-k_n\left[\sin(\overline{\alpha}_n x)-\frac{\overline{\alpha}_n}{\overline{\beta}_n}\sinh(\overline{\beta}_n x)\right]\right)^2\mathrm{d}x\right)^{-1/2}\tag{2.35c}$$

The mass normalization conditions satisfied by the mode shapes are

$$\int_0^l K_1\phi_i(x)\phi_j(x)\,\mathrm{d}x =\delta_{ij}\tag{2.36}$$

$$\int_0^l\phi_i(x)\left[C_1\frac{\mathrm{d}^4\phi_j}{\mathrm{d}x^4}(x)-C_2\frac{\mathrm{d}^2\phi_j}{\mathrm{d}x^2}(x)\right]\mathrm{d}x =\omega_i^2\delta_{ij}\tag{2.37}$$

Above, δ_{ij} is the Kronecker delta. The response of the system can then be expressed as $w(x,t)=\sum_{n=1}^{\infty}\phi_n(x)g_n(t)$, where the functions $g_n(t)$ are to be determined.

2.2 Initial Experimental Results

2.2.1 Analytical Frequency Response Function for Base Excitation

The clamped end of the string-harnessed system is fixed to a shaker during experimental testing. Therefore, the boundary conditions at the clamped end of the system in Eq. (2.32)

become, for $\omega_s \neq 0$,

$$\begin{aligned} w(0,t) &= \frac{gg_f}{\omega_s^2}\sin(\omega_s t) & C_1\frac{\partial^3 w}{\partial x^3}(l,t) - C_2\frac{\partial w}{\partial x}(l,t) &= 0 \\ \frac{\partial w}{\partial x}(0,t) &= 0 & C_1\frac{\partial^2 w}{\partial x^2}(l,t) + C_4\frac{\partial w}{\partial x}(l,t) &= 0 \end{aligned} \tag{2.38}$$

and the PDE for the transverse vibrations is given in Eq. (2.31). In Eq. (2.38), g is the gravitational acceleration, g_f is a dimensionless gravitational acceleration factor, and ω_s is the driving frequency of the shaker.

To remove the nonhomogeneous boundary condition, a function $r(x,t)$ is introduced of which the only requirement is to satisfy the same boundary conditions as $w(x,t)$. Take $r(x,t) = gg_f \sin(\omega_s t)/\omega_s^2$. Let $y(x,t) = w(x,t) - r(x,t)$, and make this substitution into the PDE of Eq. (2.31) and the boundary conditions listed in Eq. (2.38). The new PDE in terms of the function $y(x,t)$ is

$$C_1\frac{\partial^4 y}{\partial x^4} - C_2\frac{\partial^2 y}{\partial x^2} + K_1\frac{\partial^2 y}{\partial t^2} = K_1 gg_f \sin(\omega_s t) \tag{2.39}$$

and the boundary conditions are

$$\begin{aligned} y(0,t) &= 0 & C_1\frac{\partial^3 y}{\partial x^3}(l,t) - C_2\frac{\partial y}{\partial x}(l,t) &= 0 \\ \frac{\partial y}{\partial x}(0,t) &= 0 & C_1\frac{\partial^2 y}{\partial x^2}(l,t) + C_4\frac{\partial y}{\partial x}(l,t) &= 0 \end{aligned} \tag{2.40}$$

The frequencies and mode shapes are then determined by considering the unforced system; the results are those listed in Eqs. (2.34)-(2.37). Thus, the solution for the PDE in Eq. (2.39) can be expressed as $y(x,t) = \sum_{n=1}^{\infty} \phi_n(x) g_n(t)$, there the functions $g_n(t)$ are to be determined.

Because of the orthogonality condition for the mode shapes, substituting the series solution for $y(x,t)$ into the PDE, multiplying by $\phi_i(x)$, and integrating over the domain of the system yields

$$\frac{\mathrm{d}^2 g_i}{\mathrm{d}t^2}(t) + \omega_i^2 g_i(t) = gg_f K_1 \int_0^l \phi_i(x)\,\mathrm{d}x\, \sin(\omega_s t) = gg_f \overline{\phi}_i\, \sin(\omega_s t) \tag{2.41}$$

The steady-state solution for the i^{th} modal equation is then

$$g_{\text{ss},i}(t) = \frac{g g_f \overline{\phi}_i}{\omega_i^2 - \omega_s^2} \sin(\omega_s t) \tag{2.42}$$

Therefore, the steady-state solution for the original system can be found as

$$w_{\text{ss}}(x,t) = r(x,t) + y_{\text{ss}}(x,t) = g g_f \left(\frac{1}{\omega_s^2} + \sum_{n=1}^{\infty} \frac{\overline{\phi}_i \phi_i(x)}{\omega_i^2 - \omega_s^2} \right) \sin(\omega_s t) \tag{2.43}$$

The analytical expression for the FRF is then found by dividing Eq. (2.43) by the amplitude of the acceleration and taking the magnitude.

$$H(x, \omega_s) = \left| \frac{1}{\omega_s^2} + \sum_{n=1}^{\infty} \frac{\overline{\phi}_i \phi_i(x)}{\omega_i^2 - \omega_s^2} \right| \tag{2.44}$$

Here, the variable x denotes the sensing location measured from the clamped end of the system.

2.2.2 Experimental Setup

Figure 2.3 shows the test setup used for FRF validation of the homogenized models for the string-harnessed system. The experiments are conducted using a Modal Shop 2075E dual purpose electrodynamic shaker controlled by an LMS SCADAS mobile data acquisition system. The LMS SCADAS controls the shaker base acceleration using the Sine Control module. A feedback loop in the LMS Test Lab software uses a PCB Piezotronics 352A24 accelerometer to ensure the desired acceleration is met. A Polytec OFV-505 laser vibrometer and Polytec OFV-5000 vibrometer controller are used for the FRF measurements of the system. The LMS data acquisition system is also used for the laser measurement data processing. A Modal Shop 2050E09 power amplifier is used to provide the excitation signal produced by the LMS unit to the shaker.

The pre-tension in the string is applied using a hanging mass of known weight while wrapping the string around the beam. Caution is taken during wrapping the string to eliminate motion in the hanging mass in order to allow for a steady force application and to avoid variation of tension during the wrapping. Figure 2.4 shows the harnessed beam mounted on the shaker base for the experiments. As shown in this figure, the harnessing string is tied through a small hole located at the free end of the beam. Additionally, there

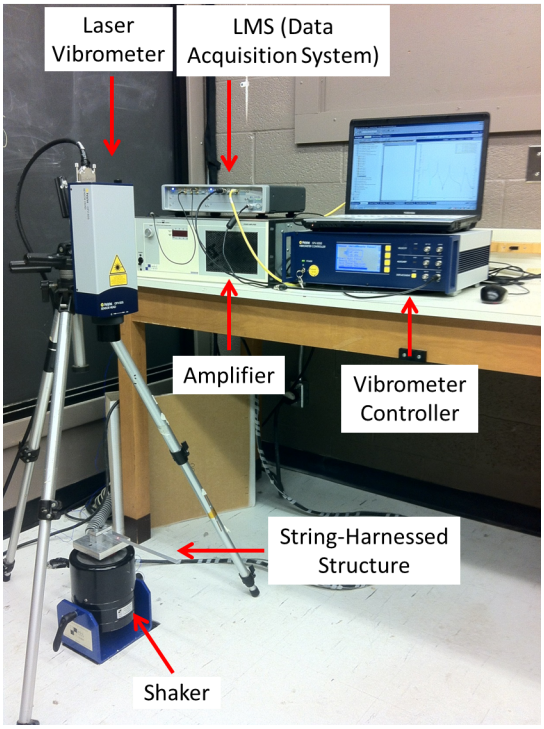

Figure 2.3: Experimental setup for FRF measurement.

is a small section of beam that extends beyond the clamp. This small section of beam is used to facilitate the clamping process of the string-harnessed system to the shaker. Lastly, a small square of reflective tape is used to improve the accuracy of the measurements from the laser vibrometer.

2.2.3 Experimental Results and Comparison of Modelling Approaches

An aluminum alloy 6061 beam specimen is used as the host structure. The clamped beam has dimension of 0.01306 m width, 0.00146 m thickness, and 0.251 m length. The modulus for the aluminum alloy 6061 is 68.9 GPa, and the density is 2768 g/m^3. A sensing location of 0.052 m from the clamped end was chosen so that it does not coincide with any nodes of the system within the frequency range of interest.

A constant base acceleration results in a smaller displacement amplitude for higher frequencies. The smaller amplitude results in a smaller accuracy in obtaining the laser

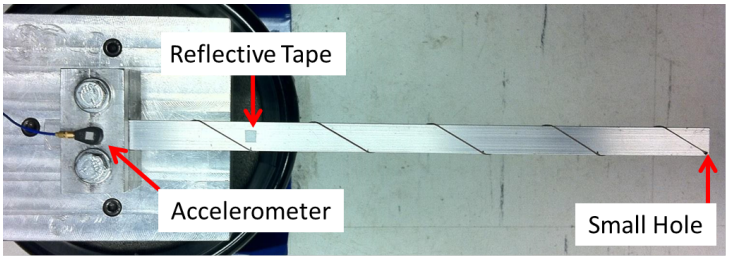

Figure 2.4: String-harnessed beam mounted on shaker.

measurements. Therefore, the FRFs are obtained individually for each mode during which both the laser sensitivity and shaker acceleration were adjusted to ensure optimal results. Table 2.1 presents the acceleration values used for the test.

Table 2.1: Acceleration profile used in initial experiments

Mode	Acceleration (g_f)	Resonance (g_f)	Anti-resonance (g_f)
1	0.05	0.03	0.2
2	1	0.1	1.2
3	1	0.5	3.5

As an initial step, the experimental FRFs for the host structure only, i.e., an unwrapped beam, are compared to the analytical FRFs using an undamped EB beam model. The results are presented in Fig. 2.5, and the natural frequencies for the analytical and experimental results are listed in Table 2.2.

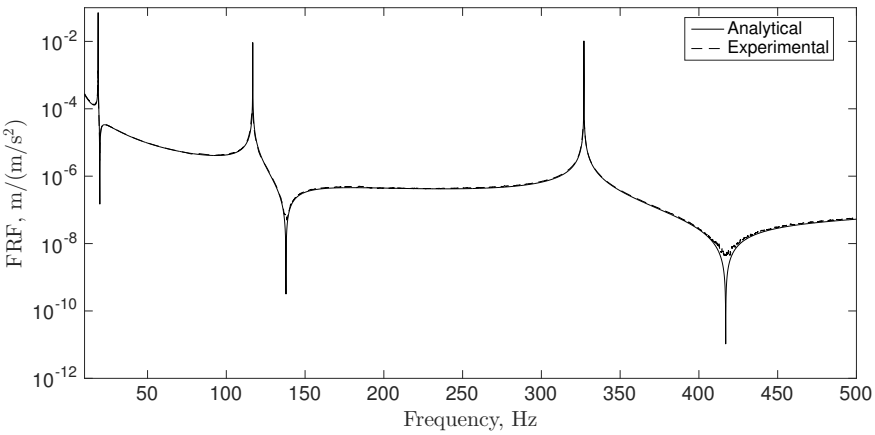

Figure 2.5: Analytical and experimental FRFs for the unwrapped beam.

Table 2.2: Experimental and analytical frequencies, in Hz, for the unwrapped beam

	Mode		
	1	2	3
Experiment	18.58	116.50	326.95
EB Model	18.64	116.79	327.01
% Error	0.3	0.25	0.02

As it is observed in Fig. 2.5, the analytical FRF matches that of the experiment quite well. This is expected considering the large length-to-thickness ratio for the beam. As shown in Table 2.2, there is good agreement between the analytical model and the experimental natural frequencies. As expected, the analytical model overpredicts the frequencies due to exclusion of shear or rotary inertia effects in the model. Since the results match quite well, this removes any uncertainty in the ability of the clamping mechanism to truly restrict displacement and slope to zero. The errors that are present in the results are likely due to human error in clamping the beam such that it is perpendicular to the clamp and the presence of the small through hole at the free end of the beam.

Next consider a string-harnessed system. For the string harness, 3 PowerPro Super 8 Slick 80lb break strength fishing lines are used. Multiple string are used in the test to ensure that the stiffening effect, as well as the added mass of the strings, is significant to the system. The material properties for the string are listed in Table 2.3. The string modulus

was determined experimentally by performing a tension test. Table 2.3 also presents the details of the test setup.

Table 2.3: Initial string-harnessed system test setup

String Type	Power Pro
String Radius (mm)	0.20955
String Modulus (GPa)	128.04
String Density (kg m^{-3})	1400
Pretension per String (N)	13.3
Number of Strings Used	3
Number of Fundamental Elements	5
Sensing Location (m)	0.052

The experimental result for the FRF of the test outlined in Table 2.3 is compared to the FRFs for the various string-harnessed system modelling approaches derived in Eq. (2.44). The experimental and analytical results for the first 3 modes of the system are presented in Fig. 2.6. The experimental and analytical natural frequencies are presented in Table. 2.4.

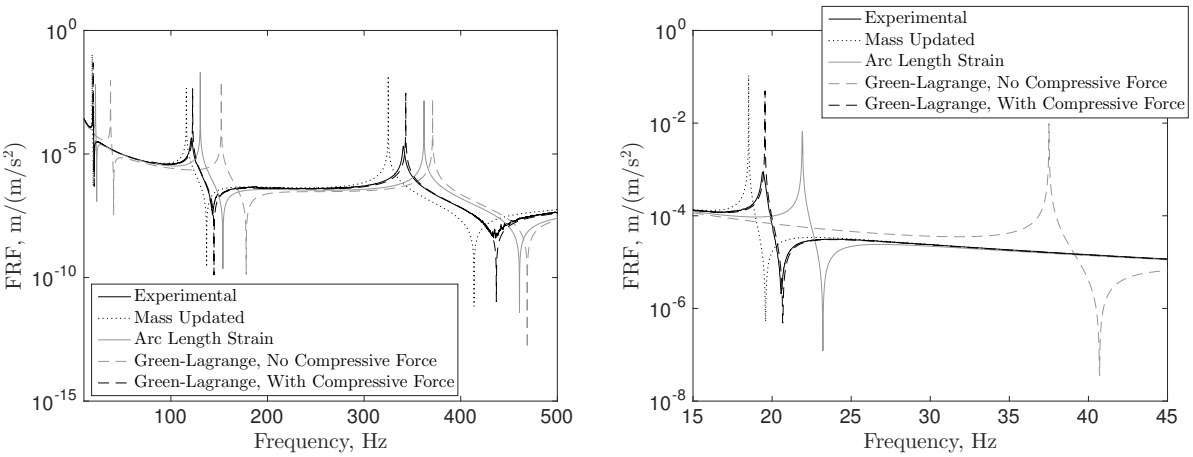

(a) First 3 modes of the system

(b) Fundamental mode of the system

Figure 2.6: Analytical and experimental FRFs for the string-harnessed system.

Table 2.4: Comparison of experimental string-harnessed natural frequencies, in Hz, to string-harnessed models

	Mode		
	1	2	3
	Experimental		
Frequency	19.42	121.25	340.6
	Mass Updated		
Frequency	18.52	116.04	324.92
% Error	-4.65	-4.30	-4.60
	Arc Length Strain		
Frequency	21.91	130.42	361.99
% Error	12.83	7.56	6.28
	G.-L., No Compressive Force		
Frequency	37.51	152.18	370.88
% Error	93.14	25.51	8.89
	G.-L., With Compressive Force		
Frequency	19.55	122.52	343.07
% Error	0.67	1.05	0.72

It is quite evident in Fig. 2.6 that amongst the four considered models that using the Green-Lagrange strain tensor with the string compressive force on the beam provides the most accurate result. In addition to the amplitude of the FRFs matching very well, Table 2.4 shows that the percentage of error in predicting the first three natural frequencies is no more than 1.05% for this model. This is significantly better than the other proposed models where the smallest absolute percentage error in predicting the frequencies is 4.30%. Some potential sources of error in the experimental results can be the small knot used to tie the strings at the free end of the system, applying the wrapping pattern perfectly along the beam, and ensuring that the tension in the strings is exactly constant throughout the system. However, care is taken in particular with the application of the wrapping pattern and the weight used to tension the strings to reduce the effect of these uncertainties and produce repeatable test measurements.

When a compressive axial force is applied to a beam, the natural frequencies of the system decrease. As expected, including the compressive force of the string on the host structure decreases the natural frequencies when compared to the case with no compressive force. Comparing the two models that use the Green-Lagrange strain tensor, it is seen that the impact of omitting the compressive force on the beam due to the string is significant.

Furthermore, the arc length strain model predicts frequencies between the Green-Lagrange strain models with and without the string compressive force. This is due to the model taking into account the work done by the beam against the string but only assuming that this takes place along the midline of the beam.

In Table 2.4 it is seen that the mass updated model underpredicts the frequencies of the system. This is expected since this model only takes into account the added mass of the string, which lowers the frequency, and does not consider the stiffening effect, which would increases the frequency. These results clearly highlight that the stiffening effect of the string is not negligible.

From the results presented in Fig. 2.6 and Table 2.4, the modelling technique employing a second-order displacement field, the Green-Lagrange strain tensor, and the string compressive force acting everywhere on the beam should be used for further analysis. Of particular interest are the mass and stiffness effects of the string harnesses for varying system parameters. From this point forward, both the diagonal and zigzag wrapping patterns presented in Fig. 2.2 will be considered.

2.3 Mass and Stiffness Effects of String-Harnessed Systems

The assumptions imposed on the string-harnessed system in Section 2.1 are still assumed to hold true. The homogenization theory approach previously used for the kinetic and strain energy derivations for transverse vibrations along the z-axis may also be used in deriving the dynamics of other coordinates of vibrations. As such, the results for the transverse along the y-axis, longitudinal, and torsional vibrations using this theory are also presented.

2.3.1 Kinetic Energy

Transverse $w(x,t)$

As in Section 2.1.1, the assumption of small transverse displacement allows rotatory inertia effects to be neglected. The kinetic energy for an arbitrary fundamental element of the hybrid structure can be found using

$$T_{\mathrm{e}} = \frac{1}{2}\rho_b \iiint_{\mathrm{beam}} \left(\frac{\partial u_z}{\partial t}\right)^2 \mathrm{d}V + \frac{1}{2}\rho_s \iiint_{\mathrm{string}} \left(\frac{\partial u_z}{\partial t}\right)^2 \mathrm{d}V \tag{2.45}$$

From substitution of the second-order displacement field in Eqs. (2.12):

$$\begin{aligned}
T_{\mathrm{e}} &= \frac{1}{2}\rho_b \iiint_{\text{beam}} \left(\frac{\partial w}{\partial t} - z\frac{\partial w}{\partial x}\frac{\partial^2 w}{\partial x \partial t}\right)^2 \mathrm{d}V + \frac{1}{2}\rho_s \iiint_{\text{string}} \left(\frac{\partial w}{\partial t} - z\frac{\partial w}{\partial x}\frac{\partial^2 w}{\partial x \partial t}\right)^2 \mathrm{d}V \\
&= \frac{1}{2}\rho_b \iiint_{\text{beam}} \left\{\left(\frac{\partial w}{\partial t}\right)^2 - 2z\frac{\partial w}{\partial t}\frac{\partial w}{\partial x}\frac{\partial^2 w}{\partial x \partial t} + z^2\left(\frac{\partial w}{\partial x}\frac{\partial^2 w}{\partial x \partial t}\right)^2\right\} \mathrm{d}V \\
&\qquad + \frac{1}{2}\rho_s \iiint_{\text{string}} \left\{\left(\frac{\partial w}{\partial t}\right)^2 - 2z\frac{\partial w}{\partial t}\frac{\partial w}{\partial x}\frac{\partial^2 w}{\partial x \partial t} + z^2\left(\frac{\partial w}{\partial x}\frac{\partial^2 w}{\partial x \partial t}\right)^2\right\} \mathrm{d}V \\
&\approx \frac{1}{2}\rho_b \iiint_{\text{beam}} \left(\frac{\partial w}{\partial t}\right)^2 \mathrm{d}V + \frac{1}{2}\rho_s \iiint_{\text{string}} \left(\frac{\partial w}{\partial t}\right)^2 \mathrm{d}V
\end{aligned}$$

The approximation is a result of keeping only up to second-order terms with respect to $w(x,t)$ and its derivatives. Applying the process of homogenization, the velocity at the centre of the fundamental element, $\frac{\partial w}{\partial t}(L/2,t)$, is taken as constant for the entire fundamental element. Then for a given wrapping pattern T_{e} is calculated. In the case of the diagonal wrapping pattern care must be taken as there is a lumped mass at the right end of the fundamental element.

Once T_{e} has been calculated it is divided by the length of the fundamental element. This produces a kinetic energy per unit length that is constant and taken to be an approximation of the kinetic energy per unit length for the entire string-harnessed system. The total kinetic energy can be expressed as

$$T_{\mathrm{tot}} = \int_0^l \frac{1}{2}K_1 \left(\frac{\partial w}{\partial t}\right)^2 \mathrm{d}x\,. \tag{2.46}$$

The constant coefficient K_1 is determined by the wrapping pattern for the string that is being considered.

Transverse $v(x,t)$

For motion along the y-axis the coordinate of vibration of interest is $v(x,t)$. The total kinetic energy in a fundamental element is given by

$$T_{\mathrm{e}} = \frac{1}{2}\rho_b \iiint_{\text{beam}} \left(\frac{\partial v}{\partial t}\right)^2 \mathrm{d}V + \frac{1}{2}\rho_s \iiint_{\text{string}} \left(\frac{\partial v}{\partial t}\right)^2 \mathrm{d}V\,.$$

Applying the same process of homogenization as presented for transverse w vibrations the total kinetic energy in the string-harnessed system can be expressed as

$$T_{\text{tot}} = \int_0^l \frac{1}{2} K_1 \left(\frac{\partial v}{\partial t} \right)^2 \mathrm{d}x \,. \tag{2.47}$$

The coefficient K_1 is determined by the wrapping pattern in consideration.

Longitudinal $u(x,t)$

For motion along the x-axis the coordinate of vibration of interest is $u(x,t)$. The total kinetic energy in a fundamental element is given by

$$T_{\text{e}} = \frac{1}{2}\rho_b \iiint_{\text{beam}} \left(\frac{\partial u}{\partial t} \right)^2 \mathrm{d}V + \frac{1}{2}\rho_s \iiint_{\text{string}} \left(\frac{\partial u}{\partial t} \right)^2 \mathrm{d}V \,.$$

Applying the process of homogenization presented in this work the total kinetic energy in the string-harnessed system can be expressed as

$$T_{\text{tot}} = \int_0^l \frac{1}{2} K_1 \left(\frac{\partial u}{\partial t} \right)^2 \mathrm{d}x \,. \tag{2.48}$$

The constant coefficient K_1 is determined by the wrapping pattern for the string that is being considered.

Torsional $\theta_x(x,t)$

For twist about the x-axis the coordinate of vibration of interest is $\theta_x(x,t)$. The total kinetic energy in a fundamental element is given by

$$T_{\text{e}} = \frac{1}{2}\rho_b \iiint_{\text{beam}} \left(y^2 + z^2\right) \left(\frac{\partial \theta_x}{\partial t} \right)^2 \mathrm{d}V + \frac{1}{2}\rho_s \iiint_{\text{string}} \left(y_s^2 + z_s^2\right) \left(\frac{\partial \theta_x}{\partial t} \right)^2 \mathrm{d}V$$

where $y_s(x)$ and $z_s(x)$ denote the y- and z-coordinate of the centre of the string. Applying the process of homogenization the total kinetic energy in the hybrid system can be expressed as

$$T_{\text{tot}} = \int_0^l \frac{1}{2} K_1 \left(\frac{\partial \theta_x}{\partial t} \right)^2 \mathrm{d}x \,. \tag{2.49}$$

The coefficient K_1 is a constant that is determined by the wrapping in consideration.

2.3.2 Strain Energy

Transverse $w(x,t)$

Recall the Green-Lagrange strain tensor from Eq. (2.14).

$$\boldsymbol{\varepsilon^{(2)}} = \begin{bmatrix} -z\frac{\partial^2 w}{\partial x^2} + \frac{z^2}{2}\left(\frac{\partial^2 w}{\partial x^2}\right)^2 + \frac{1}{2}\left(\frac{\partial w}{\partial x}\right)^2 & 0 & 0 \\ 0 & 0 & 0 \\ 0 & 0 & 0 \end{bmatrix}$$

Since $\varepsilon_{xx}^{(2)}$ is the only non-zero term in the strain tensor, this signifies that there will be no strain energy due to the vibration in the sections of string that are only in the yz-plane of the hybrid structure; this only occurs for the diagonal wrapping pattern.

The calculation for the differential strain energy in the string was performed in Section 2.1.1 and the final result given in Eq. (2.15) is stated below.

$$\mathrm{d}U_{\text{string}} = \left\{ \frac{1}{2}\left[E_s A_s z_s^2 \cos^3(\theta) + T_s z_s^2 \cos(\theta)\right]\left(\frac{\partial^2 w}{\partial x^2}\right)^2 - T_s z_s \cos(\theta)\frac{\partial^2 w}{\partial x^2} + \frac{1}{2}T_s \cos(\theta)\left(\frac{\partial w}{\partial x}\right)^2 + \frac{T_s^2}{2E_s A_s \cos(\theta)} \right\} \mathrm{d}x$$

The calculation for the differential strain energy in the beam with the string compressive force was done in Section 2.1.1 and the final result given in Eq. (2.21) is stated below.

$$\mathrm{d}U_{\text{beam}} = \left\{ \frac{1}{2}\left[E_b I_{yy} - \frac{T_s \cos(\theta) I_{yy}}{A_b}\right]\left(\frac{\partial^2 w}{\partial x^2}\right)^2 - \frac{1}{2}T_s \cos(\theta)\left(\frac{\partial w}{\partial x}\right)^2 + \frac{T_s^2 \cos^2(\theta)}{2E_b A_b} \right\} \mathrm{d}x \tag{2.50}$$

In Eq. (2.50), $I_{yy} = bh^3/12$ is the second moment of area about the y-axis.

Summing Eqs. (2.15) and (2.50) the strain energy for a differential element of the hybrid system is found.

$$\mathrm{d}U_{\text{system}} = \left\{ \frac{1}{2}\left[E_b I_{yy} + E_s A_s z_s^2 \cos^3(\theta) + T_s z_s^2 \cos(\theta) - \frac{T_s \cos(\theta) I_{yy}}{A_b}\right]\left(\frac{\partial^2 w}{\partial x^2}\right)^2 - T_s z_s \cos(\theta)\frac{\partial^2 w}{\partial x^2} + \frac{T_s^2}{2E_s A_s \cos(\theta)} + \frac{T_s^2 \cos^2(\theta)}{2E_b A_b} \right\} \mathrm{d}x \tag{2.51}$$

It is noted that in the development of Eq. (2.51) it is assumed that the longitudinal direction of the string is either in the xz- or xy-plane.

The homogenization technique outlined in Section 2.1.2 is applied to Eq. (2.51). As mentioned, Eq. (2.51) includes only the strain energy of segments of the string that lie on the xz- and xy-plane. This means that for the case of the diagonal wrapping pattern the strain energy due to pre-tension of the string in the yz-plane must be added to the result of the integration of Eq. (2.51) during homogenization. The total strain energy in the string-harnessed system can be expressed as

$$U_{\text{tot}} = \int_0^l \left(\frac{1}{2} C_1 \left(\frac{\partial^2 w}{\partial x^2} \right)^2 + C_2 \frac{\partial^2 w}{\partial x^2} + C_3 \right) \mathrm{d}x \tag{2.52}$$

The constant coefficients C_1, C_2, and C_3 are determined by the wrapping pattern for the string that is being considered. The coefficients of the kinetic and strain energy terms for the two periodic wrapping patterns shown in Fig. 2.2 are found using the method presented in the previous and current sections. These coefficients are listed in Sections 2.3.3 and 2.3.4.

Transverse $v(x,t)$

Keeping up to second-order terms the non-zero Green-Lagrange strain tensor element for the v coordinate of vibration is

$$\varepsilon_{xx}^{(2)} = -y \frac{\partial^2 v}{\partial x^2} + \frac{y^2}{2} \left(\frac{\partial^2 v}{\partial x^2} \right)^2 + \frac{1}{2} \left(\frac{\partial v}{\partial x} \right)^2 \tag{2.53}$$

Using Eq. (2.53) the differential strain energy in the string-harnessed system can be found as

$$\begin{aligned} \mathrm{d}U_{\text{system}} = \Bigg\{ \frac{1}{2} \left[E_b I_{zz} + E_s A_s y_s^2 \cos^3(\theta) + T_s y_s^2 \cos(\theta) - \frac{T_s \cos(\theta) I_{zz}}{A_b} \right] \left(\frac{\partial^2 v}{\partial x^2} \right)^2 \\ - T_s y_s \cos(\theta) \frac{\partial^2 v}{\partial x^2} + \frac{T_s^2}{2 E_s A_s \cos(\theta)} + \frac{T_s^2 \cos^2(\theta)}{2 E_b A_b} \Bigg\} \mathrm{d}x \end{aligned} \tag{2.54}$$

Applying the process of homogenization presented in the current work the total strain energy in the string-harnessed can be expressed as

$$U_{\text{tot}} = \int_0^l \left(\frac{1}{2} C_1 \left(\frac{\partial^2 v}{\partial x^2} \right)^2 + C_2 \frac{\partial^2 v}{\partial x^2} + C_3 \right) \mathrm{d}x \tag{2.55}$$

The constant coefficients C_1, C_2, and C_3 are determined by the wrapping pattern for the string in consideration. The coefficients of the kinetic and strain energy terms for the two wrapping patterns are listed in Sections 2.3.3 and 2.3.4.

Longitudinal $u(x,t)$

Keeping up to second-order terms the non-zero Green-Lagrange strain tensor element for the u coordinate of vibration is

$$\varepsilon_{xx}^{(2)} = \frac{\partial u}{\partial x} + \frac{1}{2}\left(\frac{\partial u}{\partial x}\right)^2 \tag{2.56}$$

Using Eq. (2.56) the differential strain energy in the hybrid system can be found as

$$\mathrm{d}U_{\text{system}} = \left\{\frac{1}{2}\left[E_b A_b + E_s A_s \cos^3(\theta)\right]\left(\frac{\partial u}{\partial x}\right)^2 + \frac{T_s^2}{2E_s A_s \cos(\theta)} + \frac{T_s^2 \cos^2(\theta)}{2E_b A_b}\right\} \mathrm{d}x \tag{2.57}$$

For the u coordinate of vibration a first-order Taylor series of $u(\eta,t)$ about the centre of a fundamental element is used in the homogenization process. The total strain energy in the string-harnessed system can be expressed as

$$U_{\text{tot}} = \int_0^l \left(\frac{1}{2}C_1\left(\frac{\partial u}{\partial x}\right)^2 + C_2\right) \mathrm{d}x \tag{2.58}$$

The coefficients C_1 and C_2 are constants that are determined by the wrapping pattern applied to the string. The coefficients of the kinetic and strain energy terms for the two wrapping patterns are listed in Sections 2.3.3 and 2.3.4.

Torsional $\theta_x(x,t)$

Keeping up to second-order terms the non-zero Green-Lagrange strain tensor elements for the θ_x coordinate of vibration are:

$$\begin{aligned}
\varepsilon_{xx}^{(2)} &= \frac{1}{2}\left(y^2 + z^2\right)\left(\frac{\partial \theta_x}{\partial x}\right)^2 \\
\gamma_{xy}^{(2)} &= -z\frac{\partial \theta_x}{\partial x} \\
\gamma_{xz}^{(2)} &= y\frac{\partial \theta_x}{\partial x}
\end{aligned} \tag{2.59}$$

Using Eq. (2.59) the differential strain energy in the string-harnessed system when the string is on the top or bottom of the beam, $z = \pm h/2$, can be found as

$$\mathrm{d}U_{\mathrm{system,t/b}} = \left\{ \frac{1}{2} \left[G_b J + E_s A_s z_s^2 \cos(\theta) \sin^2(\theta) + T_s \cos(\theta) \left(y_s^2 + z_s^2 \right) - \frac{T_s \cos(\theta) J}{A_b} \right] \left(\frac{\partial \theta_x}{\partial x} \right)^2 \right.$$
$$\left. \mp T_s z_s \sin(\theta) \frac{\partial \theta_x}{\partial x} + \frac{T_s^2}{2 E_s A_s \cos(\theta)} + \frac{T_s^2 \cos^2(\theta)}{2 E_b A_b} \right\} \mathrm{d}x \tag{2.60}$$

In Eq. (2.60) $J = bh^3 \left(\frac{1}{3} - \frac{64h}{\pi^5 b} \left(1 - \frac{h^4}{12 b^4} \right) \right)$ is the torsion constant for a beam with rectangular cross section when $h < b$ and G_b is the shear modulus of the beam. The differential strain energy in the harnessed system when the string is on the side of the beam, $y = \pm b/2$, is given by

$$\mathrm{d}U_{\mathrm{system,side}} = \left\{ \frac{1}{2} \left[G_b J + E_s A_s y_s^2 \cos(\theta) \sin^2(\theta) + T_s \cos(\theta) \left(y_s^2 + z_s^2 \right) - \frac{T_s \cos(\theta) J}{A_b} \right] \left(\frac{\partial \theta_x}{\partial x} \right)^2 \right.$$
$$\left. \mp T_s y_s \sin(\theta) \frac{\partial \theta_x}{\partial x} + \frac{T_s^2}{2 E_s A_s \cos(\theta)} + \frac{T_s^2 \cos^2(\theta)}{2 E_b A_b} \right\} \mathrm{d}x \tag{2.61}$$

For the θ_x coordinate of vibration a first-order Taylor series of $\theta_x(\eta, t)$ about the centre of a fundamental element is used in the homogenization process. The total strain energy in the hybrid system can be expressed as

$$U_{\mathrm{tot}} = \int_0^l \left(\frac{1}{2} C_1 \left(\frac{\partial \theta_x}{\partial x} \right)^2 + C_2 \frac{\partial \theta_x}{\partial x} + C_3 \right) \mathrm{d}x \tag{2.62}$$

The constant coefficients C_1, C_2, and C_2 are determined by the wrapping pattern applied to the string. The coefficients of the kinetic and strain energy terms for the two wrapping patterns are listed in Sections 2.3.3 and 2.3.4.

2.3.3 Coefficients for the Diagonal Wrapping Pattern

For the diagonal wrapping pattern shown in Fig. 2.2a the length of a fundamental element is $L = 2\overline{b}/\tan(\theta)$ and the centre of the string in the local Cartesian coordinates is:

$$(\eta, y, z) = \left(\eta, \tan(\theta)\eta - \overline{b}, \overline{h} \right), \quad 0 \leq \eta \leq L$$

Transverse $w(x,t)$

$$\begin{aligned}
C_1 &= E_b I_{yy} + E_s A_s \overline{h}^2 \cos^3(\theta) + T_s \cos(\theta) \left[\overline{h}^2 - \frac{I_{yy}}{A_b} \right] \\
C_2 &= -T_s \overline{h} \cos(\theta) \\
C_3 &= \frac{T_s^2 \cos^2(\theta)}{2E_b A_b} + \frac{T_s^2 \tan(\theta)}{2E_s A_s \overline{b}} \left[\frac{\overline{b}}{\sin(\theta)} + 2\overline{h} + \overline{b} \right] \\
K_1 &= \rho_b A_b + \frac{\rho_s A_s \tan(\theta)}{\overline{b}} \left[\frac{\overline{b}}{\sin(\theta)} + 2\overline{h} + \overline{b} \right]
\end{aligned} \tag{2.63}$$

It can be shown that $\overline{h}^2 - I_{yy}/A_b > 0$ always holds and therefore C_1 will always be a positive constant.

Transverse $v(x,t)$

$$\begin{aligned}
C_1 &= E_b I_{zz} + \frac{E_s A_s \overline{b}^2 \cos^3(\theta)}{3} + T_s \cos(\theta) \left[\frac{\overline{b}^2}{3} - \frac{I_{zz}}{A_b} \right] \\
C_2 &= 0 \\
C_3 &= \frac{T_s^2 \cos^2(\theta)}{2E_b A_b} + \frac{T_s^2 \tan(\theta)}{2E_s A_s \overline{b}} \left[\frac{\overline{b}}{\sin(\theta)} + 2\overline{h} + \overline{b} \right] \\
K_1 &= \rho_b A_b + \frac{\rho_s A_s \tan(\theta)}{\overline{b}} \left[\frac{\overline{b}}{\sin(\theta)} + 2\overline{h} + \overline{b} \right]
\end{aligned} \tag{2.64}$$

In Eq. (2.64), $I_{zz} = b^3 h/12$. It can be shown that $\overline{b}^2/3 - I_{zz}/A_b > 0$ always holds and therefore C_1 will always be a positive constant.

Longitudinal $u(x,t)$

$$\begin{aligned}
C_1 &= E_b A_b + E_s A_s \cos^3(\theta) \\
C_2 &= \frac{T_s^2 \cos^2(\theta)}{2E_s A_s} + \frac{T_s^2 \tan(\theta)}{2E_s A_s \overline{b}} \left[\frac{\overline{b}}{\sin(\theta)} + 2\overline{h} + \overline{b} \right] \\
K_1 &= \rho_b A_b + \frac{\rho_s A_s \tan(\theta)}{\overline{b}} \left[\frac{\overline{b}}{\sin(\theta)} + 2\overline{h} + \overline{b} \right]
\end{aligned} \tag{2.65}$$

Torsional $\theta_x(x,t)$

$$
\begin{aligned}
C_1 &= G_b J + E_s A_s \overline{h}^2 \cos(\theta)\sin^2(\theta) + T_s \cos(\theta)\left(\overline{h}^2 + \frac{\overline{b}^2}{3}\right) - \frac{T_s\cos(\theta)J}{A_b} \\
C_2 &= -T_s \overline{h}\sin(\theta) \\
C_3 &= \frac{T_s^2\cos^2(\theta)}{2E_bA_b} + \frac{T_s^2\tan(\theta)}{2E_sA_s\overline{b}}\left[\frac{\overline{b}}{\sin(\theta)} + 2\overline{h} + \overline{b}\right] \\
K_1 &= \rho_b I_{xx} + \frac{\rho_s A_s}{\cos(\theta)}\left(\overline{h}^2 + \frac{\overline{b}^2}{3}\right) + \rho_s A_s\left(2\overline{b}^2\overline{h} + \frac{2\overline{h}^3}{3} + \frac{\overline{b}^3}{3} + \overline{b}\overline{h}^2\right)\frac{\tan(\theta)}{\overline{b}}
\end{aligned}
\tag{2.66}
$$

In Eq. (2.66), $I_{xx} = I_{yy} + I_{zz}$ is the polar moment of inertia. It can be shown that $\overline{h}^2 - J/A_b > 0$ always holds and therefore C_1 will always be a positive constant.

2.3.4 Coefficients for the Zigzag Wrapping Pattern

The notation in the following sections is the same as for the diagonal wrapping pattern. As outlined in Section 2.1, for the zigzag wrapping pattern shown in Fig. 2.2b the length of a fundamental element is $L = \left(4\overline{b} + 4\overline{h}\right)/\tan(\theta)$ and the centre of the string in the local Cartesian coordinates is:

$$
(\eta, y, z) = \begin{cases}
\left(\eta, \tan(\theta)\eta - \overline{b}, \overline{h}\right), & 0 \le \eta \le \frac{2\overline{b}}{\tan(\theta)} \\
\left(\eta, \overline{b}, -\tan(\theta)\eta + 2\overline{b} + \overline{h}\right), & \frac{2\overline{b}}{\tan(\theta)} \le \eta \le \frac{2\overline{b}+2\overline{h}}{\tan(\theta)} \\
\left(\eta, -\tan(\theta)\eta + 3\overline{b} + 2\overline{h}, -\overline{h}\right), & \frac{2\overline{b}+2\overline{h}}{\tan(\theta)} \le \eta \le \frac{4\overline{b}+2\overline{h}}{\tan(\theta)} \\
\left(\eta, -\overline{b}, \tan(\theta)\eta - 4\overline{b} - 3\overline{h}\right), & \frac{4\overline{b}+2\overline{h}}{\tan(\theta)} \le \eta \le L
\end{cases}
$$

Transverse $w(x,t)$

$$
\begin{aligned}
C_1 &= E_b I_{yy} + \frac{E_s A_s \overline{h}^2 \cos^3(\theta)\left(\overline{b} + \overline{h}/3\right)}{\overline{b} + \overline{h}} + T_s\cos(\theta)\left[\frac{\overline{h}^2\left(\overline{b} + \overline{h}/3\right)}{\overline{b} + \overline{h}} - \frac{I_{yy}}{A_b}\right] \\
C_2 &= 0 \\
C_3 &= \frac{T_s^2\cos^2(\theta)}{2E_bA_b} + \frac{T_s^2}{2E_sA_s\cos(\theta)} \\
K_1 &= \rho_b A_b + \frac{\rho_s A_s}{\cos(\theta)}
\end{aligned}
\tag{2.67}
$$

Note that $\overline{h}^2\left(\overline{b}+\overline{h}/3\right)/\left(\overline{b}+\overline{h}\right)-I_{yy}/A_b>0$ always holds and therefore C_1 will always be a positive constant.

Transverse $v(x,t)$

$$\begin{aligned}
C_1 &= E_bI_{zz}+\frac{E_sA_s\overline{b}^2\cos^3(\theta)\left(\overline{b}/3+\overline{h}\right)}{\overline{b}+\overline{h}}+T_s\cos(\theta)\left[\frac{\overline{b}^2\left(\overline{b}/3+\overline{h}\right)}{\overline{b}+\overline{h}}-\frac{I_{zz}}{A_b}\right]\\
C_2 &= 0\\
C_3 &= \frac{T_s^2\cos^2(\theta)}{2E_bA_b}+\frac{T_s^2}{2E_sA_s\cos(\theta)}\\
K_1 &= \rho_bA_b+\frac{\rho_sA_s}{\cos(\theta)}
\end{aligned} \tag{2.68}$$

In Eq. (2.68) it can be shown that $\overline{b}^2\left(\overline{b}/3+\overline{h}\right)/\left(\overline{b}+\overline{h}\right)-I_{zz}/A_b>0$ always holds and therefore C_1 will always be a positive constant.

Longitudinal $u(x,t)$

$$\begin{aligned}
C_1 &= E_bA_b+E_sA_s\cos^3(\theta)\\
C_2 &= \frac{T_s^2}{2E_sA_s\cos(\theta)}+\frac{T_s^2\cos^2(\theta)}{2E_bA_b}\\
K_1 &= \rho_bA_b+\frac{\rho_sA_s}{\cos(\theta)}
\end{aligned} \tag{2.69}$$

Torsional $\theta_x(x,t)$

$$\begin{aligned}
C_1 &= G_bJ+E_sA_s\overline{bh}\cos(\theta)\sin^2(\theta)+\frac{T_s\left(\overline{b}+\overline{h}\right)^2\cos(\theta)}{3}-\frac{T_s\cos(\theta)J}{A_b}\\
C_2 &= -\frac{2T_s\overline{bh}\sin(\theta)}{\overline{b}+\overline{h}}\\
C_3 &= \frac{T_s^2\cos^2(\theta)}{2E_bA_b}+\frac{T_s^2}{2E_sA_s\cos(\theta)}\\
K_1 &= \rho_bI_{xx}+\frac{\rho_sA_s\left(\overline{b}+\overline{h}\right)^2}{3\cos(\theta)}
\end{aligned} \tag{2.70}$$

In Eq. (2.70) it can be shown that $\left(\overline{b}+\overline{h}\right)^2/3 - J/A_b > 0$ always holds and therefore C_1 is always a positive constant.

2.3.5 Vibration Analysis

Transverse $w(x,t)$

From the total kinetic and strain energy in Eqs. (2.46) and (2.52) the Lagrangian for the string-harnessed system can be found. Hamilton's principle is then applied and the PDE for the free vibration of the transverse displacement w for the string-harnessed system is

$$C_1\frac{\partial^4 w}{\partial x^4} + K_1\frac{\partial^2 w}{\partial t^2} = 0 \tag{2.71}$$

and the boundary conditions at the endpoint $x^* = 0$ or l are:

$$w(x^*,t) = 0 \qquad \text{or} \qquad \frac{\partial^3 w}{\partial x^3}(x^*,t) = 0 \tag{2.72a}$$

$$\frac{\partial w}{\partial x}(x^*,t) = 0 \qquad \text{or} \qquad C_1\frac{\partial^2 w}{\partial x^2}(x^*,t) = -C_2 \tag{2.72b}$$

The boundary conditions in the left column represent geometric boundary conditions while the boundary conditions in the right column are typically referred to as the natural boundary conditions.

To proceed with the vibration analysis a time-independent solution to the problem of Eqs. (2.71) and (2.72) is introduced and denoted $w_e(x)$. Physically this corresponds to an equilibrium solution. Performing the substitution $w(x,t) = \overline{w}(x,t) + w_e(x)$ in Eqs. (2.71) and (2.72) leads to a PDE with respect to the new function $\overline{w}(x,t)$ whose boundary conditions are homogeneous. Since $w_e(x)$ is time independent the frequencies of vibration determined from the PDE in terms of $\overline{w}(x,t)$ will be the same as the those of the original PDE in terms of $w(x,t)$.

$$C_1\frac{\partial^4 \overline{w}}{\partial x^4} + K_1\frac{\partial^2 \overline{w}}{\partial t^2} = 0 \tag{2.73}$$

$$\overline{w}(x^*,t) = 0 \qquad \text{or} \qquad \frac{\partial^3 \overline{w}}{\partial x^3}(x^*,t) = 0 \tag{2.74a}$$

$$\frac{\partial \overline{w}}{\partial x}(x^*,t) = 0 \qquad \text{or} \qquad \frac{\partial^2 \overline{w}}{\partial x^2}(x^*,t) = 0 \tag{2.74b}$$

In order to find the natural frequencies of the system the solution for the function $\overline{w}(x,t)$ must be found. Using separation of variables the solution to the PDE and boundary conditions of Eqs. (2.73) and (2.74) can be found. Subsequently, the natural frequencies for the system may be found as $\omega_n^{\text{ECM}} = \mu_n^2\sqrt{C_1/K_1}$, where the superscript ECM denotes the equivalent continuum model for w resulting from applying the homogenization method to the hybrid structure using a string model. The mode shape parameters μ_n are determined by solving the characteristic equation, [62]. In this work attention is given to clamped-clamped, clamped-free, and free-free boundary conditions.

Transverse $v(x,t)$

Hamilton's principle is applied using Eqs. (2.47) and (2.55) and leads to the PDE in the form

$$C_1\frac{\partial^4 v}{\partial x^4} + K_1\frac{\partial^2 v}{\partial t^2} = 0 \tag{2.75}$$

and the boundary conditions at the endpoint $x^* = 0$ or l are:

$$v(x^*,t) = 0 \qquad \text{or} \qquad \frac{\partial^3 v}{\partial x^3}(x^*,t) = 0 \tag{2.76a}$$

$$\frac{\partial v}{\partial x}(x^*,t) = 0 \qquad \text{or} \qquad C_1\frac{\partial^2 v}{\partial x^2}(x^*,t) = -C_2 \tag{2.76b}$$

Similar to what was done for the transverse vibrations for w a time-independent solution is found to eliminate the non-homogeneous boundary conditions. This leads to:

$$C_1\frac{\partial^4 \overline{v}}{\partial x^4} + K_1\frac{\partial^2 \overline{v}}{\partial t^2} = 0 \tag{2.77}$$

$$\overline{v}(x^*,t) = 0 \qquad \text{or} \qquad \frac{\partial^3 \overline{v}}{\partial x^3}(x^*,t) = 0 \tag{2.78a}$$

$$\frac{\partial \overline{v}}{\partial x}(x^*,t) = 0 \qquad \text{or} \qquad \frac{\partial^2 \overline{v}}{\partial x^2}(x^*,t) = 0 \tag{2.78b}$$

The natural frequencies for the system may be found as $\omega_n^{\text{ECM}} = \mu_n^2\sqrt{C_1/K_1}$, where the superscript ECM denotes the equivalent continuum model for v resulting from applying the homogenization method. The mode shape parameters μ_n are determined by the imposed boundary conditions.

Longitudinal $u(x,t)$

Hamilton's principle is applied using Eqs. (2.48) and (2.58) and leads to the PDE in the form

$$K_1 \frac{\partial^2 u}{\partial t^2} = C_1 \frac{\partial^2 u}{\partial x^2} \tag{2.79}$$

and the boundary conditions at the endpoint $x^* = 0$ or l are:

$$u(x^*,t) = 0 \qquad \text{or} \qquad \frac{\partial u}{\partial x}(x^*,t) = 0 \tag{2.80a}$$

The natural frequencies for the system may be found as $\omega_n^{\text{ECM}} = \mu_n^2 \sqrt{C_1/K_1}$, where the superscript ECM denotes the equivalent continuum model for u resulting from applying the homogenization method. The mode shape parameters μ_n are determined by the imposed boundary conditions.

Torsional $\theta_x(x,t)$

Hamilton's principle is applied using Eqs. (2.49) and (2.62) and leads to the PDE in the form

$$K_1 \frac{\partial^2 \theta_x}{\partial t^2} = C_1 \frac{\partial^2 \theta_x}{\partial x^2} \tag{2.81}$$

and the boundary conditions at the endpoint $x^* = 0$ or l are:

$$\theta_x(x^*,t) = 0 \qquad \text{or} \qquad C_1 \frac{\partial \theta_x}{\partial x}(x^*,t) = -C_2 \tag{2.82a}$$

A time-independent solution is found to eliminate the non-homogeneous boundary conditions. This leads to the PDE in the form of

$$K_1 \frac{\partial^2 \overline{\theta_x}}{\partial t^2} = C_1 \frac{\partial^2 \overline{\theta_x}}{\partial x^2} \tag{2.83}$$

$$\overline{\theta_x}(x^*,t) = 0 \qquad \text{or} \qquad \frac{\partial \overline{\theta_x}}{\partial x}(x^*,t) = 0 \tag{2.84a}$$

The natural frequencies for the system may be found as $\omega_n^{\text{ECM}} = \mu_n^2 \sqrt{C_1/K_1}$, where the superscript ECM denotes the equivalent continuum model for θ_x resulting from applying the homogenization method. The mode shape parameters μ_n are determined by the imposed boundary conditions.

2.3.6 Discussion of Boundary Conditions for Transverse $w(x,t)$

For a beam theory in which the strain tensor is expanded up to the first order in z, where z is measured along the thickness of the beam, the boundary conditions can be interpreted in terms of common notions such as displacement, slope, moment, and shear force. For example, a clamped-free Euler-Bernoulli beam with the only non-zero strain tensor element $\epsilon_{xx} = -z\frac{\partial^2 w}{\partial x^2}$ will have no displacement or slope at the clamped end and no moment or shear at the free end. This strain tensor is what is commonly seen in deriving the transverse motion in the Euler-Bernoulli beam.

However, in the current work, the addition of a string harness and the need for including higher order terms in the displacement field and the strain tensor mandates that extra care be taken when interpreting the boundary conditions. As an example, consider the natural boundary condition of Eq. (2.72b) for the zigzag wrapping pattern. In this case the boundary condition is

$$\left\{ E_b I_{yy} + \frac{E_s A_s \overline{h}^2 \cos^3(\theta)\left(\overline{b}+\overline{h}/3\right)}{\overline{b}+\overline{h}} + T_s \cos(\theta)\left[\frac{\overline{h}^2\left(\overline{b}+\overline{h}/3\right)}{\overline{b}+\overline{h}} - \frac{I_{yy}}{A_b}\right]\right\} \frac{\partial^2 w}{\partial x^2}(x^*,t) = 0 \tag{2.85}$$

While it may be tempting to reduce this to $\frac{\partial^2 w}{\partial x^2}(x^*,t) = 0$ and immediately conclude that there is no moment at a free end, some care must be taken.

Following the method outlined in [117] for laminated composite plates and shells, the authors of [44] developed the general equation of motion for an Euler-Bernoulli composite beam with higher orders of z in the strain tensor. The PDE for the transverse displacement is then given by

$$\frac{\partial^2}{\partial x^2}\left(P_x \frac{\partial^2 w}{\partial x^2}\right) - \frac{\partial^2 M_x}{\partial x^2} - \frac{\partial}{\partial x}\left(N_x \frac{\partial w}{\partial x}\right) + m\frac{\partial^2 w}{\partial t^2} = 0 \tag{2.86}$$

where m is the mass per unit length of the system. The quantities $(N_x, M_x, P_x) = \int_{\text{Area}} \sigma_{xx}\,(1, z, z^2)\,\mathrm{d}A$ are the stress resultants. N_x and M_x correspond physically to the in-plane force and the bending moment, respectively, while P_x is a higher-order stress resultant. The boundary conditions at $x^* = 0$ or l are:

$$w(x^*,t) = 0 \quad \text{or} \quad -\frac{\partial}{\partial x}\left(P_x \frac{\partial^2 w}{\partial x^2}(x^*,t)\right) + \frac{\partial M_x}{\partial x}(x^*,t) + N_x \frac{\partial w}{\partial x}(x^*,t) = 0 \tag{2.87a}$$

$$\frac{\partial w}{\partial x}(x^*,t) = 0 \quad \text{or} \quad P_x \frac{\partial^2 w}{\partial x^2}(x^*,t) - M_x(x^*,t) = 0 \tag{2.87b}$$

For the hybrid systems in this thesis the stress resultants are calculated using the definition $(N_x, M_x, P_x) = \int_{\text{Area}} \sigma_{xx}\,(1, z, z^2)\,\mathrm{d}A$. The integration is performed across the entire cross-sectional area of the hybrid system and will thus have a component due to the beam and another component due to the string. In calculating the stress resultant from the string recall that the value of the stress at the centre of the string is assumed to be the value for the entire cross section of the string. The method of homogenization used in developing the continuum model is then applied. This means an arbitrary fundamental element is considered and the Taylor series for the displacement about the centre of the element is assumed. Integrating over the length of the fundamental element and then dividing by the total length of the element yields the final results for N_x, M_x, and P_x. Throughout these steps only constant terms in N_x and P_x, and linear terms in $w(x,t)$ and constant terms for M_x are kept. The stress resultants were truncated in this manner to ensure that the final PDE for the hybrid system was linear with respect to $w(x,t)$.

Diagonal:

$$N_x = 0$$

$$M_x = T_s\overline{h}\cos(\theta) - \left\{E_bI_{yy} + E_sA_s\overline{h}^2\cos^3(\theta)\right\}\frac{\partial^2 w}{\partial x^2}$$

$$P_x = T_s\overline{h}^2\cos(\theta) - \frac{T_s\cos(\theta)I_{yy}}{A_b}$$

Zigzag:

$$N_x = 0$$

$$M_x = -\left\{E_bI_{yy} + \frac{E_sA_s\overline{h}^2\cos^3(\theta)\left(\overline{b}+\overline{h}/3\right)}{\overline{b}+\overline{h}}\right\}\frac{\partial^2 w}{\partial x^2}$$

$$P_x = \frac{T_s\overline{h}^2\cos(\theta)\left(\overline{b}+\overline{h}/3\right)}{\overline{b}+\overline{h}} - \frac{T_s\cos(\theta)I_{yy}}{A_b}$$

Returning to the natural boundary condition for the zigzag wrapping pattern in Eq. (2.85) the correct way of looking at this boundary condition is

$$-\left\{E_bI_{yy} + \frac{E_sA_s\overline{h}^2\cos^3(\theta)\left(\overline{b}+\overline{h}/3\right)}{\overline{b}+\overline{h}}\right\}\frac{\partial^2 w}{\partial x^2}(x^*,t) = \left\{T_s\cos(\theta)\left[\frac{\overline{h}^2\left(\overline{b}+\overline{h}/3\right)}{\overline{b}+\overline{h}} - \frac{I_{yy}}{A_b}\right]\right\}\frac{\partial^2 w}{\partial x^2}(x^*,t) \tag{2.88}$$

The form of Eq. (2.88) can be obtained by directly substituting the values for N_x, M_x, and P_x for the zigzag wrapping pattern into Eq. (2.87b) and also by rearranging the boundary condition in Eq. (2.85). This shows that the bending moment at a free end does not vanish in the hybrid system due to the higher-order stress resultants. After truncation of the stress resultants, it can be seen that the moment in the system, M_x, and the term $P_x\frac{\partial^2 w}{\partial x^2}$

are similar in form. This is why the boundary condition in Eq. (2.88) can be reduced to $\frac{\partial^2 w}{\partial x^2}(x^*,t)=0$, which is equivalent to no moment at the free end. In the more general case this approach must be taken so that the proper interpretation of the boundary conditions can be made.

A final note will be made with regard to the natural boundary condition of the diagonal wrapping pattern given by Eq. (2.72b). In this case we have

$$-\left\{E_b I_{yy}+E_s A_s \overline{h}^2\cos^3(\theta)\right\}\frac{\partial^2 w}{\partial x^2}(x^*,t)+T_s\overline{h}\cos(\theta)=\left\{T_s\overline{h}^2\cos(\theta)-\frac{T_s\cos(\theta)I_{yy}}{A_b}\right\}\frac{\partial^2 w}{\partial x^2}(x^*,t) \quad (2.89)$$

The form of Eq. (2.89) can be obtained by directly substituting the values for N_x, M_x, and P_x for the diagonal wrapping pattern into Eq. (2.87b) and also by rearranging the boundary condition in Eq. (2.72b) with the coefficients C_1 and C_2 for the diagonal wrapping pattern. As it can be seen, the moment in the system is composed of two parts, one that is related to the bending stiffness of the hybrid system and another that is equal to the initial moment produced by the tensioned string when the beam is perfectly horizontal. As was the case for the zigzag wrapping pattern, the bending moment in the system with a diagonal wrapping pattern also does not vanish at a free end due to the higher-order stress resultants. In the transformation of the PDE from being in terms of $w(x,t)$ to $\overline{w}(x,t)$ via $w(x,t)=\overline{w}(x,t)+w_{\mathrm{E}}(x)$, where $w_{\mathrm{E}}(x)$ is a time-independent solution, the constant $T_s\overline{h}\cos(\theta)$ from the boundary condition is removed. This change of variable was made in Section 2.3.5 with the goal of eliminating this constant and obtaining homogeneous boundary conditions. In this case Eq. (2.89) becomes

$$-\left\{E_b I_{yy}+E_s A_s \overline{h}^2\cos^3(\theta)\right\}\frac{\partial^2 \overline{w}}{\partial x^2}(x^*,t)=\left\{T_s\overline{h}^2\cos(\theta)-\frac{T_s\cos(\theta)I_{yy}}{A_b}\right\}\frac{\partial^2 \overline{w}}{\partial x^2}(x^*,t)$$

The terms are similar in form and the boundary condition can be simplified to $\frac{\partial^2 \overline{w}}{\partial x^2}(x^*,t)=0$. Again, this only tells us that for the assumptions we have made that the boundary condition is equivalent to no moment at the free end for the system in terms of $\overline{w}(x,t)$.

2.3.7 Finite Element Analysis

The finite elements analysis (FEA) method employed in this work allows displacement along the x, y, and z-axis as well as twist about the x-axis. It is assumed that cross sections of the beam remain perpendicular to the neutral axis during bending; this is a good assumption for structures with fairly large length to width ratio. Therefore, 4 independent coordinates of vibrations are considered for the FEA analysis as shown. The

following displacement field that employs up to the second-order terms in the Taylor series expansion can be presented as follows

$$u_x(x,y,z,t) = u(x,t) - y\frac{\partial v}{\partial x}(x,t) - z\frac{\partial w}{\partial x}(x,t)$$
$$u_y(x,y,z,t) = v(x,t) - z\theta_x(x,t) - \frac{y}{2}\left(\theta_x(x,t)\right)^2 - \frac{y}{2}\left(\frac{\partial v}{\partial x}(x,t)\right)^2$$
$$u_z(x,y,z,t) = w(x,t) + y\theta_x(x,t) - \frac{z}{2}\left(\theta_x(x,t)\right)^2 - \frac{z}{2}\left(\frac{\partial w}{\partial x}(x,t)\right)^2$$

Above, $u(x,t)$, $v(x,t)$, and $w(x,t)$ are the displacements along the x, y, and z-axis, respectively, and $\theta_x(x,t)$ is the twist angle about the x-axis. The Green-Lagrange strain tensor is then calculated for the FEA displacement field and up to second-order terms are kept. See Appendix A for the Green-Lagrange strain tensor used in the FEA method. Although it was assumed that cross sections remain perpendicular to the neutral axis during bending, shear strains appear due to coupling between the various coordinates of vibrations and using the Green-Lagrange strain tensor. This is clearly shown in Appendix A, Eq. (A.1). The objective of the fully coupled FEA is to demonstrate that the assumption of decoupled coordinates of vibration to obtain the equivalent continuum models is valid.

Due to the presence of the pre-tensioned string in the system the beam is initially compressed and is also subject to a pre-twist. The initial compression in the beam is accounted for in the same manner as in the homogenized model. That is, the projection of the pre-tension in the string along the longitudinal direction of the beam causes compression. Similarly, the projection of the pre-tension in the string onto the yz-plane at every point along the beam is assumed to cause a pre-twist. The initial twist in the beam is determined using the torsion formula. The initial shear at each point along the beam is determined using the beam shear formula. Using the Green-Lagrange strain tensor, and including all of these initial effects, the differential strain and kinetic energy of the string-harnessed system can be found for the FEA model. In this calculation only up to second-order terms are kept, also the rotatory inertia effect is neglected. The FEA differential strain and kinetic energy expressions are listed in Appendix A, Eqs. (A.2) to (A.4). As it may be observed from these expressions, coordinates of vibrations $u(x,t)$, $v(x,t)$, $w(x,t)$, and $\theta_x(x,t)$ are coupled due to presence of the string in the system.

The nodal displacement parameters for an arbitrary node i are denoted by $u_i(t)$, $v_i(t)$, $w_i(t)$, and $\theta_{x,i}(t)$, as well as their first derivatives $\frac{\partial u_i}{\partial x}(t)$, $\frac{\partial v_i}{\partial x}(t)$, $\frac{\partial w_i}{\partial x}(t)$, and $\frac{\partial \theta_{x,i}}{\partial x}(t)$. The interpolation function relating a single coordinate of vibration between any two nodes is a third order polynomial $a_1(t) + a_2(t)x + a_3(t)x^2 + a_4(t)x^3$ where the coefficients $a_j(t)$ are determined in terms of the nodal parameters.

Of interest from the FEA are the FRFs for the longitudinal displacement, u, the two transverse displacements, v and w, and the twist, θ_x. The following arbitrary system parameters are for numerical simulations throughout the remainder of this work

$$
\begin{aligned}
b &= 0.01\,\mathrm{m} & h &= 0.0015\,\mathrm{m} & l &= 0.25\,\mathrm{m} \\
E_b &= 6.89 \times 10^{10}\,\mathrm{N/m^2} & \rho_b &= 2700\,\mathrm{kg/m^3} & r_s &= 0.00035\,\mathrm{m} \\
E_s &= 1.5 \times 10^{11}\,\mathrm{N/m^2} & \rho_s &= 1400\,\mathrm{kg/m^3} & T_s &= 25\,\mathrm{N} \\
G_b &= 2.6 \times 10^{10}\,\mathrm{N/m^2}
\end{aligned}
$$

These values represent the properties of a harnessed aluminum beam made of 10 fundamental elements. In building the FEA model each fundamental element of the string-harnessed system is sub-divided into 30 sections of equal length. Thus the FEA model contains a total of 300 elements.

Consider the FRFs for a clamped-clamped string-harnessed system for both wrapping patterns, presented in Fig. 2.7. The sensing and actuation location is taken to be $x = l/10$ in all four FRFs and the legend in Fig. 2.7 denotes to which coordinate of vibration each FRF is related.

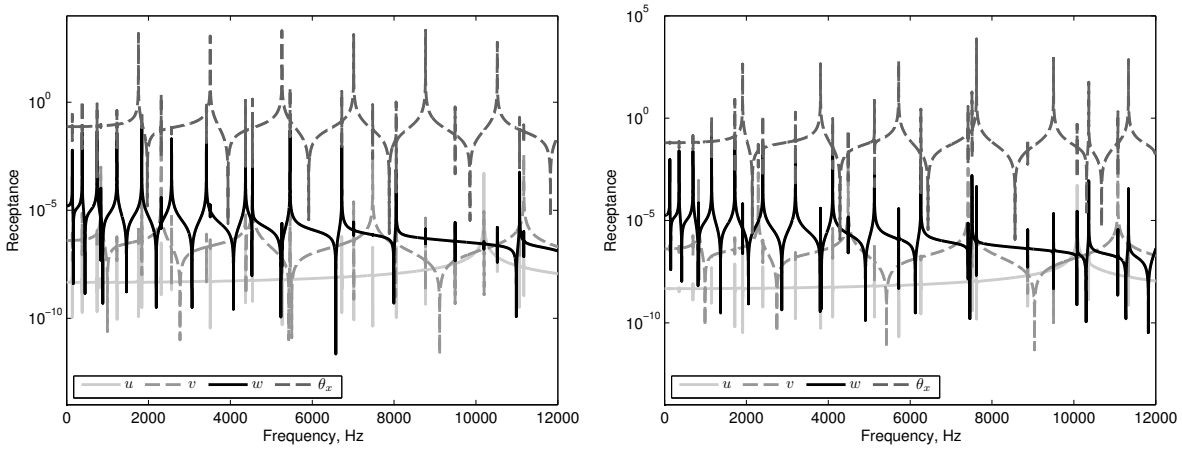

(a) Diagonal (b) Zigzag

Figure 2.7: FRFs from the FEA for clamped-clamped boundary conditions

As explained previously, from the differential strain and kinetic energy expressions of the FEA model it is known that the motions of the string-harnessed system are coupled.

As shown in Fig. 2.7, for each dominant mode the peaks pertaining to that mode is quite conspicuous and it can be seen that different coordinates of vibrations are in fact lightly coupled for the given system parameters. This type of behaviour occurs for both wrapping patterns given clamped-clamped (CC), clamped-free (CF), or free-free (FF) boundary conditions, as shown in Figs. 2.8 and 2.9. Driving point FRFs are used for this analysis with an actuation and sensing location at $x = l/10$ for the CC boundary conditions and the free end for the CF and FF boundary conditions. Caution was taken to make sure that the sensing locations do not correspond to the node locations for any of the mode within the desired frequency range. As explained before the FEA is a full-scale model that exhibits coupling between various coordinates of vibrations.

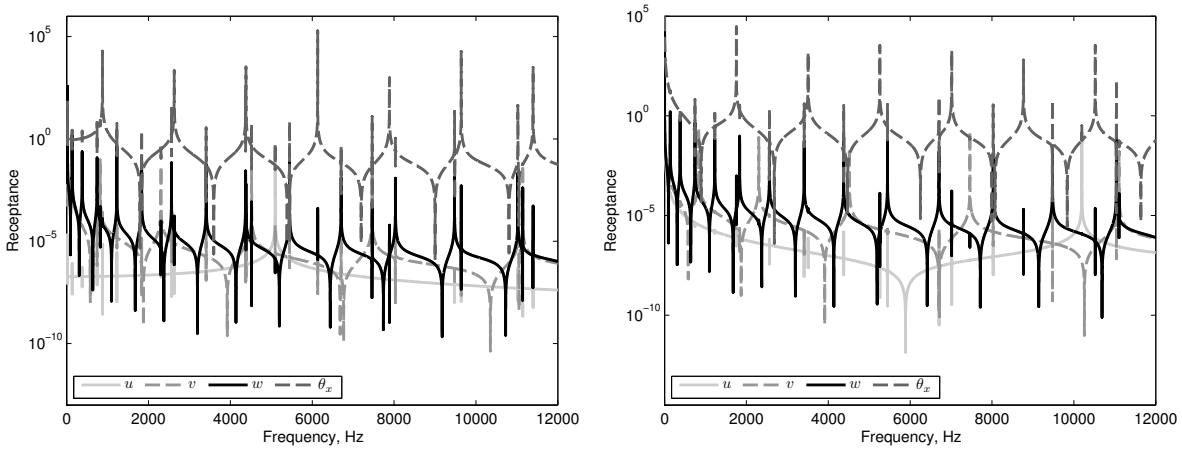

(a) Clamped-free (b) Free-free

Figure 2.8: FRFs from the FEA for the diagonal wrapping pattern.

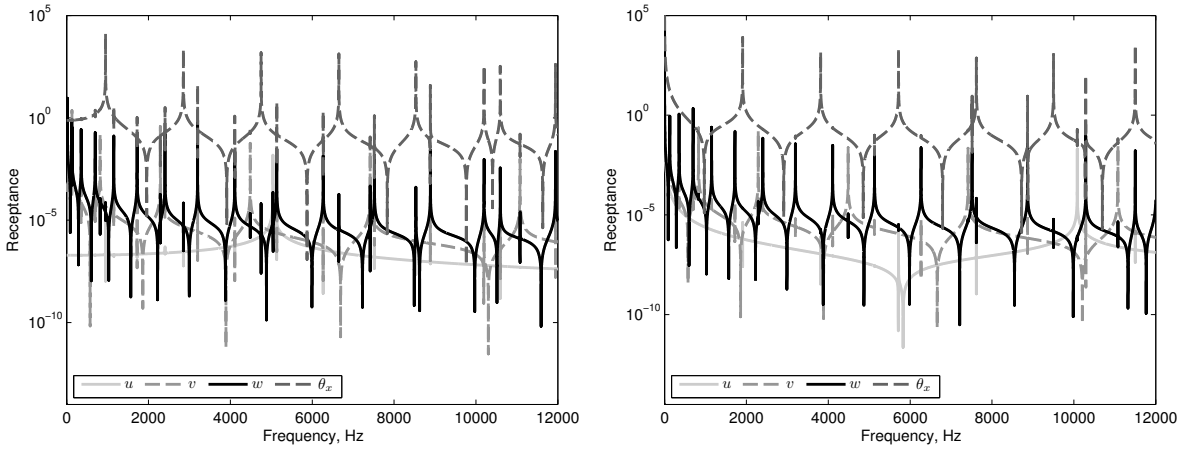

(a) Clamped-free (b) Free-free

Figure 2.9: FRFs from the FEA for the zigzag wrapping pattern.

2.3.8 Model Validation

In this section the FRFs for the equivalent continuum models (ECMs) previously derived for the 4 coordinates of vibrations are listed and compared to those from the full-scale FEA. The FRFs obtained from the ECM for each PDE represents the dominant dynamic behaviour for that coordinate of vibration. Some of the FRF results for these coordinates of vibrations for the two wrapping patterns are presented in Figs. 2.10 and 2.11. Tables 2.5 and 2.6 present the natural frequency comparisons between the homogenized model and the FEA for all boundary conditions and both wrapping patterns. In these tables the superscripts for the ECM frequency values denote which coordinate of vibration they correspond to. For FF boundary conditions there are two mode shapes associated to rigid body motion for each of the transverse coordinates, v and w, as well as one mode shape for the coordinates of vibration u and θ_x. Mode shapes were examined to assure of an accurate comparison between the corresponding frequencies in each mode for the two models. Some of these mode shapes are plotted for comparison in Figs. 2.12 to 2.15.

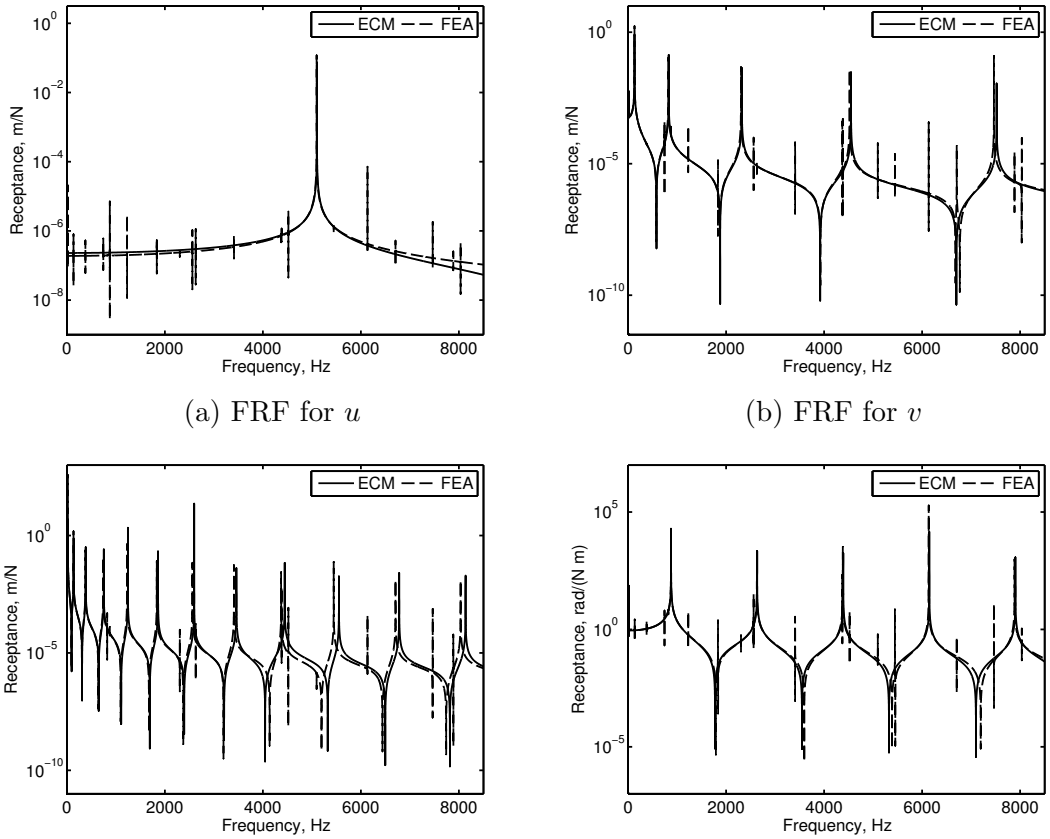

(a) FRF for u

(b) FRF for v

(c) FRF for w

(d) FRF for θ_x

Figure 2.10: FEA and ECM comparison for various coordinates of vibrations for diagonal wrapping pattern and clamped-free boundary conditions.

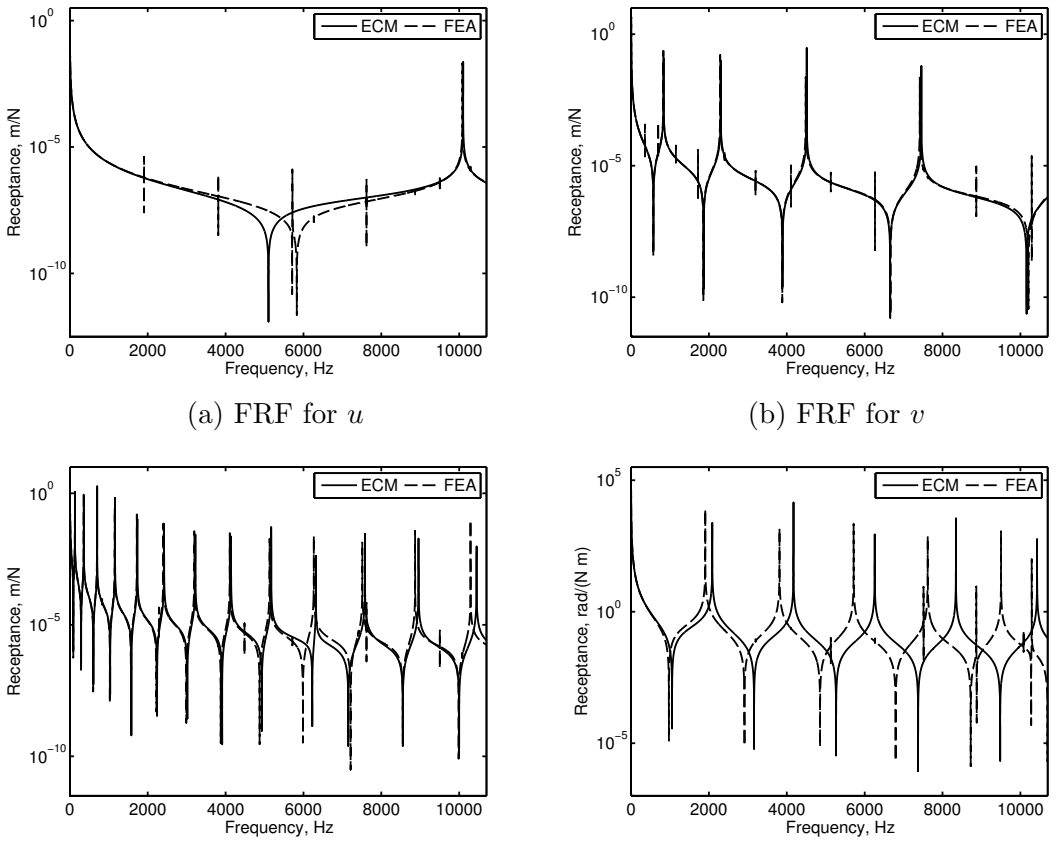

(a) FRF for u

(b) FRF for v

(c) FRF for w

(d) FRF for θ_x

Figure 2.11: FEA and ECM comparison for various coordinates of vibrations for zigzag wrapping pattern and free-free boundary conditions.

Table 2.5: ECM and FEA natural frequency comparison for diagonal wrapping pattern

	Clamped-Clamped			Clamped-Free			Free-Free		
Mode	ECMs	FEA	% Error	ECMs	FEA	% Error	ECMs	FEA	% Error
1	139.440^{w}	137.694	1.268	21.913^{w}	21.601	1.447	0	0	0
2	384.372^{w}	379.461	1.294	132.290^{v}	131.303	0.751	139.440^{w}	137.619	1.323
3	753.522^{w}	743.865	1.298	137.328^{w}	135.458	1.381	384.372^{w}	379.344	1.325
4	841.792^{v}	836.702	0.608	384.524^{w}	379.270	1.385	753.522^{w}	743.542	1.342
5	1245.610^{w}	1229.982	1.271	753.513^{w}	742.982	1.417	841.792^{v}	835.903	0.705
6	1756.371^{θ_x}	1753.708	0.152	829.045^{v}	823.155	0.716	1245.610^{w}	1228.877	1.362
7	1860.727^{w}	1835.913	1.352	878.185^{θ_x}	876.232	0.223	1756.371^{θ_x}	1753.463	0.166
8	2320.433^{v}	2308.340	0.524	1245.611^{w}	1228.341	1.406	1860.727^{w}	1835.565	1.371
9	2598.866^{w}	2564.734	1.331	1860.727^{w}	1834.426	1.434	2320.433^{v}	2303.758	0.724
10	3460.029^{w}	3414.452	1.335	2321.351^{v}	2304.459	0.733	2598.866^{w}	2562.570	1.416
11	3512.742^{θ_x}	3507.539	0.148	2598.866^{w}	2562.053	1.437	3460.029^{w}	3410.339	1.457
12	4444.215^{w}	4370.185	1.694	2634.556^{θ_x}	2628.916	0.215	3512.742^{θ_x}	3507.462	0.151
13	4548.977^{v}	4538.102	0.240	3460.029^{w}	3409.329	1.487	4444.215^{w}	4376.937	1.537
14	5269.113^{θ_x}	5261.555	0.144	4444.215^{w}	4371.849	1.655	4548.977^{v}	4515.121	0.750
15	5551.424^{w}	5457.768	1.716	4390.927^{θ_x}	4381.706	0.210	5269.113^{θ_x}	5260.356	0.166
16	6781.656^{w}	6723.681	0.862	4548.921^{v}	4520.298	0.633	5551.424^{w}	5446.869	1.920
17	7025.484^{θ_x}	7013.803	0.167	5102.937^{u}	5096.335	0.130	6781.656^{w}	6705.625	1.134
18	7519.690^{v}	7478.291	0.554	5551.424^{w}	5445.186	1.951	7025.484^{θ_x}	7016.089	0.134
19	8134.912^{w}	8051.047	1.042	6147.298^{θ_x}	6133.502	0.225	7519.690^{v}	7459.759	0.803
20	8781.855^{θ_x}	8768.383	0.154	6781.656^{w}	6705.958	1.129	8134.912^{w}	8029.230	1.316
21	9611.191^{w}	9490.357	1.273	7519.693^{v}	7464.680	0.737	8781.855^{θ_x}	8769.517	0.141
22	10205.875^{u}	10195.467	0.102	7903.669^{θ_x}	7885.556	0.230	9611.191^{w}	9478.079	1.404
23	10538.226^{θ_x}	10521.267	0.161	8134.912^{w}	8033.647	1.261	10205.875^{u}	10196.258	0.094

Table 2.6: ECM and FEA natural frequency comparison for zigzag wrapping pattern

	Clamped-Clamped			Clamped-Free			Free-Free		
Mode	ECMs	FEA	% Error	ECMs	FEA	% Error	ECMs	FEA	% Error
1	129.929^{w}	128.917	0.785	20.419^{w}	20.253	0.815	0	0	0
2	358.153^{w}	355.295	0.804	127.961^{w}	126.437	1.205	129.929^{w}	128.839	0.846
3	702.123^{w}	695.964	0.885	131.191^{v}	131.055	0.104	358.153^{w}	355.191	0.834
4	834.802^{v}	830.710	0.493	358.295^{w}	355.615	0.754	702.123^{w}	696.364	0.827
5	1160.645^{w}	1151.042	0.834	702.115^{w}	696.884	0.751	834.802^{v}	830.263	0.547
6	1733.804^{w}	1718.793	0.873	822.161^{v}	817.727	0.542	1160.645^{w}	1151.155	0.824
7	2085.798^{θ_x}	1907.211	9.364	1042.899^{θ_x}	950.673	9.701	1733.804^{w}	1719.635	0.824
8	2301.164^{v}	2288.836	0.539	1160.646^{w}	1152.099	0.742	2085.798^{θ_x}	1906.598	9.399
9	2421.594^{w}	2401.263	0.847	1733.804^{w}	1720.919	0.749	2301.164^{v}	2288.556	0.551
10	3224.016^{w}	3196.981	0.846	2302.074^{v}	2289.497	0.549	2421.594^{w}	2401.795	0.824
11	4171.597^{θ_x}	3811.180	9.457	2421.594^{w}	2403.396	0.757	3224.016^{w}	3197.594	0.826
12	4141.069^{w}	4107.860	0.808	3128.698^{θ_x}	2851.785	9.710	4171.597^{θ_x}	3812.610	9.416
13	4511.201^{v}	4486.945	0.541	3224.016^{w}	3200.070	0.748	4141.069^{w}	4106.960	0.831
14	5172.754^{w}	5126.496	0.902	4141.069^{w}	4109.386	0.771	4511.201^{v}	4486.318	0.555
15	6257.395^{θ_x}	5719.805	9.399	4511.146^{v}	4486.384	0.552	5172.754^{w}	5129.743	0.838
16	6319.071^{w}	6263.065	0.894	5214.496^{θ_x}	4751.967	9.733	6257.395^{θ_x}	5717.120	9.450
17	7457.245^{v}	7414.448	0.577	5050.856^{u}	5042.003	0.176	6319.071^{w}	6265.590	0.854
18	7580.019^{w}	7512.293	0.902	5172.754^{w}	5134.339	0.748	7457.245^{v}	7415.624	0.561
19	8343.194^{θ_x}	7621.401	9.471	6319.071^{w}	6268.446	0.808	7580.019^{w}	7512.508	0.899
20	8955.599^{w}	8871.984	0.942	7300.295^{θ_x}	6651.339	9.757	8343.194^{θ_x}	7618.926	9.506
21	10428.992^{θ_x}	9504.009	9.733	7457.248^{v}	7415.723	0.560	8955.599^{w}	8868.434	0.983
22	10101.712^{u}	10080.416	0.211	7580.019^{w}	7519.232	0.808	10428.712^{θ_x}	9502.869	9.746
23	10445.810^{w}	10364.843	0.781	9386.093^{θ_x}	8534.186	9.982	10101.712^{u}	10083.209	0.183

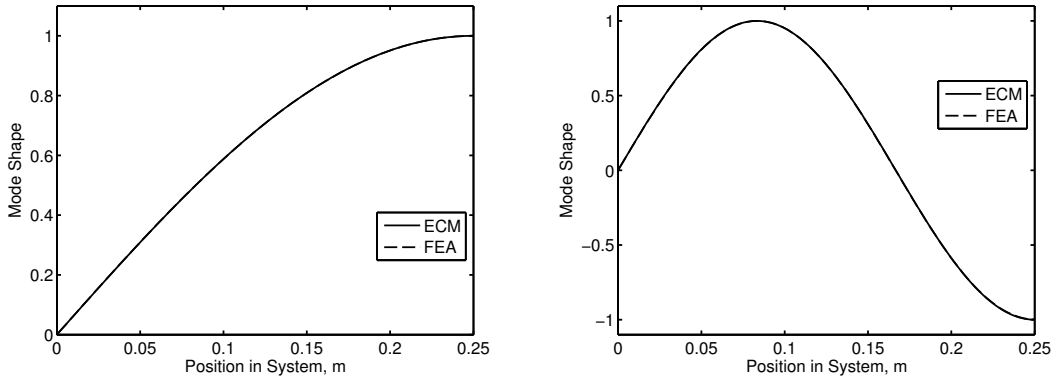

(a) Mode 1 (b) Mode 2

Figure 2.12: FEA and ECM mode shape comparison for u coordinate of vibration for zigzag wrapping pattern and clamped-free boundary conditions.

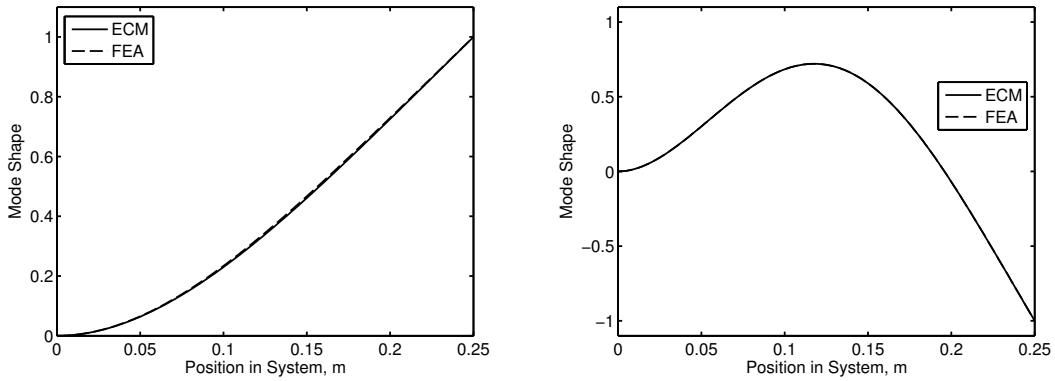

(a) Mode 1 (b) Mode 2

Figure 2.13: FEA and ECM mode shape comparison for v coordinate of vibration for zigzag wrapping pattern and clamped-free boundary conditions.

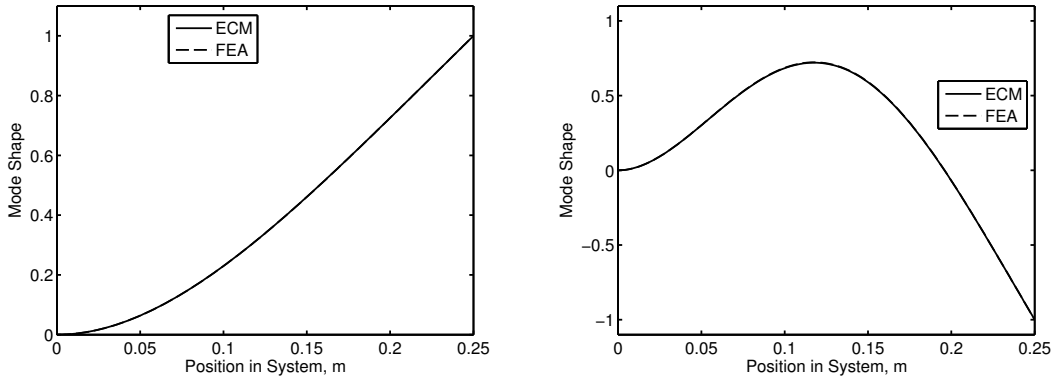

(a) Mode 1 (b) Mode 2

Figure 2.14: FEA and ECM mode shape comparison for w coordinate of vibration for zigzag wrapping pattern and clamped-free boundary conditions.

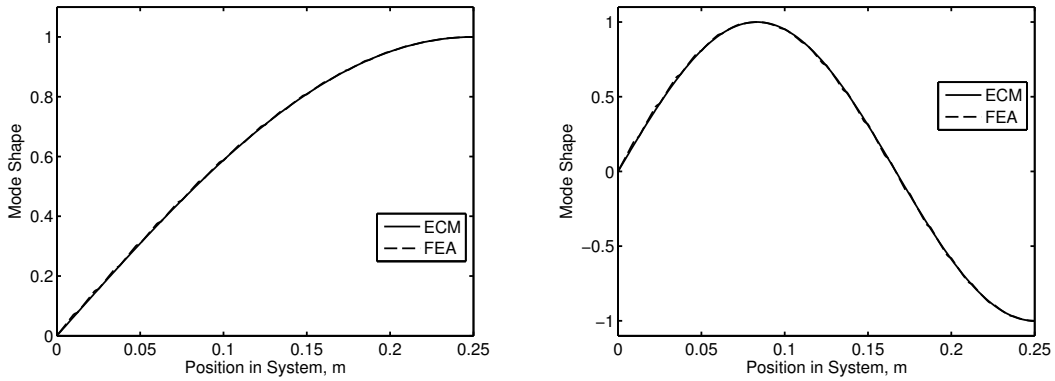

(a) Mode 1 (b) Mode 2

Figure 2.15: FEA and ECM mode shape comparison for θ_x coordinate of vibration for zigzag wrapping pattern and clamped-free boundary conditions.

It can be seen in Figs. 2.10 and 2.11 that the ECM results matches very well with the FEA in its predictions for all the coordinates of vibrations. For the torsional motion, θ_x, in the zigzag wrapping pattern the results exhibit a larger error. This is due to the strain energy derivations for the ECM that will be further discussed. The sharp peaks shown in the FEA pertain to the coupling of the coordinate shown to other coordinates of

vibrations. It should be noted that these frequencies are captured by the ECM for other coordinates as it is also shown in these figures. Additionally, in Tables 2.5 and 2.6 it is noted that the collection of the predicted natural frequencies for all the 4 coordinates of vibrations by ECM match very well with those from the FEA. This further indicates that the decoupled dynamics presented by this ECM for the 4 coordinates of vibrations give an accurate prediction for the dynamics of this system. Further discussions on the limitations of this assumption and how the frequency errors change for various system parameters will follow.

The errors in predicting the natural frequencies for the two transverse vibrations are typically smaller for the zigzag pattern. The higher error in the diagonal wrapping pattern can be attributed to the sections of string that are in the yz-plane, i.e., that do not project longitudinally along the beam. Therefore, as the string mass for those sections are distributed along the fundamental element in the ECM instead of being modelled as lumped masses, this results in slightly higher errors for the diagonal pattern. This is in contrast to the zigzag pattern in which the mass per unit length for the entire system is constant as represented by the coefficient K_1. For the longitudinal motion, u, the error between the ECM and the FEA was similar for both wrapping patterns.

The ECM model also predicts the dynamics of the torsional mode very accurately for the diagonal model however this error appears to increase to around 9% for the zigzag wrapping pattern. The string's stiffening effect varies significantly from the top/bottom to the sides of the beam for the zigzag pattern due to the larger distance from the centre of the beam cross section for the string sections on the sides. As a result, averaging the strain energy of the string within the fundamental elements induces a source of error for the frequency predictions for the torsional mode. Additionally, for the given system parameters the differential torsional strain energy for the string on the side is quite large compared to that of the beam. This can be seen when comparing Eqs. (2.60) and (2.61). In the case of the diagonal wrapping pattern only the section of the string on the top contributes to the torsional strain energy. This means that the differential strain energy due to twist is the same at every point along the system and thus the averaging performed in the homogenization process will yield a more accurate ECM for this wrapping pattern. Figure 2.16 presents the results for the torsional modes for the zigzag pattern for the same beam with a larger thickness to demonstrate how the accuracy of the ECM can be affected once a different set of system parameters is chosen. As it is shown in this figure, for the case of the thicker beam the ECM presents a much better accuracy for the torsional mode.

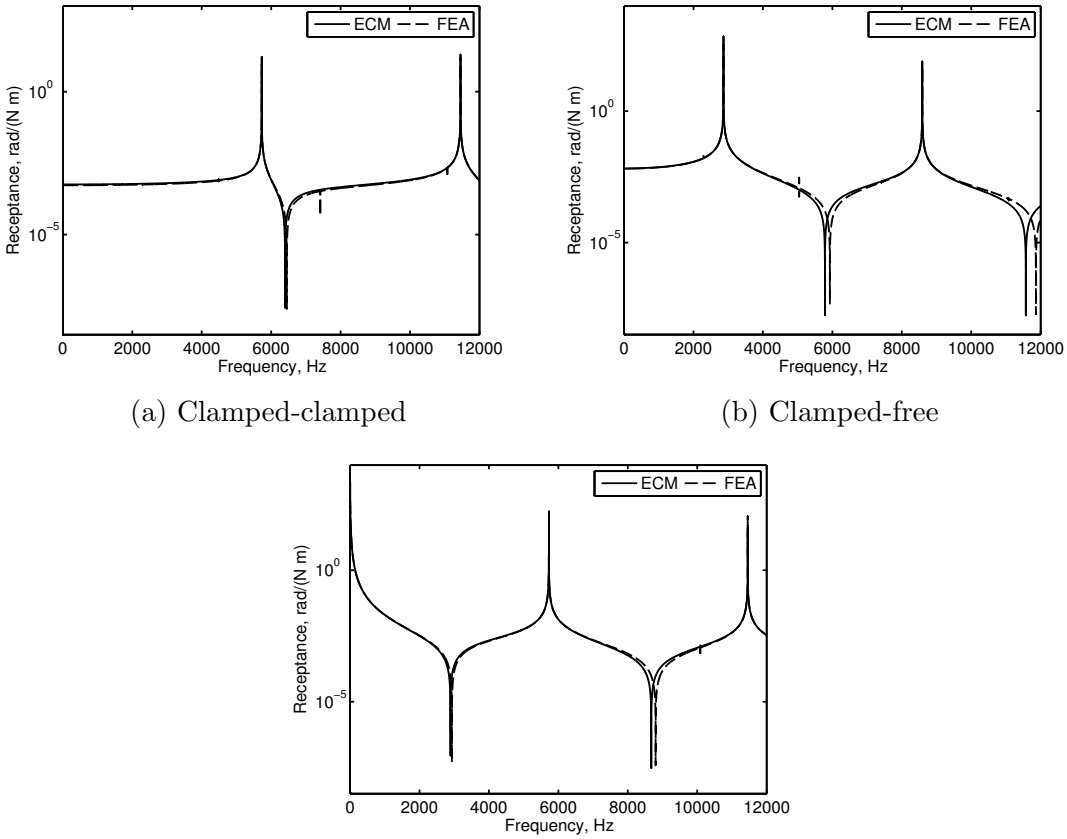

(a) Clamped-clamped

(b) Clamped-free

(c) Free-free

Figure 2.16: FEA and ECM comparison for θ_x coordinate for the zigzag pattern ($b = h =$ 0.01 m).

A major emphasis is placed on the transverse bending w in this work as presented in this section. The FRFs for the ECM model containing the first ten natural frequencies corresponding to non rigid-body motion are presented in Figs. 2.17 and 2.18. Also plotted are the FEA FRF results for the actuation and sensing along the z-axis at the same location as the ECM for both the harnessed beam and an unwrapped beam that is presented by an Euler-Bernoulli (EB) model.

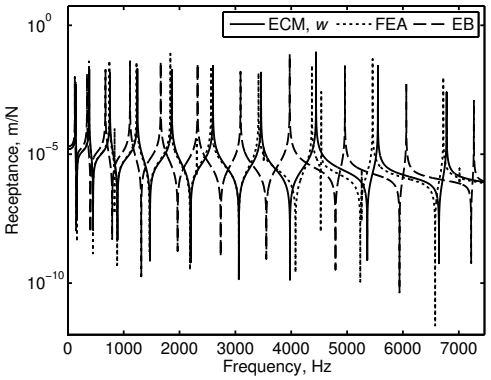

(a) Clamped-clamped

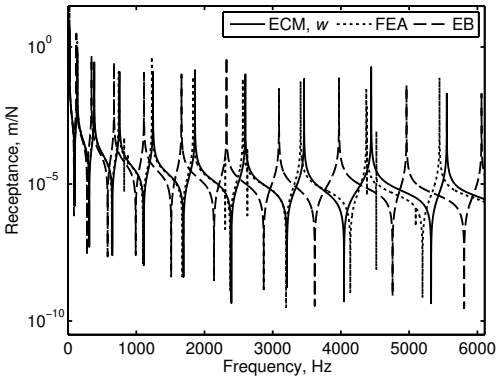

(b) Clamped-free

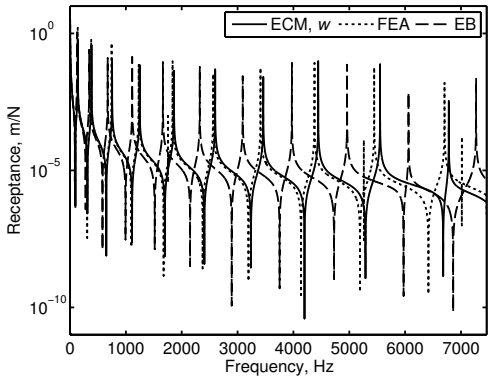

(c) Free-free

Figure 2.17: FRF comparisons between the harnessed and unwrapped beam for diagonal wrapping pattern.

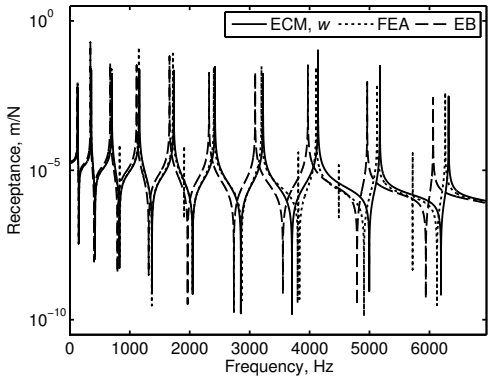

(a) Clamped-clamped

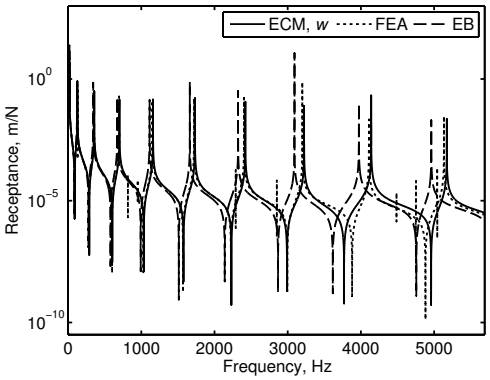

(b) Clamped-free

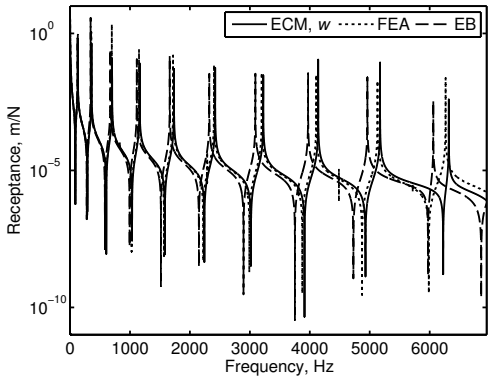

(c) Free-free

Figure 2.18: FRF comparisons between the harnessed and unwrapped beam for zigzag wrapping pattern.

It is observed that the FRFs from the ECM model agree very well with the FEA model. As previously noted, the ECM model over-predicts the natural frequencies of the harnessed system compared to the FEA. The largest absolute percentage of error in predicting the first 10 natural frequencies for the w-coordinate is 1.951% for the diagonal wrapping pattern and 1.205% for the zigzag. Figures 2.17 and 2.18 clearly show the significance of including the string effects in the model.

Homogenization techniques attempt to model the dynamic behaviour of a structure generally of a repeated pattern through some form of approximation for the repeated fundamental element. This method has several advantages compared to FEA and numerical solutions for its simplicity and closed-form solutions that are obtained for the governing

PDEs, as well as significantly smaller computational time. However, dependent upon the geometry of the system the method can become erroneous particularly for the higher modes. One important aspect is to examine the number of fundamental elements per wavelength of the mode of interest. For modes in which the number of fundamental elements per unit wavelength is less than 1, the model essentially becomes inaccurate.

2.3.9 Effects of Pre-Twist on System

In developing the equivalent continuum model for the transverse vibrations it is assumed that the initial twist of the beam due to the wrapped string is negligible. Failure to assume so will result in the violation of the periodicity condition for the structure's geometry that is mandated for obtaining a continuum model. Table 2.7 presents the initial twist experienced by the structure for both wrapping patterns and all the boundary conditions.

Table 2.7: Maximum twist due to pre-tensioned string

Boundary Condition	Diagonal	Zigzag
Clamped-Clamped	0.293°	0.886°
Clamped-Free	0.585°	1.772°
Free-Free	0.585°	1.772°

As it is shown in Table 2.7, the maximum twist value for the zigzag wrapping pattern is always larger than the diagonal wrapping pattern for a given set of boundary conditions. This occurs mainly because for a given number of fundamental elements the wrapping angle in the zigzag pattern is always larger than the diagonal. This results in an overall larger torque for the system with the zigzag pattern. To quantify the impact of the initial twist on the prediction of the natural frequencies and the FRFs for transverse vibrations, two FRFs from FEA simulations are compared in Figs. 2.19 and 2.20. The first is the FRF from the FEA of an initially twisted beam, as presented in section 2.3.7, and the second is the FRF ignoring the initial twist while accounting for the pre-tension in the string. The numeric values for the frequencies for each case are also listed and compared in Tables 2.8 and 2.9.

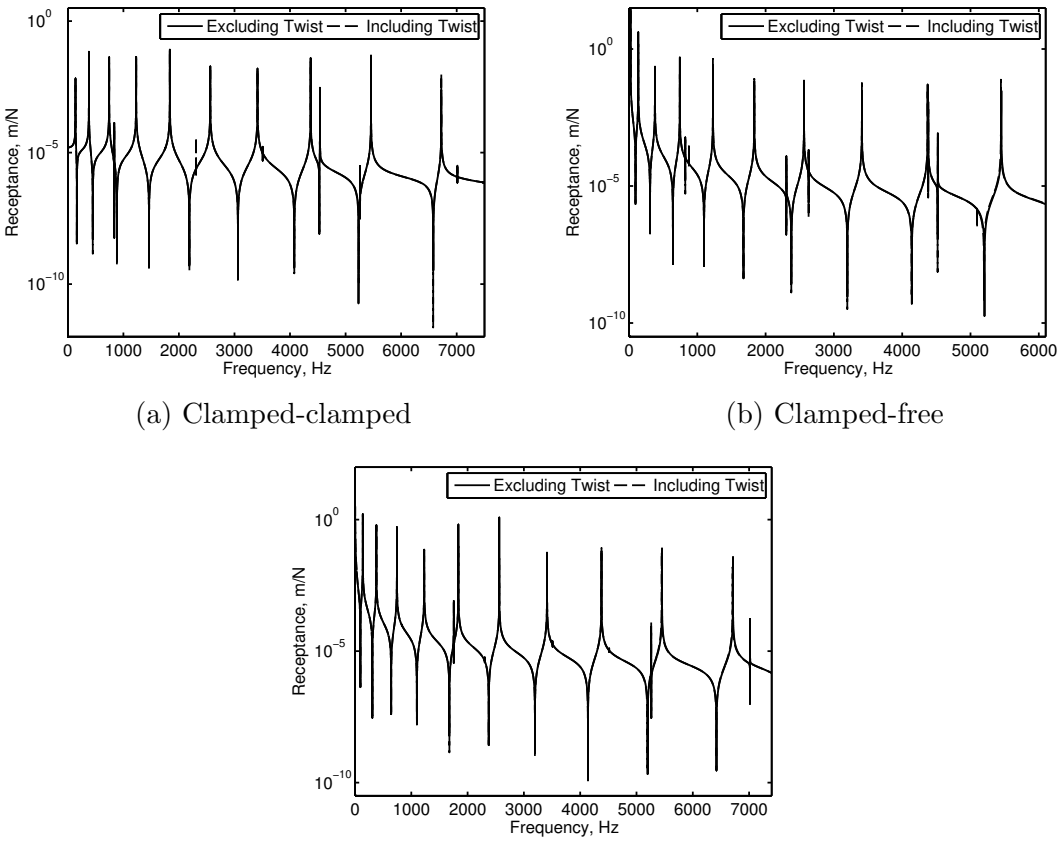

(a) Clamped-clamped

(b) Clamped-free

(c) Free-free

Figure 2.19: Comparisons between FRFs for transverse vibrations, w, including and excluding the initial twist for diagonal wrapping pattern.

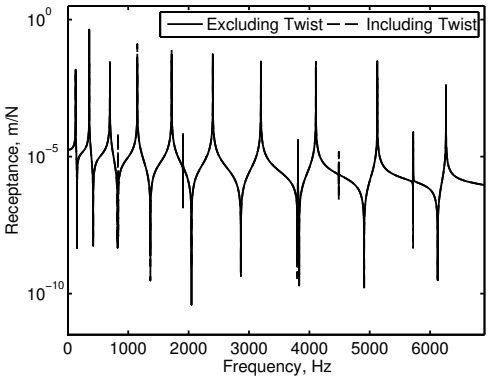

(a) Clamped-clamped

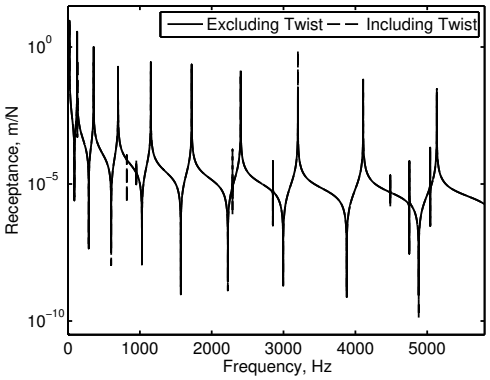

(b) Clamped-free

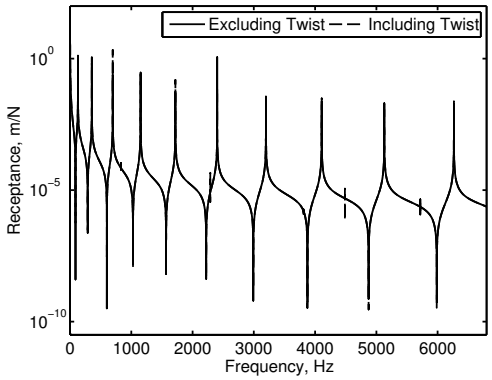

(c) Free-free

Figure 2.20: Comparisons between FRFs for transverse vibrations, w, including and excluding the initial twist for zigzag wrapping pattern.

Table 2.8: FEA natural frequencies including and excluding initial twist for transverse vibrations, w (diagonal wrapping pattern)

	Clamped-Clamped			Clamped-Free			Free-Free		
Mode	No Twist	Twist	% Incr.	No Twist	Twist	% Incr.	No Twist	Twist	% Incr.
1	137.689	137.694	0.004	21.601	21.601	0.000	137.620	137.619	0.000
2	379.454	379.461	0.002	135.593	135.458	-0.100	379.345	379.344	0.000
3	743.926	743.865	-0.008	379.268	379.270	0.001	743.540	743.542	0.000
4	1229.986	1229.982	0.000	742.940	742.982	0.006	1228.866	1228.877	0.001
5	1835.912	1835.913	0.000	1228.351	1228.341	-0.001	1835.534	1835.565	0.002
6	2564.731	2564.734	0.000	1834.378	1834.426	0.003	2562.507	2562.570	0.002
7	3414.446	3414.452	0.000	2562.052	2562.053	0.000	3410.267	3410.339	0.002
8	4370.191	4370.185	0.000	3409.308	3409.329	0.001	4377.147	4376.937	-0.005
9	5457.767	5457.768	0.000	4371.985	4371.849	-0.003	5452.844	5446.869	-0.110
10	6723.603	6723.681	0.001	5451.563	5445.186	-0.117	6712.729	6705.625	-0.106

Table 2.9: FEA natural frequencies including and excluding initial twist for transverse vibrations, w (zigzag wrapping pattern)

	Clamped-Clamped			Clamped-Free			Free-Free		
Mode	No Twist	Twist	% Incr.	No Twist	Twist	% Incr.	No Twist	Twist	% Incr.
1	128.859	128.917	0.045	20.254	20.253	-0.001	128.852	128.839	-0.010
2	355.205	355.295	0.025	126.972	126.437	-0.421	355.224	355.191	-0.009
3	696.284	695.964	-0.046	355.577	355.615	0.011	696.397	696.364	-0.005
4	1151.002	1151.042	0.003	696.766	696.884	0.017	1151.186	1151.155	-0.003
5	1718.696	1718.793	0.006	1151.876	1152.099	0.019	1719.668	1719.635	-0.002
6	2401.084	2401.263	0.007	1720.565	1720.919	0.021	2401.822	2401.795	-0.001
7	3196.748	3196.981	0.007	2402.929	2403.396	0.019	3197.613	3197.594	-0.001
8	4107.487	4107.860	0.009	3199.396	3200.070	0.021	4106.971	4106.960	0.000
9	5126.102	5126.496	0.008	4108.463	4109.386	0.022	5129.738	5129.743	0.000
10	6262.545	6263.065	0.008	5133.215	5134.339	0.022	6265.583	6265.590	0.000

From Figs. 2.19 and 2.20 it can be seen that the FRFs for both FEA simulations are very similar. The largest difference between the frequencies for the FRFs shown is about 0.421% for the system parameters shown. Therefore the assumption of no initial twist in the system when developing the ECM under the given system parameters is appropriate. However, as the initial twist in the system becomes larger it is expected that the ability of the ECM model to accurately predict the natural frequencies of the system will be reduced. In the following section the effects of various string parameters on the errors for frequency estimations for the ECM for w are analyzed. This error is partially attributed to ignoring the initial twist in the homogenized model.

2.3.10 String Parameter Effects Analysis

The natural frequencies related to the w-coordinate of the hybrid system and the string effects on the system's dynamics are considered in this section. Due to the form of the frequencies for the ECM the ratio $\omega_n^{\text{ECM}}/\mu_n^2 = \sqrt{C_1/K_1}$ will be considered in the discussion. This quantity is independent of boundary conditions and mode number, and therefore the conclusions drawn will also be independent of boundary conditions and mode number. The results for a harnessed system assuming a bar element model, as is done in [83, 84], an EB beam model without string harness, and FEA results are also presented for comparison to the presented ECM for w. The results pertaining to the model with bar element assumptions as in [83, 84] are denoted using the abbreviation BAR.

Applying the assumptions and homogenization technique in [83, 84] for the BAR model with the current wrapping patterns yields a PDE for the transverse vibrations, w, and associated boundary conditions similar in form to Eqs. (2.71) and (2.72). The PDE coefficients of the BAR model for the diagonal wrapping pattern can be found as,

$$C_1 = E_b I_{yy} + \frac{E_s A_s h^2 \cos^3(\theta)}{4} \quad , \quad K_1 = \rho_b A_b + \frac{\rho_s A_s \tan(\theta)}{b}\left[\frac{b}{\sin(\theta)} + 2h + b\right]$$

where $L = b/\tan(\theta)$ is the length of a fundamental element. For the zigzag wrapping pattern we get,

$$C_1 = E_b I_{yy} + \frac{E_s A_s h^2 \cos^3(\theta)\,(b + h/3)}{4\,(b+h)} \quad , \quad K_1 = \rho_b A_b + \frac{\rho_s A_s}{\cos(\theta)}$$

where $L = (2b + 2h)/\tan(\theta)$ is the length of a fundamental element. It should be highlighted that the main differences in the current ECM from the BAR model in [83, 84] are the manner in which the strain in the string is defined, the calculation of the wrapping angle, and inclusion of higher-order terms in the displacement field and strain tensor. Furthermore, if the strain and wrapping angle calculation in the BAR model was defined in the same manner as the ECM, then setting the string tension to zero ($T_s = 0$) in the ECM would produce the same PDE as the BAR model. Consequently, a major contribution of this work is that it allows for studying the effects of the tension in the dynamics of the hybrid system.

The first 10 non rigid-body modes for the w-coordinate for all boundary conditions are calculated using the FEA for comparison to the analytical results for the ECM, BAR, and EB models. The maximum and minimum values of the ratio ω_n/μ_n^2 across all the FEA modes will be connected with vertical lines. In the following sections, the values for

ω_n/μ_n^2 for the FEA, ECM, BAR, and EB models are plotted for comparison for various string parameters to evaluate their effects on the overall system dynamics. The system parameters used in the analysis are the same as those presented in Section 2.3.7.

To begin, the effects of varying the number of fundamental elements across the length of the structure are presented in Fig. 2.21. Since the overall length is assumed to be constant, as the number of fundamental elements increases the wrapping angle increases.

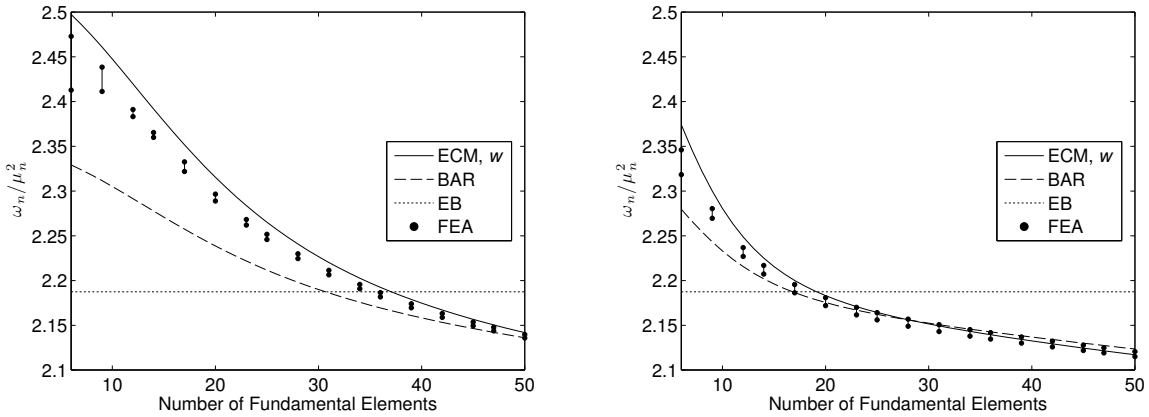

(a) Diagonal (b) Zigzag

Figure 2.21: Frequency effects for variable number of fundamental elements.

To interpret the results from a physical point of view consider the following two extreme cases shown in Fig. 2.22. It is fairly obvious that for the case shown in Fig. 2.43a there will be no changes in the string strain energy as the beam goes through transverse vibrations. Conversely, these changes are at a maximum for the string running along the length of the beam as shown in Fig. 2.43b. Similarly, an increase in the wrapping angle will make the system dynamics similar to the case shown in Fig. 2.43a, which ultimately results in a smaller stiffening effect for the string.

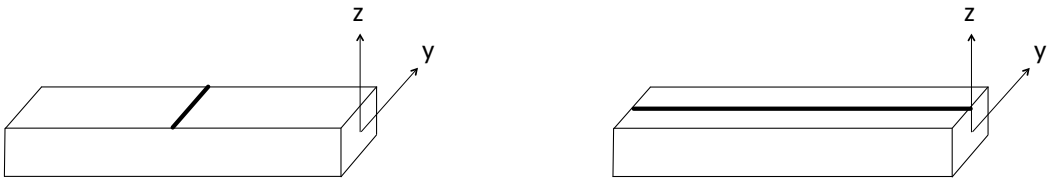

(a) String perpendicular to the longitudinal axis (b) String along the longitudinal axis

Figure 2.22: Extreme cases for a string-harnessed fundamental element.

As such, for a system with a given length the wrapping angle in both diagonal and zigzag wrapping patterns increases as the number of fundamental elements increases, which reduces the string stiffening effect. This results in smaller natural frequencies for the system with a larger number of elements which may not be intuitively obvious at a first glance. Additionally, an increase in the number of fundamental elements results in a larger mass for the string which further reduces the natural frequencies. As the total length of the string increases there is an increase in the total mass added to the hybrid structure. These arguments are supported by the results shown in Fig. 2.21.

The above physical interpretations can also be observed mathematically from the PDE for the ECM and BAR models. As the number of elements increases the wrapping angle θ increases, which results in reducing $\cos(\theta)$ and increasing $\tan(\theta)$. For both the ECM and BAR models this results in a decrease in the C_1 coefficient, which reduces the string stiffening effect. Likewise, for both models, the K_1 coefficient depends inversely on $\cos(\theta)$ and for the diagonal wrapping patterns also on $\tan(\theta)$. This means that K_1 increases as the number of elements increases; this corresponds to additional mass for the system due to an increase in the string length. Consequently, the quantity $\sqrt{C_1/K_1}$ decreases, which results in smaller frequencies as the number of fundamental elements increases, as is observed in Fig. 2.21.

The frequency changes are more obvious for a smaller number of elements and become less significant for a larger number of fundamental elements. The frequencies of the diagonal wrapping pattern are larger than those of the zigzag wrapping pattern for a given number of fundamental elements as the wrapping angle is smaller in the diagonal wrapping pattern. This results in a larger stiffening effect for the diagonal system and subsequently higher frequencies. As it can be seen the ECM and the FEA results are in very good agreement. The accuracy of the model prediction increases as the number of fundamental elements increases. Furthermore, as the number of fundamental elements increases the difference between the maximum and minimum frequency parameters for the FEA shown in Fig. 2.21 decreases and becomes closer to the single predicted values by the analytical model. This is

expected due to the increase in the number of elements per wavelength for each frequency producing ECM results with better accuracy. For the simulations presented the largest absolute percentage of error between the FEA and ECM are 3.503% and 2.407% for the diagonal and zigzag wrapping patterns, respectively. Also, the largest absolute percentage of error between the FEA and the BAR are 5.813% and 2.827% for the diagonal and zigzag wrapping pattern, respectively. For the simulations presented the maximum twist angle for the diagonal wrapping pattern varies between 0.185° and 0.674°for CC boundary conditions for the range of number of fundamental elements between 6 and 50. These values are about 0.370° and 1.347° for CF and FF boundary conditions. For the zigzag wrapping pattern these maximum twist angle values become 0.649° and 1.211° for CC boundary conditions and 1.299° and 2.422° for CF and FF boundary conditions.

Next the effect of string modulus is investigated and the results are presented in Fig. 2.23. As expected, and also supported by the results shown in Fig. 2.23, increasing the string modulus results in a stiffer system and subsequently higher natural frequencies for all models. The results presented in Fig. 2.23 can also be interpreted from the mathematical expressions derived for $\sqrt{C_1/K_1}$ for the ECM and BAR models. Since the string modulus, E_s, only appears linearly in the C_1 terms and not in the K_1 term, this supports that the quantity $\sqrt{C_1/K_1}$ is increasing as the modulus of the string increases, thus giving higher natural frequencies for the harnessed system.

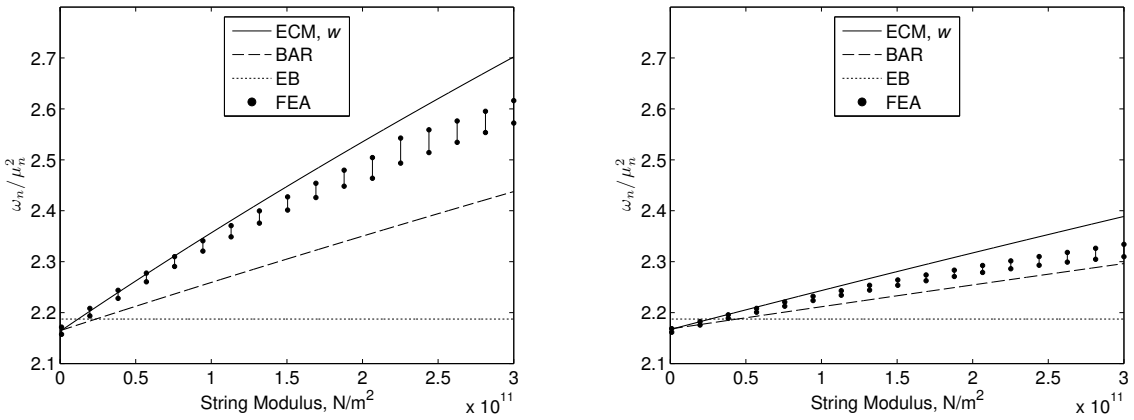

(a) Diagonal (b) Zigzag

Figure 2.23: Frequency effects for variable string modulus.

It is shown in Fig. 2.23 that for very small values of string modulus, the harnessed system has smaller natural frequencies than the beam with no harness. This is because

for sufficiently small values of modulus the mass effect of the string becomes dominant, which results in smaller frequencies than the EB model. It is observed in Fig. 2.23 that the plot for the diagonal wrapping pattern has a larger slope than the zigzag wrapping pattern. This is due to the wrapping angle being smaller for the diagonal wrapping pattern as discussed previously. This smaller angle results in both larger frequencies and a larger rate of increase for the frequencies as the string modulus increases for this pattern.

It is shown that the diagonal and zigzag wrapping patterns for the ECM agree very well with the FEA for smaller string moduli and begin to diverge as the string modulus increases. As the string modulus increases there is an increased coupling effect between the coordinates of vibrations that results in a higher error for the ECM. The coupling terms can be seen in the expression for the differential strain energy for the FEA shown in Appendix A. The largest error in the natural frequency estimations for the transverse vibrations, w, is about 5.052% for the diagonal and 3.417% for the zigzag. These error values for the BAR model are about 6.825% and 1.622%, respectively.

In Fig. 2.24 the natural frequencies versus string density are presented. As expected, increasing the string density lowers the natural frequencies for both wrapping patterns and models. Also, in the analytical expressions the density of the string only plays a role in the K_1 coefficients. Since K_1 depends linearly on ρ_s an increase in the string density increases K_1. This causes $\sqrt{C_1/K_1}$ to decrease as observed in Fig. 2.24.

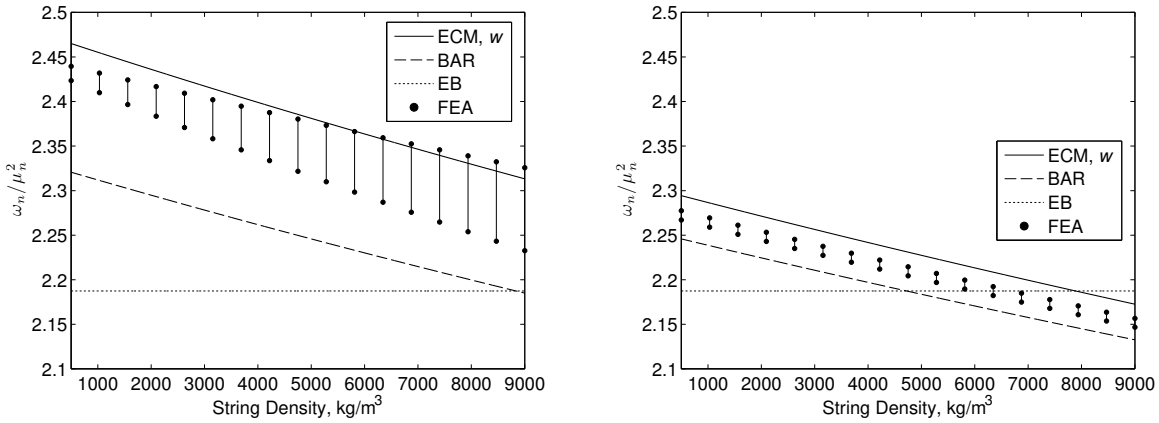

(a) Diagonal (b) Zigzag

Figure 2.24: Frequency effects for variable string density.

It should be noted that the diagonal wrapping pattern has a slightly larger string

length compared to the zigzag wrapping pattern for a given number of elements. This additional string mass will result in a slightly higher decay rate in the frequencies for the diagonal wrapping pattern as the string density increases. This is clearly shown in Fig. 2.24. However, the stiffening effect of the string is more dominant for both patterns, which is the reason for having overall higher frequencies compared to the EB model (beam with no string). Therefore, the smaller angle for the diagonal wrapping pattern results in a larger stiffening effect that ultimately results in higher frequencies for this pattern compared to the zigzag wrapping pattern despite the slightly higher total string mass for this pattern.

In Fig. 2.24 we see that the ECM over-predicts the FEA results in both wrapping patterns. For the diagonal wrapping pattern there is an increasing difference between the maximum and minimum values for the frequency parameter ω_n/μ_n^2 for the FEA. This is due to the mass for the string segment on the yz-plane being averaged over the fundamental element for this pattern instead of being modelled as a lumped mass. For the zigzag wrapping pattern the mass per unit length in the homogenized ECM and FEA models is equal thus the results are in better agreement. The range between the minimum and maximum FEA values is a result of the ratio ω_n/μ_n^2 varying across the modes for a given set of boundary conditions. The maximum absolute percentage of error between the FEA and ECM model is 3.609% and 1.205% for the diagonal and zigzag wrapping patterns, respectively. Also, the maximum absolute percentage of error between the FEA and BAR model is 6.050% and 1.389% for the diagonal and zigzag wrapping patterns, respectively.

The increasing error for the ECM with respect to the FEA for the diagonal wrapping pattern as the string density increases clearly indicates a need for a more accurate model due to the additional lumped mass for the string sections on the yz-plane shown in Fig. 2.2a. This states that the assumptions that result in constant coefficients for the beam-like ECM need to be further improved for much higher string density values.

Next, the effects of string radius are considered and the results presented in Figs. 2.25 and 2.26. The string radius plays a role in both the stiffness and mass of the hybrid system. As the string radius increases, the total strain energy in the system increases and will consequently increase the natural frequencies. However, an increase in the string radius will result in a larger mass for the system that will lower the frequencies. Figure 2.25 shows that the stiffening effect is more dominant.

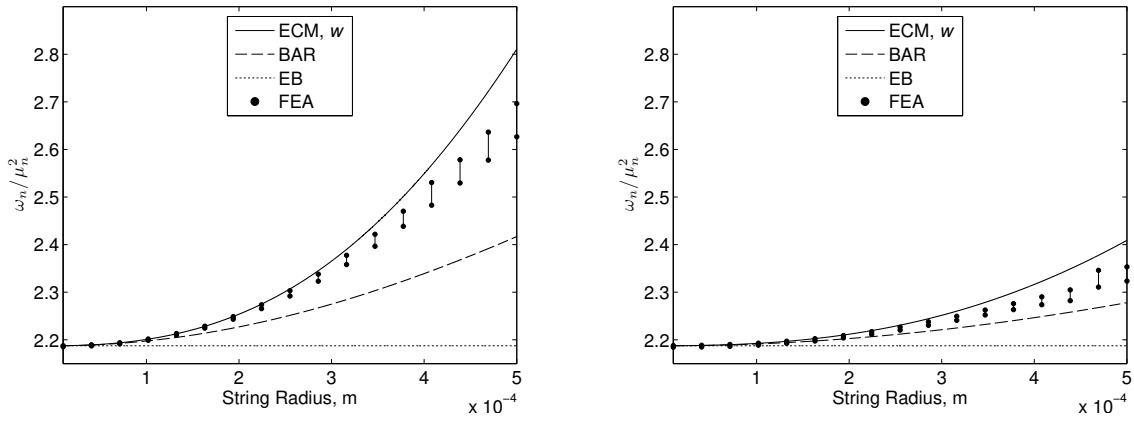

(a) Diagonal (b) Zigzag

Figure 2.25: Frequency effects for variable string radius, $\rho_s = 1400$ kg/m^3.

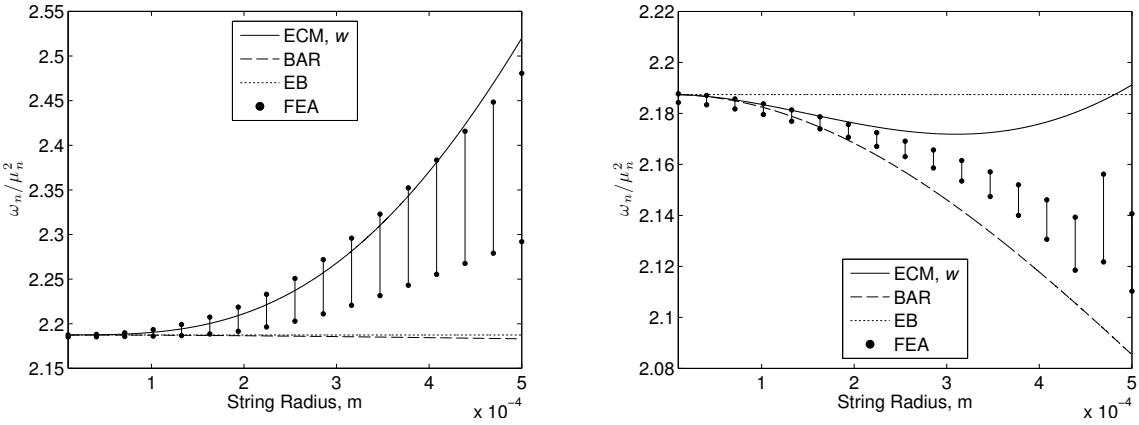

(a) Diagonal (b) Zigzag

Figure 2.26: Frequency effects for variable string radius, $\rho_s = 9000$ kg/m^3.

As shown in Fig. 2.25 the diagonal wrapping pattern has a more drastic change in frequencies as the radius increases when compared to the zigzag wrapping pattern. This is again due to the wrapping angle for the diagonal wrapping pattern being smaller than the zigzag wrapping pattern that results in stronger stiffening effects for the string. Figure 2.25 also shows that the frequencies obtained from the ECM are always greater than the BAR

model. Also, the ECM frequencies increase at a faster rate than the BAR model as the string radius increases. The maximum errors between the FEA and ECM in Fig. 2.25 for the diagonal and zigzag wrapping patterns are 7.006% and 3.685%, respectively. The maximum errors between the FEA and BAR for the diagonal and zigzag wrapping patterns are 10.360% and 3.338%, respectively.

For comparison consider a system in which the density of the string is increased from $\rho_s = 1400$ kg/m^3 to $\rho_s = 9000$ kg/m^3. It can be seen from Fig. 2.26 that the zigzag and diagonal wrapping patterns exhibit different behaviours as the string radius increases. This difference stems from the zigzag wrapping pattern being more affected by added mass than the diagonal system. As discussed previously, the larger angle for the zigzag wrapping pattern will reduce the string stiffening effects for this pattern. Therefore, the two wrapping patterns experience a different rate of change of frequencies as seen in Figs. 2.26a and 2.26b. The maximum errors between the FEA and ECM in Fig. 2.26 for the diagonal and zigzag wrapping patterns are 9.950% and 3.835%, respectively. The maximum errors between the FEA and BAR for the diagonal and zigzag wrapping patterns are 11.996% and 2.808%, respectively.

In Figs. 2.25 and 2.26 it is observed that the difference between the maximum and minimum values for the frequency parameters ω_n/μ_n^2 is larger for the diagonal pattern compared to the zigzag for the FEA. As was the case with varying string density, this larger difference is due to the fact that the diagonal wrapping pattern has sections of string that are only in the yz-plane. The increasing error for the ECM with respect to the FEA as the string radius increases indicates a need for a more accurate model for larger values of string radius. It should be noted for the BAR model that as the radius increases the model tends toward a constant value. This makes the ECM model a more accurate model when compared to the BAR. Also, the coupling terms presented in the strain energy expression for the FEA in Appendix A depend on E_sA_s and T_s. Therefore, increasing any of these parameters will result in a larger coupling between different coordinates of vibrations that result in a larger error for the ECM model. This is clearly shown in Figs. 2.25 and 2.26.

Looking into the analytical model for the ECM wrapping patterns, we can see how the string radius plays a role in the stiffness and mass coefficients C_1 and K_1, respectively. In the C_1 coefficient r_s affects the cross-sectional area A_s, the constants $\overline{h}$ and $\overline{b}$, as well as the wrapping angle θ. For an increasing r_s there will be an increase in A_s, $\overline{h}$, and $\overline{b}$ and a decrease in $\cos(\theta)$. It cannot be concluded if C_1 will be increasing or decreasing for changing radius as it will depend on the system parameter values. However, in the K_1 coefficients, an increase in the radius always causes an increase in K_1. Therefore, the changes of $\sqrt{C_1/K_1}$ could not be directly determined as also supported by the differences in Figs. 2.25 and 2.26.

Lastly, the effects of tension in the harnessing string on the natural frequencies are presented in Figs. 2.27 and 2.28. From a physical point of view it is expected that an increase in tension should increase the frequencies of the system. This behaviour is observed in Fig. 2.27, and is more dominant in Fig. 2.28.

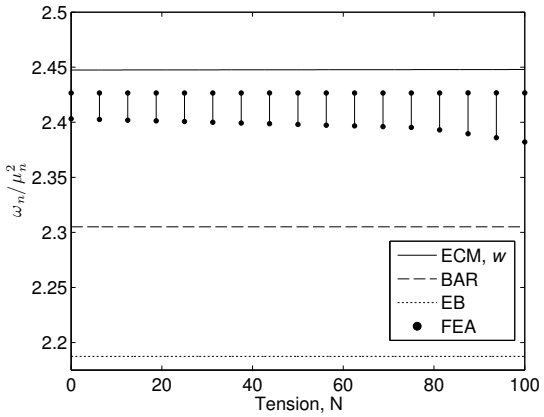

(a) Diagonal

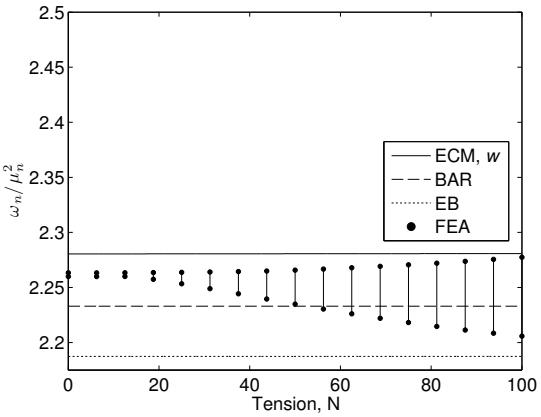

(b) Zigzag

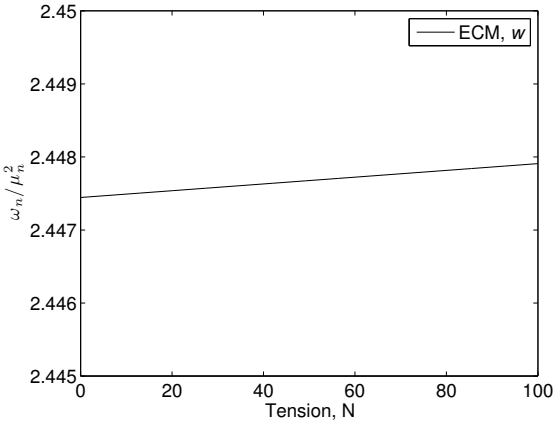

(c) Diagonal, zoom-in

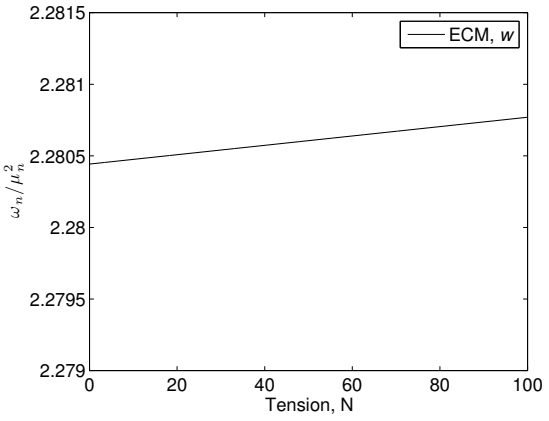

(d) Zigzag, zoom-in

Figure 2.27: Frequency effects for variable string tension, $E_b = 6.89 \times 10^{10}$ N/m^2, $E_s = 1.5 \times 10^{11}$ N/m^2, $r_s = 0.00035$ m, $G_b = 2.6 \times 10^{10}$ N/m^2.

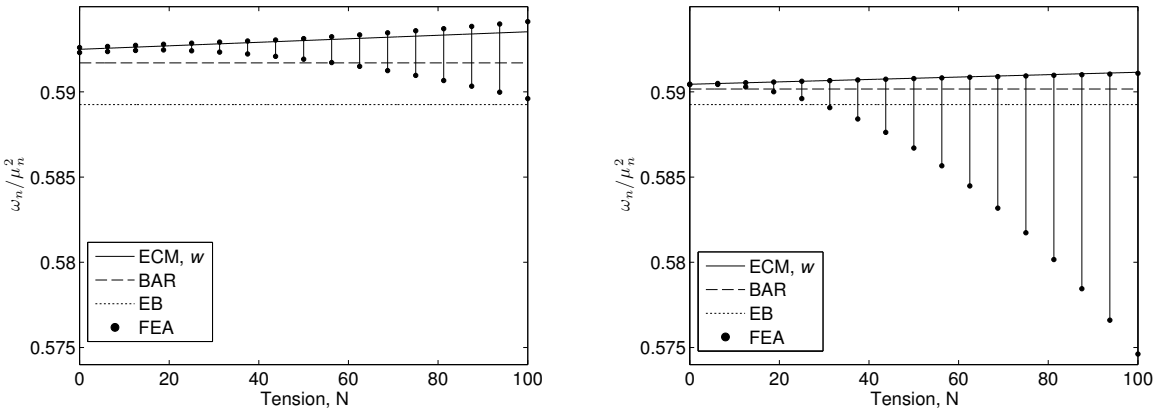

(a) Diagonal

(b) Zigzag

Figure 2.28: Frequency effects for variable string tension, $E_b = 5 \times 10^9$ N/m^2, $E_s = 1 \times 10^{10}$ N/m^2, $r_s = 0.0001$ m, $G_b = 1 \times 10^{12}$ N/m^2.

As shown in Figs. 2.27 and 2.28, the degree to which the string tension impacts the hybrid system's natural frequencies depends on the system parameters, most importantly the bending stiffness of the beam, string modulus, shear modulus, and string radius. As shown in these figures, tension plays an important role in the dynamics of the harnessed system particularly for the higher modes. Inclusion of this effect is an advantage of the modelling technique presented in this paper compared to the previously established BAR model. In Fig. 2.27 the largest absolute error between the FEA and the ECM was 2.763% and 3.400% for the diagonal and zigzag wrapping patterns, respectively. Also, the largest absolute error between the FEA and the BAR model was 5.011% and 1.948% for the diagonal and zigzag wrapping patterns, respectively. In Fig. 2.28 the largest absolute error between the FEA and the ECM was 0.665% and 2.877% for the diagonal and zigzag wrapping patterns, respectively. The largest absolute error between the FEA and the BAR model was 0.408% and 2.706% for the diagonal and zigzag wrapping patterns, respectively.

Comparing Figs. 2.27 and 2.28, the difference between the maximum and minimum values for the FEA is smaller in Fig. 2.28 than in Fig. 2.27. In Fig. 2.28 the modulus of the string and the radius of the string were both decreased. This means that the effect of the string on the hybrid system will be dominated by the dynamics of the beam. Therefore we expect the hybrid system to behave similarly to an EB beam and thus the ratio ω_n/μ_n^2 will not vary much across the modes.

Although in the BAR model the assumption of a pre-tensioned string was employed,

due to the exclusion of the higher-order terms in the displacement field and the strain tensor the natural frequencies do not depend on tension. The pre-tension in the BAR model only appears in the non-homogeneous boundary conditions in a similar manner to the ECM where the coefficient C_2 depends on tension. As a result, the frequencies of the BAR model are not affected by pre-tension. The larger frequencies and their higher rate of increase due to an increase of tension for the diagonal wrapping pattern compared to the zigzag wrapping pattern are due to the wrapping angle being smaller for the diagonal wrapping pattern, as discussed previously in this paper. For both Figs. 2.27 and 2.28 it can be observed that the results from the ECM and FEA models are in good agreement. Also, from the expression for C_1 for the wrapping patterns of the ECM, we see that it depends linearly on T_s. Therefore, an increase in the tension increases the value for C_1 and subsequently $\sqrt{C_1/K_1}$, thus increasing the system's natural frequencies.

In Figs. 2.27 and 2.28 it can be seen that for smaller values of tension the ECM predicts the FEA results very well. As the string tension increases the errors between the FEA and ECM increase dramatically. This is due to a larger initial twist in the beam when the string tension is increased. This effect is more highlighted in the zigzag pattern due to the larger string angle. For system parameters shown in Fig. 2.27 the maximum initial twist angle for the diagonal wrapping pattern is 1.170° for CC boundary conditions and 2.341° for CF and FF boundary conditions. These values become 3.544° and 7.087° respectively for the zigzag pattern. For the system parameters shown in Fig. 2.28 these twist angles are 0.023° and 0.045° for the diagonal pattern and 0.071° and 0.141° for the zigzag pattern.

In summary, for a beam structure of a given length an increase in the number of fundamental elements or the string density results in smaller frequencies. Also, an increase in the string modulus or the tension causes an increase in the frequencies. Finally, the effect of string radius on a system's natural frequencies is undetermined as other system parameters will define the dominance of either the stiffening or density effect of the string. Furthermore, the frequencies of the ECM are typically larger than the BAR model developed in [83, 84]. Exceptions occurred for large numbers of fundamental elements. Among major contributions of the current modelling technique compared to the previously developed BAR model by the authors are utilization of the higher-order Green-Lagrange instead of the infinitesimal strain tensor to obtain a higher accuracy, the dependence of the system's dynamics on the string tension, as well as the inclusion of the compression in the beam due to the string tension.

2.4 Experimental Results

The final section concerning periodic wrapping patterns is the experimental validation of the homogenized model developed for string-harnessed beam structures. The FRFs and natural frequencies obtained from the model are compared to those from experiments. Various system configurations with clamped-free boundary conditions and a constant wrapping angle, the zigzag wrapping pattern, are considered for comparison.

2.4.1 Analytical Model Details

The analytical model for the zigzag wrapping pattern was determined in Section 2.3.5 and given in Eqs. (2.71) and (2.72) using the coefficients listed in Eqs. (2.67). The PDE for the free transverse vibrations with clamped-free boundary conditions is presented below.

$$C_1 \frac{\partial^4 w}{\partial x^4} + K_1 \frac{\partial^2 w}{\partial t^2} = 0 \tag{2.90}$$

$$w\left(0,t\right) = 0 \quad , \quad \frac{\partial w}{\partial x}\left(0,t\right) = 0 \quad , \quad \frac{\partial^2 w}{\partial x^2}\left(l,t\right) = 0 \quad , \quad \frac{\partial^3 w}{\partial x^3}\left(l,t\right) = 0 \tag{2.91}$$

The natural frequencies of the system were found as

$$\omega_n = \beta_n^2 \sqrt{\frac{C_1}{K_1}} \tag{2.92}$$

where $\beta_n = \left(\beta l\right)_n / l$ and $\left(\beta l\right)_n$ represents the n^{th} solution to the characteristic equation $0 = 1 + \cos(\beta l)\cosh(\beta l)$. For each frequency ω_n, the corresponding mass normalized mode shape is

$$\phi_n(x) = A_n \left\{\cos(\beta_n x) - \cosh(\beta_n x) - k_n \left[\sin(\beta_n x) - \sinh(\beta_n x)\right]\right\} \tag{2.93a}$$

$$k_n = \frac{\cos(\beta_n l) + \cosh(\beta_n l)}{\sin(\beta_n l) + \sinh(\beta_n l)} \tag{2.93b}$$

$$\beta_n^4 = \frac{K_1 \omega^2}{C_1} \tag{2.93c}$$

$$A_n = \left(K_1 \int_0^l \left(\cos(\beta_n x) - \cosh(\beta_n x) - k_n \left[\sin(\beta_n x) - \sinh(\beta_n x)\right]\right)^2 \, \mathrm{d}x \right)^{-1/2} \tag{2.93d}$$

The mass-normalization conditions are given by

$$\int_0^l K_1 \phi_i(x) \phi_j(x)\, \mathrm{d}x = \delta_{ij} \tag{2.94}$$

$$\int_0^l C_1 \phi_i(x) \frac{\mathrm{d}^4 \phi_j}{\mathrm{d}x^4}(x)\, \mathrm{d}x = \omega_i^2 \delta_{ij} \tag{2.95}$$

The above results are obtained by setting $C_2 = C_4 = 0$ in Eqs. (2.33)-(2.37).

During experiments, the clamped end of the string-harnessed system is fixed to the shaker. The FRF of the system was determined in Section 2.2.1 and is listed below. ω_s denotes the driving frequency of the shaker and x is the sensing location measured from the clamped end.

$$H(x, \omega_s) = \left| \frac{1}{\omega_s^2} + \sum_{i=1}^{\infty} \frac{\overline{\phi}_i \phi_i(x)}{\omega_i^2 - \omega_s^2} \right| \tag{2.96a}$$

$$\overline{\phi}_i = K_1 \int_0^l \phi_i(x)\, \mathrm{d}x \tag{2.96b}$$

2.4.2 Unwrapped Beam Experimental and Analytical FRFs

The experimental setup outlined in Section 2.2.2 is also used for the experimental results presented in the current section. An aluminium alloy 6061 beam specimen is used as the host structure. Two beams with different dimensions are used and referred to as beam 1 and beam 2. Beam 1 has 0.01306 m width, 0.00216 m thickness, and 0.3099 m length while beam 2 has 0.01306 m width, 0.00146 m thickness, and 0.2510 m length. The modulus for the aluminium alloy 6061 is 68.9 GPa and the density is 2768 kg/m^3. These values are listed in Table 2.10.

Table 2.10: Beam material and geometric properties

Beam property	Beam 1	Beam 2
Beam width, m	0.01306	0.01306
Beam thickness, m	0.00216	0.00146
Beam modulus, GPa	68.9	68.9
Beam density, kg/m^3	2768	2768
Beam length, m	0.310	0.251

As an initial step, the experimental FRFs for the host structures only, i.e., an unwrapped beam, are compared to the analytical FRFs using an undamped Euler-Bernoulli (EB) beam model. The results are presented in Fig. 2.29 and the natural frequencies for the analytical and experimental results are listed in Table 2.11. The sensing location for the FRF measurements is at 0.021 m from the clamp end for beam 1 and 0.052 m for beam 2. The measurement locations are chosen so that they do not coincide with any node of the first six modes within the frequency range of interest. The distances between the closest node of a mode to the sensing locations are about 0.049 m and 0.005 m for beams 1 and 2, respectively.

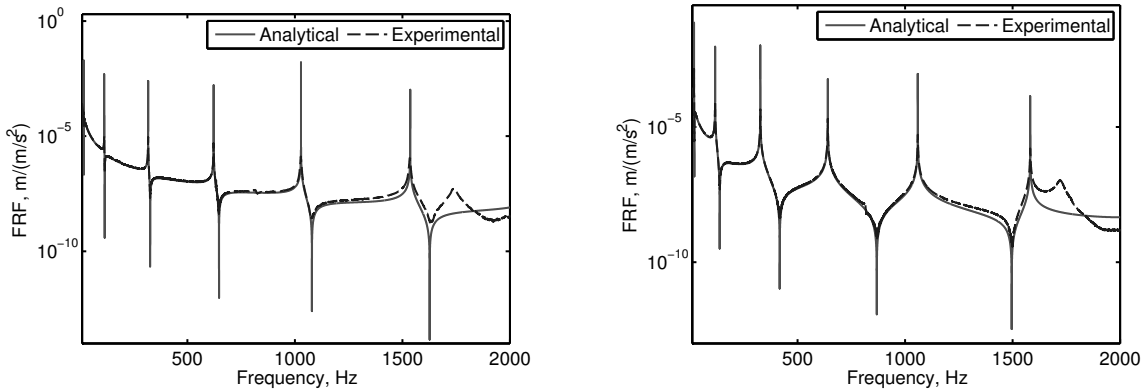

(a) Beam 1 (b) Beam 2

Figure 2.29: Analytical and experimental FRFs for the unwrapped beams.

Table 2.11: Experimental and analytical frequencies, in Hz, for the unwrapped beams

	Mode					
Result	1	2	3	4	5	6
			Beam 1			
Experiment	18.00	112.97	317.50	621.55	1027.5	1534.5
EB Model	18.09	113.39	317.50	622.17	1028.5	1536.4
Error, %	0.5	0.37	0	0.10	0.097	0.12
			Beam 2			
Experiment	18.58	116.50	326.95	640.45	1059.3	1582.1
EB Model	18.64	116.79	327.01	640.81	1059.3	1582.4
Error, %	0.3	0.25	0.02	0.056	0	0.02

As it is observed in Fig. 2.29, the analytical FRFs match with those of the experiments quite well. This is expected considering the large length-to-thickness ratio for both of these beams. As shown in Table 2.11, there is good agreement between the analytical model and the experimental natural frequencies. As expected, the analytical model over-predicts the frequencies due to exclusion of shear or rotary inertia effects in the model.

It should be noted that the peaks at approximately 1,700 Hz in Fig. 2.29 do not represent a resonant mode in the beam of interest. In the experimental setup there is approximately a 0.01 m length of beam extending beyond the clamp as seen in Fig. 2.4. The 1,700 Hz frequency shown pertains to the fundamental mode of the extended section and is the cause for this additional peak shown in the FRFs for both beams. For this reason the additional peak is not predicted by the analytical model. This point is further discussed in the following section.

High Frequency Peak

To investigate the high frequency peak that appears after the sixth mode in the experimental results, FRF measurements were made at the 2 sensing locations shown in Fig. 2.30. The FRF results are shown in Fig. 2.31.

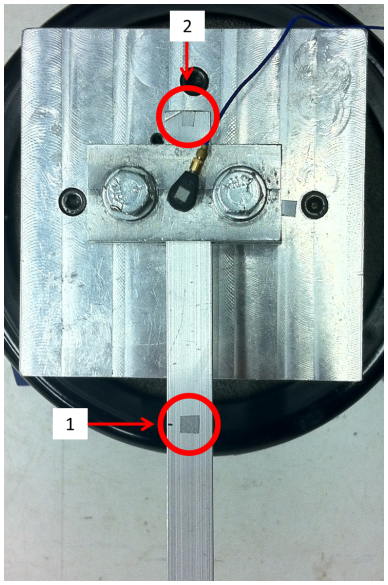

Figure 2.30: Additional sensing locations.

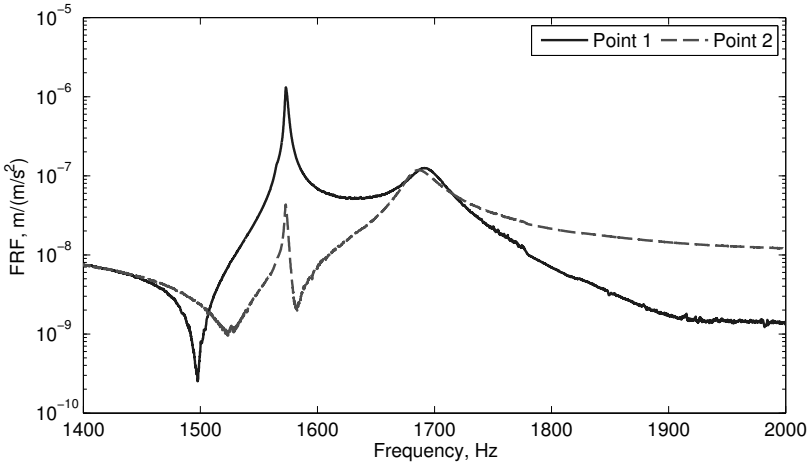

Figure 2.31: Zoom in plot of the high frequency peak at 2 sensing locations.

As the shaker provides excitation to the beam, both sections of the beam extending beyond the clamp are excited. As shown in the FRF plot for point 2, located on the short extended section on the opposite side of the beam in this study, the peak around the 1,700 Hz is the most conspicuous in this plot. This indicates that the frequency of 1,700 Hz is the fundamental frequency for the short extended section. As such it is not captured by the model presented for the long section that is of interest for this paper; even though, this peak also appears in all the FRF plots for the longer section of the beam. Also, the peak just below 1,600 Hz in this plot pertains to the 6^{th} bending mode for the long section as also shown in the FRF plot for point 1.

2.4.3 String-Harnessed System Experimental and Analytical FRFs

For the string-harnessed system experimental tests, two different types of fishing line are used for the strings. The first string is a SpiderWire Stealth Braid 50 pound break strength fishing line and the second is a PowerPro Super 8 Slick 80 pound break strength fishing line; the material properties are listed in Table 2.12. The modulus of each fishing line was determined experimentally by performing a tension test. Table 2.12 also presents the details of the test setups used for each harnessed beam. The sensing locations shown are measured from the clamped end.

Table 2.12: String-harnessed system test setups

	Test				
Setup property	1	2	3	4	5
Beam	Beam 1	Beam 1	Beam 1	Beam 1	Beam 2
String type	Spider Wire	Power Pro	Power Pro	Power Pro	Power Pro
String radius, mm	0.17018	0.20955	0.20955	0.20955	0.20955
String modulus, GPa	62.43	128.04	128.04	128.04	128.04
String density, kg/m^3	1271	1400	1400	1400	1400
Pretension per string, N	8.3	8.3	40.0	8.3	13.3
Number of strings Used	1	1	1	1	3
Number of Fundamental Elements	5	5	5	15	5
Sensing location, m	0.021	0.021	0.021	0.021	0.052

In tests 1-4 beam 1 is used as the host structure while other system parameters change during these tests. This allows for a fair comparison between these tests to validate the ability of the proposed model. Test 5 is performed on a different host structure (beam 2) along with multiple strings harnessing the system and a higher total value of pretension. The purpose of this test is to demonstrate the significance of this model due to the larger differences observed between the natural frequencies of the harnessed and unwrapped beam.

A constant base acceleration results in a smaller displacement amplitude for higher frequencies. The smaller amplitude results in a smaller accuracy in obtaining the laser measurements. Therefore, the FRFs are obtained individually for each mode during which both the laser sensitivity and shaker acceleration were adjusted to ensure optimal results. For test 5, a variable acceleration profile produced the best results. Smaller base acceleration near the resonant peaks ensures the minimization of nonlinear effects, while a larger base acceleration value around anti-resonances allows for more accurate measurements. Table 2.13 presents the acceleration values used for each of these tests. The acceleration profile for tests 1-4 is used to obtain the FRF shown in Fig. 2.29a for the unwrapped beam 1, and the acceleration profile for test 5 is used to obtain the FRF in Fig. 2.29b for the unwrapped beam 2.

Table 2.13: Acceleration profile used for experiments

Test no.	Mode	Acceleration (g_f)	Resonance (g_f)	Anti-resonance (g_f)
Tests 1-4	1	0.05	-	-
	2	0.4	-	-
	3	0.5	-	-
	4	0.9	-	-
	5	1.2	-	-
	6	1.2	-	-
Test 5	1	0.05	0.03	0.2
	2	1	0.1	1.2
	3	1	0.5	3.5
	4	3	0.5	10
	5	10	1	15
	6	15	1.5	15

The experimental results for the FRFs of the tests outlined in Table 2.12 are compared to the FRFs for the string-harnessed model developed in the current work and given by Eq. (2.96). For brevity, the string-harnessed system model is referred to as the STR model. Additionally, the FRF for a model that employs a bar member assumption for the string, a first-order displacement field, and a first-order strain tensor will also be included. The aforementioned modelling approach represents initial co-authored work for periodically wrapped harnessed systems developed in [83, 84]. This is the same modelling technique referenced in the numerical simulations and is once again referred to as the BAR model.

The experimental and analytical FRFs for the string-harnessed system are presented in Figs. 2.32 to 2.36. The experimental natural frequencies for the unwrapped and string-harnessed systems are presented in Table 2.14. Also, the experimental natural frequencies for the string-harnessed system are compared to those from the BAR and STR models in Table 2.15. Finally, zoom-in FRF plots for the individual modes are presented in Figs. 2.37 to 2.41. In these figures, the experimental results for both the unwrapped beam and the string-harnessed system, as well as analytical results for the STR and BAR models are presented for a closer comparison.

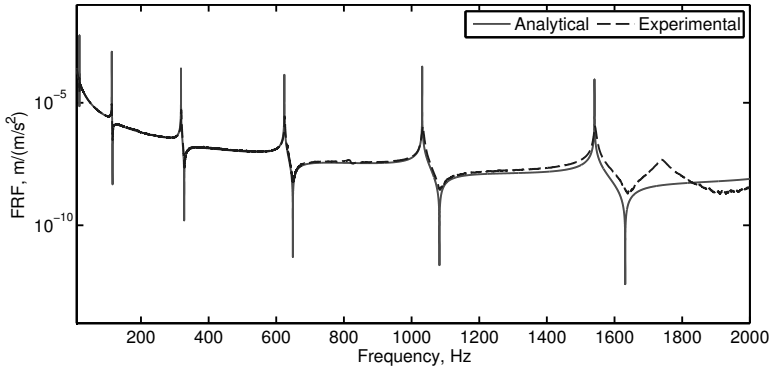

Figure 2.32: FRF comparison between experimental and STR model results for test 1.

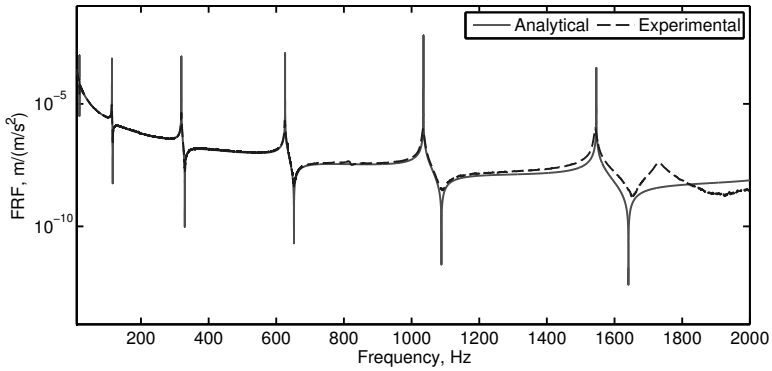

Figure 2.33: FRF comparison between experimental and STR model results for test 2.

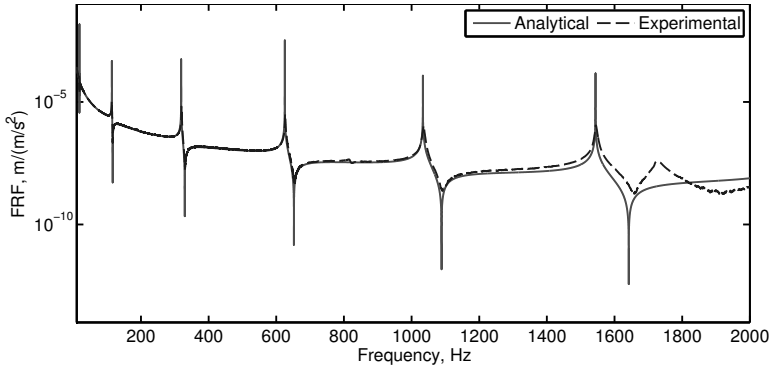

Figure 2.34: FRF comparison between experimental and STR model results for test 3.

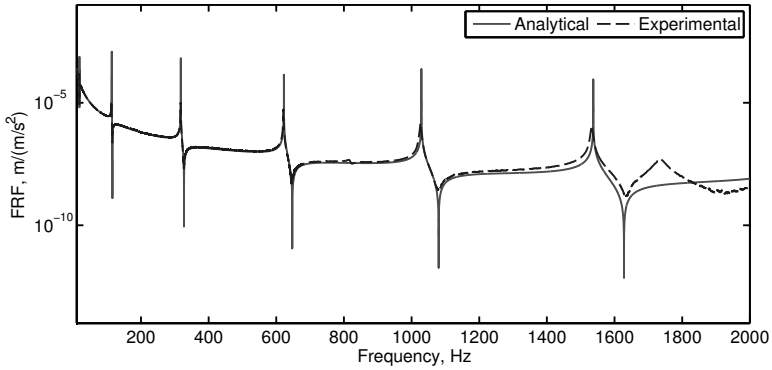

Figure 2.35: FRF comparison between experimental and STR model results for test 4.

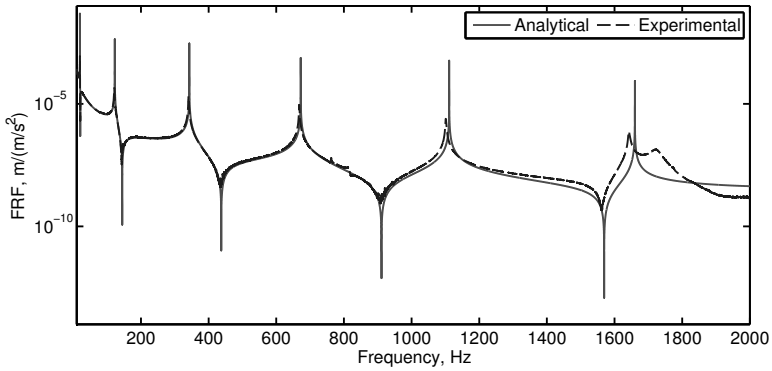

Figure 2.36: FRF comparison between experimental and STR model results for test 5.

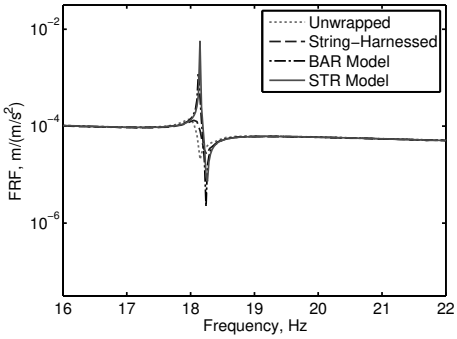

(a) Mode 1

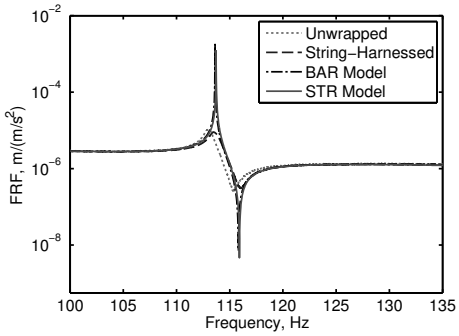

(b) Mode 2

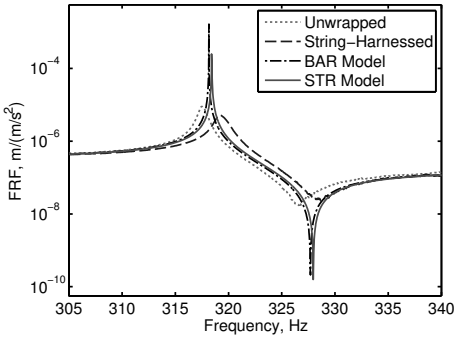

(c) Mode 3

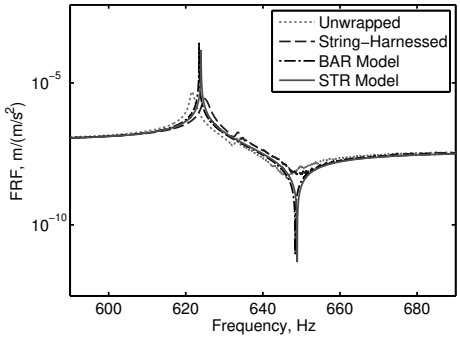

(d) Mode 4

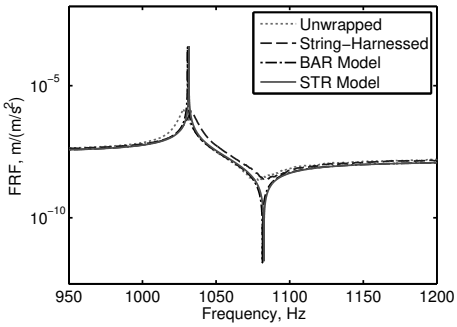

(e) Mode 5

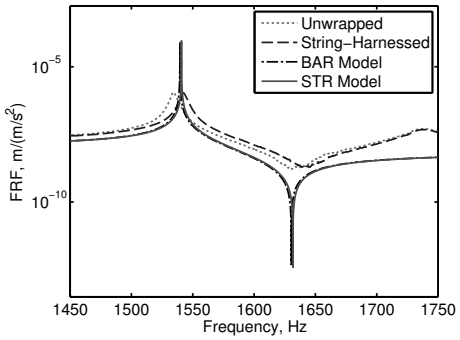

(f) Mode 6

Figure 2.37: Zoom in of the natural frequencies for test 1.

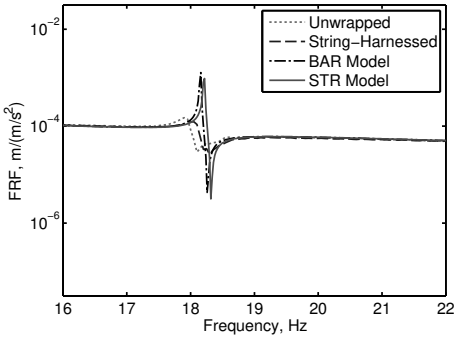

(a) Mode 1

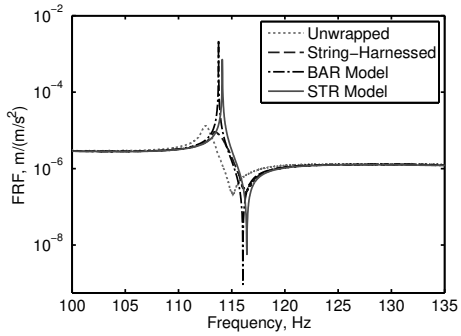

(b) Mode 2

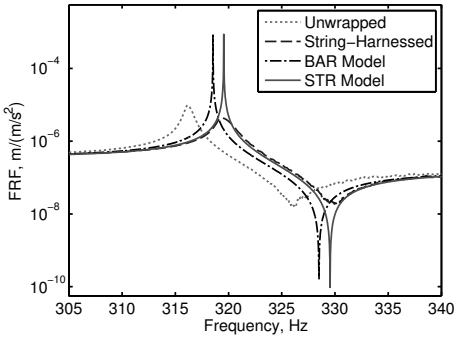

(c) Mode 3

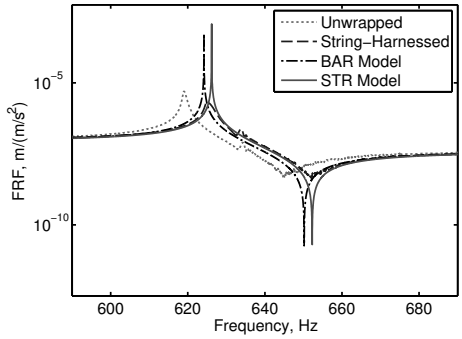

(d) Mode 4

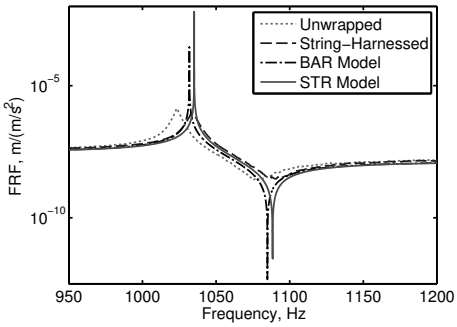

(e) Mode 5

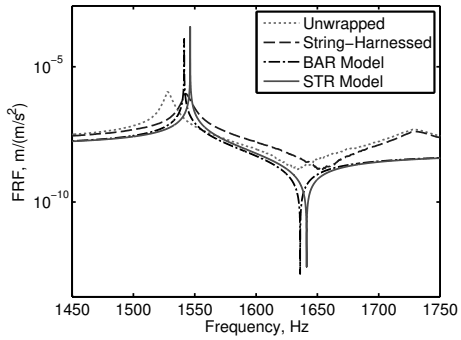

(f) Mode 6

Figure 2.38: Zoom in of the natural frequencies for test 2.

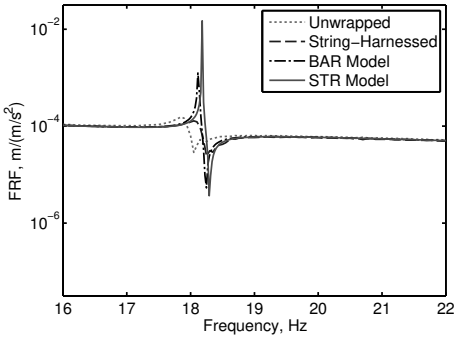

(a) Mode 1

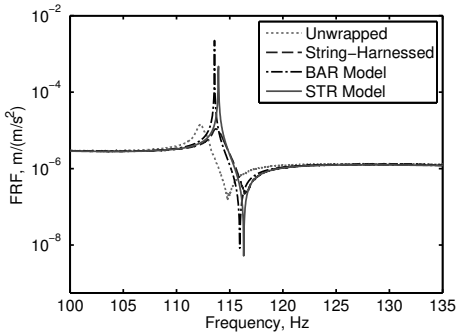

(b) Mode 2

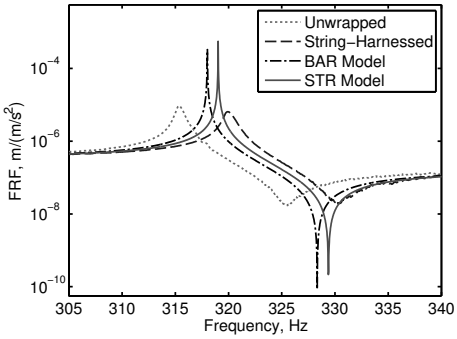

(c) Mode 3

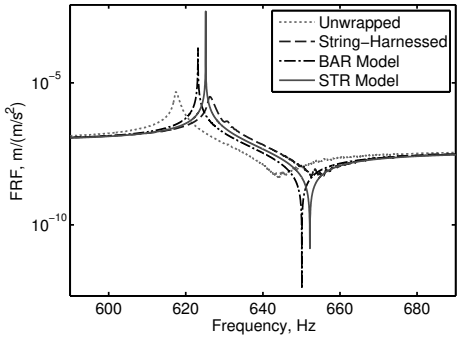

(d) Mode 4

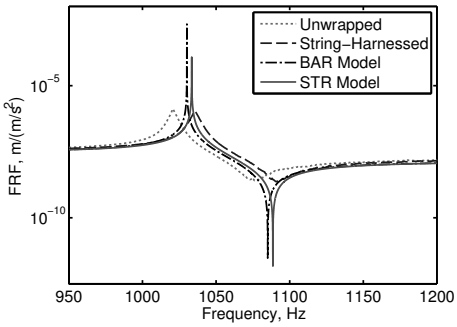

(e) Mode 5

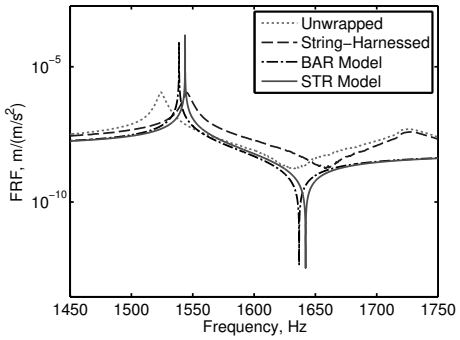

(f) Mode 6

Figure 2.39: Zoom in of the natural frequencies for test 3.

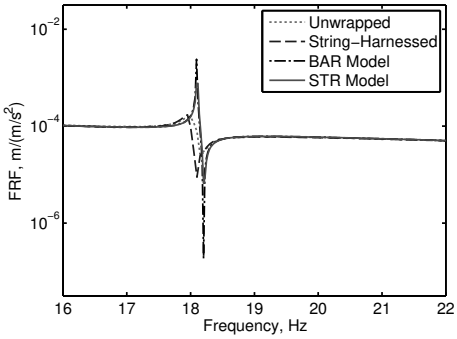

(a) Mode 1

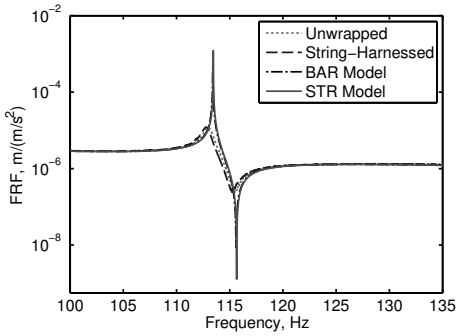

(b) Mode 2

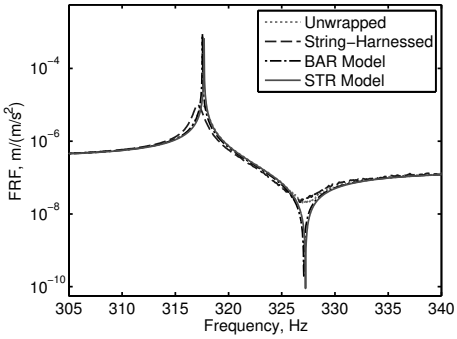

(c) Mode 3

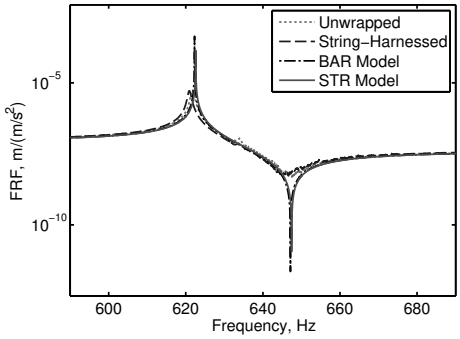

(d) Mode 4

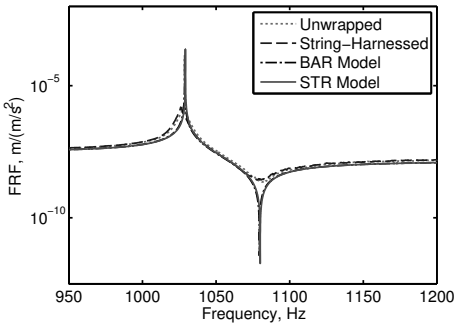

(e) Mode 5

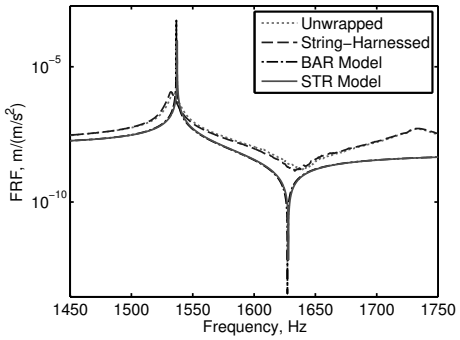

(f) Mode 6

Figure 2.40: Zoom in of the natural frequencies for test 4.

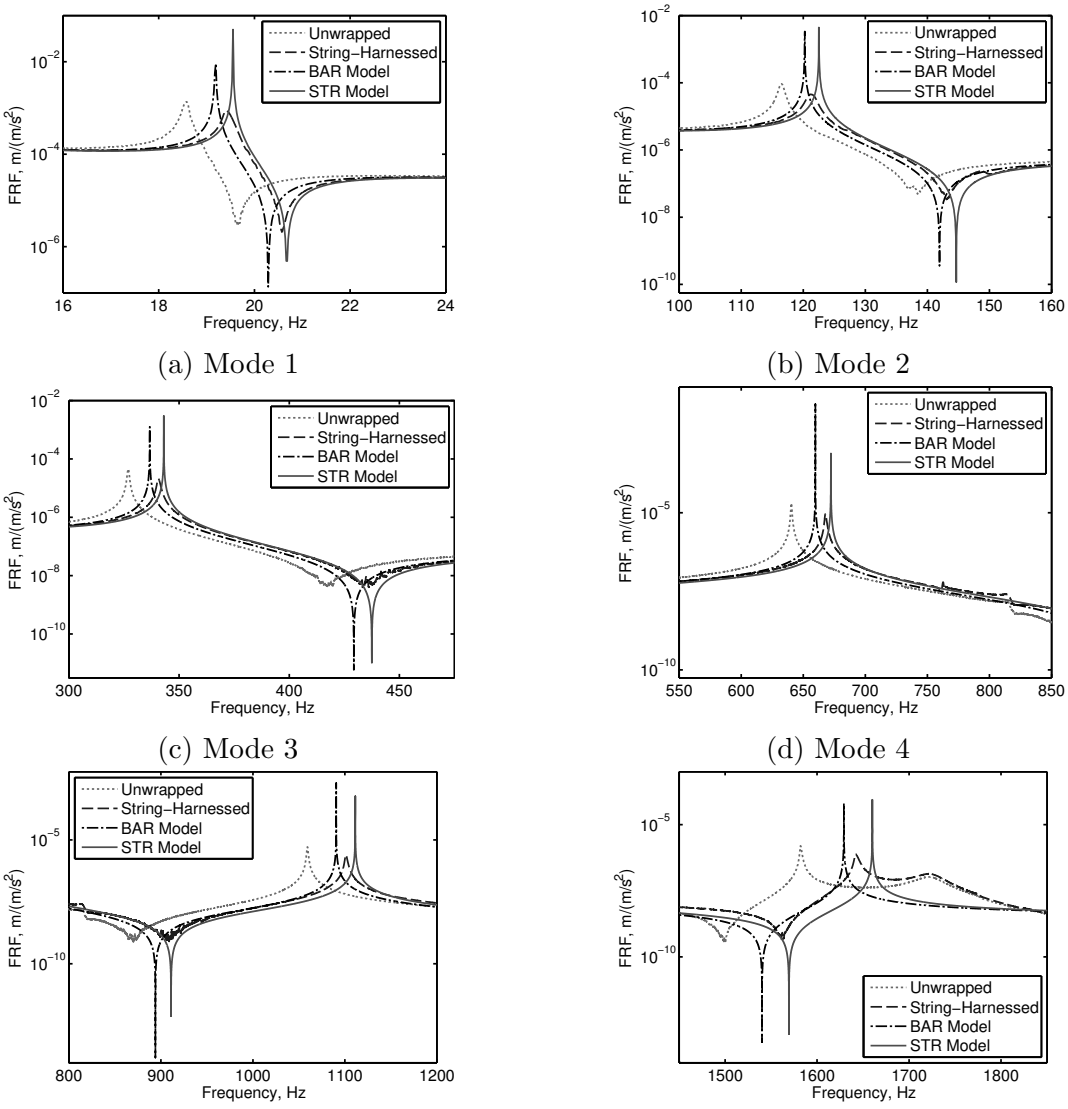

(a) Mode 1

(b) Mode 2

(c) Mode 3

(d) Mode 4

(e) Mode 5

(f) Mode 6

Figure 2.41: Zoom in of the natural frequencies for test 5.

Table 2.14: Experimental natural frequencies, in Hz, for unwrapped beam and string-harnessed system

	Mode					
Result	1	2	3	4	5	6
			Test 1			
Unwrapped	18.00	112.97	317.50	621.55	1027.5	1534.5
String-harnessed	18.05	113.48	319.15	624.85	1033.0	1542.5
Frequency increase, %	0.3	0.45	0.520	0.531	0.54	0.52
			Test 2			
Unwrapped	17.90	112.55	316.15	619.00	1023.0	1528.0
String-harnessed	18.05	113.44	319.35	625.05	1033.5	1542.5
Frequency increase, %	0.84	0.79	1.01	0.977	1.03	0.949
			Test 3			
Unwrapped	17.85	112.22	315.35	617.45	1020.5	1524.0
String-harnessed	18.05	113.7	319.95	626.25	1035.5	1545.0
Frequency increase, %	1.1	1.32	1.46	1.43	1.47	1.38
			Test 4			
Unwrapped	18.00	112.98	317.55	621.65	1027.5	1534.0
String-harnessed	17.95	112.79	317.10	620.90	1026.0	1532.0
Frequency increase, %	-0.3	-0.17	-0.14	-0.12	-0.15	-0.13
			Test 5			
Unwrapped	18.58	116.50	326.95	640.45	1059.3	1582.1
String-harnessed	19.42	121.25	340.60	667.80	1101.1	1642.0
Frequency increase, %	4.5	4.08	4.17	4.270	3.95	3.79

Table 2.15: Comparison of experimental string-harnessed natural frequencies, in Hz, to STR and BAR models

	Mode					
Result	1	2	3	4	5	6
			Test 1			
String-harnessed	18.05	113.48	319.15	624.85	1033.0	1542.5
STR model	18.15	113.72	318.42	623.97	1031.5	1540.8
Error STR, %	0.5	0.21	-0.23	-0.14	-0.15	-0.11
BAR model	18.13	113.62	318.15	623.45	1030.6	1539.5
Error BAR, %	0.4	0.13	-0.31	-0.224	-0.23	-0.19
			Test 2			
String-harnessed	18.05	113.44	319.35	625.05	1033.5	1542.5
STR model	18.21	114.12	319.55	626.19	1035.1	1546.3
Error STR, %	0.89	0.60	0.063	0.183	0.16	0.25
BAR model	18.15	113.76	318.54	624.20	1031.9	1541.4
Error BAR, %	0.57	0.28	-0.26	-0.14	-0.16	-0.071
			Test 3			
String-harnessed	18.05	113.70	319.95	626.25	1035.5	1545.0
STR model	18.18	113.94	319.02	625.16	1033.4	1543.8
Error STR, %	0.72	0.21	-0.29	-0.174	-0.20	-0.080
BAR model	18.12	113.57	318.00	623.16	1030.1	1538.8
Error BAR, %	0.4	-0.11	-0.608	-0.493	-0.52	-0.40
			Test 4			
String-harnessed	17.95	112.79	317.10	620.90	1026.0	1532.0
STR model	18.11	113.46	317.70	622.56	1029.1	1537.4
Error STR, %	0.86	0.60	0.19	0.268	0.31	0.35
BAR model	18.10	113.41	317.54	622.26	1028.6	1536.6
Error BAR, %	0.82	0.55	0.14	0.219	0.26	0.30
			Test 5			
String-harnessed	19.42	121.25	340.60	667.80	1101.1	1642.0
STR model	19.55	122.52	343.07	672.27	1111.3	1660.1
Error STR, %	0.70	1.05	0.724	0.670	0.928	1.10
BAR model	19.19	120.24	336.67	659.74	1090.6	1629.2
Error BAR, %	-1.2	-0.834	-1.15	-1.21	-0.954	-0.782

2.4.4 Comparison Between Experimental and STR Model Results

The FRF plots in Figs. 2.37 - 2.41 clearly indicate that the results from the STR model are in better agreement with the experimental FRFs compared to the BAR model. The largest absolute percentage of error between the frequencies from the STR model and the experiments is 1.10%. As shown in Table 2.15 the errors in using the STR model to predict the experimental results for the 6 modes of a given test are not strictly all positive or negative values. This can be attributed to the fact that the STR model is similar in form to an Euler-Bernoulli beam model, whereas, the physical system is not expected to behave exactly as an Euler-Bernoulli beam model. To elaborate, consider the analytical expression for the frequencies of the STR model reformulated as $\omega_n/\beta_n^2 = \sqrt{C_1/K_1}$. For a given set of system parameters, the values of C_1 and K_1 are constant, and it follows that ω_n/β_n^2 is constant for all the modes in the model. The analytical value for ω_n/β_n^2 and the experimental values are presented in Fig. 2.42.

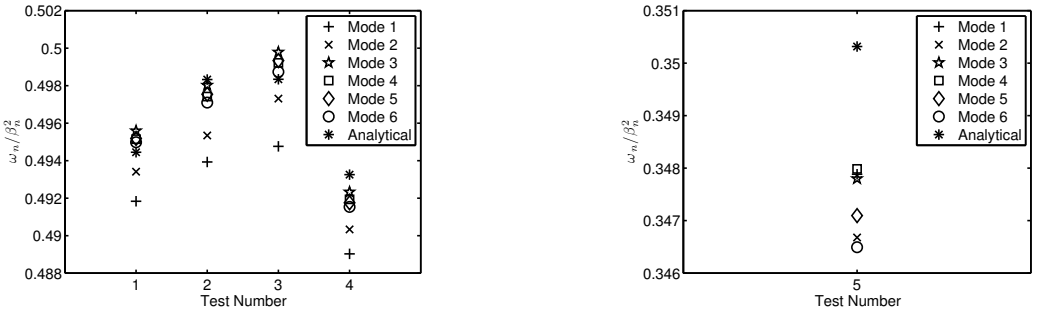

(a) Tests 1 - 4 (b) Test 5

Figure 2.42: Experimental and analytical values of ω_n/β_n^2.

For tests 2, 4, and 5 the analytical value for $\omega_n/\beta_n^2 = \sqrt{C_1/K_1}$ is greater than all of the experimental results for a given test. Therefore, in these cases, the STR model overestimates the modes obtained. In tests 1 and 3 the analytical value is greater than the experimental results for the first two modes and smaller than the experimental results for the higher modes. In these cases the first two modes are overestimated and the higher modes are underestimated. Finally, the values for ω_n/β_n^2 are smaller for test 5 compared to tests 1 - 4 as a beam of smaller thickness and length is used. The percentage of difference between the maximum and minimum experimental values for ω_n/β_n^2 is 0.76%, 0.83%, 1.0%, 0.67%, and 0.430% for tests 1 through 5, respectively.

It can also be examined how changes in the system parameters affect the natural frequencies of the string-harnessed system. First consider the change in string between tests 1 and 2. By changing the SpiderWire string for test 1 to the PowerPro string for test 2, the modulus, density, and radius of the string are increased. In particular, the modulus is increased by 105.1%, the density is increased by 10.2%, and the radius is increased by 23.1%. As it is expected, increasing the modulus of the string results in a higher overall stiffness for the string-harnessed system. Intuitively, this should result in a larger frequency difference between the string-harnessed and the unwrapped systems. On the other hand, increasing the string density should result in smaller natural frequencies for the harnessed system. Finally, an increase of string radius affects both mass and overall stiffness for the harnessed system. The overall impact of the changes in string radii on the system's frequencies depends on which one of the stiffness or density effects are more dominant; this will be determined by the other system parameters.

As expected, the small additional system's mass from test 1 to 2 due to the increased density is outweighed by the additional stiffness due to the much larger modulus of elasticity. Hence, the difference between the string-harnessed and unwrapped frequencies in going from test 1 to test 2 is expected to be larger. This behaviour is also observed experimentally and can be seen by comparing Figs. 2.37 and 2.38 and the results shown in Table 2.14.

Also, the developed model includes the effects for density, modulus, and radius of the string and, as it is shown in the results from this model, the overall effect of these parameters on the system's frequencies is an increase. Recall that the frequencies for the STR model are predicted by $\omega_n = \beta_n^2\sqrt{C_1/K_1}$, in Eq. (2.92), where, C_1 is the stiffness coefficient and K_1 is the mass per unit length coefficient. An increase in the string modulus will result in an increase in the C_1 coefficient while the K_1 coefficient remains unchanged. Therefore, as seems intuitively obvious, an increase in the string modulus will increase the overall stiffness of the system and also the natural frequencies. Similarly, if the density of the string is increased, the C_1 coefficient remains unchanged while the K_1 coefficient increases due to its dependence on ρ_s. Hence, increasing the string density increases the mass per unit length of the system and correspondingly the frequencies decrease. Finally, variations to the string radius, r_s, play a role in the values of A_s, $\overline{b}$, $\overline{h}$, and $\cos(\theta)$. An increase in r_s causes an increase in A_s, $\overline{b}$, and $\overline{h}$, and a decrease in $\cos(\theta)$. Since the coefficient K_1 depends on A_s and $\cos^{-1}(\theta)$, an increase in the string radius always causes an increase in K_1. On the contrary, the effect of varying string radius on the C_1 coefficient may be an increase or a decrease and will depend on the other system parameters. The overall changes shown in the frequencies in the STR model are compatible with those observed from the test results.

Another important factor that plays a substantial role in the dynamics of a string-harnessed system is the tension in the cables. To examine this effect the tension is varied from 8.3 N to 40 N, a 382% increase, between tests 2 and 3. Intuitively, it is expected that an increase in the string tension will also increase the stiffness, thus increasing the natural frequencies. The experimental results presented in Table 2.14 demonstrate this change. As it is observed from these results, the frequency shifts between the tests are more noticeable for the higher modes. This effect can also be seen in Figs. 2.38 and 2.39 where both the model and test results are presented. As shown in Eq. (2.67), for the STR model the tension, T_s, only plays a role in the C_1 coefficient. Thus an increase in T_s will result in a larger value for C_1, which is representative of the overall system's stiffness resulting in higher natural frequency predictions by the STR model. Therefore, the proposed analytical model accurately captures the changes in the dynamic behaviour for this system as tension varies. This is a major improvement for this model compared to the BAR model presented in [83, 84].

Recall the results for ω_n/β_n^2 in Fig. 2.42. When the string radius and modulus increases from test 1 to 2 and the string tension increases from test 2 to 3, the percentage of difference between the maximum and minimum values of ω_n/β_n^2 for the experiments increases from test 1 to test 2 and this difference increases further from test 2 to 3. This indicates that as the stiffening effects of the string increase for a given host structure, the distribution of the experimental frequencies becomes less likely to look like those for an EB model. Since the STR model predicts only a single value for ω_n/β_n^2, this demonstrates the need for further improvement in the model. Furthermore, an increase in the string stiffening effect will cause the coupling between various coordinates of vibrations to become more prominent and is an additional element that must be further incorporated in the model, [86].

Another factor to analyze for a string-harnessed system is the cable pattern. For this reason, the number of fundamental elements is tripled from test 2 to 4. To determine the expected change in the frequencies of the system when the number of fundamental elements is increased, consider the two cases presented in Fig. 2.43. When the string is running along the width of the beam as shown in Fig. 2.43a, there will be no additional strain energy in the string as the system undergoes transverse vibrations. Alternatively, for the case of the string running along the length of the beam shown in Fig. 2.43b, the strain energy in the string during vibrations will be maximized. Accordingly, as the number of elements increases, the wrapping angle, θ, increases and the wrapping pattern becomes more similar to the extreme case shown in Fig. 2.43a. This leads to an overall smaller strain energy stored in the string and, therefore, smaller stiffening effect as the number of fundamental elements increases. Also, as the number of fundamental elements increases, the total string length increases and results in a larger mass for the system.

Combined, these effects indicate smaller natural frequencies for a system of larger number of fundamental elements.

(a) String along the width of the beam (b) String along the length of the beam

Figure 2.43: Extreme geometries for the string-harnessed beam.

Also, comparing the experimental results in Figs. 2.38 and 2.40 clearly show that the difference between the frequencies of the string-harnessed system and unwrapped beam decreases as the number of fundamental elements is increased. As shown in Table 2.14, increasing the fundamental elements from 5 to 15 causes the experimental string-harnessed frequencies to become even smaller than those for the unwrapped beam. For test 2 the average percentage increase of the frequencies for the string-harnessed system compared to the unwrapped beam is 0.933%, while for test 4 the average percentage increase is -0.17%. This indicates that in test 4, the additional mass of the string is more dominant than the stiffening effect for the string. In the STR model, as the number of fundamental elements increases for a given beam length, the wrapping angle, θ, also increases. Since the coefficient C_1 depends on $\cos(\theta)$ and $\cos^3(\theta)$, this change results in a smaller C_1 value. On the other hand, the coefficient K_1 will be larger as it depends on $\cos^{-1}(\theta)$. Subsequently, the frequencies of the STR model will decrease as the number of fundamental elements increases. For all the given system parameters with an exception of those for test 4, the STR model accurately predicts the trend for the frequency shifts between the unwrapped and harnessed beams. As it is shown in test 4, the experimental frequencies for the harnessed beam are smaller than those for the unwrapped beam in contrast to the model predictions. This is because of the additional mass of the string due to a larger number of fundamental elements used for this test that is likely underestimated for in the model.

When the number of fundamental elements is increased from 5, in test 2, to 15, in test 4, the stiffening effect of the string decreases. Additionally, when the number of fundamental elements increases it is expected that STR model will produce more accurate results. This is generally true about homogenization techniques as they employ the assumption of periodicity. Generally speaking when the number of fundamental elements per wavelength for the mode of interest increases, the homogenized model gives better accuracies in its frequency estimations. As a result of both the reduction of the stiffening effects and better

accuracy for larger number of fundamental elements, the percentage difference between the maximum and minimum values for decreases from test 2 to test 4.

From the previous discussions, multiple changes in the systems parameters may be considered to further highlight the ability of the STR model to capture the system's dynamics. Specifically, consider test 3 and test 4 for which the tension is reduced and the number of fundamental elements is increased. Each of these changes will cause the frequencies of the string-harnessed system to decrease as can be seen in both Table 2.14 and Figs. 2.39 and 2.39. Furthermore, it is seen in Table 2.14 that the percentage frequency shifts between the harnessed and the unwrapped beam are larger between tests 3 and 4 compared to those between tests 2 and 4. This is expected since both number of elements and the tension are different between tests 3 and 4. This clearly demonstrates the ability of the STR model to predict the behaviour of the frequencies of the system when multiple system parameters are changed simultaneously. Also, it is observed through the experiments that changing the string from SpiderWire to PowerPro and using higher tension values results in a larger frequency difference between the unwrapped and the string-harnessed beams. Finally, using a different type of string and a larger number of fundamental elements from test 1 to test 4 results in smaller frequencies due to both the additional string mass and the reduction of the string stiffening effects when the wrapping angle changes.

Tests 1 to 4 are primarily conducted for comparison to show the effectiveness of the developed model in predicting the system's natural frequencies when several system parameters change. System parameters in test 5 are chosen in a way to obtain much larger differences between the natural frequencies of the unwrapped and the harnessed system under consideration in this test to demonstrate the importance of modelling string effects. The average shift between the frequencies of the two systems is about 4.12% with the largest shift of 4.5% in the first mode.

A fundamental quantity for obtaining the frequencies using the STR model is C_1/K_1. The quantity C_1/K_1 for a wrapped beam is similar to E_bI_b/ρ_bA_b for an unwrapped beam; C_1 is the overall bending stiffness coefficient and K_1 is the mass per unit length coefficient. For comparison, the values for E_bI_b/ρ_bA_b and C_1/K_1 for each of the tests are presented in Table 2.16.

Table 2.16: Ratios for Euler-Bernoulli and string-harnessed analytical models

	E_bI_b/ρ_bA_b	C_1/K_1
Test 1	9.5961	9.6516
Test 2	9.5961	9.8036
Test 3	9.5961	9.8042
Test 4	9.5961	9.6051
Test 5	4.4019	4.8448

In Table 2.16 it can be seen that the change in C_1/K_1 from test 1 to test 2 is larger than the change from test 2 to test 3. This is particularly interesting since the modulus of the string is increased 105.1% from test 1 to test 2, whereas the increase in tension is much larger at 382% from test 2 to test 3. As such, this indicates that the effect of changing the type of string, in particular the modulus of the string, has a greater effect on the frequencies than increasing the tension in the string. It can also be seen in Table 2.16 that the value of C_1/K_1 decreases from test 2 to test 4, where the number of fundamental elements is increased from 5 to 15. This highlights the impact of the loss in stiffening effect from the string and an increased mass per unit length when the number of fundamental elements is increased. For test 5, the C_1/K_1 value is smaller when compared to tests 1 - 4 since a thinner beam was used for the host structure.

To conclude, the absolute percentage of error in using the STR model to predict the experimental results is plotted versus mode number for comparison for each of the 5 tests in Fig. 2.44. As shown in this figure the error in the model frequency predictions are highest for test 5 where multiple strings are used on a shorter and thinner beam.

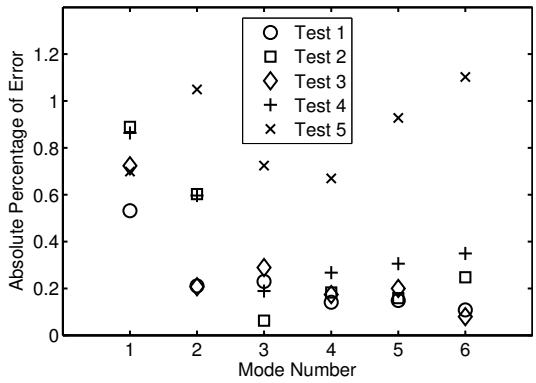

Figure 2.44: Absolute percentage of error between analytical and experimental frequencies for the string-harnessed systems.

2.4.5 STR and BAR Model Comparison

As shown previously, both the STR and the BAR models produce equivalent continuum models for the transverse vibrations similar to an Euler-Bernoulli model. The error in the natural frequency predictions by each of the STR and BAR models are listed in Table 2.15 and the absolute errors are presented in Fig. 2.45.

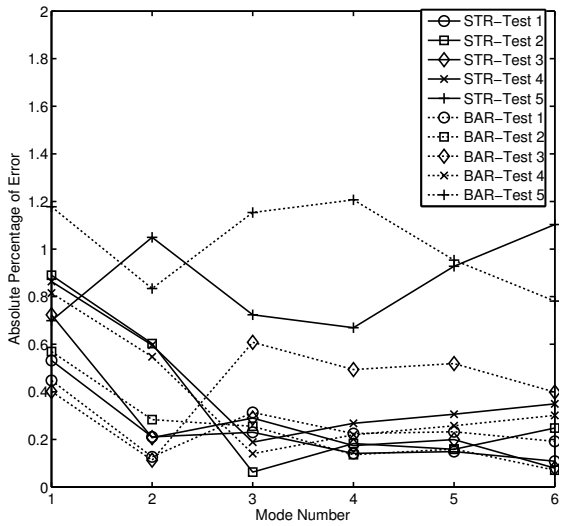

Figure 2.45: Absolute percentage of error between experimental and analytical results for the STR and BAR models.

Looking at the error values produced by each model for tests 3 and 5, which have higher tension values, the advantage of using the STR model becomes evident. This is particularly more noticeable for the higher modes. Also, as discussed previously, employing the assumption of the BAR model, [83, 84], for the string elements results in a model that lacks in dependence on the string tension, which is counterintuitive. For both models, the largest error is produced for test 5 where multiple strings are used. Finally, it is shown in [86] that increasing the ratio for the string to beam cross-sectional area results in a larger error in predicting the natural frequencies. As such, using multiple strings on a thinner beam in this test explains the higher frequency errors for test 5 compared to the previous 4 tests.

In summary, the proposed STR model for string-harnessed structures accurately predicts the experimental frequencies and FRFs for multiple test setups. Additionally, this model is able to accurately predict the changes in the system's frequencies subject to all system parameter changes such as string modulus, string radius, tension, number of fundamental elements, number of string harnesses, and dimensions of the host beam structure. The most important improvement for the STR model compared with the BAR model is the dependence of its predicted natural frequencies on the string tension.

2.5 Chapter Summary

In this chapter, an energy equivalent homogenization technique was used to determine a simple constant coefficient model for periodically wrapped string-harnessed systems. The model was in the form of a constant coefficient Euler-Bernoulli beam model. Increasing the modulus or tension in the string, as well as wrapping the string less frequently around the beam resulted in an increase in the frequencies of the system. Increasing the density of the string resulted in a decrease in the frequencies of the system. Changing the radius of the string affected both the added stiffness and added mass due to the string and the effect on the frequencies depends on the other system parameters.

Experimental tests were performed to assess the accuracy of the homogenized string-harnessed model. Five distinct tests were performed for clamped-free boundary conditions and considered different types of strings, number of strings, tension applied, and number of wraps around the host structure (fundamental elements). In these tests the first six modes of the system were captured and the largest absolute percentage of error in a single mode was 1.10%, which demonstrates the strength of the developed model. Furthermore, it was shown that the stiffening effect of including strings is quite significant. For the 3 strings

test performed there was an average increase of 4.1% in the frequencies when compared with a beam without any strings.

Chapter 3

Perturbation Theory for Euler-Bernoulli Models

In this chapter a perturbation theory for a spatially dependent Euler-Bernoulli beam model is developed. Using a Lindstedt-Poincaré perturbation theory method, two corrections to the frequencies and one correction to the mode shapes are found. Furthermore, various methods for determining reference values of the spatially dependent quantities from which perturbations occur, necessary values in the perturbation theory, are considered. Previously in the literature only a single correction to the frequency and a one method for choosing the reference values were considered in [75]. Numerical simulations are performed to investigate the accuracy of the proposed perturbation theory. The work presented in this chapter is to be submitted in [93].

3.1 Lindstedt-Poincaré Method

3.1.1 Problem Statement

Consider a spatially varying Euler-Bernoulli (EB) model for free transverse vibrations with bending stiffness given by $EI(x)$ and mass per unit length given by $\rho A(x)$. Assume that $EI(x)$ and $\rho A(x)$ are C^∞-functions on $[0,l] \setminus P_{EI}$ and $[0,l] \setminus P_{\rho A}$. That is, the functions have derivatives of all orders except at a finite set of points. The PDE in consideration is

$$\frac{\partial^2}{\partial x^2}\left[EI(x)\frac{\partial^2 w(x,t)}{\partial x^2}\right] + \rho A(x)\frac{\partial^2 w(x,t)}{\partial t^2} = 0 \tag{3.1}$$

for $0 < x < l$ and $t > 0$. The boundary conditions at $x^* = 0$ or l are:

$$w(x^*,t) = 0 \qquad \text{or} \qquad \frac{\partial}{\partial x}\left[EI(x)\frac{\partial^2 w(x,t)}{\partial x^2}\right]_{x=x^*} = 0 \tag{3.2}$$

$$\frac{\partial w(x^*,t)}{\partial x} = 0 \qquad \text{or} \qquad EI(x^*)\frac{\partial^2 w(x^*,t)}{\partial x^2} = 0 \tag{3.3}$$

The first boundary condition in Eqs. (3.2) and (3.3) are the geometric boundary conditions and correspond to zero displacement and zero slope, respectively. The second boundary condition in Eqs. (3.2) and (3.3) are the natural boundary conditions and correspond to zero shear and zero moment, respectively.

The problem is next nondimensionalized using a yet undetermined reference value for the bending stiffness, EI^*, and a yet undetermined reference value for the mass per unit length, ρA^*. These reference values are the values from which the respective parameters of the system are considered perturbed and are at this point not fixed. Introduce the length scale l and the time scale $l^2\sqrt{\rho A^*/EI^*}$. Let W, X, and T denote the dimensionless variables associated with w, x, and t, respectively. The dimensionless PDE is

$$\frac{\partial^2}{\partial X^2}\left[\left\{1 + \frac{EI(X) - EI^*}{EI^*}\right\}\frac{\partial^2 W(X,T)}{\partial X^2}\right] + \left\{1 + \frac{\rho A(X) - \rho A^*}{\rho A^*}\right\}\frac{\partial^2 W(X,T)}{\partial T^2} = 0 \tag{3.4}$$

Assume a separable solution to Eq. (3.4) of the form $W(X,T) = u(X)e^{i\omega T}$. This leads to a spatial ordinary differential equation (ODE)

$$\frac{\mathrm{d}^2}{\mathrm{d}X^2}\left[\left\{1 + \frac{EI(X) - EI^*}{EI^*}\right\}\frac{\mathrm{d}^2 u(X)}{\mathrm{d}X^2}\right] - \omega^2\left\{1 + \frac{\rho A(X) - \rho A^*}{\rho A^*}\right\}u(X) = 0 \tag{3.5}$$

3.1.2 Perturbation Theory

Since the reference values EI^* and ρA^* were chosen such that perturbations occur from these values, introduce a small parameter ϵ in Eq. (3.5)

$$\frac{\mathrm{d}^2}{\mathrm{d}X^2}\left[\left\{1 + \epsilon\widehat{EI}(X)\right\}\frac{\mathrm{d}^2 u(X)}{\mathrm{d}X^2}\right] - \omega^2\left\{1 + \epsilon\widehat{\rho A}(X)\right\}u(X) = 0 \tag{3.6}$$

Applying the same steps that were applied to the PDE to the boundary conditions.

The boundary conditions at $X^* = 0$ or 1 are

$$u(X^*) = 0 \qquad \text{or} \qquad \frac{\mathrm{d}}{\mathrm{d}X}\left[\left\{1 + \epsilon\widehat{EI}(X)\right\}\frac{\mathrm{d}^2 u(X)}{\mathrm{d}X^2}\right]_{X=X^*} = 0 \tag{3.7a}$$

$$\frac{\mathrm{d}u(X^*)}{\mathrm{d}X} = 0 \qquad \text{or} \qquad \left\{1 + \epsilon\widehat{EI}(X)\right\}\frac{\mathrm{d}^2 u(X^*)}{\mathrm{d}X^2} = 0 \tag{3.7b}$$

The perturbation theory used is the Lindstedt-Poincaré method, see [104] for one of many texts on the subject. In this technique, the natural frequencies and mode shapes are expanded in powers of the small parameter ϵ

$$u(X) = u_0(X) + \epsilon u_1(X) + \epsilon^2 u_2(X) + \ldots \tag{3.8a}$$

$$\omega = \omega_0 + \epsilon\omega_1 + \epsilon^2\omega_2 + \ldots \tag{3.8b}$$

The expansions in Eq. (3.8) are then substituted into the PDE and boundary conditions in Eqs. (3.6) and (3.7). Terms with similar powers of ϵ are grouped together and these define a sequence of problems that must be solved to determine the frequencies and mode shapes.

3.1.3 Mass Normalization Condition

Once the mode shapes of the system are determined from the perturbation theory they are mass normalized. This is quite common in a vibrations analysis as the mass normalization allows for the various modes of the system to be decoupled when determining the time response of the system. The mass normalized mode shapes are denoted by $\overline{\phi}(x)$ and the nondimensional mode shapes are denoted by $\phi(X)$. The mass normalization condition in nondimensional form is given by

$$1 = \int_0^1 \left\{1 + \epsilon\widehat{\rho A}(X)\right\}\phi^2(X)\,\mathrm{d}X \tag{3.9}$$

To determine the mass normalization condition corresponding to each $\mathcal{O}(\epsilon^i)$ problem of the perturbation theory, substitute the expansion of the mode shape in terms of ϵ into Eq. (3.9). The mass normalization conditions for the $\mathcal{O}(1)$ and $\mathcal{O}(\epsilon)$ are

$$\mathcal{O}(1): \qquad 1 = \int_0^1 \phi_0^2(X)\,\mathrm{d}X \tag{3.10a}$$

$$\mathcal{O}(\epsilon): \qquad 0 = \int_0^1 2\phi_0(X)\phi_1(X) + \widehat{\rho A}(X)\phi_0^2(X)\,\mathrm{d}X \tag{3.10b}$$

3.1.4 $\mathcal{O}(1)$ Problem

The ODE for the $\mathcal{O}(1)$ problem is

$$\frac{\mathrm{d}^4 u_0}{\mathrm{d}X^4} - \omega_0^2 u_0 = 0 \tag{3.11}$$

for $0 < X < 1$. Clamped-clamped (CC), clamped-free (CF), and free-free (FF) boundary conditions are considered. The solution for the ODE in Eq. (3.11) is readily available and is simply presented for each of the boundary conditions considered. The presented solutions also satisfy the mass normalization condition for the $\mathcal{O}(1)$ problem.

Clamped-Clamped Solution

The boundary conditions for a CC system are

$$u_0(0) = 0 \quad , \quad \frac{\mathrm{d}u_0(0)}{\mathrm{d}X} = 0 \quad , \quad u_0(1) = 0 \quad , \quad \frac{\mathrm{d}u_0(1)}{\mathrm{d}X} = 0$$

The characteristic equation, which determines the frequencies ω_{n0}, is

$$0 = 1 - \cos(\sqrt{\omega_0})\cosh(\sqrt{\omega_0})$$

and the n^{th} mode shape of the system is

$$\phi_{n0}(X) = \cos(\sqrt{\omega_{n0}}X) - \cosh(\sqrt{\omega_{n0}}X) - \frac{\cos(\sqrt{\omega_{n0}}) - \cosh(\sqrt{\omega_{n0}})}{\sin(\sqrt{\omega_{n0}}) - \sinh(\sqrt{\omega_{n0}})}\left\{\sin(\sqrt{\omega_{n0}}X) - \sinh(\sqrt{\omega_{n0}}X)\right\} \tag{3.12}$$

Clamped-Free Solution

The boundary conditions for a CF system are

$$u_0(0) = 0 \quad , \quad \frac{\mathrm{d}u_0(0)}{\mathrm{d}X} = 0 \quad , \quad \frac{\mathrm{d}^2 u_0(1)}{\mathrm{d}X^2} = 0 \quad , \quad \frac{\mathrm{d}^3 u_0(1)}{\mathrm{d}X^3} = 0$$

The characteristic equation, which determines the frequencies ω_{n0}, is

$$0 = 1 + \cos(\sqrt{\omega_0})\cosh(\sqrt{\omega_0})$$

and the n^{th} mode shape of the system is

$$\phi_{n0}(X) = \cos(\sqrt{\omega_{n0}}X) - \cosh(\sqrt{\omega_{n0}}X) - \frac{\cos(\sqrt{\omega_{n0}}) + \cosh(\sqrt{\omega_{n0}})}{\sin(\sqrt{\omega_{n0}}) + \sinh(\sqrt{\omega_{n0}})}\left\{\sin(\sqrt{\omega_{n0}}X) - \sinh(\sqrt{\omega_{n0}}X)\right\} \tag{3.13}$$

Free-Free Solution

The boundary conditions for a FF system are

$$\frac{\mathrm{d}^2 u_0(0)}{\mathrm{d}X^2} = 0 \quad , \quad \frac{\mathrm{d}^3 u_0(0)}{\mathrm{d}X^3} = 0 \quad , \quad \frac{\mathrm{d}^2 u_0(1)}{\mathrm{d}X^2} = 0 \quad , \quad \frac{\mathrm{d}^3 u_0(1)}{\mathrm{d}X^3} = 0$$

The characteristic equation, which determines the frequencies ω_{n0}, is

$$0 = 1 - \cos(\sqrt{\omega_0})\cosh(\sqrt{\omega_0})$$

and the n^{th} mode shape of the system is

$$\phi_{n0}(X) = \cos(\sqrt{\omega_{n0}}X) + \cosh(\sqrt{\omega_{n0}}X) - \frac{\cos(\sqrt{\omega_{n0}}) - \cosh(\sqrt{\omega_{n0}})}{\sin(\sqrt{\omega_{n0}}) - \sinh(\sqrt{\omega_{n0}})}\left\{\sin(\sqrt{\omega_{n0}}X) + \sinh(\sqrt{\omega_{n0}}X)\right\} \tag{3.14}$$

3.1.5 $\mathcal{O}(\epsilon)$ Problem

The ODE for the $\mathcal{O}(\epsilon)$ problem is

$$\frac{\mathrm{d}^4 u_{n1}}{\mathrm{d}X^4} - \omega_{n0}^2 u_{n1} = 2\omega_{n0}\omega_{n1}\phi_{n0} + \omega_{n0}^2 \widehat{\rho A}\phi_{n0} - \frac{\mathrm{d}^2}{\mathrm{d}X^2}\left[\widehat{EI}\frac{\mathrm{d}^2\phi_{n0}}{\mathrm{d}X^2}\right] \tag{3.15}$$

for $0 < X < 1$. As is typically done in the perturbation theory, a solution to the ODE exists when the solvability condition is satisfied. The solvability condition is a corollary to the Fredholm Alternative and states that a solution to the ODE exists if and only if the inner product of the non-homogeneous term in Eq. (3.15) and the $\mathcal{O}(1)$ solution is 0.

$$0 = \int_0^1 \left\{2\omega_{n0}\omega_{n1}\phi_{n0} + \omega_{n0}^2 \widehat{\rho A}\phi_{n0} - \frac{\mathrm{d}^2}{\mathrm{d}X^2}\left[\widehat{EI}\frac{\mathrm{d}^2\phi_{n0}}{\mathrm{d}X^2}\right]\right\}\phi_{n0}\,\mathrm{d}X \tag{3.16}$$

From the solvability condition in Eq. (3.16) the value for ω_{n1} is found. Using integration by parts and that CC, CF, and FF boundary conditions are under consideration, the

solvability condition yields

$$
\begin{aligned}
0 =& \int_0^1 2\omega_{n0}\omega_{n1}\phi_{n0}^2 + \omega_{n0}^2\widehat{\rho A}\phi_{n0}^2 - \frac{\mathrm{d}^2}{\mathrm{d}X^2}\left[\widehat{EI}\frac{\mathrm{d}^2\phi_{n0}}{\mathrm{d}X^2}\right]\phi_{n0}\,\mathrm{d}X \\
0 =& 2\omega_{n0}\omega_{n1}\int_0^1 \phi_{n0}^2\,\mathrm{d}X + \omega_{n0}^2\int_0^1 \widehat{\rho A}\phi_{n0}^2\,\mathrm{d}X - \int_0^1 \frac{\mathrm{d}^2}{\mathrm{d}X^2}\left[\widehat{EI}\frac{\mathrm{d}^2\phi_{n0}}{\mathrm{d}X^2}\right]\phi_{n0}\,\mathrm{d}X \\
2\omega_{n0}\omega_{n1} =& -\int_0^1 \frac{\mathrm{d}}{\mathrm{d}X}\left[\widehat{EI}\frac{\mathrm{d}^2\phi_{n0}}{\mathrm{d}X^2}\right]\frac{\mathrm{d}\phi_{n0}}{\mathrm{d}X}\,\mathrm{d}X - \omega_{n0}^2\int_0^1 \widehat{\rho A}\phi_{n0}^2\,\mathrm{d}X \\
\omega_{n1} =& \frac{1}{2\omega_{n0}}\int_0^1 \widehat{EI}\left(\frac{\mathrm{d}^2\phi_{n0}}{\mathrm{d}X^2}\right)^2\mathrm{d}X - \frac{\omega_{n0}}{2}\int_0^1 \widehat{\rho A}\,\phi_{n0}^2\,\mathrm{d}X
\end{aligned}
\tag{3.17}
$$

Recall the assumption that $EI(x)$ and $\rho A(x)$ are C^∞-functions everywhere except on a set of points $P = P_{EI} \cup P_{\rho A}$ of size $m-1$. It follows that $\widehat{EI}(X)$ and $\widehat{\rho A}(X)$ are C^∞-functions on the set $\widehat{P} = P/l$. Suppose that the points in $\widehat{P}$ are ordered as $0 < X_{P_1} < X_{P_2} < \ldots < X_{P_{m-1}} < 1$ and denote $X_0 = 0$ and $X_m = 1$. The ODE in Eq. (3.15) is solved over each of the m intervals $[X_{i-1}, X_i]$ with the general solution on the i^{th} interval given by

$$
\begin{aligned}
u_{n1}^{(i)}(X) =& A_{n1}^{(i)}\cos(\sqrt{\omega_{n0}}X) + B_{n1}^{(i)}\sin(\sqrt{\omega_{n0}}X) + C_{n1}^{(i)}\cosh(\sqrt{\omega_{n0}}X) + D_{n1}^{(i)}\sinh(\sqrt{\omega_{n0}}X) \\
&+ \frac{\omega_{n1}}{2\omega_{n0}}X\frac{\mathrm{d}\phi_{n0}}{\mathrm{d}X} + u_{n1,p}^{(i)}(X)
\end{aligned}
\tag{3.18}
$$

The coefficients $A_{n1}^{(i)}$, $B_{n1}^{(i)}$, $C_{n1}^{(i)}$ and $D_{n1}^{(i)}$ in Eq. (3.18) are determined by applying the

boundary conditions. The particular solution to the ODE, denoted by $u_{n1,p}^{(i)}(X)$, is

$$\begin{aligned}
u_{n1,p}^{(i)}(x) =& \frac{\sqrt{\omega_{n0}}}{2}\Bigg[\cos(\sqrt{\omega_{n0}}X)\int \sin(\sqrt{\omega_{n0}}X)\,\widehat{\rho A}^{(i)}\phi_{n0}\,\mathrm{d}X \\
&- \sin(\sqrt{\omega_{n0}}X)\int \cos(\sqrt{\omega_{n0}}X)\,\widehat{\rho A}^{(i)}\phi_{n0}\,\mathrm{d}X \\
&- \cosh(\sqrt{\omega_{n0}}X)\int \sinh(\sqrt{\omega_{n0}}X)\,\widehat{\rho A}^{(i)}\phi_{n0}\,\mathrm{d}X \\
&+ \sinh(\sqrt{\omega_{n0}}X)\int \cosh(\sqrt{\omega_{n0}}X)\,\widehat{\rho A}^{(i)}\phi_{n0}\,\mathrm{d}X\Bigg] \\
&- \frac{1}{2\sqrt{\omega_{n0}^3}}\Bigg[\cos(\sqrt{\omega_{n0}}X)\int \sin(\sqrt{\omega_{n0}}X)\,\frac{\mathrm{d}^2}{\mathrm{d}X^2}\left[\widehat{EI}^{(i)}\frac{\mathrm{d}^2\phi_{n0}}{\mathrm{d}X^2}\right]\mathrm{d}X \\
&\quad - \sin(\sqrt{\omega_{n0}}X)\int \cos(\sqrt{\omega_{n0}}X)\,\frac{\mathrm{d}^2}{\mathrm{d}X^2}\left[\widehat{EI}^{(i)}\frac{\mathrm{d}^2\phi_{n0}}{\mathrm{d}X^2}\right]\mathrm{d}X \\
&\quad - \cosh(\sqrt{\omega_{n0}}X)\int \sinh(\sqrt{\omega_{n0}}X)\,\frac{\mathrm{d}^2}{\mathrm{d}X^2}\left[\widehat{EI}^{(i)}\frac{\mathrm{d}^2\phi_{n0}}{\mathrm{d}X^2}\right]\mathrm{d}X \\
&\quad + \sinh(\sqrt{\omega_{n0}}X)\int \cosh(\sqrt{\omega_{n0}}X)\,\frac{\mathrm{d}^2}{\mathrm{d}X^2}\left[\widehat{EI}^{(i)}\frac{\mathrm{d}^2\phi_{n0}}{\mathrm{d}X^2}\right]\mathrm{d}X\Bigg]
\end{aligned} \tag{3.19}$$

Since the ODE is solved over each section, a set of continuity conditions must be applied. The continuity conditions are continuity of displacement, slope, moment, and shear. These are obtained mathematically from Eq. (3.15). For an arbitrary point $X_j \in \widehat{P}$.

$$u_{n1}^{(j)}(X_{P_j}) = u_{n1}^{(j+1)}(X_{P_j}) \tag{3.20a}$$

$$\frac{\mathrm{d}u_{n1}^{(j)}(X_{P_j})}{\mathrm{d}X} = \frac{\mathrm{d}u_{n1}^{(j+1)}(X_{P_j})}{\mathrm{d}X} \tag{3.20b}$$

$$\frac{\mathrm{d}^2u_{n1}^{(j)}(X_{P_j})}{\mathrm{d}X^2} = \frac{\mathrm{d}^2u_{n1}^{(j+1)}(X_{P_j})}{\mathrm{d}X^2} + \left(\widehat{EI}^{(j+1)}(X_{P_j}) - \widehat{EI}^{(j)}(X_{P_j})\right)\frac{\mathrm{d}^2\phi_{n0}(X_{P_j})}{\mathrm{d}X^2} \tag{3.20c}$$

$$\frac{\mathrm{d}^3u_{n1}^{(j)}(X_{P_j})}{\mathrm{d}X^3} = \frac{\mathrm{d}^3u_{n1}^{(j+1)}(X_{P_j})}{\mathrm{d}X^3} + \frac{\mathrm{d}}{\mathrm{d}X}\left[\left(\widehat{EI}^{(j+1)}(X) - \widehat{EI}^{(j)}(X)\right)\frac{\mathrm{d}^2\phi_{n0}}{\mathrm{d}X^2}\right]_{X=X_{P_j}} \tag{3.20d}$$

The boundary conditions for the $\mathcal{O}(\epsilon)$ problem are simplified using the $\mathcal{O}(1)$ problem boundary conditions. The boundary conditions for a CC system are

$$u_{n1}^{(1)}(0) = 0 \quad , \quad \frac{\mathrm{d}u_{n1}^{(1)}(0)}{\mathrm{d}X} = 0 \quad , \quad u_{n1}^{(m)}(1) = 0 \quad , \quad \frac{\mathrm{d}u_{n1}^{(m)}(1)}{\mathrm{d}X} = 0 \tag{3.21}$$

The boundary conditions for a CF system are

$$u_{n1}^{(1)}(0) = 0 \quad , \quad \frac{\mathrm{d}u_{n1}^{(1)}(0)}{\mathrm{d}X} = 0 \quad , \quad \frac{\mathrm{d}^2 u_{n1}^{(m)}(1)}{\mathrm{d}X^2} = 0 \quad , \quad \frac{\mathrm{d}^3 u_{n1}^{(m)}(1)}{\mathrm{d}X^3} = 0 \tag{3.22}$$

The boundary conditions for a FF system are

$$\frac{\mathrm{d}^2 u_{n1}^{(1)}(0)}{\mathrm{d}X^2} = 0 \quad , \quad \frac{\mathrm{d}^3 u_{n1}^{(1)}(0)}{\mathrm{d}X^3} = 0 \quad , \quad \frac{\mathrm{d}^2 u_{n1}^{(m)}(1)}{\mathrm{d}X^2} = 0 \quad , \quad \frac{\mathrm{d}^3 u_{n1}^{(m)}(1)}{\mathrm{d}X^3} = 0 \tag{3.23}$$

Applying the boundary conditions at $X = 0$, the first section of the mode shape for a CC and CF system is

$$\begin{aligned} u_{n1}^{(1)}(X) =& A_{n1}^{(1)} \{\cos(\sqrt{\omega_{n0}}X) - \cosh(\sqrt{\omega_{n0}}X)\} + B_{n1}^{(1)} \{\sin(\sqrt{\omega_{n0}}X) - \sinh(\sqrt{\omega_{n0}}X)\} \\ &+ \frac{\omega_{n1}}{2\omega_{n0}} X \frac{\mathrm{d}\phi_{n0}}{\mathrm{d}X} + u_{n1,p}^{(1)}(X) - u_{n1,p}^{(1)}(0)\cosh(\sqrt{\omega_{n0}}X) - \frac{1}{\sqrt{\omega_{n0}}} \frac{\mathrm{d}u_{n1,p}^{(1)}(0)}{\mathrm{d}X} \sinh(\sqrt{\omega_{n0}}X) \\ =& A_{n1}^{(1)} \{\cos(\sqrt{\omega_{n0}}X) - \cosh(\sqrt{\omega_{n0}}X)\} + B_{n1}^{(1)} \{\sin(\sqrt{\omega_{n0}}X) - \sinh(\sqrt{\omega_{n0}}X)\} \\ &+ \frac{\omega_{n1}}{2\omega_{n0}} X \frac{\mathrm{d}\phi_{n0}}{\mathrm{d}X} + \widetilde{u}_{n1}^{(1)}(X) \end{aligned} \tag{3.24}$$

The first section of the mode shape for a FF system is:

$$\begin{aligned} u_{n1}^{(1)}(X) =& A_{n1}^{(1)} \{\cos(\sqrt{\omega_{n0}}X) + \cosh(\sqrt{\omega_{n0}}X)\} + B_{n1}^{(1)} \{\sin(\sqrt{\omega_{n0}}X) + \sinh(\sqrt{\omega_{n0}}X)\} \\ &+ \frac{\omega_{n1}}{2\omega_{n0}} X \frac{\mathrm{d}\phi_{n0}}{\mathrm{d}X} + u_{n1,p}^{(1)}(X) - \frac{1}{\omega_{n0}} \frac{\mathrm{d}^2 u_{n1,p}^{(1)}(0)}{\mathrm{d}X^2} \cosh(\sqrt{\omega_{n0}}X) \\ &- \frac{1}{\sqrt{\omega_{n0}^3}} \frac{\mathrm{d}^3 u_{n1,p}^{(1)}(0)}{\mathrm{d}X^3} \sinh(\sqrt{\omega_{n0}}X) \\ =& A_{n1}^{(1)} \{\cos(\sqrt{\omega_{n0}}X) + \cosh(\sqrt{\omega_{n0}}X)\} + B_{n1}^{(1)} \{\sin(\sqrt{\omega_{n0}}X) + \sinh(\sqrt{\omega_{n0}}X)\} \\ &+ \frac{\omega_{n1}}{2\omega_{n0}} X \frac{\mathrm{d}\phi_{n0}}{\mathrm{d}X} + \widetilde{u}_{n1}^{(1)}(X) \end{aligned} \tag{3.25}$$

Next the continuity conditions are applied in order, from the continuity conditions at X_1 to the continuity conditions at X_{m-1}. Once this has been performed, the general form of the mode shape over each section for a CC and CF system is:

$$\begin{aligned} u_{n1}^{(i)}(X) =& A_{n1}^{(1)} \{\cos(\sqrt{\omega_{n0}}X) - \cosh(\sqrt{\omega_{n0}}X)\} + B_{n1}^{(1)} \{\sin(\sqrt{\omega_{n0}}X) - \sinh(\sqrt{\omega_{n0}}X)\} \\ &+ \frac{\omega_{n1}}{2\omega_{n0}} X \frac{\mathrm{d}\phi_{n0}}{\mathrm{d}X} + \widetilde{u}_{n1}^{(i)}(X) \end{aligned} \tag{3.26}$$

and the general form of the mode shape over each section for a FF system is:

$$u_{n1}^{(i)}(X) = A_{n1}^{(1)}\left\{\cos(\sqrt{\omega_{n0}}X) + \cosh(\sqrt{\omega_{n0}}X)\right\} + B_{n1}^{(1)}\left\{\sin(\sqrt{\omega_{n0}}X) + \sinh(\sqrt{\omega_{n0}}X)\right\} + \frac{\omega_{n1}}{2\omega_{n0}}X\frac{\mathrm{d}\phi_{n0}}{\mathrm{d}X} + \widetilde{u}_{n1}^{(i)}(X) \tag{3.27}$$

It is seen in Eqs. (3.26) and (3.27) that there are only two unknown coefficients that remain to be determined. The expressions of $\widetilde{u}_{n1}^{(i)}(X)$ for the various boundary conditions can be found in Appendix B.1.

Next, the boundary conditions at $X = 1$ are applied. Only the first boundary condition needs to be applied as the second boundary condition is automatically satisfied due to the choice of ω_{n1} from the solvability condition. Apply the third boundary condition listed in Eqs. (3.21)-(3.23). The expression for the mode shape over the i^{th} section for a CC system is:

$$u_{n1}^{(i)}(X) = A_{n1}^{(1)}\phi_{n0}(X) + \frac{\omega_{n1}}{2\omega_{n0}}X\frac{\mathrm{d}\phi_{n0}}{\mathrm{d}X} + \widetilde{u}_{n1}^{(i)}(X) - \frac{\widetilde{u}_{n1}^{(m)}(1)\left\{\sin(\sqrt{\omega_{n0}}X) - \sinh(\sqrt{\omega_{n0}}X)\right\}}{\left\{\sin(\sqrt{\omega_{n0}}) - \sinh(\sqrt{\omega_{n0}})\right\}} \tag{3.28}$$

The expression for the mode shape over the i^{th} section for a CF system is:

$$u_{n1}^{(i)}(X) = A_{n1}^{(1)}\phi_{n0}(X) + \frac{\omega_{n1}}{2\omega_{n0}}X\frac{\mathrm{d}\phi_{n0}}{\mathrm{d}X} + \widetilde{u}_{n1}^{(i)}(X) + \frac{\frac{\mathrm{d}^2\widetilde{u}_{n1}^{(m)}(1)}{\mathrm{d}X^2}\left\{\sin(\sqrt{\omega_{n0}}X) - \sinh(\sqrt{\omega_{n0}}X)\right\}}{\omega_{n0}\left\{\sin(\sqrt{\omega_{n0}}) + \sinh(\sqrt{\omega_{n0}})\right\}} \tag{3.29}$$

The expression for the mode shape over the i^{th} section for a FF system is:

$$u_{n1}^{(i)}(X) = A_{n1}^{(1)}\phi_{n0}(X) + \frac{\omega_{n1}}{2\omega_{n0}}X\frac{\mathrm{d}\phi_{n0}}{\mathrm{d}X} + \widetilde{u}_{n1}^{(i)}(X) + \frac{\frac{\mathrm{d}^2\widetilde{u}_{n1}^{(m)}(1)}{\mathrm{d}X^2}\left\{\sin(\sqrt{\omega_{n0}}X) + \sinh(\sqrt{\omega_{n0}}X)\right\}}{\omega_{n0}\left\{\sin(\sqrt{\omega_{n0}}) - \sinh(\sqrt{\omega_{n0}})\right\}} \tag{3.30}$$

The final step is to determine the coefficient $A_{n1}^{(1)}$ by applying the mass normalization condition of Eq. (3.10b). The coefficient $A_{n1}^{(1)}$ for a CC system is

$$A_{n1}^{(1)} = -\int_0^1 \frac{\omega_{n1}}{2\omega_{n0}}X\phi_{n0}\frac{\mathrm{d}\phi_{n0}}{\mathrm{d}X} + \phi_{n0}\widetilde{u}_{n1}(X) - \frac{\widetilde{u}_{n1}^{(m)}(1)\left\{\sin(\sqrt{\omega_{n0}}X) - \sinh(\sqrt{\omega_{n0}}X)\right\}}{\left\{\sin(\sqrt{\omega_{n0}}) - \sinh(\sqrt{\omega_{n0}})\right\}}\phi_{n0} + \frac{1}{2}\widehat{\rho A}(X)\phi_{n0}^2\,\mathrm{d}X \tag{3.31}$$

The coefficient $A_{n1}^{(1)}$ for a CF system is

$$A_{n1}^{(1)} = -\int_0^1 \frac{\omega_{n1}}{2\omega_{n0}} X\phi_{n0}\frac{\mathrm{d}\phi_{n0}}{\mathrm{d}X} + \phi_{n0}\widetilde{u}_{n1} + \frac{\frac{\mathrm{d}^2\widetilde{u}_{n1}^{(m)}(1)}{\mathrm{d}X^2}\left\{\sin(\sqrt{\omega_{n0}}X) - \sinh(\sqrt{\omega_{n0}}X)\right\}}{\omega_{n0}\left\{\sin(\sqrt{\omega_{n0}}) + \sinh(\sqrt{\omega_{n0}})\right\}}\phi_{n0} + \frac{1}{2}\widehat{\rho A}(X)\phi_{n0}^2\,\mathrm{d}X \tag{3.32}$$

The coefficient $A_{n1}^{(1)}$ for a FF system is

$$A_{n1}^{(1)} = -\int_0^1 \frac{\omega_{n1}}{2\omega_{n0}} X\phi_{n0}\frac{\mathrm{d}\phi_{n0}}{\mathrm{d}X} + \phi_{n0}\widetilde{u}_{n1} + \frac{\frac{\mathrm{d}^2\widetilde{u}_{n1}^{(m)}(1)}{\mathrm{d}X^2}\left\{\sin(\sqrt{\omega_{n0}}X) + \sinh(\sqrt{\omega_{n0}}X)\right\}}{\omega_{n0}\left\{\sin(\sqrt{\omega_{n0}}) - \sinh(\sqrt{\omega_{n0}})\right\}}\phi_{n0} + \frac{1}{2}\widehat{\rho A}(X)\phi_{n0}^2\,\mathrm{d}X \tag{3.33}$$

3.1.6 $\mathcal{O}(\epsilon^2)$ Problem

The ODE for the $\mathcal{O}(\epsilon^2)$ problem is

$$\frac{\mathrm{d}^4 u_{n2}}{\mathrm{d}X^4} - \omega_{n0}^2 u_{n2} = 2\omega_{n0}\omega_{n2}\phi_{n0} + 2\omega_{n0}\omega_{n1}\phi_{n1} + \omega_{n1}^2\phi_{n0} + \omega_{n0}^2\widehat{\rho A}\phi_{n1} + 2\omega_{n0}\omega_{n1}\widehat{\rho A}\phi_{n0} - \frac{\mathrm{d}^2}{\mathrm{d}X^2}\left[\widehat{EI}\frac{\mathrm{d}^2\phi_{n1}}{\mathrm{d}X^2}\right] \tag{3.34}$$

for $0 < X < 1$. A solution to the ODE exists when the following solvability condition is satisfied.

$$0 = \int_0^1 \left\{2\omega_{n0}\omega_{n2}\phi_{n0} + 2\omega_{n0}\omega_{n1}\phi_{n1} + \omega_{n1}^2\phi_{n0} + \omega_{n0}^2\widehat{\rho A}\phi_{n1} + 2\omega_{n0}\omega_{n1}\widehat{\rho A}\phi_{n0} - \frac{\mathrm{d}^2}{\mathrm{d}X^2}\left[\widehat{EI}\frac{\mathrm{d}^2\phi_{n1}}{\mathrm{d}X^2}\right]\right\}\phi_{n0}\,\mathrm{d}X \tag{3.35}$$

From the solvability condition in Eq. (3.35) the value for ω_{n2} is found. Using integration by parts and that CC, CF, and FF boundary conditions are under consideration, the solvability condition yields:

$$\omega_{n2} = -\frac{\omega_{n1}^2}{2\omega_{n0}} + \frac{1}{2\omega_{n0}}\int_0^1 \widehat{EI}\frac{\mathrm{d}^2\phi_{n1}}{\mathrm{d}X^2}\frac{\mathrm{d}^2\phi_{n0}}{\mathrm{d}X^2} - \omega_{n0}^2\widehat{\rho A}\phi_{n0}\phi_{n1} - \omega_{n0}\omega_{n1}\widehat{\rho A}(X)\phi_{n0}^2\,\mathrm{d}X \tag{3.36}$$

3.1.7 Final Dimensional Solution

Dependence on Reference Values

To determine the final expressions for the natural frequencies and mode shapes in terms of the reference values EI^* and ρA^* the parameter ϵ is removed. This is done by using the relationships $\epsilon\widehat{EI}(X) = (EI(X) - EI^*)/EI^*$ and $\epsilon\widehat{\rho A}(X) = (\rho A(X) - \rho A^*)/\rho A^*$. First, determine the dependence of the first correction to the frequencies in terms of the reference values.

$$\begin{aligned}
\epsilon\omega_{n1} =& \frac{1}{2\omega_{n0}} \int_0^1 \epsilon\widehat{EI} \left(\frac{\mathrm{d}^2\phi_{n0}}{\mathrm{d}X^2}\right)^2 \mathrm{d}X - \frac{\omega_{n0}}{2} \int_0^1 \epsilon\widehat{\rho A}\, \phi_{n0}^2 \,\mathrm{d}X \\
=& \frac{1}{EI^*} \left\{ \frac{\int_0^1 EI(X) \left(\frac{\mathrm{d}^2\phi_{n0}}{\mathrm{d}X^2}\right)^2 \mathrm{d}X}{2\omega_{n0}} \right\} - \frac{1}{\rho A^*} \left\{ \frac{\omega_{n0}}{2} \int_0^1 \rho A(X)\, \phi_{n0}^2 \,\mathrm{d}X \right\} \\
=& \frac{\alpha_{n1}}{EI^*} - \frac{\alpha_{n2}}{\rho A^*}
\end{aligned} \tag{3.37}$$

Above, it is seen that the expression for the first correction to the natural frequency is calculated solely in terms of the nondimensional bending stiffness and mass per unit length, the reference values, and the $\mathcal{O}(1)$ solution. The same procedure is applied to the first mode shape correction and the second frequency correction. The first correction to the mode shape is expressed as

$$\epsilon\phi_{n1}(X) = \frac{f_{n1}(X)}{\rho A^*} - \frac{f_{n2}(X)}{EI^*} + \frac{\phi_{n0}(X)}{2} \tag{3.38}$$

and the second frequency correction is expressed as

$$\epsilon^2\omega_{n2} = \frac{\alpha_{n1}}{EI^*} - \frac{\alpha_{n2}}{\rho A^*} + \frac{\beta_{n1}}{(EI^*)^2} + \frac{\beta_{n2}}{EI^*\rho A^*} + \frac{\beta_{n3}}{(\rho A^*)^2} \tag{3.39}$$

where

$$\beta_{n1} = -\frac{\alpha_{n1}^2}{2\omega_{n0}} - \frac{1}{2\omega_{n0}} \int_0^1 EI(X) \frac{\mathrm{d}^2\phi_{n0}}{\mathrm{d}X^2} \frac{\mathrm{d}^2 f_{n2}}{\mathrm{d}X^2} \,\mathrm{d}X \tag{3.40a}$$

$$\beta_{n2} = \frac{1}{2\omega_{n0}} \int_0^1 EI(X) \frac{\mathrm{d}^2\phi_{n0}}{\mathrm{d}X^2} \frac{\mathrm{d}^2 f_{n1}}{\mathrm{d}X^2} \,\mathrm{d}X + \frac{\omega_{n0}}{2} \int_0^1 \rho A(X) \phi_{n0} f_{n2} \,\mathrm{d}X \tag{3.40b}$$

$$\beta_{n3} = \frac{\alpha_{n2}^2}{2\omega_{n0}} - \frac{\omega_{n0}}{2} \int_0^1 \rho A(X) \phi_{n0} f_{n1} \,\mathrm{d}X \tag{3.40c}$$

The expressions of $f_{n1}(X)$ and $f_{n2}(X)$ for the various boundary conditions are given in Appendix C.1. The final expressions for the natural frequencies with two corrections and the mode shapes with one correction are

$$\omega_n = \omega_{n0} + \frac{2\alpha_{n1}}{EI^*} - \frac{2\alpha_{n2}}{\rho A^*} + \frac{\beta_{n1}}{(EI^*)^2} + \frac{\beta_{n2}}{EI^*\rho A^*} + \frac{\beta_{n3}}{(\rho A^*)^2} \tag{3.41}$$

$$\phi_n(X) = \frac{3}{2}\phi_{n0}(X) + \frac{f_{n1}(X)}{\rho A^*} - \frac{f_{n2}(X)}{EI^*} \tag{3.42}$$

Reintroduction of Dimensions

Dimension are reintroduced for the final solution using the length scale l and time scale $l^2\sqrt{\rho A^*/EI^*}$. For the mass normalized mode shapes, the dimensions of $1/\sqrt{\text{kg}}$ must be introduced. From the length and time scales used it follows that the mass scale is $l\rho A^*$. From the nondimensional results in Eqs. (3.41) and (3.42), the dimensional solution is

$$\overline{\omega}_n = \frac{1}{l^2}\sqrt{\frac{EI^*}{\rho A^*}}\left\{\omega_{n0} + \frac{2\alpha_{n1}}{EI^*} - \frac{2\alpha_{n2}}{\rho A^*} + \frac{\beta_{n1}}{(EI^*)^2} + \frac{\beta_{n2}}{EI^*\rho A^*} + \frac{\beta_{n3}}{(\rho A^*)^2}\right\} \tag{3.43}$$

$$\overline{\phi}_n(x) = \frac{1}{\sqrt{l\rho A^*}}\left\{\frac{3}{2}\phi_{n0}(x/l) + \frac{f_{n1}(x/l)}{\rho A^*} - \frac{f_{n2}(x/l)}{EI^*}\right\} \tag{3.44}$$

3.2 Reference Values Selection

The final expression for the natural frequencies and mode shapes of the system are in terms of the reference values EI^* and ρA^*. The value of these are yet to be determined and the method in which they are determined will influence the accuracy of the results. Multiple methods for determining the reference values are proposed.

3.2.1 Minimizing L_p Norm of Difference

The first proposed method for determining the reference values is to minimize the difference between the reference value and the associated spatially varying function. This is achieved

by considering the L_p norm for continuous functions. Mathematically,

$$EI^* = \min_{EI^* \in \mathbb{R}} \left\{ \left(\int_0^l |EI\,(x) - EI^*|^p \, \mathrm{d}x \right)^{1/p} \right\} \tag{3.45a}$$

$$\rho A^* = \min_{\rho A^* \in \mathbb{R}} \left\{ \left(\int_0^l |\rho A\,(x) - \rho A^*|^p \, \mathrm{d}x \right)^{1/p} \right\} \tag{3.45b}$$

where p is a positive integer.

Performing the minimization of the L_p norm of the difference results in a single value for EI^* and ρA^*, which does not depend on the mode number. Generally, the minimization procedure cannot be solved exactly to determine the optimal reference values. In the specific case that $p = 2$, however, an exact expression is found for the reference values.

$$EI^* = \frac{\int_0^l EI\,(x) \, \mathrm{d}x}{l} \quad , \quad \rho A^* = \frac{\int_0^l \rho A\,(x) \, \mathrm{d}x}{l} \tag{3.46}$$

In the case of $p = 2$ it is seen that the optimal reference values correspond to the average value for the bending stiffness and mass per unit length over the length of the system.

3.2.2 Minimizing L_p Norm of Perturbation

The next proposed method also considers an L_p norm minimization and applies the minimization to the terms that introduce perturbations in the nondimensional ODE in Eq. (3.5). This is expressed mathematically as

$$EI^* = \min_{EI^* \in \mathbb{R}} \left\{ \left(\int_0^1 \left| \frac{EI\,(X) - EI^*}{EI^*} \right|^p \, \mathrm{d}X \right)^{1/p} \right\} \tag{3.47a}$$

$$\rho A^* = \min_{\rho A^* \in \mathbb{R}} \left\{ \left(\int_0^1 \left| \frac{\rho A\,(X) - \rho A^*}{\rho A^*} \right|^p \, \mathrm{d}X \right)^{1/p} \right\} \tag{3.47b}$$

where p is a positive integer.

Performing the minimization of the L_p norm of the perturbations results in a single value for EI^* and ρA^*, which does not depend on the mode number. Minimizing the perturbations can be interpreted as minimizing the error between the reference value and the associated function over the length of the system.

It should be noted that the minimization in this case is with respect to the nondimensional length X whereas the minimization of the L_p norm of the difference was with respect to the dimensional length x. The choice of the nondimensional domain for the perturbation minimization was due to this being the domain in consideration when applying the perturbation theory. Minimizing the expressions in Eq. (3.47) over either the dimensional or nondimensional domains will result in the same reference values.

3.2.3 Minimizing Gradient Norm

The final proposed method is the minimization of the norm of the gradient of the frequencies. In this case the L_2 (Euclidean) norm is used and the expression for the dimensional natural frequencies in Eq. (3.43) is considered. The gradient of the frequencies is taken with respect to EI^* and ρA^*. The motivation for the gradient minimization approach is that small variations to the reference values should produce larger changes in the frequency prediction when EI^* and ρA^* does not give accurate results compared to when the values are optimally chosen. In other words, stable equilibrium points for the gradient of the frequency expression are assumed to correspond to locations of optimal reference values.

Additionally, constraints are added to the minimization procedure. The first constraint is that the sum of the corrections for the natural frequency is zero. This constraint is imposed to produce simple expressions for the frequencies and is motivated by previous work in [75]. The second set of constraints is with respect to the range of allowable values for the reference values. It is imposed that the reference values cannot be less than or greater than the minimum and maximum values of the respective spatially varying functions.

The mathematical expression for the gradient norm minimization method is

$$\text{minimize:} \qquad \left\|\nabla\overline{\omega}_n\right\|_2 \tag{3.48a}$$

$$\text{subject to:} \qquad \min_{x\in[0,l]} EI\left(x\right) \leq EI^* \leq \max_{x\in[0,l]} EI\left(x\right) \tag{3.48b}$$

$$\min_{x\in[0,l]} \rho A\left(x\right) \leq \rho A^* \leq \max_{x\in[0,l]} \rho A\left(x\right) \tag{3.48c}$$

$$\frac{2\alpha_{n1}}{EI^*} - \frac{2\alpha_{n2}}{\rho A^*} + \frac{\beta_{n1}}{\left(EI^*\right)^2} + \frac{\beta_{n2}}{EI^*\rho A^*} + \frac{\beta_{n3}}{\left(\rho A^*\right)^2} = 0 \tag{3.48d}$$

The Euclidean norm of the gradient for the dimensional frequencies is given by

$$\|\nabla\overline{\omega}_n\|_2 = \frac{1}{2l^2}\left\{\frac{1}{EI^*\rho A^*}\left(\omega_{n0} - \frac{2\alpha_{n1}}{EI^*} - \frac{2\alpha_{n2}}{\rho A^*} - \frac{3\beta_{n1}}{\left(EI^*\right)^2} - \frac{\beta_{n2}}{EI^*\rho A^*} + \frac{\beta_{n3}}{\left(\rho A^*\right)^2}\right)^2 + \frac{EI^*}{\left(\rho A^*\right)^3}\left(\omega_{n0} + \frac{2\alpha_{n1}}{EI^*} - \frac{6\alpha_{n2}}{\rho A^*} + \frac{\beta_{n1}}{\left(EI^*\right)^2} + \frac{3\beta_{n2}}{EI^*\rho A^*} + \frac{5\beta_{n3}}{\left(\rho A^*\right)^2}\right)^2\right\}^{1/2} \tag{3.49}$$

Performing the gradient norm minimization, a value for EI_n^* and ρA_n^* are determined for each mode of the system. In this procedure, it is possible for various modes to have the same value for EI_n^* or ρA_n^*. This would be the case if the bending stiffness or mass per unit length were constant throughout the system. The gradient norm minimization producing different reference values for each mode of the system is in contrast to the two previous methods where a single value was produced for all the modes of the system.

Single Frequency Correction

In the case of a single correction to the frequency, the gradient norm minimization procedure becomes

$$\text{minimize:} \quad \frac{1}{2l^2}\left\{\frac{1}{EI^*\rho A^*}\left(\omega_{n0} - \frac{\alpha_{n1}}{EI^*} - \frac{\alpha_{n2}}{\rho A^*}\right)^2 + \frac{EI^*}{\left(\rho A^*\right)^3}\left(\omega_{n0} + \frac{\alpha_{n1}}{EI^*} - \frac{3\alpha_{n2}}{\rho A^*}\right)^2\right\}^{1/2} \tag{3.50a}$$

$$\text{subject to:} \quad \min_{x\in[0,l]} EI\left(x\right) \leq EI^* \leq \max_{x\in[0,l]} EI\left(x\right) \tag{3.50b}$$

$$\min_{x\in[0,l]} \rho A\left(x\right) \leq \rho A^* \leq \max_{x\in[0,l]} \rho A\left(x\right) \tag{3.50c}$$

$$\frac{\alpha_{n1}}{EI^*} - \frac{\alpha_{n2}}{\rho A^*} = 0 \tag{3.50d}$$

In this case, the reference values can be found explicitly and are given by $EI_n^* = 2\alpha_{n1}/\omega_{n0}$ and $\rho A_n^* = 2\alpha_{n2}/\omega_{n0}$, where α_{n1} and α_{n2} are given in Eq. (3.37). The norm of the gradient is 0 for this choice of reference values. Furthermore, these reference values correspond exactly to the results of [75]. Thus, the proposed method in Eq. (3.48) is a generalization of the method for determining reference values that was described in [75]

Existence of Solution

Due to the presence in Eq. (3.48) of the constraint that the sum of the corrections is zero, it is not immediately obvious if a solution always exists for the minimization procedure. The existence of a solution can be determined by proving that there is at least one point that satisfies the constraints of the system.

First consider the case of a constant bending stiffness and mass per unit length over the entire length of the system. Straightforward substitution into the minimization procedure shows that the reference values should be taken as the constant and the constraints of the system will be satisfied. Without loss of generality, assume that both $EI(x)$ and $\rho A(x)$ are spatially dependent. For convenience, write the expression for the dimensional frequencies as

$$\overline{\omega}_n\left(EI^*, \rho A^*\right) = \frac{1}{l^2}\sqrt{\frac{EI^*}{\rho A^*}}\left[\omega_{n0} + \Omega_n\left(EI^*, \rho A^*\right)\right] \tag{3.51}$$

In Eq. (3.51), $\Omega_n\left(EI^*, \rho A^*\right)$ is the sum of the corrections to the natural frequencies.

To show that there is at least one point that satisfies the final constraint of the minimization procedure, consider the following two extreme cases. First, consider the reference values $EI_1^* = \max_{x\in[0,l]} EI(x)$ and $\rho A_1^* = \min_{x\in[0,l]} \rho A(x)$. For this choice of reference values, the expression $\omega_{n0}\sqrt{EI_1^*/\rho A_1^*}/l^2$ will overestimate the natural frequency for the n^{th} mode. The perturbation theory will compensate for this overestimation by producing a negative sum of corrections, $\Omega_n\left(EI_1^*, \rho A_1^*\right) < 0$. Next, consider the reference values $EI_2^* = \min_{x\in[0,l]} EI(x)$ and $\rho A_2^* = \max_{x\in[0,l]} \rho A(x)$. For this choice of reference values, the expression $\omega_{n0}\sqrt{EI_2^*/\rho A_2^*}/l^2$ will underestimate the natural frequency for the n^{th} mode. The perturbation theory will compensate for this underestimation by producing a positive sum of corrections, $\Omega_n\left(EI_2^*, \rho A_2^*\right) > 0$.

The first set of constraints in the minimization procedure create upper and lower bounds for the reference values. Considering a two-dimensional Euclidean space, the bounds on the reference values form a convex set. Since the set is convex, a path exists from $(EI_1^*, \rho A_1^*)$ to $(EI_2^*, \rho A_2^*)$. Since $\Omega_n\left(EI_1^*, \rho A_1^*\right) < 0 < \Omega_n\left(EI_2^*, \rho A_2^*\right)$, it follow from a corollary to the intermediate value theorem [36] that there exists a point $(EI_3^*, \rho A_3^*)$ such that $\Omega_n\left(EI_3^*, \rho A_3^*\right) = 0$. Therefore there exists at least one set of reference values that satisfies all the constraints of the minimization problem.

3.3 Simulation Results for Simple Cases

3.3.1 Stepped Beam

The first simple test case that is considered is a stepped beam with two homogeneous sections described by

$$EI(x) = \begin{cases} 1\,, & 0 \le x \le l_0 \\ \tau\,, & l_0 \le x \le l \end{cases} \quad \text{and} \quad \rho A(x) = \begin{cases} 1\,, & 0 \le x \le l_0 \\ \gamma\,, & l_0 \le x \le l \end{cases}$$

It is assumed that τ, $\gamma > 0$. Using the notation from the perturbation theory, the point where $EI(x)$ and $\rho A(x)$ are not C^∞-functions is $P_{EI} = P_{\rho A} = \{l_0\}$.

For the case of a stepped beam, an expression for the reference values determined using the norm minimization methods of Sections 3.2.1 and 3.2.2 can be found. As the bending stiffness and mass per unit length of the stepped system are similar in form, the expression found for the bending stiffness reference value is similar to the expression for the mass per unit length reference value. The expressions for the bending stiffness reference value using the L_p norm of the difference and the L_p norm of the perturbation are given by, respectively:

$$EI^*_{\text{diff}} = \frac{l_0^{1/(p-1)} + \tau\,(l-l_0)^{1/(p-1)}}{l_0^{1/(p-1)} + (l-l_0)^{1/(p-1)}} \tag{3.52}$$

$$EI^*_{\text{pert}} = \frac{l_0^{1/(p-1)} + \tau^{p/(p-1)}\,(l-l_0)^{1/(p-1)}}{l_0^{1/(p-1)} + \tau^{1/(p-1)}\,(l-l_0)^{1/(p-1)}} \tag{3.53}$$

In Eqs. (3.52) and (3.53), $p \ge 2$. It can be shown that if the minimization procedure is attempted with $p = 1$, then the reference values are not unique. Therefore this case is not considered.

The effect of the p-value and ratio l_0/l on EI^* is presented in Fig. 3.1. In Fig. 3.1 the case of $\tau > 1$ is considered. The figure for the case of $0 < \tau < 1$ is obtained by reflecting the results in Fig. 3.1 about the line $EI^* = 1$.

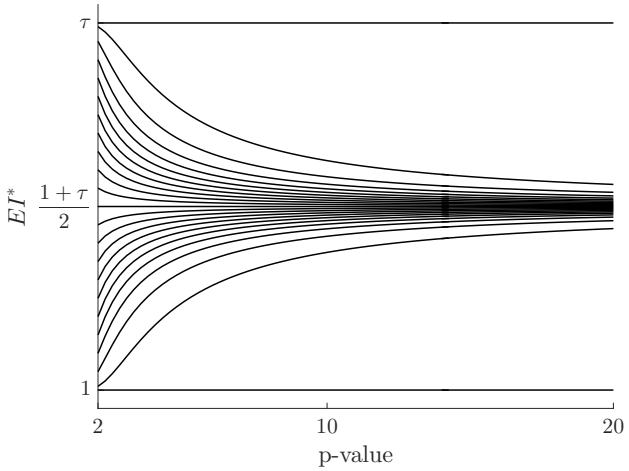

Figure 3.1: EI^* for various p and l_0/l values.

As the value of p increases, it is seen in Fig. 3.1 that the value of EI^* approaches $(1+\tau)/2$. That is to say EI^* approaches the average bending stiffness value of the two sections $(1+\tau)/2$, regardless of the length of each of the two sections. This holds true for both norm minimization methods and is found by taking the limit as p approaches infinity in Eqs. (3.52) and (3.53). For smaller p-values, the length of each of the homogeneous sections will play a role in the reference value. Physical interpretation can be given to the case of $p = 2$ for the norm minimization of the difference. In this case $EI^*_{\text{diff}} = l_0/l + \tau\,(l - l_0)\,/l$ and this is the average of the bending stiffness in the system using the length of each section as a weight.

It is observed in Fig. 3.1 that certain choices for l_0/l will produce a result for EI^* that is independent of p. When $l_0/l = 1$ there is only one homogeneous section in the beam with bending stiffness 1. Therefore in this case the reference value is taken as $EI^* = 1$ for both norm minimization methods. Similarly, when $l_0/l = 0$ there is only one homogeneous section in the beam with bending stiffness τ. Therefore in this case the reference value is taken as $EI^* = \tau$ for both norm minimization methods. Lastly, it is seen that there is a p independent line at $EI^* = (1+\tau)/2$. From Eqs. (3.52) and (3.53), assuming $EI^* = (1+\tau)/2$ allows the corresponding value for l_0/l to be determined. For the norm of the difference the value is $l_0/l = 1/2$ and for the norm of the perturbation the value is $l_0/l = \tau/(1+\tau)$.

To investigate the ability of the perturbation theory to predict the natural frequencies and mode shapes of the system, the error between the perturbation theory and an analytical model is calculated for multiple cases. The first 10 transverse bending modes are

considered. Denoting the perturbation and analytical results by a subscript 'p' and 'a', respectively, the sum of the absolute percentage of error of the frequencies is calculated as:

$$\sum_{n=1}^{10} 100 \left| \frac{\omega_{n,\mathrm{p}} - \omega_{n,\mathrm{a}}}{\omega_{n,\mathrm{a}}} \right| \tag{3.54}$$

and the sum of the absolute percentage of error of the mode shapes is given by:

$$\sum_{n=1}^{10} 100 \frac{\int_0^l \left(\phi_{n,\mathrm{p}}(x) - \phi_{n,\mathrm{a}}(x)\right)^2 \, \mathrm{d}x}{\int_0^l \phi_{n,\mathrm{a}}^2(x) \, \mathrm{d}x} \tag{3.55}$$

Clamped-clamped (CC), clamped-free (CF), and free-free (FF) boundary conditions are considered and the error results for variable τ are presented in Figs. 3.2 and 3.3, and the error results for variable γ are presented in Figs. 3.4 and 3.5. In each of the presented figures the results for the various proposed methods of determining the reference values are given. A first and second-order correction for the gradient minimization are considered; a first-order correction corresponds to the results that would be obtained using the method presented in [75]. The p-value listed for the norm minimization methods is the value that minimizes the total error in the frequencies and mode shapes across the variable parameter and was determined separately for each boundary conditions and l_0/l value.

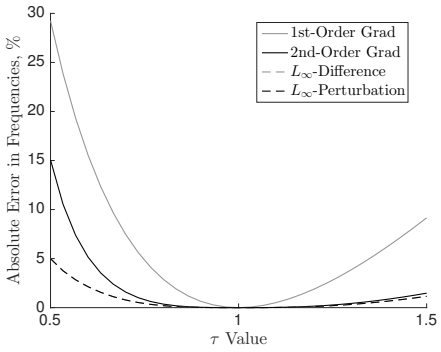

(a) CC and $l_0/l = 1/4$

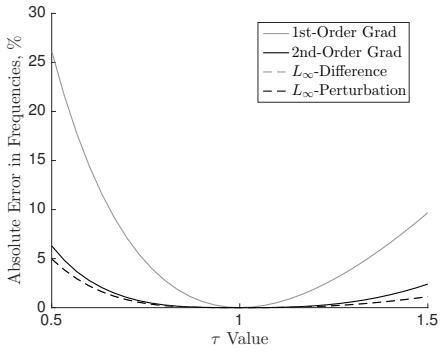

(b) CC and $l_0/l = 3/4$

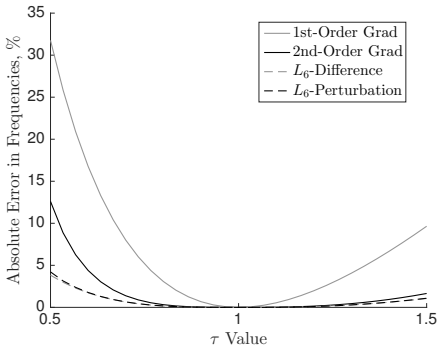

(c) CF and $l_0/l = 1/4$

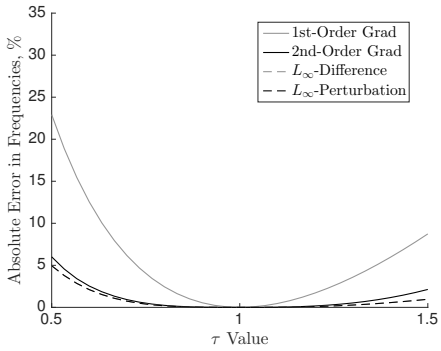

(d) CF and $l_0/l = 3/4$

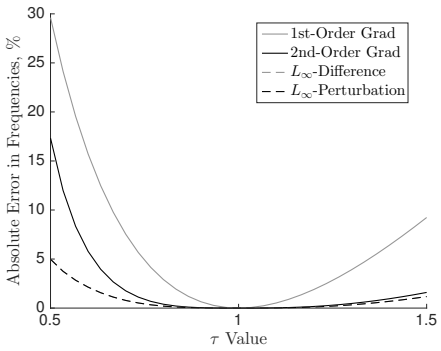

(e) FF and $l_0/l = 1/4$

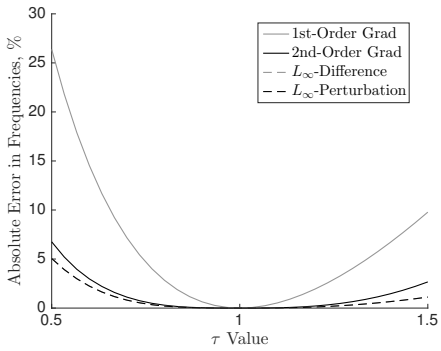

(f) FF and $l_0/l = 3/4$

Figure 3.2: Sum of absolute error in frequencies for variable τ.

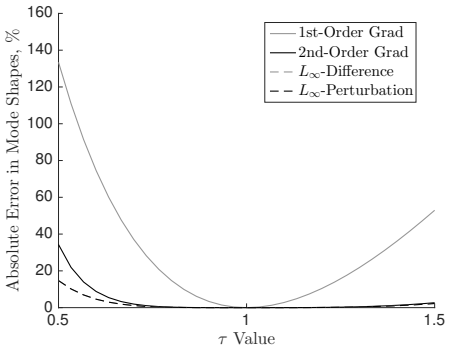

(a) CC and $l_0/l = 1/4$

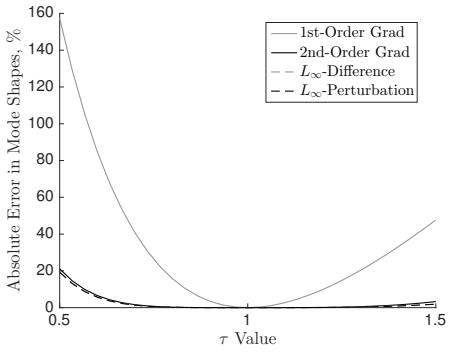

(b) CC and $l_0/l = 3/4$

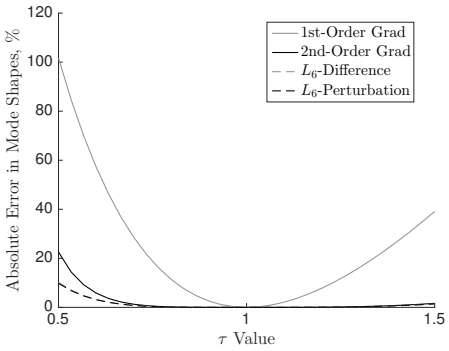

(c) CF and $l_0/l = 1/4$

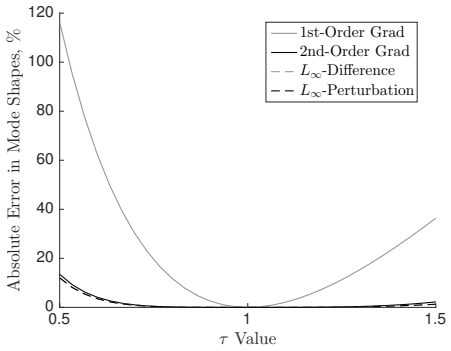

(d) CF and $l_0/l = 3/4$

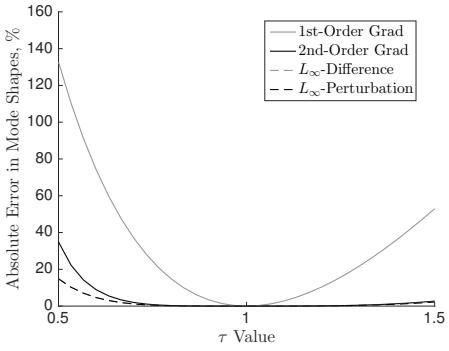

(e) FF and $l_0/l = 1/4$

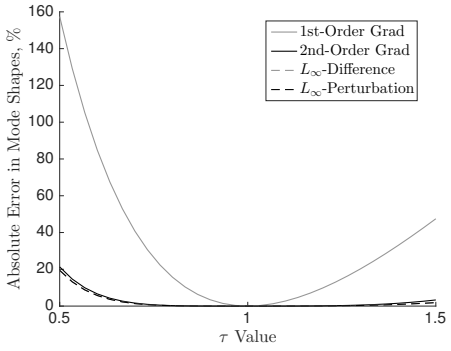

(f) FF and $l_0/l = 3/4$

Figure 3.3: Sum of absolute error in mode shapes for variable τ.

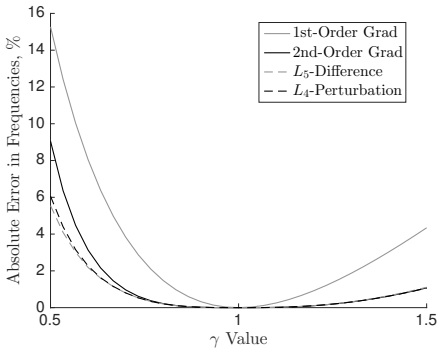

(a) CC and $l_0/l = 1/4$

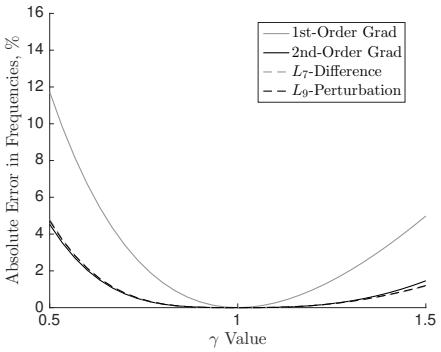

(b) CC and $l_0/l = 3/4$

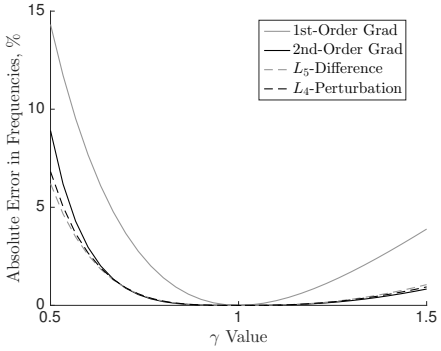

(c) CF and $l_0/l = 1/4$

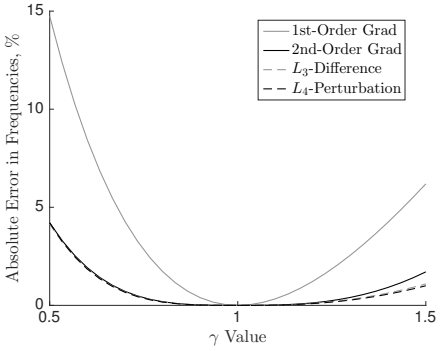

(d) CF and $l_0/l = 3/4$

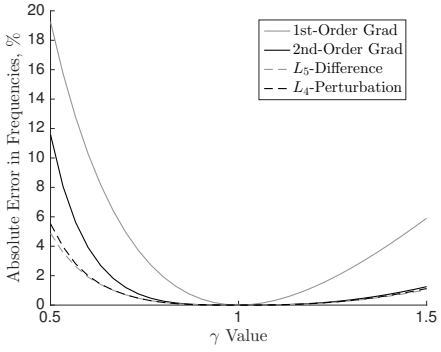

(e) FF and $l_0/l = 1/4$

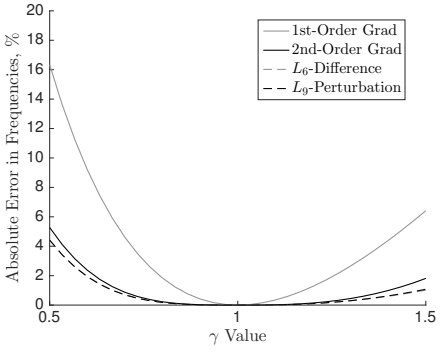

(f) FF and $l_0/l = 3/4$

Figure 3.4: Sum of absolute error in frequencies for variable γ.

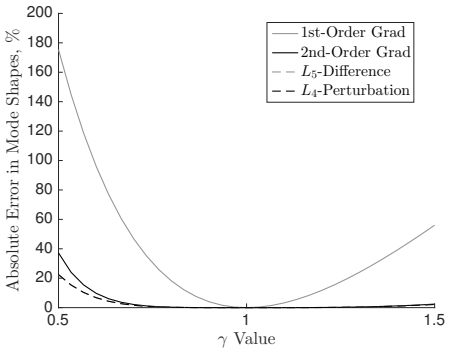

(a) CC and $l_0/l = 1/4$

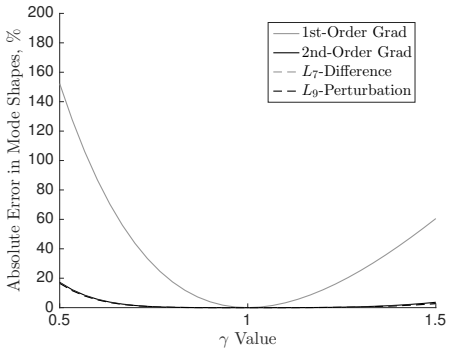

(b) CC and $l_0/l = 3/4$

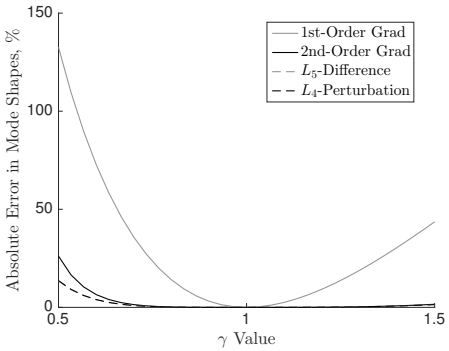

(c) CF and $l_0/l = 1/4$

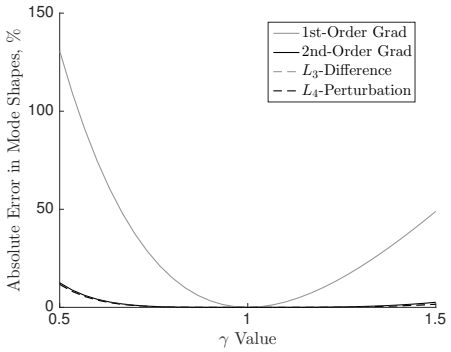

(d) CF and $l_0/l = 3/4$

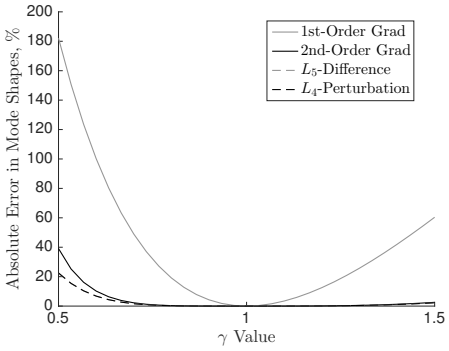

(e) FF and $l_0/l = 1/4$

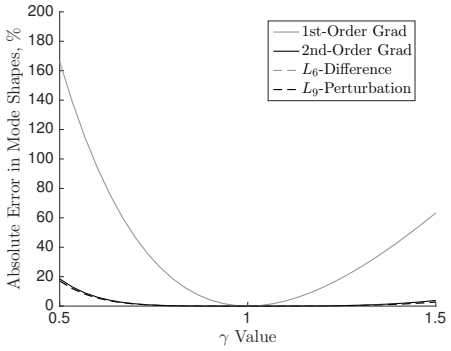

(f) FF and $l_0/l = 3/4$

Figure 3.5: Sum of absolute error in mode shapes for variable γ.

In Figs. 3.2 - 3.5 it is seen that when both τ and γ are 1 that the sum of the error for the frequencies and mode shapes is 0. This makes sense as when both τ and γ are 1 the system becomes a homogeneous beam, and in this case the perturbation theory results exactly match those of the analytical model. Furthermore, throughout all the figures it is observed that the first-order gradient minimization always produces that largest sum of error, while the norm minimization methods always produces the smallest sum of error. Typically, the second-order gradient minimization method produces a sum of error that is only slightly larger than the norm minimization methods. It is expected that the norm minimization methods produce the smallest errors as the p-value was optimally chosen. Overall, the CF boundary conditions typically produced the smallest sum of errors for both the frequencies and mode shapes when compared to the CC and FF boundary conditions.

Next consider the shape of the curves in Figs. 3.2 - 3.5. As the value of τ or γ moves away from 1, there is an increase in the sum of the errors for both the natural frequencies and the mode shapes. This is expected since the further the values of τ and γ are from 1 the larger the perturbation is in the system. The larger perturbation inherently leads to larger errors from the perturbation theory in the prediction of the frequencies and mode shapes. It is seen that for both the frequencies and mode shapes, the largest sum of error for a given set of system parameters always occurs when either τ or γ is 0.5. In addition, it is seen that the curves for the reference value selection methods utilizing two corrections are less affected by variations in τ and γ near unity when compared to the first-order gradient minimization where only one correction to the frequency is considered. This is expected as a higher number of corrections in the perturbation theory leads to more accurate results over a larger range of values for the variables.

Furthermore, it is observed that the results for the error in the frequencies and mode shapes are not symmetric about the vertical line given by $\tau = 1$ in Figs. 3.2 and 3.3 and are not symmetric about the vertical line $\gamma = 1$ in Figs. 3.4 and 3.5. This is due to an increase in the bending stiffness affecting the system and the resulting perturbation theory solution differently than a decrease in the bending stiffness. A similar argument holds when considering the mass per unit length of the system. Although the results obtained are not symmetric about either $\tau = 1$ or $\gamma = 1$, the results obtained for the cases of $l_0/l = 1/4$ and $l_0/l = 3/4$ can be related to each other. The error obtained in the $l_0/l = 1/4$ case for a given τ is equal to the error obtained in the $l_0/l = 3/4$ case for $1/\tau$, and vice versa. A similar result holds true when considering the case of variable γ.

Lastly, the p-value that minimizes the sum of the error is investigated. For variable τ in Figs. 3.2 and 3.3, typically the optimal reference value was obtained when the value of p becomes infinitely large. This indicates that for variable bending stiffness the optimal reference value is typically the average bending stiffness of the two sections. For variable

γ in Figs. 3.4 and 3.5, the optimal reference values were found when the value of p was between 3 and 9, inclusively. In contrast to the variable τ results, this seems to indicate that the length of each of the sections plays a role in determining the optimal reference values. Therefore for variable mass per unit length the optimal reference value should be determined using a p-value of less than 10.

Consider next the fundamental mode shapes for two systems, each with $l_0/l = 1/4$, where one system has $\tau = 1.5$ and $\gamma = 1$ and the other has $\tau = 1$ and $\gamma = 1.5$. For CC, CF, and FF boundary conditions, Figs. 3.6 - 3.8 present the results for displacement, moment, and shear associated with the fundamental mode. The values for p in the two systems are taken from the previous results for variable τ and variable γ.

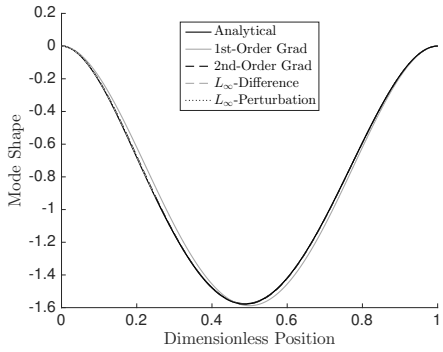

(a) Displacement, $\tau = 1.5$

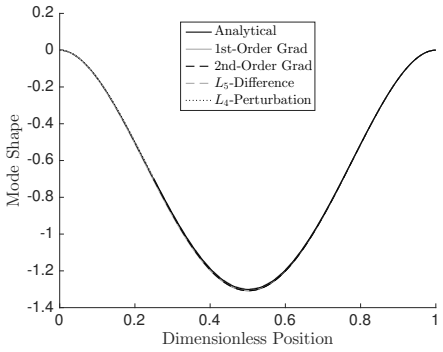

(b) Displacement, $\gamma = 1.5$

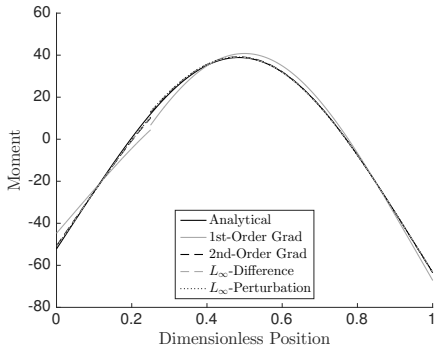

(c) Moment, $\tau = 1.5$

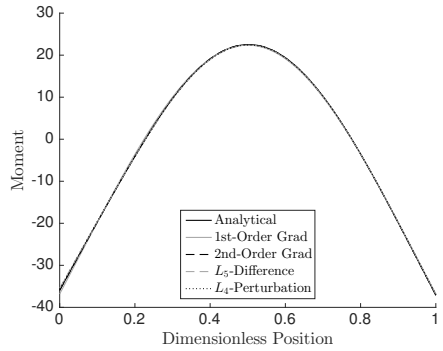

(d) Moment, $\gamma = 1.5$

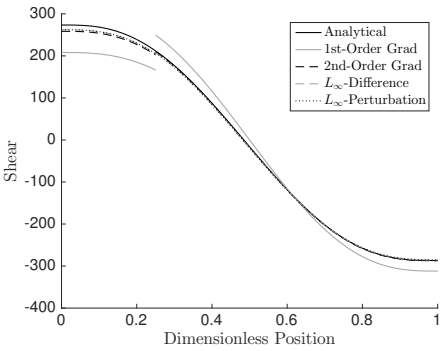

(e) Shear, $\tau = 1.5$

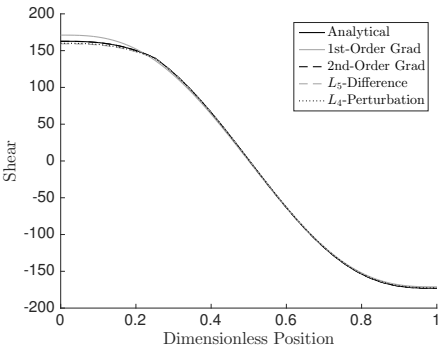

(f) Shear, $\gamma = 1.5$

Figure 3.6: Fundamental mode shape displacement, moment, and shear for a CC system.

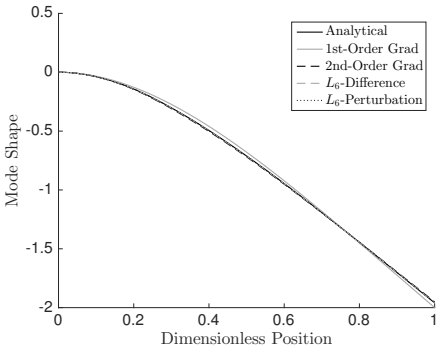

(a) Displacement, $\tau = 1.5$

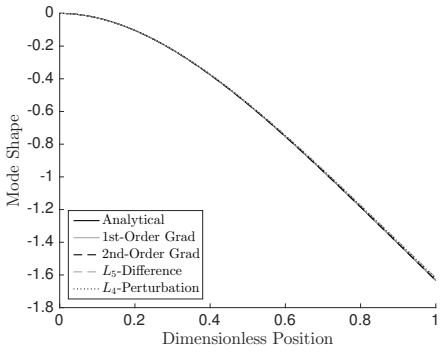

(b) Displacement, $\gamma = 1.5$

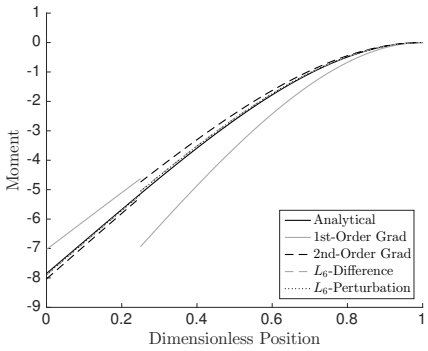

(c) Moment, $\tau = 1.5$

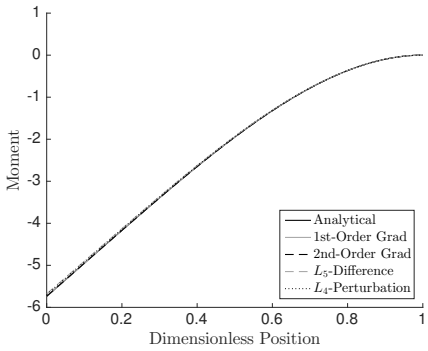

(d) Moment, $\gamma = 1.5$

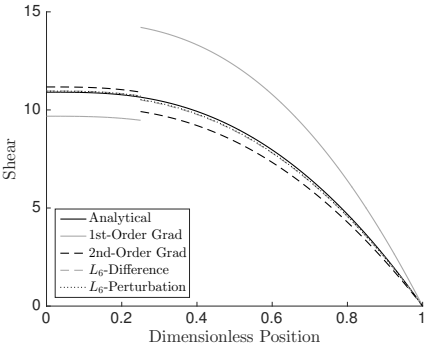

(e) Shear, $\tau = 1.5$

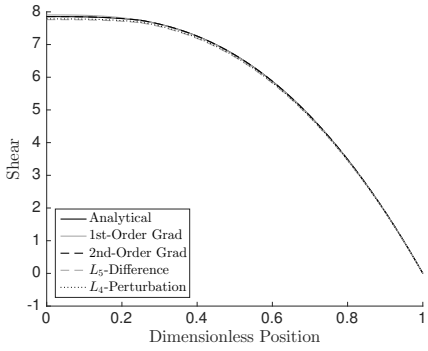

(f) Shear, $\gamma = 1.5$

Figure 3.7: Fundamental mode shape displacement, moment, and shear for a CF system.

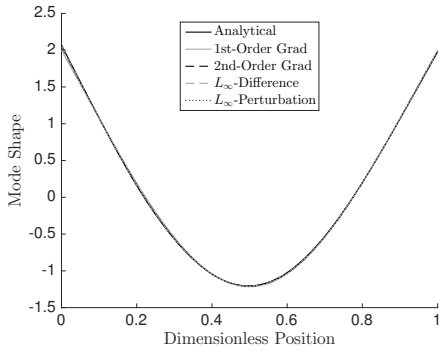

(a) Displacement, $\tau = 1.5$

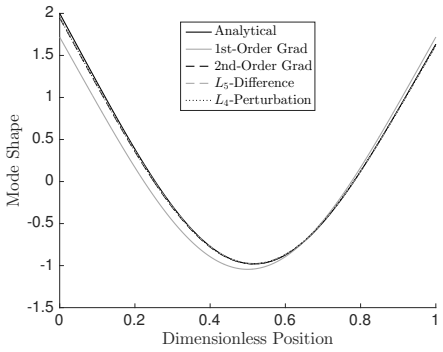

(b) Displacement, $\gamma = 1.5$

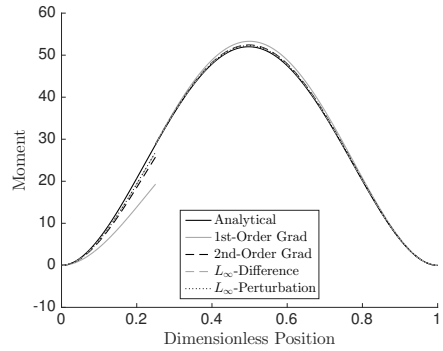

(c) Moment, $\tau = 1.5$

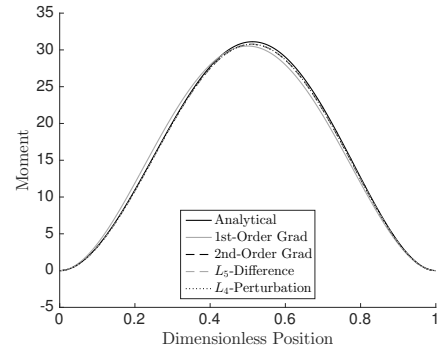

(d) Moment, $\gamma = 1.5$

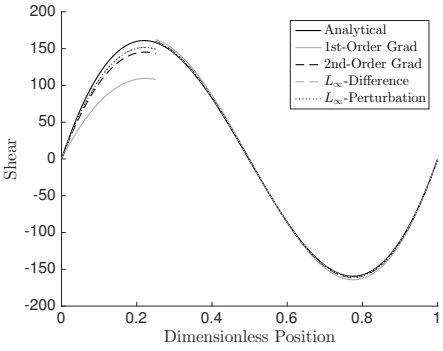

(e) Shear, $\tau = 1.5$

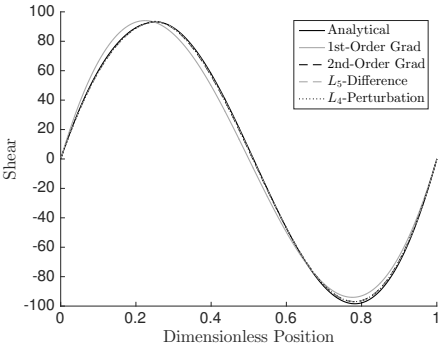

(f) Shear, $\gamma = 1.5$

Figure 3.8: Fundamental mode shape displacement, moment, and shear for a FF system.

In Figs. 3.6 - 3.8 it is seen for the system with $\tau = 1.5$ and $\gamma = 1$ that there is a discontinuity in the moment and shear associated with the fundamental mode at $l_0/l = 1/4$. This discontinuity does not appear in the moment and shear associated with the fundamental mode for the system with $\tau = 1$ and $\gamma = 1.5$. The discontinuity in the moment can be investigated by analyzing the expression for the moment in the system. Consider the moment of the nondimensional system, obtained from Eq. (3.6):

$$M(X) = \left\{1 + \epsilon\widehat{EI}(X)\right\} \frac{\mathrm{d}^2\phi(X)}{\mathrm{d}X^2} \tag{3.56}$$

The perturbation theory of the current work considers a single correction to the mode shapes, that is $\phi(X) = \phi_0(X) + \epsilon\phi_1(X)$. Let X_P denote a location where the bending stiffness and mass per unit length of the system are not C^∞-functions. Consider the following:

$$\begin{aligned}
&M\left(X_P^-\right) - M\left(X_P^+\right) \\
&= \left\{1 + \epsilon\widehat{EI}(X_P^-)\right\} \left\{\frac{\mathrm{d}^2\phi_0(X_P^-)}{\mathrm{d}X^2} + \frac{\mathrm{d}^2\epsilon\phi_1(X_P^-)}{\mathrm{d}X^2}\right\} - \left\{1 + \epsilon\widehat{EI}(X_P^+)\right\} \left\{\frac{\mathrm{d}^2\phi_0(X_P^+)}{\mathrm{d}X^2} + \frac{\mathrm{d}^2\epsilon\phi_1(X_P^+)}{\mathrm{d}X^2}\right\} \\
&= \left(EI(X_P^+) - EI(X_P^-)\right) \left\{\frac{EI(X_P^-) - EI^*}{(EI^*)^2} \frac{\mathrm{d}^2\phi_0(X_P)}{\mathrm{d}X^2} + \frac{1}{EI^*} \frac{\mathrm{d}^2\epsilon\phi_1(X_P^+)}{\mathrm{d}X^2}\right\}
\end{aligned} \tag{3.57}$$

It is seen in Eq. (3.57) that if the bending stiffness of the system is continuous, then the moment in the system from the perturbation theory results will be continuous. If the bending stiffness of the system is discontinuous, then the moment in the system from the perturbation theory results may or may not be discontinuous. Furthermore, the continuity of the moment is not influenced by the mass per unit length of the system. For the stepped beam, the bending stiffness in the system is continuous when $\tau = 1$ and discontinuous otherwise. For a system with $\tau = 1.5$, this discontinuity causes the jumps seen in Figs. 3.6c, 3.7c, and 3.8c for the moment, whereas for the system with $\tau = 1$ in Figs. 3.6d, 3.7d, and 3.8d the bending stiffness is continuous and thus so is the moment.

The shear in the system, $S(X) = \frac{\mathrm{d}}{\mathrm{d}X}M(X)$ is analyze in a similar manner as the moment in the system. Let X_P denote a location where the bending stiffness and mass per unit length of the system are not C^∞-functions. Consider the following

$$\begin{aligned}
&S\left(X_P^-\right) - S\left(X_P^+\right) \\
&= \left(EI(X_P^+) - EI(X_P^-)\right) \left\{\frac{EI(X_P^-) - EI^*}{(EI^*)^2} \frac{\mathrm{d}^3\phi_0(X_P)}{\mathrm{d}X^3} + \frac{\frac{\mathrm{d}EI(X_P^-)}{\mathrm{d}X}}{(EI^*)^2} \frac{\mathrm{d}^2\phi_0(X_P)}{\mathrm{d}X^2} - \frac{1}{EI^*} \frac{\mathrm{d}^3\epsilon\phi_1(X_P^+)}{\mathrm{d}X^3}\right\} \\
&\quad + \left(\frac{\mathrm{d}EI(X_P^+)}{\mathrm{d}X} - \frac{\mathrm{d}EI(X_P^-)}{\mathrm{d}X}\right) \left\{\frac{EI(X_P^-) - EI^*}{(EI^*)^2} \frac{\mathrm{d}^2\phi_0(X_P)}{\mathrm{d}X^2} - \frac{1}{EI^*} \frac{\mathrm{d}^2\epsilon\phi_1(X_P^+)}{\mathrm{d}X^2}\right\}
\end{aligned} \tag{3.58}$$

It is seen Eq. (3.58) that if bending stiffness of the system and its first derivative are continuous, then the shear in the system from the perturbation theory results will be continuous. If the bending stiffness of the system or the first derivative is discontinuous, then the shear in the system from the perturbation theory results may or may not be discontinuous. Furthermore, the continuity of the shear is not influenced by the mass per unit length of the system. For the stepped beam, the bending stiffness in the system and its first derivative are continuous when $\tau = 1$ and discontinuous otherwise. For a system with $\tau = 1.5$, this discontinuity causes the jumps seen in Figs. 3.6e, 3.7e, and 3.8e for the shear, whereas for the system with $\tau = 1$ in Figs. 3.6f, 3.7f, and 3.8f the bending stiffness and its first derivative are continuous and thus so is the shear.

Overall, the perturbation theory results presented in Figs. 3.6 - 3.8 show a better overall match to the analytical results for the system with $\tau = 1$ and $\gamma = 1.5$ when compared to the system with $\tau = 1.5$ and $\gamma = 1$. This is mainly due to the absence of discontinuities when the mass per unit length is continuous. With regard to the reference value selection methods, the method with fewer corrections to the frequencies and mode shapes produced the least accurate results, as expected. The norm minimization methods typically provided the most accurate results, in particular with respect to the magnitude of the jump in the moment and shear when there is a discontinuity. This increase in accuracy at the discontinuous point is quantified by calculating the absolute percentage of error of the various proposed methods in predicting the value of the moment and shear when compared to the analytical model. The results are presented in Table 3.1

Table 3.1: Absolute error in perturbation theory compared to analytical model in moment and shear at discontinuity

Value Selection Method	Moment $l_0/l = 1/4^-$	Moment $l_0/l = 1/4^+$	Shear $l_0/l = 1/4^-$	Shear $l_0/l = 1/4^+$
		Clamped-Clamped		
1st-Order Grad, %	62.94	44.40	21.44	17.84
2nd-Order Grad, %	15.99	5.32	4.55	0.67
L_∞-Difference, %	12.48	9.04	3.28	2.06
L_∞-Perturbation, %	12.48	9.04	3.28	2.06
		Clamped-Free		
1st-Order Grad, %	9.90	35.02	11.05	33.43
2nd-Order Grad, %	2.33	7.73	2.42	6.87
L_6-Difference, %	0.64	1.89	0.58	1.36
L_6-Perturbation, %	0.56	1.60	0.49	1.09
		Free-Free		
1st-Order Grad, %	32.74	0.89	31.64	2.54
2nd-Order Grad, %	10.24	0.32	9.53	0.82
L_∞-Difference, %	6.28	0.22	5.64	0.52
L_∞-Perturbation, %	6.28	0.22	5.64	0.52

Table 3.1 confirms that the norm minimization methods typically produce the most accurate results at the discontinuity, with the second-order gradient method results with only slightly higher errors. The most noticeable difference is in the errors between the first-order gradient method and the norm minimization methods. By comparison, the error using the first-order gradient minimization is typically 5 times larger, and up to 30 times larger in the case of CF boundary conditions. This highlights a significant advantage of using additional corrections to the mode shapes, particularly if the moment and shear of the system are of interest.

The final numerical simulations for the stepped beam consider a variable location for the discontinuity l_0/l. Various systems are considered with CC, CF, and FF boundary conditions and the results are presented in Figs. 3.9 - 3.12. The p-value listed for the norm minimization methods is the value that minimizes the total error for variable l_0/l and was determined separately for each system. Note that the optimizing procedure was performed anew since a different variable parameter is under consideration and thus the optimal values are not necessarily the same as in the case of variable τ and γ.

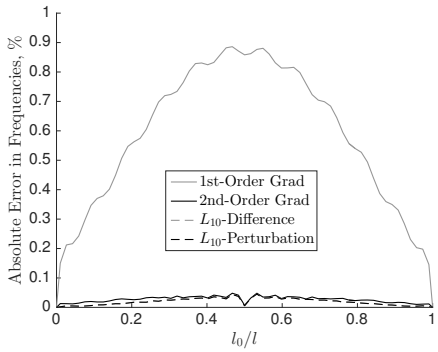

(a) CC, $\tau = 0.9$, and $\gamma = 1$

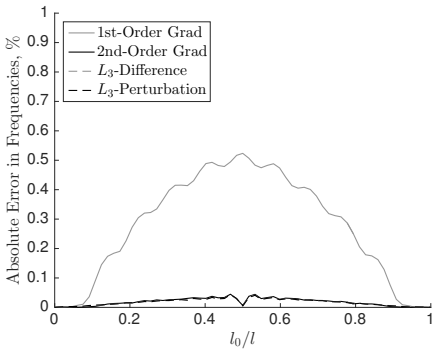

(b) CC, $\tau = 1$, and $\gamma = 0.9$

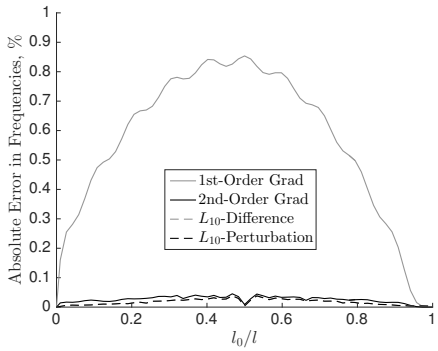

(c) CF, $\tau = 0.9$, and $\gamma = 1$

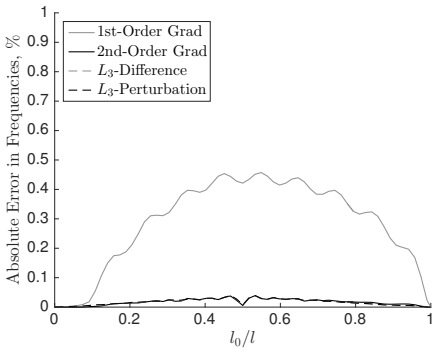

(d) CF, $\tau = 1$, and $\gamma = 0.9$

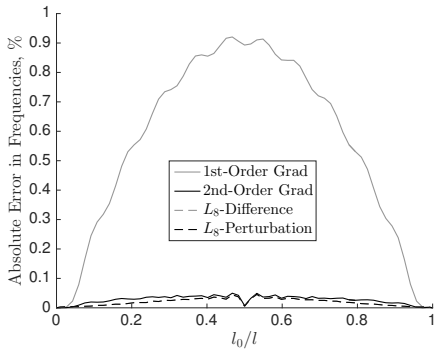

(e) FF, $\tau = 0.9$, and $\gamma = 1$

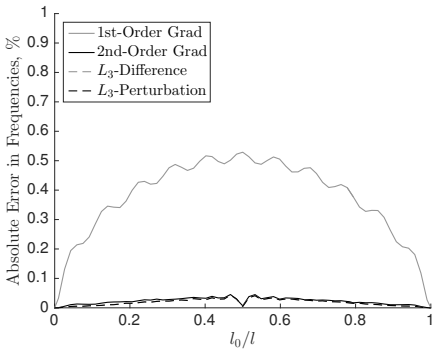

(f) FF, $\tau = 1$, and $\gamma = 0.9$

Figure 3.9: Sum of absolute error in frequencies for variable l_0/l and decrease in system parameter.

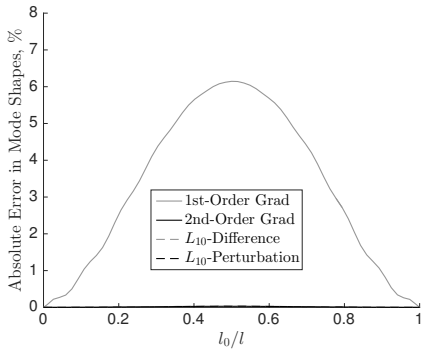

(a) CC, $\tau = 0.9$, and $\gamma = 1$

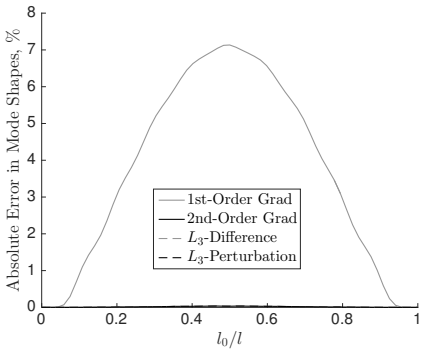

(b) CC, $\tau = 1$, and $\gamma = 0.9$

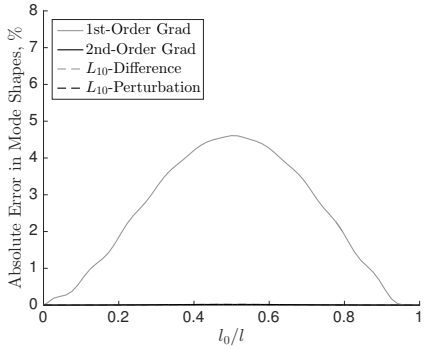

(c) CF, $\tau = 0.9$, and $\gamma = 1$

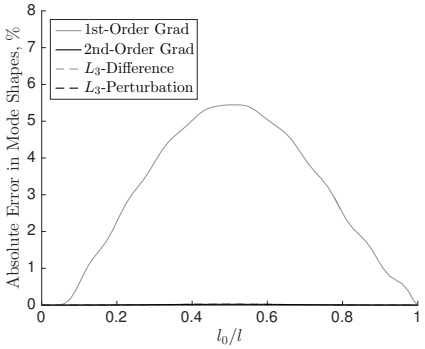

(d) CF, $\tau = 1$, and $\gamma = 0.9$

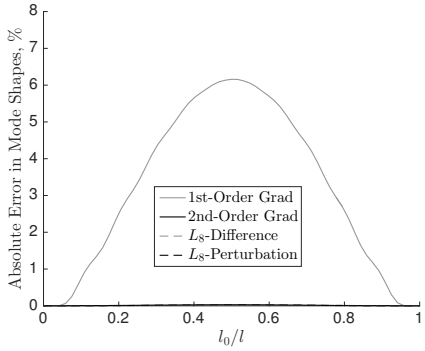

(e) FF, $\tau = 0.9$, and $\gamma = 1$

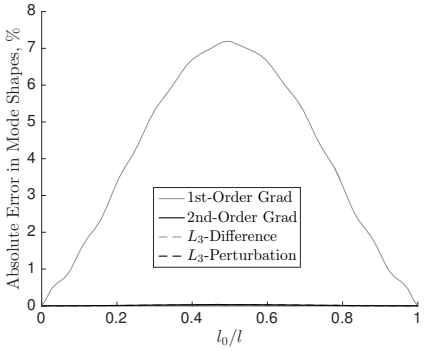

(f) FF, $\tau = 1$, and $\gamma = 0.9$

Figure 3.10: Sum of absolute error in mode shapes for variable l_0/l and decrease in system parameter.

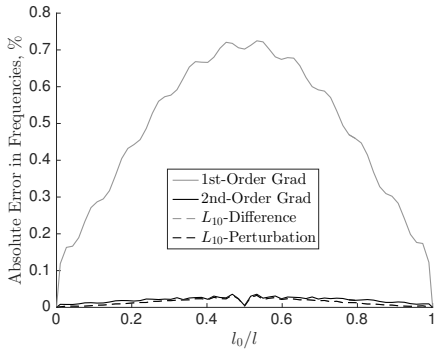

(a) CC, $\tau = 1.1$, and $\gamma = 1$

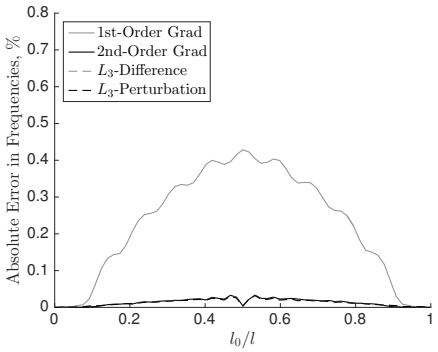

(b) CC, $\tau = 1$, and $\gamma = 1.1$

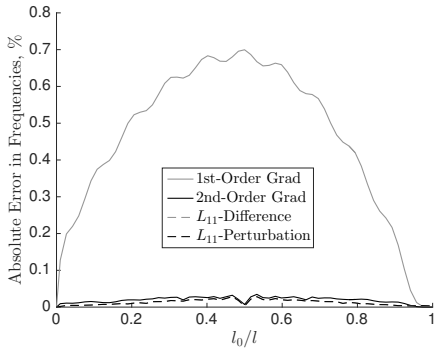

(c) CF, $\tau = 1.1$, and $\gamma = 1$

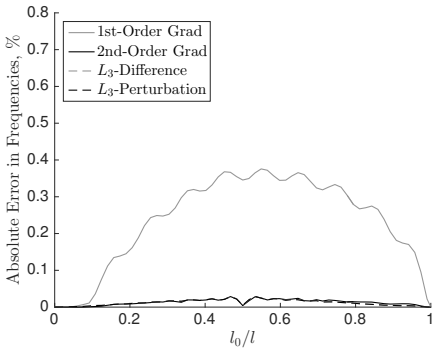

(d) CF, $\tau = 1$, and $\gamma = 1.1$

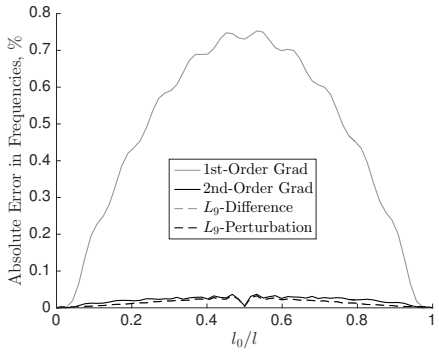

(e) FF, $\tau = 1.1$, and $\gamma = 1$

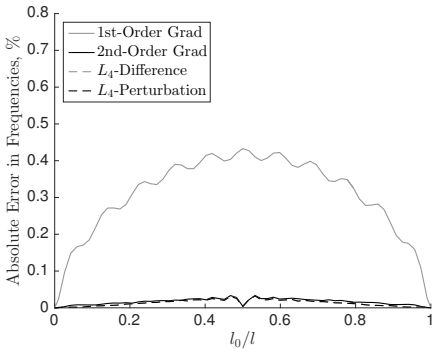

(f) FF, $\tau = 1$, and $\gamma = 1.1$

Figure 3.11: Sum of absolute error in frequencies for variable l_0/l and increase in system parameter.

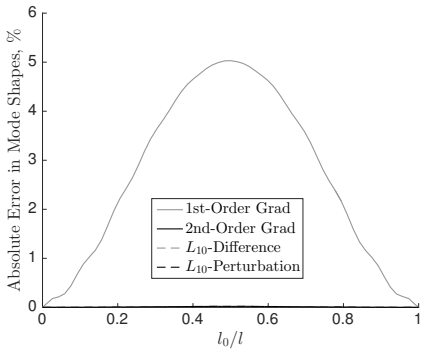

(a) CC, $\tau = 1.1$, and $\gamma = 1$

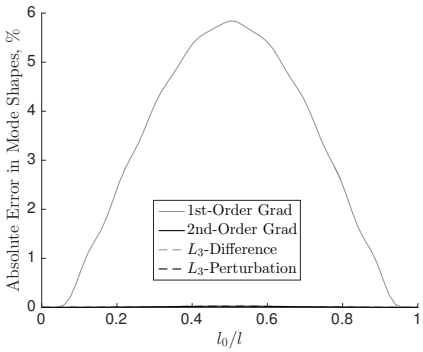

(b) CC, $\tau = 1$, and $\gamma = 1.1$

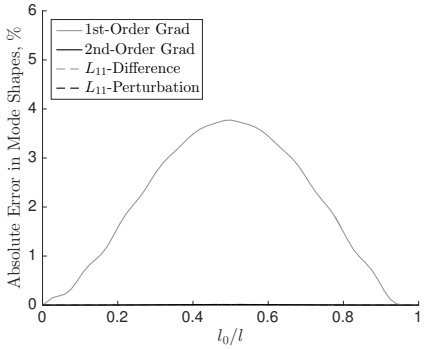

(c) CF, $\tau = 1.1$, and $\gamma = 1$

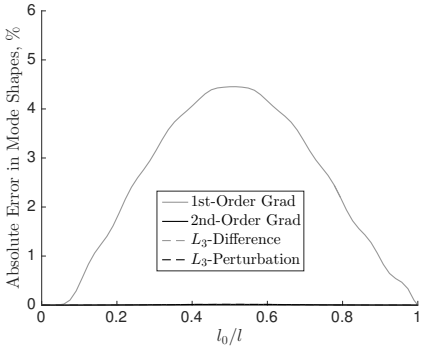

(d) CF, $\tau = 1$, and $\gamma = 1.1$

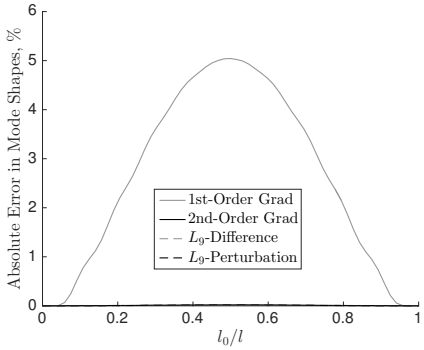

(e) FF, $\tau = 1.1$, and $\gamma = 1$

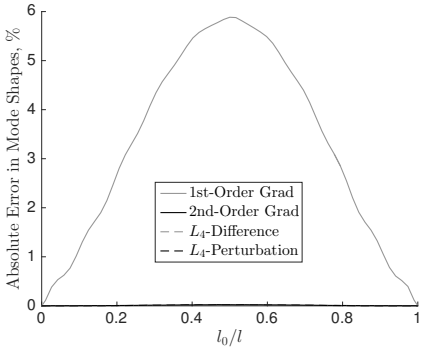

(f) FF, $\tau = 1$, and $\gamma = 1.1$

Figure 3.12: Sum of absolute error in mode shapes for variable l_0/l and increase in system parameter.

In Figs. 3.9 - 3.12 where a 10% increase or decrease in the system bending stiffness or mass per unit length is considered it is seen that the errors reported by the various methods are quite small. As expected, the first-order gradient method produces the largest sum of errors for both the frequencies and mode shapes due to fewer corrections considered in the perturbation theory. Across all the simulations, the largest error in the frequencies was 0.921% for the first-order gradient method, 0.050% for the second-order gradient method, 0.046% for the norm minimization of the difference, and 0.046% for the norm minimization of the perturbation. The largest error in the mode shapes was 7.1912% for the first-order gradient method, 0.0374% for the second-order gradient method, 0.0368% for the norm minimization of the difference, and 0.0368% for the norm minimization of the perturbation. This demonstrates the ability of the perturbation theory and the proposed methods for selecting the reference values in accurately predicting the frequencies and mode shapes even in the case of a fairly significant change in the system parameters.

The cases of variable bending stiffness typically produce larger errors in the natural frequencies and mode shapes when compared to the cases of variable mass per unit length in Figs. 3.9 - 3.12. This behaviour was also observed previously when variable τ and γ were considered, and also when comparing the displacement, moment, and shear associated with the fundamental mode of the system. Also similar to previous numerical simulation results, the errors for variable l_0/l given CF boundary conditions were typically smaller than those reported for a system with CC or FF boundary conditions.

Lastly, in Figs. 3.9 - 3.12 the largest errors occurred when l_0/l was near 1/2, with the error at $l_0/l = 1/2$ sometimes being smaller than neighbouring points. When the step in the system is near $l_0/l = 1/2$, both sections of the beam will play an equally important role in the system behaviour. Therefore it is increasingly difficult to choose a reference value from which the system properties are perturbed and the sum of the errors increases. Also in the figures it is seen that the sum of the errors is 0 when l_0/l is 0 or 1 as in these cases the system is a homogeneous beam with no step.

3.3.2 Periodically Grooved Beam

The second test case that is considered is a grooved beam for which schematics are presented in Fig. 3.13. The beam is assumed to have a thickness of h and the grooves are such that at their peak the system has a thickness of ch. This means that for $c > 1$ the beam increases in thickness due to the groove, as in Fig. 3.13a, and for $0 < c < 1$ the beam decreases in thickness due to the groove, as in Fig. 3.13b. If $c = 1$ then the grooves do not change the thickness of the beam and the system is homogeneous. Any number of the single grooved elements are combined side-by-side to form a multiple grooved system, as in Fig. 3.13c.

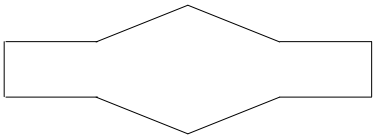

(a) Single grooved element with $c > 1$

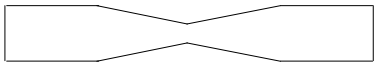

(b) Single grooved element with $0 < c < 1$

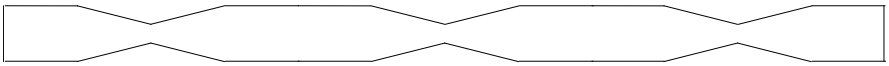

(c) Multiple grooves with $0 < c < 1$

Figure 3.13: Schematics of grooved beams.

Denoting the length of a single grooved element by L, the bending stiffness of a single grooved element can be expressed as:

$$EI\left(x\right) = \begin{cases} 1\,, & 0 \leq x \leq \frac{L}{4} \\ \left[1 + (c-1)\frac{x - L/4}{L/4}\right]^3, & \frac{L}{4} \leq x \leq \frac{L}{2} \\ \left[c + (1-c)\frac{x - L/2}{L/4}\right]^3, & \frac{L}{2} \leq x \leq \frac{3L}{4} \\ 1\,, & \frac{3L}{4} \leq x \leq L \end{cases}$$

And the mass per unit length of a single grooved element can be expressed as:

$$\rho A\left(x\right) = \begin{cases} 1\,, & 0 \leq x \leq \frac{L}{4} \\ \left[1 + (c-1)\frac{x - L/4}{L/4}\right], & \frac{L}{4} \leq x \leq \frac{L}{2} \\ \left[c + (1-c)\frac{x - L/2}{L/4}\right], & \frac{L}{2} \leq x \leq \frac{3L}{4} \\ 1\,, & \frac{3L}{4} \leq x \leq L \end{cases}$$

The total length of the system is taken to be 1. For the grooved beam, the bending stiffness and mass per unit length are both continuous functions with discontinuous derivatives at the start, middle, and end of each groove.

To investigate the ability of the perturbation theory to predict the natural frequencies and mode shapes of the system, the sum of the absolute error in the frequencies and mode shapes are found using Eqs. (3.54) and (3.55), respectively. For the case of a grooved beam, the analytical solution is presented by a finite element analysis (FEA), the details of which can be found in Appendix E.

Clamped-clamped (CC), clamped-free (CF), and free-free (FF) boundary conditions are considered and the errors for variable c^3 values of a system with 5 grooves and unit length are presented in Fig. 3.14. In each of the presented figures, the results for the various proposed methods of determining the reference values are given. A first and second-order correction for the gradient minimization are considered and the p-values for the norm minimization methods are chosen such that they minimize the total error in the frequencies and mode shapes for variable c^3.

The range of values for c^3 were chosen such that a 50% decrease in the bending stiffness is considered, up to an increase of 50% in the bending stiffness. Correspondingly, this results in a 20.6% decrease and an increase of 14.5% in the mass per unit length. For this particular case the value c^3 represents the ratio of the bending stiffness of the centre of the groove to the bending stiffness of a non-grooved section and is further from 1 than the value c which is the ratio of the mass per unit length of the centre of the groove to the mass per unit length of a non-grooved section. Due to this, c^3 is chosen for the independent variable in the presentation of the results.

As expected in Figs. 3.14, when $c = 1$ the value of the sum of error for the frequencies and mode shapes is 0. This is due to the case of $c = 1$ corresponding to a homogeneous beam, and thus the perturbation theory results exactly match the FEA results. Overall, it is observed that the gradient minimization method with one correction produces the largest errors. This is to be expected since there are fewer corrections in this method when compared to the other three methods.

In Figs. 3.15 - 3.18, the sum of the absolute error in the frequencies and mode shapes for variable c^3 value is presented for each of the various reference selection methods. Additionally, various total number of grooves in the system are considered for a fixed length system.

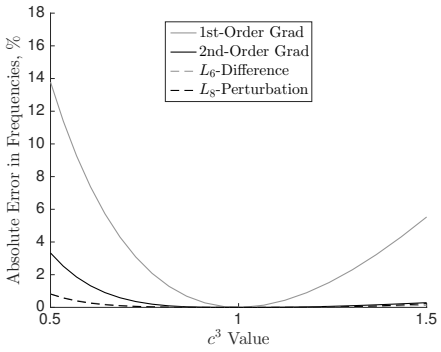

(a) CC, frequencies

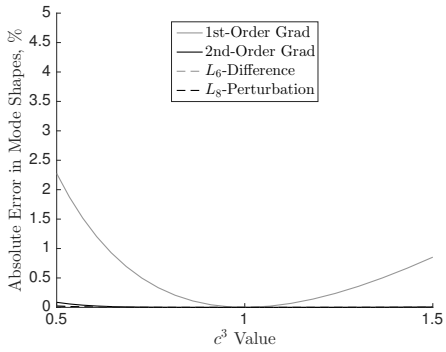

(b) CC, mode shapes

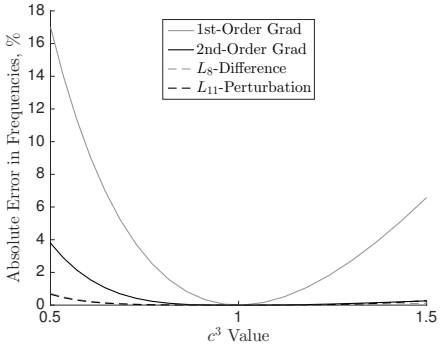

(c) CF, frequencies

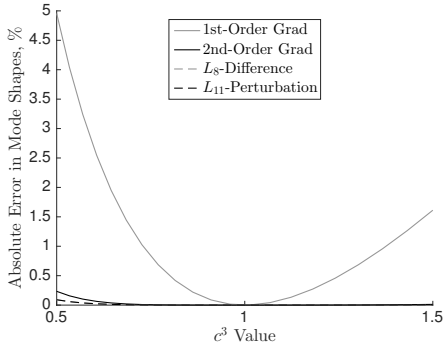

(d) CF, mode shapes

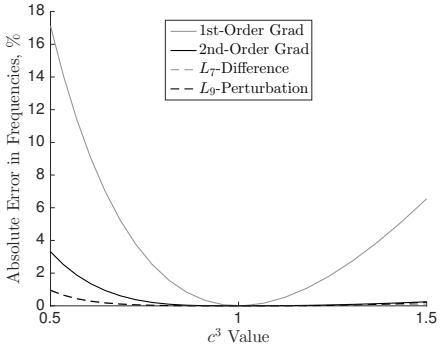

(e) FF, frequencies

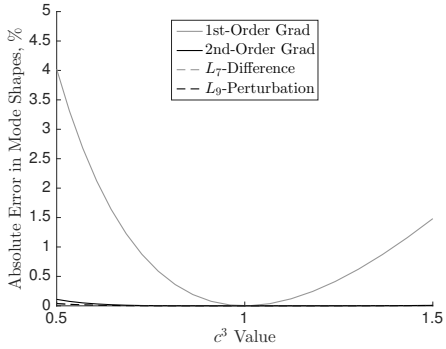

(f) FF, mode shapes

Figure 3.14: Sum of absolute error in frequencies and mode shapes for variable c and 5 grooves.

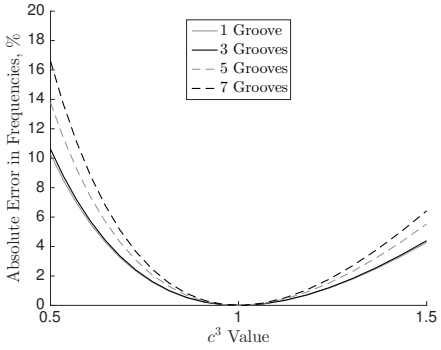

(a) CC, frequencies

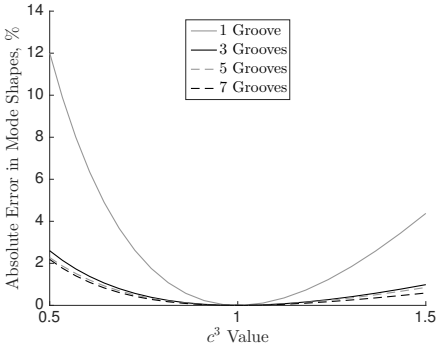

(b) CC, mode shapes

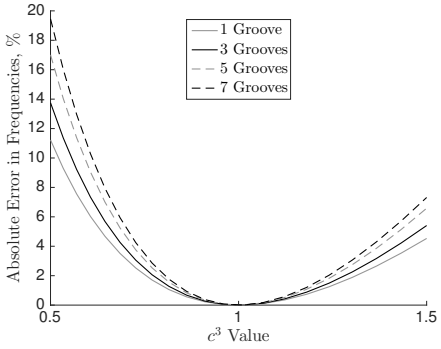

(c) CF, frequencies

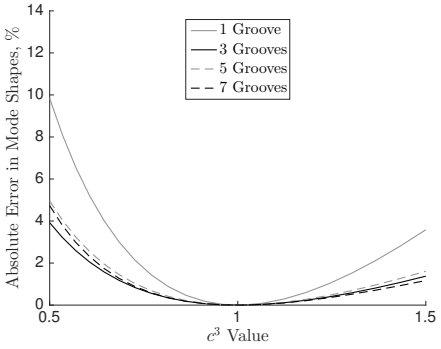

(d) CF, mode shapes

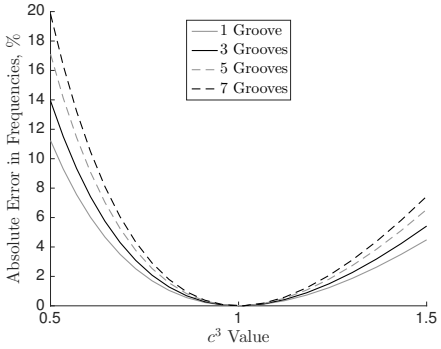

(e) FF, frequencies

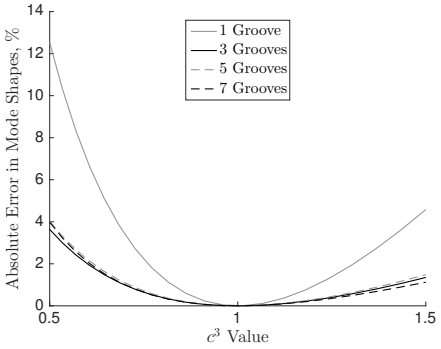

(f) FF, mode shapes

Figure 3.15: Sum of absolute error in frequencies and mode shapes for first-order gradient minimization with variable c.

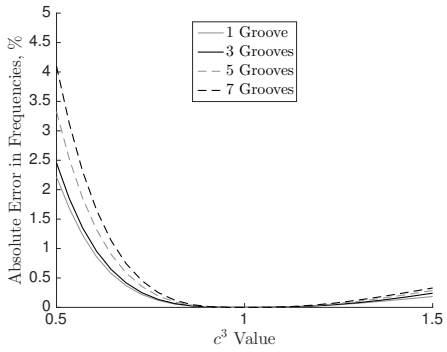

(a) CC, frequencies

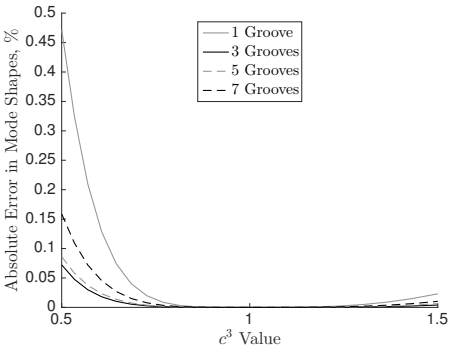

(b) CC, mode shapes

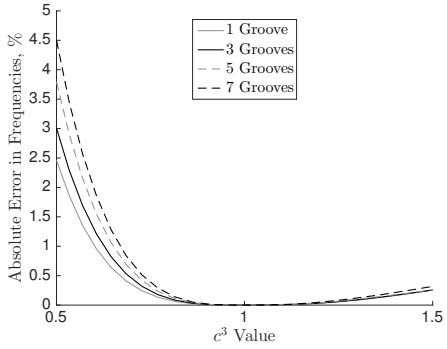

(c) CF, frequencies

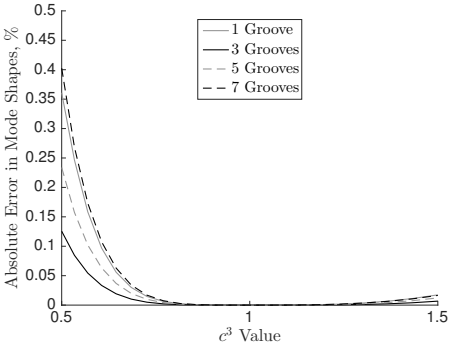

(d) CF, mode shapes

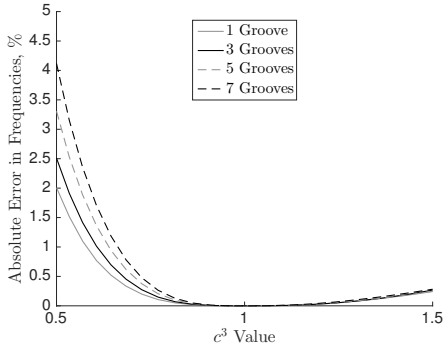

(e) FF, frequencies

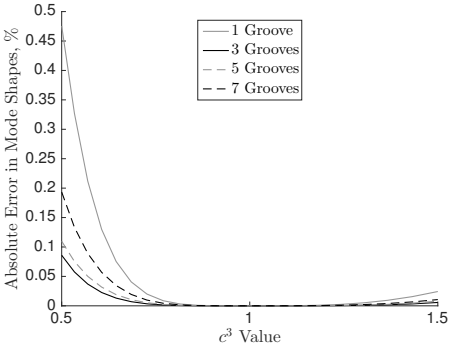

(f) FF, mode shapes

Figure 3.16: Sum of absolute error in frequencies and mode shapes for second-order gradient minimization with variable c.

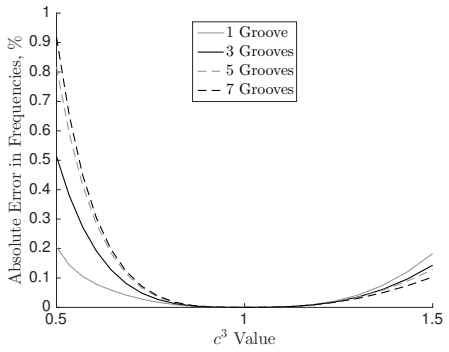

(a) CC, frequencies

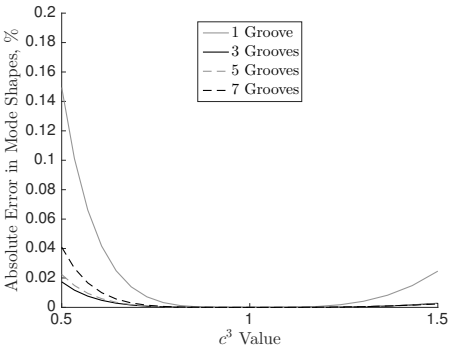

(b) CC, mode shapes

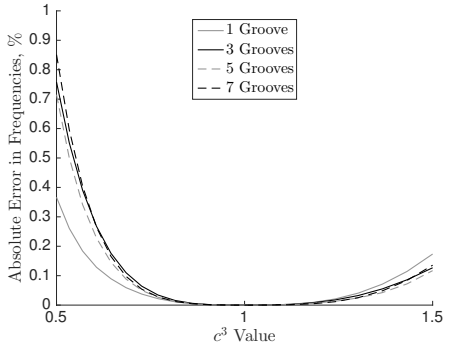

(c) CF, frequencies

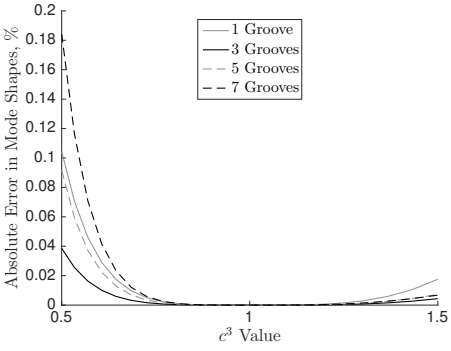

(d) CF, mode shapes

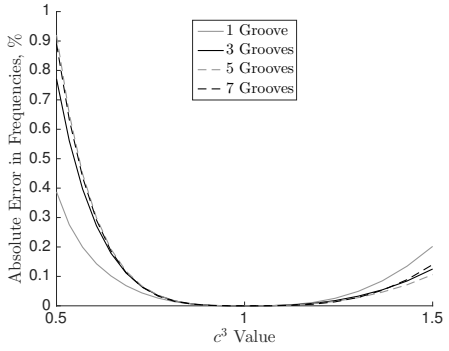

(e) FF, frequencies

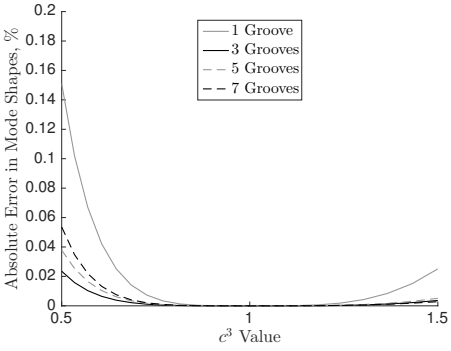

(f) FF, mode shapes

Figure 3.17: Sum of absolute error in frequencies and mode shapes for norm minimization of difference with variable c.

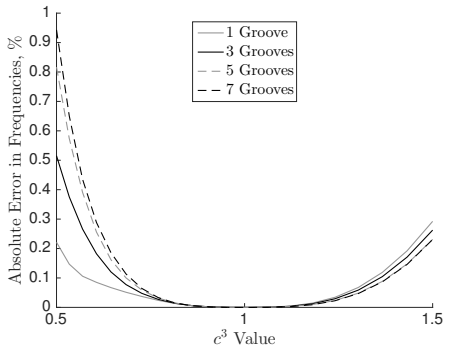

(a) CC, frequencies

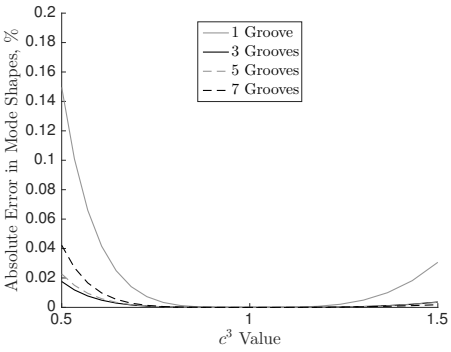

(b) CC, mode shapes

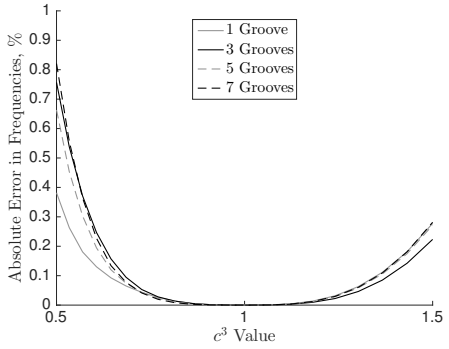

(c) CF, frequencies

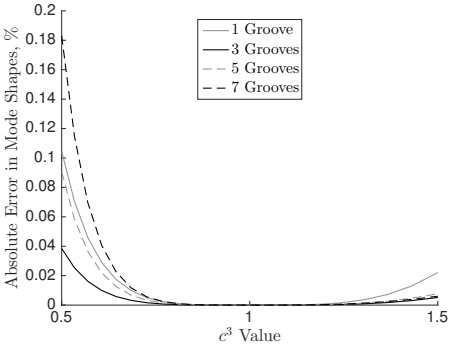

(d) CF, mode shapes

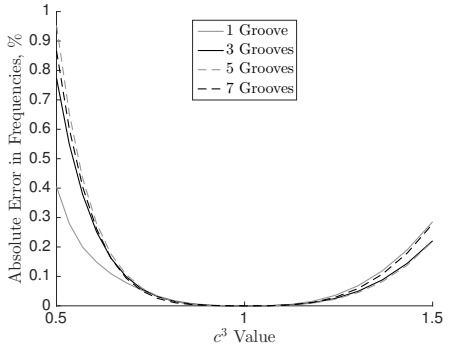

(e) FF, frequencies

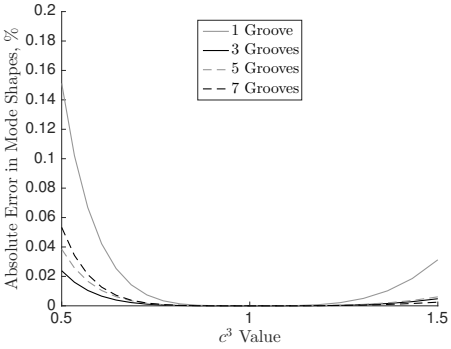

(f) FF, mode shapes

Figure 3.18: Sum of absolute error in frequencies and mode shapes for norm minimization of perturbation with variable c.

First, consider the errors reported going from the first-order gradient minimization method in Fig. 3.15, to the second-order gradient minimization method in Fig. 3.16, to the minimization of the norm of the difference and perturbation in Figs. 3.17 and 3.18. For both the sum of the error in the frequencies and mode shapes, the errors decrease dramatically from the first-order to the second-order gradient minimization methods. Then, going from the second-order gradient minimization to the norm minimization methods the errors are again reduced. The largest sum of error for the natural frequencies for the first and second-order gradient minimization, the norm minimization of the difference, and the norm minimization of the perturbation is 19.835%, 4.501%, 0.921%, and 0.953%, respectively. The largest sum of error for the mode shapes for the first and second-order gradient minimization, the norm minimization of the difference, and the norm minimization of the perturbation is 12.524%, 0.476%, 0.184%, and 0.183%, respectively.

Secondly, from the presented figures it is seen that the errors in the frequencies and mode shapes follow a similar behaviour, regardless of the number of grooves in the system. This behaviour is not symmetric about $c^3 = 1$. In addition, the difference between the error results for variable number of grooves is relatively small. Another common feature for the four reference value selection methods is the sum of errors reported when $c^3 < 1$ are higher than when $c^3 > 1$ when considering is a similar distance from the point $c^3 = 1$. To explain this, as well as the lack of symmetry, consider the values for c^3 that are a distance Δ from $c^3 = 1$. In this case the percentage change in the bending stiffness is the same we have $c = \sqrt[3]{1 \pm \Delta}$ for a given Δ. With respect to the mass per unit length, the percentage change will be larger when considering the case of $c^3 < 1$, *i.e.* Δ being subtracted, than for $c^3 > 1$. Therefore for points c^3 that are equidistant from $c^3 = 1$ the values with $c^3 < 1$ will have a larger change in the mass per unit length and hence will exhibit higher errors than for the $c^3 > 1$ case. This is the reason for the highest error observed for $c^3 = 0.5$ and the lack of symmetry in the results.

Most importantly, the results of Figs. 3.15 - 3.18 highlight the advantage of using an additional number of corrections to the frequencies and mode shape in the perturbation theory. The results of the second-order gradient and norm minimization methods are significantly less sensitive to changes in the value of c near $c = 1$ when compared to the first-order method. This highlights the significant advantage of including additional corrections in the perturbation theory as the ensuing model is more robust in terms of changes to the system parameters.

With respect to the sum of the absolute error in the frequencies in the gradient minimization methods in Figs. 3.15 and 3.16 it is seen that quite frequently the system with a single groove results in the smallest values. The error then increases as the number of grooves increases, with the exception for the FF boundary conditions using the second-

order gradient method. In this case for $c^3 > 1$ the results for a system with 3 grooves is larger than for a system with 5 grooves. This behaviour seen for the gradient minimization methods demonstrates that a system with more rapidly varying parameters, that is for larger number of grooves, results in higher errors in the frequencies.

Next consider the sum of the absolute error in Figs. 3.17 and 3.18 for the norm minimization of the difference and perturbation. In the results it is seen that there is no consistent pattern as the number of grooves changes across the boundary conditions and whether $c^3 < 1$ or $c^3 > 1$. Likely the main factor that contributes to this lack of consistency compared to the gradient minimization methods is that the norm minimization methods determine a single value for EI^* and ρA^* rather than a distinct value for each mode in the gradient minimization methods. However, it can be seen that the pattern for the results obtained using the norm minimization of the difference are quite similar to the pattern for the results obtained using the norm minimization of the perturbation.

Consider next the fundamental mode shapes for a system with a single groove in the system and $c^3 = 1.1$; the value for c was arbitrarily chosen. For CC, CF, and FF boundary conditions, Figs. 3.19 - 3.21 present the results for the displacement, moment, and shear associated with the fundamental mode. The values for p used are 7 and 9 for the norm minimization of the difference and perturbation, respectively, as these are the optimal values for all the boundary conditions.

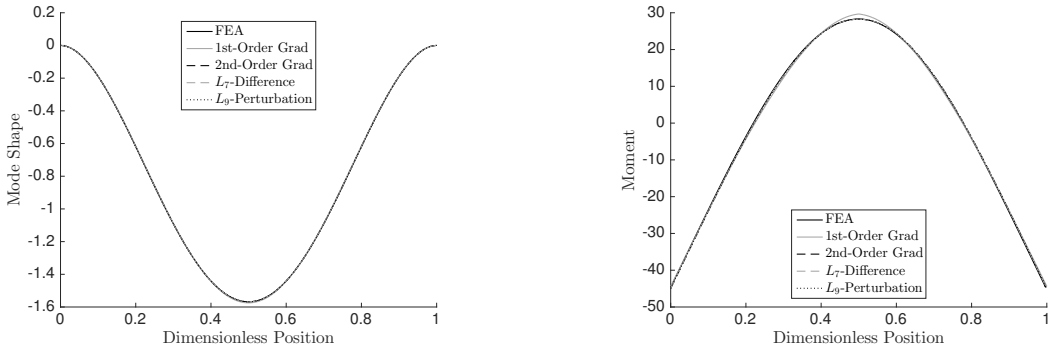

(a) Displacement

(b) Moment

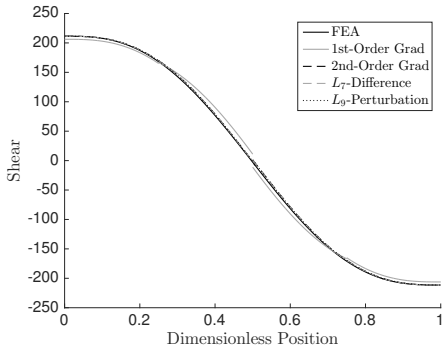

(c) Shear

Figure 3.19: Fundamental mode shape displacement, moment, and shear for a CC system.

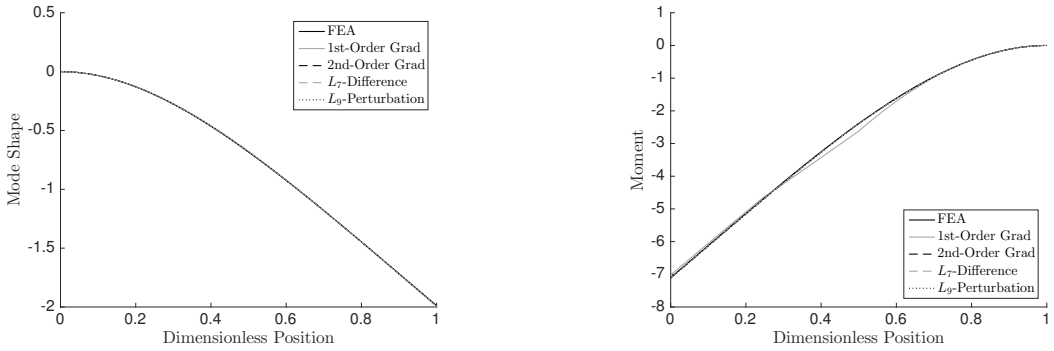

(a) Displacement

(b) Moment

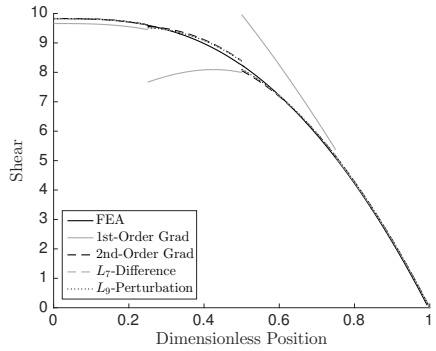

(c) Shear

Figure 3.20: Fundamental mode shape displacement, moment, and shear for a CF system.

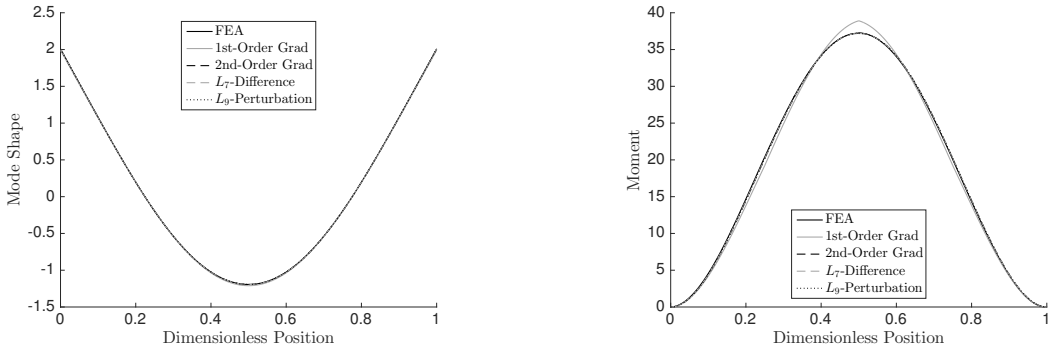

(a) Displacement

(b) Moment

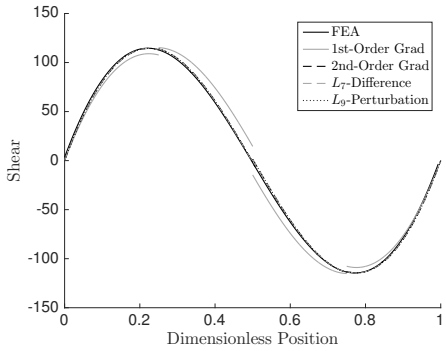

(c) Shear

Figure 3.21: Fundamental mode shape displacement, moment, and shear for a FF system.

For a system with a single groove the bending stiffness is continuous at all points in the system, however the first derivative is discontinuous at the points where the groove begins, peaks, and ends. Since the bending stiffness is continuous, it is expected from Eq. (3.57) that the moment in the system predicted by the perturbation theory will also be continuous. Indeed, this is the case in Figs. 3.19b, 3.20b, and 3.21b. As the first derivative of the bending stiffness is not continuous, from Eq. (3.58) the shear in the system predicted by the perturbation theory may or may not be continuous. In Figs. 3.19c, 3.20c, and 3.21c, it is seen that for the system under consideration that the shear in the system will be discontinuous at each of the points where the bending stiffness is discontinuous.

For the system parameters considered, it is seen in Figs. 3.19a, 3.20a, and 3.21a that the mode shape displacement predicted by the perturbation theory strongly agrees with the FEA results for all the boundary conditions considered and all methods for choosing the reference values. The advantage of including additional corrections to the mode shapes in the perturbation theory is clearly highlighted in the results for the moment, and in particular the shear. Specifically, the correction to the shear results for a CF system in Fig. 3.20c are quite impressive. This demonstrates that if the moment and shear in a system are to be predicted using a perturbation theory approach, it is quite imperative to include at least one correction to the mode shapes to obtain reasonably accurate results.

The final numerical simulations for the grooved beam consider a variable number of grooves in a system with fixed length. The case of $c^3 = 1.1$ is first considered to compare the various methods for obtaining the reference values in the perturbation theory in Fig. 3.22. The value for c^3 was chosen arbitrarily and corresponds to a 10% increase in the bending stiffness and a 0.032% increase in the mass per unit length at the peak of the grooves. As a new system parameter is being varied, variable number of grooves, the optimal p-values are recalculated and are not necessarily the same as those found for variable c^3.

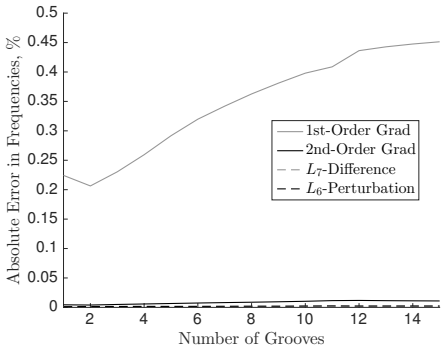

(a) CC, frequencies

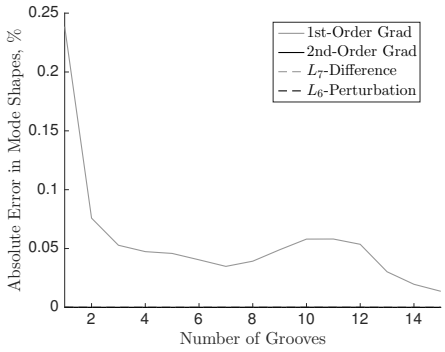

(b) CC, mode shapes

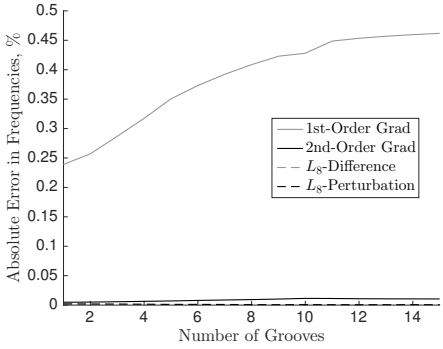

(c) CF, frequencies

(d) CF, mode shapes

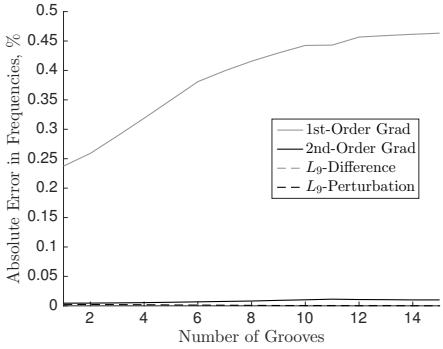

(e) FF, frequencies

(f) FF, mode shapes

Figure 3.22: Sum of absolute error in frequencies and mode shapes for variable number of grooves and $c^3 = 1.1$.

Overall, it is clear for the first-order gradient minimization method that there is a larger sum of error in the frequencies as the number of grooves increases. This behaviour is consistent with previous results for variable c^3 value. Additionally, there are no cases where the sum of the error is 0 since for a variable number of grooves there is no case that corresponds to a homogeneous beam as was the case with previous simulations. As expected, the first-order gradient minimization method produces the largest error of the presented methods since there are fewer corrections to the frequencies and mode shapes.

In Figs. 3.23 - 3.26, the sum of the absolute error in the frequencies and mode shapes for variable number of grooves is presented for each of the various reference selection methods. Additionally, various values for c^3 are considered with CC, CF, and FF boundary conditions.

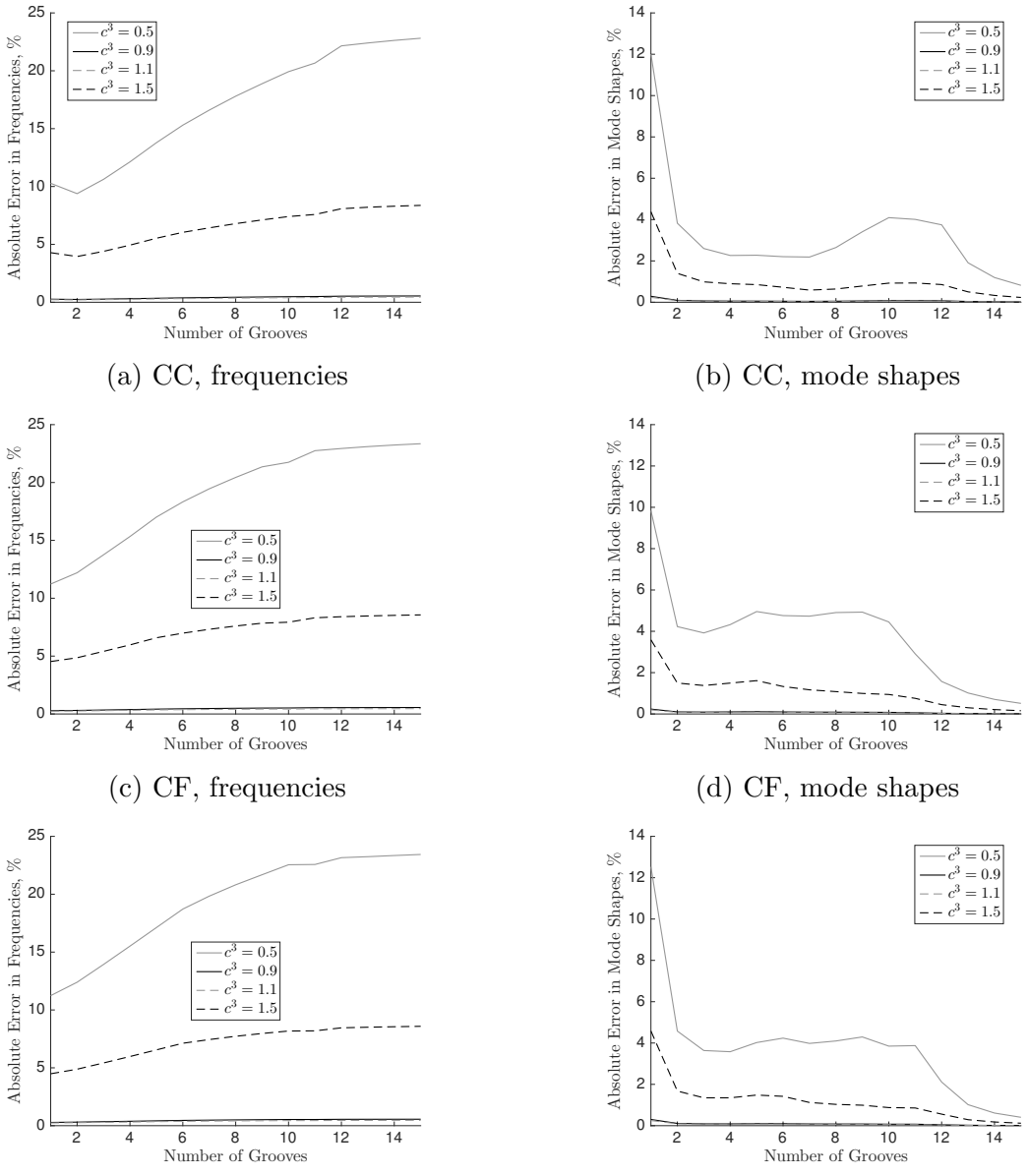

(a) CC, frequencies

(b) CC, mode shapes

(c) CF, frequencies

(d) CF, mode shapes

(e) FF, frequencies

(f) FF, mode shapes

Figure 3.23: Sum of absolute error in frequencies and mode shapes for first-order gradient minimization with variable number of grooves.

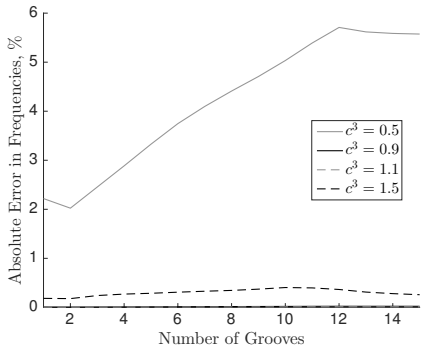

(a) CC, frequencies

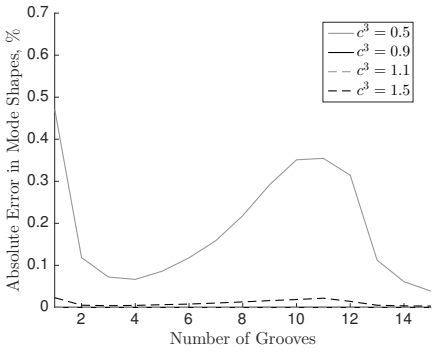

(b) CC, mode shapes

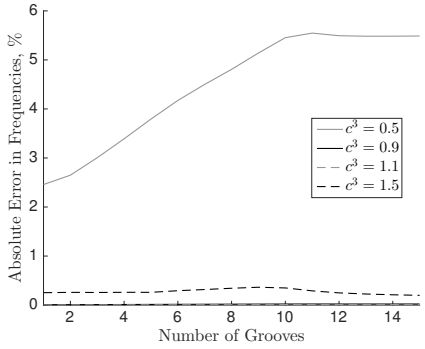

(c) CF, frequencies

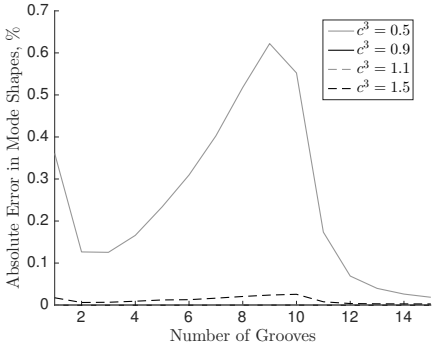

(d) CF, mode shapes

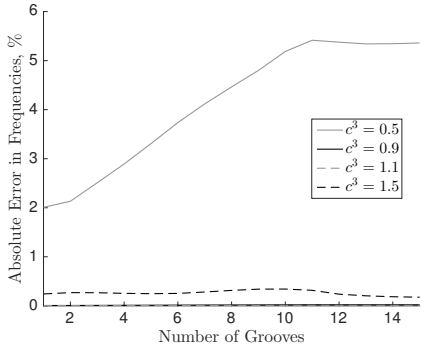

(e) FF, frequencies

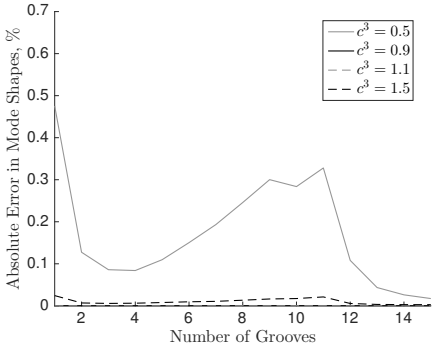

(f) FF, mode shapes

Figure 3.24: Sum of absolute error in frequencies and mode shapes for second-order gradient minimization with variable number of grooves.

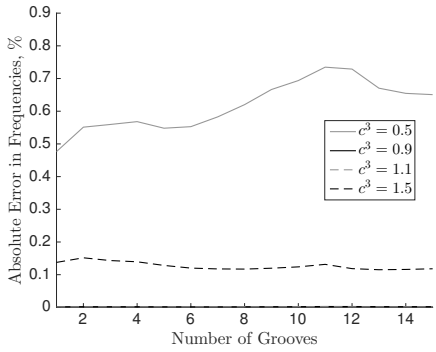

(a) CC, frequencies

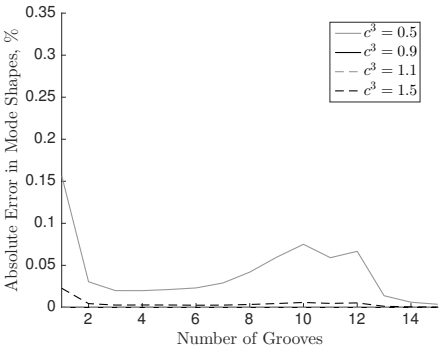

(b) CC, mode shapes

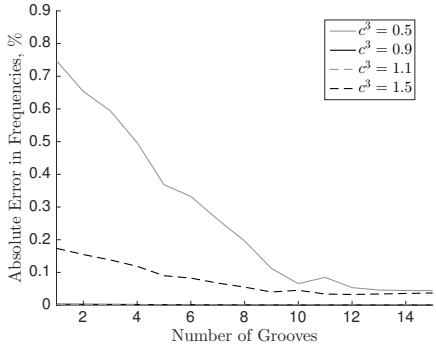

(c) CF, frequencies

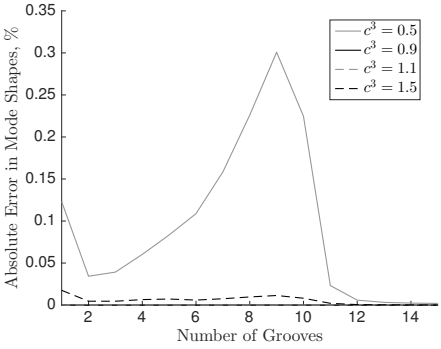

(d) CF, mode shapes

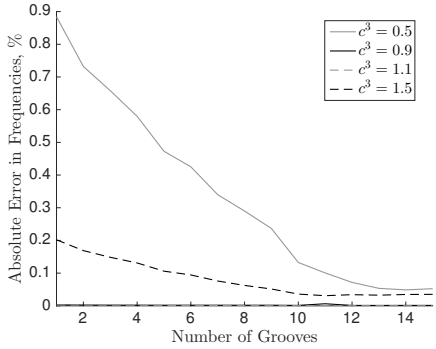

(e) FF, frequencies

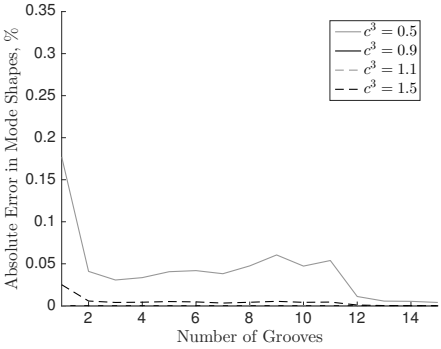

(f) FF, mode shapes

Figure 3.25: Sum of absolute error in frequencies and mode shapes for norm minimization of difference with variable number of grooves.

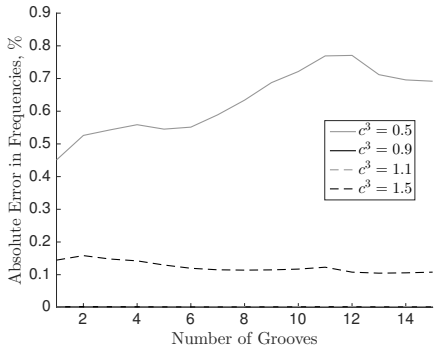

(a) CC, frequencies

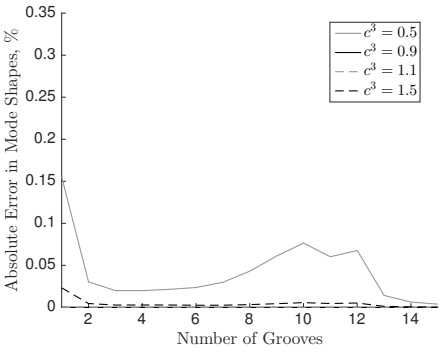

(b) CC, mode shapes

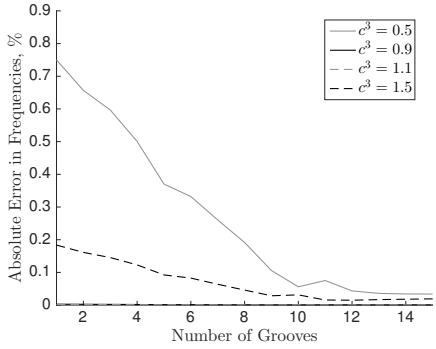

(c) CF, frequencies

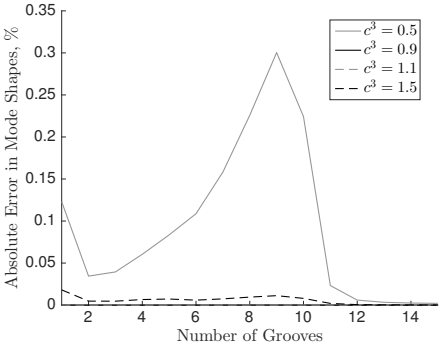

(d) CF, mode shapes

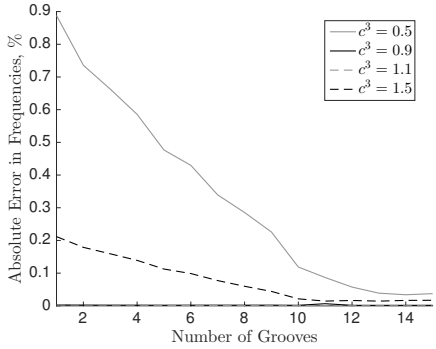

(e) FF, frequencies

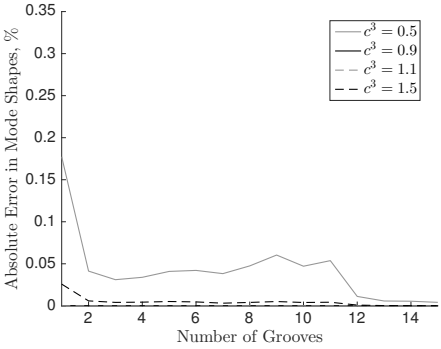

(f) FF, mode shapes

Figure 3.26: Sum of absolute error in frequencies and mode shapes for norm minimization of perturbation with variable number of grooves.

First, consider the errors reported going from the first-order gradient minimization method in Fig. 3.23, to the second-order gradient minimization method in Fig. 3.24, to the minimization of the norm of the difference and perturbation in Figs. 3.25 and 3.26. As was previously observed for variable c^3 values, the sum of the error in the frequencies and mode shapes exhibit a significant decrease for variable number of grooves from the first to second-order gradient minimization methods. Then, going from the second-order gradient minimization method to the norm minimization methods the errors are further reduced for both the frequencies and mode shapes. The largest sum of error for the natural frequencies for the first and second-order gradient minimization, the norm minimization of the difference, and the norm minimization of the perturbation is 23.436%, 5.709%, 0.884%, and 0.888%. The largest sum of error for the mode shapes for the first and second-order gradient minimization, the norm minimization of the difference, and the norm minimization of the perturbation is 12.524%, 0.622%, 0.301%, and 0.300%. All of the maximum sum of errors occurred for the case when $c^3 = 0.5$.

Secondly, from the presented figures, it is observed that the highest errors are reported for the cases with larger variations in the system properties, $c^3 = 0.5$ with the largest errors and $c^3 = 1.5$ with the second largest. The smallest errors occurred for the case of $c^3 = 1.1$ and the second smallest occurred for the case of $c^3 = 0.9$. This is expected since for equidistance c^3 values from $c^3 = 1$ the errors are larger when $c^3 < 1$ than when $c^3 > 1$, as previously discussed.

With respect to the sum of the absolute error in the frequencies in the gradient minimization methods in Figs. 3.23 and 3.24 it is seen that the error increases as the number of grooves increases and ultimately reaches an upper bound. This increase is larger for the first-order gradient minimization method and the results approach the upper bound much sooner, that is a fewer number of grooves, for the second-order gradient minimization compared to the first-order gradient minimization. This is an advantage for the second-order gradient minimization. Additionally, the pattern of the errors observed for the results with variable number of grooves in Figs. 3.23 and 3.24 is consistent with the pattern of the errors observed for the results with variable c^3 in Figs. 3.15 and 3.16.

Next consider the sum of the absolute error in Figs. 3.25 and 3.26 for the norm minimization of the difference and perturbation. The behaviour of the results are observed to be different than for the gradient norm minimization and is likely due to the norm minimization methods producing a single value for EI^* and ρA^*. However, it can be seen that the pattern for the results obtained using the norm minimization of the difference are quite similar to the pattern for the results obtained using the norm minimization of the perturbation. With respect to the boundary conditions, it is seen for the CC boundary conditions that the errors are quite consistent as the number of grooves is varied with a

slight overall increase in the errors for the case of $c^3 = 0.5$. For the CF and FF boundary conditions there is a noticeable decrease in the sum of the absolute error in the frequencies as the number of grooves increases, especially for the cases when $c^3 = 0.5$ and $c^3 = 1.5$.

Finally, it is seen for the norm minimization methods that the pattern of the errors observed for the results with variable number of grooves in Figs. 3.25 and 3.26 is not consistent with the pattern of the errors observed for the results with variable c^3 in Figs. 3.17 and 3.18. This is due to the pattern for the errors being related to the choice of p-value. For each of the cases of variable c^3 and variable number of grooves the process to determine the optimal p-value was performed and produced different results for the two cases. The process was performed in each case to obtain the optimal results for the given variable system parameter to highlight the potential accuracy of the norm minimization methods. Furthermore, the pattern of the errors would be different if the optimal p-value was determine for each individual data point, and would ultimately results in lower levels of error for the frequencies and mode shapes.

Overall, it has been seen through numerical simulation of two distinct systems that there is a significant improvement in the results for the frequencies and mode shapes when additional corrections are considered. Furthermore, the various proposed manners in which to determine the reference values in the perturbation theory each produce quite accurate results. The optimally chosen results for L_p norm minimization produced the smallest errors, with only slightly larger errors from the second-order gradient minimization. However, the L_p norm minimization methods rely on knowledge of the frequencies and mode shapes *a priori*, this is in contrast to the gradient minimization method.

3.4 Lindstedt-Poincaré Method with Lumped Masses

3.4.1 Problem Statement

To apply the perturbation theory to both wrapping patterns that are considered for string-harnessed system, the details in Section 3.1 are updated to include lumped masses. Let δ denote the Dirac delta function. The PDE and boundary conditions that consider lumped masses are given by

$$\frac{\partial^2}{\partial x^2}\left[EI(x)\frac{\partial^2 w}{\partial x^2}\right] + \left\{\rho A(x) + \sum_{k=0}^{m} M_k \delta(x - x_k)\right\}\frac{\partial^2 w}{\partial t^2} = 0 \tag{3.59}$$

$$w(x^*,t)=0 \qquad \text{or} \qquad \frac{\partial}{\partial x}\left[EI(x)\frac{\partial^2 w}{\partial x^2}\right]_{x=x^*}=0 \tag{3.60}$$

$$\frac{\partial w}{\partial x}(x^*,t)=0 \qquad \text{or} \qquad EI(x)\frac{\partial^2 w}{\partial x^2}\bigg|_{x=x^*}=0 \tag{3.61}$$

The functions $EI(x)$ and $\rho A(x)$ are C^∞-functions on $[0,l]\setminus P$. For the case of string-harnessed systems, the finite set P contains all the points where a string goes from one face of the host structure to another. Assume that P contains $m-1$ points. A similar sequence of steps are applied as in the case without lumped masses.

The problem is nondimensionalized using a reference value EI^* for the bending stiffness and ρA^* for the mass per unit length. These references values are the values from which the respective functions of the system are considered perturbed. Introduce the length scale l the time scale $l^2\sqrt{\rho A^*/EI^*}$, and let X, T, W denote the dimensionless quantities associated with x, t, and w, respectively.

$$\begin{aligned}0=&\frac{\partial^2}{\partial X^2}\left[\left\{1+\frac{EI(X)-EI^*}{EI^*}\right\}\frac{\partial^2 W(X,T)}{\partial X^2}\right]\\&+\left(\left\{1+\frac{\rho A(X)-\rho A^*}{\rho A^*}\right\}+\sum_{k=0}^{m}\frac{M_k}{l\rho A^*}\delta\left(X-X_k\right)\right)\frac{\partial^2 W(X,T)}{\partial T^2}\end{aligned} \tag{3.62}$$

Assume a separable solution to Eq. (3.62) of the form $W(X,T)=u(X)e^{i\omega T}$. This leads to a spatial ordinary differential equation (ODE)

$$\begin{aligned}0=&\frac{\mathrm{d}^2}{\mathrm{d}X^2}\left[\left\{1+\frac{EI(X)-EI^*}{EI^*}\right\}\frac{\mathrm{d}^2 u(X)}{\mathrm{d}X^2}\right]\\&-\omega^2\left(\left\{1+\frac{\rho A(X)-\rho A^*}{\rho A^*}\right\}+\sum_{k=0}^{m}\frac{M_k}{l\rho A^*}\delta\left(X-X_k\right)\right)u(X)\end{aligned} \tag{3.63}$$

3.4.2 Perturbation Theory

Since the reference values EI^* and ρA^* were chosen such that perturbations occur from these values, introduce a small parameter ϵ in Eq. (3.63)

$$\frac{\mathrm{d}^2}{\mathrm{d}X^2}\left[\left\{1+\epsilon\widehat{EI}(X)\right\}\frac{\mathrm{d}^2 u(X)}{\mathrm{d}X^2}\right]-\omega^2\left(\left\{1+\epsilon\widehat{\rho A}(X)\right\}+\sum_{k=0}^{m}\epsilon\widehat{M}_k\delta\left(X-X_k\right)\right)u(X)=0 \tag{3.64}$$

Applying the same steps that were applied to the PDE to the boundary conditions. The boundary conditions at $X^* = 0$ or 1 are:

$$u(X^*) = 0 \qquad \text{or} \qquad \frac{\mathrm{d}}{\mathrm{d}X}\left[\left\{1+\epsilon\widehat{EI}(X)\right\}\frac{\mathrm{d}^2u(X)}{\mathrm{d}X^2}\right]_{X=X^*} = 0 \tag{3.65a}$$

$$\frac{\mathrm{d}u(X^*)}{\mathrm{d}X} = 0 \qquad \text{or} \qquad \left\{1+\epsilon\widehat{EI}(X)\right\}\frac{\mathrm{d}^2u(X^*)}{\mathrm{d}X^2} = 0 \tag{3.65b}$$

As was done for the previous model without lumped masses, the Lindstedt-Poincaré method is applied and the natural frequencies and mode shapes are expanded in terms of the small parameter ϵ.

$$u(X) = u_0(X) + \epsilon u_1(X) + \epsilon^2 u_2(X) + \ldots \tag{3.66a}$$

$$\omega = \omega_0 + \epsilon\omega_1 + \epsilon^2\omega_2 + \ldots \tag{3.66b}$$

The expansions in Eq. (3.66) are then substituted into the PDE and boundary conditions in Eqs. (3.64) and (3.65). Terms with similar powers of ϵ are grouped together and these define a sequence of problems that must be solved to determine the frequencies and mode shapes.

3.4.3 Mass Normalization Condition

Once the mode shapes of the system are determined from the perturbation theory they are mass normalized; this is quite common in a vibrations analysis. The mass normalized mode shapes are denoted by $\overline{\phi}(x)$ and the nondimensional mode shapes are denoted by $\phi(X)$. The mass normalization condition in nondimensional form is given by

$$1 = \int_0^1 \left\{\left\{1+\epsilon\widehat{\rho A}(X)\right\} + \sum_{k=0}^{m}\epsilon\widehat{M}_k\delta\left(X-X_k\right)\right\}\phi^2(X)\,\mathrm{d}X \tag{3.67}$$

To determine the mass normalization condition corresponding to each $\mathcal{O}(\epsilon^i)$ problem of the perturbation theory, substitute the expansion of the mode shape in terms of ϵ into Eq. (3.67). The mass normalization conditions for the $\mathcal{O}(1)$ and $\mathcal{O}(\epsilon)$ are

$$\mathcal{O}(1): \qquad 1 = \int_0^1 \phi_0^2(X)\,\mathrm{d}X \tag{3.68a}$$

$$\mathcal{O}(\epsilon): \qquad 0 = \int_0^1 2\phi_0(X)\phi_1(X) + \widehat{\rho A}(X)\phi_0^2(X)\,\mathrm{d}X + \sum_{k=0}^{m}\widehat{M}_k\phi_0^2(X_k) \tag{3.68b}$$

3.4.4 $\mathcal{O}(1)$ Problem

The $\mathcal{O}(1)$ problem for the system with lumped masses is the same as for the previous EB model in Section 3.1.4. The solutions for the various boundary conditions are presented for completeness.

Clamped-Clamped Solution

The boundary conditions for a CC system are

$$u_0(0) = 0 \quad , \quad \frac{\mathrm{d}u_0(0)}{\mathrm{d}X} = 0 \quad , \quad u_0(1) = 0 \quad , \quad \frac{\mathrm{d}u_0(1)}{\mathrm{d}X} = 0$$

The characteristic equation, which determines the frequencies ω_{n0}, is

$$0 = 1 - \cos(\sqrt{\omega_0})\cosh(\sqrt{\omega_0})$$

and the n^{th} mode shape of the system is

$$\phi_{n0}(X) = \cos(\sqrt{\omega_{n0}}X) - \cosh(\sqrt{\omega_{n0}}X) - \frac{\cos(\sqrt{\omega_{n0}}) - \cosh(\sqrt{\omega_{n0}})}{\sin(\sqrt{\omega_{n0}}) - \sinh(\sqrt{\omega_{n0}})}\left\{\sin(\sqrt{\omega_{n0}}X) - \sinh(\sqrt{\omega_{n0}}X)\right\} \tag{3.69}$$

Clamped-Free Solution

The boundary conditions for a CF system are

$$u_0(0) = 0 \quad , \quad \frac{\mathrm{d}u_0(0)}{\mathrm{d}X} = 0 \quad , \quad \frac{\mathrm{d}^2u_0(1)}{\mathrm{d}X^2} = 0 \quad , \quad \frac{\mathrm{d}^3u_0(1)}{\mathrm{d}X^3} = 0$$

The characteristic equation, which determines the frequencies ω_{n0}, is

$$0 = 1 + \cos(\sqrt{\omega_0})\cosh(\sqrt{\omega_0})$$

and the n^{th} mode shape of the system is

$$\phi_{n0}(X) = \cos(\sqrt{\omega_{n0}}X) - \cosh(\sqrt{\omega_{n0}}X) - \frac{\cos(\sqrt{\omega_{n0}}) + \cosh(\sqrt{\omega_{n0}})}{\sin(\sqrt{\omega_{n0}}) + \sinh(\sqrt{\omega_{n0}})}\left\{\sin(\sqrt{\omega_{n0}}X) - \sinh(\sqrt{\omega_{n0}}X)\right\} \tag{3.70}$$

Free-Free Solution

The boundary conditions for a FF system are

$$\frac{\mathrm{d}^2 u_0(0)}{\mathrm{d}X^2} = 0 \quad , \quad \frac{\mathrm{d}^3 u_0(0)}{\mathrm{d}X^3} = 0 \quad , \quad \frac{\mathrm{d}^2 u_0(1)}{\mathrm{d}X^2} = 0 \quad , \quad \frac{\mathrm{d}^3 u_0(1)}{\mathrm{d}X^3} = 0$$

The characteristic equation, which determines the frequencies ω_{n0}, is

$$0 = 1 - \cos(\sqrt{\omega_0})\cosh(\sqrt{\omega_0})$$

and the n^{th} mode shape of the system is

$$\phi_{n0}(X) = \cos(\sqrt{\omega_{n0}}X) + \cosh(\sqrt{\omega_{n0}}X) - \frac{\cos(\sqrt{\omega_{n0}}) - \cosh(\sqrt{\omega_{n0}})}{\sin(\sqrt{\omega_{n0}}) - \sinh(\sqrt{\omega_{n0}})} \left\{\sin(\sqrt{\omega_{n0}}X) + \sinh(\sqrt{\omega_{n0}}X)\right\} \tag{3.71}$$

3.4.5 $\mathcal{O}(\epsilon)$ Problem

The ODE for the $\mathcal{O}(\epsilon)$ problem is

$$\frac{\mathrm{d}^4 u_{n1}}{\mathrm{d}X^4} - \omega_{n0}^2 u_{n1} = 2\omega_{n0}\omega_{n1}\phi_{n0} + \omega_{n0}^2 \widehat{\rho A}\phi_{n0} + \sum_{k=0}^{m} \omega_{n0}^2 \widehat{M}_k \delta\left(X - X_k\right)\phi_{n0} - \frac{\mathrm{d}^2}{\mathrm{d}X^2}\left[\widehat{EI}\frac{\mathrm{d}^2\phi_{n0}}{\mathrm{d}X^2}\right] \tag{3.72}$$

for $0 < X < 1$. A solution to the ODE exists when the following solvability condition is satisfied.

$$0 = \int_0^1 \left\{ 2\omega_{n0}\omega_{n1}\phi_{n0} + \omega_{n0}^2 \widehat{\rho A}\phi_{n0} + \sum_{k=0}^{m} \omega_{n0}^2 \widehat{M}_k \delta\left(X - X_k\right)\phi_{n0} - \frac{\mathrm{d}^2}{\mathrm{d}X^2}\left[\widehat{EI}\frac{\mathrm{d}^2\phi_{n0}}{\mathrm{d}X^2}\right] \right\} \phi_{n0}\,\mathrm{d}X \tag{3.73}$$

From the solvability condition in Eq. (3.73) the value for ω_{n1} is found. Using integration by parts and that CC, CF, and FF boundary conditions are under consideration, the solvability condition yields:

$$\omega_{n1} = \frac{1}{2\omega_{n0}} \int_0^1 \widehat{EI}\left(\frac{\mathrm{d}^2\phi_{n0}}{\mathrm{d}X^2}\right)^2 \mathrm{d}X - \frac{\omega_{n0}}{2}\int_0^1 \widehat{\rho A}\,\phi_{n0}^2\,\mathrm{d}X - \frac{\omega_{n0}}{2}\sum_{k=1}^{m} \widehat{M}_k \phi_{n0}(X_k)^2 \tag{3.74}$$

Recall the assumption that $EI(x)$ and $\rho A(x)$ are C^∞-functions everywhere except on a set of points P of size $m-1$. It follows that $\widehat{EI}(X)$ and $\widehat{\rho A}(X)$ are C^∞-functions on the set $\widehat{P} = P/l$. Suppose that the points in $\widehat{P}$ are ordered as $0 < X_{P_1} < X_{P_2} < \ldots < X_{P_{m-1}} < 1$ and denote $X_0 = 0$ and $X_m = 1$. The ODE in Eq. (3.72) is solved over each of the m intervals $[X_{i-1}, X_i]$. The general solution on the i^{th} interval is the same as in Section 3.1.5 since the lumped masses are not present inside the intervals over which a solution is found, but rather at the interface of each of the intervals. The general solution over the i^{th} interval is

$$\begin{aligned} u_{n1}^{(i)}(X) =& A_{n1}^{(i)} \cos(\sqrt{\omega_{n0}} X) + B_{n1}^{(i)} \sin(\sqrt{\omega_{n0}} X) + C_{n1}^{(i)} \cosh(\sqrt{\omega_{n0}} X) + D_{n1}^{(i)} \sinh(\sqrt{\omega_{n0}} X) \\ &+ \frac{\omega_{n1}}{2\omega_{n0}} X \frac{\mathrm{d}\phi_{n0}}{\mathrm{d}X} + u_{n1,p}^{(i)}(X) \end{aligned} \tag{3.75}$$

with

$$\begin{aligned} u_{n1,p}^{(i)}(x) =& \frac{\sqrt{\omega_{n0}}}{2} \Bigg[\cos(\sqrt{\omega_{n0}} X) \int \sin(\sqrt{\omega_{n0}} X)\, \widehat{\rho A}^{(i)} \phi_{n0}\, \mathrm{d}X \\ &- \sin(\sqrt{\omega_{n0}} X) \int \cos(\sqrt{\omega_{n0}} X)\, \widehat{\rho A}^{(i)} \phi_{n0}\, \mathrm{d}X \\ &- \cosh(\sqrt{\omega_{n0}} X) \int \sinh(\sqrt{\omega_{n0}} X)\, \widehat{\rho A}^{(i)} \phi_{n0}\, \mathrm{d}X \\ &+ \sinh(\sqrt{\omega_{n0}} X) \int \cosh(\sqrt{\omega_{n0}} X)\, \widehat{\rho A}^{(i)} \phi_{n0}\, \mathrm{d}X \Bigg] \\ &- \frac{1}{2\sqrt{\omega_{n0}^3}} \Bigg[\cos(\sqrt{\omega_{n0}} X) \int \sin(\sqrt{\omega_{n0}} X) \frac{\mathrm{d}^2}{\mathrm{d}X^2} \left[\widehat{EI}^{(i)} \frac{\mathrm{d}^2 \phi_{n0}}{\mathrm{d}X^2} \right] \mathrm{d}X \\ &- \sin(\sqrt{\omega_{n0}} X) \int \cos(\sqrt{\omega_{n0}} X) \frac{\mathrm{d}^2}{\mathrm{d}X^2} \left[\widehat{EI}^{(i)} \frac{\mathrm{d}^2 \phi_{n0}}{\mathrm{d}X^2} \right] \mathrm{d}X \\ &- \cosh(\sqrt{\omega_{n0}} X) \int \sinh(\sqrt{\omega_{n0}} X) \frac{\mathrm{d}^2}{\mathrm{d}X^2} \left[\widehat{EI}^{(i)} \frac{\mathrm{d}^2 \phi_{n0}}{\mathrm{d}X^2} \right] \mathrm{d}X \\ &+ \sinh(\sqrt{\omega_{n0}} X) \int \cosh(\sqrt{\omega_{n0}} X) \frac{\mathrm{d}^2}{\mathrm{d}X^2} \left[\widehat{EI}^{(i)} \frac{\mathrm{d}^2 \phi_{n0}}{\mathrm{d}X^2} \right] \mathrm{d}X \Bigg] \end{aligned} \tag{3.76}$$

Since the ODE is solved over each section, a set of continuity conditions must be applied. The continuity conditions are continuity of displacement, slope, moment, and shear and can be obtained mathematically from Eq. (3.72). When lumped masses are present in the

system, they affect the continuity of the shear. For an arbitrary point $X_j \in \widehat{P}$.

$$u_{n1}^{(j)}(X_{P_j}) = u_{n1}^{(j+1)}(X_{P_j}) \tag{3.77a}$$

$$\frac{\mathrm{d}u_{n1}^{(j)}(X_{P_j})}{\mathrm{d}X} = \frac{\mathrm{d}u_{n1}^{(j+1)}(X_{P_j})}{\mathrm{d}X} \tag{3.77b}$$

$$\frac{\mathrm{d}^2u_{n1}^{(j)}(X_{P_j})}{\mathrm{d}X^2} = \frac{\mathrm{d}^2u_{n1}^{(j+1)}(X_{P_j})}{\mathrm{d}X^2} + \left(\widehat{EI}^{(j+1)}(X_{P_j}) - \widehat{EI}^{(j)}(X_{P_j})\right)\frac{\mathrm{d}^2\phi_{n0}(X_{P_j})}{\mathrm{d}X^2} \tag{3.77c}$$

$$\begin{aligned}\frac{\mathrm{d}^3u_{n1}^{(j)}(X_{P_j})}{\mathrm{d}X^3} =& \frac{\mathrm{d}^3u_{n1}^{(j+1)}(X_{P_j})}{\mathrm{d}X^3} + \frac{\mathrm{d}}{\mathrm{d}X}\left[\left(\widehat{EI}^{(j+1)}(X) - \widehat{EI}^{(j)}(X)\right)\frac{\mathrm{d}^2\phi_{n0}}{\mathrm{d}X^2}\right]_{X=X_{P_j}} \\ & - \omega_{n0}^2\widehat{M}_j\phi_{n0}(X_{P_j})\end{aligned} \tag{3.77d}$$

The boundary conditions for the $\mathcal{O}(\epsilon)$ problem are simplified using the $\mathcal{O}(1)$ problem boundary conditions. For the case of lumped masses, the boundary conditions are updated to include the possibility of a lumped mass at free ends of the system. The boundary conditions for a CC system are:

$$u_{n1}^{(1)}(0) = 0 \quad , \quad \frac{\mathrm{d}u_{n1}^{(1)}(0)}{\mathrm{d}X} = 0 \quad , \quad u_{n1}^{(m)}(1) = 0 \quad , \quad \frac{\mathrm{d}u_{n1}^{(m)}(1)}{\mathrm{d}X} = 0 \tag{3.78}$$

The boundary conditions for a CF system are:

$$u_{n1}^{(1)}(0) = 0 \quad , \quad \frac{\mathrm{d}u_{n1}^{(1)}(0)}{\mathrm{d}X} = 0 \quad , \quad \frac{\mathrm{d}^2u_{n1}^{(m)}(1)}{\mathrm{d}X^2} = 0 \quad , \quad \frac{\mathrm{d}^3u_{n1}^{(m)}(1)}{\mathrm{d}X^3} = -\omega_{n0}^2\widehat{M}_m\phi_{n0}(1) \tag{3.79}$$

The boundary conditions for a FF system are:

$$\frac{\mathrm{d}^2u_{n1}^{(1)}(0)}{\mathrm{d}X^2} = 0 \ , \ \frac{\mathrm{d}^3u_{n1}^{(1)}(0)}{\mathrm{d}X^3} = \omega_{n0}^2\widehat{M}_0\phi_{n0}(0) \ , \ \frac{\mathrm{d}^2u_{n1}^{(m)}(1)}{\mathrm{d}X^2} = 0 \ , \ \frac{\mathrm{d}^3u_{n1}^{(m)}(1)}{\mathrm{d}X^3} = -\omega_{n0}^2\widehat{M}_m\phi_{n0}(1) \tag{3.80}$$

Applying the boundary conditions at $X = 0$, the first section of the mode shape for a CC and CF system is:

$$\begin{aligned}u_{n1}^{(1)}(X) =& A_{n1}^{(1)}\left\{\cos(\sqrt{\omega_{n0}}X) - \cosh(\sqrt{\omega_{n0}}X)\right\} + B_{n1}^{(1)}\left\{\sin(\sqrt{\omega_{n0}}X) - \sinh(\sqrt{\omega_{n0}}X)\right\} \\ & + \frac{\omega_{n1}}{2\omega_{n0}}X\frac{\mathrm{d}\phi_{n0}}{\mathrm{d}X} + \left\{u_{n1,p}^{(1)}(X) - u_{n1,p}^{(1)}(0)\cosh(\sqrt{\omega_{n0}}X) - \frac{1}{\sqrt{\omega_{n0}}}\frac{\mathrm{d}u_{n1,p}^{(1)}(0)}{\mathrm{d}X}\sinh(\sqrt{\omega_{n0}}X)\right\} \\ =& A_{n1}^{(1)}\left\{\cos(\sqrt{\omega_{n0}}X) - \cosh(\sqrt{\omega_{n0}}X)\right\} + B_{n1}^{(1)}\left\{\sin(\sqrt{\omega_{n0}}X) - \sinh(\sqrt{\omega_{n0}}X)\right\} \\ & + \frac{\omega_{n1}}{2\omega_{n0}}X\frac{\mathrm{d}\phi_{n0}}{\mathrm{d}X} + \widetilde{u}_{n1}^{(1)}(X) + m_{n1}^{(1)}(X)\end{aligned} \tag{3.81}$$

The first section of the mode shape for a FF system is:

$$\begin{aligned}u_{n1}^{(1)}(X) =&A_{n1}^{(1)}\left\{\cos(\sqrt{\omega_{n0}}X)+\cosh(\sqrt{\omega_{n0}}X)\right\}+B_{n1}^{(1)}\left\{\sin(\sqrt{\omega_{n0}}X)+\sinh(\sqrt{\omega_{n0}}X)\right\}\\&+\frac{\omega_{n1}}{2\omega_{n0}}X\frac{\mathrm{d}\phi_{n0}}{\mathrm{d}X}+\left\{u_{n1,p}^{(1)}(X)-\frac{1}{\omega_{n0}}\frac{\mathrm{d}^2u_{n1,p}^{(1)}(0)}{\mathrm{d}X^2}\cosh(\sqrt{\omega_{n0}}X)\right.\\&\left.-\frac{1}{\sqrt{\omega_{n0}^3}}\frac{\mathrm{d}^3u_{n1,p}^{(1)}(0)}{\mathrm{d}X^3}\sinh(\sqrt{\omega_{n0}}X)\right\}+\sqrt{\omega_{n0}}\widehat{M}_0\phi_{n0}(0)\sinh(\sqrt{\omega_{n0}}X)\\=&A_{n1}^{(1)}\left\{\cos(\sqrt{\omega_{n0}}X)+\cosh(\sqrt{\omega_{n0}}X)\right\}+B_{n1}^{(1)}\left\{\sin(\sqrt{\omega_{n0}}X)+\sinh(\sqrt{\omega_{n0}}X)\right\}\\&+\frac{\omega_{n1}}{2\omega_{n0}}X\frac{\mathrm{d}\phi_{n0}}{\mathrm{d}X}+\widetilde{u}_{n1}^{(1)}(X)+m_{n1}^{(1)}(X)\end{aligned}\tag{3.82}$$

In Eqs. (3.81) and (3.82), $\widetilde{u}_{n1}^{(1)}(X)$ is equal to the terms within the brackets and $m_{n1}^{(1)}(X)$ is equal to the final term. In Eq. (3.81), $m_{n1}^{(1)}(X)=0$.

Next the continuity conditions are applied in order, from the continuity conditions at X_1 to the continuity conditions at X_{m-1}. Once this has been performed, the general form of the mode shape over each section for a CC and CF system is:

$$\begin{aligned}u_{n1}^{(i)}(X) =&A_{n1}^{(1)}\left\{\cos(\sqrt{\omega_{n0}}X)-\cosh(\sqrt{\omega_{n0}}X)\right\}+B_{n1}^{(1)}\left\{\sin(\sqrt{\omega_{n0}}X)-\sinh(\sqrt{\omega_{n0}}X)\right\}\\&+\frac{\omega_{n1}}{2\omega_{n0}}X\frac{\mathrm{d}\phi_{n0}}{\mathrm{d}X}+\widetilde{u}_{n1}^{(i)}(X)+m_{n1}^{(i)}(X)\end{aligned}\tag{3.83}$$

and the general form of the mode shape over each section for a FF system is:

$$\begin{aligned}u_{n1}^{(i)}(X) =&A_{n1}^{(1)}\left\{\cos(\sqrt{\omega_{n0}}X)+\cosh(\sqrt{\omega_{n0}}X)\right\}+B_{n1}^{(1)}\left\{\sin(\sqrt{\omega_{n0}}X)+\sinh(\sqrt{\omega_{n0}}X)\right\}\\&+\frac{\omega_{n1}}{2\omega_{n0}}X\frac{\mathrm{d}\phi_{n0}}{\mathrm{d}X}+\widetilde{u}_{n1}^{(i)}(X)+m_{n1}^{(i)}(X)\end{aligned}\tag{3.84}$$

It is seen in Eqs. (3.83) and (3.84) that there are only two unknown coefficients that remain to be determined. The expressions of $\widetilde{u}_{n1}^{(i)}(X)$ and $m_{n1}^{(i)}$ for the various boundary conditions can be found in Appendix B.2.

Next, the boundary conditions at $X=1$ are applied. Only the first boundary condition needs to be applied as the second boundary condition is automatically satisfied due to the choice of ω_{n1} from the solvability condition. Apply the third boundary condition listed in Eqs. (3.78)-(3.80). The expression for the mode shape over the i^{th} section for a CC system

is:

$$u_{n1}^{(i)}(X) = A_{n1}^{(1)}\phi_{n0}(X) + \frac{\omega_{n1}}{2\omega_{n0}} X \frac{\mathrm{d}\phi_{n0}}{\mathrm{d}X} + \widetilde{u}_{n1}^{(i)}(X) - \frac{\widetilde{u}_{n1}^{(m)}(1)\left\{\sin(\sqrt{\omega_{n0}}X) - \sinh(\sqrt{\omega_{n0}}X)\right\}}{\left\{\sin(\sqrt{\omega_{n0}}) - \sinh(\sqrt{\omega_{n0}})\right\}} + m_{n1}^{(i)}(X) - \frac{m_{n1}^{(m)}(1)\left\{\sin(\sqrt{\omega_{n0}}X) - \sinh(\sqrt{\omega_{n0}}X)\right\}}{\left\{\sin(\sqrt{\omega_{n0}}) - \sinh(\sqrt{\omega_{n0}})\right\}} \tag{3.85}$$

The expression for the mode shape over the i^{th} section for a CF system is:

$$u_{n1}^{(i)}(X) = A_{n1}^{(1)}\phi_{n0}(X) + \frac{\omega_{n1}}{2\omega_{n0}} X \frac{\mathrm{d}\phi_{n0}}{\mathrm{d}X} + \widetilde{u}_{n1}^{(i)}(X) + \frac{\frac{\mathrm{d}^2\widetilde{u}_{n1}^{(m)}(1)}{\mathrm{d}X^2}\left\{\sin(\sqrt{\omega_{n0}}X) - \sinh(\sqrt{\omega_{n0}}X)\right\}}{\omega_{n0}\left\{\sin(\sqrt{\omega_{n0}}) + \sinh(\sqrt{\omega_{n0}})\right\}} + m_{n1}^{(i)}(X) + \frac{\frac{\mathrm{d}^2 m_{n1}^{(m)}(1)}{\mathrm{d}X^2}\left\{\sin(\sqrt{\omega_{n0}}X) - \sinh(\sqrt{\omega_{n0}}X)\right\}}{\omega_{n0}\left\{\sin(\sqrt{\omega_{n0}}) + \sinh(\sqrt{\omega_{n0}})\right\}} \tag{3.86}$$

The expression for the mode shape over the i^{th} section for a FF system is:

$$u_{n1}^{(i)}(X) = A_{n1}^{(1)}\phi_{n0}(X) + \frac{\omega_{n1}}{2\omega_{n0}} X \frac{\mathrm{d}\phi_{n0}}{\mathrm{d}X} + \widetilde{u}_{n1}^{(i)}(X) + \frac{\frac{\mathrm{d}^2\widetilde{u}_{n1}^{(m)}(1)}{\mathrm{d}X^2}\left\{\sin(\sqrt{\omega_{n0}}X) + \sinh(\sqrt{\omega_{n0}}X)\right\}}{\omega_{n0}\left\{\sin(\sqrt{\omega_{n0}}) - \sinh(\sqrt{\omega_{n0}})\right\}} + m_{n1}^{(i)}(X) + \frac{\frac{\mathrm{d}^2 m_{n1}^{(m)}(1)}{\mathrm{d}X^2}\left\{\sin(\sqrt{\omega_{n0}}X) + \sinh(\sqrt{\omega_{n0}}X)\right\}}{\omega_{n0}\left\{\sin(\sqrt{\omega_{n0}}) - \sinh(\sqrt{\omega_{n0}})\right\}} \tag{3.87}$$

The final step is to determine the coefficient $A_{n1}^{(1)}$ by applying the mass normalization condition of Eq. (3.68b). The coefficient $A_{n1}^{(1)}$ for a CC system is

$$A_{n1}^{(1)} = -\int_0^1 \frac{\omega_{n1}}{2\omega_{n0}} X\phi_{n0}\frac{\mathrm{d}\phi_{n0}}{\mathrm{d}X} + \phi_{n0}\widetilde{u}_{n1}(X) - \frac{\widetilde{u}_{n1}^{(m)}(1)\left\{\sin(\sqrt{\omega_{n0}}X) - \sinh(\sqrt{\omega_{n0}}X)\right\}}{\left\{\sin(\sqrt{\omega_{n0}}) - \sinh(\sqrt{\omega_{n0}})\right\}}\phi_{n0} + \phi_{n0}m_{n1} - \frac{m_{n1}^{(m)}(1)\left\{\sin(\sqrt{\omega_{n0}}X) - \sinh(\sqrt{\omega_{n0}}X)\right\}}{\left\{\sin(\sqrt{\omega_{n0}}) - \sinh(\sqrt{\omega_{n0}})\right\}}\phi_{n0} + \frac{1}{2}\widehat{\rho A}(X)\phi_{n0}^2\,\mathrm{d}X - \frac{1}{2}\sum_{k=1}^{m-1}\widehat{M}_k\phi_{n0}(X_k)^2 \tag{3.88}$$

The coefficient $A_{n1}^{(1)}$ for a CF system is

$$A_{n1}^{(1)} = -\int_0^1 \frac{\omega_{n1}}{2\omega_{n0}} X\phi_{n0}\frac{\mathrm{d}\phi_{n0}}{\mathrm{d}X} + \phi_{n0}\widetilde{u}_{n1} + \frac{\frac{\mathrm{d}^2\widetilde{u}_{n1}^{(m)}(1)}{\mathrm{d}X^2}\left\{\sin(\sqrt{\omega_{n0}}X) - \sinh(\sqrt{\omega_{n0}}X)\right\}}{\omega_{n0}\left\{\sin(\sqrt{\omega_{n0}}) + \sinh(\sqrt{\omega_{n0}})\right\}}\phi_{n0}$$
$$+ \phi_{n0}m_{n1} + \frac{\frac{\mathrm{d}^2 m_{n1}^{(m)}(1)}{\mathrm{d}X^2}\left\{\sin(\sqrt{\omega_{n0}}X) - \sinh(\sqrt{\omega_{n0}}X)\right\}}{\omega_{n0}\left\{\sin(\sqrt{\omega_{n0}}) + \sinh(\sqrt{\omega_{n0}})\right\}}\phi_{n0} + \frac{1}{2}\widehat{\rho A}(X)\phi_{n0}^2\,\mathrm{d}X$$
$$- \frac{1}{2}\sum_{k=1}^{m}\widehat{M}_k\phi_{n0}(X_k)^2 \tag{3.89}$$

The coefficient $A_{n1}^{(1)}$ for a FF system is

$$A_{n1}^{(1)} = -\int_0^1 \frac{\omega_{n1}}{2\omega_{n0}} X\phi_{n0}\frac{\mathrm{d}\phi_{n0}}{\mathrm{d}X} + \phi_{n0}\widetilde{u}_{n1} + \frac{\frac{\mathrm{d}^2\widetilde{u}_{n1}^{(m)}(1)}{\mathrm{d}X^2}\left\{\sin(\sqrt{\omega_{n0}}X) + \sinh(\sqrt{\omega_{n0}}X)\right\}}{\omega_{n0}\left\{\sin(\sqrt{\omega_{n0}}) - \sinh(\sqrt{\omega_{n0}})\right\}}\phi_{n0}$$
$$+ \phi_{n0}m_{n1} + \frac{\frac{\mathrm{d}^2 m_{n1}^{(m)}(1)}{\mathrm{d}X^2}\left\{\sin(\sqrt{\omega_{n0}}X) + \sinh(\sqrt{\omega_{n0}}X)\right\}}{\omega_{n0}\left\{\sin(\sqrt{\omega_{n0}}) - \sinh(\sqrt{\omega_{n0}})\right\}}\phi_{n0} + \frac{1}{2}\widehat{\rho A}(X)\phi_{n0}^2\,\mathrm{d}X$$
$$- \frac{1}{2}\sum_{k=0}^{m}\widehat{M}_k\phi_{n0}(X_k)^2 \tag{3.90}$$

3.4.6 $\mathcal{O}(\epsilon^2)$ Problem

The ODE for the $\mathcal{O}(\epsilon^2)$ problem is

$$\frac{\mathrm{d}^4 u_{n2}}{\mathrm{d}X^4} - \omega_{n0}^2 u_{n2} = 2\omega_{n0}\omega_{n2}\phi_{n0} + 2\omega_{n0}\omega_{n1}\phi_{n1} + \omega_{n1}^2\phi_{n0} + \omega_{n0}^2\widehat{\rho A}\phi_{n1} + 2\omega_{n0}\omega_{n1}\widehat{\rho A}\phi_{n0}$$
$$+ \sum_{k=0}^{m}\left\{\omega_{n0}^2\phi_{n1} + 2\omega_{n0}\omega_{n1}\phi_{n0}\right\}\widehat{M}_k\delta\left(X - X_k\right) - \frac{\mathrm{d}^2}{\mathrm{d}X^2}\left[\widehat{EI}\frac{\mathrm{d}^2\phi_{n1}}{\mathrm{d}X^2}\right] \tag{3.91}$$

for $0 < X < 1$. A solution to the ODE exists when the following solvability condition is satisfied.

$$0 = \int_0^1 \Bigg\{ 2\omega_{n0}\omega_{n2}\phi_{n0} + 2\omega_{n0}\omega_{n1}\phi_{n1} + \omega_{n1}^2\phi_{n0} + \omega_{n0}^2\widehat{\rho A}\phi_{n1} + 2\omega_{n0}\omega_{n1}\widehat{\rho A}\phi_{n0}$$
$$+ \sum_{k=0}^{m}\left\{\omega_{n0}^2\phi_{n1} + 2\omega_{n0}\omega_{n1}\phi_{n0}\right\}\widehat{M}_k\delta\left(X - X_k\right) - \frac{\mathrm{d}^2}{\mathrm{d}X^2}\left[\widehat{EI}\frac{\mathrm{d}^2\phi_{n1}}{\mathrm{d}X^2}\right]\Bigg\}\phi_{n0}\,\mathrm{d}X \tag{3.92}$$

From the solvability condition in Eq. (3.92) the value for ω_{n2} is found. Using integration by parts and that CC, CF, and FF boundary conditions are under consideration, the solvability condition yields:

$$\begin{aligned}\omega_{n2} =& -\frac{\omega_{n1}^2}{2\omega_{n0}} + \frac{1}{2\omega_{n0}}\int_0^1 \widehat{EI}\frac{\mathrm{d}^2\phi_{n1}}{\mathrm{d}X^2}\frac{\mathrm{d}^2\phi_{n0}}{\mathrm{d}X^2} - \omega_{n0}^2\widehat{\rho A}\phi_{n0}\phi_{n1} - \omega_{n0}\omega_{n1}\widehat{\rho A}(X)\phi_{n0}^2\,\mathrm{d}X \\ & - \frac{1}{2}\sum_{k=0}^{m}\widehat{M}_k\phi_{n0}(X_k)\left\{\omega_{n0}\phi_{n1}(X_k) + \omega_{n1}\phi_{n0}(X_k)\right\} \end{aligned} \tag{3.93}$$

3.4.7 Final Dimensional Solution

Dependence on Reference Values

To determine the final expressions for the natural frequencies and mode shapes in terms of the reference values EI^* and ρA^* the parameter ϵ is removed. This is done by using the relationships $\epsilon\widehat{EI}(X) = (EI(X) - EI^*)/EI^*$, $\epsilon\widehat{\rho A}(X) = (\rho A(X) - \rho A^*)/\rho A^*$, and $\epsilon\widehat{M}_k = M_k/(l\rho A^*)$. This is the same approach used in Section 3.1.7. The result for the first correction to the natural frequencies is

$$\begin{aligned}\epsilon\omega_{n1} =& \frac{1}{2\omega_{n0}}\int_0^1 \epsilon\widehat{EI}\left(\frac{\mathrm{d}^2\phi_{n0}}{\mathrm{d}X^2}\right)^2\mathrm{d}X - \frac{\omega_{n0}}{2}\int_0^1 \epsilon\widehat{\rho A}\,\phi_{n0}^2\,\mathrm{d}X - \frac{\omega_{n0}}{2}\sum_{k=1}^{m}\epsilon\widehat{M}_k\phi_{n0}(X_k)^2 \\ =& \frac{1}{EI^*}\left\{\frac{\int_0^1 EI(X)\left(\frac{\mathrm{d}^2\phi_{n0}}{\mathrm{d}X^2}\right)^2\mathrm{d}X}{2\omega_{n0}}\right\} - \frac{1}{\rho A^*}\left\{\frac{\omega_{n0}}{2}\int_0^1 \rho A(X)\,\phi_{n0}^2\,\mathrm{d}X \right. \\ & \left. + \frac{\omega_{n0}}{2}\sum_{k=1}^{m}\frac{M_k}{l}\phi_{n0}(X_k)^2\right\} \\ =& \frac{\alpha_{n1}}{EI^*} - \frac{\alpha_{n2}}{\rho A^*}\end{aligned} \tag{3.94}$$

The first correction to the mode shape is expressed as

$$\epsilon\phi_{n1}(X) = \frac{f_{n1}(X)}{\rho A^*} - \frac{f_{n2}(X)}{EI^*} + \frac{\phi_{n0}(X)}{2} \tag{3.95}$$

and the second frequency correction is expressed as

$$\epsilon^2\omega_{n2} = \frac{\alpha_{n1}}{EI^*} - \frac{\alpha_{n2}}{\rho A^*} + \frac{\beta_{n1}}{(EI^*)^2} + \frac{\beta_{n2}}{EI^*\rho A^*} + \frac{\beta_{n3}}{(\rho A^*)^2} \tag{3.96}$$

where

$$\beta_{n1} = -\frac{\alpha_{n1}^2}{2\omega_{n0}} - \frac{1}{2\omega_{n0}} \int_0^1 EI(X) \frac{\mathrm{d}^2\phi_{n0}}{\mathrm{d}X^2} \frac{\mathrm{d}^2 f_{n2}}{\mathrm{d}X^2} \,\mathrm{d}X \tag{3.97a}$$

$$\begin{aligned}\beta_{n2} =& \frac{1}{2\omega_{n0}} \int_0^1 EI(X) \frac{\mathrm{d}^2\phi_{n0}}{\mathrm{d}X^2} \frac{\mathrm{d}^2 f_{n1}}{\mathrm{d}X^2} \,\mathrm{d}X + \frac{\omega_{n0}}{2} \int_0^1 \rho A(X) \phi_{n0} f_{n2} \,\mathrm{d}X \\ &+ \frac{\omega_{n0}}{2l} \sum_{k=0}^{m} M_k \phi_{n0}(X_k) f_{n2}(X_k)\end{aligned} \tag{3.97b}$$

$$\beta_{n3} = \frac{\alpha_{n2}^2}{2\omega_{n0}} - \frac{\omega_{n0}}{2} \int_0^1 \rho A(X) \phi_{n0} f_{n1} \,\mathrm{d}X - \frac{\omega_{n0}}{2l} \sum_{k=0}^{m} M_k \phi_{n0}(X_k) f_{n1}(X_k) \tag{3.97c}$$

The expressions of $f_{n1}(X)$ and $f_{n2}(X)$ for the various boundary conditions are given in Appendix C.2. The final expressions for the natural frequencies with two corrections and the mode shapes with one correction are

$$\omega_n = \omega_{n0} + \frac{2\alpha_{n1}}{EI^*} - \frac{2\alpha_{n2}}{\rho A^*} + \frac{\beta_{n1}}{(EI^*)^2} + \frac{\beta_{n2}}{EI^* \rho A^*} + \frac{\beta_{n3}}{(\rho A^*)^2} \tag{3.98}$$

$$\phi_n(X) = \frac{3}{2}\phi_{n0}(X) + \frac{f_{n1}(X)}{\rho A^*} - \frac{f_{n2}(X)}{EI^*} \tag{3.99}$$

The final form of the frequencies and mode shapes in Eqs. (3.98) and (3.99) is identical to those in Section 3.1.7 for the case without lumped masses. Only the values for α, β, and $f(X)$ are different.

Reintroduction of Dimensions

Dimension are reintroduced for the final solution using the length scale l and time scale $l^2\sqrt{\rho A^*/EI^*}$. For the mass normalized mode shapes, the dimensions of $1/\sqrt{\mathrm{kg}}$ must be introduced. From the length and time scales used it follows that the mass scale is $l\rho A^*$. This mass scale also arose naturally during the nondimensionalization procedure to obtain Eq. (3.62). From the nondimensional results in Eqs. (3.98) and (3.99), the dimensional solution is

$$\overline{\omega}_n = \frac{1}{l^2}\sqrt{\frac{EI^*}{\rho A^*}} \left\{ \omega_{n0} + \frac{2\alpha_{n1}}{EI^*} - \frac{2\alpha_{n2}}{\rho A^*} + \frac{\beta_{n1}}{(EI^*)^2} + \frac{\beta_{n2}}{EI^* \rho A^*} + \frac{\beta_{n3}}{(\rho A^*)^2} \right\} \tag{3.100}$$

$$\overline{\phi}_n(x) = \frac{1}{\sqrt{l\rho A^*}} \left\{ \frac{3}{2}\phi_{n0}(x/l) + \frac{f_{n1}(x/l)}{\rho A^*} - \frac{f_{n2}(x/l)}{EI^*} \right\} \tag{3.101}$$

3.5 Reference Values Selection with Lumped Masses

The final expression for the natural frequencies and mode shapes of the system are in terms of the reference values EI^* and ρA^*. The values of these are yet to be determined and the method in which they are determined will influence the accuracy of the results. The same methods for determining the reference values in Section 3.2 are updated for the case of lumped masses.

3.5.1 Minimizing L_p Norm of Difference

Updating the minimization of the L_p norm of the difference presented in Section 3.2.1 to include lumped masses yields

$$\rho A^* = \min_{\rho A^* \in \mathbb{R}} \left\{ \left(\int_0^l \left| \rho A(x) + \sum_{k=0}^{m} M_k \delta(x - x_k) - \rho A^* \right|^p \, \mathrm{d}x \right)^{1/p} \right\}$$

Since the multiplication of distributions is not well defined, the value for p must be restricted to 1. In the case that $p = 1$

$$\int_0^l \left| \rho A(x) + \sum_{k=0}^{m} M_k \delta(x - x_k) - \rho A^* \right| \, \mathrm{d}x = \int_0^l \left| \rho A(x) - \rho A^* \right| \, \mathrm{d}x + \sum_{k=0}^{m} M_k$$

It can be seen that in the case of $p = 1$, the result of the minimization with lumped masses is equivalent to the minimization of $\int_0^l |\rho A(x) - \rho A^*| \, \mathrm{d}x$. This is due to the sum of the lumped masses being a constant value and thus independent of ρA^*. Therefore the minimization of the L_p norm of the difference is

$$EI^* = \min_{EI^* \in \mathbb{R}} \left\{ \left(\int_0^l \left| EI(x) - EI^* \right|^p \, \mathrm{d}x \right)^{1/p} \right\} \tag{3.102a}$$

$$\rho A^* = \min_{\rho A^* \in \mathbb{R}} \left\{ \left(\int_0^l \left| \rho A(x) - \rho A^* \right|^p \, \mathrm{d}x \right)^{1/p} \right\} \tag{3.102b}$$

where $p = 1$ must be used if there are lumped masses in the system.

3.5.2 Minimizing L_p Norm of Perturbation

Updating the minimization of the L_p norm of the perturbation presented in Section 3.2.2 means that care must taken due to the presence of the Dirac delta distribution. As was the case in Section 3.5.1, the minimization procedure is only well defined when $p = 1$. Selecting this value for the minimization procedure leads to the following case when lumped masses are present:

$$EI^* = \min_{EI^* \in \mathbb{R}} \left\{ \int_0^1 \left| \frac{EI(X) - EI^*}{EI^*} \right| \mathrm{d}X \right\} \tag{3.103a}$$

$$\rho A^* = \min_{\rho A^* \in \mathbb{R}} \left\{ \int_0^1 \left| \frac{\rho A(X) - \rho A^*}{\rho A^*} \right| \mathrm{d}X + \sum_{k=0}^{m} \frac{M_k}{l\, \rho A^*} \right\} \tag{3.103b}$$

3.5.3 Minimizing Gradient Norm

The minimization of the gradient norm presented in Section 3.2.3 is updated to include lumped masses by omitting the upper bound on the value for ρA^*. The constraints on the mass per unit length reference value are removed due to the presence of the Dirac delta distributions, which do not allow for upper bounds to be properly defined. The expression for the Euclidean norm of the frequency and the constraint that the sum of the corrections equals 0 remains the same since the final forms of the expression for the natural frequencies of the system with and without lumped masses were identical. The minimization of the gradient norm when considering lumped masses can be written as:

$$\text{minimize:} \qquad \left\| \nabla \overline{\omega}_n \right\|_2 \tag{3.104a}$$

$$\text{subject to:} \qquad \min_{x \in [0,l]} EI\,(x) \leq EI^* \leq \max_{x \in [0,l]} EI\,(x) \tag{3.104b}$$

$$\min_{x \in [0,l]} \rho A\,(x) \leq \rho A^* \tag{3.104c}$$

$$\frac{2\alpha_{n1}}{EI^*} - \frac{2\alpha_{n2}}{\rho A^*} + \frac{\beta_{n1}}{\left(EI^*\right)^2} + \frac{\beta_{n2}}{EI^* \rho A^*} + \frac{\beta_{n3}}{\left(\rho A^*\right)^2} = 0 \tag{3.104d}$$

where:

$$\begin{aligned} \left\| \nabla \overline{\omega}_n \right\|_2 = \frac{1}{2l^2} \Bigg\{ & \frac{1}{EI^* \rho A^*} \left(\omega_{n0} - \frac{2\alpha_{n1}}{EI^*} - \frac{2\alpha_{n2}}{\rho A^*} - \frac{3\beta_{n1}}{\left(EI^*\right)^2} - \frac{\beta_{n2}}{EI^* \rho A^*} + \frac{\beta_{n3}}{\left(\rho A^*\right)^2} \right)^2 \\ & + \frac{EI^*}{\left(\rho A^*\right)^3} \left(\omega_{n0} + \frac{2\alpha_{n1}}{EI^*} - \frac{6\alpha_{n2}}{\rho A^*} + \frac{\beta_{n1}}{\left(EI^*\right)^2} + \frac{3\beta_{n2}}{EI^* \rho A^*} + \frac{5\beta_{n3}}{\left(\rho A^*\right)^2} \right)^2 \Bigg\}^{1/2} \end{aligned} \tag{3.105}$$

To prove the existence of a solution to the minimization procedure in Eq. (3.104), the same technique involving a corollary to the intermediate value theorem as in Section 3.2.3 can be used.

In summary, a perturbation theory with two corrections to the frequencies and one correction to the mode shapes was developed for an EB beam model, in addition to various ways to determine the reference values. Numerical simulations were used to quantify the errors associated with each method to select the reference values and were shown to be in good agreement. The perturbation theory was then further developed to include lumped masses so that it may be applied to string-harnessed systems, specifically the diagonal wrapping pattern.

3.6 Chapter Summary

In this chapter, the Lindstedt-Poincaré perturbation method was applied to a spatially dependent Euler-Bernoulli beam model. Two cases were considered, a system with and without lumped masses. In the perturbation theory, one correction was found for the mode shapes and two corrections were found for the frequencies. Additionally in the perturbation theory, reference values for the bending stiffness and mass per unit length from which the system is considered perturbed must be determined. The best approach for choosing these reference values was a minimization of the norm of the gradient of the frequencies.

Chapter 4

Exact Modelling and Analysis of String-Harnessed Structures

In this chapter a spatially dependent model is derived for the transverse vibrations of string-harnessed systems. The advantages of a spatially dependent model is the ability to consider non-periodic wrapping patterns for the string, in addition to periodic wrapping patterns. The perturbation theory previously developed is used to determine the frequencies and mode shapes of the system and results are verified experimentally. The work presented in this chapter is to be submitted in [91, 92].

4.1 Modelling

Consider a string-harnessed system with n strings, each of which may have a distinct wrapping pattern. Figure 4.1 presents a schematic for a system with one string and a variable wrapping pattern and indicates the Cartesian coordinates that are used to describe the system. The assumptions of Section 2.1 still hold true. That is to say there is no slip between the string and the host structure, Euler-Bernoulli (EB) assumptions are used for the host structure, and the parameters of the system are such that any initial twisting behaviour due to the presence of the strings is negligible.

Furthermore, the same assumptions are used to determine the displacement field in the system. Assuming a small transverse displacement $z = w(x, t)$ along the midline of the

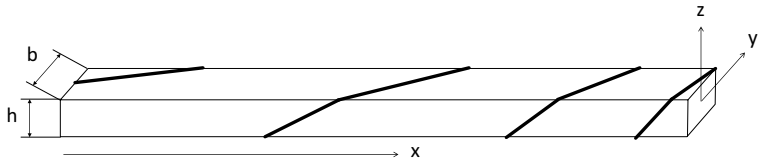

Figure 4.1: String-harnessed system with a single string and variable wrapping angle.

beam, the second-order displacement field is

$$u_x(x,t) = -z\frac{\partial w}{\partial x} \tag{4.1a}$$

$$u_y(x,t) = 0 \tag{4.1b}$$

$$u_z(x,t) = w - \frac{z}{2}\left(\frac{\partial w}{\partial x}\right)^2 \tag{4.1c}$$

The position of the centre of the i^{th} string is given by $(x, y, z) = (x, y_{s,i}(x), z_{s,i}(x))$. It is assumed that the centre of the string has a single position for a given x value. It should be noted that the functions $y_{s,i}$ and $z_{s,i}$ are not differentiable at locations where the string goes from one face of the host structure to another. Since these points are countable, $y_{s,i}$ and $z_{s,i}$ are smooth functions almost everywhere (*a.e.*). The modulus, density, pre-tension, and radius of the i^{th} string will be denoted by $E_{s,i}$, $\rho_{s,i}$, $T_{s,i}$, and $r_{s,i}$, respectively.

4.1.1 Kinetic Energy

From the assumption of small transverse displacements, the effect of rotary inertia can be ignored. The kinetic energy of the beam and the strings is given by:

$$T_{\text{system}} = \frac{1}{2}\rho_b \iiint_{\text{beam}} \left(\frac{\partial u_z}{\partial t}\right)^2 \mathrm{d}V + \sum_{i=1}^{n} \frac{1}{2}\rho_{s,i} \iiint_{i\text{th string}} \left(\frac{\partial u_z}{\partial t}\right)^2 \mathrm{d}V \tag{4.2}$$

Using the displacement field in Eq. (4.1) and keeping only higher-order terms gives

$$\begin{aligned} T_{\text{system}} &= \frac{1}{2}\rho_b A_b \int_0^l \left(\frac{\partial w}{\partial t}\right)^2 \mathrm{d}x + \sum_{i=1}^{n} \frac{1}{2}\rho_{s,i} A_{s,i} \int_0^l \sqrt{1 + \left(\frac{\mathrm{d}y_{s,i}}{\mathrm{d}x}\right)^2 + \left(\frac{\mathrm{d}z_{s,i}}{\mathrm{d}x}\right)^2} \left(\frac{\partial w}{\partial t}\right)^2 \mathrm{d}x \\ &= \frac{1}{2}\int_0^l \left(\rho_b A_b + \sum_{i=1}^{n} \frac{\rho_{s,i} A_{s,i}}{\Psi_i(x)}\right)\left(\frac{\partial w}{\partial t}\right)^2 \mathrm{d}x \end{aligned} \tag{4.3}$$

Above, $A_{s,i} = \pi r_{s,i}^2$ is the cross-section area of the i^{th} string and

$$\Psi_i(x) = \left(1 + \left(\frac{\mathrm{d}y_{s,i}}{\mathrm{d}x}\right)^2 + \left(\frac{\mathrm{d}z_{s,i}}{\mathrm{d}x}\right)^2\right)^{-1/2}$$

denotes the cosine of the angle formed by the i^{th} string with respect to the longitudinal axis.

It should be noted that the integral in Eq. (4.3) is well defined since the integrand is bounded and continuous *a.e.*. Boundedness follows since the derivatives of $y_{s,i}$ and $z_{s,i}$ are equal to or less than the magnitude of the tangent of the angle formed by the string with respect to the x-axis. This comes from the assumption that the string must form a straight line on a given face of the beam. Next, since it is assumed that a finite number of strings are present in the system, the number of points where the derivatives of $y_{s,i}$ and $z_{s,i}$ do not exist is countable and therefore form a null set. Consequently $y_{s,i},\ z_{s,i} \in C^\infty[0,l]$ *a.e.* and it follows that $\Psi_i \in C^\infty[0,l]$ *a.e.*. This shows that the integrand is continuous *a.e.* and the integral in Eq. (4.3) is Riemann integrable.

In Chapter 2 the diagonal wrapping pattern, which includes lumped masses, was considered. As such, lumped masses are added to the exact modelling of the string harnessed system for generality. Let there be a total of $m+1$ lumped masses, each of total mass M_k located at x_k. Assume that the locations of the lumped masses are $0 = x_0 < x_1 < \ldots < x_{m-1} < x_m = l$. Lumped masses at the boundaries are included for full generality. The final expression for the kinetic energy in the system is:

$$T_{\text{system}} = \frac{1}{2}\int_0^l \left(\rho_b A_b + \sum_{i=1}^{n} \frac{\rho_{s,i} A_{s,i}}{\Psi_i(x)} + \sum_{k=0}^{m} M_k \delta(x - x_k)\right)\left(\frac{\partial w}{\partial t}\right)^2 \mathrm{d}x \tag{4.4}$$

In Eq. (4.4), δ is the Dirac delta function.

4.1.2 Strain Energy

Following the same approach of Section 2.1.1, the Green-Lagrange strain tensor is employed. Using the displacement field from Eq. (4.1) the single non-zero term in the Green-Lagrange strain tensor is strain along the longitudinal axis.

$$\epsilon_{xx} = -z\frac{\partial^2 w}{\partial x^2} + \frac{z^2}{2}\left(\frac{\partial^2 w}{\partial x^2}\right)^2 + \frac{1}{2}\left(\frac{\partial w}{\partial x}\right)^2 \tag{4.5}$$

First consider the strain energy in the strings. Since it is assumed that each string is pre-tensioned, there is a pre-strain of $T_{s,i}/E_{s,i}A_{s,i}$ along the i^{th} string. In addition to the pre-strain, there will be strain due to deformations when the system undergoes vibrations. Recall for the periodic wrapping patterns that the strain tensor transformation led to a longitudinal strain in the string of the form $\epsilon_{xx}\cos^2(\theta)$. In the general case, the cosine of the angle is denoted by $\Psi(x)$ and thus the strain along the i^{th} string is given by $\epsilon_{xx}\Psi^2$. Next, it is assumed that the strain at then centre of the string is taken as the strain amount for the entire cross section of the string. Assuming Hooke's law holds and denoting a differential element of string by $\mathrm{d}s$, the total strain energy in the strings is

$$U_{\text{strings}} = \sum_{i=1}^{n} \int_{\text{length } i} \iint_{\text{area } i} \frac{1}{2} E_{s,i} \left(\frac{T_{s,i}}{E_{s,i}A_{s,i}} + \boldsymbol{\epsilon}_{xx}|_{z=z_{s,i}} \Psi_i^2 \right)^2 \mathrm{d}A\,\mathrm{d}s \tag{4.6}$$

The length of the i^{th} string is related to the Cartesian coordinates by $s = x/\Psi_i$. Making this change of coordinates in Eq. (4.6) leads to the Jacobian determinant $1/\Psi_i + x\,\Psi_i^2 \left(\frac{\mathrm{d}y_{s,i}}{\mathrm{d}x}\frac{\mathrm{d}^2 y_{s,i}}{\mathrm{d}x^2} + \frac{\mathrm{d}z_{s,i}}{\mathrm{d}x}\frac{\mathrm{d}^2 z_{s,i}}{\mathrm{d}x^2} \right)$. Note that each string is assumed to form a straight line over every section of the host structure and thus $\frac{\mathrm{d}^2 y_{s,i}}{\mathrm{d}x^2} = \frac{\mathrm{d}^2 z_{s,i}}{\mathrm{d}x^2} = 0$ *a.e.* and so the Jacobian determinant reduces to $1/\Psi_i$ *a.e.*. Perform the integration in Eq. (4.6) and keep only up to second-order terms.

$$\begin{aligned}
U_{\text{strings}} &= \sum_{i=1}^{n} \int_0^l \iint_{\text{area } i} \frac{E_{s,i}}{2\Psi_i} \left(\frac{T_{s,i}}{E_{s,i}A_{s,i}} + \boldsymbol{\epsilon}_{xx}|_{z=z_{s,i}} \Psi_i^2 \right)^2 \mathrm{d}A\,\mathrm{d}x \\
&= \sum_{i=1}^{n} \int_0^l \frac{E_{s,i}A_{s,i}}{2\Psi_i} \left(\frac{T_{s,i}}{E_{s,i}A_{s,i}} + \boldsymbol{\epsilon}_{xx}|_{z=z_{s,i}} \Psi_i^2 \right)^2 \mathrm{d}x \\
&\approx \sum_{i=1}^{n} \int_0^l \left\{ \frac{E_{s,i}A_{s,i}\Psi_i^3 z_{s,i}^2}{2} \left(\frac{\partial^2 w}{\partial x^2} \right)^2 \right. \\
&\quad \left. + T_{s,i}\Psi_i \left(-z_{s,i}\frac{\partial^2 w}{\partial x^2} + \frac{z_{s,i}^2}{2} \left(\frac{\partial^2 w}{\partial x^2} \right)^2 + \frac{1}{2} \left(\frac{\partial w}{\partial x} \right)^2 \right) + \frac{T_{s,i}^2}{2E_{s,i}A_{s,i}\Psi_i} \right\} \mathrm{d}x \\
&= \int_0^l \sum_{i=1}^{n} \left\{ \frac{E_{s,i}A_{s,i}\Psi_i^3 z_{s,i}^2}{2} \left(\frac{\partial^2 w}{\partial x^2} \right)^2 \right. \\
&\quad \left. + T_{s,i}\Psi_i \left(-z_{s,i}\frac{\partial^2 w}{\partial x^2} + \frac{z_{s,i}^2}{2} \left(\frac{\partial^2 w}{\partial x^2} \right)^2 + \frac{1}{2} \left(\frac{\partial w}{\partial x} \right)^2 \right) + \frac{T_{s,i}^2}{2E_{s,i}A_{s,i}\Psi_i} \right\} \mathrm{d}x
\end{aligned} \tag{4.7}$$

In Eq. (4.7) the interchange of summation and integration is justified as the summation is finite.

Next the strain energy in the beam is calculated, beginning with the pre-strain due to the presence of the strings. The i^{th} string will pre-strain the beam in the longitudinal direction an amount of $-T_{s,i}\Psi_i/E_bA_b$. Therefore the total pre-strain in the beam is $\sum_{i=1}^{n} -T_{s,i}\Psi_i/E_bA_b$. Assuming the beam obeys Hooke's law, the strain energy is found as:

$$\begin{aligned}
U_{\text{Beam}} &= \int_0^l \int_{-b/2}^{b/2} \int_{-h/2}^{h/2} \frac{1}{2} E_b \left(\sum_{i=1}^{n} \frac{-T_{s,i}\Psi_i}{E_bA_b} + \boldsymbol{\epsilon}_{xx} \right)^2 \mathrm{d}z\,\mathrm{d}y\,\mathrm{d}x \\
&\approx \int_0^l \int_{-b/2}^{b/2} \int_{-h/2}^{h/2} \left\{ \frac{E_b z^2}{2} \left(\frac{\partial^2 w}{\partial x^2} \right)^2 + \frac{E_b}{2} \left(\sum_{i=1}^{n} \frac{-T_{s,i}\Psi_i}{E_bA_b} \right)^2 \right. \\
&\quad \left. + E_b \left(\sum_{i=1}^{n} \frac{-T_{s,i}\Psi_i}{E_bA_b} \right) \left(-z \frac{\partial^2 w}{\partial x^2} + \frac{z^2}{2} \left(\frac{\partial^2 w}{\partial x^2} \right)^2 + \frac{1}{2} \left(\frac{\partial w}{\partial x} \right)^2 \right) \right\} \mathrm{d}z\,\mathrm{d}y\,\mathrm{d}x \\
&= \int_0^l \left\{ \frac{E_bI_b}{2} \left(\frac{\partial^2 w}{\partial x^2} \right)^2 + \frac{1}{2E_{s,i}A_{s,i}} \left(\sum_{i=1}^{n} T_{s,i}\Psi_i \right)^2 \right. \\
&\quad \left. - \left(\sum_{i=1}^{n} \frac{T_{s,i}\Psi_i}{A_b} \right) \left(\frac{I_b}{2} \left(\frac{\partial^2 w}{\partial x^2} \right)^2 + \frac{A_b}{2} \left(\frac{\partial w}{\partial x} \right)^2 \right) \right\} \mathrm{d}x
\end{aligned} \tag{4.8}$$

The approximation symbol in Eq. (4.8) is used as only up to second-order terms are kept.

Summing the strain in the strings from Eq. (4.7) and the strain in the beam from Eq. (4.8), the total strain energy in the system is found.

$$\begin{aligned}
U_{\text{system}} = \int_0^l \left\{ \frac{1}{2} \left(E_bI_b + \sum_{i=1}^{n} \left\{ E_{s,i}A_{s,i}\Psi_i^3 z_{s,i}^2 + T_{s,i}\Psi_i z_{s,i}^2 - \frac{T_{s,i}\Psi_i I_b}{A_b} \right\} \right) \left(\frac{\partial^2 w}{\partial x^2} \right)^2 \right. \\
\left. - \sum_{i=1}^{n} \left\{ T_{s,i}\Psi_i z_{s,i} \right\} \frac{\partial^2 w}{\partial x^2} + \frac{1}{2E_{s,i}A_{s,i}} \left(\sum_{i=1}^{n} T_{s,i}\Psi_i \right)^2 + \sum_{i=1}^{n} \left[\frac{T_{s,i}^2}{2E_{s,i}A_{s,i}\Psi_i} \right] \right\} \mathrm{d}x
\end{aligned} \tag{4.9}$$

4.1.3 Vibration Analysis

Applying Hamilton's principle with the total kinetic and strain energy of the system from Eqs. (4.4) and (4.9), respectively, the partial differential equation (PDE) for the free transverse vibrations of the string-harnessed system is found as

$$\frac{\partial^2}{\partial x^2} \left[EI(x) \frac{\partial^2 w}{\partial x^2} \right] + \left\{ \rho A(x) + \sum_{k=0}^{m} M_k \delta(x - x_k) \right\} \frac{\partial^2 w}{\partial t^2} = \frac{\mathrm{d}^2 \widehat{T}}{\mathrm{d}x^2}(x) \tag{4.10}$$

$$EI(x) = E_b I_b + \sum_{i=1}^{n} \left\{ E_{s,i} A_{s,i} \Psi_i^3 z_{s,i}^2 + T_{s,i} \Psi_i z_{s,i}^2 - \frac{T_{s,i} \Psi_i I_b}{A_b} \right\} \tag{4.11a}$$

$$\rho A(x) = \rho_b A_b + \sum_{i=1}^{n} \frac{\rho_{s,i} A_{s,i}}{\Psi_i} \tag{4.11b}$$

$$\widehat{T}(x) = \sum_{i=1}^{n} \{ T_{s,i} \Psi_i z_{s,i} \} \tag{4.11c}$$

The first boundary condition, at either $x^* = 0$ or l, is

$$w(x^*, t) = 0 \qquad \text{or} \qquad \frac{\partial}{\partial x} \left[EI(x) \frac{\partial^2 w}{\partial x^2} \right]_{x=x^*} = \frac{\mathrm{d}\widehat{T}}{\mathrm{d}x}(x^*) \tag{4.12}$$

and the second boundary condition is

$$\frac{\partial w}{\partial x}(x^*, t) = 0 \qquad \text{or} \qquad EI(x) \frac{\partial^2 w}{\partial x^2} \bigg|_{x=x^*} = \widehat{T}(x^*) \tag{4.13}$$

The imposed boundary conditions are the first ones listed in Eqs. (4.12) and (4.13) and are interpreted as zero displacement and zero slope. The natural boundary conditions are the second ones listed in Eqs. (4.12) and (4.13) and are related to shear and moment in the system, respectively. For a further analysis of the natural boundary conditions, consider the expression for the moment in the string-harnessed system.

$$M_x = - \left(E_b I_b + \sum_{i=1}^{n} \left\{ E_{s,i} A_{s,i} \Psi_i^3 z_{s,i}^2 \right\} \right) \frac{\partial^2 w}{\partial x^2} + \sum_{i=1}^{n} \{ T_{s,i} \Psi_i z_{s,i} \} \tag{4.14}$$

In Eq. (4.14) it is seen that the moment in the system is due the bending stiffness of the host structure, the initial moment produced by the pre-tension in the string, and a stiffening effect due to the presence of the string. Since second-order terms were kept in the displacement field and strain tensor, this results in higher-order stress resultants in the system. Calculating the higher-order stress resultants yields

$$P_x = \sum_{i=1}^{n} \left\{ T_{s,i} \Psi_i z_{s,i}^2 - \frac{T_{s,i} \Psi_i I_b}{A_b} \right\} \tag{4.15}$$

It can be seen that the boundary condition in Eq. (4.13) is in fact $M_x = P_x \frac{\partial^2 w}{\partial x^2}$. Therefore the natural boundary condition for the string-harnessed system indicates that the moment

in the system is equal to higher-order stress resultants. In terms of M_x and P_x, the natural boundary condition in Eq. (4.12) can be written as $\frac{\partial M_x}{\partial x} = \frac{\partial}{\partial x}\left(P_x \frac{\partial^2 w}{\partial x^2}\right)$. Hence it is seen that the shear in the string-harnessed system is equal to higher-order stress resultant terms.

The PDE and boundary conditions in Eqs. (4.10)-(4.13) are not homogeneous. Prior to determining a solution to the problem, a time-independent solution that satisfies the PDE and boundary conditions is introduced to eliminate the non-homogeneous terms. Denote this time-independent solution by $w_{\mathrm{e}}(x)$ and perform the substitution $w(x,t) = \overline{w}(x,t) + w_{\mathrm{e}}(x)$. Since a time independent solution has been introduced, the frequencies of $\overline{w}(x,t)$ are the same as for $w(x,t)$. The homogeneous PDE and boundary conditions at $x^* = 0$ or l are

$$\frac{\partial^2}{\partial x^2}\left[EI(x)\frac{\partial^2 \overline{w}}{\partial x^2}\right] + \left\{\rho A(x) + \sum_{k=0}^{m} M_k \delta(x - x_k)\right\}\frac{\partial^2 \overline{w}}{\partial t^2} = 0 \tag{4.16}$$

$$\overline{w}(x^*,t) = 0 \qquad \text{or} \qquad \frac{\partial}{\partial x}\left[EI(x)\frac{\partial^2 \overline{w}}{\partial x^2}\right]_{x=x^*} = 0 \tag{4.17}$$

$$\frac{\partial \overline{w}}{\partial x}(x^*,t) = 0 \qquad \text{or} \qquad EI(x)\frac{\partial^2 \overline{w}}{\partial x^2}\bigg|_{x=x^*} = 0 \tag{4.18}$$

4.2 Simulation Results for String-Harnessed System

The final form of the equation for the transverse vibrations of the string-harnessed system is a spatially dependent EB model. Typically, spatially dependent models are not solvable except under specific circumstances and thus methods to estimate the frequencies and mode shapes are frequently employed. For the string-harnessed system model the perturbation theory developed in Chapter 3 is applied.

4.2.1 Periodic Wrapping Patterns

The same system parameters previously used in Section 2.3.7 for numerical simulations are considered for both diagonal and zigzag wrapping patterns. The system parameters are restated and will be used for all simulations in this section: $b = 0.01$ m, $h = 0.0015$ m,

$l = 0.25$ m, $E_b = 6.89 \times 10^{10}$ N/m^2, $\rho_b = 2700$ kg/m^3, $r_s = 0.00035$ m, $E_s = 1.5 \times 10^{11}$ N/m^2, $\rho_s = 1400$ kg/m^3, and $T = 25$ N. It is further assumed that there are 6 fundamental elements that form the system. This is the smallest number of elements for which the homogenization procedure reports a ratio of the wavelength to the length of fundamental element greater than one for the first ten modes of the system. This also holds for all the boundary conditions considered. Due to the tenth mode having the shortest wavelength, it is this mode that provides the restriction on the number of fundamental elements under consideration.

As a periodic wrapping pattern is considered in the current simulations, the frequency results obtained using the homogenization method of Chapter 2 will be included and compared to the perturbation theory results. For notational convenience, the results of the homogenization method will be denoted by "HOM". The error of the HOM and perturbation theory results in predicting the natural frequencies and mode shapes is determined using an analytical solution for the diagonal wrapping pattern and an FEA for the zigzag wrapping pattern. Due to the manner in which the bending stiffness and mass per unit length depend on the position in the system, it is not possible to solve the PDE for a zigzag system exactly. The details of the analytical solution for the diagonal wrapping pattern are given in Appendix D and the FEA details for the zigzag wrapping pattern are given in Appendix E.

In the current simulations, the focus is on the error in predicting the natural frequencies and mode shapes of the system. The error in the frequencies is calculated as $\left(\omega_{n,\mathrm{p}} - \omega_{n,\mathrm{e}}\right)/\omega_{n,\mathrm{e}}$ and the error of the mode shapes is calculated as

$$\frac{\int_0^l \left(\phi_{n,\mathrm{p}}(x) - \phi_{n,\mathrm{e}}(x)\right)^2 \,\mathrm{d}x}{\int_0^l \phi_{n,\mathrm{e}}^2(x)\,\mathrm{d}x}$$

where the subscript 'e' represents the exact solution.

First the Young's modulus of the string is varied and the absolute percentage of error in the fundamental frequency and associated mode shape is presented in Fig. 4.2 for the diagonal wrapping pattern and in Fig. 4.3 for the zigzag wrapping pattern. In the figures, the gradient minimization method is denoted by "Grad. 1" when there is a single correction to the frequencies and "Grad. 2" when there are two corrections to the frequencies. Additionally, in Fig. 4.2, "L_1" denotes the norm minimization method. Recall that for the diagonal wrapping pattern that the case of $p = 1$ must be used and there is no difference between the difference and perturbation norm minimization. Finally, in Fig. 4.3, "Diff." and "Pert." along with a p value is used to denote the difference and perturbation norm minimization methods, respectively. In addition to the p-value that minimizes the

error, the results for $p = 1$ are included as well to represent a case in which knowledge of the frequencies and mode shapes is not known beforehand. This notation will be used throughout this chapter.

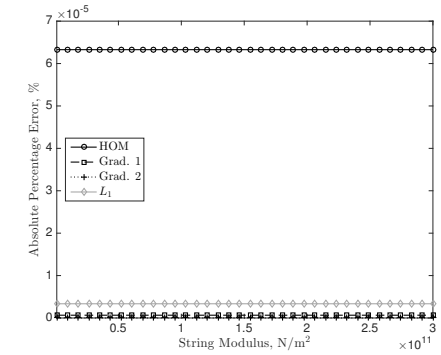

(a) CC, frequencies

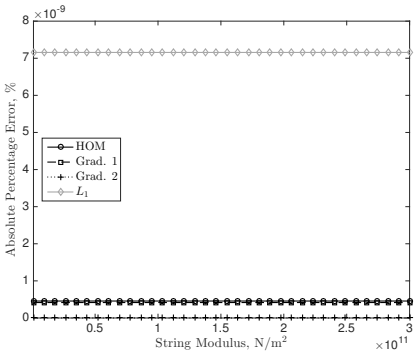

(b) CC, mode shapes

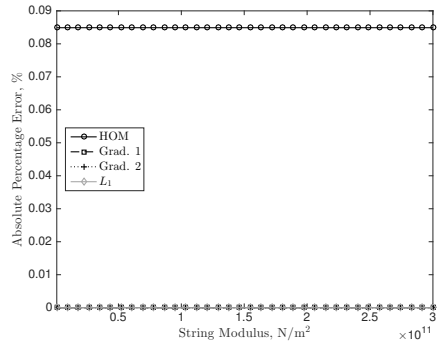

(c) CF, frequencies

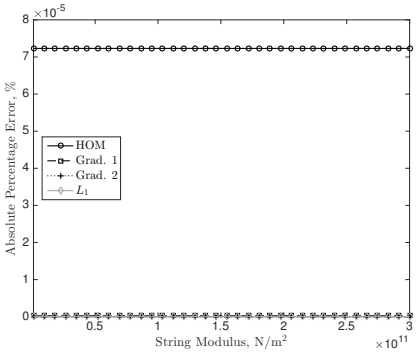

(d) CF, mode shapes

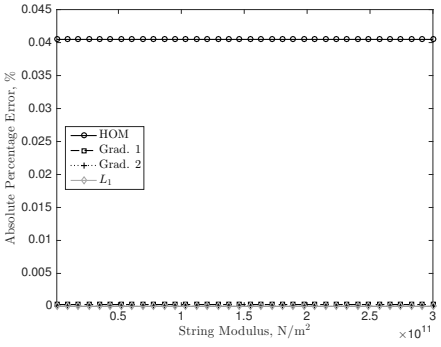

(e) FF, frequencies

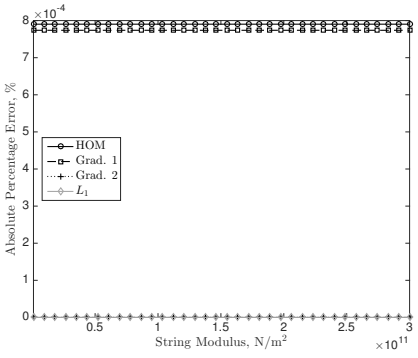

(f) FF, mode shapes

Figure 4.2: Absolute error in fundamental frequency and associated mode shape for variable string modulus and diagonal wrapping pattern.

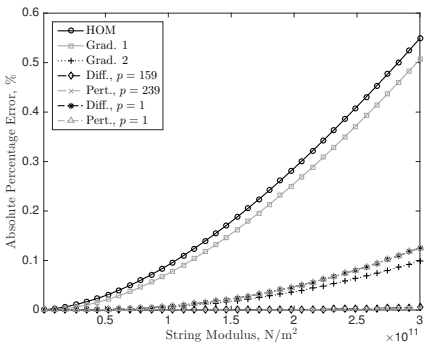

(a) CC, frequencies

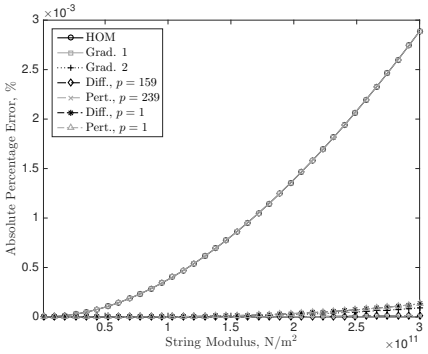

(b) CC, mode shapes

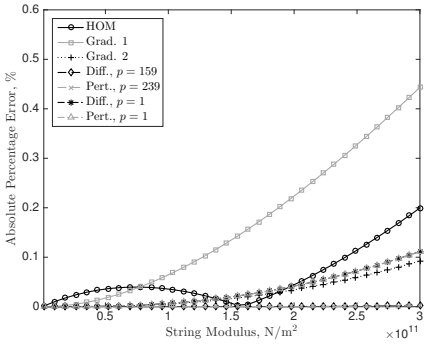

(c) CF, frequencies

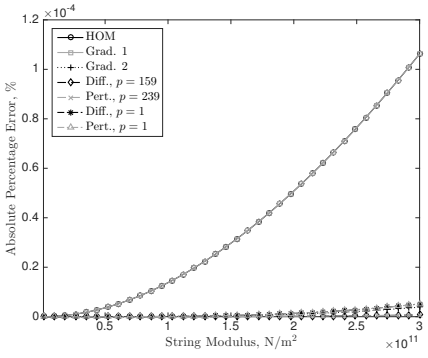

(d) CF, mode shapes

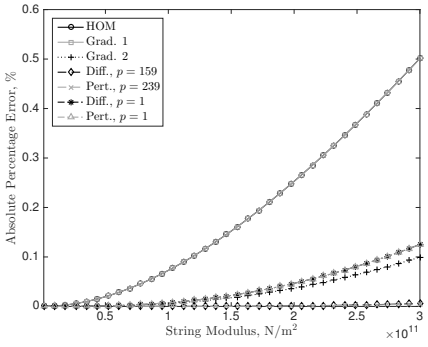

(e) FF, frequencies

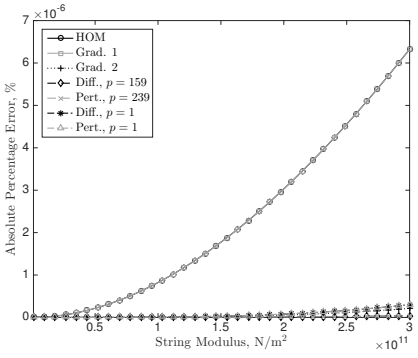

(f) FF, mode shapes

Figure 4.3: Absolute error in fundamental frequency and associated mode shape for variable string modulus and zigzag wrapping pattern.

It is seen for the diagonal wrapping pattern in Fig. 4.2 that the error in the frequency and mode shape is not affected by changes in the string modulus. Since the diagonal wrapping pattern has a constant bending stiffness throughout the system, the reference value determined by the perturbation theory is exactly this value. Hence, as the string modulus is increased, there are no additional errors introduced in the results. Furthermore, for the diagonal pattern, the perturbation theory with additional corrections typically produced smaller errors. Overall, the error in predicting the frequency and mode shape is very small, less than 0.1%.

It is seen for the zigzag wrapping pattern in Fig. 4.3 that the error in the frequency and mode shape increases as the modulus of the string increases. This behaviour is expected since as the modulus of the string increases so does the size of the perturbations, hence resulting in larger errors. It can also be seen in Fig. 4.3 that for CF boundary conditions the HOM model results for the fundamental frequency initially increase, then decrease to 0, and then once again increase as the modulus of the string increases. Due to the constant mass per unit length of the string-harnessed system, the behaviour observed for the HOM model is due to an initial underprediction of the added stiffness, followed by an overprediction of the added stiffness. Overall, the smallest errors were typically reported by the norm minimization methods with optimal p-values and the second smallest errors were typically reported by the gradient minimization with 2 corrections. Overall, the absolute error in the fundamental frequency was less than 0.6% and the absolute error in the associated mode shape was very small, less than 0.0003%.

To analyze the error across multiple modes, the average of the sum of the absolute percentage of error for the first 10 modes is presented in Table 4.1. In this table, it is clearly shown that the perturbation theory with additional corrections produces significantly smaller errors than the perturbation theory with a single correction to the frequencies. This is expected as additional corrections produce more accurate results. Furthermore, it is seen that the HOM method produces significantly larger average sum of error than the higher-order perturbation theory. This clearly highlights the advantages of using the perturbation theory over the homogenization approach.

In terms of producing the smallest average error, the gradient minimization method with additional corrections proved the best for the diagonal wrapping pattern while the perturbation norm minimization with optimal p produced the smallest error for the zigzag wrapping pattern. This was observed across all the boundary conditions and for both the frequency and mode shape errors. Assuming for the zigzag wrapping pattern that the frequencies are not known ahead of time, *i.e.* an optimal p cannot be determined, the second-order gradient minimization method resulted in the smallest average absolute error across the boundary conditions considered.

Table 4.1: Natural frequency and mode shape average absolute sum of error for the first 10 modes given variable string modulus

	Frequency Results			Mode Shape Results		
Result	CC	CF	FF	CC	CF	FF
			Diagonal Pattern ($\times 10^{-3}$)			
HOM	493.052	1188.713	1099.427	13.831	86.634	118.590
Grad. 1	4.505	15.411	19.579	13.250	84.825	116.918
Grad. 2	0.014	0.082	0.106	0.000	0.014	0.022
L_1	0.061	0.423	0.472	0.001	0.038	0.059
			Zigzag Pattern ($\times 10^{0}$)			
HOM	3.108	1.001	2.138	0.354	0.049	0.092
Grad. 1	1.979	1.721	1.917	0.354	0.049	0.092
Grad. 2	0.291	0.275	0.299	0.005	0.001	0.002
Diff., p opt.	0.011	0.008	0.017	0.001	0.000	0.000
Pert., p opt.	0.009	0.007	0.015	0.001	0.000	0.000
Diff., $p = 1$	0.382	0.339	0.379	0.008	0.002	0.003
Pert., $p = 1$	0.382	0.339	0.379	0.008	0.002	0.003

Next, the number of fundamental elements is varied while keeping the length of the system constant and the results for the fundamental frequency and associated mode shape absolute error for the diagonal and zigzag wrapping patterns are presented in Figs. 4.4 and 4.5, respectively. As the number of fundamental elements increases, the wrapping angle also increases. This leads to a reduction in the added stiffness due to the string and an increase in the added mass, resulting in a decrease in the frequencies. In the results for variable number of fundamental elements the cases of 5 or fewer elements HOM results are not presented. As previously explained, the number of fundamental elements was restricted such that the ratio of wavelength to fundamental element length is greater than one for the first ten modes of the system. Finally, since a different variable system parameter is being considered, the process to determine the optimal p-value for the norm minimization methods is performed anew.

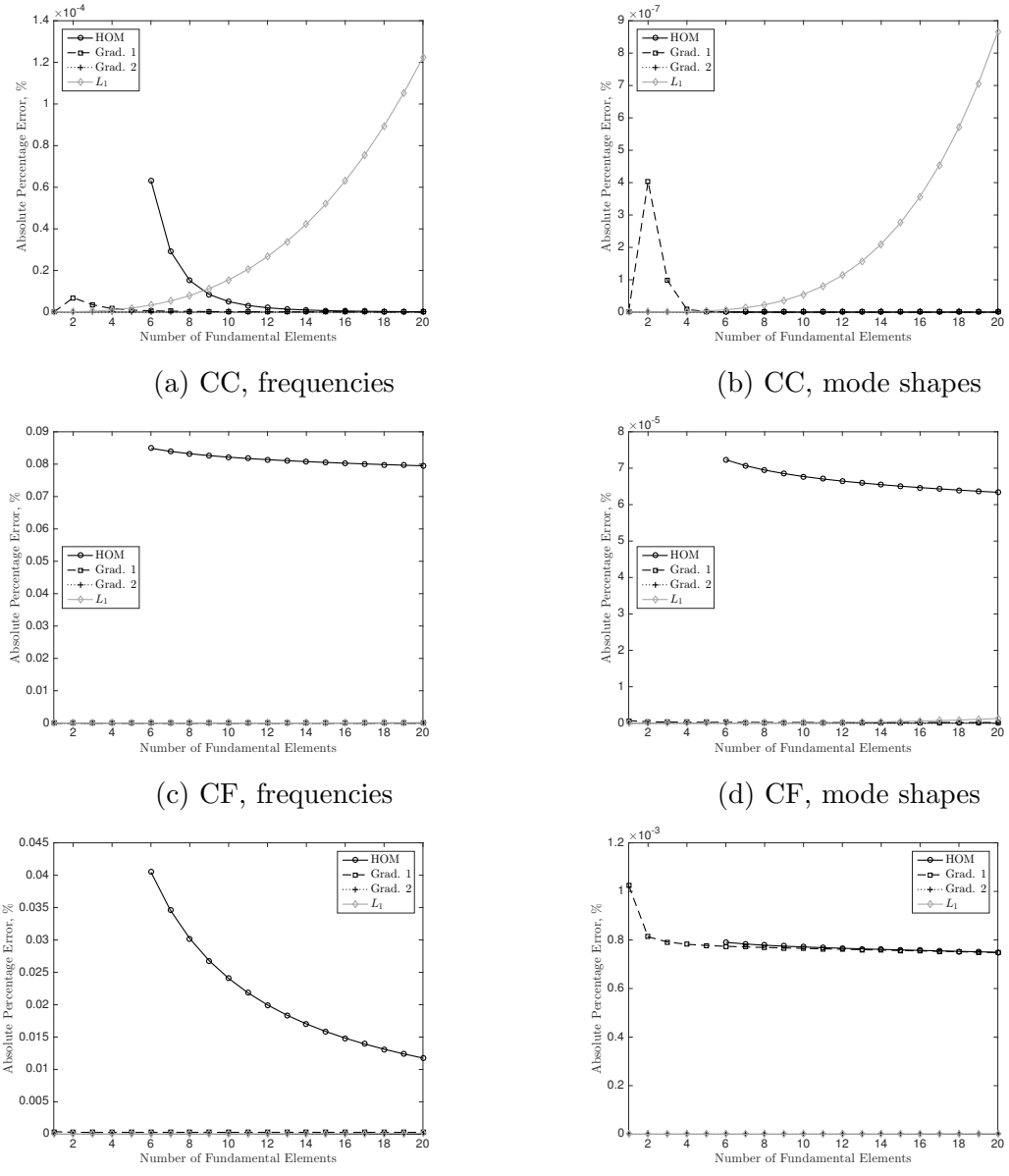

(a) CC, frequencies

(b) CC, mode shapes

(c) CF, frequencies

(d) CF, mode shapes

(e) FF, frequencies

(f) FF, mode shapes

Figure 4.4: Absolute error in fundamental frequency and associated mode shape for variable number of fundamental elements and diagonal wrapping pattern.

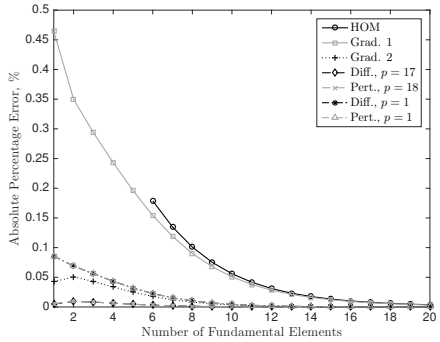

(a) CC, frequencies

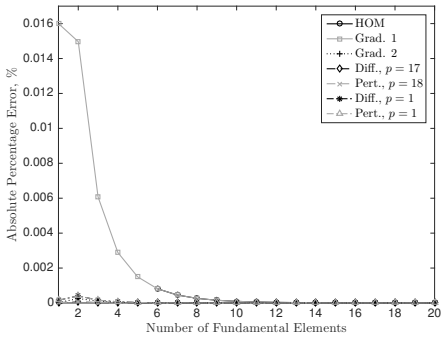

(b) CC, mode shapes

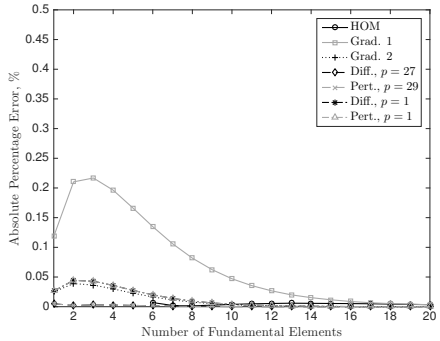

(c) CF, frequencies

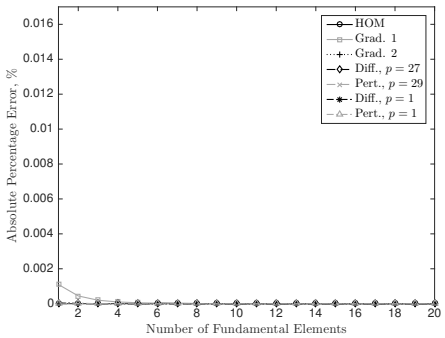

(d) CF, mode shapes

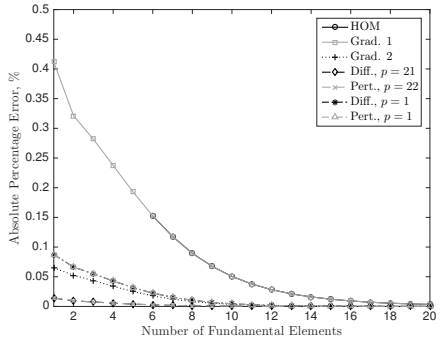

(e) FF, frequencies

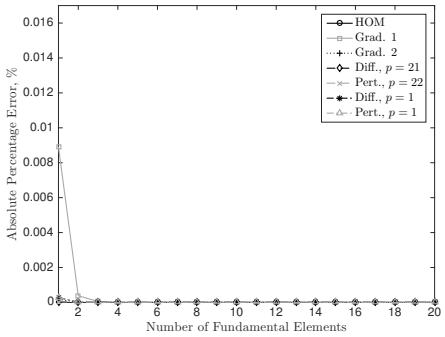

(f) FF, mode shapes

Figure 4.5: Absolute error in fundamental frequency and associated mode shape for variable number of fundamental elements and zigzag wrapping pattern.

Figure 4.4 demonstrates that for the diagonal pattern the absolute error typically decreases as the number of elements increases, with the notable exception of the norm minimization with CC boundary conditions. The increase observed for the L_1 results is due to this method being independent of the lumped masses in the system. Therefore, as the number of fundamental elements increases so does the number of lumped masses in the system. These additional lumped masses will cause increasing error as the number of fundamental elements increases. This highlights an advantage for using the gradient minimization method as the errors are decreasing for increasing number of fundamental elements. Overall, the HOM results were quite large compared to the perturbation theory results. In general for all the results presented, the error in predicting the frequency and associated mode shape was quite small, less than 0.1%.

Figure 4.5 indicates that the overall the errors decrease as the number of fundamental elements increases. In addition, it is seen for CF and FF boundary conditions that for small numbers of fundamental elements it occurs that the perturbation theory errors will sometimes increase as the number of fundamental elements increases. Furthermore, this behaviour is seen for certain results to occur in either CC or CF boundary conditions but not the other. This indicates that this increasing error behaviour is dependent on the boundary conditions applied and the perturbation theory results under consideration, rather than a specific effect. A decrease in error as the number of fundamental elements increases is expected as in this case the mass per unit length of the system is exactly known and the perturbations in the string-harnessed system bending stiffness become smaller. These effects will result in a more accurate perturbation theory. Across the various presented methods for predicting the frequency and mode shape, the norm minimization methods with optimal p-value usually predicted the smallest errors. The next best method was the second-order gradient minimization. Overall, the mode shapes were very well predicted, with errors less than 0.016%, and the error in the frequency was less than 0.5%.

Table 4.2 presents the average of the sum of the absolute percentage of error for the first 10 modes for variable number of fundamental elements. These results, as expected, indicate that the perturbation theory with additional corrections provide more accurate results than the first-order method, regardless of how the reference values are determined. In addition, the HOM typically produces a higher average error for the frequencies and mode shapes when compared to the second-order perturbation methods, in particular for the diagonal wrapping pattern with multiple lumped masses. This underlines the advantage of using the perturbation method over the HOM method, particularly when lumped masses are present. The increase in accuracy for the diagonal wrapping pattern is due to the HOM distributing the lumped masses over the entire system during homogenization, whereas the perturbation theory considers the exact location of the lumped masses. Furthermore, an

advantage of the perturbation theory is the ability to consider systems with a very small number of fundamental elements.

The second-order gradient minimization method produced the smallest average sum of absolute error for both frequencies and mode shapes for the diagonal wrapping pattern. The norm minimization using the perturbation with optimal p-value produced the smallest average sum of absolute error for both frequencies and mode shapes for the zigzag wrapping pattern. For each wrapping pattern, the most accurate method was also independent of boundary conditions. If an optimal p-value cannot be determined ahead of time, then for the results presented the second-order gradient minimization method produces the most accurate results for the zigzag wrapping pattern for both the frequencies and mode shapes, and given any of the boundary conditions.

Table 4.2: Natural frequency and mode shape average absolute sum of error for the first 10 modes given variable number of fundamental elements

	Frequency Results			Mode Shape Results		
Result	CC	CF	FF	CC	CF	FF
			Diagonal Pattern ($\times 10^{-3}$)			
HOM	239.971	1160.185	839.155	6.103	60.496	102.493
Grad. 1	3.026	10.215	15.536	6.311	66.786	105.633
Grad. 2	0.237	0.107	0.667	0.002	0.013	0.029
L_1	0.498	0.823	1.286	0.005	0.048	0.081
			Zigzag Pattern ($\times 10^{0}$)			
HOM	0.602	0.096	0.408	0.035	0.005	0.004
Grad. 1	0.902	0.793	0.856	0.242	0.117	0.156
Grad. 2	0.098	0.098	0.103	0.003	0.002	0.003
Diff., p opt.	0.018	0.014	0.018	0.001	0.000	0.001
Pert., p opt.	0.017	0.014	0.018	0.001	0.000	0.001
Diff., $p = 1$	0.134	0.122	0.131	0.004	0.003	0.004
Pert., $p = 1$	0.134	0.122	0.131	0.004	0.003	0.004

Variations in the density of the string are considered next and the absolute percentage of error in the fundamental frequency and associated mode shape is presented in Fig. 4.6 for the diagonal wrapping pattern and in Fig. 4.7 for the zigzag wrapping pattern.

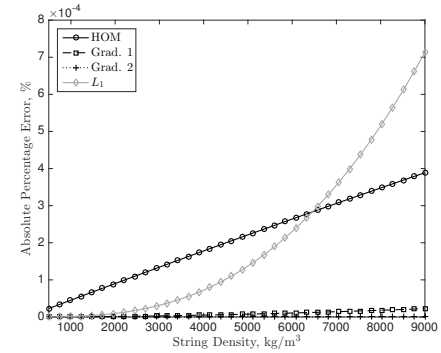

(a) CC, frequencies

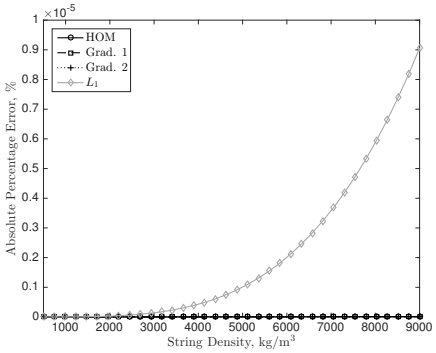

(b) CC, mode shapes

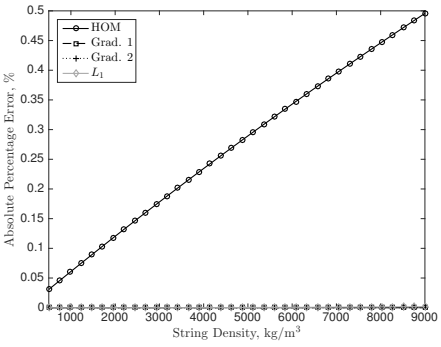

(c) CF, frequencies

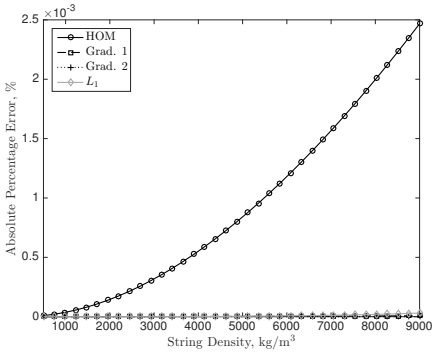

(d) CF, mode shapes

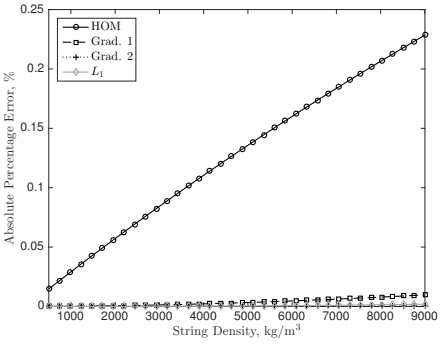

(e) FF, frequencies

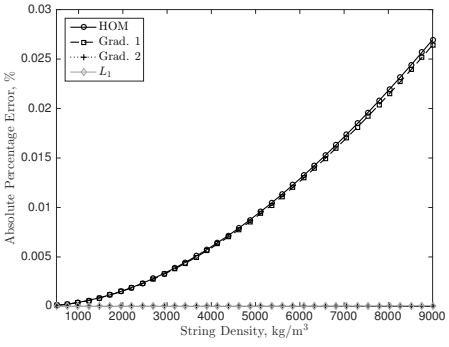

(f) FF, mode shapes

Figure 4.6: Absolute error in fundamental frequency and associated mode shape for variable string density and diagonal wrapping pattern.

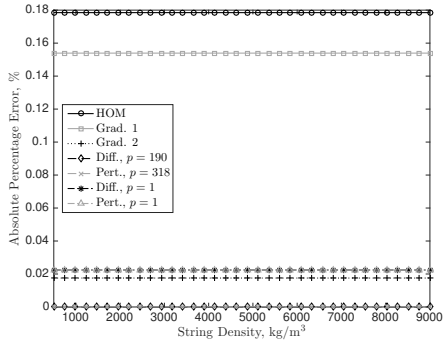

(a) CC, frequencies

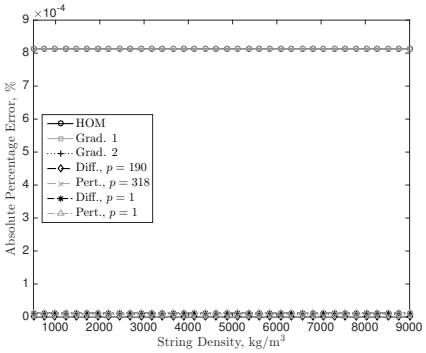

(b) CC, mode shapes

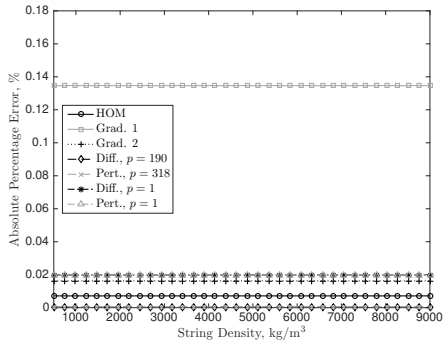

(c) CF, frequencies

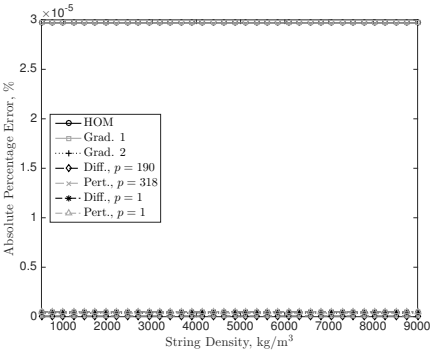

(d) CF, mode shapes

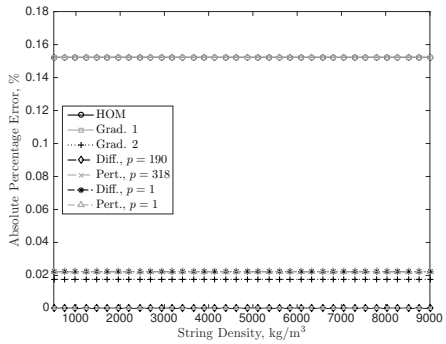

(e) FF, frequencies

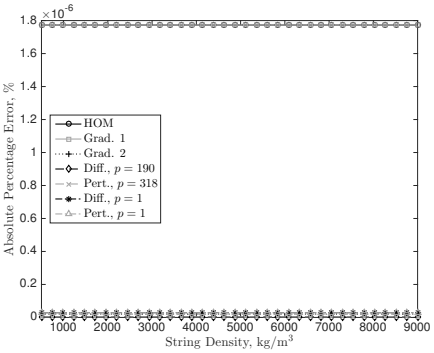

(f) FF, mode shapes

Figure 4.7: Absolute error in fundamental frequency and associated mode shape for variable string density and zigzag wrapping pattern.

It is seen for the diagonal wrapping pattern in Fig. 4.6 that the error in the frequency and mode shape increases as the density of the string increases. Furthermore, for the diagonal wrapping pattern, the second-order gradient minimization perturbation method consistently resulted in the smallest errors in the frequency and mode shape. As the density of the string increases, so does the value of the lumped masses. Due to this, the L_1 results, which is not influenced by the lumped masses, demonstrate a larger rate of increase in error compared to the other perturbation results, in particular for the CC boundary conditions. Again, this clearly shows an advantage for using the gradient minimization method for the diagonal wrapping pattern. Overall, the error in predicting the frequency is less than 0.5%, and the error for the mode shapes is quite small, less than 0.03%.

It is seen for the zigzag wrapping pattern in Fig. 4.7 that the error in the frequency and mode shape is not affected by changes in the string density. Since the zigzag wrapping pattern has a constant mass per unit length throughout the system, the reference value determined by the perturbation theory is exactly this value. Hence, as the string density is increased, there are no additional errors introduced in the results. The smallest errors were typically reported by the norm minimization methods with optimal p-value and the second smallest errors were typically reported by the second-order gradient minimization. Overall, the absolute error in the fundamental frequency was small, less than 0.18%, and the error in the associated mode shape was very small, less than 0.001%.

To analyze the error across multiple modes, the average of the sum of the absolute percentage of error for the first 10 modes is presented in Table 4.3. In this table, it is clearly shown that the perturbation theory with additional corrections produces significantly smaller errors than the first-order perturbation theory, as expected. Furthermore, it is seen that the HOM method produces significantly larger average sum of error than the second-order perturbation theory results. Once again, this demonstrates the advantage of using the perturbation theory over the HOM.

In terms of producing the smallest average error, the gradient minimization method with two corrections to the frequencies and one correction to the mode shape proved the best for the diagonal wrapping pattern while the norm minimizations with optimal p produced the smallest error for the zigzag wrapping pattern. This was observed across all the boundary conditions and for both the sum of error for frequencies and mode shapes. Assuming for the zigzag wrapping pattern that an optimal p cannot be determined, the second-order gradient minimization method resulted in the smallest average absolute error across the boundary conditions considered.

Table 4.3: Natural frequency and mode shape average absolute sum of error for the first 10 modes given variable string density

	Frequency Results			Mode Shape Results		
Result	CC	CF	FF	CC	CF	FF
			Diagonal Pattern ($\times 10^{-3}$)			
HOM	1623.782	3714.771	3389.699	175.974	1026.455	1397.085
Grad. 1	57.846	192.183	245.077	168.356	1002.587	1374.167
Grad. 2	0.819	4.686	5.590	0.047	3.420	5.448
L_1	3.606	24.667	27.780	0.245	9.863	15.206
			Zigzag Pattern ($\times 10^{0}$)			
HOM	2.806	0.568	1.806	0.285	0.039	0.074
Grad. 1	1.628	1.415	1.575	0.285	0.039	0.074
Grad. 2	0.178	0.168	0.182	0.002	0.000	0.001
Diff., p opt.	0.002	0.003	0.004	0.000	0.000	0.000
Pert., p opt.	0.003	0.004	0.003	0.000	0.000	0.000
Diff., $p = 1$	0.234	0.208	0.233	0.003	0.001	0.001
Pert., $p = 1$	0.234	0.208	0.233	0.003	0.001	0.001

Consider next Figs. 4.8 and 4.9, which contain the absolute error in the fundamental frequency and mode shape when a variable string radius is considered. As the radius of the string is increased, there will be more added mass as well as a larger stiffening effect. The overall effect on the frequencies will depend on the additional system parameters and may cause an increase or decrease.

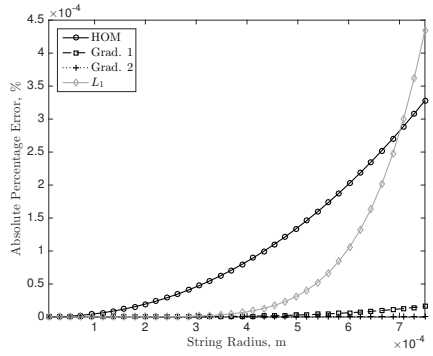

(a) CC, frequencies

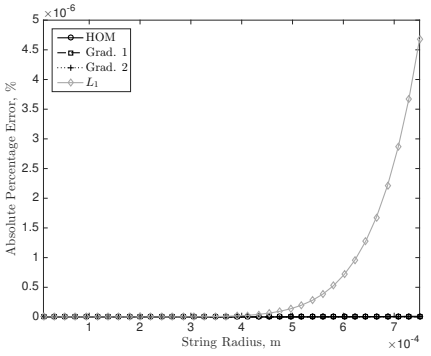

(b) CC, mode shapes

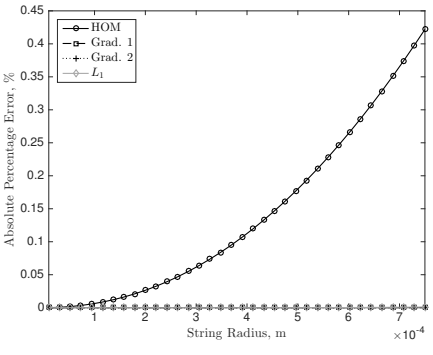

(c) CF, frequencies

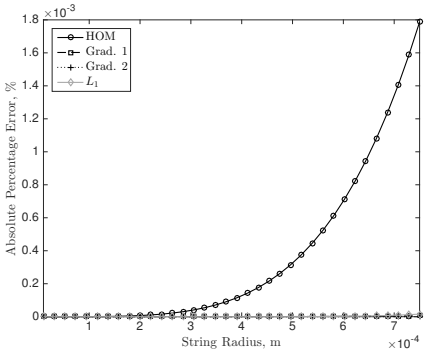

(d) CF, mode shapes

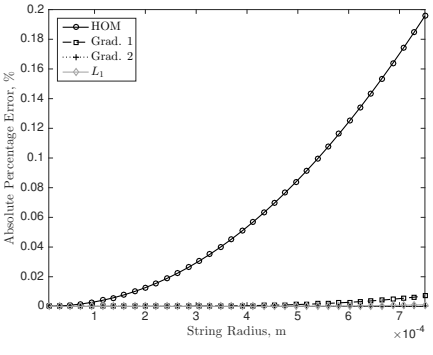

(e) FF, frequencies

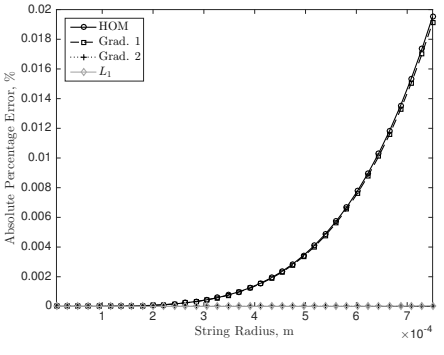

(f) FF, mode shapes

Figure 4.8: Absolute error in fundamental frequency and associated mode shape for variable string radius and diagonal wrapping pattern.

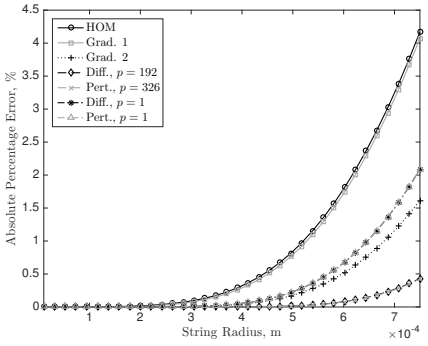

(a) CC, frequencies

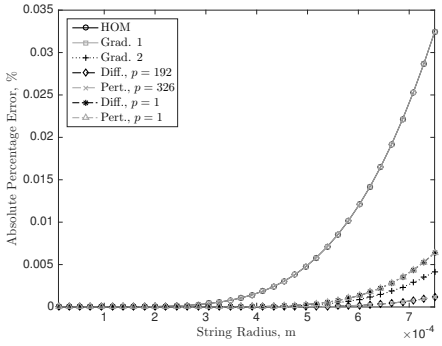

(b) CC, mode shapes

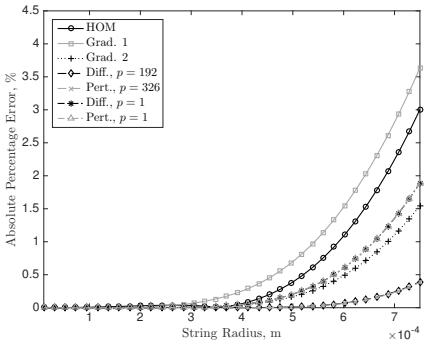

(c) CF, frequencies

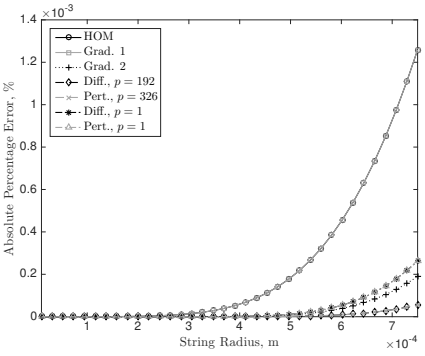

(d) CF, mode shapes

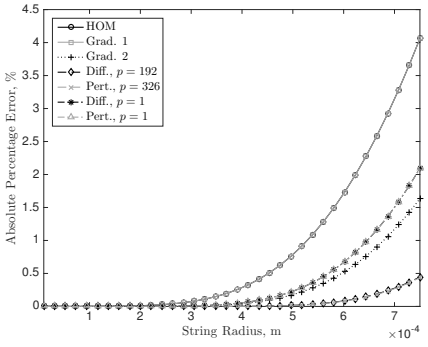

(e) FF, frequencies

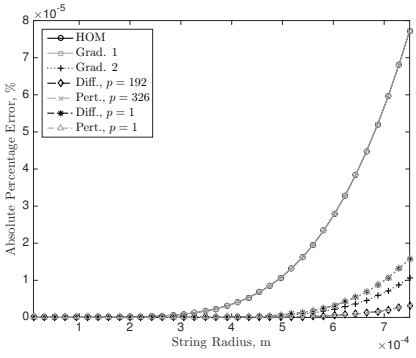

(f) FF, mode shapes

Figure 4.9: Absolute error in fundamental frequency and associated mode shape for variable string radius and zigzag wrapping pattern.

It is shown in Fig. 4.8 that increasing the radius of the string increases the error in the prediction of the fundamental frequency and mode shape for all the presented results. Typically, the HOM method produced the largest errors, with the exception for CC boundary conditions where the norm minimization produced the largest errors. As the radius of the string increases so does the value of the lumped masses. As the L_1 results are independent of the lumped masses, it is seen that the errors increase at a much quicker rate for the CC boundary conditions as the radius increases. Once again this demonstrates the appropriateness of using the gradient norm minimization over the norm minimization of the difference and perturbation. In general across all the boundary conditions, the error is quite small, less than 0.45% for the frequency and less than 0.02% for the mode shape.

It is shown in Fig. 4.9 that increasing the radius of the string increases the error in the prediction of the fundamental frequency and mode shape for all the presented results. Typically, the HOM and first-order perturbation theory produced the largest errors while the norm minimization methods with optimal p produced the smallest errors. The second-order gradient method produced the second smallest errors for the frequency and mode shape. It is expected that increasing the string radius would increase the error as this will result in larger perturbations in the bending stiffness, hence larger errors in the perturbation theory results. In general, the absolute percentage of error for the mode shapes was quite small, less than 0.035%, and it is seen that the error in the frequency is quite sensitive to changes in the string radius, reaching a maximum of 4.17% in the HOM for CC boundary conditions.

The results for the average sum of error in the frequencies and mode shapes for the first 10 modes given variable string radius are tabulated in Table 4.4. These results show a significant improvement in the accuracy when using the second-order perturbation theory instead of the HOM results. This illustrates the noteworthy increase in accuracy over a large range of system parameters when using the second-order perturbation theory. As anticipated, the perturbation theory with additional corrections results in a smaller average error when compared to the perturbation theory with fewer corrections.

The second-order gradient minimization provided the smallest average error for the frequencies and mode shapes across all the boundary conditions for the diagonal wrapping pattern. The norm minimization using the perturbation with optimal p provided the smallest average error for the frequencies and mode shapes across all the boundary conditions for the zigzag wrapping pattern. If it is not possible to determine an optimal p-value for the norm minimizations, for the cases considered the second-order gradient minimization would provide the best estimates for the frequencies and mode shapes for the zigzag wrapping pattern.

Table 4.4: Natural frequency and mode shape average absolute sum of error for the first 10 modes given variable string radius

	Frequency Results			Mode Shape Results		
Result	CC	CF	FF	CC	CF	FF
			Diagonal Pattern ($\times 10^{-3}$)			
HOM	817.325	1903.430	1745.006	66.775	396.230	540.126
Grad. 1	21.872	73.220	93.292	63.910	387.254	531.575
Grad. 2	0.248	1.409	1.709	0.012	0.863	1.375
L_1	1.082	7.430	8.353	0.061	2.474	3.813
			Zigzag Pattern ($\times 10^{0}$)			
HOM	10.415	6.356	8.928	1.779	0.321	0.533
Grad. 1	8.650	7.671	8.570	1.779	0.321	0.533
Grad. 2	2.623	2.544	2.755	0.110	0.037	0.041
Diff., p opt.	0.514	0.479	0.605	0.033	0.013	0.010
Pert., p opt.	0.497	0.464	0.589	0.032	0.013	0.010
Diff., $p = 1$	3.510	3.180	3.561	0.189	0.052	0.066
Pert., $p = 1$	3.510	3.180	3.561	0.189	0.052	0.066

Finally, the tension in the string is varied and the results for the fundamental frequency and associated mode shape absolute error for the diagonal and zigzag wrapping patterns are presented in Figs. 4.10 and 4.11, respectively. As the tension in the string increases, there is an increase in the stiffening effect and thus an increase in the frequencies is expected.

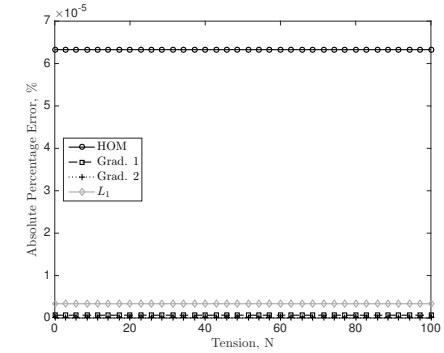

(a) CC, frequencies

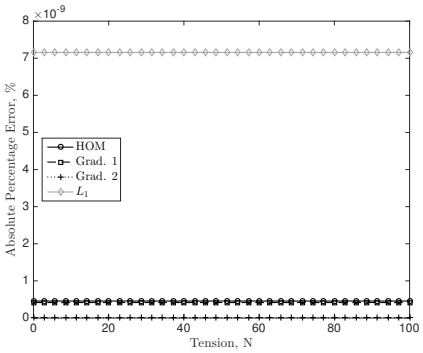

(b) CC, mode shapes

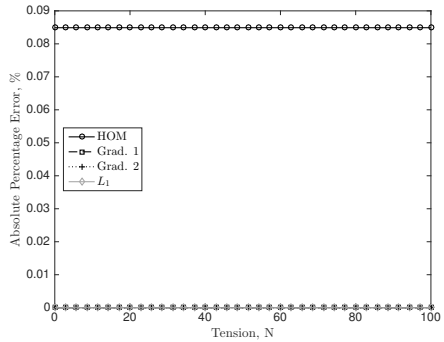

(c) CF, frequencies

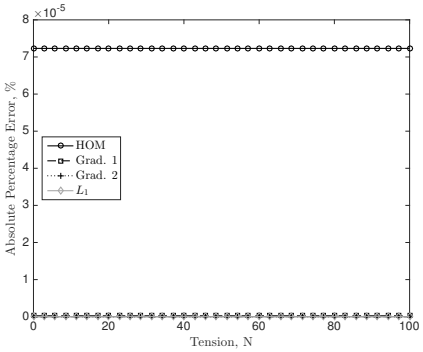

(d) CF, mode shapes

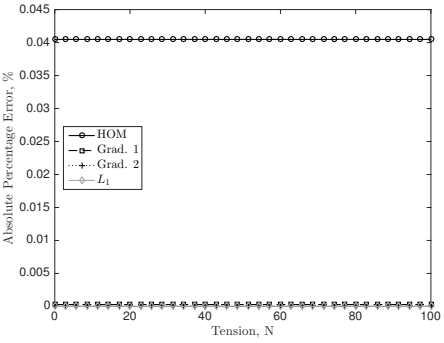

(e) FF, frequencies

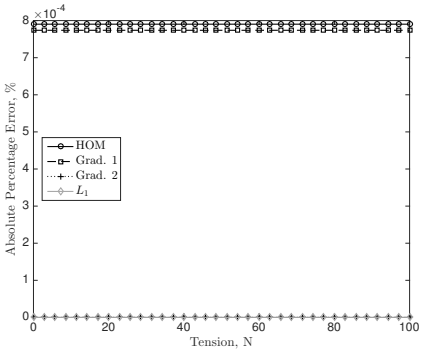

(f) FF, mode shapes

Figure 4.10: Absolute error in fundamental frequency and associated mode shape for variable string tension and diagonal wrapping pattern.

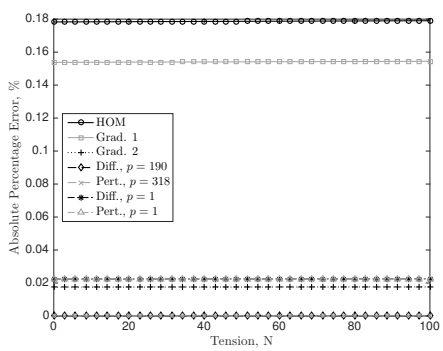

(a) CC, frequencies

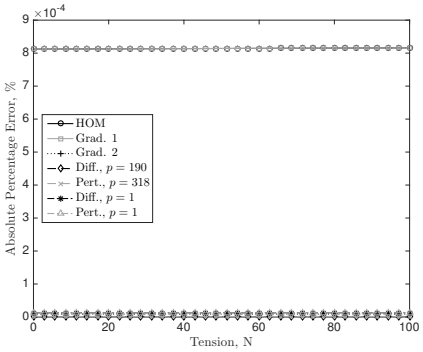

(b) CC, mode shapes

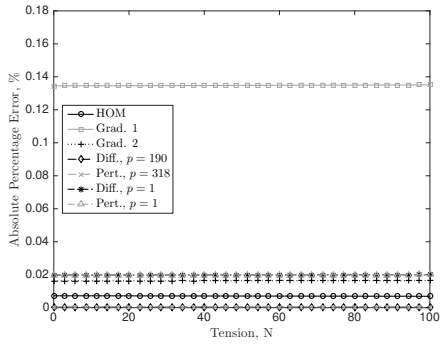

(c) CF, frequencies

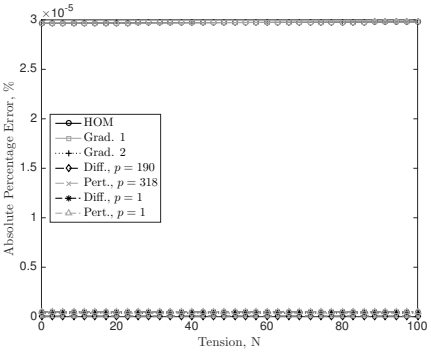

(d) CF, mode shapes

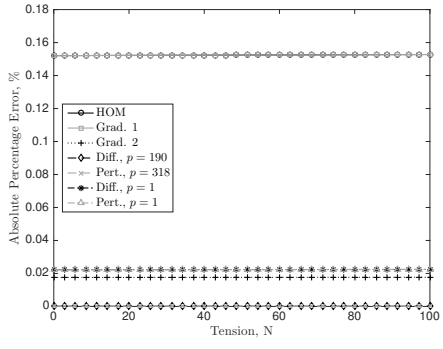

(e) FF, frequencies

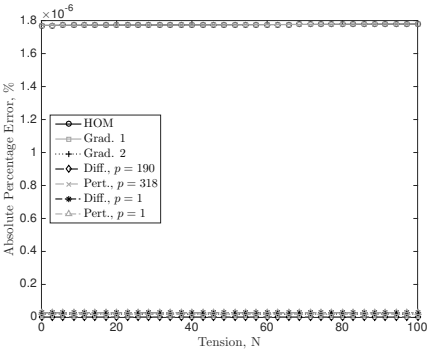

(f) FF, mode shapes

Figure 4.11: Absolute error in fundamental frequency and associated mode shape for variable string tension and zigzag wrapping pattern.

Figure 4.10 for the diagonal wrapping pattern demonstrates that the error in the frequency and mode shape is not affected by changes in the string tension. Since the diagonal wrapping pattern has a constant bending stiffness throughout the system, the reference value determined by the perturbation theory is exactly this value. Hence, as the string tension is increases, there are no additional errors introduced in the results. Overall for the diagonal wrapping pattern, the HOM typically predicts the largest absolute error and the perturbation theory results with additional corrections predict the smallest absolute error. In general for all the results presented, the error in predicting the frequency and associated mode shape was quite good, less than 0.1%.

Figure 4.11 for the zigzag wrapping pattern demonstrates that the error in the frequency and mode shape is not greatly affected by changes in the string tension. In the numerical simulations of Section 2.3.10 it was shown that the frequency of the system did not vary much for the system parameters that were considered. Therefore in the figures above the error does not change much with variable tension since the system behaviour is not greatly affected by changes in the tension. It is expected, however, that increasing the string tension yields an increase in the errors. As the string tension increases so do the size of the perturbations in the system's bending stiffness, leading to larger errors in the perturbation theory. Taking the results for the second-order gradient minimization arbitrarily, it is shown in Fig. 4.12 that increasing the tension in the string does in fact increase the error in the system. In this figure only a single set of results are presented since otherwise it becomes difficult to visualize the increase in error. Due to the smaller frequencies for the CF boundary conditions, it is seen in Fig. 4.12 that there are larger numerical errors than for the CC and FF boundary conditions. Across the various presented methods for predicting the frequency and mode shape of the zigzag wrapping pattern, the norm minimization methods with optimal p-value usually predicted the smallest errors. The next best method was the second-order gradient minimization. Overall, the mode shapes were very well predicted, with errors less than 0.001%, and the error in the frequency was less than 0.18%.

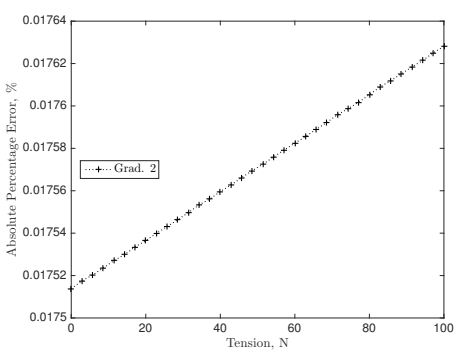

(a) CC, frequencies

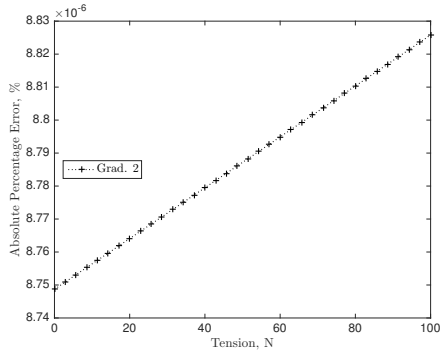

(b) CC, mode shapes

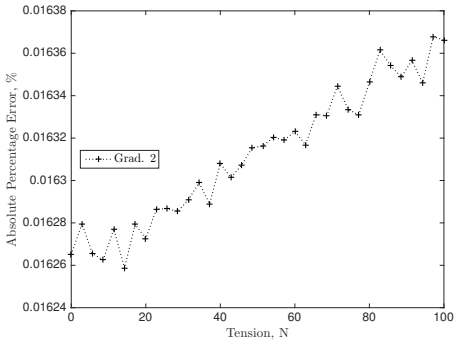

(c) CF, frequencies

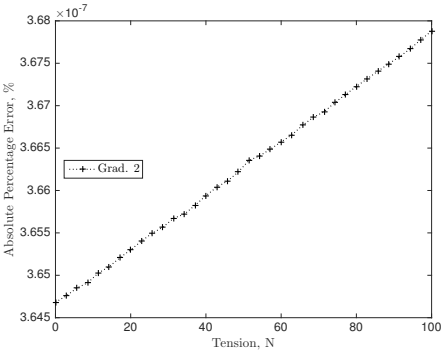

(d) CF, mode shapes

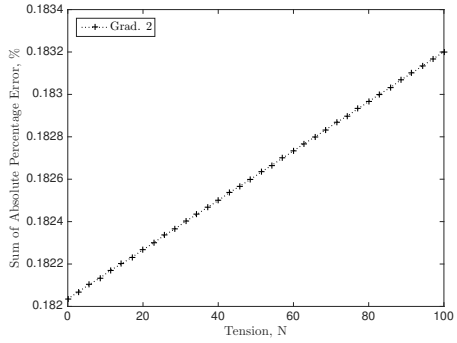

(e) FF, frequencies

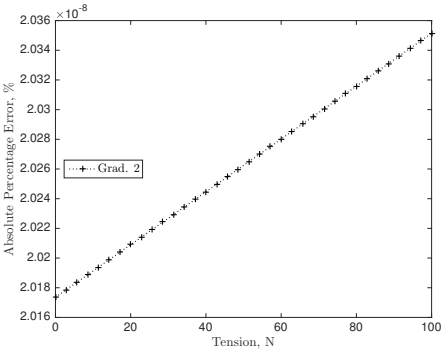

(f) FF, mode shapes

Figure 4.12: Zoom-in of absolute error in fundamental frequency and associated mode shape for variable string tension and zigzag wrapping pattern.

Table 4.5 presents the average of the sum of the absolute percentage of error for the first 10 modes for variable string tension. These results, as expected, indicate that the perturbation theory with additional corrections provide more accurate results than the first-order method, regardless of how the reference values are determined. In addition, the HOM produces a higher average error for the frequencies and mode shapes when compared to the second-order perturbation methods, in particular for the diagonal wrapping pattern with multiple lumped masses. This is an advantage of using the perturbation method over the HOM method, particularly when lumped masses are present.

The second-order gradient minimization method produced the smallest average sum of absolute error for both frequencies and mode shapes for the diagonal wrapping pattern. The norm minimizations with optimal p-value produced the smallest average sum of absolute error for both frequencies and mode shapes for the zigzag wrapping pattern. For each wrapping pattern, the most accurate method was also independent of boundary conditions. If an optimal p-value cannot be determined ahead of time, then for the results presented the second-order gradient minimization method produces the most accurate results for the zigzag wrapping pattern for both the frequencies and mode shapes, and given any of the boundary conditions.

Table 4.5: Natural frequency and mode shape average absolute sum of error for the first 10 modes given variable string tension

	Frequency Results			Mode Shape Results		
Result	CC	CF	FF	CC	CF	FF
			Diagonal Pattern ($\times 10^{-3}$)			
HOM	493.052	1188.713	1099.427	13.831	86.634	118.590
Grad. 1	4.505	15.411	19.579	13.250	84.825	116.918
Grad. 2	0.014	0.082	0.106	0.000	0.014	0.022
L_1	0.061	0.423	0.472	0.001	0.038	0.059
			Zigzag Pattern ($\times 10^{0}$)			
HOM	2.809	0.569	1.808	0.286	0.039	0.074
Grad. 1	1.630	1.417	1.577	0.286	0.039	0.074
Grad. 2	0.178	0.168	0.183	0.002	0.000	0.001
Diff., p opt.	0.002	0.003	0.004	0.000	0.000	0.000
Pert., p opt.	0.003	0.004	0.003	0.000	0.000	0.000
Diff., $p = 1$	0.235	0.208	0.233	0.003	0.001	0.001
Pert., $p = 1$	0.235	0.208	0.233	0.003	0.001	0.001

In summary, from the numerical simulations with periodic wrapping patterns and multiple variations to the system parameters it is clear that there is a significant advantage in using the perturbation theory with additional corrections over the HOM model. Specifically, a smaller average sum of error was observed for the second-order perturbation theory when compared to a first-order theory, regardless of how the reference were determined. In addition, the perturbation theory is capable of considering system setups for which the HOM model is considered unreliable, that is for a small number of fundamental elements.

A clear pattern was observed with regards to the perturbation theory reference value selection method that should be employed to obtain the most accurate results. For the diagonal pattern, the second-order gradient minimization always produced the smallest average sum of error for the first 10 modes of the system. This held true for both frequencies and mode shapes and all three boundary conditions considered. For the zigzag pattern, the norm minimization methods with optimally chosen p values, specifically the perturbation minimization, produced the smallest average sum of error for the first 10 modes of the system. If it is assumed that the frequencies of the system are not known ahead of time and an optimal p-value cannot be determined, then it is seen form the presented results that the second-order gradient minimization method would provide the most accurate method for determining the frequencies and mode shapes of the zigzag system.

Finally, driving point FRFs are presented for the periodically wrapped system in Fig. 4.13. In addition, to highlight the stiffening effect of the string, the FRF for an unwrapped beam is also presented in the figure. The unwrapped beam FRF was determined using an EB model. For CF and FF boundary conditions, the actuation and sensing location is the free right end. For the CC boundary conditions, the actuation and sensing location is $x = 0.025$ m from the left clamped end. These locations for the driving point FRFs were chosen such that they do not correspond to any node of any mode of interest. The system parameters employed are the same as those listed at the beginning of Section 4.2.1. Finally, for this single system setup the optimal p-value was determined for the norm minimization methods by minimizing the frequency and mode shape errors for the first twn modes of the system.

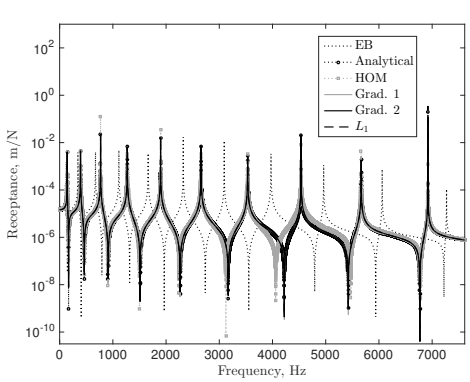

(a) Diagonal, CC

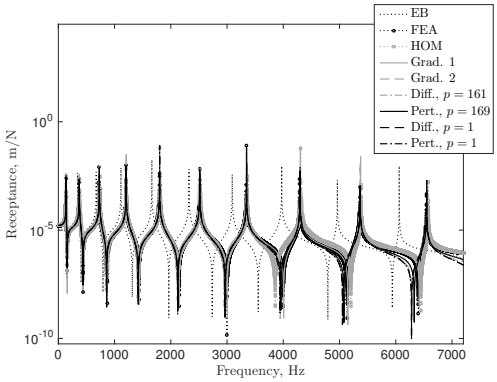

(b) Zigzag, CC

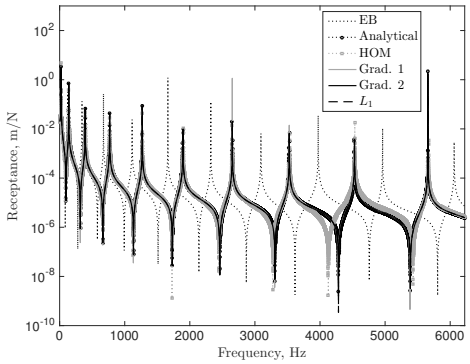

(c) Diagonal, CF

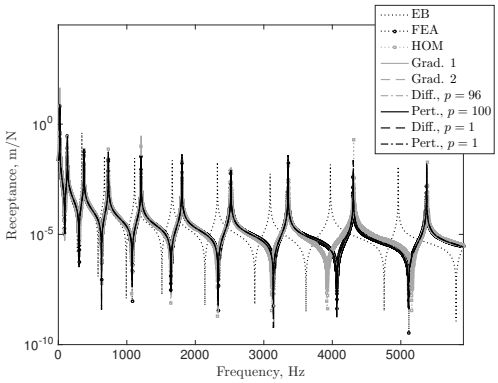

(d) Zigzag, CF

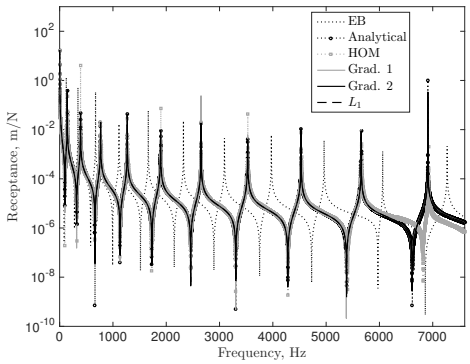

(e) Diagonal, FF

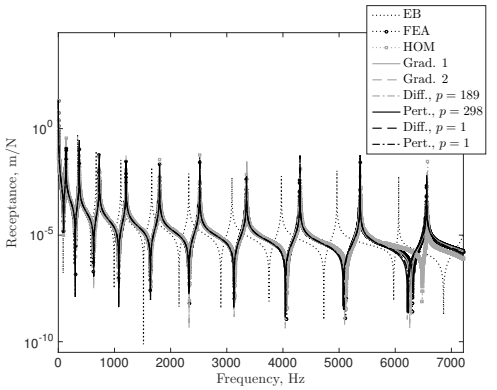

(f) Zigzag, FF

Figure 4.13: FRFs for an unwrapped beam (EB), and string-harnessed beam using perturbation theory and exact solution for periodic wrapping pattern.

Figure 4.13 clearly demonstrate that the perturbation theory results agree quite strongly with the analytical and FEA results for the diagonal and zigzag wrapping patterns, respectively. The accuracy of the FRFs is measured by comparing the location of the natural frequencies, the location of antiresonances, as well as the amplitude. Additionally, the perturbation theory results compared to the HOM results are observed be a better match to the exact FRFs. This demonstrates the advantage of using the perturbation theory over the HOM model. Finally, it is seen in Fig. 4.13 that the shift in the FRFs between the unwrapped and string-harnesses systems is quite noticeable. This highlights the significant impact of a string harness, particularly with respect to the added stiffness to the system.

4.2.2 Non-Periodic Wrapping Pattern: Variable Wrapping Angle

Description of System

Consider a system setup where an initial wrapping angle is given and then is either increased or decreased a predetermined amount each time the string goes from one side of the beam to the next. Specifically, for the diagonal wrapping pattern the wrapping angle will change after each lumped mass. For the numerical simulations, two initial wrapping angles are considered. The first initial wrapping angle is the constant angle across the system necessary to obtain two fundamental elements. This will be referred to as the Base 2 case. The second initial wrapping angle is the constant angle across the system necessary to obtain 10 fundamental elements. This will be referred to as the Base 10 case. Schematics of some of the wrapping patterns considered, including the maximum and minimum percentage change considered over each section, are presented in Fig. 4.14 for the diagonal pattern and in Fig. 4.15 for the zigzag pattern.

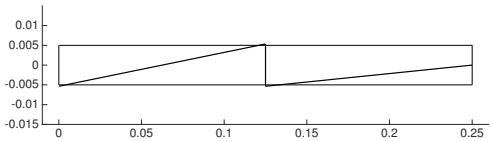

(a) Base 2, -49.9% (Minimum)

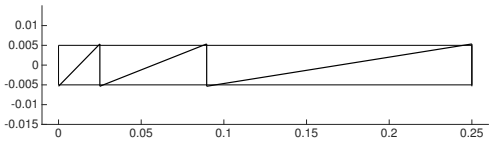

(b) Base 10, -59.4% (Minimum)

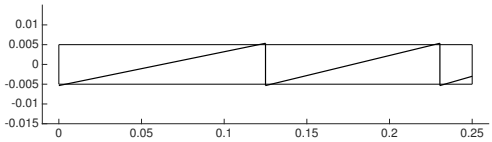

(c) Base 2, 18.4%

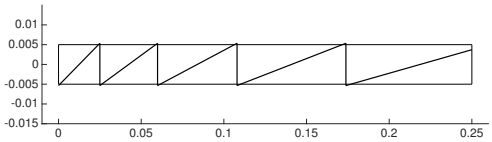

(d) Base 10, -26.4%

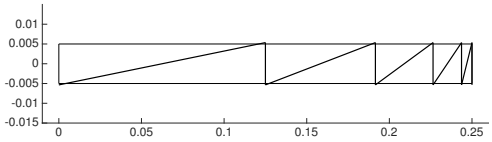

(e) Base 2, 86.7% (Maximum)

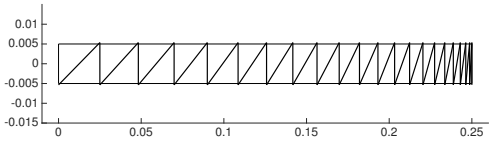

(f) Base 10, 6.5% (Maximum)

Figure 4.14: Schematics of variable wrapping angle cases for the diagonal pattern.

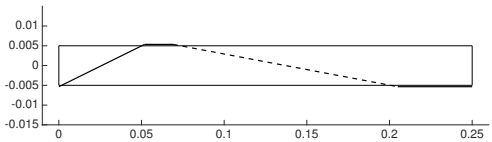

(a) Base 2, -37.9% (Minimum)

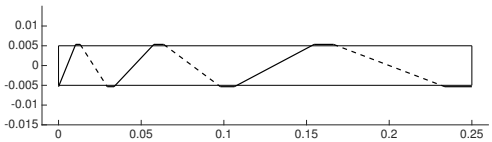

(b) Base 10, -15.0% (Minimum)

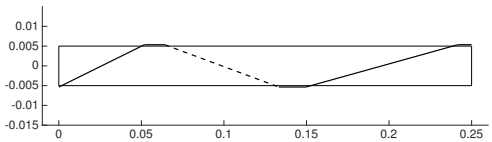

(c) Base 2, -13.2%

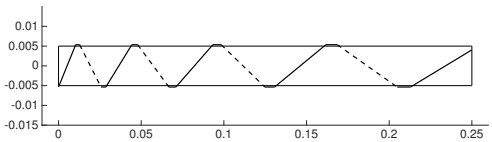

(d) Base 10, -7.1%

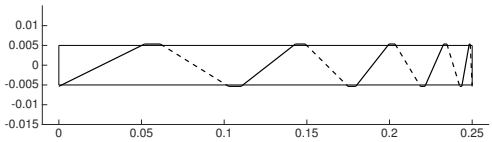

(e) Base 2, 11.6% (Maximum)

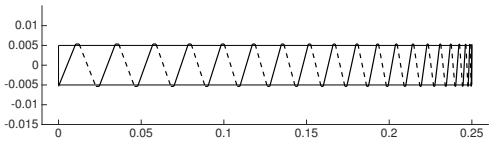

(f) Base 10, 0.9% (Maximum)

Figure 4.15: Schematics of variable wrapping angle cases for the zigzag pattern.

Frequency Response Functions

A first step in determining the accuracy of the perturbation theory model is to compare the frequency response functions (FRFs) to the analytical and FEA solutions, which ever is appropriate based on the wrapping pattern. The cases of the minimum percentage change in the wrapping angle for both Base 2 and Base 10 cases are considered. The FRFs containing the first 10 bending modes for the CC, CF, and FF boundary conditions are presented in Figs. 4.16 and 4.17.

For all of the results in Figs. 4.16 and 4.17, driving point FRFs are presented. For CF and FF boundary conditions, the actuation and sensing location is the free right end. For the CC boundary conditions, the actuation and sensing location is $x = 0.025$ m from the left clamped end. These locations for the driving point FRFs were chosen such that they do not correspond to any node of any mode of interest.

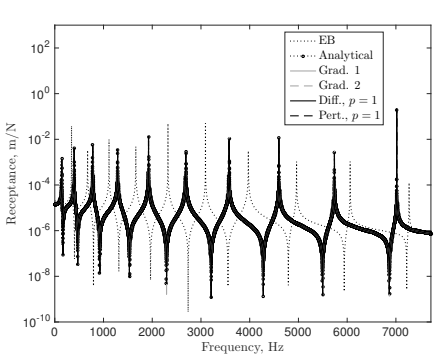

(a) Diagonal, CC

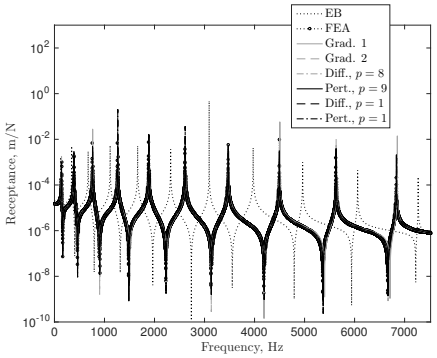

(b) Zigzag, CC

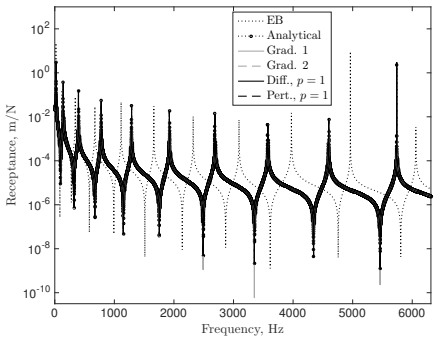

(c) Diagonal, CF

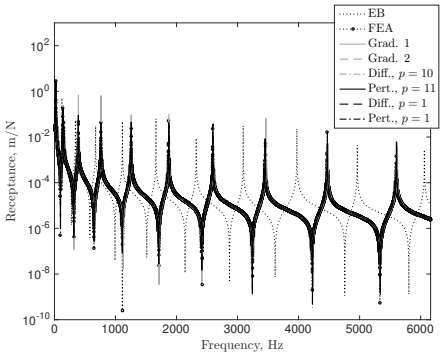

(d) Zigzag, CF

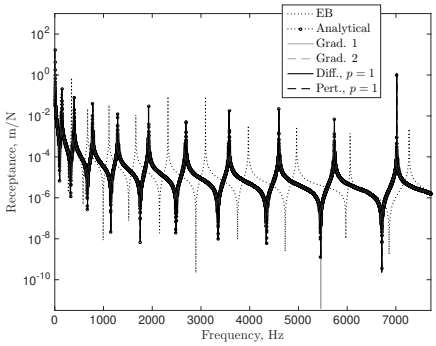

(e) Diagonal, FF

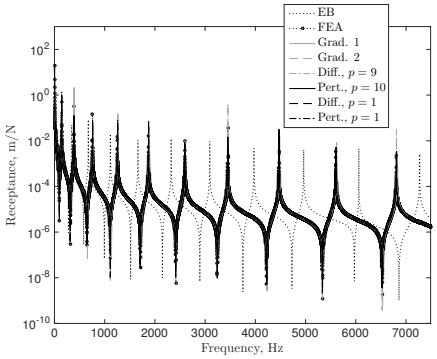

(f) Zigzag, FF

Figure 4.16: FRFs for an unwrapped beam (EB), and string-harnessed beam using perturbation theory and exact solution for variable string wrapping angle with Base 2.

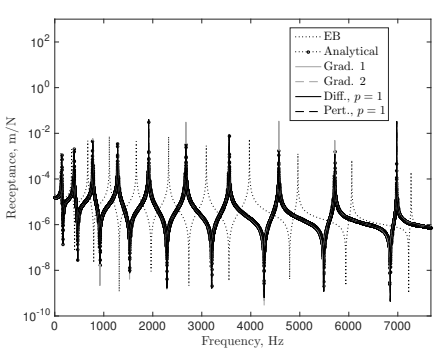

(a) Diagonal, CC

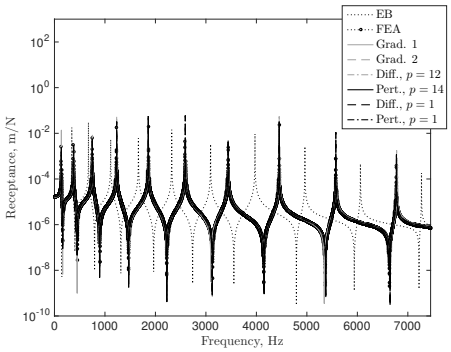

(b) Zigzag, CC

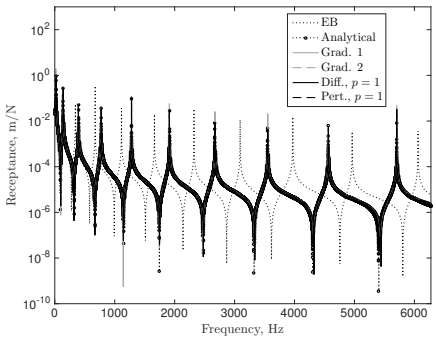

(c) Diagonal, CF

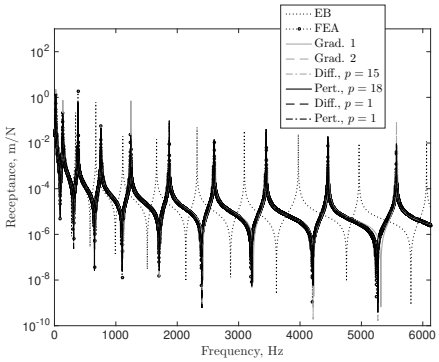

(d) Zigzag, CF

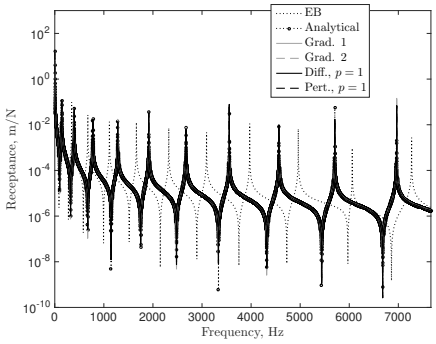

(e) Diagonal, FF

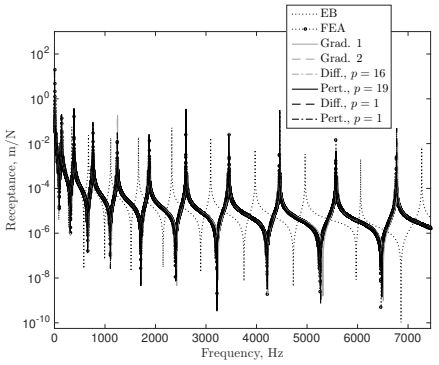

(f) Zigzag, FF

Figure 4.17: FRFs for an unwrapped beam (EB), and string-harnessed beam using perturbation theory and exact solution for variable string wrapping angle with Base 10.

Figures 4.16 and 4.17 clearly demonstrate that the perturbation theory results agree quite strongly with the analytical and FEA results for the diagonal and zigzag wrapping patterns, respectively. The FRFs agree in terms of natural frequencies, location of antiresonance, and amplitude. Furthermore, all the perturbation theory results, regardless of how the reference values were determined or the number of corrections used, agreed very well. For all of the FRFs presented, the largest absolute error in the first 10 natural frequencies for the diagonal wrapping pattern is 0.095% and for the zigzag wrapping pattern is 0.443%. Finally, it is seen in Figs. 4.16 and 4.17 that there is a very obvious shift in the FRFs of the unwrapped system and the string-harnessed system. This highlights the significant impact of a string harness, particularly with respect to the added stiffness to the system.

Fundamental Frequency

Using the perturbation theory, the frequencies of the non-periodic string-harnessed system are found. Of particular interest is the fundamental frequency as it is the most easily excited. The fundamental frequency for both wrapping patterns given Base 2 is presented in Fig.4.16 and given Base 10 in Fig. 4.17. In these figures, the fundamental frequency for variable percentage change in the wrapping angle is considered.

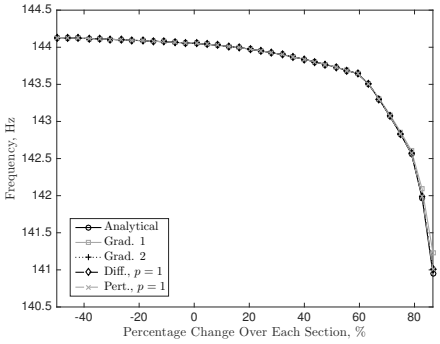

(a) Diagonal, CC

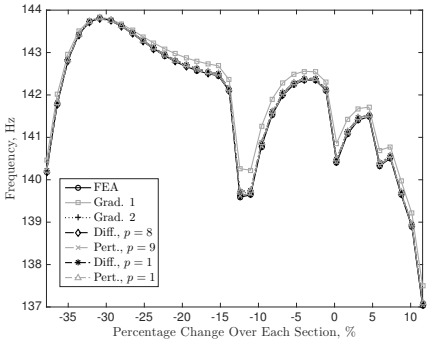

(b) Zigzag, CC

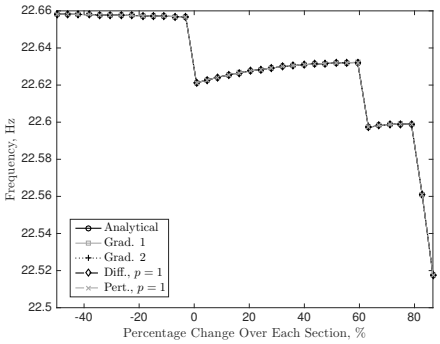

(c) Diagonal, CF

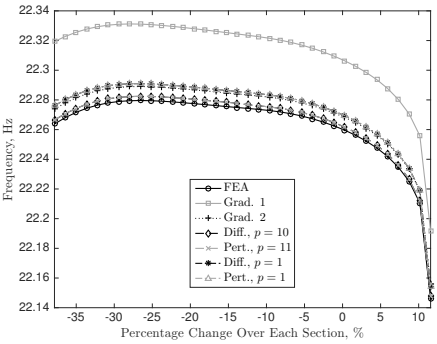

(d) Zigzag, CF

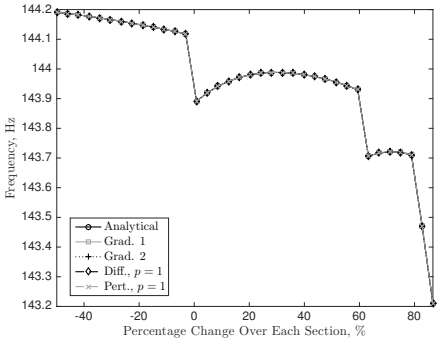

(e) Diagonal, FF

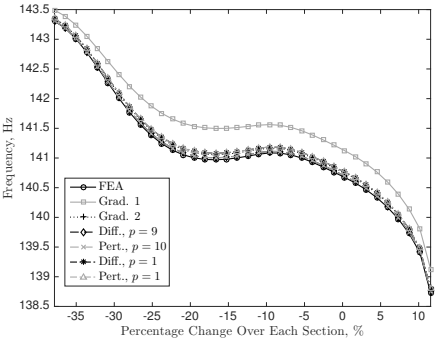

(f) Zigzag, FF

Figure 4.18: Fundamental frequency for variable percentage change in wrapping angle with Base 2.

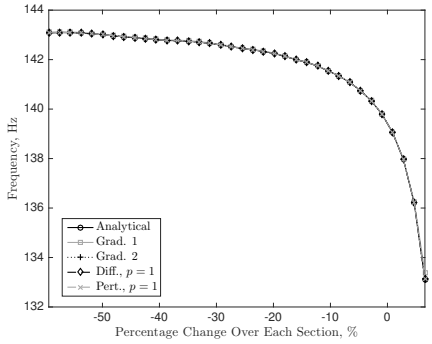

(a) Diagonal, CC

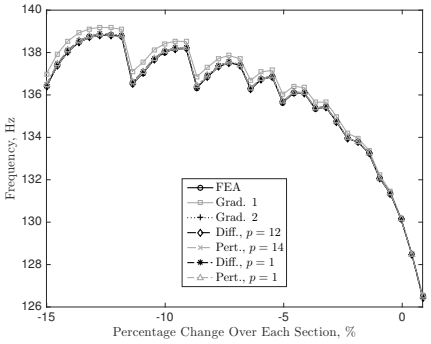

(b) Zigzag, CC

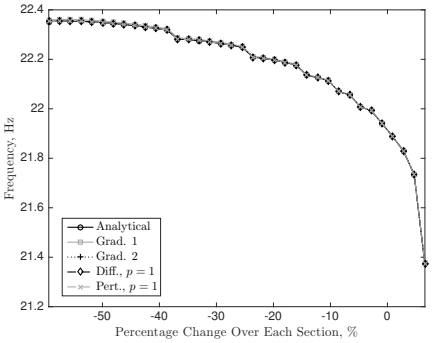

(c) Diagonal, CF

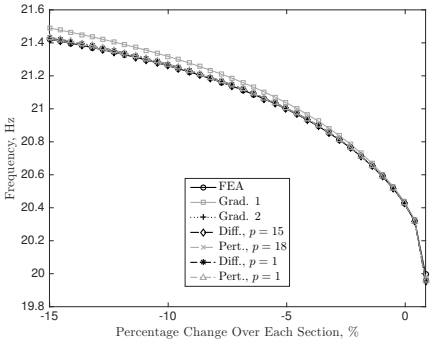

(d) Zigzag, CF

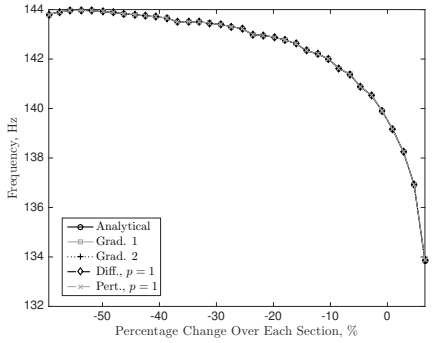

(e) Diagonal, FF

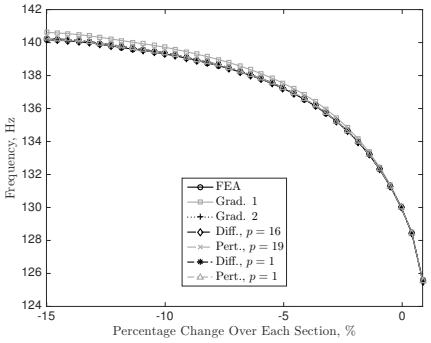

(f) Zigzag, FF

Figure 4.19: Fundamental frequency for variable percentage change in wrapping angle with Base 10.

Figures 4.18 and 4.19 clearly demonstrate a notable impact of the percentage change in the wrapping angle on the value of the fundamental frequency. Quantitatively, the percentage difference between the smallest and largest analytical values of the fundamental frequency for the diagonal pattern with Base 2 is 2.25% for CC, 0.62% for CF, and 0.69% for FF boundary conditions. For the diagonal pattern with Base 10 this percentage difference is 7.49% for CC, 4.60% for CF, and 7.56% for FF boundary conditions. For the zigzag pattern with Base 2 this percentage difference is 4.95% for CC, 0.60% for CF, and 3.30% for FF boundary conditions. For the zigzag pattern with Base 10 this percentage difference is 9.74% for CC, 7.13% for CF, and 11.62% for FF boundary conditions.

The diagonal wrapping pattern results in the figures clearly show that the multiple perturbation theory results all agree very well with the analytical results. The zigzag wrapping pattern results in the figures show that the Grad. 1 perturbation results always overpredict the FEA and the other perturbation theory results are all quite similar to the FEA. This is expected as additional corrections in the perturbation theory leads to more accurate results. Furthermore, for the zigzag wrapping pattern, the norm minimization results with optimal p-value provided the most accurate frequency prediction to the FEA.

The behaviour in Figs. 4.18 and 4.19 for the Base 2 and Base 10 results shows that in both cases there is an overall decrease in the fundamental frequency as the percentage change in the wrapping angle over each section increases. This behaviour is expected since as the string is more tightly wrapped, there is a decrease in the bending stiffness and an increase in the mass per unit length. Comparing the diagonal pattern results for the Base 2 and Base 10, there is a larger overall decrease in the frequencies for the Base 10 case. This occurs since the Base 10 case allows for significantly more lumped masses to be added into the system as the string is more tightly wrapped. The CC boundary conditions results are similar in both the Base 2 and Base 10 cases and in both the CF and FF boundary conditions there are sudden decreases in the value of the frequency. As the system is more tightly wrapped, additional lumped masses are introduced at the right free end for the system causing a sudden increase in the kinetic energy of the system, resulting in a sudden decrease in the frequency.

Comparing the zigzag pattern results for the Base 2 and Base 10, there is a larger overall decrease in the frequencies for the Base 10 case. This occurs since the Base 10 case allows for significantly more total string mass to be added into the system as the string is more tightly wrapped. Furthermore, it is observed that the boundary conditions as well as the initial wrapping angle (Base 2 or Base 10) play a significant role in the behaviour of the fundamental frequency when the percentage change in the wrapping angle is varied. Many different types of behaviours are observed in the results, such as seemingly random results in Fig. 4.18b, sudden decreases in the value of the frequency in Figs. 4.18e and 4.19b, and

smooth results as in Fig. 4.19f. Such variability in the response of the system to variations in the percentage change in the wrapping angle over each section indicates the importance of developing a model for string-harnessed systems and gaining physical intuition.

Physical intuition for the effect of changes in the system parameters on the frequencies begins from the PDE for the free transverse vibrations in Eq. (3.59). Assume a separable solution of the form $w(x,t) = u(x)e^{i\omega t}$ and integrate over the domain of the system. Performing integration by parts, the square of the frequency can be expressed as

$$\omega^2 = \frac{\frac{1}{2}\int_0^l EI(x)\left(\frac{\mathrm{d}^2 u}{\mathrm{d}x^2}\right)^2 \mathrm{d}x}{\frac{1}{2}\int_0^l \left\{\rho A(x) + \sum_{k=0}^{m} M_k \delta(x - x_k)\right\} u^2 \,\mathrm{d}x} \tag{4.19}$$

The numerator of Eq. (4.19) is the strain energy of the system and the denominator is a quantity related to the kinetic energy of the system for a given displacement $u(x)$. Continuing with the analysis of Eq. (4.19), unit normalized mode shapes $u_n(x)$ are employed. Unit normalized mode shapes are used instead of mass normalized mode shapes as the latter would cause the denominator of Eq. (4.19) to be unity due to the mass normalization condition.

The strain energy due to the n^{th} unit normalized mode shape is $\frac{1}{2}\int_0^l EI(x)\left(\frac{\mathrm{d}^2 u_n}{\mathrm{d}x^2}\right)^2 \mathrm{d}x$. If the value of $EI(x)$ is increased by a scalar multiple, then the strain in the system will increase while the kinetic energy related integral is unchanged. This leads to an increase in the frequencies, as expected. Next, consider how the form of $EI(x)$ affects the strain energy in the system. To begin, the second derivative for the unit normalized fundamental mode shape is presented in Fig. 4.20. In Fig. 4.20 the perturbation theory results for the gradient minimization with second-order corrections and Base 2 are used for both the diagonal and zigzag wrapping patterns. A small percentage change in the wrapping angle of 0.8248% and 0.2720% over each section was chosen arbitrarily for the diagonal and zigzag wrapping pattern, respectively.

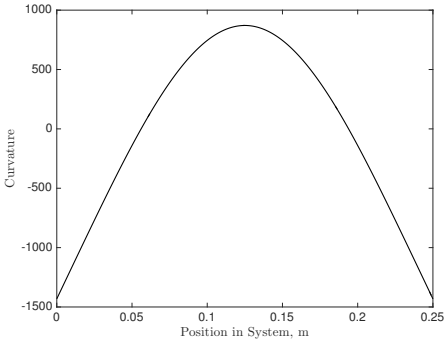

(a) Diagonal, CC

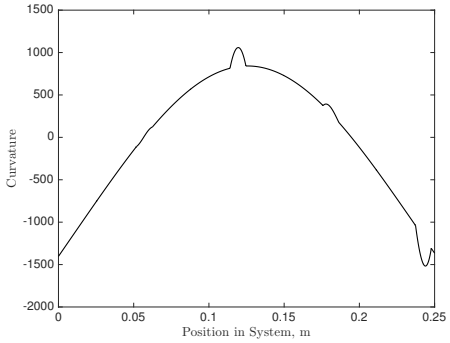

(b) Zigzag, CC

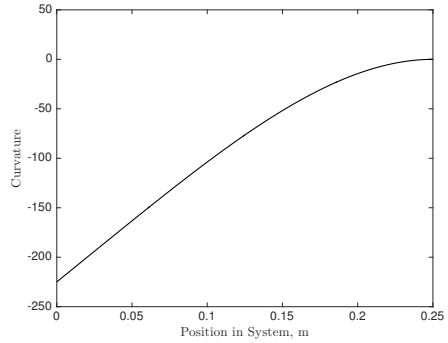

(c) Diagonal, CF

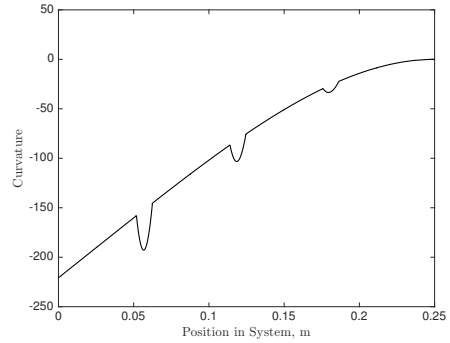

(d) Zigzag, CF

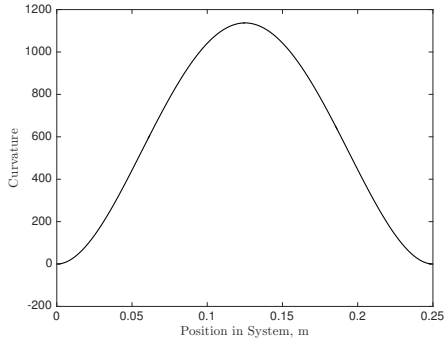

(e) Diagonal, FF

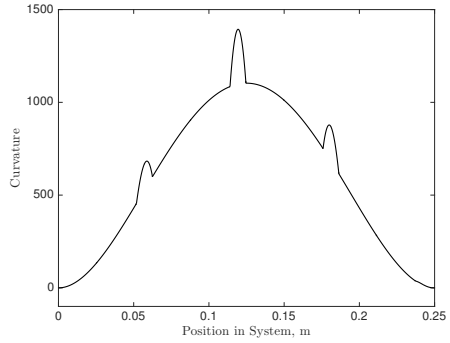

(f) Zigzag, FF

Figure 4.20: Second derivative of unit normalized fundamental mode shape for Base 2 system with small positive percentage change in wrapping angle over each section.

For a string-harnessed system, the bending stiffness is constant when the string is on the top or bottom face of the beam and is parabolic when the string is on the side of the beam. When the string is on the side of the beam, the parabolic shape has positive curvature and minimum value of $E_b I_b - T\frac{I_b}{A_b}$. When the bending stiffness decreases, locally the string-harnessed system is more compliant and thus will exhibit a higher curvature at these locations. These sections of sudden increase in curvature can be seen as additional "peaks" in Fig. 4.20 for the zigzag wrapping pattern. As there are no sections of the string running diagonally on the side of the host structure for the diagonal wrapping pattern, there are no additional "peaks" observed in Fig. 4.20. An alternative method to describe the presence of the peaks is that the moment of the system must be continuous and differentiable, hence locations where the bending stiffness has parabolic decreases it must also be that the magnitude of the curvature has parabolic increases.

Next, consider the integrand of the numerator in Eq. (4.19), namely $EI(x)\left(\frac{\mathrm{d}^2 u_n}{\mathrm{d}x^2}\right)^2$. Using the same unit normalized mode shape as before, the integrand associated with the fundamental mode is presented in Fig. 4.21.

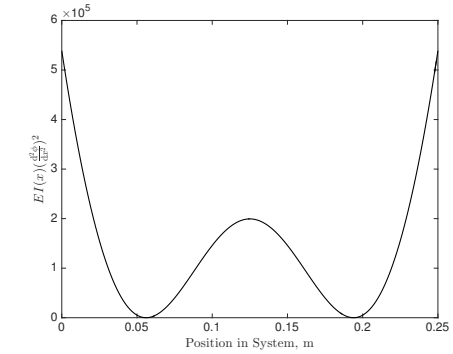

(a) Diagonal, CC

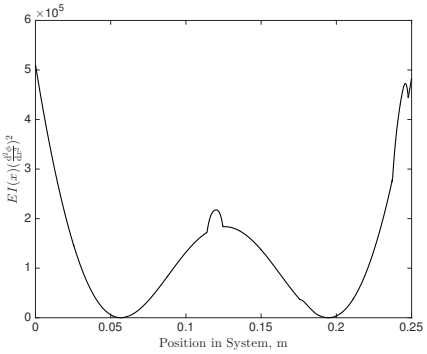

(b) Zigzag, CC

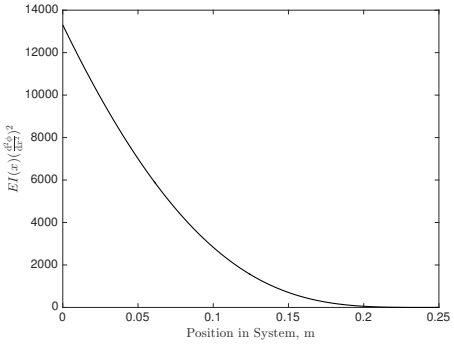

(c) Diagonal, CF

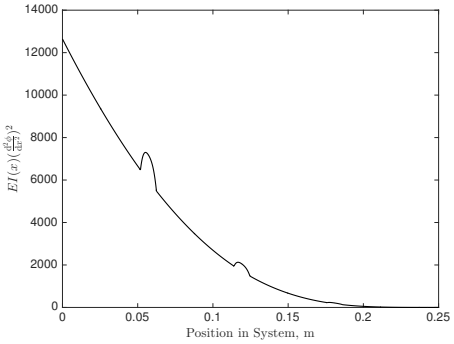

(d) Zigzag, CF

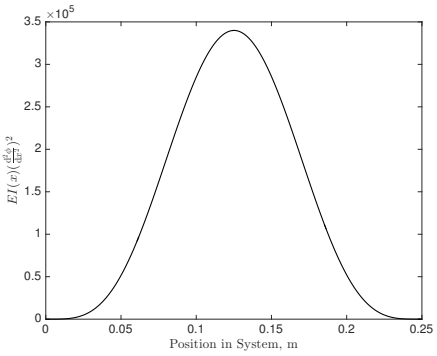

(e) Diagonal, FF

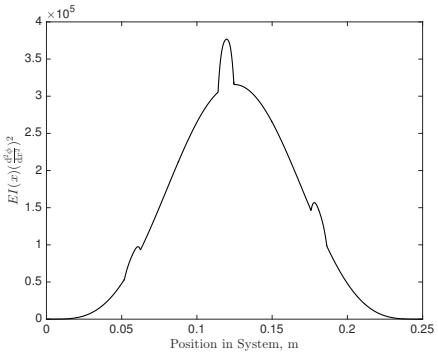

(f) Zigzag, FF

Figure 4.21: Second derivative of unit normalized fundamental mode shape multiplied by $EI(x)$ for Base 2 system with small positive percentage change in wrapping angle over each section.

It is seen in Fig. 4.21 that the overall shape of the integrand is similar between the diagonal and zigzag wrapping patterns. Furthermore, it is seen that the locations of increased curvature in the unit normalized mode shape cause an increase in the value of the integrand over the section of the side string. As expected, since for the diagonal wrapping pattern there are no peaks of increased curvature, there are no peaks in the integrand results. Using this insight, a small variation in the wrapping pattern that moves a section of string on the side of the beam closer to areas of higher curvature will increase the strain energy locally in the system. Additionally, the local strain energy in the system will increase if a small variation in the wrapping pattern introduces a new section of string on the side of the beam at a clamped end, a location which has a high value for the curvature.

The kinetic energy related component in the system for the n^{th} unit normalized mode shape is $\frac{1}{2}\int_0^l \{\rho A(x) + \sum_{k=0}^{m} M_k \delta(x - x_k)\}\, u_n^2 \, \mathrm{d}x$. If the value of $\rho A(x)$ is increased by a scalar multiple, then the kinetic energy related component in the system will increase while the strain energy is unchanged. This leads to a decrease in the frequencies, as expected. Next, consider how the form of $\rho A(x)$ affects the kinetic energy related component of the system. The unit normalized fundamental mode shapes that were considered previously for the strain energy in the system are presented in Fig. 4.22 for both the diagonal and zigzag wrapping patterns.

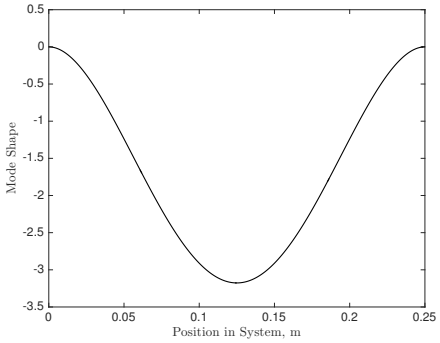

(a) Diagonal, CC

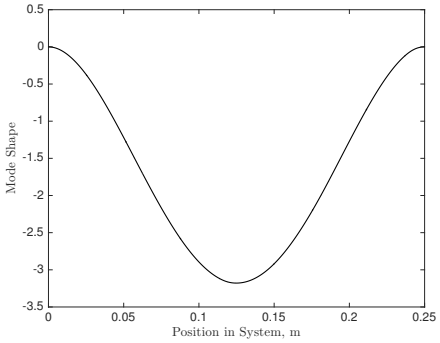

(b) Zigzag, CC

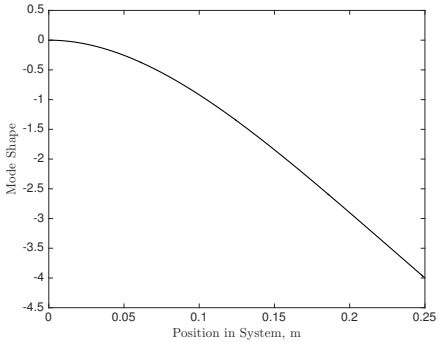

(c) Diagonal, CF

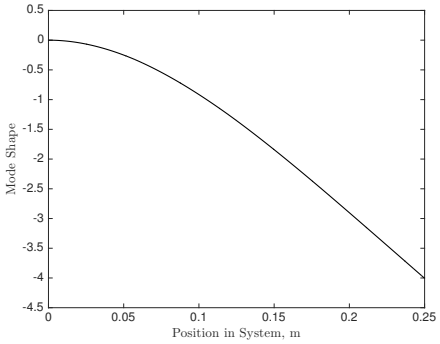

(d) Zigzag, CF

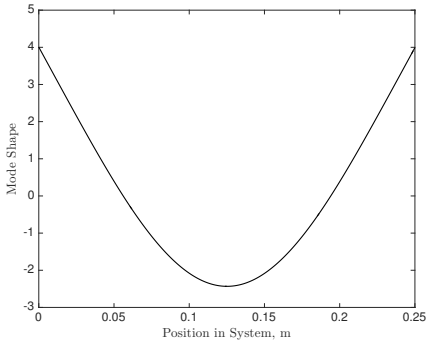

(e) Diagonal, FF

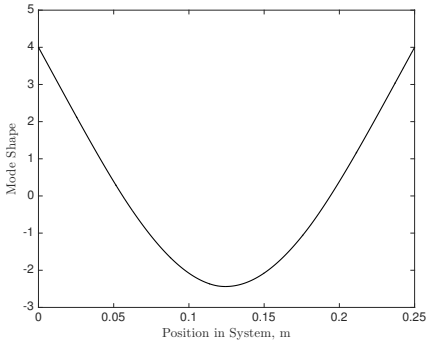

(f) Zigzag, FF

Figure 4.22: Unit normalized fundamental mode shape for Base 2 system with small positive percentage change in wrapping angle over each section.

Figure 4.22 clearly shows that the unit normalized mode shapes for the diagonal and zigzag wrapping patterns are almost identical. Referring back to the expression for the kinetic energy related component, it is clear that small variations in the wrapping pattern that add mass near locations of peaks in the mode shape displacement will increase this quantity. Additionally, the kinetic energy related component of the system will increase if a small variation in the wrapping pattern introduces a lumped mass at a free end, a location which has a large displacement in the mode shape.

Given a variable percentage change in the wrapping angle over each section, Figs. 4.23 and 4.24 present the strain energy and kinetic energy related components for the unit normalized fundamental mode for the diagonal and zigzag wrapping patterns, respectively. The behaviour of each of these components can be used to determine the square of the fundamental frequency, as per Eq. (4.19). For the diagonal wrapping pattern results, a vertical line is included to denote locations at which an additional lumped mass is introduced at the right end of the system. For the zigzag wrapping pattern results, a dotted vertical line is included to denote locations at which a section of string on the side of the beam begins to be added to the system and a dashed vertical line is included to denote locations at which the same section of string on the side of the beam is done being added to the system.

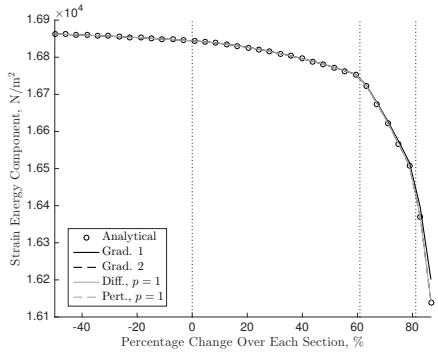

(a) Strain related integral, CC

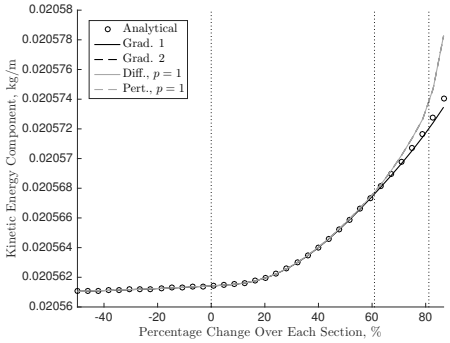

(b) Kinetic related integral, CC

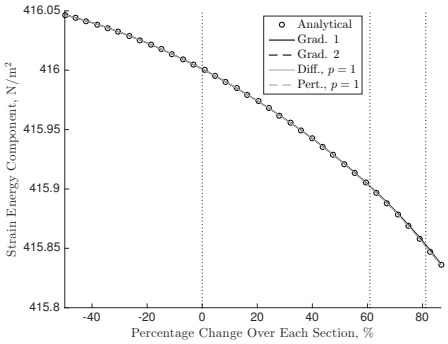

(c) Strain related integral, CF

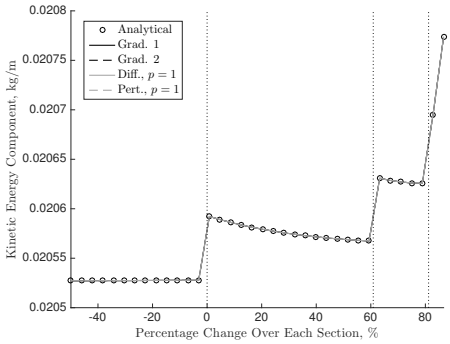

(d) Kinetic related integral, CF

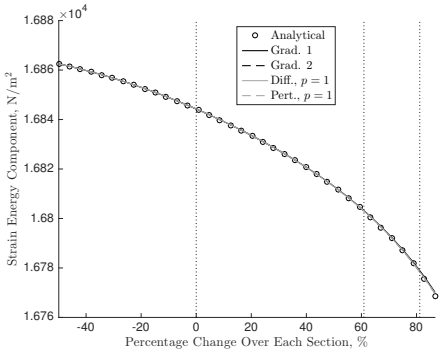

(e) Strain related integral, FF

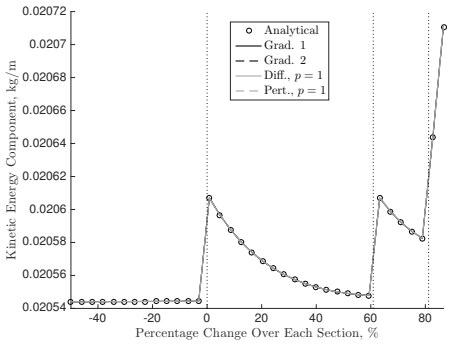

(f) Kinetic related integral, FF

Figure 4.23: Diagonal wrapping pattern strain and kinetic energy related components for unit normalized fundamental mode shape for Base 2 system.

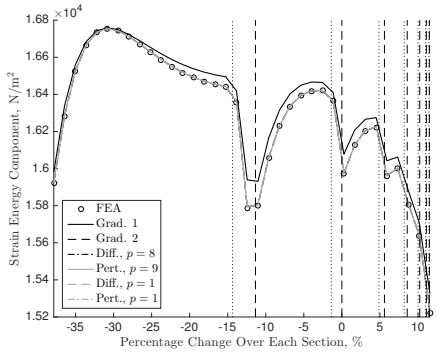

(a) Strain related integral, CC

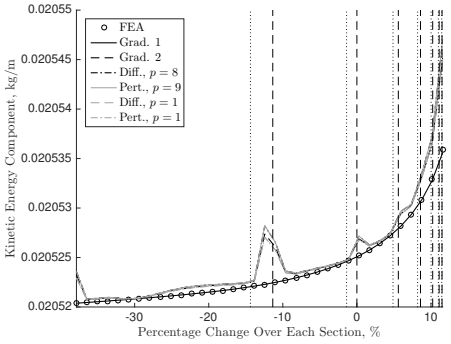

(b) Kinetic related integral, CC

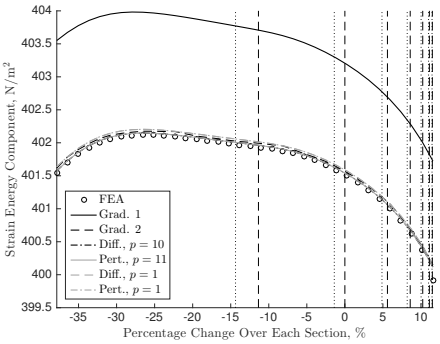

(c) Strain related integral, CF

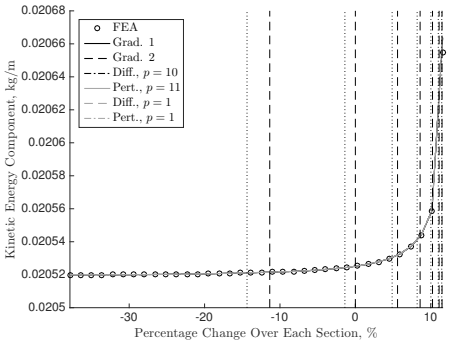

(d) Kinetic related integral, CF

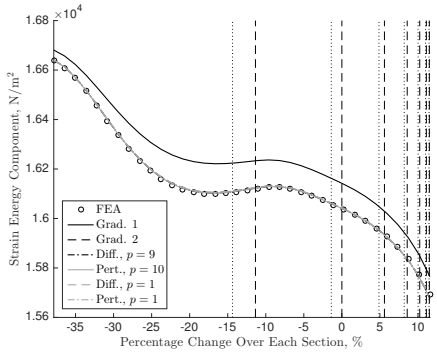

(e) Strain related integral, FF

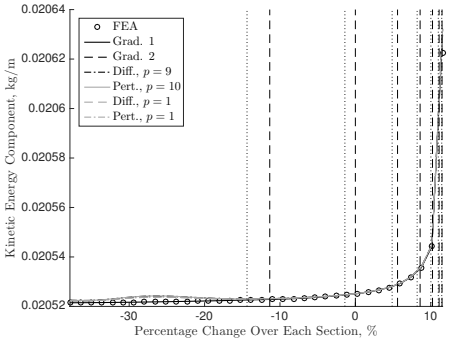

(f) Kinetic related integral, FF

Figure 4.24: Zigzag wrapping pattern strain and kinetic energy related components for unit normalized fundamental mode shape for Base 2 system.

For both the diagonal and zigzag wrapping patterns, the overall effect of increasing the percentage change in the wrapping angle over each section is a decrease in the bending stiffness and increase in the mass per unit length. This directly results in a decrease in the strain energy in the system and an increase in the kinetic energy component of the system. This overall behaviour is clearly observed in Figs. 4.23 and 4.24. In addition, it is seen that the perturbation theory results agree quite well with the analytical and FEA results. In particular, for the zigzag wrapping pattern the perturbation theory results with additional corrections typically provided a better match than the perturbation theory results with a single frequency correction. One exception to this was for the kinetic energy related component given CC boundary conditions, although the variations from the FEA for the higher-order perturbation theory were quite small.

For the diagonal wrapping pattern, when a lumped mass is added at the right end of a CF or FF system, it is expected that there is a sudden increase in the kinetic energy. Indeed this is the observed behaviour near the vertical lines in Figs. 4.23d and 4.23f. For CC boundary conditions, the mode shape has zero displacement at the right end and thus an additional lumped mass does not cause a sudden increase in the kinetic energy. Since there are no sections of string running diagonally on the side of the beam for the diagonal pattern, the strain energy does not experience any sudden changes. This is indeed the case in Fig. 4.23.

For the zigzag pattern, as the percentage change in the wrapping angle is increased there are multiple simultaneous effects. First, there are additional sections of string on the side of the beam being added at the right end of the system that cause an increase in the local strain energy. Second, the wrapping angle is increased and causes a smaller added stiffness from the string. This results in a decrease in the strain energy and is attributed to the local increase in the strain energy of the side section of string causing a decreasing in the overall strain energy for the remainder of the system. Finally, as the percentage change in the wrapping angle is increased there are side sections of string that move from low curvature areas, to higher curvature areas, and back to low curvature areas. This behaviour is clearly observed in Fig. 4.24a to the left of the first vertical line. Overall, these three effects will combine in different manners for the various boundary conditions and this is evidenced by the varying behaviour for the CC, CF, and FF boundary conditions. Since there are no lumped masses added to the system for the zigzag wrapping pattern, it is expected that the kinetic energy does not experience any sudden changes in the value. This is indeed the case in Fig. 4.24.

Error in Predicting Frequencies and Mode Shapes

For the diagonal and zigzag wrapping patterns given Base 2, the error in predicting the fundamental frequency and mass normalized mode shape for variable percentage change in the wrapping angle over each section is presented in Fig. 4.25 and 4.26, respectively. For the diagonal wrapping pattern the error is calculated with respect to the analytical solution and for the zigzag wrapping pattern the error is calculated with respect to the FEA solution.

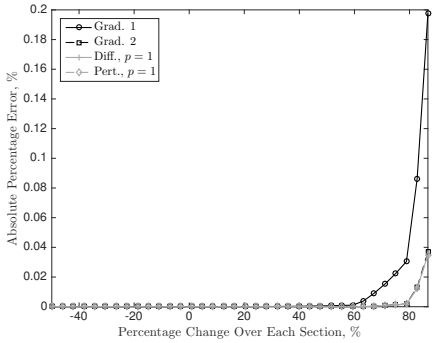

(a) Frequency, CC

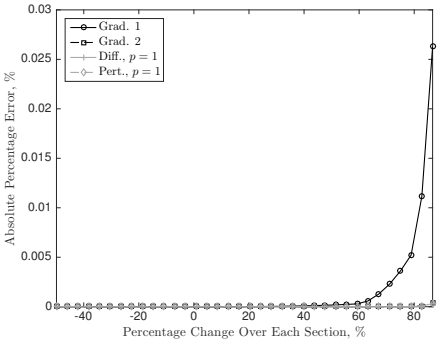

(b) Mode shape, CC

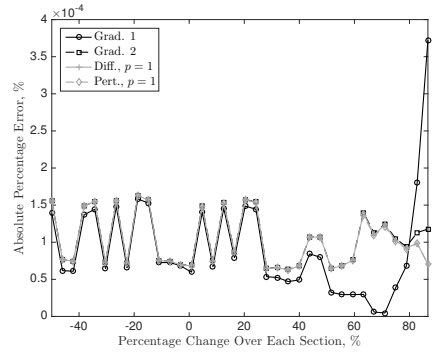

(c) Frequency, CF

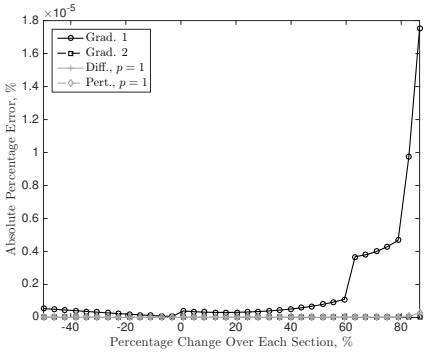

(d) Mode shape, CF

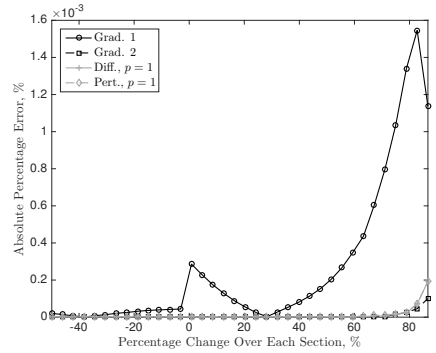

(e) Frequency, FF

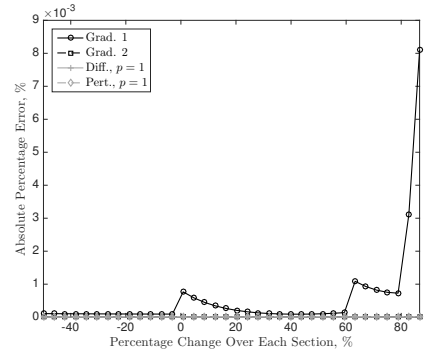

(f) Mode shape, FF

Figure 4.25: Absolute percentage of error in fundamental frequency and mass normalized mode shape given diagonal wrapping pattern with Base 2 for variable percentage change in wrapping angle.

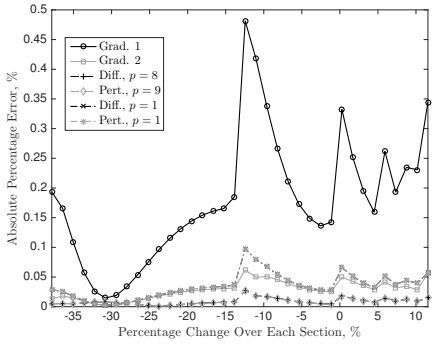

(a) Frequency, CC

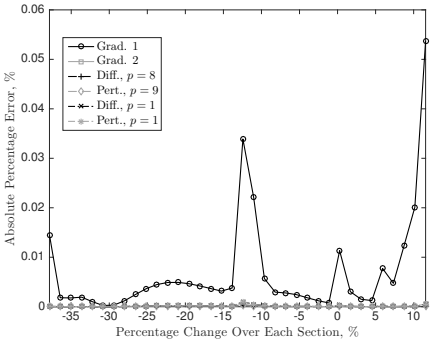

(b) Mode shape, CC

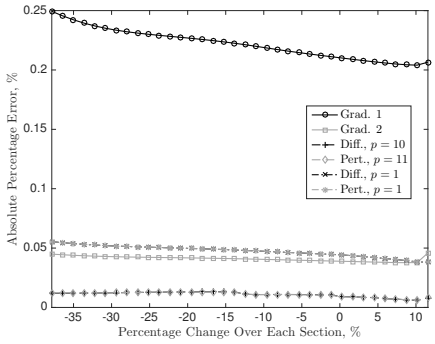

(c) Frequency, CF

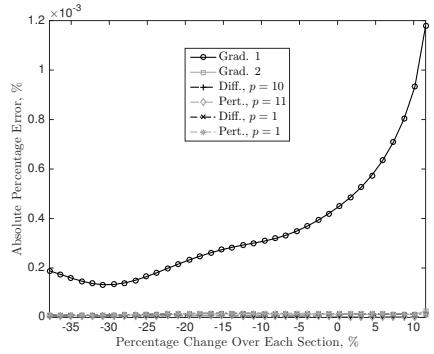

(d) Mode shape, CF

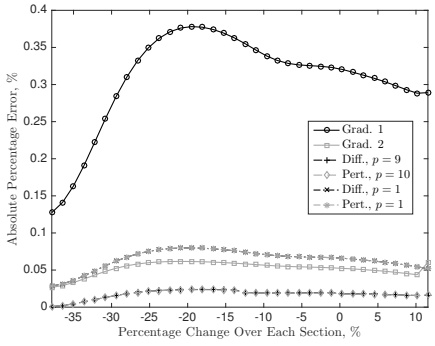

(e) Frequency, FF

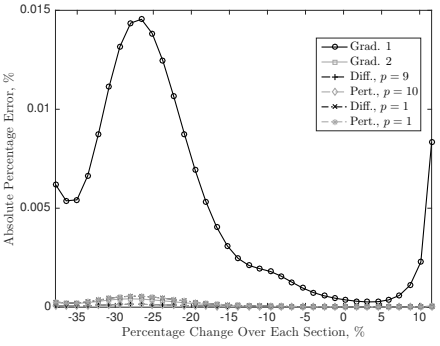

(f) Mode shape, FF

Figure 4.26: Absolute percentage of error in fundamental frequency and mass normalized mode shape given zigzag wrapping pattern with Base 2 for variable percentage change in wrapping angle.

Considering the diagonal wrapping pattern results in Fig. 4.25, it is seen that the error in both the frequency and mode shape increases rapidly as the percentage change in the wrapping angle in the system approaches the maximum possible value. This increasing error is attributed to the additional lumped masses that are introduced into the system as the string is more tightly wrapped. In particular for some of the CF and FF boundary conditions it is seen that there are sudden increases in the errors corresponding to points where lumped masses are added into the system. Overall, the error in predicting the frequency and mode shape is small, less than 0.2%.

Considering the zigzag wrapping pattern results in Fig. 4.26, it is seen that the boundary conditions significantly affected the results for the error. It is observed for the fundamental frequency that sudden increases in the error occur when the frequency suddenly decreases. The behaviour is most noticeable for the CC boundary conditions. It is therefore concluded that the error increases when sections of side string are moved towards or introduced at locations of high curvature. For the CC boundary conditions this increase in errors occurs more frequently since as the string is more tightly wrapped side sections of string are introduced at the clamped end, a location of high curvature. For the CF and FF boundary conditions the right end of the system has zero curvature, therefore side sections of string are not introduced at a location of high curvature and there are no sudden increases. It is clear that the perturbation theory with a single correction to the frequencies produces the largest errors; the norm minimization with optimally determined p-value resulting in the smallest errors. Overall, the absolute error in the frequencies was less than 0.5% and the absolute error in the associated mode shape was quite small, less than 0.06%.

To analyze the error across multiples, the average of the sum of the absolute percentage of error for the first 10 modes is presented in Table 4.6. The results are determined by considering a variable percentage change in the wrapping angle over each section. In this table, it is clearly shown that the perturbation theory with additional corrections produces significantly smaller errors than the perturbation theory with a single correction to the frequencies, as expected.

In terms of producing the smallest average sum of error, the norm minimization of the difference ($p = 1$) proved the best for the diagonal wrapping pattern while the norm minimization of the perturbation with optimal p produced the smallest average sum of error the for the zigzag wrapping pattern. This was observed across all the boundary conditions and for both the frequency and mode shape errors. Assuming for the zigzag wrapping pattern that the frequencies are not known ahead of time, the second-order gradient minimization method resulted in the smallest average sum of absolute error across the boundary conditions considered.

Table 4.6: Natural frequency and mode shape average absolute sum of error for the first 10 modes given variable percentage change in the wrapping angle over each section with Base 2

	Frequency Results			Mode Shape Results		
Result	CC	CF	FF	CC	CF	FF
			Diagonal Pattern ($\times 10^{-3}$)			
Grad. 1	49.595	13.549	16.097	210.108	107.289	147.398
Grad. 2	6.149	0.966	1.056	1.234	0.215	0.305
Diff., $p = 1$	5.740	0.923	1.046	0.985	0.158	0.244
Pert., $p = 1$	5.791	0.940	1.067	0.993	0.160	0.247
			Zigzag Pattern ($\times 10^{0}$)			
Grad. 1	2.188	2.424	2.576	1.495	1.378	1.757
Grad. 2	0.293	0.344	0.347	0.019	0.019	0.024
Diff., p opt.	0.064	0.078	0.092	0.007	0.008	0.010
Pert., p opt.	0.062	0.078	0.092	0.007	0.008	0.010
Diff., $p = 1$	0.391	0.456	0.479	0.028	0.028	0.036
Pert., $p = 1$	0.391	0.456	0.479	0.028	0.028	0.036

Consider next Figs. 4.27 and 4.28, which contain the absolute error in the fundamental frequency and mode shape for variable percentage change in the wrapping angle over each section given Base 10.

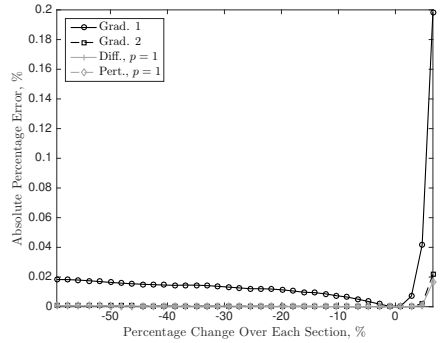

(a) Frequency, CC

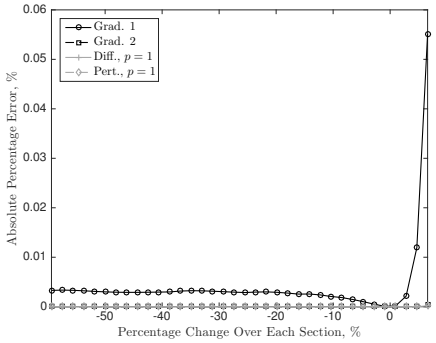

(b) Mode shape, CC

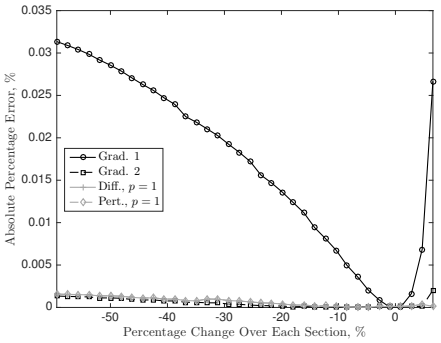

(c) Frequency, CF

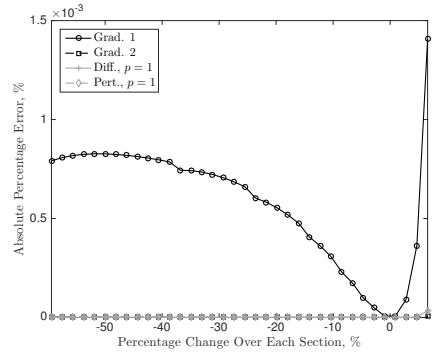

(d) Mode shape, CF

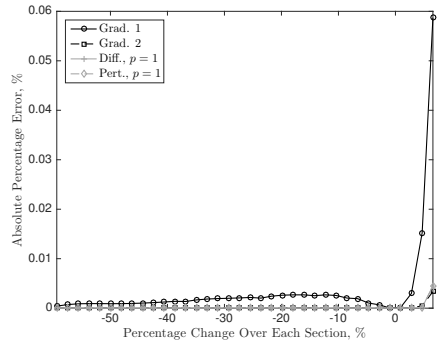

(e) Frequency, FF

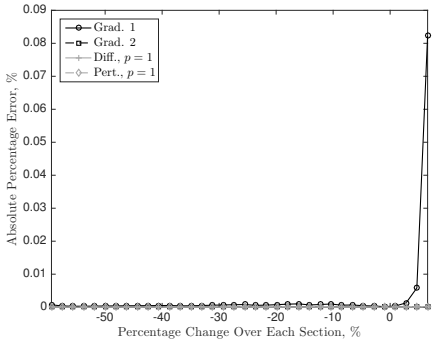

(f) Mode shape, FF

Figure 4.27: Absolute percentage of error in fundamental frequency and mass normalized mode shape given diagonal wrapping pattern with Base 10 for variable percentage change in wrapping angle.

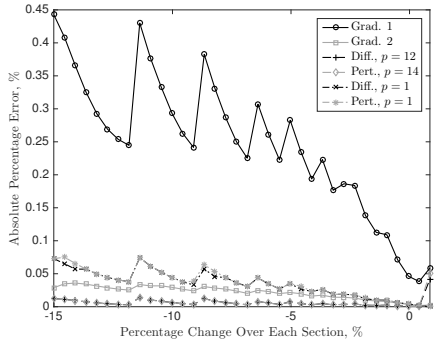

(a) Frequency, CC

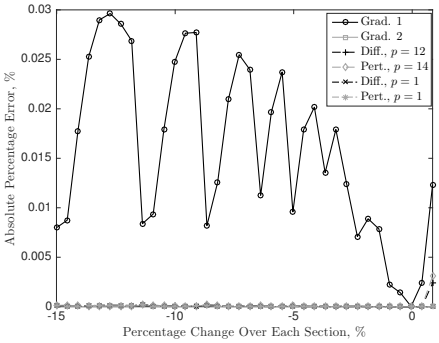

(b) Mode shape, CC

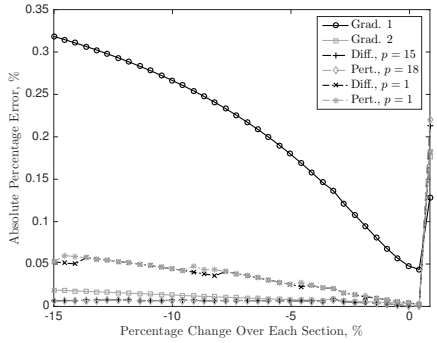

(c) Frequency, CF

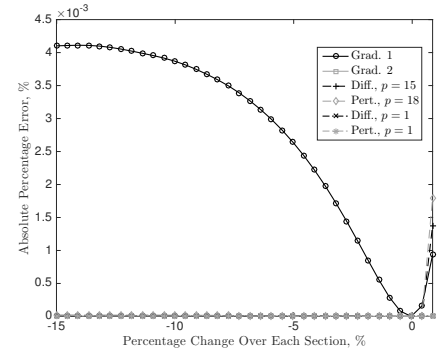

(d) Mode shape, CF

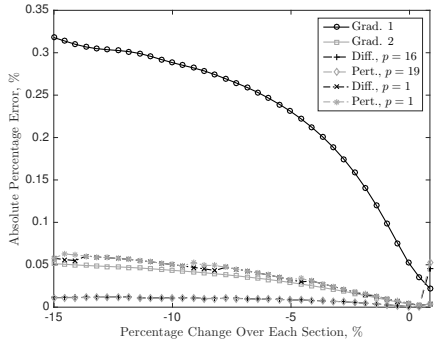

(e) Frequency, FF

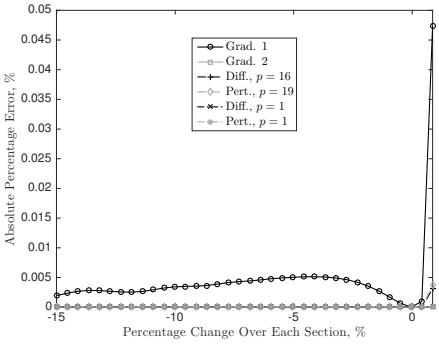

(f) Mode shape, FF

Figure 4.28: Absolute percentage of error in fundamental frequency and mass normalized mode shape given zigzag wrapping pattern with Base 10 for variable percentage change in wrapping angle.

Figure 4.27 demonstrates that for the diagonal pattern the errors decrease as the percentage change in the wrapping angle over each section is increased, up until the system is periodically wrapped. Then, the errors increase as the system becomes more tightly wrapped. For the diagonal wrapping pattern, as the system goes from more loosely wrapped to a periodically wrapped system the bending stiffness and mass per unit length, excluding the lumped masses, become more constant throughout the system. This results in smaller errors in the perturbation theory. As the system becomes more tightly wrapped with a positive percentage change in the wrapping angle over each section the errors increase due to the large amount of lumped masses added into the system. omparing the various results, the perturbation theory with a single correction to the frequencies produced larger errors that the perturbation theory with additional corrections, as expected. In general for all the results presented, the error in predicting the frequency was less than 0.2% and the error in predicting the associated mode shape was quite small, less than 0.09%.

Figure 4.28 demonstrates that the boundary conditions had a significant role in the errors for the zigzag wrapping pattern. Similar to the explanation given when analyzing the Base 2 results, the increases in errors correspond to decreases in the frequency value. In particular for the CC boundary conditions side sections of string are frequently added at a location of high curvature, resulting in multiple sudden decreases in the frequency value. Therefore, multiple instances where the error increases in the perturbation theory results are observed. Across the various presented methods for predicting the frequency and mode shape, the perturbation theory with a single correction to the frequency typically produced the largest absolute error. Overall, the absolute error in the frequency was less than 0.45% and the absolute error in the mode shape is quite small, less than 0.05%.

Table 4.7 presents the average of the sum of the absolute percentage of error for the first 10 modes for variable percentage change in the wrapping angle over each section. The results are determined by considering a variable percentage change in the wrapping angle over each section. These results, as expected, indicate that the perturbation theory with additional corrections provide more accurate results than the first-order perturbation theory, regardless of how the reference values are determined.

The norm minimization of the difference ($p = 1$) produced the smallest average sum of absolute error for both the frequencies and mode shapes for the diagonal wrapping pattern. The norm minimization using the difference with optimal p-value produced the smallest average sum of absolute error for both frequencies and mode shapes for the zigzag wrapping pattern. For each wrapping pattern, the most accurate method was also independent of boundary conditions. If an optimal p-value cannot be determined ahead of time, then for the results presented the second-order gradient minimization method produces the most

accurate results for the zigzag wrapping pattern for both the frequencies and mode shapes, and given any of the boundary conditions.

Table 4.7: Natural frequency and mode shape average absolute sum of error for the first 10 modes given variable percentage change in the wrapping angle over each section with Base 10

	Frequency Results			Mode Shape Results		
Result	CC	CF	FF	CC	CF	FF
			Diagonal Pattern ($\times 10^{-3}$)			
Grad. 1	111.484	108.381	84.094	908.989	731.719	890.520
Grad. 2	9.242	4.663	4.048	5.401	2.782	4.398
Diff., $p = 1$	8.012	4.383	3.668	4.136	2.468	3.991
Pert., $p = 1$	8.022	4.390	3.671	4.140	2.469	3.993
			Zigzag Pattern ($\times 10^{0}$)			
Grad. 1	2.177	2.266	2.247	3.407	2.604	3.100
Grad. 2	0.207	0.216	0.251	0.020	0.016	0.021
Diff., p opt.	0.057	0.065	0.070	0.028	0.024	0.029
Pert., p opt.	0.057	0.065	0.070	0.029	0.024	0.030
Diff., $p = 1$	0.300	0.330	0.331	0.023	0.018	0.023
Pert., $p = 1$	0.310	0.341	0.341	0.023	0.018	0.024

To summarize, from the numerical simulations with variable percentage change in the wrapping angle it is obvious that there is a significant advantage in using the perturbation theory with additional corrections when compared to a single correction for the frequencies. A clear pattern was observed with regards to the perturbation theory reference value selection method that should be employed to obtain the most accurate results. For the diagonal wrapping pattern, the norm minimization using the difference with $p = 1$ always produced the smallest average sum of error for the first 10 modes of the system. It should also be noted that the second-order gradient minimization method for the diagonal wrapping pattern reported errors that were on average 15% larger than the optimal method. For the zigzag wrapping pattern, the norm minimization methods with optimal p value produced similarly accurate results for the average sum of error for the first 10 modes of the system. If it is assumed that the frequencies of the system are not known ahead of time, then an optimal p-value cannot be determined. If this is the case, then it is seen from the presented results that the second-order gradient minimization method would provide the most accurate method for determining the frequencies and mode shapes of the zigzag system.

4.2.3 Non-Periodic Wrapping Pattern: Variable Number of Strings

Description of System

The wrapping patterns used in these numerical simulations come from the previous non-periodic example with variable wrapping angle. From the previous example, the smallest change in the wrapping angle for the Base 10 system is used. This means that the pattern in Fig. 4.14b is used for the diagonal wrapping pattern, and the pattern in Fig. 4.15b is used for the zigzag wrapping pattern. For each of these wrapping patterns, a single string is added to the system with the parameters listed in Section 2.3.7. Then, a second string is added from the left end of the beam up to a given point. This location will be referred to as the switching location as it is the position where the system switches from 2 strings to 1. In the current set of simulations, the switching location is varied.

In addition to varying the switching location, two different sets of string parameters will be considered for the second string that is added to the system. In the first case, a second string with the same parameters as those listed in Section 2.3.7 will be used. This will be referred to as the identical string case. In the second case, a string with a higher modulus, $E_{s2} = 1.875 \times 10^{11}$ N/m^2, and higher density, $\rho_{s2} = 8000$ kg/m^3, compared to the original system parameters are used. This will be referred to as the alternative string case.

Frequency Response Functions

A first step in determining the accuracy of the perturbation theory model is to compare the FRFs to the analytical and FEA solutions, which ever is appropriate based on the wrapping pattern. The case of the second string being present on the left half of the beam, for both an identical and an alternative string added, are considered. The FRFs containing the first 10 bending modes for the CC, CF, and FF boundary conditions are presented in Figs. 4.29 and 4.30. In addition, to highlight the stiffening effect of the string, the FRF for an unwrapped beam is also presented in the figures. The unwrapped beam FRF was determined using an EB model.

For all of the results in Figs. 4.16 and 4.17, driving point FRFs are presented. For CF and FF boundary conditions, the actuation and sensing location is the free right end. For the CC boundary conditions, the actuation and sensing location is $x = 0.025$ m from the left clamped end. These locations for the driving point FRFs were chosen such that they do not correspond to any node of any mode of interest.

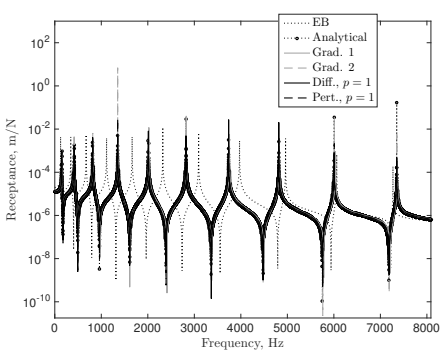

(a) Diagonal, CC

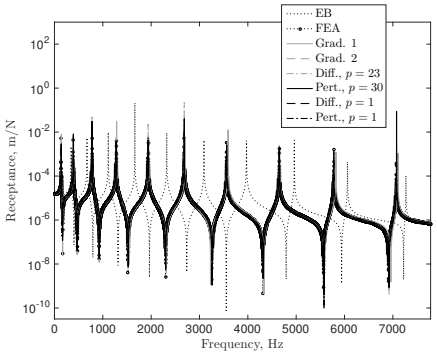

(b) Zigzag, CC

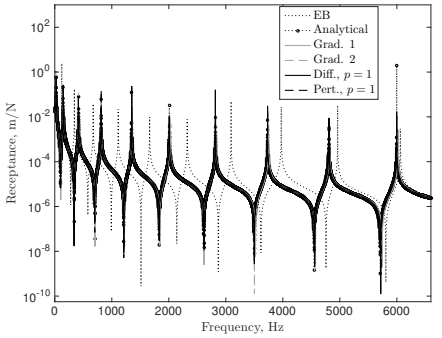

(c) Diagonal, CF

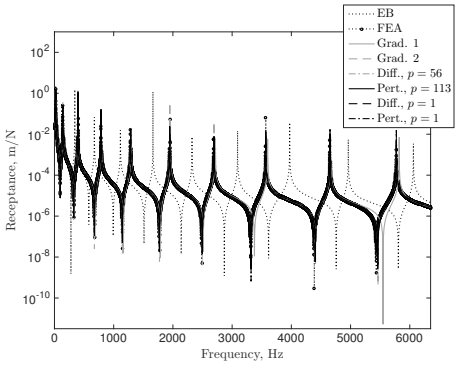

(d) Zigzag, CF

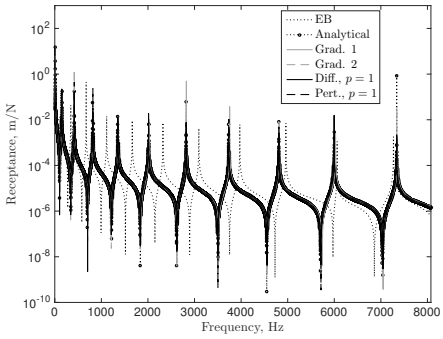

(e) Diagonal, FF

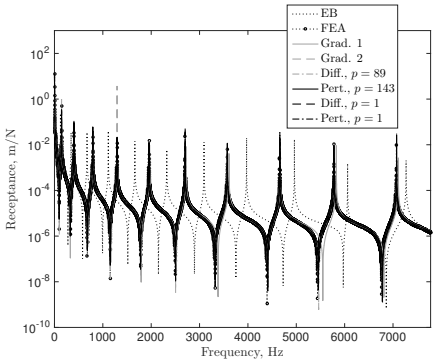

(f) Zigzag, FF

Figure 4.29: FRFs for an unwrapped beam (EB), and string-harnessed beam using perturbation theory and exact solution for identical second string.

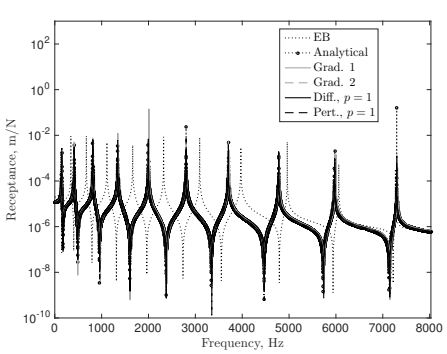

(a) Diagonal, CC

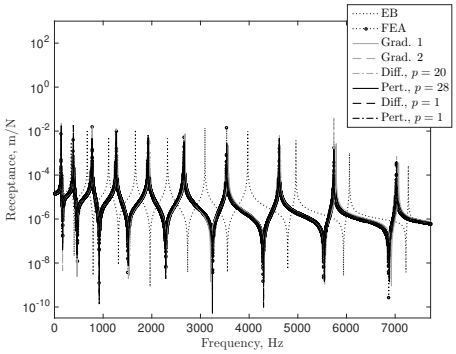

(b) Zigzag, CC

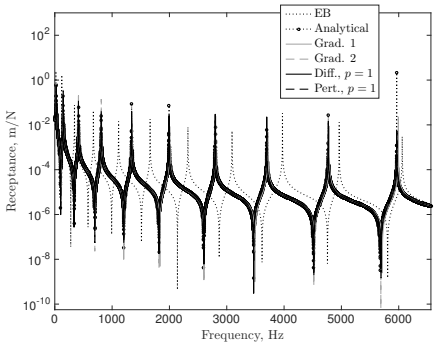

(c) Diagonal, CF

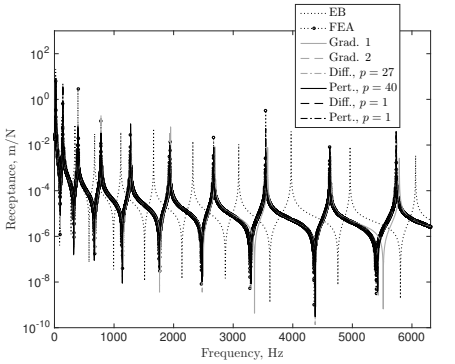

(d) Zigzag, CF

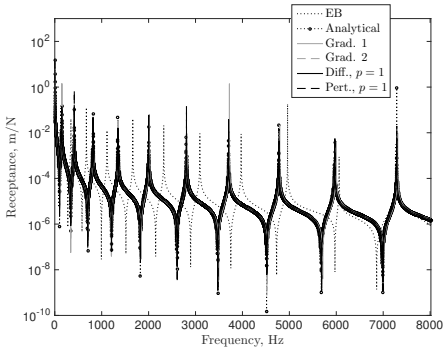

(e) Diagonal, FF

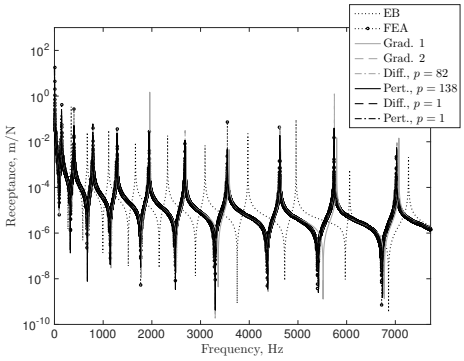

(f) Zigzag, FF

Figure 4.30: FRFs for an unwrapped beam (EB), and string-harnessed beam using perturbation theory and exact solution for alternative second string.

Figures 4.29 and 4.30 clearly demonstrate that the perturbation theory results agree quite strongly with the analytical and FEA results for the diagonal and zigzag wrapping patterns, respectively. The FRFs agree in terms of natural frequencies, location of antiresonance, and amplitude. Furthermore, all the perturbation theory results, regardless of how the reference values were determined or the number of corrections used, agreed very well. For all of the FRFs presented, the largest absolute error in the first 10 natural frequencies for the diagonal wrapping pattern is 0.892% and for the zigzag wrapping pattern is 1.245%. Finally, it is seen in Figs. 4.29 and 4.30 that there is a very obvious shift in the FRFs of the unwrapped system and the string-harnessed system. This highlights the significant impact of a string harness, particularly with respect to the added stiffness to the system.

Fundamental Frequency

The fundamental frequency for variable switching location is presented in Fig. 4.31 for an identical second string and in Fig. 4.32 for an alternative second string. In these figures both wrapping patterns are considered.

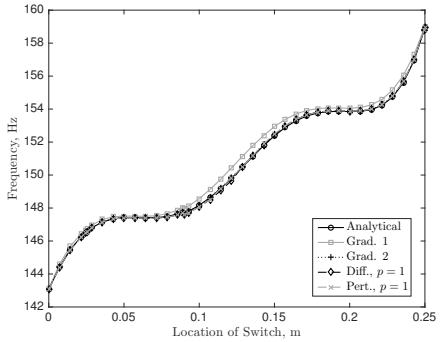

(a) Diagonal, CC

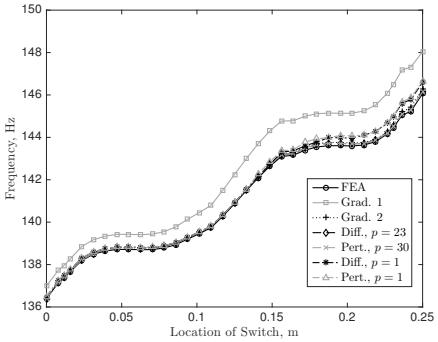

(b) Zigzag, CC

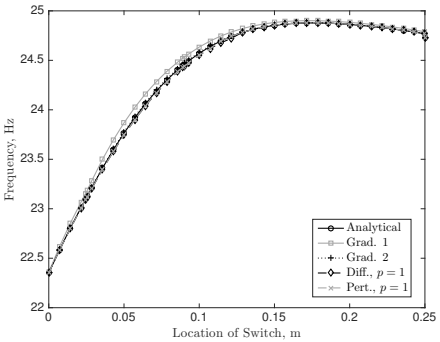

(c) Diagonal, CF

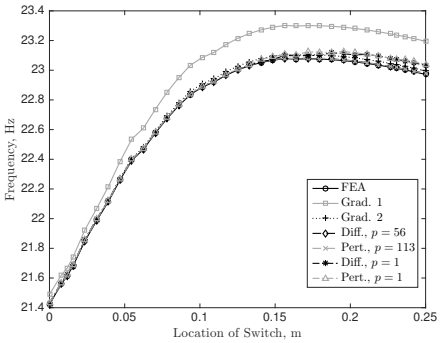

(d) Zigzag, CF

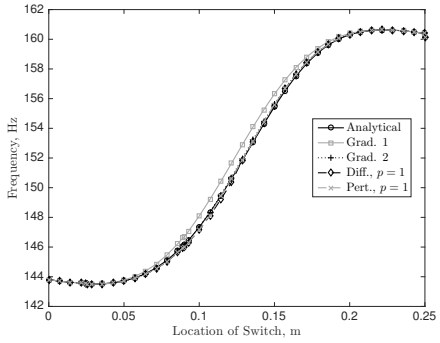

(e) Diagonal, FF

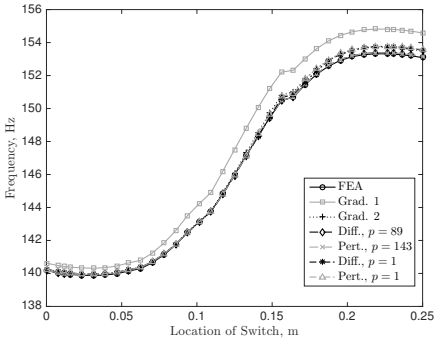

(f) Zigzag, FF

Figure 4.31: Fundamental frequency for variable switching location with identical second string.

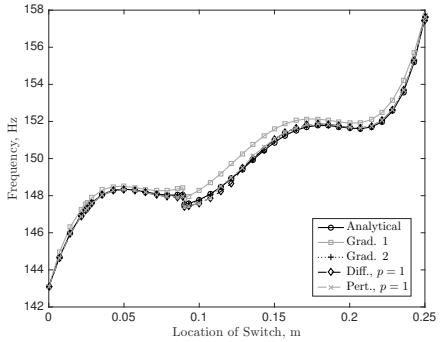

(a) Diagonal, CC

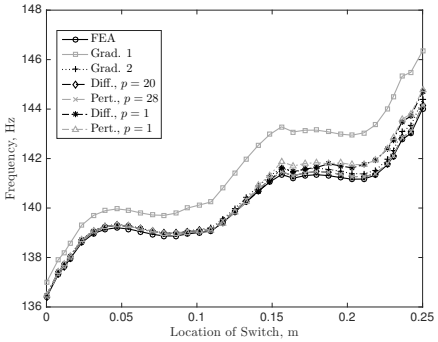

(b) Zigzag, CC

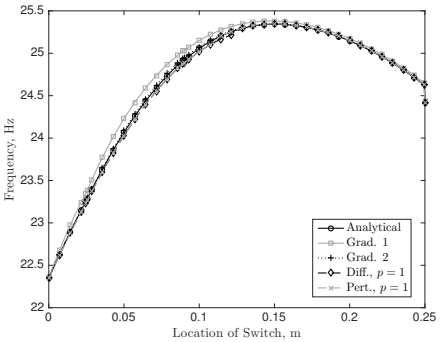

(c) Diagonal, CF

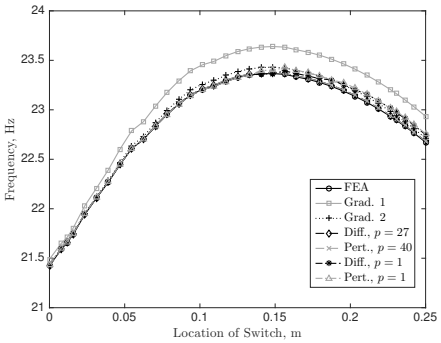

(d) Zigzag, CF

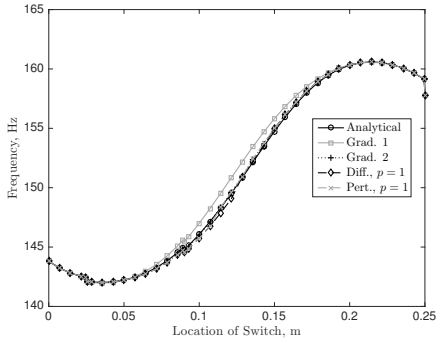

(e) Diagonal, FF

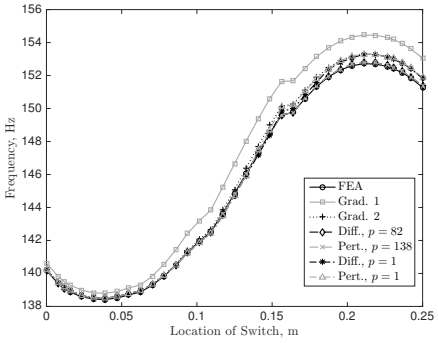

(f) Zigzag, FF

Figure 4.32: Fundamental frequency for variable switching location with alternative second string.

Figures 4.31 and 4.32 clearly show that the switching location from 2 strings to 1 plays an important role in the value of the fundamental frequency. In addition, the parameters of the second string as well as the boundary conditions are shown to play a role in the results for the fundamental frequency. Quantitatively, the percentage difference between the smallest and largest analytical values of the fundamental frequency for the diagonal pattern with identical second string is 11.09% for CC, 11.30% for CF, and 11.94% for FF boundary conditions. For the diagonal pattern with alternative string this percentage difference is 10.16% for CC, 13.38% for CF, and 13.07% for FF boundary conditions. For the zigzag pattern with identical second string this percentage difference is 7.09% for CC, 7.73% for CF, and 9.61% for FF boundary conditions. For the zigzag pattern with alternative string this percentage difference is 5.60% for CC, 9.08% for CF, and 10.33% for FF boundary conditions. These large differences between the maximum and minimum values highlight the importance of developing a model for non-periodically wrapped string-harnessed systems.

Considering the diagonal wrapping pattern results, the various perturbation theory results all match quite well with the analytical results with the exception of the Grad. 1 results, which typically overpredicts compared to the analytical results. This is expected as including additional corrections in the frequencies and mode shapes will result in more accurate predictions. In the zigzag wrapping pattern results it is also seen that the Grad. 1 results overpredict the exact results. Additionally, it is seen that the norm minimization methods with optimally determined p-value provide the most accurate results. This is particularly noticeable as the switching location becomes nearer to the right end of the system.

Overall, it is seen that the effect of adding a second string for the parameters considered is an overall increase in the fundamental frequency of the system. This indicates that the added stiffening effect of the second string is greater than the added mass. Furthermore, the pattern of the fundamental frequency observed for a given set of boundary conditions are similar between the cases of identical and alternative second string being added to the system. The results in Figs. 4.31 and 4.32 demonstrate that the overall increase in the frequency is smaller for the alternative string than for the identical string. Hence, the increased density of the alternative string has a larger effect than the increased modulus. Finally, although the overall change in the frequency is larger for the identical string, it occurs for certain switching locations that the frequency value of the system with the alternative string is larger than the frequency of the system with the identical string. This indicates that the boundary conditions and the location of the switch will play an important role in determining if the added mass or added stiffness will be the dominant effect.

Using the physical intuition developed from the previous numerical results section on

variable wrapping angle, the behaviours in Figs. 4.31 and 4.32 are interpreted. First consider CC boundary conditions, which result in a fundamental mode shape with maximum displacement at the centre of the system and larger curvature at the clamped ends and at the centre of the system. In Figs. 4.31a, 4.31b, 4.32a, and 4.32b it is seen that there is a rapid increase in the CC fundamental frequency when the switching location is near the location of increased curvature as these locations will add more stiffness in the system than mass. At locations where the curvature of the system is relatively small, the effect of added mass will be more observable and this results in very little change to the fundamental frequency.

For a system with CF boundary conditions, the fundamental mode shape has the largest displacement at the free end of the system, along with zero curvature at this location. The maximum curvature value is at the clamped end, along with zero displacement at this location. This means that it is expected that when the switching location is near the clamped end that the effect of added stiffness will be much larger than the added mass, resulting in an increase in the frequency. Additionally, it is expected that when the switching location is near the free end that the added mass mass will have a larger influence than the added stiffness on the frequency. This behaviour is clearly seen in Figs. 4.31c, 4.31d, 4.32c, and 4.32d. Comparing the results of an identical and the alternative string added to the system, it is seen that the increase in the fundamental frequency from the initial value to the maximum is larger for the alternative string since this has a larger modulus. Also, the value for the frequency when both strings are present over the entire system is lower for the case of alternative string since this has a larger density than the original string.

Lastly, FF boundary conditions produce a fundamental frequency with larger displacement at the free ends and at the centre of the system, and the maximum curvature is located at the centre of the system. Further, the curvature of the system is 0 at the free ends. From a physical point of view, it is therefore expected that the added mass effect will be more dominant than the added stiffness effect at the free ends of the system while the opposite is true at the centre of the system where the largest curvature is experienced. Figures 4.31c, 4.31d, 4.32c, and 4.32d demonstrate that the fundamental frequency decreases, to varying degrees, when the switching location is near the end points of the system and increases significantly when the switching location is near the centre of the system. This behaviour corresponds exactly to what is expected form the physical point of view. Finally, the larger density of the alternative second string compared to the original string results in a greater rate at which the frequency decreases when the switching location is near a free end.

Error in Predicting Frequencies and Mode Shapes

For the diagonal and zigzag wrapping patterns given an identical second string added to the system, the error in predicting the fundamental frequency and mass normalized mode shape for variable switching location is presented in Fig. 4.33 and 4.34, respectively. For the diagonal wrapping pattern the error is calculated with respect to the analytical solution and for the zigzag wrapping pattern the error is calculated with respect to the FEA solution.

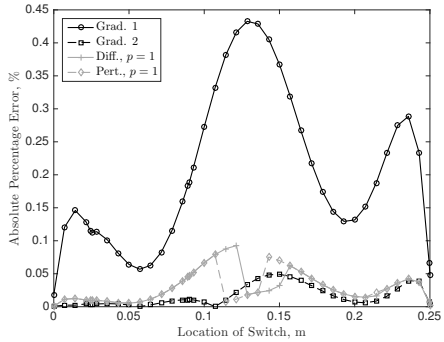

(a) Frequency, CC

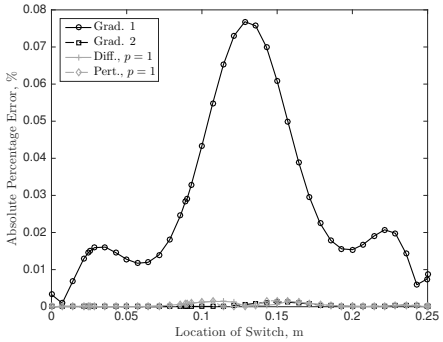

(b) Mode shape, CC

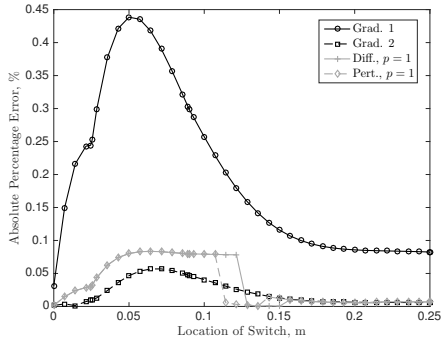

(c) Frequency, CF

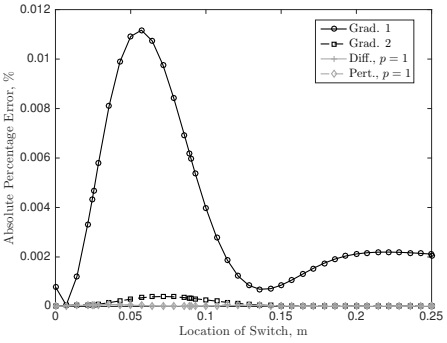

(d) Mode shape, CF

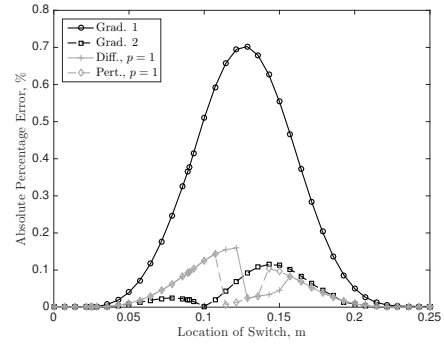

(e) Frequency, FF

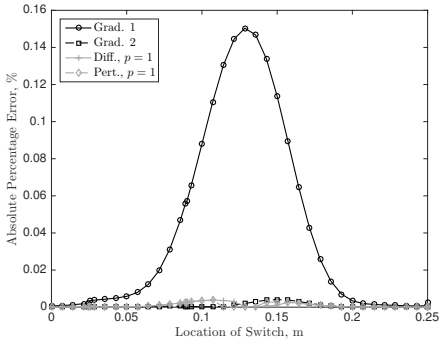

(f) Mode shape, FF

Figure 4.33: Absolute percentage of error in fundamental frequency and mass normalized mode shape given diagonal wrapping pattern with identical second string for variable switching location.

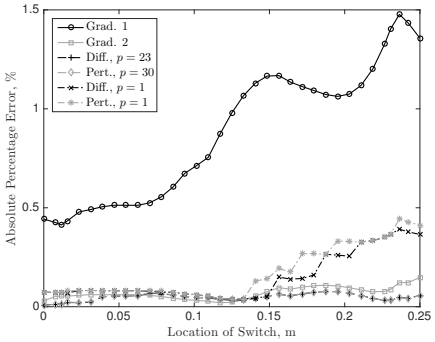

(a) Frequency, CC

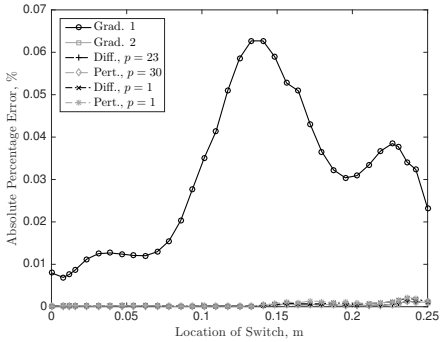

(b) Mode shape, CC

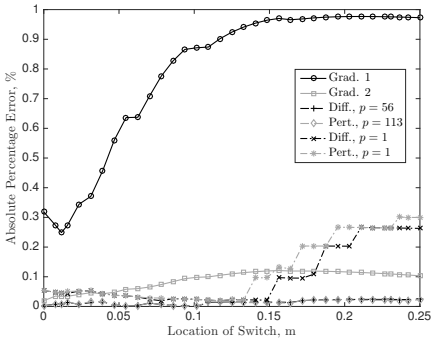

(c) Frequency, CF

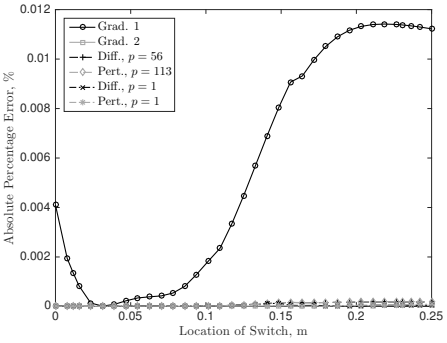

(d) Mode shape, CF

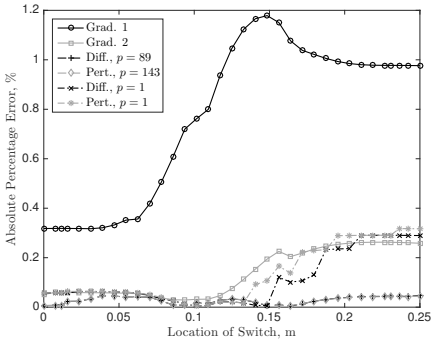

(e) Frequency, FF

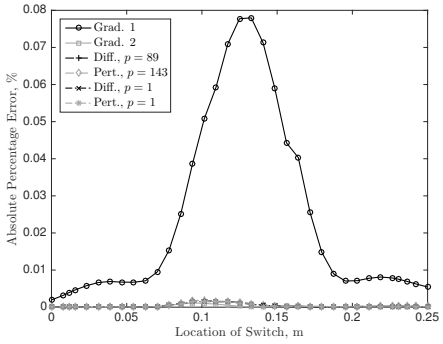

(f) Mode shape, FF

Figure 4.34: Absolute percentage of error in fundamental frequency and mass normalized mode shape given zigzag wrapping pattern with identical second string for variable switching location.

Considering the diagonal wrapping pattern results in Fig. 4.33, it is seen that the error in both the frequency and mode shape attains the maximum near a switching location of $x = l/2$ for CC and FF boundary conditions. For CF boundary conditions the maximum errors for the frequency and mode shape was observed near a switching location of $x = l/4$. It is therefore concluded that the diagonal wrapping pattern exhibits higher errors when the switching location is near an area of high curvature. Furthermore, it is seen in Fig. 4.33 that the norm minimization methods exhibit a sudden decrease in the error when the switching location is near areas of large displacement. This behaviour is not observed for the gradient minimization method and the smoothly varying errors of this method are seen as a benefit for using the gradient minimization. For the various perturbation theory results presented, the perturbation theory with additional corrections always produced smaller errors when compared to the perturbation theory with a single correction to the frequencies. Overall, the error in predicting the frequency was less than 0.8% and the error in predicting the associated mode shape was less than 0.16%.

In Fig. 4.34 it is clearly seen that perturbation theory results with additional corrections resulted in smaller errors than for the Grad. 1 method. Additionally, for all the perturbation theory results presented, the errors in the frequencies experience an overall increase as the switching location increases. As the second string is added into the system, the perturbations in the mass per unit length and bending stiffness become increasing larger, resulting in larger errors. As with the diagonal wrapping pattern, it is seen for the zigzag wrapping pattern the norm minimization results experience sudden jumps in the errors reported for the frequencies. Such a behaviour is not present in the Grad. 2 method results and the smooth errors are considered an advantage of this method over the norm minimization methods. Additionally, when comparing the behaviour of the errors to the behaviour of the frequencies for variable switching location, it is seen that typically the errors increase at the same time that the frequency in the system increases. Since the fundamental frequency of the system increases most rapidly when the switching location is near areas of high curvature, it can be concluded that when the switching location is near an area of high curvature that the errors in predicting the frequency will increase. Finally, It is clear that the norm minimization with optimally determined p-value resulted in the smallest errors. Overall, the absolute error in the frequencies was less than 1.5% and the absolute error in the associated mode shape was very small, less than 0.08%.

To analyze the error across multiple modes, the average of the sum of the absolute percentage of error for the first 10 modes is presented in Table 4.8. The results are determined by considering a variable switching location from 2 strings to 1 string. In this table, it is clearly shown that the perturbation theory with additional corrections produces significantly smaller errors than the perturbation theory with a single correction to the

frequencies, as expected.

In terms of producing the smallest average sum of error, the second-order gradient minimization method proved the best for the diagonal wrapping pattern while the norm minimization using the difference with optimal p produced the smallest average sum of error the for the zigzag wrapping pattern. This was observed across all the boundary conditions and for both the frequency and mode shape errors. Assuming for the zigzag wrapping pattern that the frequencies are not known ahead of time, the second-order gradient minimization method typically resulted in the smallest average sum of absolute error across the boundary conditions considered. The exception was for FF boundary conditions where the norm minimization using the difference with $p = 1$ provided slightly more accurate estimates for the frequencies.

Table 4.8: Natural frequency and mode shape average absolute sum of error for the first 10 modes given variable switching location with identical second string

	Frequency Results			Mode Shape Results		
Result	CC	CF	FF	CC	CF	FF
			Diagonal Pattern ($\times 10^0$)			
Grad. 1	2.181	2.164	2.295	8.236	7.084	10.033
Grad. 2	0.222	0.232	0.263	0.146	0.117	0.184
Diff., $p = 1$	0.336	0.336	0.367	0.217	0.165	0.254
Pert., $p = 1$	0.327	0.322	0.354	0.211	0.160	0.247
			Zigzag Pattern ($\times 10^0$)			
Grad. 1	6.240	6.056	6.111	4.663	3.627	5.014
Grad. 2	0.643	0.789	0.925	0.098	0.089	0.125
Diff., p opt.	0.233	0.188	0.221	0.121	0.103	0.144
Pert., p opt.	0.237	0.189	0.222	0.120	0.104	0.145
Diff., $p = 1$	0.857	0.820	0.857	0.122	0.104	0.150
Pert., $p = 1$	1.017	0.979	1.011	0.124	0.108	0.155

Consider next Figs. 4.35 and 4.36, which contain the absolute error in the fundamental frequency and mode shape for variable switching location given the alternative second string parameters. Recall that the alternative string has a higher modulus and higher density than the original string parameters.

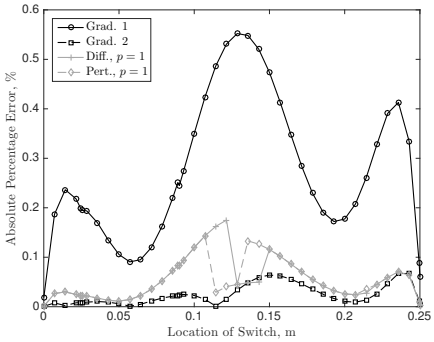

(a) Frequency, CC

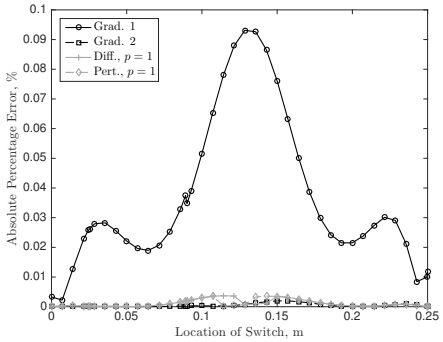

(b) Mode shape, CC

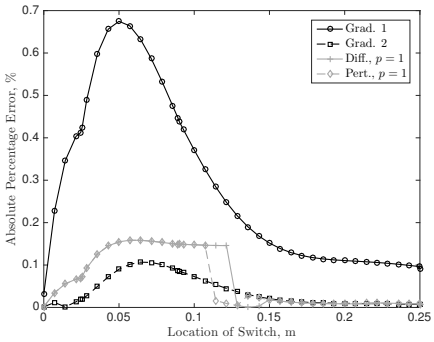

(c) Frequency, CF

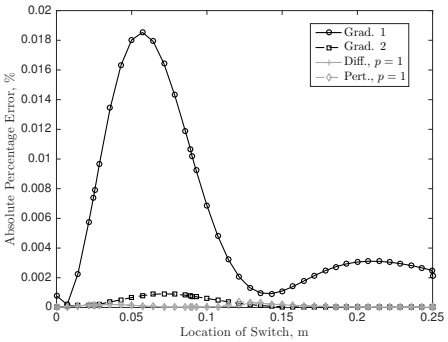

(d) Mode shape, CF

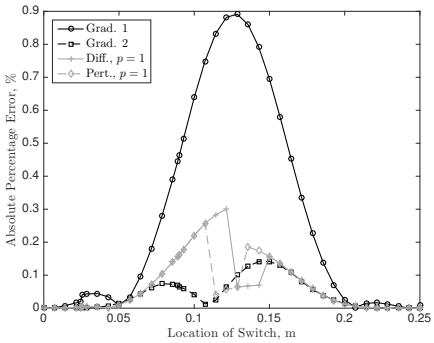

(e) Frequency, FF

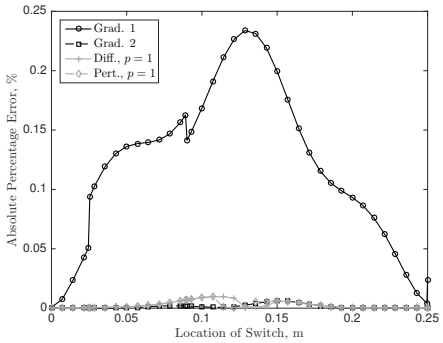

(f) Mode shape, FF

Figure 4.35: Absolute percentage of error in fundamental frequency and mass normalized mode shape given diagonal wrapping pattern with alternative second string for variable switching location.

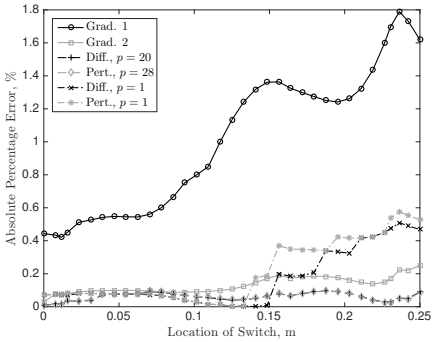

(a) Frequency, CC

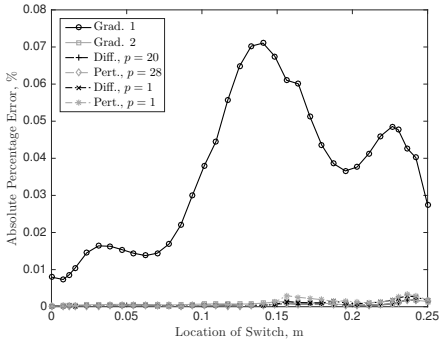

(b) Mode shape, CC

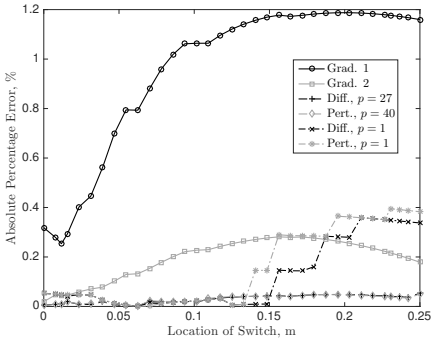

(c) Frequency, CF

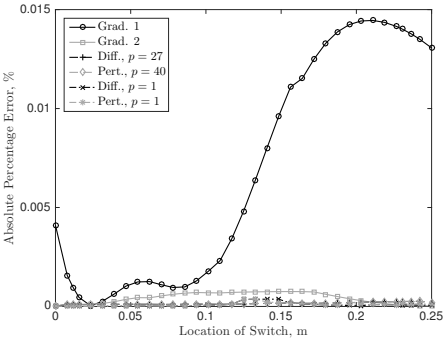

(d) Mode shape, CF

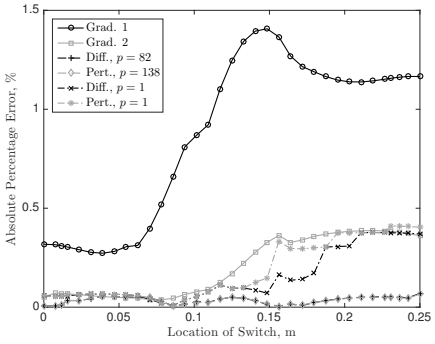

(e) Frequency, FF

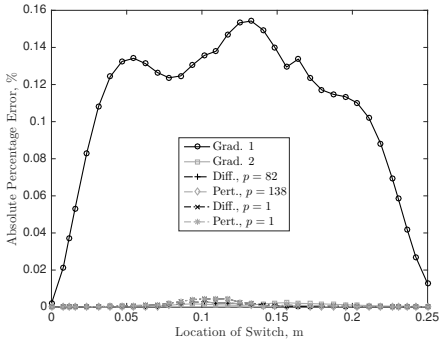

(f) Mode shape, FF

Figure 4.36: Absolute percentage of error in fundamental frequency and mass normalized mode shape given zigzag wrapping pattern with alternative second string for variable switching location.

Figures 4.35 and 4.36 for the alternative string results present similar behaviours as those in Figs. 4.33 and 4.34 for the identical string. Namely, it is clearly seen that the Grad. 1 method results in the largest errors for both the frequency and mode shape. In addition, for the norm minimization methods there are sudden increases and decreases in the errors, which produce non-smooth errors. This does not occur for the gradient minimization method and highlights an advantage to using this method.

Figure 4.35 demonstrates that for the diagonal pattern with CC and FF boundary conditions the absolute error attains the maximum value in the frequency and mode shape near a switching location of $x = l/2$. For CF boundary conditions the frequency and mode shape attains its maximum near a switching location of $x = l/4$. Hence the error in predicting the frequencies peaks at locations where the switch is made in a high curvature area. For all the results presented, the error in predicting the frequency was less than 0.9% and the error in predicting the associated mode shape was less than 0.25%. Figure 4.36 for the zigzag wrapping pattern demonstrates that, as was the case with the identical string, the errors in the frequency increases when the value of the frequency increases. Therefore when the switching location is near an area of high curvature it is expected that the error in predicting the fundamental frequency will increase. Overall, the absolute error in the frequency was less than 1.8% and the absolute error in the mode shape is less than 0.16%.

Table 4.9 presents the average of the sum of the absolute percentage of error for the first 10 modes for variable switching location. The results are determined by considering a variable switching location from 2 strings to 1 string. These results, as expected, indicate that the perturbation theory with additional corrections provide more accurate results than the first-order perturbation theory, regardless of how the reference values are determined.

The second-order gradient minimization method produced the smallest average sum of absolute error for both the frequencies and mode shapes for the diagonal wrapping pattern. The norm minimization using the difference with optimal p-value produced the smallest average sum of absolute error for both frequencies and mode shapes for the zigzag wrapping pattern. For each wrapping pattern, the most accurate method was also independent of boundary conditions. If an optimal p-value cannot be determined ahead of time, then for the results presented the norm minimization using the difference with $p = 1$ produced the most accurate estimates for the frequencies and the second-order gradient minimization method produced the most accurate estimates for the mode shapes.

Table 4.9: Natural frequency and mode shape average absolute sum of error for the first 10 modes given variable switching location with alternative second string

	Frequency Results			Mode Shape Results		
Result	CC	CF	FF	CC	CF	FF
			Diagonal Pattern ($\times 10^0$)			
Grad. 1	2.643	2.686	2.804	6.078	5.394	7.875
Grad. 2	0.261	0.284	0.319	0.104	0.085	0.137
Diff., $p = 1$	0.608	0.611	0.662	0.299	0.229	0.349
Pert., $p = 1$	0.593	0.587	0.636	0.301	0.231	0.347
			Zigzag Pattern ($\times 10^0$)			
Grad. 1	7.227	6.983	7.029	4.405	4.177	5.125
Grad. 2	1.125	1.300	1.429	0.128	0.136	0.171
Diff., p opt.	0.292	0.248	0.267	0.152	0.141	0.189
Pert., p opt.	0.297	0.252	0.268	0.152	0.141	0.189
Diff., $p = 1$	1.044	1.003	1.049	0.170	0.151	0.208
Pert., $p = 1$	1.324	1.264	1.308	0.172	0.159	0.213

To summarize, from the numerical simulations with variable switching location it is obvious that there is a significant advantage in using the perturbation theory with additional corrections when compared to a single correction for the frequencies. A clear pattern was observed with regards to the perturbation theory reference value selection method that should be employed to obtain the most accurate results. For the diagonal wrapping pattern, the second-order gradient minimization method always produced the smallest average sum of error for the first 10 modes of the system. For the zigzag wrapping pattern, the norm minimization method using the difference with optimal p value produced the smallest average sum of error for the first 10 modes of the system. If it is assumed that the frequencies of the system are not known ahead of time, the second-order gradient minimization method typically provided the most accurate method for determining the frequencies and mode shapes of the zigzag system. The exception was for the alternative string where the norm minimization using the difference and $p = 1$ predicted the frequencies most accurately in the absence of known values.

4.3 Experimental Validation

4.3.1 System Description

The non-periodic string-harnessed system wrapping pattern considered experimentally is presented in Fig. 4.37. Non-periodicity is introduced into the system by varying the wrapping angle by a prescribed percentage increase or decrease each time the string goes from one face of the host structure to another.

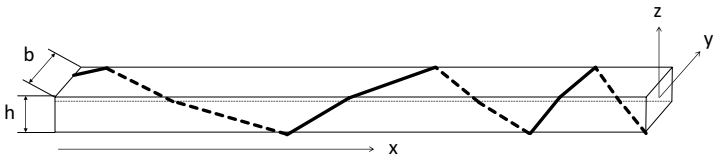

Figure 4.37: String-harnessed system with variable wrapping angle.

A clamped-free system is considered and the perturbation theory approach developed in Chapter 3 is applied to determine the natural frequencies and mode shapes. The clamped end of the beam is attached to a shaker and this provides the excitation to the system.

4.3.2 Frequency Response Function

To calculate the FRF using the results of the perturbation theory, first find the FRF assuming a set of mode shapes that are exact for the spatially varying problem. Denote this set of mode shapes by $\left\{\widehat{\phi}_n(x)\right\}_{n=1}^{\infty}$ and denote the frequency associated with the n^{th} mode shape by $\widehat{\omega}_n$. Let the mode shapes satisfy the normalization conditions

$$\delta_{ij} = \int_0^l \rho A(x)\widehat{\phi}_i(x)\widehat{\phi}_j(x)\,\mathrm{d}x \tag{4.20a}$$

$$\widehat{\omega}_i^2\delta_{ij} = \int_0^l \widehat{\phi}_i(x)\frac{\mathrm{d}^2}{\mathrm{d}x^2}\left[EI(x)\frac{\mathrm{d}^2\widehat{\phi}_j(x)}{\mathrm{d}x^2}\right]\,\mathrm{d}x \tag{4.20b}$$

where δ_{ij} is the Kronecker delta. Again, the normalization conditions are chosen such that the modes of the system can be decoupled when determining the time response of the system.

As the clamped portion of the system is attached to a shaker, the boundary conditions of the system must be updated to include the motion of the base. Therefore for $\omega_s \neq 0$ the experimental boundary conditions are

$$\overline{w}(0,t) = \frac{gg_f}{\omega_s^2}\sin(\omega_s t) \quad , \quad \frac{\partial \overline{w}(0,t)}{\partial x} = 0 \quad , \quad EI(l)\frac{\partial^2 \overline{w}(l,t)}{\partial x^2} = 0 \quad , \quad \frac{\partial}{\partial x}\left[EI(x)\frac{\partial^2 \overline{w}(x,t)}{\partial x^2}\right]_{x=l} = 0 \tag{4.21}$$

In the boundary conditions, the driving frequency of the shaker is ω_s, the gravitational acceleration is g, and g_f denotes a dimensionless gravitational acceleration factor. The PDE for the transverse motion of the system is that same as that obtained in Eq. (4.16) with the lumped masses set to 0.

$$\frac{\partial^2}{\partial x^2}\left[EI(x)\frac{\partial^2 \overline{w}}{\partial x^2}\right] + \rho A(x)\frac{\partial^2 \overline{w}}{\partial t^2} = 0 \tag{4.22}$$

First, the nonhomogeneous boundary conditions are removed by introducing a function that satisfies the boundary conditions in Eq. (4.21). Such a function is $r(x,t) = gg_f \sin(\omega_s t)/\omega_s^2$. Make the substitution $\overline{w}(x,t) = y(x,t) + r(x,t)$ into the PDE and boundary conditions. The PDE in terms of $y(x,t)$ that is to be solved is

$$\frac{\partial^2}{\partial x^2}\left[EI(x)\frac{\partial^2 y}{\partial x^2}\right] + \rho A(x)\frac{\partial^2 y}{\partial t^2} = \rho A(x) g g_f \sin(\omega_s t) \tag{4.23}$$

and the boundary conditions are

$$y(0,t) = 0 \quad , \quad \frac{\partial y(0,t)}{\partial x} = 0 \quad , \quad EI(l)\frac{\partial^2 y(l,t)}{\partial x^2} = 0 \quad , \quad \frac{\partial}{\partial x}\left[EI(x)\frac{\partial^2 y(x,t)}{\partial x^2}\right]_{x=l} = 0 \tag{4.24}$$

The solution to the PDE in Eq. (4.23) with the boundary conditions in Eq. (4.24) can be expressed in terms of the mode shapes as $y(x,t) = \sum_{n=1}^{\infty} g_n(t)\widehat{\phi}_n(x)$. The functions $g_n(t)$ are yet to be determined.

Substitute the series solution for $y(x,t)$ into the PDE in Eq. (4.23), multiply by $\widehat{\phi}_i(x)$, and integrate over the length of the domain. Then, applying the normalization conditions in Eq. (4.20) yields

$$\ddot{g}_i(t) + \widehat{\omega}_i^2 g_i(t) = g g_f \int_0^l \rho A(x)\widehat{\phi}_i(x)\,\mathrm{d}x\, \sin(\omega_s t) = g g_f \widetilde{\phi}_i \sin(\omega_s t) \tag{4.25}$$

For the FRF, the steady-state solution is of interest. For the case of the clamped end excited by a shaker the steady-state solution is

$$g_{ss,i}(t) = \frac{g g_f \widetilde{\phi}_i}{\widehat{\omega}_i^2 - \omega_s^2}\sin(\omega_s t) \tag{4.26}$$

Using the steady-state solution for the $g_i(t)$, the steady state for the transverse vibrations of the string-harnessed system given by Eq. (4.22) is

$$\overline{w}_{ss}(x,t) = r(x,t) + y_{ss}(x,t) = gg_f \left(\frac{1}{\omega_s^2} + \sum_{i=1}^{\infty} \frac{\widetilde{\phi}_i \widehat{\phi}_i(x)}{\widehat{\omega}_i^2 - \omega_s^2} \right) \sin(\omega_s t) \tag{4.27}$$

The FRF is obtained by dividing the steady-state response for the displacement by the amplitude of the input acceleration to the shaker, and then taking the magnitude.

$$H(x,\omega_s) = \left| \frac{1}{\omega_s^2} + \sum_{i=1}^{\infty} \frac{\widetilde{\phi}_i \widehat{\phi}_i(x)}{\widehat{\omega}_i^2 - \omega_s^2} \right| \tag{4.28}$$

In Eq. (4.28) the sensing location x is measured from the clamped end and is the FRF of the system assuming exact mode shapes for the spatially varying system. To obtain the FRF using the perturbation theory results, the frequencies obtained from the perturbation theory are used for $\widehat{\omega}_i$ and the mode shapes obtained from the perturbation theory are used for $\widehat{\phi}_i(x)$.

4.3.3 Experimental Setup

The experimental setup used for the non-periodic wrapping pattern tests is the same that was previously used for the periodic wrapping pattern tests in Section 2.2.2. Furthermore, the non-periodic string wrapping pattern is applied in the same manner as the periodic wrapping pattern. A hanging mass is used to applied a pre-tension in the string and then it is wrapped around the host structure. There is a small hole at the free end of the system that is used to tie the string and reflective tape is added to ensure optimal measurements. Figure 4.38 shows one of the test setups used in the non-periodic wrapping pattern tests.

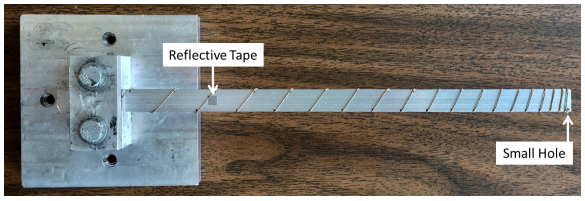

Figure 4.38: String-harnessed beam with non-periodic wrapping pattern.

The host structure is an aluminium alloy 6061 beam with 0.01306 m width, 0.00146 m thickness, and 0.251 m length. The modulus is 68.9 GPa and the density is 2768 kg/m^3.

This is the same beam that was used in the periodic wrapping pattern tests and was referred to as Beam 2.

4.3.4 String-Harnessed System Experimental and Analytical FRFs

A PowerPro Super 8 Slick 80 lb break strength fishing line is used for the experimental tests. This is the same type of string used for the periodic wrapping pattern tests in Section 2.4.3 with a radius of 0.20955 mm, a density of 1400 kg/m^3, and a modulus of 128.04 GPa. A first round of tests are performed with a single string pre-tensioned with 8.3 N. A second round of tests with three string harnesses, all with the same wrapping pattern, is performed with each of the three strings pre-tensioned with 13.3 N. A sensing location of 0.0513 m $\pm$ 0.0013 m was used with variations as a result of the variable wrapping pattern.

Beginning from the free end of the system, the wrapping angle of the string is varied by a fixed percentage each time the string goes from one side of the host structure to another. Multiple wrapping patterns are produced by varying the percentage change in the wrapping angle over each section. Figure 4.39 presents a top-down view of the wrapping patterns that are considered for both the single and three string tests along with the percentage change over each section noted. In Fig. 4.39, the dashed lines represent a section of string on the bottom face of the beam. Each of the wrapping patterns are setup so that the string is attached to the small hole at the free end of the beam and also so that the wrapping angle at the clamped end is roughly similar across all the tests.

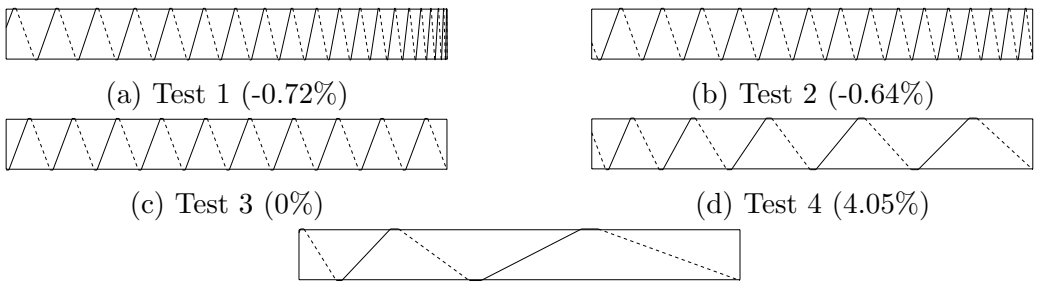

(a) Test 1 (-0.72%)

(b) Test 2 (-0.64%)

(c) Test 3 (0%)

(d) Test 4 (4.05%)

(e) Test 5 (18.27%)

Figure 4.39: Wrapping patterns for non-periodic tests with percentage change in wrapping angle noted.

Using the same acceleration profile as the periodic wrapping pattern tests in Section 2.4.3, the FRFs for the non-periodic wrapping patterns are obtained. Figures 4.40-4.44 present the FRFs for the single string tests and Figs. 4.45-4.49 present the FRFs

for the three strings tests. In these figures experimental results are presented for the string-harnessed system, denoted by "Exp. SH", as well as experimental results for the unwrapped system, denoted by "Exp. Un.". Also included in the results is the FRF for a mass updated system, denoted by "MU". The mass updated model neglects the stiffening effect of the string and accounts only for the added mass. Using EB beam assumption, an analytical solution for the MU model can be found and the details are presented in Appendix D.

Additionally in the figures, two FRF results for the perturbation theory are presented. The first is the perturbation theory using the gradient minimization method to determine the reference values, denoted "Pert., Grad.", and the second is the L_p norm minimization with optimally chosen p with the best result take from the difference and perturbation norm minimization approaches, denoted "Pert., Opt.". In the numerical simulations it was seen that without prior knowledge of the frequencies of the system, the gradient minimization method typically produced the most accurate results for the perturbation theory method. It is of interest to determine how these results compare to the case when the frequencies are known beforehand to optimally choose the reference values.

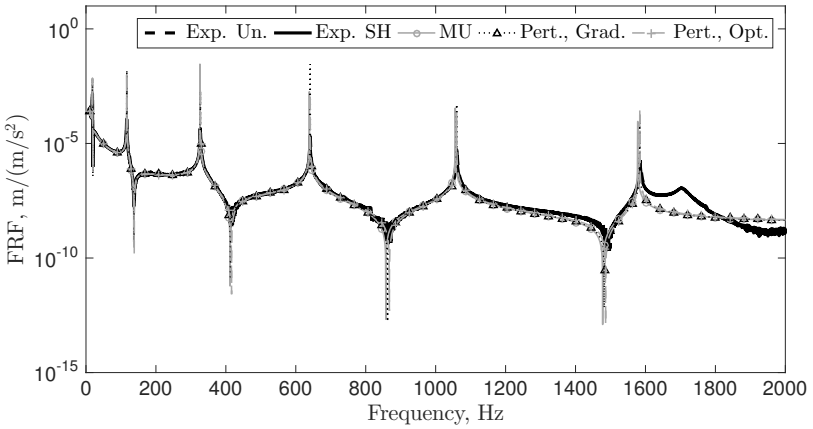

Figure 4.40: Single string analytical and experimental FRF comparison, test 1.

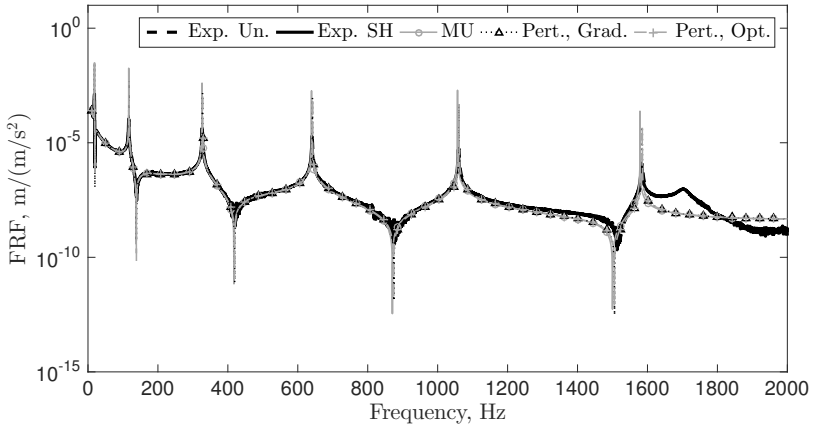

Figure 4.41: Single string analytical and experimental FRF comparison, test 2.

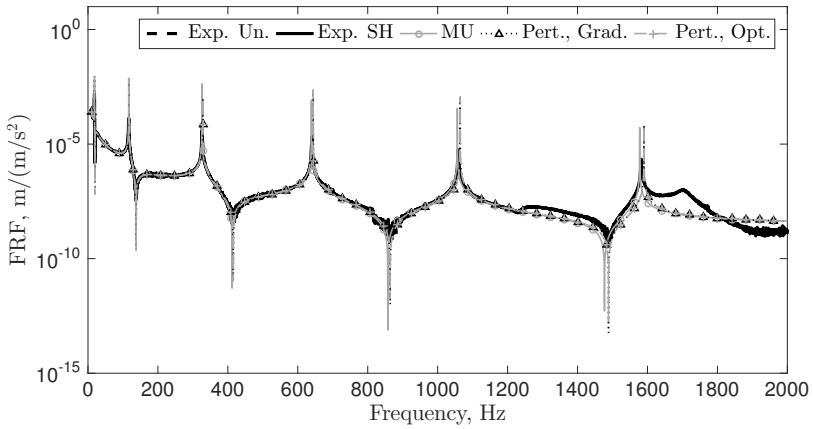

Figure 4.42: Single string analytical and experimental FRF comparison, test 3.

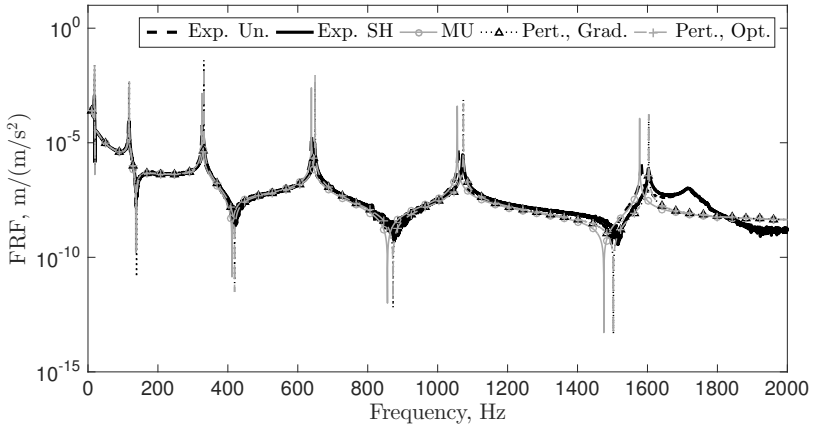

Figure 4.43: Single string analytical and experimental FRF comparison, test 4.

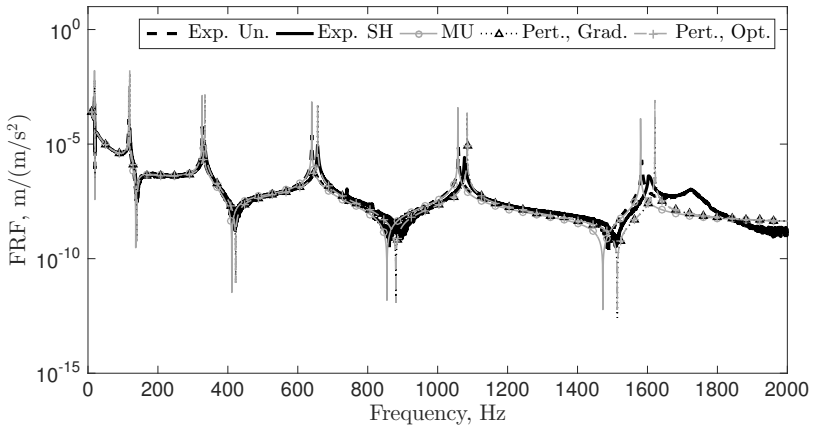

Figure 4.44: Single string analytical and experimental FRF comparison, test 5.

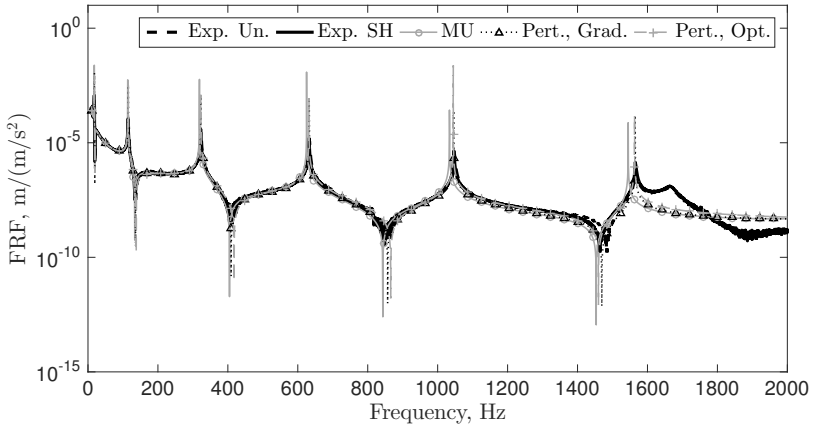

Figure 4.45: Three strings analytical and experimental FRF comparison, test 1.

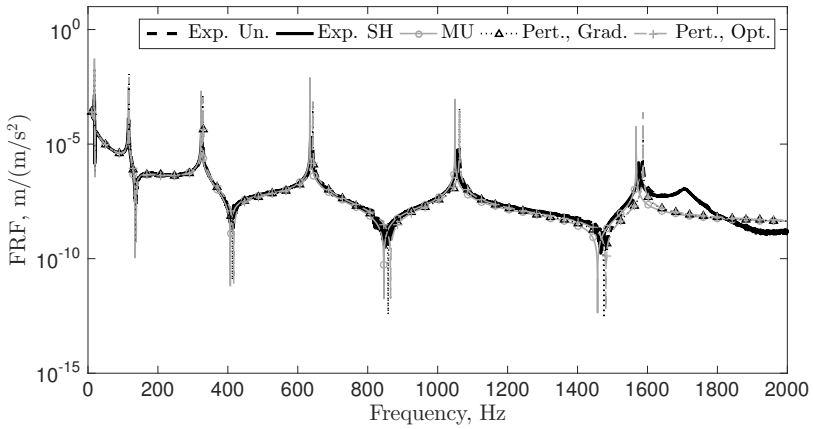

Figure 4.46: Three strings analytical and experimental FRF comparison, test 2.

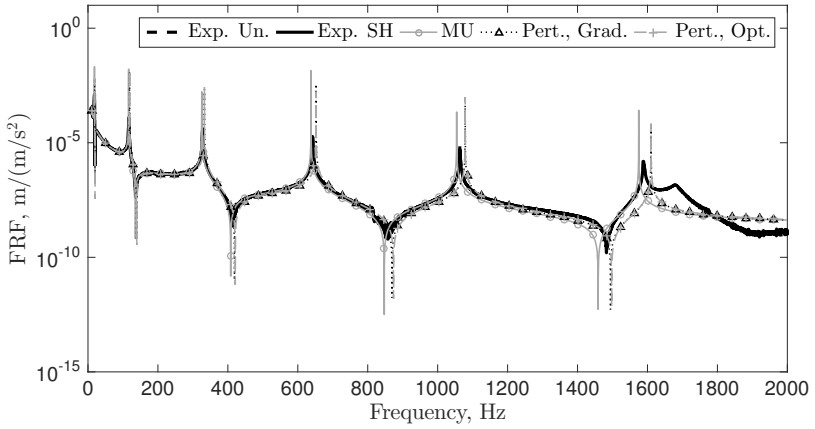

Figure 4.47: Three strings analytical and experimental FRF comparison, test 3.

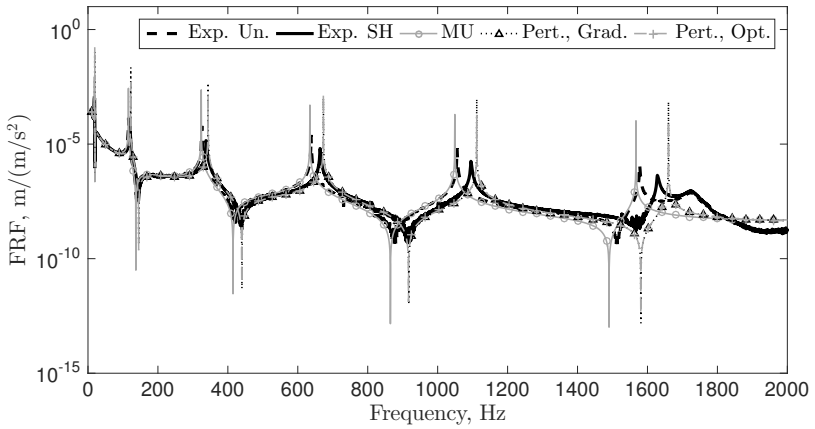

Figure 4.48: Three strings analytical and experimental FRF comparison, test 4.

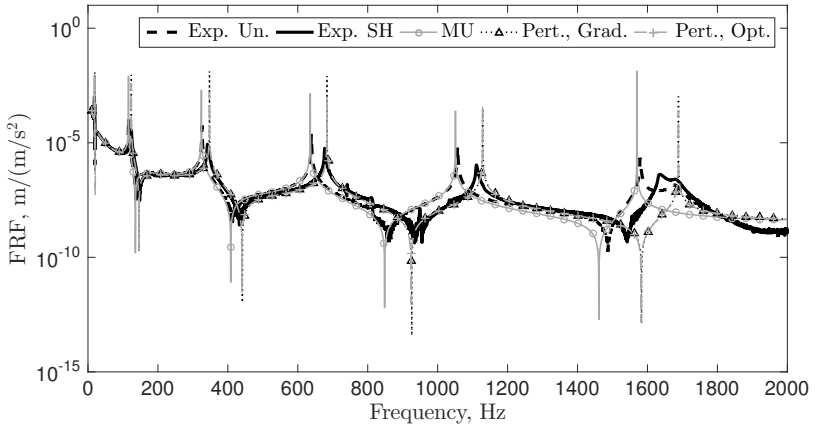

Figure 4.49: Three strings analytical and experimental FRF comparison, test 5.

Very good agreement is observed between the analytical and experimental results in Figs. 4.40 - 4.49 with respect to the amplitude, value of the natural frequencies, and location of antiresonances. As was observed in previous tests for periodic wrapping patterns, there is an additional peak near 1700 Hz due to the small section of beam that extends beyond the clamp. Furthermore, it should be noted that the value of the resonant peaks of the experimental and analytical models do not match due to the absence of damping in the analytical model. Additionally, there is no observable difference between the perturbation theory FRFs, indicating that without prior knowledge of the frequencies excellent results are achieved.

It is quite clear from the results in Figs. 4.40 - 4.49 that the perturbation theory FRFs provide a much better match for the experimental string-harnessed FRFs than the mass updated model. The results for Tests 4 and 5 in particular clearly highlight this. The perturbation theory results providing a more accurate FRF than the mass updated model indicates the importance of including the effect of stiffening in the analytical model. Furthermore, it is seen through experimentation that the frequencies of the string-harnessed system can be significantly larger than those of the unwrapped system. One of the limitations of the mass updated model is the inability to predict frequencies that are larger than those of an unwrapped system. This is due to the added mass in the model causing a decrease in the frequencies and clearly highlights the advantage of using the proposed model and perturbation theory.

Two effects are observed on the natural frequencies going from Test 1 to Test 5 as the wrapping pattern is increasingly more loosely wrapped. When the string-harnessed system

is more loosely wrapped, the total added mass by the string decreases. This has the effect of increasing the frequencies of the system. The second effect is an increase in the stiffening effect due to the string as the system is more loosely wrapped. The increase in the string stiffening effect is due to an overall decrease in the wrapping angle as the string is more loosely wrapped and will cause an increase in the frequencies of the system. Therefore, due to both of these effects, in going from Test 1 to Test 5 it is expected that the natural frequencies of the string-harnessed system will increase. The natural frequencies are listed in Table 4.10 and indeed an increase in the frequencies from Test 1 to Test 5 is observed for both the single and three string tests.

It is also shown in Table 4.10 that the perturbation theory results for the proposed model of a string-harnessed system are quite accurate in predicting the natural frequencies of the system when compared to experimental results. Also, the errors reported by the gradient and optimally chosen references values for the perturbation theory are almost identical. Plots of the absolute percentage of error for all the tests performed are presented in Fig. 4.50 for the gradient results and in Fig. 4.51 for the optimally determined results. For the gradient norm minimization perturbation theory results the largest absolute error obtained for the single string tests is 1.11%, with an average absolute error of 0.48%, and the largest absolute error obtained for the three strings tests is 3.28%, with an average absolute error of 1.33%. For the norm minimization with optimal p-value perturbation theory results the largest absolute error obtained for the single string tests is 1.11%, with an average absolute error of 0.48%, and the largest absolute error obtained for the three strings tests is 3.27%, with an average absolute error of 1.32%.

Table 4.10: Natural frequencies, in Hz, of the experimental and analytical string-harnessed tests.

	Mode						Mode					
Result	1	2	3	4	5	6	1	2	3	4	5	6
	Test 1, Single String						*Test 1, Multiple Strings*					
String-harnessed	18.535	116.25	326.65	640.30	1059.8	1583.2	18.270	114.55	322.20	632.00	1046.3	1565.1
Pert., Grad.	18.650	116.85	327.17	641.19	1060.1	1583.6	18.411	115.29	322.75	632.64	1045.8	1564.8
Error, %	0.618	0.52	0.16	0.14	0.03	0.03	0.774	0.66	0.17	0.10	-0.05	-0.02
Pert., Opt.	18.649	116.85	327.17	641.18	1060.1	1583.6	18.396	115.18	322.42	631.98	1044.7	1563.1
Error, %	0.618	0.52	0.16	0.14	0.03	0.03	0.689	0.55	0.069	-0.003	-0.15	-0.13
	Test 2, Single String						*Test 2, Multiple Strings*					
String-harnessed	18.570	116.25	326.55	640.05	1058.9	1581.6	18.450	115.65	324.90	636.65	1053.7	1574.4
Pert., Grad.	18.688	117.02	327.59	641.98	1061.3	1585.2	18.759	117.32	328.14	642.75	1062.6	1587.5
Error, %	0.636	0.66	0.319	0.301	0.22	0.23	1.68	1.44	0.997	0.958	0.84	0.831
Pert., Opt.	18.688	117.02	327.59	641.98	1061.3	1585.2	18.759	117.32	328.14	642.74	1062.6	1587.5
Error, %	0.636	0.66	0.319	0.301	0.22	0.23	1.68	1.44	0.996	0.957	0.84	0.831
	Test 3, Single String						*Test 3, Multiple Strings*					
String-harnessed	18.555	116.35	326.25	639.75	1058.4	1581.4	18.620	116.65	327.60	642.20	1063.6	1588.2
Pert., Grad.	18.725	117.35	328.58	643.88	1064.4	1590.0	18.977	118.96	333.04	652.47	1078.6	1610.2
Error, %	0.918	0.859	0.714	0.646	0.57	0.54	1.92	1.98	1.66	1.600	1.41	1.39
Pert., Opt.	18.725	117.35	328.58	643.88	1064.4	1590.0	18.977	118.96	333.04	652.47	1078.6	1610.2
Error, %	0.918	0.859	0.714	0.646	0.57	0.54	1.92	1.98	1.66	1.599	1.41	1.39
	Test 4, Single String						*Test 4, Multiple Strings*					
String-harnessed	18.660	117.50	329.95	647.90	1071.4	1602.1	18.770	120.00	337.55	663.65	1095.1	1628.2
Pert., Grad.	18.800	118.24	331.35	649.41	1073.5	1603.6	19.342	122.42	343.48	673.14	1111.8	1660.0
Error, %	0.751	0.63	0.425	0.233	0.20	0.092	3.05	2.02	1.76	1.43	1.52	1.95
Pert., Opt.	18.800	118.24	331.35	649.41	1073.5	1603.6	19.342	122.42	343.47	673.12	1111.7	1660.0
Error, %	0.751	0.63	0.425	0.233	0.20	0.092	3.05	2.02	1.75	1.43	1.52	1.95
	Test 5, Single String						*Test 5, Multiple Strings*					
String-harnessed	18.800	119.15	332.40	656.45	1076.7	1603.3	19.270	123.50	341.60	676.60	1110.7	1635.0
Pert., Grad.	19.003	119.43	334.43	656.91	1084.4	1621.2	19.617	123.90	347.37	683.45	1128.7	1688.6
Error, %	1.08	0.23	0.610	0.070	0.71	1.11	1.80	0.32	1.69	1.01	1.62	3.28
Pert., Opt.	19.003	119.43	334.43	656.91	1084.4	1621.1	19.615	123.88	347.33	683.36	1128.7	1688.5
Error, %	1.08	0.23	0.610	0.070	0.71	1.11	1.79	0.31	1.68	0.999	1.62	3.27

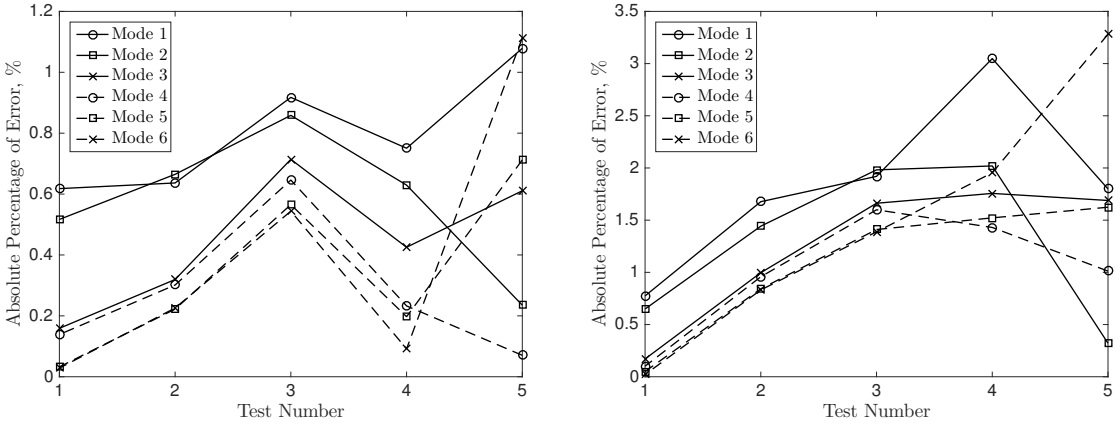

(a) Single string (b) Three strings

Figure 4.50: Absolute percentage of error of perturbation theory with gradient method model frequencies compared to experimental frequencies.

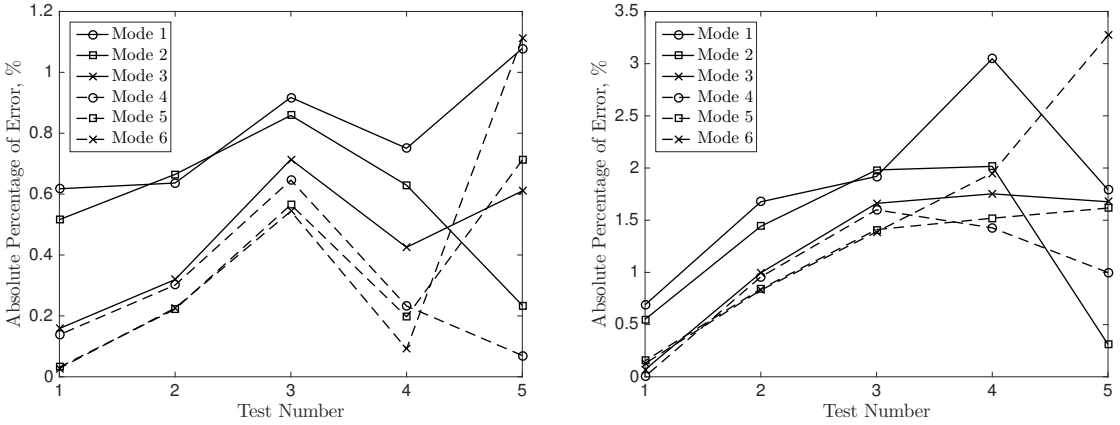

(a) Single string (b) Three strings

Figure 4.51: Absolute percentage of error of perturbation theory with optimal reference model frequencies compared to experimental frequencies.

Figures 4.50 and 4.51 further demonstrate that the results obtained by the two perturbation theory results are essentially identical to one another. In these figures, it is demonstrated that for both the single and three string tests the absolute percentage of error is relatively consistent for each of the five tests. Consistency in the error indicates that

as the wrapping pattern is varied the analytical model does not introduce additional error into the prediction of the natural frequencies and therefore accurately captures changes from one test to another. Finally, it is seen that the error is larger in the three strings test when compared to the single string test for a given wrapping pattern, in particular for the tests which are more loosely wrapped. This is attributable to the larger string-to-host-structure cross-sectional area for the three strings test compared to the single string test; a similar result was observed experimentally for the periodic pattern tests in Section 2.4.4.

During testing the string-harnessed system FRF was first obtained, then the string(s) carefully removed, and the FRF for the unwrapped beam was obtained. Figure 4.52 presents the experimental natural frequencies for the string-harnessed and unwrapped systems, as well as the perturbation theory string-harnessed model frequencies, given both approaches, for the single string tests. Figure 4.53 presents the experimental natural frequencies for the string-harnessed and unwrapped systems, as well as the perturbation theory string-harnessed model frequencies, given both approaches, for the three strings tests. Table 4.11 presents the experimental natural frequencies and the percentage change going from unwrapped to string-harnessed.

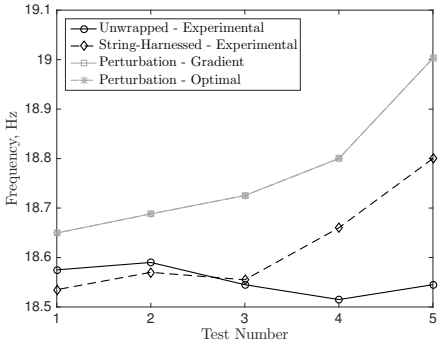

(a) Mode 1

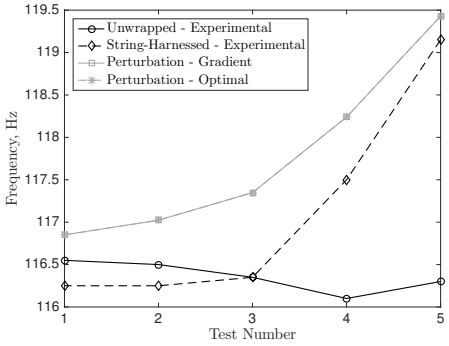

(b) Mode 2

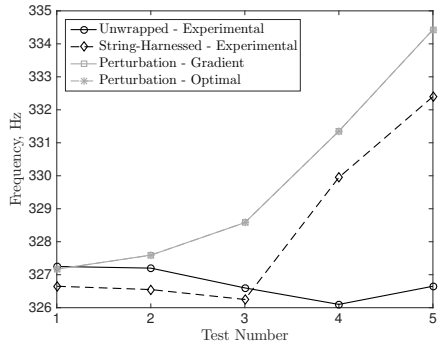

(c) Mode 3

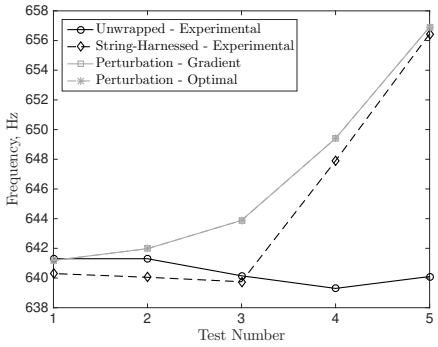

(d) Mode 4

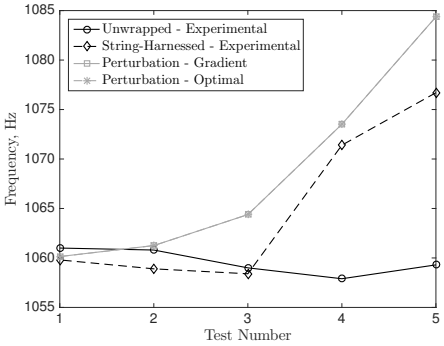

(e) Mode 5

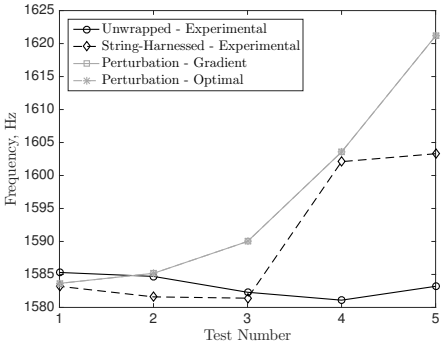

(f) Mode 6

Figure 4.52: Single string analytical string-harnessed natural frequencies and experimental natural frequencies for unwrapped and string-harnessed systems.

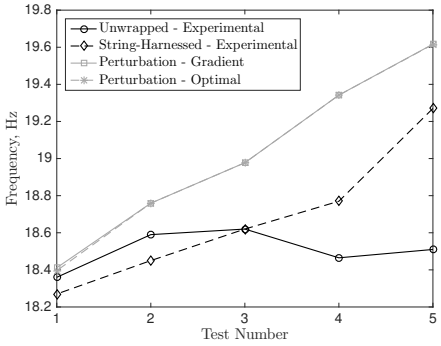

(a) Mode 1

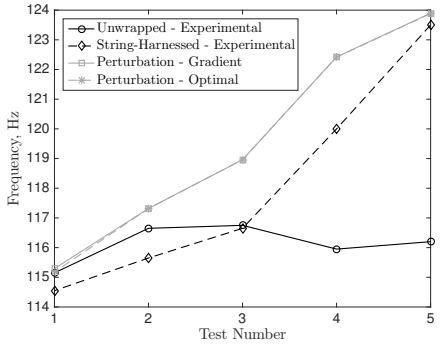

(b) Mode 2

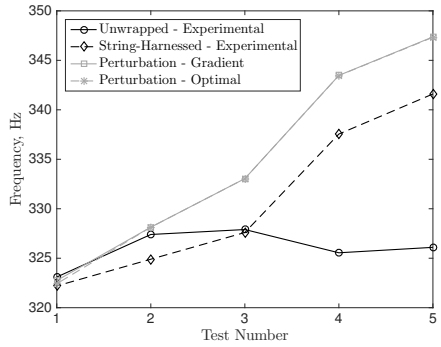

(c) Mode 3

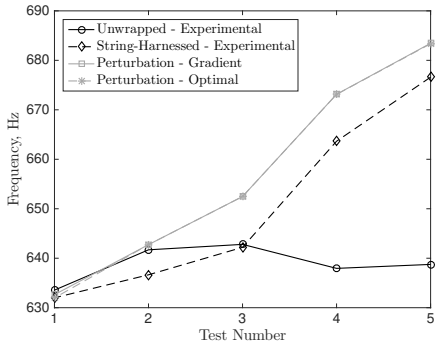

(d) Mode 4

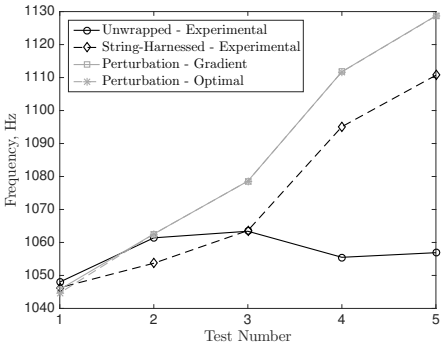

(e) Mode 5

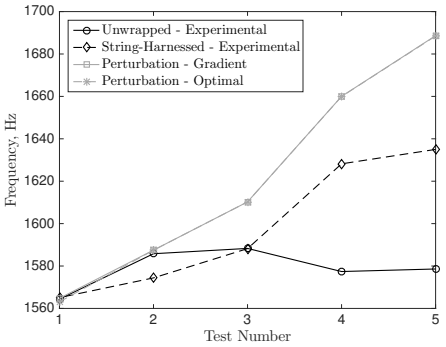

(f) Mode 6

Figure 4.53: Three strings analytical string-harnessed natural frequencies and experimental natural frequencies for unwrapped and string-harnessed systems.

Small variations in the frequency for the unwrapped system are observed in Figs. 4.52 and 4.53 due to human error in clamping the system at the same exact length between the various tests. However since the string-harnessed results were obtained and then the string(s) removed to then obtain the unwrapped results, this provides a fair comparison between the frequencies for a given test number. In particular, this allows for a fair comparison of the percentage change in the frequency from the unwrapped to the string-harnessed system between the various tests.

For both the single and three string tests, it is seen in Table 4.11 that the string-harnessed system frequencies are typically smaller than the unwrapped system for Tests 1 and 2. When the strings are tightly wrapped, as in Tests 1 and 2, it is seen that the added mass effect is larger than the stiffening effect. This causes a decrease in the frequencies of the system when the string is added. For both the single and three string tests, it is seen in Table 4.11 that the string-harnessed system frequencies are larger than the unwrapped system for Tests 4 and 5. When the strings are loosely wrapped, as in Tests 4 and 5, it is seen that the added stiffening effect is larger than the mass effect. This causes an increase in the frequencies of the system when the string is added. It is also seen that the magnitude of the frequency increase for the three strings tests is much larger than for the single string tests. When the mass effect is dominant, the three strings added 3 times more mass than the single string, creating a larger decrease in the frequencies. When the stiffening effect is dominant, the three string add significantly more stiffness than the single string, creating a larger increase in the frequencies.

Additionally, it is seen in Table 4.11 that experimentally the overall stiffening effect of the strings was not negligible. In particular for Test 5 the percentage increase in the frequency from an unwrapped system to a string-harnessed system was as large as 2.554% for a single string system and 6.28% for a three strings system. This highlights the importance of the modelling the strings accurately in the system and that the stiffening effect cannot be ignored.

In summary, it has been shown experimentally that the stiffening effect of string harnesses is significant, in particular for more loosely wrapped patterns where the string-harnessed frequencies are significantly larger than an unwrapped system. The natural frequencies and FRFs for the perturbation theory results of the proposed string-harnessed system model were shown to match quite well with experimental results, for both single and three string tests. Two methods for determining the perturbation theory reference values were considered, one with and one without prior knowledge of the frequencies of the string-harnessed system. It was seen for the cases considered that there is very little advantage in terms of the errors obtained of using the optimally chosen reference values over the gradient method. This highlight the ability of the gradient method to predict

Table 4.11: Unwrapped and string-harnessed experimental natural frequencies, in Hz.

	Mode						Mode					
Result	1	2	3	4	5	6	1	2	3	4	5	6
	Test 1, Single String						*Test 1, Multiple Strings*					
Unwrapped	18.575	116.55	327.25	641.30	1061.1	1585.3	18.360	115.15	323.10	633.55	1048.0	1564.4
String-harnessed	18.535	116.25	326.65	640.30	1059.8	1583.2	18.270	114.55	322.20	632.00	1046.3	1565.1
Frequency change, %	-0.22	-0.26	-0.18	-0.156	-0.11	-0.13	-0.490	-0.52	-0.28	-0.245	-0.16	0.04
	Test 2, Single String						*Test 2, Multiple Strings*					
Unwrapped	18.590	116.50	327.20	641.30	1060.8	1584.7	18.590	116.65	327.40	641.70	1061.4	1585.8
String-harnessed	18.570	116.25	326.55	640.05	1058.9	1581.6	18.450	115.65	324.90	636.65	1053.7	1574.4
Frequency change, %	-0.108	-0.21	-0.20	-0.195	-0.18	-0.20	-0.753	-0.857	-0.764	-0.787	-0.73	-0.719
	Test 3, Single String						*Test 3, Multiple Strings*					
Unwrapped	18.570	116.45	326.90	640.70	1059.8	1583.2	18.620	116.75	327.90	642.80	1063.4	1588.3
String-harnessed	18.610	116.70	327.75	642.80	1063.5	1588.8	18.620	116.65	327.60	642.20	1063.6	1588.2
Frequency change, %	0.215	0.21	0.26	0.328	0.35	0.35	0	-0.086	-0.091	-0.093	0.02	-0.006
	Test 4, Single String						*Test 4, Multiple Strings*					
Unwrapped	18.515	116.10	326.10	639.30	1057.9	1581.1	18.465	115.95	325.55	637.95	1055.5	1577.4
String-harnessed	18.660	117.50	329.95	647.90	1071.4	1602.1	18.770	120.00	337.55	663.65	1095.1	1628.2
Frequency change, %	0.783	1.21	1.18	1.35	1.28	1.33	1.65	3.49	3.686	4.029	3.75	3.22
	Test 5, Single String						*Test 5, Multiple Strings*					
Unwrapped	18.545	116.30	326.65	640.10	1059.3	1583.2	18.510	116.20	326.10	638.75	1056.9	1578.6
String-harnessed	18.800	119.15	332.40	656.45	1076.7	1603.3	19.270	123.50	341.60	676.60	1110.7	1635.0
Frequency change, %	1.38	2.45	1.76	2.554	1.64	1.27	4.11	6.28	4.753	5.926	5.09	3.57

the frequencies of the system with great accuracy. Finally, the string-harnessed perturbation theory results were compared to a mass updated model to highlight the importance of modelling the stiffening effect of the strings. These results validate the ability of the proposed model to accurately model non-periodic wrapping patterns for string-harnessed systems.

4.4 Chapter Summary

In this chapter, a spatially dependent model for string-harnessed system that can account for periodic and non-periodic wrapping patterns was developed. The perturbation theory previously developed in this thesis was then used to determine the frequencies and mode shapes. For periodic wrapping patterns, it was clearly shown that the perturbation theory results were more accurate than using a homogenized model as in Chapter 2. Additionally through this analytical study, it was found that adding string in locations of high displacement in a mode shape lowers the frequency of that mode. Further, adding string in locations of high curvature in a mode shape raises the frequency of that mode. Interestingly, sections of string on the side of the beam increased the strain energy locally.

Experimental tests were performed to assess the accuracy of the perturbation theory results for the string-harnessed model. Multiple wrapping patterns were considered, four non-periodic and one periodic, and tested for a system with a single string as well as with three strings. The FRFs for the perturbation theory results matched exceptionally well with the experimental FRFs. For the single string tests, the largest percentage increase in a frequency compared to an unwrapped system for a single mode was 2.554%. For the three strings tests, the largest percentage increase in a frequency compared to an unwrapped system for a single mode was 6.28%. Such significant increases in the frequencies due to the additional of strings clearly highlights their significance in adding stiffness to the system.

Chapter 5

Model Approximation for String-Harnessed Systems

In this chapter the applicability of a constant coefficient model to accurately predict the frequencies and mode shapes of a string-harnessed system is investigated. The frequencies and mode shapes of the system are predicted using perturbation theory and an inverse problem approach is employed to obtain the constant coefficients in the approximation model. Multiple numerical simulations are performed for both periodic and non-periodic wrapping patterns and results are compared to experiments. An initial version of this model approximation was presented by the author in [89] and the work presented in this chapter is to be submitted in [90].

5.1 Simple Euler-Bernoulli Approximation

5.1.1 Mathematical Details

The perturbation theory results of the previous section were shown to predict the frequencies and mode shapes quite well, particularly when using the second-order gradient minimization method. Furthermore, it was demonstrated that the frequencies and frequency response functions (FRFs) for the perturbation theory results matched quite well with experiments for various system setups.

Although the perturbation theory can be used to solve the spatially dependent problem, and hence consider non-periodic wrapping patterns, one drawback is the lack of a

concise explicit solution. The goal of the current chapter is to investigate the ability of various constant coefficient models to accurately predict the frequencies and mode shapes of the spatially dependent model. To achieve this, the perturbation theory results for the frequencies and mode shapes are used as the exact quantities that the approximate model aims to predict.

As evidenced in the previous chapter, without prior knowledge of the frequencies and mode shapes of the system, the second-order gradient minimization method to determine the reference values was the most accurate. For this reason, this method for choosing the reference values is the sole focus for the approximate model. Specifically, in the current chapter it is assumed that the frequencies and mode shapes are given by

$$\omega_n = \frac{\omega_{n0}}{l^2}\sqrt{\frac{EI_n^*}{\rho A_n^*}} \tag{5.1}$$

$$\phi_n(x) = \frac{1}{\sqrt{l\rho A_n^*}}\left\{\frac{3}{2}\phi_{n0}(x) + \frac{f_{n1}(x)}{\rho A_n^*} - \frac{f_{n2}(x)}{EI_n^*}\right\} \tag{5.2}$$

where the expressions for ω_{n0} and $\phi_n(x)$ are found by solving the $\mathcal{O}(1)$ problem in Section 3.4.4, the expressions for $f_{n1}(x)$ and $f_{n2}(x)$ are found in Appendix C, and EI_n^* and ρA_n^* are obtained via the gradient minimization method outlined in Chapter 3.

A simple Euler-Bernoulli (EB) model is considered as the approximate model for the string-harnessed system. Letting $\widehat{w}(x,t)$ denote the transverse displacement of the approximate model, the partial differential equation (PDE) for the free transverse vibrations of the model is

$$\widehat{EI}\,\frac{\partial^4 \widehat{w}(x,t)}{\partial x^4} + \widehat{\rho A}\,\frac{\partial^2 \widehat{w}(x,t)}{\partial t^2} = 0 \tag{5.3}$$

for $x \in [0,l]$ and $t > 0$. The unknown coefficients $\widehat{EI}$ and $\widehat{\rho A}$ are to be determined and represent an equivalent bending stiffness and equivalent mass per unit length that approximate the string-harnessed system.

The boundary conditions for the approximate model are

$$\widehat{w}(x^*,t) = 0 \qquad \text{or} \qquad \widehat{EI}\,\frac{\partial^3 \widehat{w}(x^*,t)}{\partial x^3} = 0 \tag{5.4a}$$

$$\frac{\partial \widehat{w}(x^*,t)}{\partial x} = 0 \qquad \text{or} \qquad \widehat{EI}\,\frac{\partial^2 \widehat{w}(x^*,t)}{\partial x^2} = 0 \tag{5.4b}$$

where $x^* = 0$ or l. The left hand boundary conditions listed in Eq. (5.4) represent zero displacement and zero slope. These are the geometric boundary conditions. The right hand

boundary conditions listed in Eq. (5.4) represent zero shear and zero moment. These are the natural boundary conditions. As in previous chapters, attention is given to clamped-clamped (CC), clamped-free (CF), and free-free (FF) boundary conditions.

The frequencies and mode shapes of the approximation model are readily available and are given by

$$\widehat{\omega}_n = \frac{\omega_{n0}}{l^2}\sqrt{\frac{\widehat{EI}}{\widehat{\rho A}}} \tag{5.5}$$

$$\widehat{\phi}_n = \frac{1}{\sqrt{l\widehat{\rho A}}}\phi_{n0}(x) \tag{5.6}$$

In Eqs. (5.5) and (5.6), the quantities ω_{n0} and $\phi_{n0}(x)$ are exactly those that are used in the perturbation theory results in Eqs. (5.1) and (5.2).

5.1.2 Approximation Method 1 - Metric Minimization

The metric minimization approach considers the square of the difference between the frequencies and mode shapes and determines the values of $\widehat{EI}$ and $\widehat{\rho A}$ that provide a local minimum. Both the frequencies and mode shapes are included in the metric since if only the frequencies were considered then only a value for the ratio $\widehat{EI}/\widehat{\rho A}$ could be determined. Obtaining results for both $\widehat{EI}$ and $\widehat{\rho A}$ allows for additional insight into how the approximation method varies these quantities to account for changes in the frequencies. Since the frequencies and mode shapes differ in units, these quantities are first nondimensionalized. Use the length scale l, time scale $l^2\sqrt{\widehat{\rho A}/\widehat{EI}}$, and the mass scale $\widehat{\rho A}\, l$.

The metric containing the first m nondimensional frequencies and mode shapes is

$$d_1 = \left\{ \sum_{n=1}^{m} \left(\omega_{n0} - \omega_{n0}\sqrt{\frac{\widehat{\rho A}}{\widehat{EI}}}\sqrt{\frac{EI_n^*}{\rho A_n^*}} \right)^2 + \sum_{n=1}^{m} \int_0^1 \left(\phi_{n0} - \frac{\sqrt{\widehat{\rho A}}}{\sqrt{\rho A_n^*}} \left\{ \frac{3}{2}\phi_{n0} + \frac{f_{n1}}{\rho A_n^*} - \frac{f_{n2}}{EI_n^*} \right\} \right)^2 \mathrm{d}X \right\}^{1/2} \tag{5.7}$$

Expanding the integrand, terms can be grouped by similar powers of $\widehat{\rho A}$. Define the integrals

$$S_{1n} = \int_0^1 \phi_{n0} \left\{ \frac{3}{2}\phi_{n0} + \frac{f_{n1}}{\rho A_n^*} - \frac{f_{n2}}{EI_n^*} \right\} \mathrm{d}X \qquad \text{and} \qquad S_{2n} = \int_0^1 \left\{ \frac{3}{2}\phi_{n0} + \frac{f_{n1}}{\rho A_n^*} - \frac{f_{n2}}{EI_n^*} \right\}^2 \mathrm{d}X$$

The metric to be minimized can be written compactly as

$$d_1 = \left\{ \sum_{n=1}^{m} \omega_{n0}^2 \left(1 - \sqrt{\frac{\widehat{\rho A}}{\widehat{EI}}} \sqrt{\frac{EI_n^*}{\rho A_n^*}} \right)^2 + \sum_{n=1}^{m} \left\{ 1 - \frac{2\sqrt{\widehat{\rho A}}}{\sqrt{\rho A_n^*}} S_{1n} + \frac{\widehat{\rho A}}{\rho A_n^*} S_{2n} \right\} \right\}^{1/2} \tag{5.8}$$

To determine the minimal value of Eq. (5.8), stationary points are found. That is to say the points where the equations $\frac{\partial d_1}{\partial \widehat{EI}} = 0$ and $\frac{\partial d_1}{\partial \widehat{\rho A}} = 0$ are simultaneously satisfied. Solving for the unknown coefficients in the approximation model leads to a single solution, which is the global minimum.

$$\widehat{EI} = \frac{\left\{ \sum_{n=1}^{m} \omega_{n0}^2 \frac{EI_n^*}{\rho A_n^*} \right\}^2 \left\{ \sum_{n=1}^{m} \frac{1}{\sqrt{\rho A_n^*}} S_{1n} \right\}^2}{\left\{ \sum_{n=1}^{m} \omega_{n0}^2 \sqrt{\frac{EI_n^*}{\rho A_n^*}} \right\}^2 \left\{ \sum_{n=1}^{m} \frac{1}{\rho A_n^*} S_{2n} \right\}^2} \tag{5.9a}$$

$$\widehat{\rho A} = \frac{\left\{ \sum_{n=1}^{m} \frac{1}{\sqrt{\rho A_n^*}} S_{1n} \right\}^2}{\left\{ \sum_{n=1}^{m} \frac{1}{\rho A_n^*} S_{2n} \right\}^2} \tag{5.9b}$$

5.1.3 Approximation Method 2 - Error Minimization

The second approximation method follows a similar set of steps as the metric minimization method but instead considers the error in the frequencies and mode shapes. Specifically, the square of the frequency errors are considered as this leads a simple expression for the coefficients of the approximation model. The value of the sum of the error in the first m frequencies and mode shapes is given by

$$\Delta = \sum_{n=1}^{m} \left(\frac{\frac{\omega_{n0}}{l^2} \sqrt{\frac{\widehat{EI}}{\widehat{\rho A}}} - \frac{\omega_{n0}}{l^2} \sqrt{\frac{EI_n^*}{\rho A_n^*}}}{\frac{\omega_{n0}}{l^2} \sqrt{\frac{EI_n^*}{\rho A_n^*}}} \right)^2 + \sum_{n=1}^{m} \frac{\int_0^l \left(\frac{1}{\sqrt{l\widehat{\rho A}}} \phi_{n0} - \frac{1}{\sqrt{l\rho A_n^*}} \left\{ \frac{3}{2} \phi_{n0} + \frac{f_{n1}}{\rho A_n^*} - \frac{f_{n2}}{EI_n^*} \right\} \right)^2 \mathrm{d}x}{\int_0^l \left(\frac{1}{\sqrt{l\rho A_n^*}} \left\{ \frac{3}{2} \phi_{n0} + \frac{f_{n1}}{\rho A_n^*} - \frac{f_{n2}}{EI_n^*} \right\} \right)^2 \mathrm{d}x} \tag{5.10}$$

Using the expressions for S_{n1} and S_{n2} defined in the first approximation method, the expression for the sum of the errors can be written as

$$\Delta = \sum_{n=1}^{m} \left(\sqrt{\frac{\widehat{EI}}{\widehat{\rho A}}} \sqrt{\frac{\rho A_n^*}{EI_n^*}} - 1 \right)^2 + \sum_{n=1}^{m} \left(\frac{\rho A_n^*}{\widehat{\rho A}} \frac{1}{S_{2n}} - \frac{2\sqrt{\rho A_n^*}}{\sqrt{\widehat{\rho A}}} \frac{S_{1n}}{S_{2n}} + 1 \right) \tag{5.11}$$

From the expression for Δ in Eq. (5.11), a local minimum is found by locating the stationary points. Determining the values of $\widehat{EI}$ and $\widehat{\rho A}$ that simultaneously satisfy $\frac{\partial \Delta}{\partial \widehat{EI}} = 0$ and $\frac{\partial \Delta}{\partial \widehat{\rho A}} = 0$ gives

$$\widehat{EI} = \frac{\left\{\sum_{n=1}^{m} \sqrt{\frac{\rho A_n^*}{EI_n^*}}\right\}^2 \left\{\sum_{n=1}^{m} \rho A_n^* \frac{1}{S_{2n}}\right\}^2}{\left\{\sum_{n=1}^{m} \frac{\rho A_n^*}{EI_n^*}\right\}^2 \left\{\sum_{n=1}^{m} \sqrt{\rho A_n^*} \frac{S_{1n}}{S_{n2}}\right\}^2} \tag{5.12a}$$

$$\widehat{\rho A} = \frac{\left\{\sum_{n=1}^{m} \rho A_n^* \frac{1}{S_{2n}}\right\}^2}{\left\{\sum_{n=1}^{m} \sqrt{\rho A_n^*} \frac{S_{1n}}{S_{n2}}\right\}^2} \tag{5.12b}$$

5.1.4 Approximation Method 3 - Modal Participation Factor (MPF)

The third approximation method uses the modal participation factors from the response of the system due to a unit impulse in a weighted average of the perturbation theory reference values EI_n^* and ρA_n^*. Using the perturbation theory mode shapes, the transverse displacement of the string-harnessed system can be expressed as $w(x,t) = \sum_{n=1}^{\infty} g_n(t)\phi_n(x)$. Assuming a unit impulse is applied to the system at a location $x = x_i$, the functions $g_n(t)$ are determined. The steady-state response of the system is given by

$$w(x,t) = \sum_{n=1}^{\infty} \frac{\phi_n(x_i)}{\omega_n} \phi_n(x) \sin(\omega_n t) \tag{5.13}$$

In Eq. (5.13), the ω_n are the frequencies obtained from the perturbation theory. The quantity $\phi_n(x_i)/\omega_n$ is the modal participation factor of the n^{th} mode given a unit impulse at $x = x_i$, see [62].

Using the absolute value of the modal participation factors $\gamma_n^i = |\phi_n(x_i)/\omega_n|$, a weighted average is used to determine the unknown coefficients in the approximate model given an impulse at $x = x_i$.

$$\widehat{EI}_i = \frac{\sum_{n=1}^{m} \gamma_n^i EI_n^*}{\sum_{n=1}^{m} \gamma_n^i} \tag{5.14a}$$

$$\widehat{\rho A}_i = \frac{\sum_{n=1}^{m} \gamma_n^i \rho A_n^*}{\sum_{n=1}^{m} \gamma_n^i} \tag{5.14b}$$

It is obvious that the location of the impulse will directly affect the modal participation factors and the resulting estimates for the approximate bending stiffness and mass per unit length. One such example would be applying the impulse at the node of any of the modes. This would result in the modal participation factor being 0 and is not representative of the overall dynamics of the structure. To overcome this, the average of N evenly spaced impulse locations are used and then the limit as $N \to \infty$ is considered.

$$\begin{aligned}
\widehat{EI} =& \lim_{n\to\infty} \frac{1}{N} \sum_{i=1}^{N} \widehat{EI}_i \\
=& \frac{1}{l} \lim_{n\to\infty} \sum_{i=1}^{N} \frac{\sum_{n=1}^{m} \left| \frac{\phi_n(il/N)}{\omega_n} \right| EI_n^*}{\sum_{n=1}^{m} \left| \frac{\phi_n(il/N)}{\omega_n} \right|} \frac{l}{N} \\
=& \frac{1}{l} \int_0^l \frac{\sum_{n=1}^{m} \left| \frac{\phi_n(x)}{\omega_n} \right| EI_n^*}{\sum_{n=1}^{m} \left| \frac{\phi_n(x)}{\omega_n} \right|} \mathrm{d}x
\end{aligned} \tag{5.15}$$

Applying the steps used to determine $\widehat{EI}$ in Eq. (5.15), the expression for $\widehat{\rho A}$ is found. The final expression for the unknown coefficients in the approximate model using the modal participation factor method is

$$\widehat{EI} = \frac{1}{l} \sum_{n=1}^{m} \left\{ EI_n^* \int_0^l \frac{\left| \frac{\phi_n(x)}{\omega_n} \right|}{\sum_{n=1}^{m} \left| \frac{\phi_n(x)}{\omega_n} \right|} \mathrm{d}x \right\} \tag{5.16a}$$

$$\widehat{\rho A} = \frac{1}{l} \sum_{n=1}^{m} \left\{ \rho A_n^* \int_0^l \frac{\left| \frac{\phi_n(x)}{\omega_n} \right|}{\sum_{n=1}^{m} \left| \frac{\phi_n(x)}{\omega_n} \right|} \mathrm{d}x \right\} \tag{5.16b}$$

Above, the summation and integration may be interchanged since the summation is finite.

5.1.5 Approximation Method 4 - Proper Orthogonal Decomposition (POD)

The final approximation method employs the results of a proper orthogonal decomposition (POD) in a weighted average of the perturbation theory reference values EI_n^* and ρA_n^*. The POD is commonly used in vibration applications to determine the mode shapes and the power associated with each of the modes in the displacement of an experimental

test. Typically, see for example [25, 42, 41], there is a set of N discrete measurement locations where the displacement of the system is measured at M times. For the model approximation, the goals are threefold. First, instead of experimental results the transverse displacement, results of a string-harnessed system given by the perturbation theory and a unit impulse are employed. Secondly, the discretization of N measurement locations at M times is extended from the discrete case to the continuous case. Finally, as was done with the modal participation factor approximation method, the results are averaged over multiple impulse locations.

The steps for the discretized version of the POD are as follows. A matrix $\boldsymbol{W}(i,j)$ is created from the displacement results at the i^{th} sensing location at the j^{th} time. From this matrix of displacement results, the correlation matrix $\boldsymbol{R} = \frac{1}{M}\boldsymbol{W}^\top\boldsymbol{W}$ is formed. The eigenvalues and eigenvectors of $\boldsymbol{R}$ represent the proper orthogonal values (POVs) and proper orthogonal modes (POMs), respectively. The goal is to outline a similar set of steps to determine the POVs when the measurements are no longer discretized in time and space.

Assume a unit impulse at $x = x_i$ and let $w(x,t)$ denote the displacement of the system calculated using the perturbation theory results. The correlation between any two points is given by $R(x_i,x_j) = \frac{1}{M}\sum_{k=1}^{M} w(x_i,t_k)w(x_j,t_k)$. Assume there is a fixed total measurement time, $\overline{T}$, and take the limit as M, the number of points in time when a measurement is made, approaches infinity.

$$\begin{aligned} R(x_i,x_j) &= \lim_{M\to\infty}\frac{1}{M}\sum_{k=1}^{M} w(x_i,t_k)w(x_j,t_k) \\ &= \frac{1}{\overline{T}}\lim_{M\to\infty}\sum_{k=1}^{M} w(x_i,t_k)w(x_j,t_k)\frac{\overline{T}}{M} \\ &= \frac{1}{\overline{T}}\int_0^{\overline{T}} w(x_i,t)w(x_j,t)\,\mathrm{d}t \end{aligned} \tag{5.17}$$

It is seen in Eq. (5.17) that the correlation is continuous in time and no longer depends on a discretization.

Once the correlation matrix is found, an eigenvalue problem is solved in the discrete case. Component wise, the problem can be formulated as $\sum_{k=1}^{N} R(x_i,x_k)f(x_k) = \lambda(N)f(x_i)$. Here, the eigenvalue depends on the number of sensing locations N. As it can be seen, increasing N will cause the left hand side of the component wise eigenvalue to increase. Since it is expected for $f(x_i)$ to remain the same, it must be that the eigenvalue

increases. Consider the case where the correlation matrix is replaced by the correlation function in Eq. (5.17) and the number of points which discretize the spatial domain approaches infinity.

$$\begin{aligned}
\lim_{N\to\infty}\sum_{k=1}^{N} R(x_i,x_k)f(x_k) &= \lim_{N\to\infty}\lambda(N)f(x_i)\\
\lim_{N\to\infty}\sum_{k=1}^{N} R(x_i,kl/N)f(kl/N)\frac{l}{N} &= \lim_{N\to\infty}\frac{l}{N}\lambda(N)f(x_i)\\
\int_0^l R(x_i,s)f(s)\,\mathrm{d}s &= \left[\lim_{N\to\infty}\frac{l}{N}\lambda(N)\right]f(x_i)\\
\int_0^l R(x_i,s)f(s)\,\mathrm{d}s &= \overline{\lambda}f(x_i) \qquad (5.18)
\end{aligned}$$

Equation (5.18) holds for each point x_i and thus the eigenvalue problem for the proper orthogonal decomposition which is independent of a spatial discretization is

$$\int_0^l R(x,s)f(s)\,\mathrm{d}s = \overline{\lambda}f(x) \qquad (5.19)$$

Since only a finite number of modes from the perturbation theory are used to determine the displacement of the system due to a unit impulse, the eigenfunction of the problem in Eq. (5.19) can be expressed as the finite sum $f(x) = \sum_{n=1}^{m} c_n\phi_n(x)$. In the expression for the eigenfunction the mode shapes from the perturbation theory are used. For $\overline{\lambda} \neq 0$, substitution of the eigenfunction in Eq. (5.19) leads to

$$\sum_{n=1}^{m}\overline{\lambda}c_n\phi_n(x) = \sum_{n=1}^{m}\sum_{j=1}^{m} c_jA_{nj}\phi_n(x) \qquad (5.20)$$

where

$$A_{nj} = \sum_{k=1}^{m}\left(\frac{1}{\overline{T}}\int_0^{\overline{T}} g_n(t)g_k(t)\,\mathrm{d}t\right)\left(\int_0^l \phi_k(s)\phi_j(s)\,\mathrm{d}s\right)$$

From Eq. (5.20), it follows that $\overline{\lambda}c_n = \sum_{j=1}^{m} c_jA_{nj}$ for each n. This is a component wise expression for the eigenvalue problem $Ac = \overline{\lambda}c$, where c is a vector of the c_n in the expansion for the eigenfunction.

Once the eigenvalues $\overline{\lambda}_n$ and associated eigenfunctions $f_n(x) = \sum_{n=1}^{m} c_n\phi_n(x)$ are determined, each eigenfunction $f_n(x)$ is associated with the mode shape which is most similar

from the perturbation theory. This is achieved by looking at the values of c. Typically, the entries in c are small with the exception of a single value whose absolute value is near 1. Once this association is done, the eigenvalues $\overline{\lambda}_n$ that represent the power associated with the mode are associated with a mode from the perturbation theory. This is the manner in which the weights in the weighted average of the perturbation theory reference values are determined. For a system with a unit impulse at $x = x_i$, the coefficients in the approximate model are

$$\widehat{EI}_i = \frac{\sum_{n=1}^{m} \overline{\lambda}_n^i EI_n^*}{\sum_{n=1}^{m} \overline{\lambda}_n^i} \tag{5.21a}$$

$$\widehat{\rho A}_i = \frac{\sum_{n=1}^{m} \overline{\lambda}_n^i \rho A_n^*}{\sum_{n=1}^{m} \overline{\lambda}_n^i} \tag{5.21b}$$

As with the modal participation factor, the location of the unit impulse plays an important role in the values determined for the approximate model. Therefore, an average using multiple actuation locations is determined. Since for the proper orthogonal decomposition method it is not possible to extend the results easily to the continuous case, a quadrature method is employed to determine the average. Assuming that $P+1$ equally spaced actuation locations are considered, using the trapezoidal method for numerical integration leads to the final expression for the unknown coefficients.

$$\widehat{EI} = \frac{1}{2P} \sum_{i=1}^{P} \left\{ \widehat{EI}_i + \widehat{EI}_{i+1} \right\} \tag{5.22a}$$

$$\widehat{\rho A} = \frac{1}{2P} \sum_{i=1}^{P} \left\{ \widehat{\rho A}_i + \widehat{\rho A}_{i+1} \right\} \tag{5.22b}$$

5.2 Numerical Results

5.2.1 Periodic Wrapping Patterns

The same system parameters as those used in Section 4.2 are employed for the current numerical simulations. That is to say, a system with 6 fundamental elements and the following system parameters are used: $b = 0.01$ m, $h = 0.0015$ m, $l = 0.25$ m, $E_b = 6.89 \times 10^{10}$, N/m^2, $\rho_b = 2700$ kg/m^3, $r_s = 0.00035$ m, $E_s = 1.5 \times 10^{11}$ N/m^2, $\rho_s = 1400$

kg/m^3, and $T_s = 25$ N. Furthermore, a total sampling interval of 0.1 s and $P = 25$ actuation locations are used in the POD method throughout all the simulations.

In addition to the results obtained from the approximation methods, the results of the previously developed homogenization method are presented. The abbreviation "HOM" will be used to denote the equivalent continuum model obtained by homogenization. For completeness, the coefficients of the HOM model are presented here using the notation of the current section. For the diagonal wrapping pattern, the coefficients of the HOM model are given by

$$\begin{aligned}\widehat{EI} =& E_b I_b + E_s A_s \overline{h}^2 \cos^3(\theta) + T_s \cos(\theta) \left[\overline{h}^2 - \frac{I_b}{A_b}\right] \\ \widehat{\rho A} =& \rho_b A_b + \frac{\rho_s A_s \tan(\theta)}{\overline{b}} \left[\frac{\overline{b}}{\sin(\theta)} + 2\overline{h} + \overline{b}\right]\end{aligned}$$

and $L = 2\overline{b}/\tan(\theta)$ is the length of a single fundamental element. For the zigzag wrapping pattern, the coefficients of the HOM model are given by

$$\begin{aligned}\widehat{EI} =& E_b I_b + \frac{E_s A_s \overline{h}^2 \cos^3(\theta)(\overline{b} + \overline{h}/3)}{\overline{b} + \overline{h}} + T_s \cos(\theta) \left[\frac{\overline{h}^2(\overline{b} + \overline{h}/3)}{\overline{b} + \overline{h}} - \frac{I_b}{A_b}\right] \\ \widehat{\rho A} =& \rho_b A_b + \frac{\rho_s A_s}{\cos(\theta)}\end{aligned}$$

and $L = (4\overline{b} + 4\overline{h})/\tan(\theta)$ is the length of a single fundamental element.

As was done for the numerical simulations of the string-harnessed systems in Chapter 4, an analytical solution for the diagonal wrapping pattern is employed and an FEA is used for the zigzag wrapping pattern. Collectively, these results will be referred to as the 'exact results' throughout this chapter. The details of the analytical solution are given in Appendix D and the FEA details are given in Appendix E.

Consider first the effect of variable string modulus on the frequency results. Figures 5.1 and 5.2 present the fundamental and tenth mode frequency for the exact, perturbation theory, the HOM, as well as the various proposed methods for model approximation results. Multiple boundary conditions are considered with the diagonal wrapping pattern considered in Fig. 5.1 and the zigzag wrapping pattern considered in Fig. 5.2.

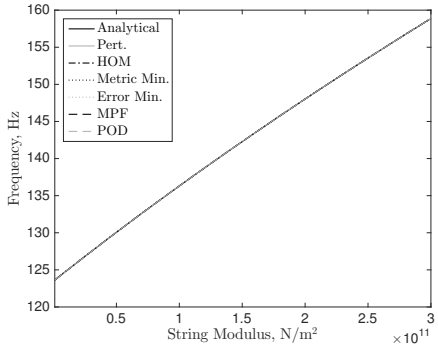

(a) CC, Mode 1

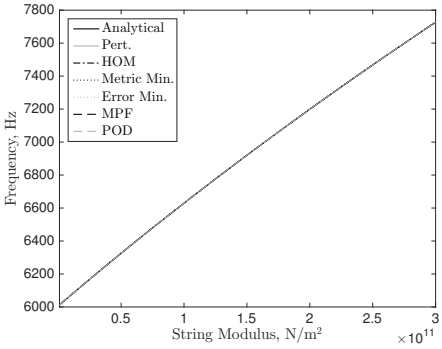

(b) CC, Mode 10

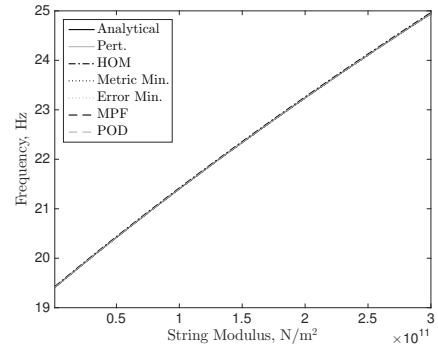

(c) CF, Mode 1

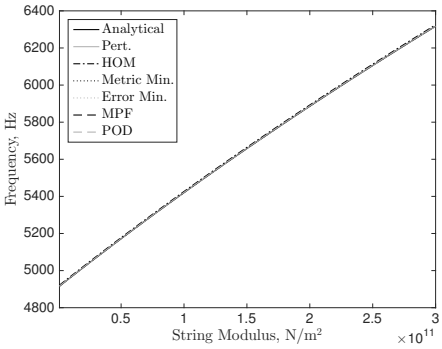

(d) CF, Mode 10

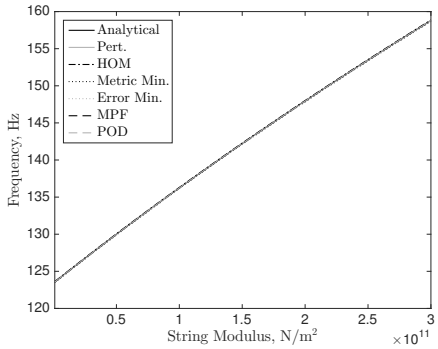

(e) FF, Mode 1

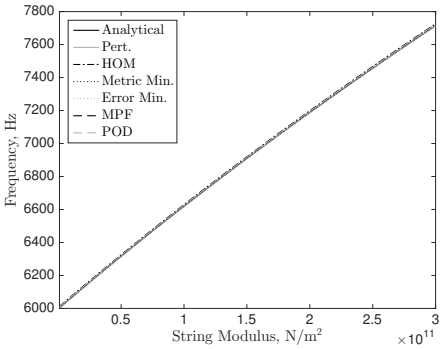

(f) FF, Mode 10

Figure 5.1: Frequency results for fundamental and tenth mode given variable string modulus and diagonal wrapping pattern.

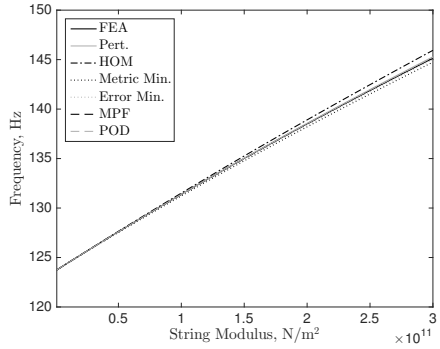

(a) CC, Mode 1

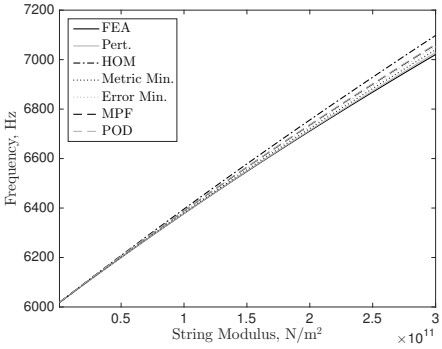

(b) CC, Mode 10

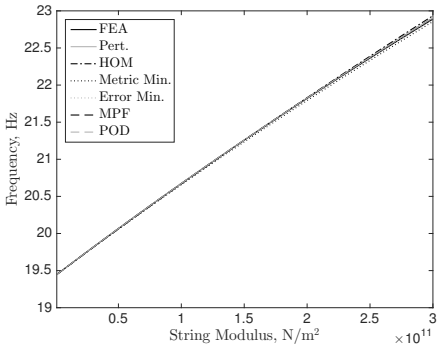

(c) CF, Mode 1

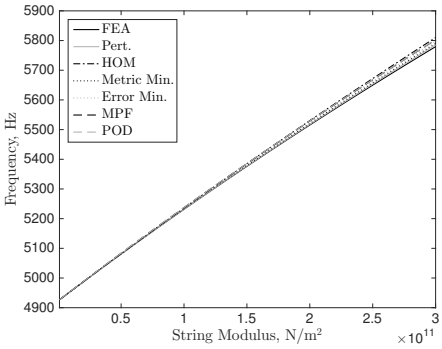

(d) CF, Mode 10

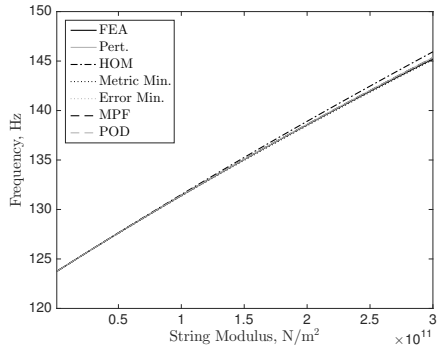

(e) FF, Mode 1

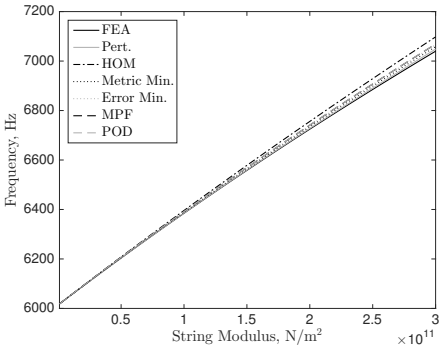

(f) FF, Mode 10

Figure 5.2: Frequency results for fundamental and tenth mode given variable string modulus and zigzag wrapping pattern.

As the modulus of the string is increased, there is an increase in the stiffening effect due to the string. As a result, the frequencies for the string-harnessed system are expected to increase with increasing string modulus. This behaviour is clearly observed in the fundamental and tenth modes of the system given various boundary conditions for both the diagonal and zigzag wrapping patterns in Figs. 5.1 and 5.2.

Focusing on the diagonal wrapping pattern results in Fig. 5.1, it is seen that the various results for the frequencies match very well with the analytical results. This indicates that the perturbation theory is quite accurate in predicting the frequencies of the string-harnessed system, and also that the various proposed methods for model approximation are capable of matching the perturbation theory results with minimal error. In contrast, it is seen in Fig. 5.2 for the zigzag wrapping pattern that the HOM slightly overpredicts the values of the frequencies. Furthermore, the various proposed methods for approximation produce noticeable, yet relatively small, differences in the frequencies, particularly for higher values of the string modulus. These differences are also more noticeable for the tenth mode when compared to the fundamental mode.

Next, the effect of variable string modulus on the results for the coefficients $\widehat{EI}$ and $\widehat{\rho A}$, as determined by the approximation methods outlined in the current work, is presented in Figs. 5.3 and 5.4. In addition, the HOM coefficient values are presented for comparison. The results for variable string modulus given a diagonal and zigzag wrapping pattern are presented in Figs. 5.3 and 5.4, respectively.

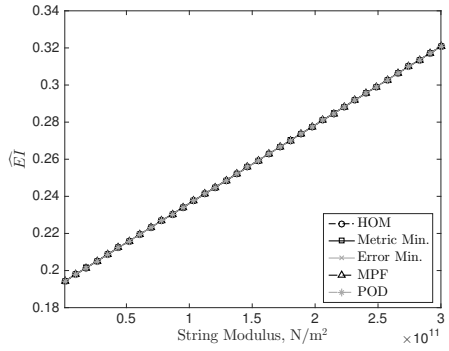

(a) $\widehat{EI}$, CC

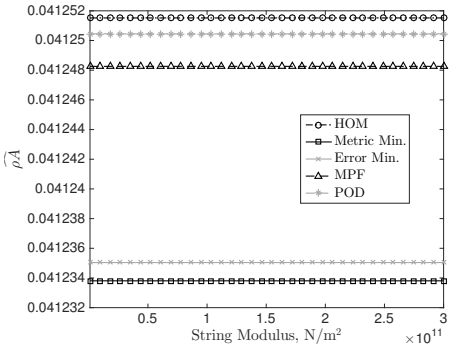

(b) $\widehat{\rho A}$, CC

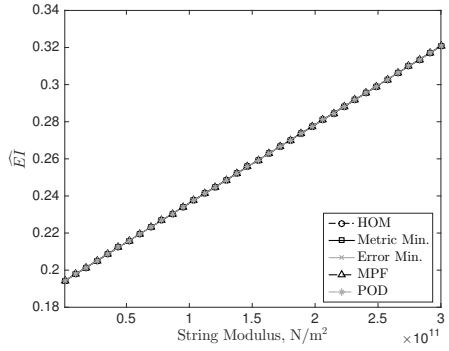

(c) $\widehat{EI}$, CF

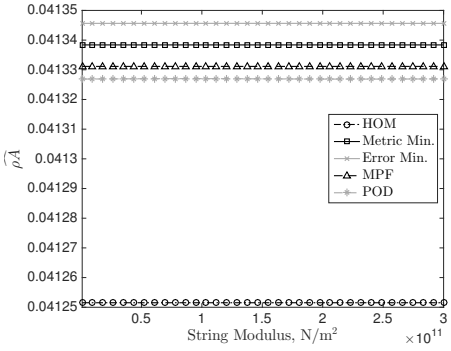

(d) $\widehat{\rho A}$, CF

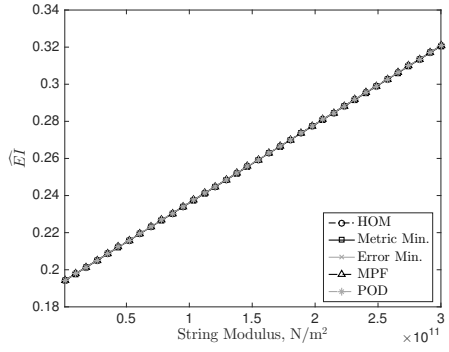

(e) $\widehat{EI}$, FF

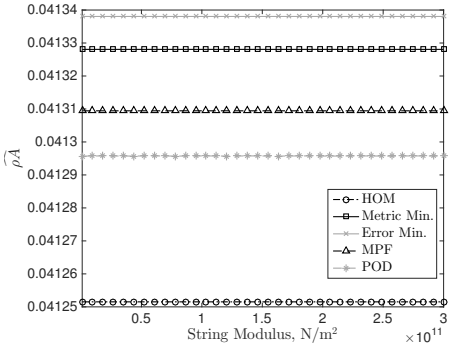

(f) $\widehat{\rho A}$, FF

Figure 5.3: Results for $\widehat{EI}$ and $\widehat{\rho A}$ coefficients for diagonal wrapping pattern with variable string modulus.

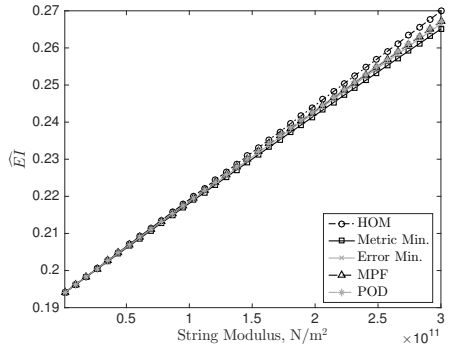

(a) $\widehat{EI}$, CC

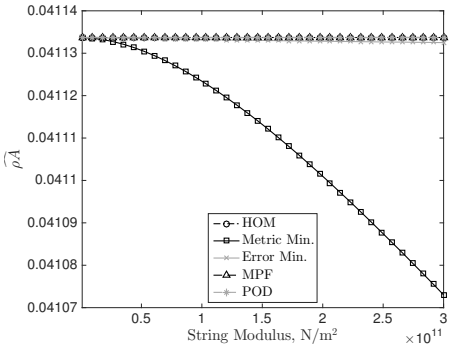

(b) $\widehat{\rho A}$, CC

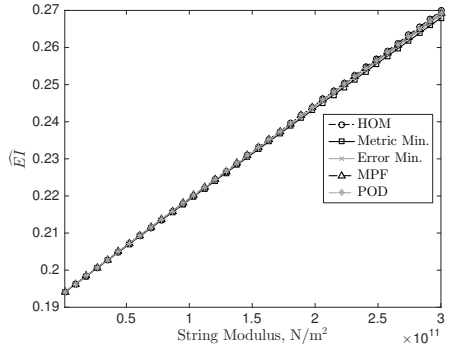

(c) $\widehat{EI}$, CF

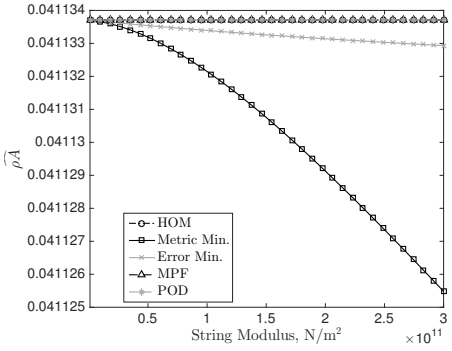

(d) $\widehat{\rho A}$, CF

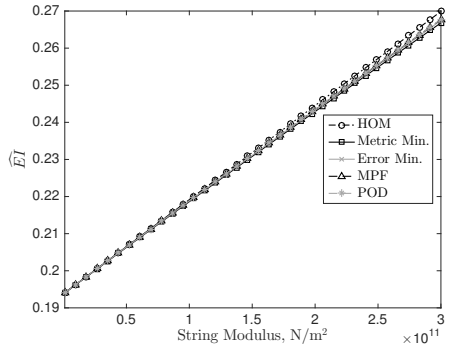

(e) $\widehat{EI}$, FF

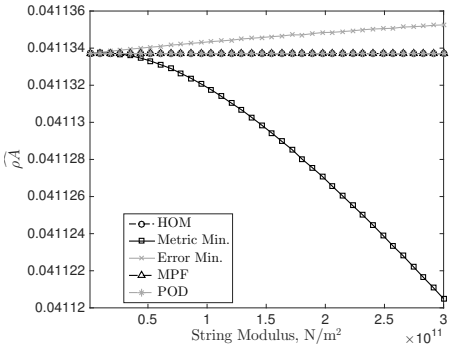

(f) $\widehat{\rho A}$, FF

Figure 5.4: Results for $\widehat{EI}$ and $\widehat{\rho A}$ coefficients for zigzag wrapping pattern with variable string modulus.

With respect to the $\widehat{EI}$ coefficient, it is seen for both the diagonal and zigzag wrapping patterns that an increase in the string modulus leads to an increase in $\widehat{EI}$. Since increasing the modulus of the string increases the stiffness in the system, this behaviour is expected.

It is seen in Fig. 5.3 for the diagonal wrapping pattern that an increase in the string modulus leads to no change in the $\widehat{\rho A}$ coefficient. This behaviour is due to the added stiffness of the string being a constant value throughout the entire system in the diagonal wrapping pattern. Hence as the string modulus is increased the reference values ρA_n^* and the nondimensional mode shapes determined by the perturbation theory do not change. For this reason the value for $\widehat{\rho A}$ is unaffected by changes in the string modulus. As expected, the HOM value for $\widehat{\rho A}$ is constant across the various boundary conditions since this method produces a single value.

Figure 5.4 demonstrates that for the zigzag wrapping pattern the value for $\widehat{\rho A}$ is typically constant, with the exception for the metric and error minimizations. It is expected that as the string modulus increases that this should not affect the results for $\widehat{\rho A}$. For the metric and error minimization methods, it is seen in the expressions for the unknown coefficients that the integrals S_{1n} and S_{2n} depend both on the values of EI_n^* and ρA_n^*, as well as the corrections to the mode shape cause by perturbations in the bending stiffness and mass per unit length. As the string modulus is increased, and since the bending stiffness is not a constant throughout the entire system with a zigzag wrapping pattern, the values for EI_n^* and the correction in the nondimensional mode shape are altered. For these reasons, the value of $\widehat{\rho A}$ is not constant for the metric and error minimization with variable string modulus.

The first step in quantifying the accuracy of each of the proposed approximation models is to examine the error between these and the perturbation theory results. It is quite important to investigate this since the perturbation theory results are taken as the exact values that the models should match. To this end, the percentage error in the fundamental frequency and associated mode shape are considered for variable string modulus. The error in the mode shape is calculated by

$$\frac{\int_0^l \left(\phi_{\text{Approx.}}(x) - \phi_{\text{Pert.}}(x)\right)^2 \, \mathrm{d}x}{\int_0^l \phi_{\text{Pert.}}^2(x) \, \mathrm{d}x}$$

The results for the diagonal wrapping pattern are presented in Fig. 5.5 and the zigzag pattern in Fig. 5.6.

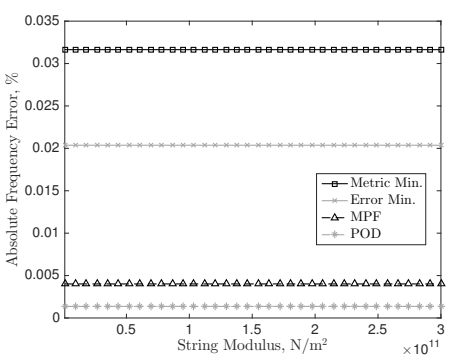

(a) Frequencies, CC

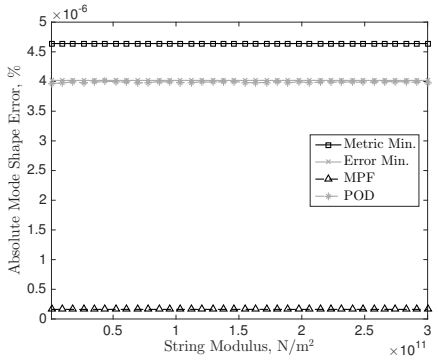

(b) Mode shapes, CC

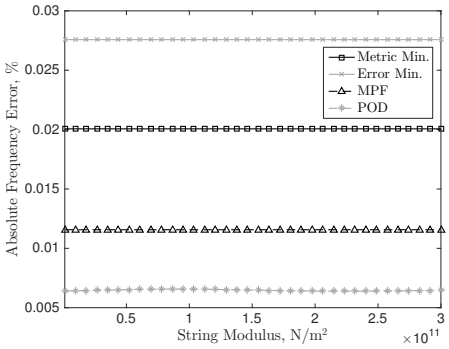

(c) Frequencies, CF

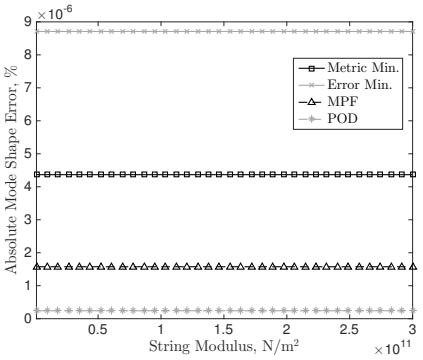

(d) Mode shapes, CF

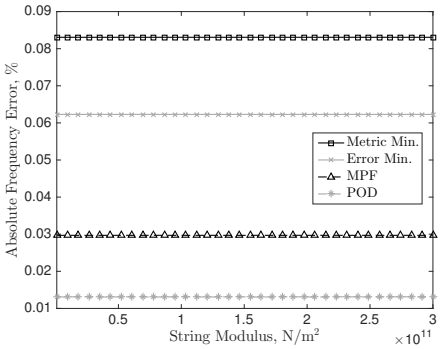

(e) Frequencies, FF

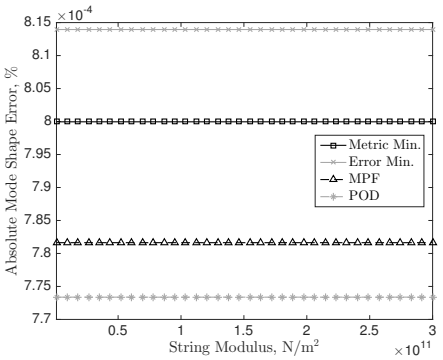

(f) Mode shapes, FF

Figure 5.5: Error in fundamental frequency and mode shape of approximate models to perturbation theory given variable string modulus and diagonal wrapping pattern.

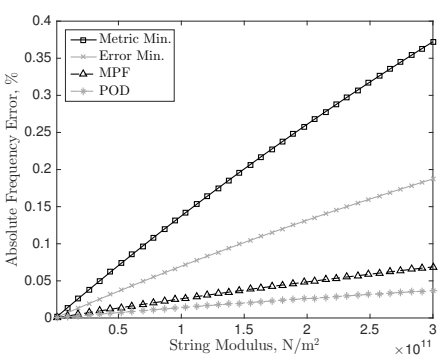

(a) Frequencies, CC

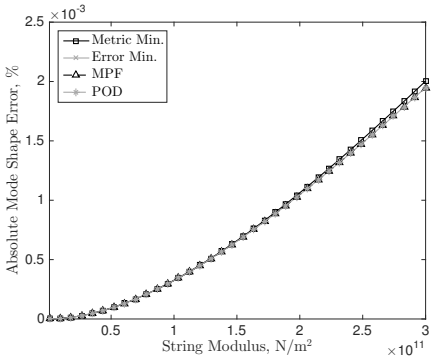

(b) Mode shapes, CC

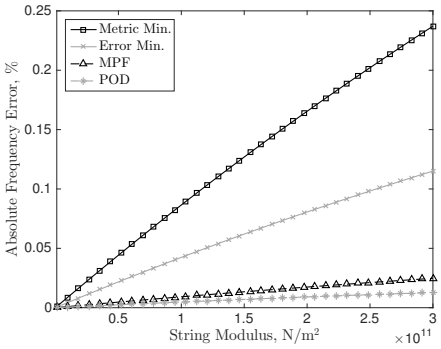

(c) Frequencies, CF

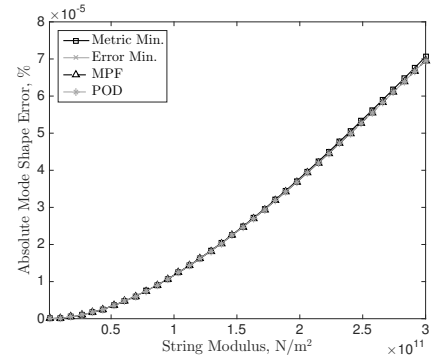

(d) Mode shapes, CF

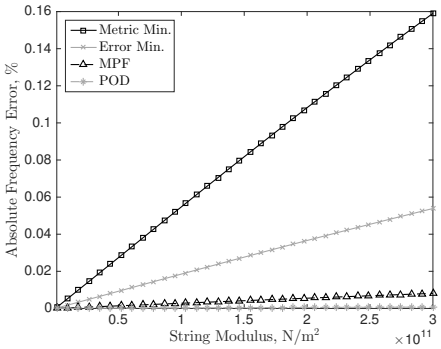

(e) Frequencies, FF

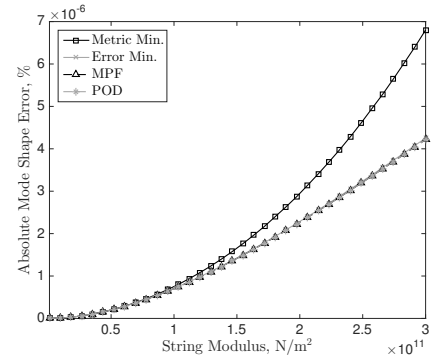

(f) Mode shapes, FF

Figure 5.6: Error in fundamental frequency and mode shape of approximate models to perturbation theory given variable string modulus and zigzag wrapping pattern.

It is seen in Fig. 5.5 that the error between the proposed methods and the perturbation theory results is unaffected by changes in the string modulus. This is due to the diagonally wrapped system having a constant value for the bending stiffness in the system. In this case, the approximation methods simply choose this value for the unknown coefficient $\widehat{EI}$ and the error in the models is due to variable mass per unit length caused by lumped masses. When the string modulus is varied, this does not affect the mass per unit length of the string-harnessed system and thus no additional error is introduced, causing a constant value for the error.

For the case of the zigzag wrapping pattern in Fig. 5.6, it is observed that the error in the fundamental frequency and mode shape increases as the modulus of the string increases. As the modulus of the string increases, the frequencies of the string-harnessed system are less likely to follow the pattern of a constant coefficient EB model. This type of behaviour was previously seen in Section 2.3.10. This directly corresponds to higher errors when using the proposed models as they attempt to predict the frequencies using a constant coefficient EB model.

A clear pattern is seen in Figs. 5.5 and 5.6 with respect to the errors reported for the frequencies by the various proposed models. It is seen for the fundamental frequency that the POD method always produces the most accurate result to the perturbation theory, then the MPF, and finally the metric and error minimization methods produce the largest errors. When a system is excited by a unit impulse, the fundamental mode accounts for a significant contribution of the total displacement response. Because of this, the MPF and POD methods place a large weight on matching the fundamental mode in comparison to the higher modes. For this reason, the MPF and POD are expected to provide quite accurate estimates for the fundamental mode of the system. As the POD is seen to be more accurate than the MPF for the numerical simulations, this indicates that the POD places more importance on matching the fundamental mode than the MPF. With respect to the mode shape, it is observed that for both wrapping patterns and all boundary conditions that the levels of error are quite small and quite similar across the various proposed methods.

In addition to the accuracy of the proposed methods for the fundamental frequency and mode shape, the error with respect to the perturbation theory over multiple modes is considered. To this end, the sum of the absolute error of the first 10 modes of the system is considered and the average value of this sum for variable string modulus is reported. The results for both wrapping patterns, each of the proposed approximation methods, and the various boundary conditions are presented in Table 5.1.

Table 5.1: Average sum of absolute percentage of error to perturbation theory for the first 10 natural frequencies and associated mode shapes for variable string modulus

	Frequency Results			Mode Shape Results		
Result	CC	CF	FF	CC	CF	FF
	Diagonal Pattern			*Diagonal Pattern*		
Metric Min.	0.5542	0.4579	0.5663	0.01383277	0.08690176	0.11976672
Error Min.	0.5307	0.4578	0.5311	0.01383255	0.08689404	0.11975214
MPF	0.4979	0.4808	0.5995	0.01385824	0.08692482	0.11987199
POD	0.4931	0.5012	0.6966	0.01383255	0.08697584	0.12008665
	Zigzag Pattern			*Zigzag Pattern*		
Metric Min.	1.1416	0.7221	0.6788	0.28091905	0.03531647	0.06974415
Error Min.	0.6564	0.4138	0.3320	0.28079071	0.03531444	0.06973624
MPF	0.7414	0.5086	0.2661	0.28079079	0.03531448	0.06973638
POD	0.8399	0.5527	0.2725	0.28079079	0.03531448	0.06973637

It is seen in Table 5.1 that the error minimization method always produces the smallest sum of absolute error for the mode shapes, regardless of wrapping pattern or boundary conditions. Furthermore, it is seen that typically the error minimization method produces the smallest error in the average sum of the absolute error for the frequencies. In the cases where the error minimization is not the most accurate method, CC boundary conditions with a diagonal wrapping pattern and FF boundary conditions with a zigzag wrapping pattern, it is observed that the error in the frequencies is quite similar to that of the the most accurate methods, the MPF and POD. Overall, the error minimization is the best approach for approximating the string-harnessed when multiple modes are in consideration.

The error minimization does not always produce the smallest average sum of absolute error for the frequencies due to the form of the objective function in Eq. (5.10). Using the results of Table 5.1 for the mode shapes and the square of the frequency results, it is seen that for the objective function the component involving the mode shapes will have a greater influence on its value when compared to the frequencies. For this reason, the error minimization produces the smallest average sum of absolute error for the mode shapes. Furthermore, changing the results for $\widehat{EI}$ and $\widehat{\rho A}$ slightly to obtain more accurate frequency results in the error minimization method would lead to an increase in the mode shape error, the component that is seen as more important in the objective function. In contrast, the MPF and POD methods rely solely on a weighted average of the perturbation theory results. Therefore, the MPF and POD methods at times produce values for the unknown coefficients that produce more accurate frequency results than the error minimization, at

the cost of larger errors in the mode shape results.

Finally, the average sum of absolute error, given variable string modulus, of the perturbation theory, the HOM method, and the four proposed approximation methods to the exact solutions is presented in Table 5.2. The results for both wrapping patterns and the various boundary conditions are presented.

Table 5.2: Average sum of absolute percentage of error to exact solution for the first 10 natural frequencies and associated mode shapes for variable string modulus

	Frequency Results			Mode Shape Results		
Result	CC	CF	FF	CC	CF	FF
	Diagonal Pattern			*Diagonal Pattern*		
Perturbation	0.0000	0.0001	0.0001	0.00000017	0.00001359	0.00002160
HOM	0.4931	1.1887	1.0994	0.01383303	0.08639492	0.11854532
Metric Min.	0.5541	0.4578	0.5662	0.01379329	0.08529998	0.11742475
Error Min.	0.5307	0.4578	0.5309	0.01379307	0.08529006	0.11740543
MPF	0.4979	0.4807	0.5994	0.01381879	0.08532523	0.11753883
POD	0.4931	0.5012	0.6965	0.01382800	0.08534698	0.11768770
	Zigzag Pattern			*Zigzag Pattern*		
Perturbation	0.2911	0.2745	0.2986	0.00496480	0.00121895	0.00170672
HOM	3.1079	1.0006	2.1380	0.35367788	0.04910780	0.09235113
Metric Min.	0.9572	0.5639	0.4839	0.35398185	0.04910468	0.09236657
Error Min.	0.6590	0.4419	0.3572	0.35368200	0.04909923	0.09234990
MPF	0.9455	0.7536	0.5327	0.35367789	0.04909883	0.09235114
POD	1.0936	0.8145	0.5697	0.35367788	0.04909883	0.09235113

In Table 5.2, it is seen for the diagonal wrapping pattern that the error between the perturbation theory and the analytical results is quite small for both the frequency and mode shapes, given all the boundary conditions. Due to the accuracy of the perturbation theory for the diagonal wrapping pattern, the errors between the approximation methods and the analytical results, Table 5.2, are almost identical to the error between the approximation methods and the perturbation theory, Table 5.1. On the other hand, it is seen for the case of the zigzag wrapping pattern that the error between the perturbation theory and the FEA is not negligible. Comparing the zigzag wrapping pattern errors of the approximation methods to the perturbation theory, Table 5.1, with the errors of the approximation methods to the FEA, Table 5.2, it is observed that the values are significantly changed. Furthermore, in certain cases the error with respect to the FEA will be larger than the

error with respect to the perturbation theory, and other times the error with respect to the FEA will be smaller than the error with respect to the perturbation theory. The former case occurs, for example, when the perturbation theory overpredicts the FEA frequencies and an approximation method overpredicts the perturbation theory frequencies. The latter case occurs, for example, when the perturbation theory overpredicts the FEA frequencies and an approximation method slightly underpredicts the perturbation theory frequencies.

In Table 5.2 the average sum of absolute error for the HOM method is typically larger than any of the proposed approximation methods when considering the frequencies. The exception occurs for CC boundary conditions and a diagonal wrapping pattern, however in this case the results are quite similar across the 5 results. A noticeable increase in accuracy is observed in the frequency results for the zigzag wrapping pattern when comparing the proposed approximation methods to the HOM method. The results in Table 5.2 clearly indicate that using either of the proposed approximation methods will yield similar or smaller levels of error in predicting the frequencies compared to the HOM method for the diagonal wrapping pattern, and offer a considerable increase in accuracy in predicting the frequencies compared to the HOM method for the zigzag wrapping pattern. The sum of absolute error for the mode shapes is almost identical regardless of the method used or the boundary conditions.

With respect to the four approximation methods, it is seen in Table 5.2 that the error minimization method typically produces the smallest sum of absolute error for the first 10 frequencies of the system. The next smallest average error is given by the metric minimization method. This is expected since the error and metric minimization methods place equal weight on matching the frequencies and mode shapes of all the modes of interest. As previously mentioned the MPF and POD place a higher weight on matching the lower modes, particularly the fundamental mode, and therefore larger errors in the higher modes will occur. This then results in a larger sum of the absolute error for both the MPF and POD methods. This indicates that the method that should be implemented to approximate the string-harnessed system will depend on the importance, for the user, of the fundamental mode with respect to the higher modes of the system.

Consider next the effect of variable string density on the frequency results. Figures 5.7 and 5.8 present the fundamental and tenth mode frequency for the exact, perturbation theory, the HOM, as well as the various proposed methods for model approximation results. Multiple boundary conditions are considered and the diagonal wrapping pattern is considered in Fig. 5.7, and the zigzag wrapping pattern is considered in Fig. 5.8.

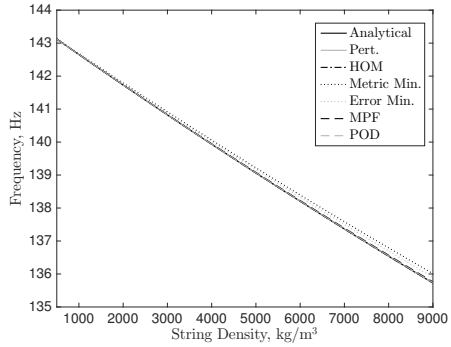

(a) CC, Mode 1

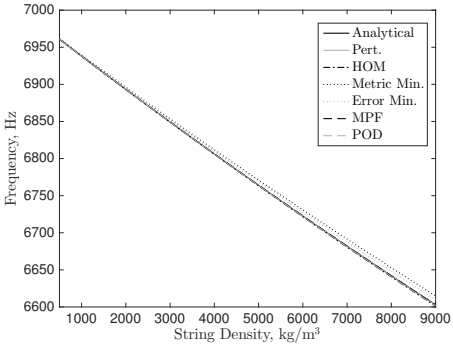

(b) CC, Mode 10

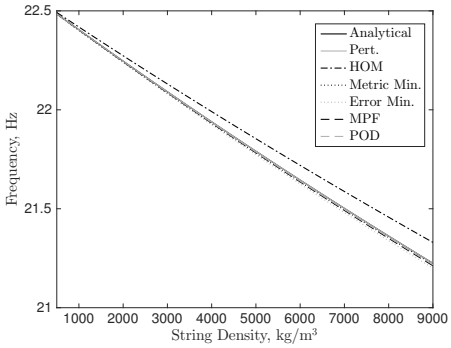

(c) CF, Mode 1

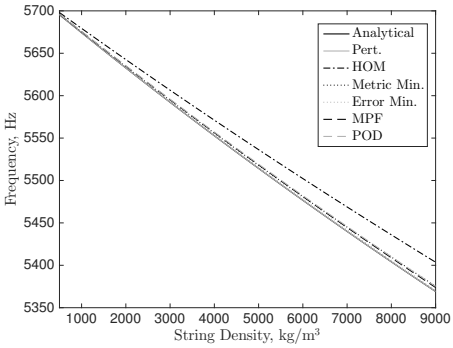

(d) CF, Mode 10

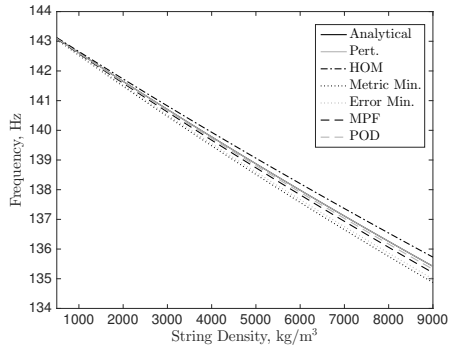

(e) FF, Mode 1

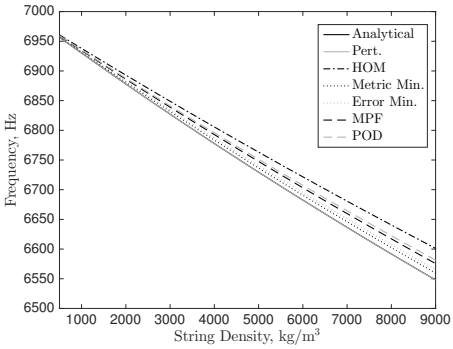

(f) FF, Mode 10

Figure 5.7: Frequency results for fundamental and tenth mode given variable string density and diagonal wrapping pattern.

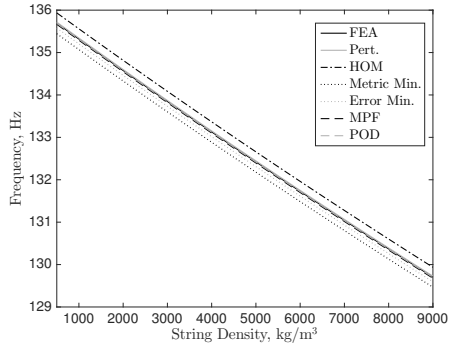

(a) CC, Mode 1

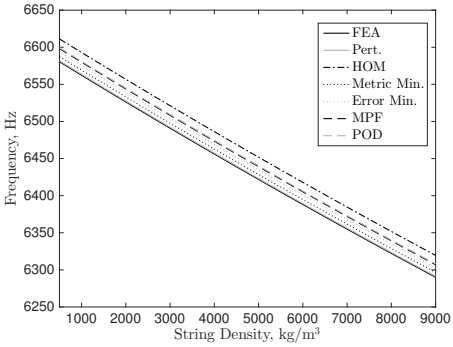

(b) CC, Mode 10

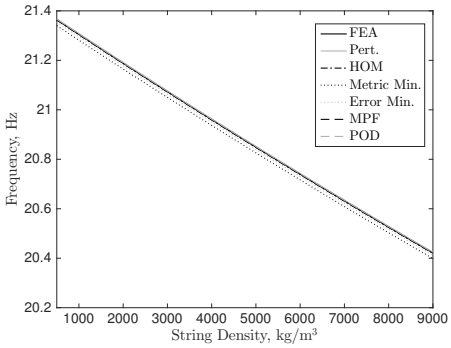

(c) CF, Mode 1

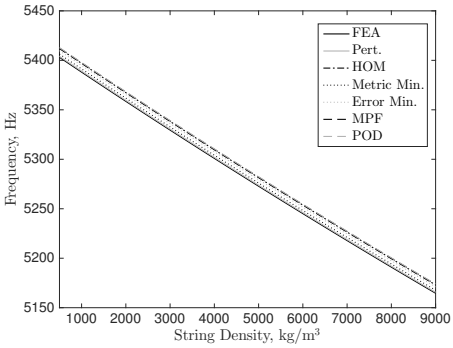

(d) CF, Mode 10

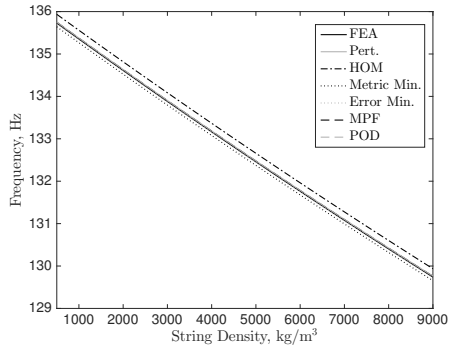

(e) FF, Mode 1

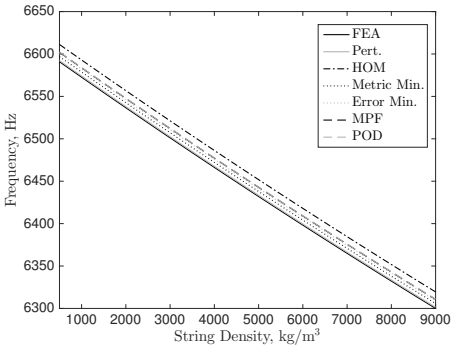

(f) FF, Mode 10

Figure 5.8: Frequency results for fundamental and tenth mode given variable string density and zigzag wrapping pattern.

As the density of the string is increased, there is an increase in the total mass added to the system by the string. As a result, the frequencies for the string-harnessed system are expected to decrease with increasing string density. This behaviour is clearly observed in the fundamental and tenth modes of the system given various boundary conditions for both the diagonal and zigzag wrapping patterns in Figs. 5.7 and 5.8.

For the diagonal wrapping pattern results in Fig. 5.7, it is observed that as the density of the string increases, the differences in the frequencies predicted by the approximation methods are more noticeable. Furthermore, for the case of CF boundary conditions, it is seen that the HOM model overpredicts the analytical results somewhat significantly when compared to the approximation methods. For the zigzag wrapping pattern results in Fig. 5.8, it is first observed that the HOM model overpredicts the frequencies when compared to the FEA results, particularly for CC and FF boundary conditions. Since the mass per unit length in the zigzag pattern with constant wrapping angle is the same at each point in the system, the mass per unit length in the HOM model is exactly the actual value of the string-harnessed system. Therefore it is concluded that the overprediction in the case of variable string density is due to the overprediction of the added stiffness of the string to the system, as was seen in the case of variable string modulus. This highlights the advantages of using the model approximation methods instead of the HOM method. Furthermore, the various approximation methods are all quite accurate when compared to the FEA and perturbation theory results.

Next, the results for the coefficients $\widehat{EI}$ and $\widehat{\rho A}$ from the various approximation methods and the HOM method are presented for variable string density. The results for the diagonal wrapping pattern are presented in Fig. 5.9 and the results for the zigzag wrapping pattern are presented in Fig. 5.10.

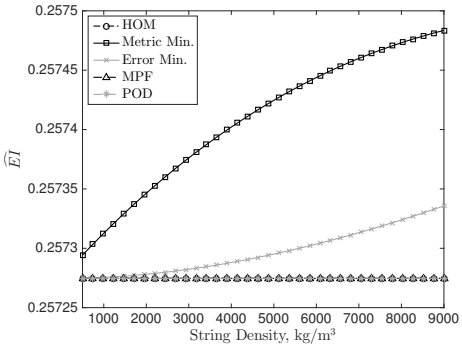

(a) $\widehat{EI}$, CC

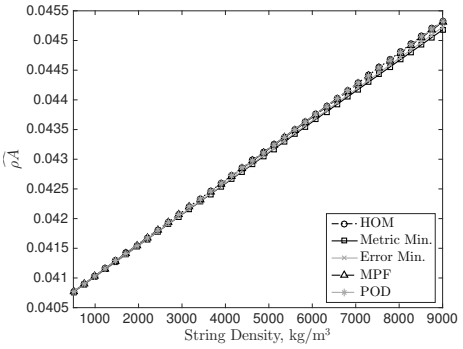

(b) $\widehat{\rho A}$, CC

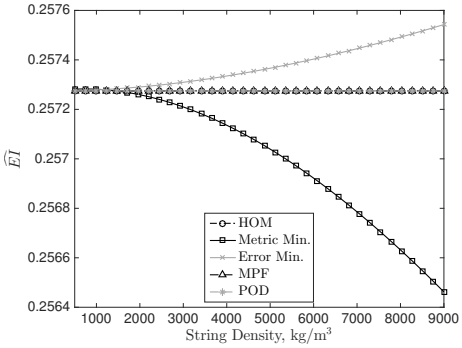

(c) $\widehat{EI}$, CF

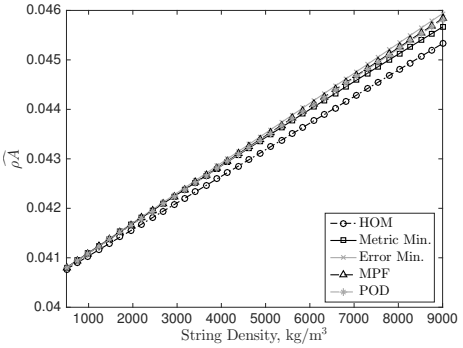

(d) $\widehat{\rho A}$, CF

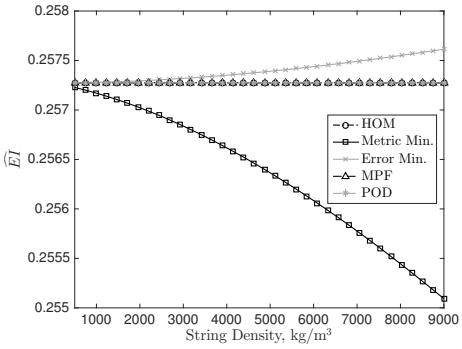

(e) $\widehat{EI}$, FF

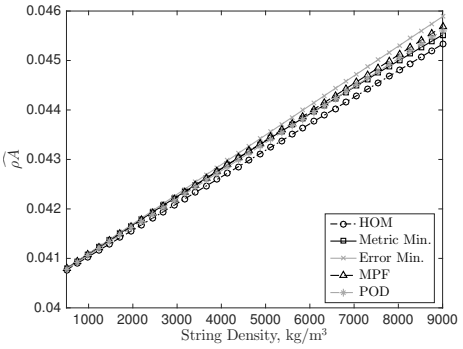

(f) $\widehat{\rho A}$, FF

Figure 5.9: Results for $\widehat{EI}$ and $\widehat{\rho A}$ coefficients for diagonal wrapping pattern with variable string density.

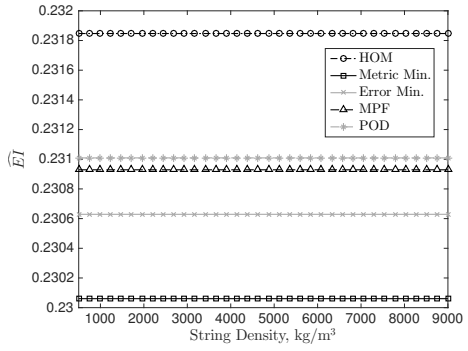

(a) $\widehat{EI}$, CC

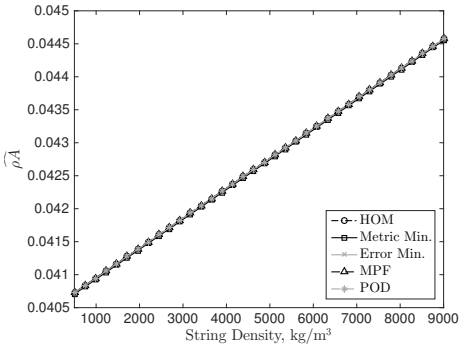

(b) $\widehat{\rho A}$, CC

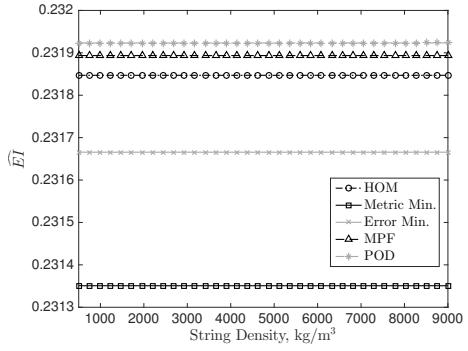

(c) $\widehat{EI}$, CF

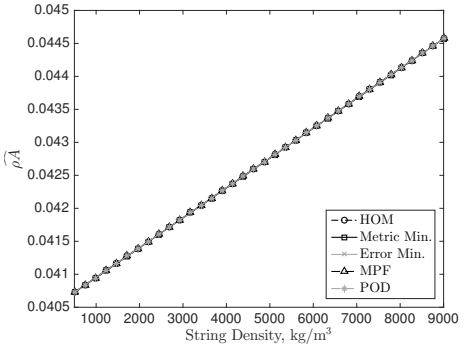

(d) $\widehat{\rho A}$, CF

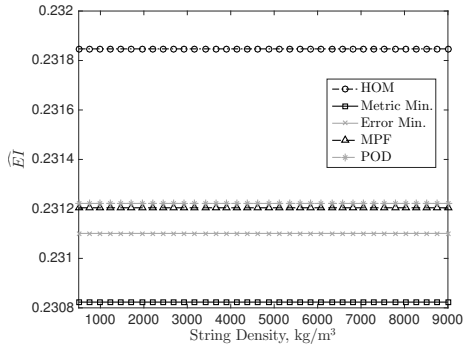

(e) $\widehat{EI}$, FF

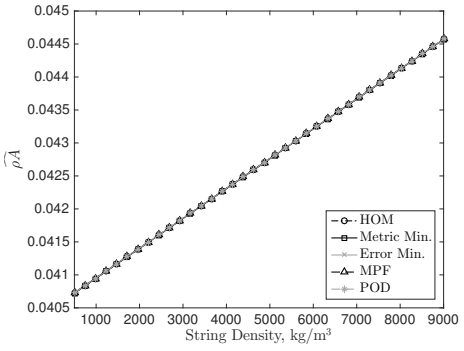

(f) $\widehat{\rho A}$, FF

Figure 5.10: Results for $\widehat{EI}$ and $\widehat{\rho A}$ coefficients for zigzag wrapping pattern with variable string density.

With respect to the $\widehat{\rho A}$ coefficient, it is seen for both the diagonal and zigzag wrapping patterns that an increase in the string density leads to a decrease in $\widehat{\rho A}$. Since increasing the density of the string increases the total mass of the system, this behaviour is expected.

Figure 5.9 demonstrates that for the diagonal wrapping pattern the value for $\widehat{EI}$ is typically constant, with the exception for the metric and error minimizations. It is expected that as the string density increases that this should not affect the results for $\widehat{EI}$. For the metric and error minimization methods, it is seen in the expressions for the unknown coefficients that the integrals S_{1n} and S_{2n} depend both on the values of EI_n^* and ρA_n^*, as well as the corrections to the mode shape cause by perturbations in the bending stiffness and mass per unit length. As the string density is increased, and since the mass per unit length is not a constant throughout the entire system due to lumped masses in a diagonal wrapping pattern, the values for ρA_n^* and the correction in the nondimensional mode shape are altered. For these reasons, the value of $\widehat{EI}$ is not constant for the metric and error minimization with variable string modulus.

It is seen in Fig. **??** for the zigzag wrapping pattern that an increase in the string density leads to no change in the $\widehat{EI}$ coefficient. This behaviour is due to the added mass of the string being a constant value throughout the entire system in the zigzag wrapping pattern. Hence as the string density is increased the reference values EI_n^* and the nondimensional mode shapes determined by the perturbation theory do not change. For this reason the value for $\widehat{EI}$ is unaffected by changes in the string density. As expected, the HOM value for $\widehat{EI}$ is constant across the various boundary conditions since this method produces a single value.

The first step in quantifying the accuracy of each of the proposed approximation models given variable string density is to examine the error between these and the perturbation theory results. Recall that the perturbation theory results were the results the approximate models attempted to match. The results for the diagonal wrapping pattern are presented in Fig. 5.11 and the zigzag pattern in Fig. 5.12.

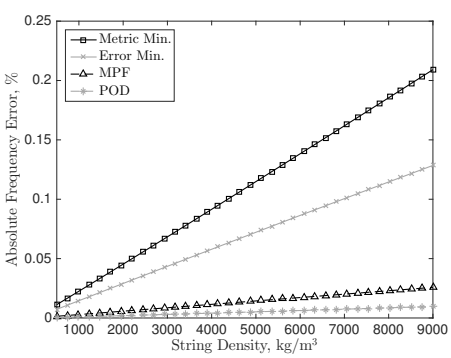

(a) Frequencies, CC

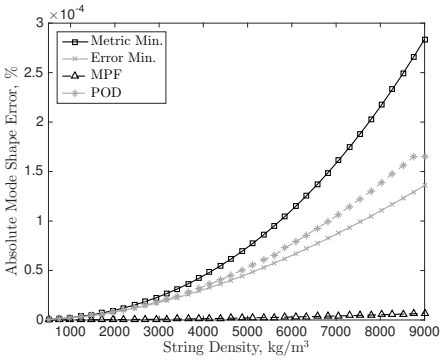

(b) Mode shapes, CC

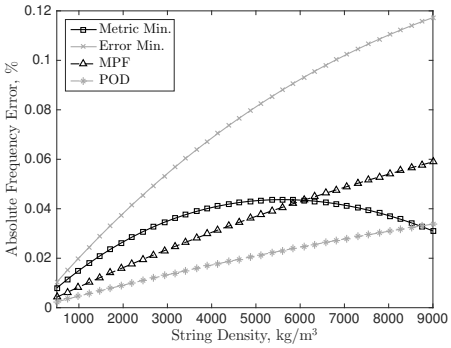

(c) Frequencies, CF

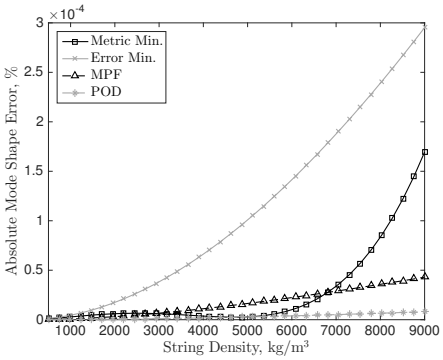

(d) Mode shapes, CF

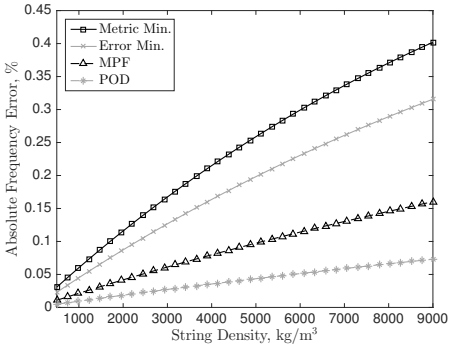

(e) Frequencies, FF

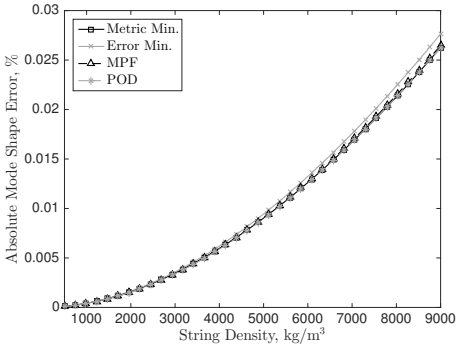

(f) Mode shapes, FF

Figure 5.11: Error in fundamental frequency and mode shape of approximate models to perturbation theory given variable string density and diagonal wrapping pattern.

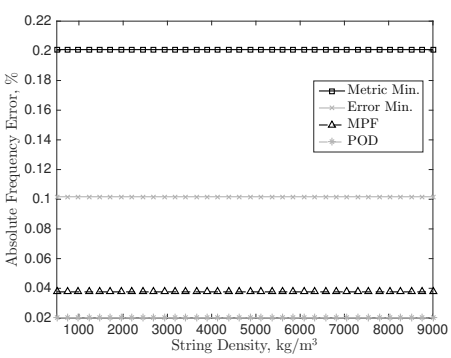

(a) Frequencies, CC

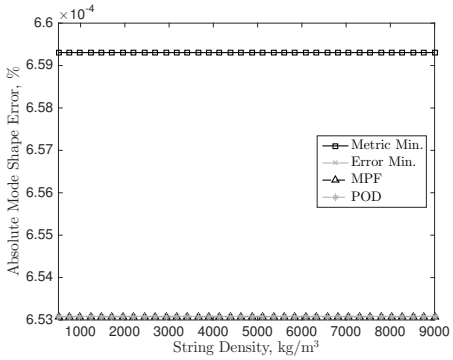

(b) Mode shapes, CC

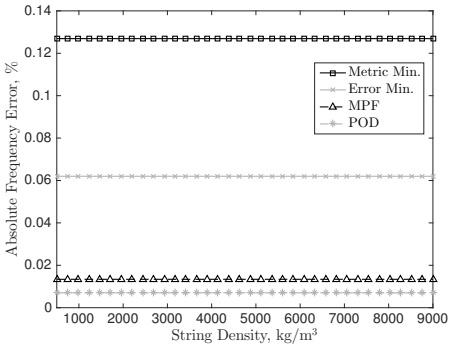

(c) Frequencies, CF

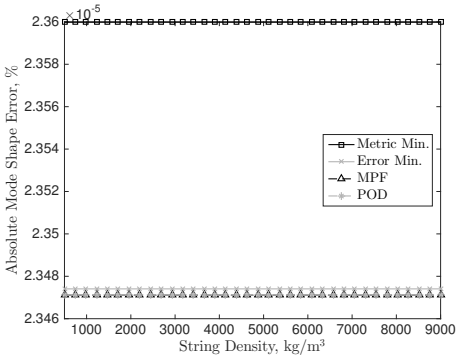

(d) Mode shapes, CF

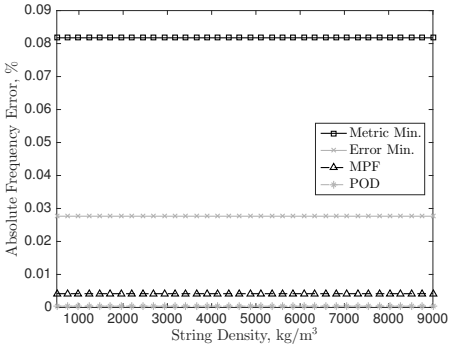

(e) Frequencies, FF

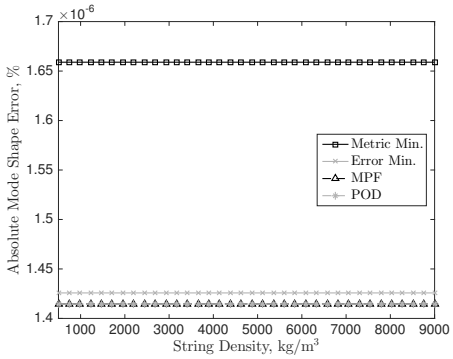

(f) Mode shapes, FF

Figure 5.12: Error in fundamental frequency and mode shape of approximate models to perturbation theory given variable string density and zigzag wrapping pattern.

For the case of the diagonal wrapping pattern in Fig. 5.11, it is observed that the error in the fundamental frequency and mode shape typically increases as the density of the string increases. In the case of a diagonal wrapping pattern, the frequencies of the string-harnessed system are less likely to follow the pattern of a constant coefficient EB model due to the increased value of the lumped masses. This type of behaviour was previously seen in Section 2.3.10. This directly corresponds to higher errors when using the proposed approximation models as these attempt to predict the frequencies using a constant coefficient EB model.

It is seen in Fig. 5.12 that the error between the proposed methods and the perturbation theory results is unaffected by changes in the string modulus. This is due to the periodic zigzag wrapping pattern having a constant value for the mass per unit length in the system. In this case, the approximation methods simply choose this value for the unknown coefficient $\widehat{\rho A}$ and the error in the models is due to variable bending stiffness, which is a result of the wrapping pattern. When the string density is varied, this does not affect the bending stiffness of the string-harnessed system and thus no additional error is introduces, resulting in a constant value for the error.

A clear pattern is seen in Figs. 5.11 and 5.12 with respect to the errors reported for the frequencies by the various proposed models. It is seen for the fundamental frequency that the POD method typically produces the most accurate result to the perturbation theory, then the MPF, and finally the metric and error minimization methods produce the largest errors. The exception to this occurs for the CF boundary conditions given a diagonal wrapping pattern; in this case the metric minimization becomes more accurate as the string density is increased. As previously discussed, the MPF and POD methods place a large weight on matching the fundamental mode in comparison to the higher modes. For this reason, the MPF and POD are expected to provide quite accurate estimates for the fundamental mode of the system. As the POD is seen to be more accurate than the MPF for the numerical simulations, this indicates that the POD places more importance on matching the fundamental mode than the MPF. With respect to the mode shape, typically the POD method was the most accurate, with the exception of CC boundary conditions given a diagonal wrapping pattern.

In addition to the accuracy of the proposed methods for the fundamental frequency and mode shape, the error with respect to the perturbation theory over multiple modes is considered. To this end, the sum of the absolute error of the first 10 modes of the system is considered and the average value of this sum for variable string density is reported. The results for both wrapping patterns, each of the proposed approximation methods, and the various boundary conditions are presented in Table 5.3.

Table 5.3: Average sum of absolute percentage of error to perturbation theory for the first 10 natural frequencies and associated mode shapes for variable string density

	Frequency Results			Mode Shape Results		
Result	CC	CF	FF	CC	CF	FF
	Diagonal Pattern			*Diagonal Pattern*		
Metric Min.	1.8236	1.5168	1.7626	0.17794972	1.09842261	1.51250195
Error Min.	1.7398	1.4908	1.6615	0.17788884	1.09640330	1.50871525
MPF	1.6293	1.5252	1.8443	0.17820201	1.09683959	1.51046329
POD	1.6239	1.5750	2.1288	0.17789378	1.09744048	1.51315811
	Zigzag Pattern			*Zigzag Pattern*		
Metric Min.	1.1625	0.7339	0.6829	0.24112735	0.03043608	0.05995000
Error Min.	0.6696	0.4213	0.3339	0.24106923	0.03043515	0.05994641
MPF	0.7580	0.5191	0.2677	0.24106931	0.03043518	0.05994652
POD	0.8590	0.5640	0.2742	0.24106931	0.03043518	0.05994652

It is seen in Table 5.3 that the error minimization method always produces the smallest sum of absolute error for the mode shapes, regardless of wrapping pattern or boundary conditions. Furthermore, it is seen that typically the error minimization method produces the smallest error in the average sum of the absolute error for the frequencies. As previously discussed, the error minimization does not always produce the smallest average sum of absolute error for the frequencies due to the form of the objective function in Eq. (5.10). In the cases where the error minimization is not the most accurate method, CC boundary conditions with a diagonal wrapping pattern and FF boundary conditions with a zigzag wrapping pattern, it is observed that the error in the frequencies is quite similar to that of the the most accurate methods, the MPF and POD. Overall, the error minimization is the best approach for approximating the string-harnessed system when multiple modes are in consideration.

Finally, the average sum of absolute error given variable string density for the perturbation theory, the HOM method, and the four proposed approximation methods to the exact solutions is presented in Table 5.4. The results for both wrapping patterns and the various boundary conditions are presented.

Table 5.4: Average sum of absolute percentage of error to FEA for the first 10 natural frequencies and associated mode shapes for variable string density

	Frequency Results			Mode Shape Results		
Result	CC	CF	FF	CC	CF	FF
	Diagonal Pattern			*Diagonal Pattern*		
Perturbation	0.0008	0.0047	0.0056	0.00004742	0.00341893	0.00544510
HOM	1.6238	3.7148	3.3897	0.17597441	1.01529834	1.39658479
Metric Min.	1.8228	1.5124	1.7576	0.17552036	1.01097539	1.38552200
Error Min.	1.7391	1.4864	1.6565	0.17546223	1.00852313	1.38076869
MPF	1.6288	1.5209	1.8400	0.17578122	1.00915826	1.38316501
POD	1.6239	1.5712	2.1256	0.17590023	1.00944547	1.38519427
	Zigzag Pattern			*Zigzag Pattern*		
Perturbation	0.1779	0.1678	0.1823	0.00207755	0.00049619	0.00070953
HOM	2.8064	0.5677	1.8058	0.28537941	0.03863969	0.07357553
Metric Min.	1.0420	0.6293	0.5491	0.28551285	0.03863529	0.07358162
Error Min.	0.6564	0.4152	0.2798	0.28538189	0.03863285	0.07357486
MPF	0.8628	0.6538	0.4171	0.28537941	0.03863261	0.07357554
POD	0.9978	0.7179	0.4550	0.28537941	0.03863261	0.07357553

In Table 5.4, it is seen for the diagonal wrapping pattern that the error between the perturbation theory and the analytical solution is quite small for both the frequency and mode shapes, given all the boundary conditions. Due to the accuracy of the perturbation theory for the diagonal wrapping pattern, the errors between the approximation methods and the analytical solution, Table 5.4, are almost identical to the error between the approximation methods and the perturbation theory, Table 5.3. On the other hand, it is seen for the case of the zigzag wrapping pattern that the error between the perturbation theory and the FEA is not negligible. Comparing the errors of the approximation methods to the perturbation theory, Table 5.3, with the errors of the approximation methods to the FEA, Table 5.4, it is observed that the values are significantly changed. Furthermore, in certain cases the error with respect to the FEA will be larger than the error with respect to the perturbation theory, and other times the error with respect to the FEA will be smaller than the error with respect to the perturbation theory. As previously discussed, this will depend on whether the perturbation theory over or underpredicts the FEA results, and whether an approximation method over or underpredicts the perturbation theory results.

It is seen in the table of average sum of absolute errors that typically the HOM method results are larger than the proposed approximation methods. The exceptions to this are for

the diagonal wrapping pattern with CC boundary conditions, the same case that was the exception in Table 5.2 for variable string modulus, and zigzag wrapping pattern with CF boundary conditions. In these cases, however, it is seen that the average sum of absolute error is fairly similar between the five approximate methods and thus there is no significant advantage in one approximate model over the other compared to the HOM. It is clear in Table 5.4 that there is an advantage in using any of the proposed approximation models over the HOM. The sum of absolute error for the mode shapes is fairly constant for the proposed methods regardless of wrapping pattern or boundary conditions.

Comparing the four proposed approximation methods, it is evident from Table 5.4 that the error minimization typically results in the smallest average sum of the absolute error in the first 10 frequencies of the system. The exception occurred for CC boundary conditions given the diagonal wrapping pattern. In the cases where the error minimization results in the most accurate average results for the frequencies, the second most accurate method varied between the metric minimization and the MPF method.

The final numerical results that are presented for a periodically wrapped system are frequency response functions (FRFs). The system parameters used are those listed at the beginning of the current section. Figure 5.13 presents driving point FRFs with an actuation and sensing location of $x = 0.025$ for CC boundary conditions and the free end for CF and FF boundary conditions. In Fig. 5.13, both wrapping patterns are considered as well as the various boundary conditions. Note that since damping is not included in the models, the values of the resonant peaks are not relevant but rather their location is of importance.

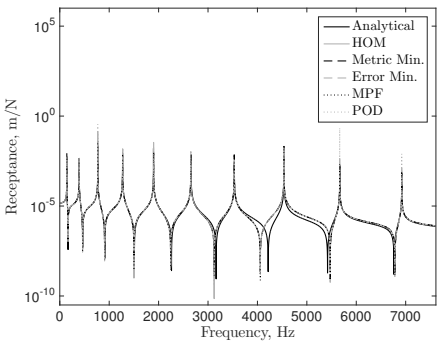

(a) Diagonal, CC

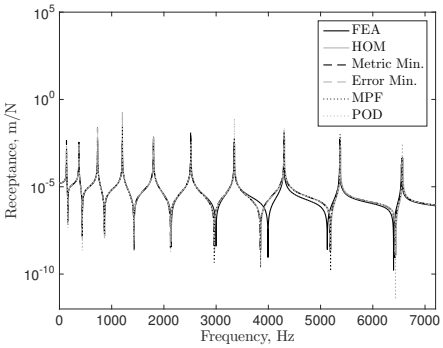

(b) Zigzag, CC

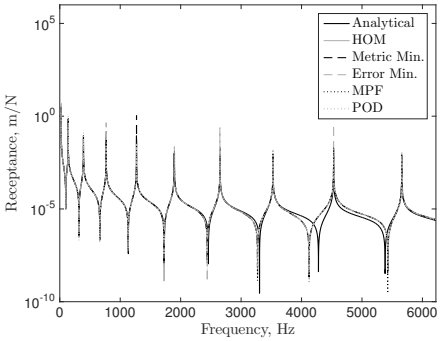

(c) Diagonal, CF

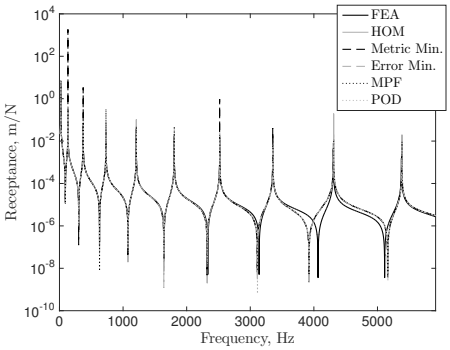

(d) Zigzag, CF

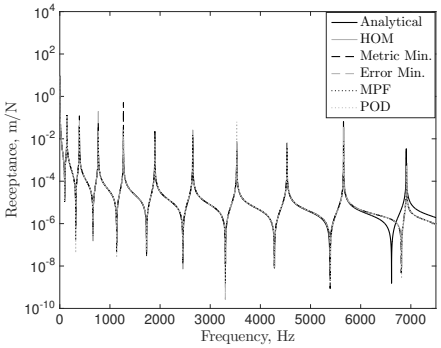

(e) Diagonal, FF

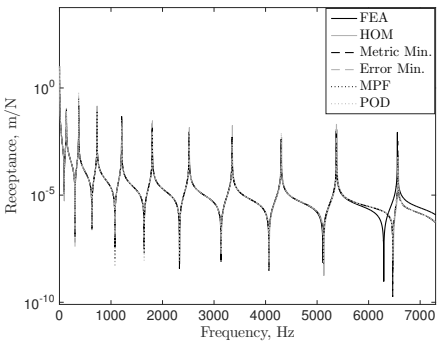

(f) Zigzag, FF

Figure 5.13: FRFs of exact solution and model approximations for periodic wrapping patterns given various boundary conditions.

Figures 5.13a, 5.13c, and 5.13e containing the results for the diagonal wrapping pattern demonstrate that there is very little difference in the results of the four proposed methods and the HOM method. This is somewhat expected as the level of errors reported in Tables 5.2 and 5.4 for the four proposed methods and the HOM method are quite similar. Additionally, the FRFs for the approximate models match quite well with the analytical FRF with respect to the locations of resonance and antiresonance, as well as in amplitude. There is a slight difference in the location of the antiresonances for the seventh mode and higher.

For the zigzag wrapping pattern FRFs in Figs. 5.13b, 5.13d, and 5.13f, the four proposed method results are overall quite similar to one another with respect to the location of resonances and antiresonances, as well as amplitude. In addition, it is seen that the proposed methods for model approximation provide a much more accurate estimate for the FEA FRF than the HOM method. This highlights the advantage of using the approximation methods to accurately predict the FRF of the string-harnessed system.

In summary, it has been shown that the model approximation methods provide similar or improved accuracy when compared to the HOM model with respect to the prediction of the natural frequencies, mode shapes, and as a result the FRFs. It was seen that there is significant improvement for the case of a zigzag wrapping pattern. Further, the MPF and POD were shown to provide more accurate results when the fundamental mode of the system is of the utmost importance, whereas the metric and error minimization methods provide the most accurate results when multiple modes of the system are simultaneously considered.

5.2.2 Non-Periodic Wrapping Patterns

The first non-periodic wrapping pattern that is considered allows for a variable wrapping angle. Beginning with a fixed initial wrapping angle, the wrapping angle is then varied by a prescribed amount each time the string goes from one side of the host structure to another. In particular, for the diagonal wrapping pattern the change in the wrapping angle occurs after each lumped mass.

In the current chapter, the initial wrapping angle is taken as the wrapping angle required for the system to be composed of two fundamental elements. From this initial wrapping angle a minimum and maximum percentage change over each section are defined for the numerical simulations. For the wrapping patterns considered, the largest percentage change in the angle over each section considered is the largest possible value which does not cause

the string to wrap over itself. Figure 5.14 contains schematics of the wrapping patterns considered for various cases, including the maximum and minimum values.

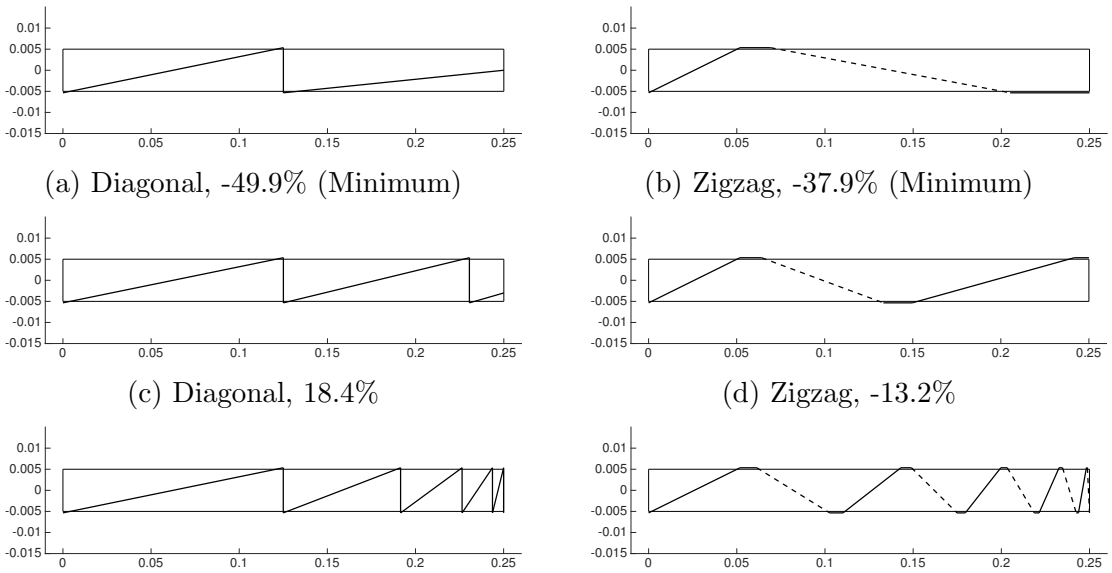

(a) Diagonal, -49.9% (Minimum)

(b) Zigzag, -37.9% (Minimum)

(c) Diagonal, 18.4%

(d) Zigzag, -13.2%

(e) Diagonal, 86.7% (Maximum)

(f) Zigzag, 11.6% (Maximum)

Figure 5.14: Schematics of variable wrapping angle systems for diagonal and zigzag wrapping patterns.

Consider first the effect of variable percentage of change in the wrapping angle over each section on the frequency results. Figures 5.15 and 5.16 present the fundamental and tenth mode frequency results for the exact, perturbation theory, as well as the various proposed methods for model approximation results. For the non-periodic cases the homogenization technique cannot be applied and therefore there are no HOM model results. Multiple boundary conditions are considered and the diagonal wrapping pattern is considered in Fig. 5.15 and the zigzag wrapping pattern is considered in Fig. 5.16.

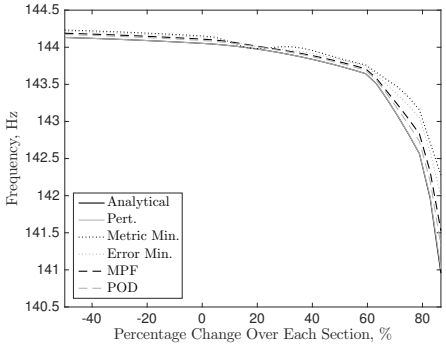

(a) CC, Mode 1

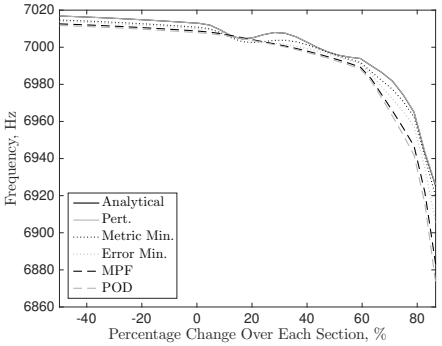

(b) CC, Mode 10

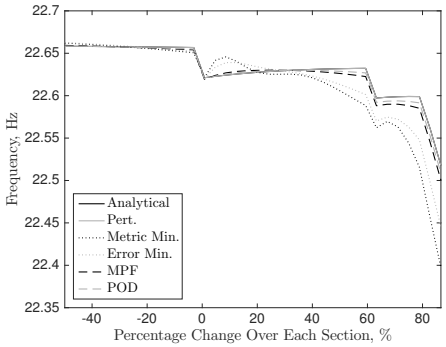

(c) CF, Mode 1

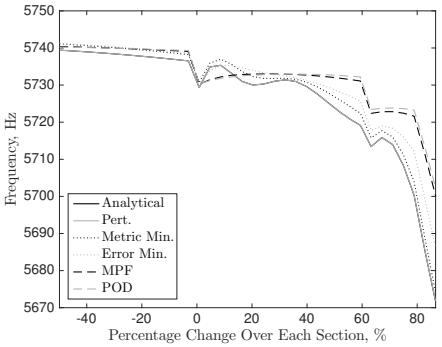

(d) CF, Mode 10

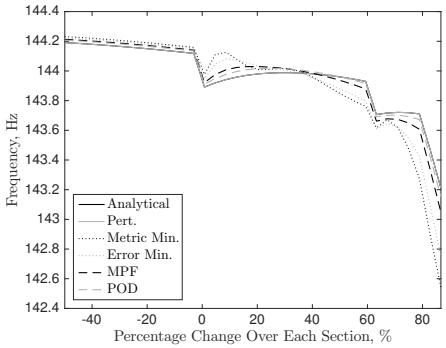

(e) FF, Mode 1

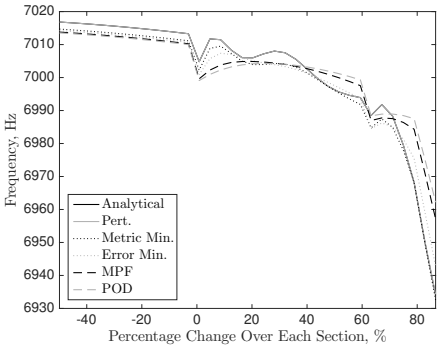

(f) FF, Mode 10

Figure 5.15: Frequency results for fundamental and tenth mode given variable percentage change in wrapping angle over each section and diagonal wrapping pattern.

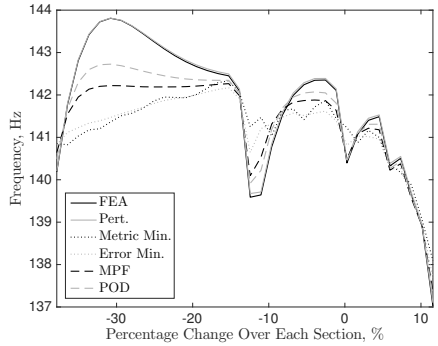

(a) CC, Mode 1

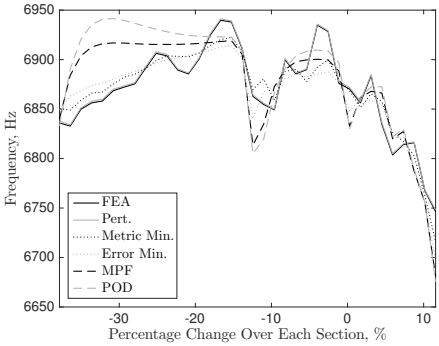

(b) CC, Mode 10

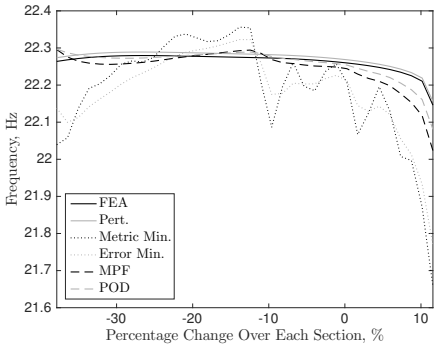

(c) CF, Mode 1

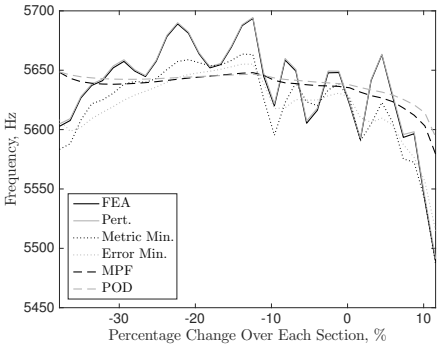

(d) CF, Mode 10

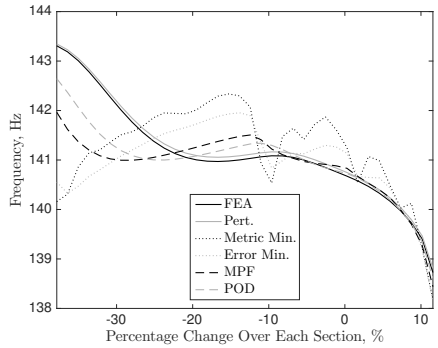

(e) FF, Mode 1

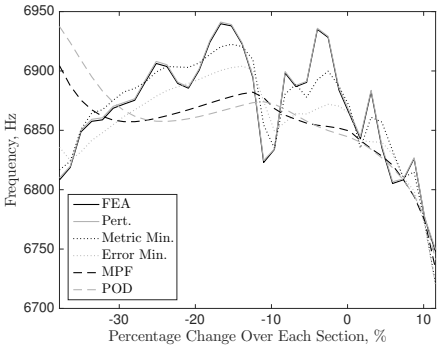

(f) FF, Mode 10

Figure 5.16: Frequency results for fundamental and tenth mode given variable percentage change in wrapping angle over each section and zigzag wrapping pattern.

As the percentage change over each section is increased, there is a reduction in the stiffening effect due to the string in addition to an increase in the total mass added to the system by the string. As a result, the overall behaviour of the frequencies for the string-harnessed system are expected to decrease with increasing percentage change in the wrapping angle over each section. This behaviour is quite clear for the various boundary conditions and both wrapping patterns in Figs. 5.15 and 5.16.

For both the diagonal and zigzag wrapping patterns, it is seen that for the fundamental mode the MPF and POD methods results are more similar to the behaviour of the exact and perturbation theory results than the metric and error minimization methods. In addition, it is seen that for the tenth mode the metric and error minimization methods are more similar to the behaviour of the exact and perturbation theory results than the MPF and POD methods. These differences in behaviour are attributed to the manner in which each method determines the unknown coefficients. The MPF and POD methods place a larger emphasis on matching the fundamental mode, and for this reason their results are most similar to the exact and perturbation theory results for the fundamental mode. For the metric and error minimization methods, equal importance is placed on all the modes. This creates more accurate frequency behaviour to the exact and perturbation theory results for the tenth mode when compared to the fundamental mode.

For the metric minimization, the difference between the model and perturbation theory are of interest and therefore there will be a tendency for the frequency results of the method to be more similar to the higher modes. For the error minimization, the error between the model and perturbation theory frequencies are of interest. In this case, matching the fundamental frequency more closely would result in much larger errors for the higher modes, whereas matching the higher modes more closely will not result in significantly large errors for the fundamental mode. Therefore, the error minimization method tries to match the higher modes somewhat more accurately while keeping the error in the fundamental mode relatively small, thus creating more accurate frequency behaviour to the exact and perturbation theory results for the tenth mode when compared to the fundamental mode.

Next, the effect of variable percentage change in wrapping angle over each section on the results for the coefficients $\widehat{EI}$ and $\widehat{\rho A}$, as determined by the approximation methods outlined in the current work, is presented. The results for variable string modulus given a diagonal and zigzag wrapping pattern are presented in Figs. 5.17 and 5.18, respectively.

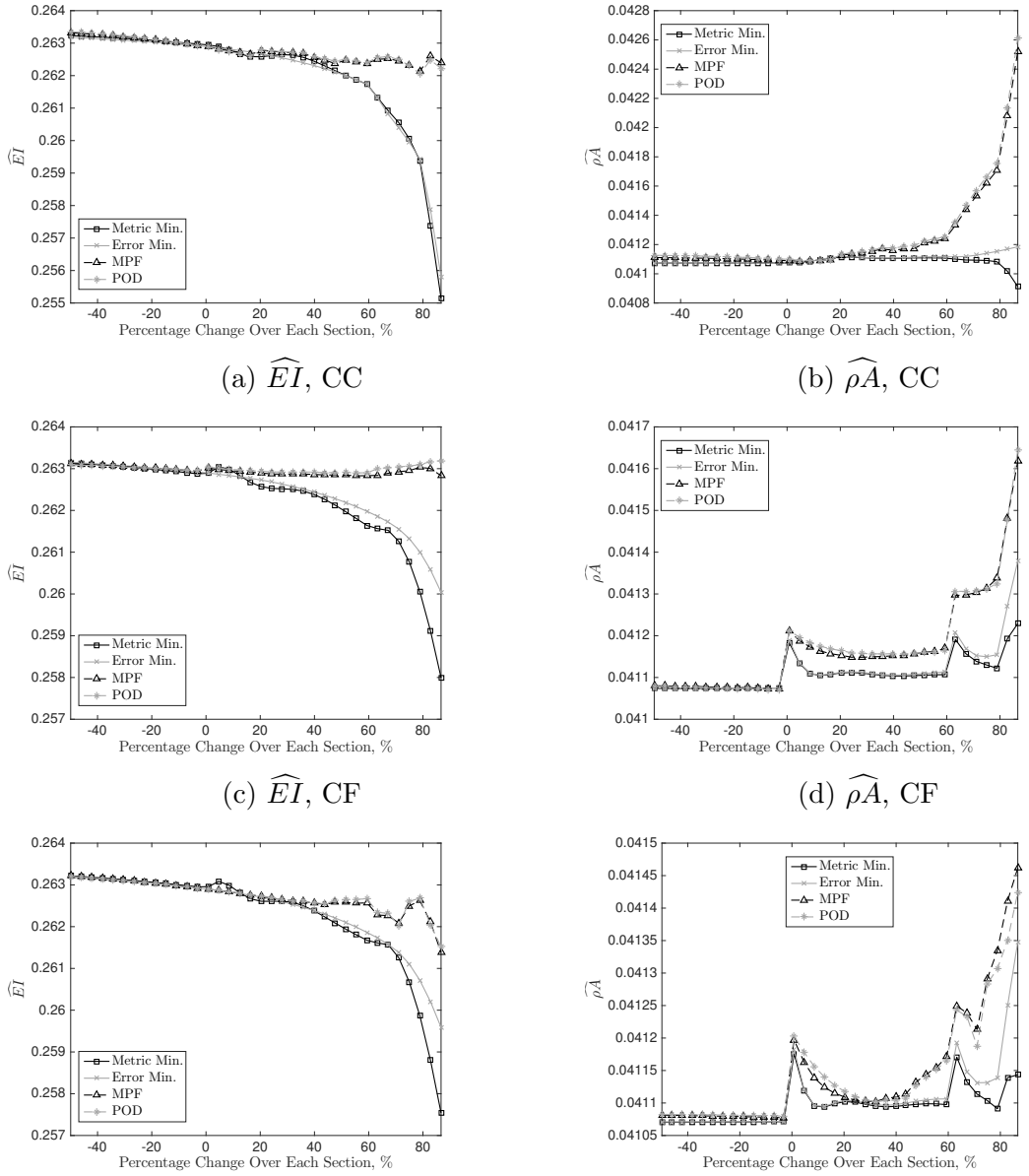

(a) $\widehat{EI}$, CC (b) $\widehat{\rho A}$, CC

(c) $\widehat{EI}$, CF (d) $\widehat{\rho A}$, CF

(e) $\widehat{EI}$, FF (f) $\widehat{\rho A}$, FF

Figure 5.17: Results for $\widehat{EI}$ and $\widehat{\rho A}$ coefficients for diagonal wrapping pattern with variable percentage change in wrapping angle over each section.

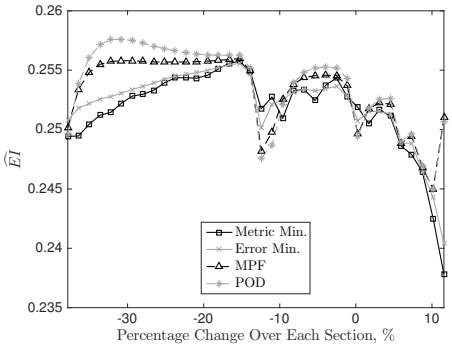

(a) $\widehat{EI}$, CC

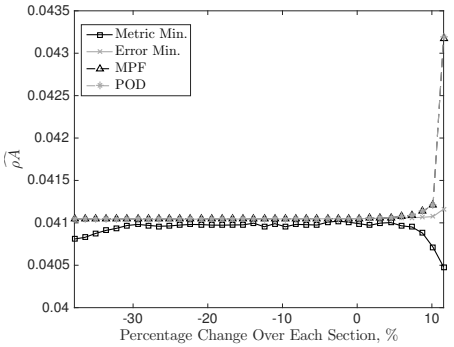

(b) $\widehat{\rho A}$, CC

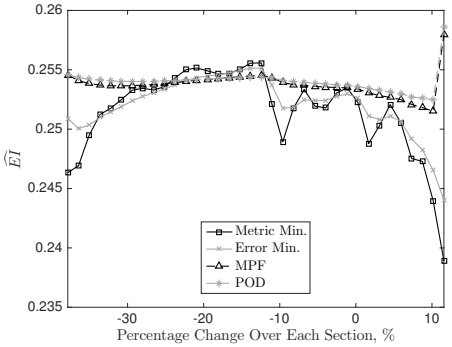

(c) $\widehat{EI}$, CF

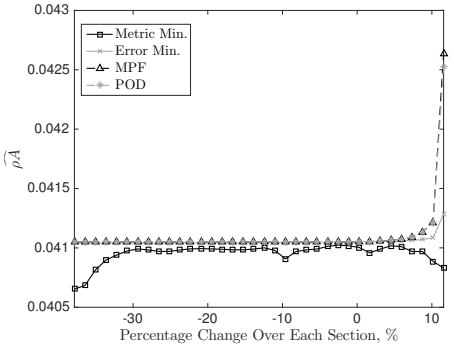

(d) $\widehat{\rho A}$, CF

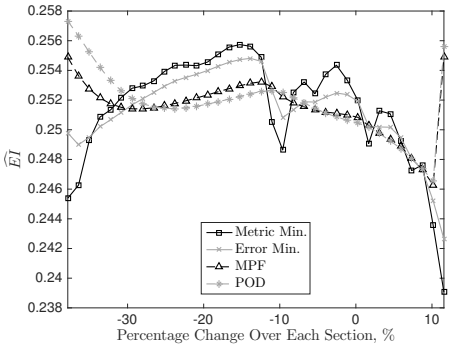

(e) $\widehat{EI}$, FF

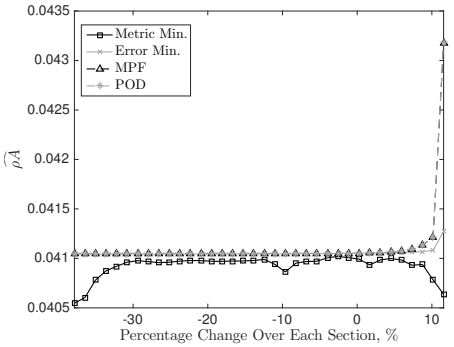

(f) $\widehat{\rho A}$, FF

Figure 5.18: Results for $\widehat{EI}$ and $\widehat{\rho A}$ coefficients for zigzag wrapping pattern with variable percentage change in wrapping angle over each section.

For the diagonal wrapping pattern coefficients in Fig. 5.17, it is seen for the metric and error minimization methods that the pattern for the $\widehat{EI}$ coefficient is similar in behaviour to the tenth mode frequency results in Fig. 5.15. The MPF and POD methods predict a fairly constant value for $\widehat{EI}$, especially when compared to the variations observed in the metric and error minimization methods. With respect to the $\widehat{\rho A}$ variable, it is observed that all four of the proposed methods demonstrate a sudden increase in value when a lumped mass is added to the free end of the system. Since the CC boundary conditions has no free end, there are no sudden jumps in the equivalent value for the mass per unit length. Opposite to the case of the equivalent bending stiffness, it is seen for the diagonal pattern that the metric and error minimization methods predict a fairly constant value for $\widehat{\rho A}$, and the MPF and POD methods predict more significant changes. In particular, when the wrapping pattern becomes increasingly tight, large percentage change in the wrapping angle over each section, the value for $\widehat{\rho A}$ increases.

Consider the zigzag wrapping pattern $\widehat{EI}$ and $\widehat{\rho A}$ coefficients in Fig. 5.18. It is observed that, similar to the diagonal wrapping pattern case, the metric and error minimization methods predict values for $\widehat{EI}$ that are similar in behaviour to the frequency results for the tenth mode in Fig. 5.16. For the MPF and POD methods, the behaviour of $\widehat{EI}$ is similar to the behaviour of the frequency results for the fundamental mode in Fig. 5.16. The pattern for the coefficient $\widehat{\rho A}$ is similar to the diagonal wrapping pattern case in that the metric and error minimization methods predict fairly constant values and the MPF and POD methods predict fairly constant values and a large increase in $\widehat{\rho A}$ occurs when the is tightly wrapped and the total mass of the string-harnessed system increases quite dramatically.

The first step in quantifying the accuracy of each of the proposed approximation models is to examine the error between these and the perturbation theory results. To this end, the percentage error in the fundamental frequency and associated mode shape are considered for variable percentage change in the wrapping angle over each section. The results for the diagonal wrapping pattern are presented in Fig. 5.19 and the zigzag pattern in Fig. 5.20.

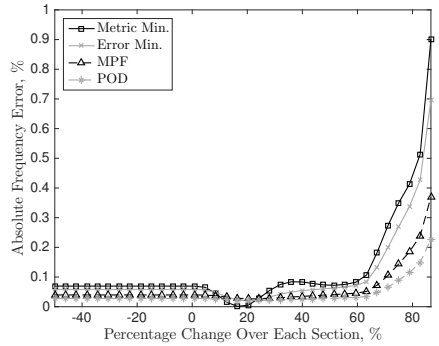

(a) Frequencies, CC

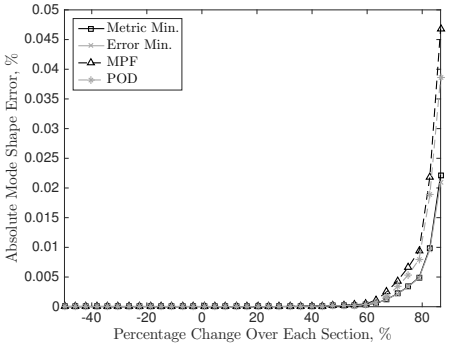

(b) Mode shapes, CC

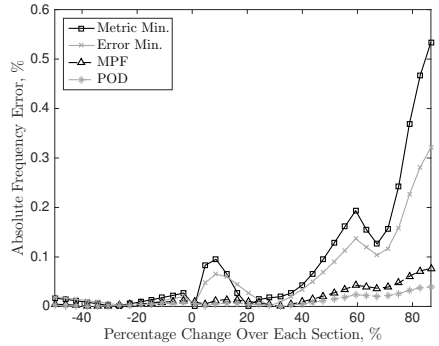

(c) Frequencies, CF

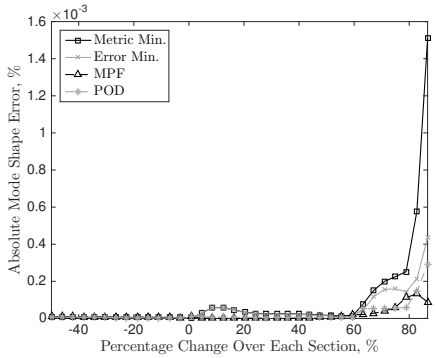

(d) Mode shapes, CF

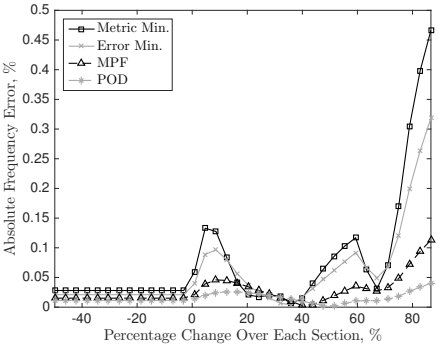

(e) Frequencies, FF

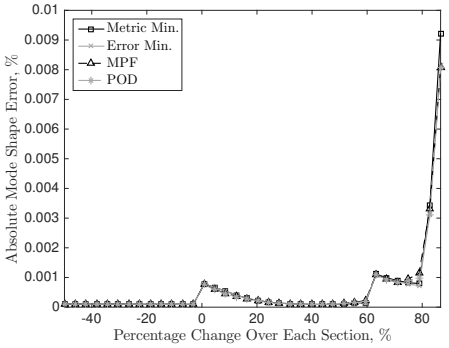

(f) Mode shapes, FF

Figure 5.19: Error in fundamental frequency and mode shape of approximate models to perturbation theory given variable percentage change in wrapping angle over each section and diagonal wrapping pattern.

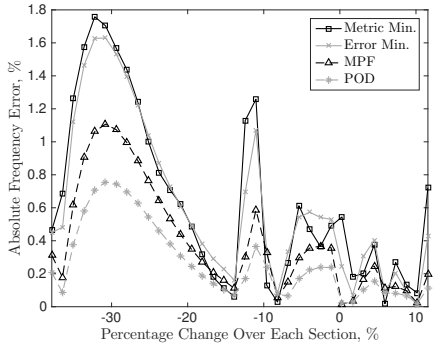

(a) Frequencies, CC

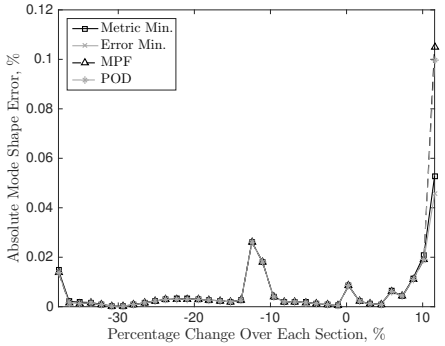

(b) Mode shapes, CC

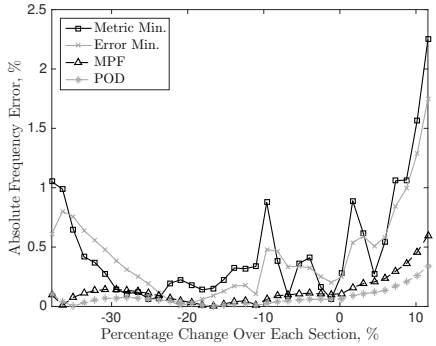

(c) Frequencies, CF

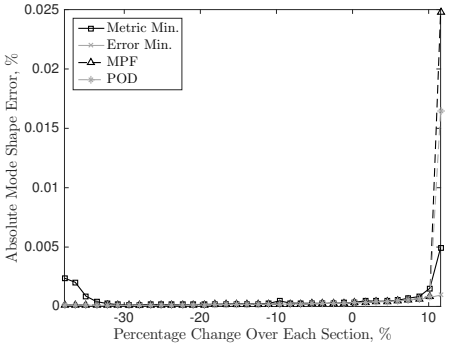

(d) Mode shapes, CF

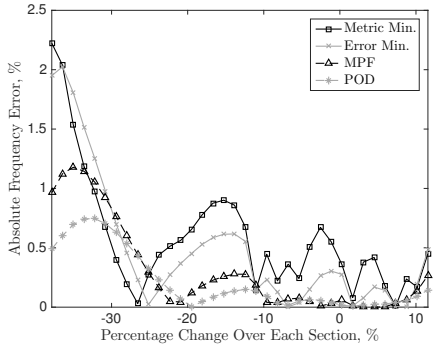

(e) Frequencies, FF

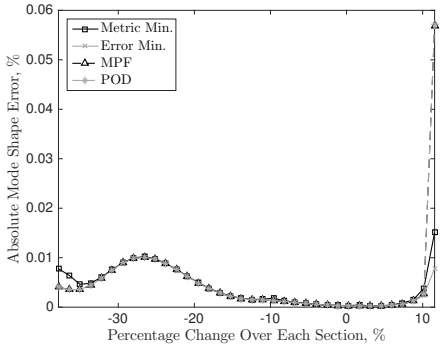

(f) Mode shapes, FF

Figure 5.20: Error in fundamental frequency and mode shape of approximate models to perturbation theory given variable percentage change in wrapping angle over each section and zigzag wrapping pattern.

A clear pattern is seen in Figs. 5.19 and 5.20 with respect to the errors reported for the frequencies by the various proposed models. It is seen for the fundamental frequency that overall the POD method produces the most accurate results to the perturbation theory, then typically the MPF method. The metric and error minimization methods produce similar levels of error and are typically the methods producing the largest error in the fundamental frequency. With respect to the mode shape, it is observed that for both wrapping pattern and all boundary conditions that the errors reported are quite similar across the four proposed approximation methods and attain their largest values as the percentage change in wrapping angle over each section reaches the largest simulated value. This increase in error as the system is more tightly wrapped occurs due to larger changes in the mass per unit length across the system. Having a significant variation in the mass per unit length over the system makes matching the mode shapes of a constant coefficient model to the perturbation theory results more difficult.

Furthermore, the behaviour observed for the errors in Figs. 5.19 and 5.20 is explained by referring back to the frequency results in Figs. 5.15 and 5.16. The erratic behaviour that is seen for the errors in the metric and error minimization methods is caused by these methods choosing the unknown coefficients $\widehat{EI}$ and $\widehat{\rho A}$ in a manner that matches the higher mode frequencies. Since the pattern of the frequencies for different modes differ significantly, this results in erratic looking errors for the fundamental mode. A similar effect occurs for the MPF and POD methods, however the results for the errors are smaller and less erratic due to these methods placing a higher importance on matching the fundamental mode.

Alternatively, the behaviour of over and underprediction by the MPF and POD methods can be explained by considering the perturbation theory reference value results. Considering the case of zigzag wrapping pattern, the EI^* and ρA^* results are presented in Fig. 5.21 for the first three modes of the system.

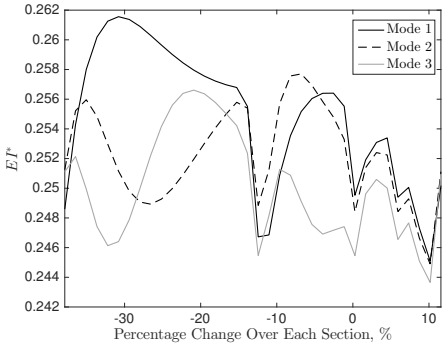

(a) EI^*, CC

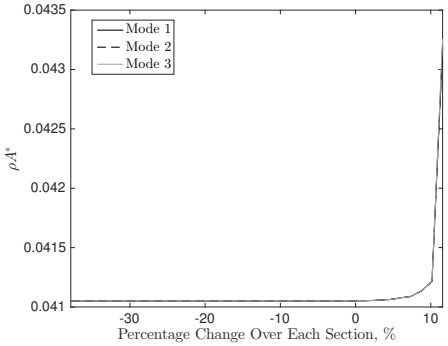

(b) ρA^*, CC

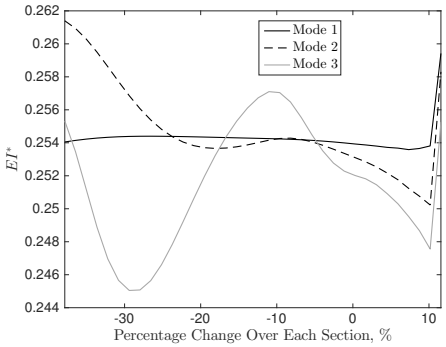

(c) EI^*, CF

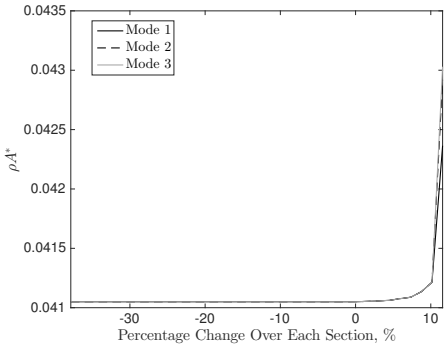

(d) ρA^*, CF

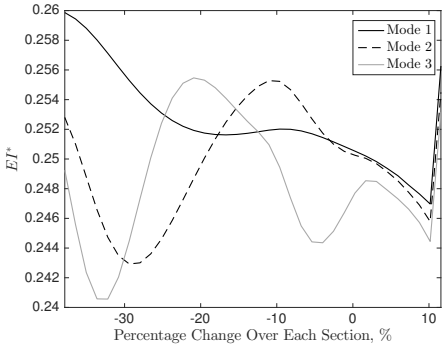

(e) EI^*, FF

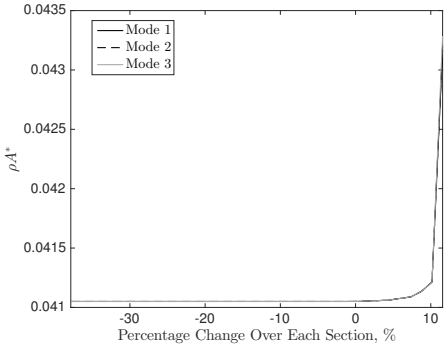

(f) ρA^*, FF

Figure 5.21: EI^* and ρA^* perturbation theory zigzag pattern reference values for the first three modes with variable percentage change in wrapping angle over each section.

Figure 5.21 demonstrates that the various modes of the system produce quite different results for EI^* and almost identical results for ρA^*. When calculating the coefficient $\widehat{EI}$ and $\widehat{\rho A}$ in the approximate model, the MPF and POD methods use a weighted average of the reference values. The fundamental mode will have the largest impact with the second and third modes typically having the second and third highest weights, respectively. With respect to ρA^*, since the various results are almost identical the coefficient $\widehat{\rho A}$ for the given results will be identical to the reference value results. Indeed this is the case as can be seen in Fig. 5.18. Due to this, the error in the fundamental frequency of the approximate system will be mainly determined by the results for $\widehat{EI}$. It can be said with certainty that in the cases where EI_2^* and EI_3^* are larger than EI_1^*, this will cause $\widehat{EI}$ to be larger than EI_1^*. Similarly, when EI_2^* and EI_3^* are smaller than EI_1^*, this will cause $\widehat{EI}$ to be smaller than EI_1^*. When the value of $\widehat{EI}$ switches between being greater or less than EI_1^*, as occurs quite frequently for the CC boundary conditions, this causes the over and underestimations for the fundamental frequency. This in turn produces the behaviour observed in the error results of Fig. 5.20.

In addition to the accuracy of the proposed methods for the fundamental frequency and mode shape, the error with respect to the perturbation theory over multiple modes is considered. The average sum of the absolute error for the first 10 modes of the system is considered for variable percentage change in the wrapping angle over each section. The results for both wrapping patterns, each of the proposed approximation methods, and the various boundary conditions are presented in Table 5.5.

Table 5.5: Average sum of absolute percentage of error to perturbation theory for the first 10 natural frequencies and associated mode shapes for variable percentage change in wrapping angle over each section

	Frequency Results			Mode Shape Results		
Result	CC	CF	FF	CC	CF	FF
	Diagonal Pattern			*Diagonal Pattern*		
Metric Min.	0.5421	0.5690	0.5118	0.18949615	0.10246722	0.14062479
Error Min.	0.5160	0.5089	0.4826	0.18919540	0.10238435	0.14046582
MPF	0.6480	0.6380	0.5725	0.20016456	0.10329072	0.14101297
POD	0.7319	0.6874	0.6353	0.19656606	0.10347849	0.14081312
	Zigzag Pattern			*Zigzag Pattern*		
Metric Min.	4.4114	4.9432	5.0506	1.23950332	1.13718130	1.45510951
Error Min.	4.3155	4.8462	4.8081	1.23659956	1.13479331	1.45111304
MPF	4.8227	5.4738	5.3970	1.24502002	1.13869867	1.45859132
POD	5.4387	5.7140	5.9376	1.24429157	1.13742125	1.45863841

It is seen in Table 5.5 that the error minimization method always produces the smallest sum of absolute error for the frequencies and mode shapes, regardless of wrapping pattern or boundary conditions. For the case of variable percentage change in the wrapping angle over each section, this clearly demonstrates the robustness of the error minimization methods when the error across multiple modes are considered. The metric minimization consistently produced the second smallest average sum of error for both the frequencies and mode shapes. Furthermore, it is seen that the POD methods consistently produced the largest average sum of error in the frequencies. The largest error in the mode shapes was produced by either the MPF or POD methods. This indicates that when the behaviour of the frequencies given a variable parameter changes significantly between the various modes of interest, then an approximation methods that equally takes into account each of the modes is advantageous over methods that focus more strongly on approximating the fundamental modes.

Finally, the average sum of absolute error, given variable percentage change in the wrapping angle over each section of the perturbation theory and the four proposed approximation methods to the exact solutions, is presented in Table 5.6. The results for both wrapping patterns and the various boundary conditions are presented.

Table 5.6: Average sum of absolute percentage of error for the first 10 natural frequencies and associated mode shapes for variable percentage change in wrapping angle over each section

	Frequency Results			Mode Shape Results		
Result	CC	CF	FF	CC	CF	FF
	Diagonal Pattern			*Diagonal Pattern*		
Perturbation	0.0061	0.0010	0.0011	0.00123393	0.00021471	0.00030529
Metric Min.	0.5456	0.5689	0.5115	0.21090951	0.10767100	0.14789943
Error Min.	0.5150	0.5095	0.4830	0.21030989	0.10750870	0.14758242
MPF	0.6440	0.6389	0.5734	0.21933421	0.10821060	0.14792257
POD	0.7279	0.6882	0.6362	0.22093270	0.10826750	0.14783881
	Zigzag Pattern			*Zigzag Pattern*		
Perturbation	0.2926	0.3436	0.3474	0.01917092	0.01885087	0.02380681
Metric Min.	4.4793	4.9896	5.1967	1.50064981	1.38345182	1.76573695
Error Min.	4.3716	4.8832	4.8955	1.49461768	1.37837738	1.75726479
MPF	4.9288	5.6007	5.4455	1.49946644	1.38070209	1.76172728
POD	5.5617	5.8560	5.9739	1.49956755	1.38022966	1.76181359

In Table 5.6, it is seen for the diagonal wrapping pattern that the error between the perturbation theory and the analytical results is small for both the frequency and mode shapes, given all the boundary conditions. Due to the accuracy of the perturbation theory for the diagonal wrapping pattern, the errors between the approximation methods and the analytical results, Table 5.6, are very similar to the error between the approximation methods and the perturbation theory, Table 5.5. On the other hand, it is seen for the case of the zigzag wrapping pattern that the error between the perturbation theory and the FEA is not negligible. Comparing the errors of the approximation methods to the perturbation theory, Table 5.6, with the errors of the approximation methods to the FEA, Table 5.5, it is observed that the values are changed more drastically than for the diagonal wrapping pattern. Unlike the cases for the periodic wrapping patterns, for this non-periodic wrapping pattern case the order of most to least accurate method in terms of predicting the frequencies does not change when going from the error compared with perturbation theory to error compared to exact results.

With respect to the four approximation methods, it is seen in Table 5.6 that the error minimization method always produces the smallest sum of absolute error for the first 10 frequencies and mode shapes of the system. The metric minimization provides the second smallest average error for the frequencies and is typically the second smallest average error

for the mode shapes. The POD and MPF methods produce the largest average errors.

Finally, the FRFs for the case of the smallest percentage change in wrapping angle over each section considered are presented for the approximation methods and the exact solutions. This case corresponds to the wrapping pattern presented in Fig. 5.14a for the diagonal wrapping pattern and Fig. 5.14b for the zigzag wrapping pattern. Figure 5.22 presents driving point FRFs with an actuation and sensing location of $x = 0.025$ for CC boundary conditions and the free end for CF and FF boundary conditions. In Fig. 5.22, both wrapping patterns are considered as well as the various boundary conditions. Note that since damping is not included in the models, the values of the resonant peaks are not relevant but rather their location is of interest.

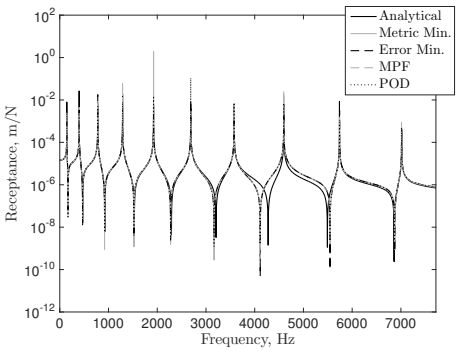

(a) Diagonal, CC

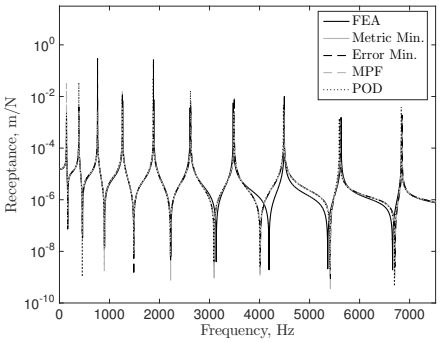

(b) Zigzag, CC

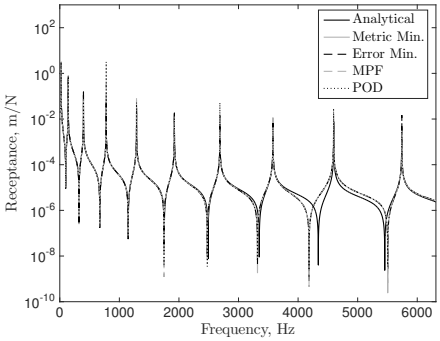

(c) Diagonal, CF

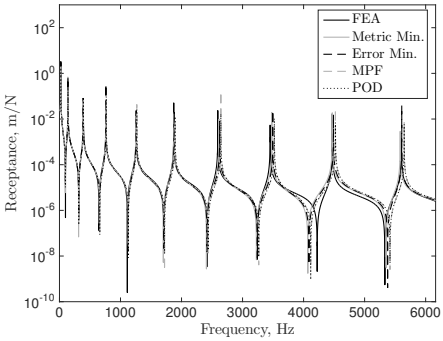

(d) Zigzag, CF

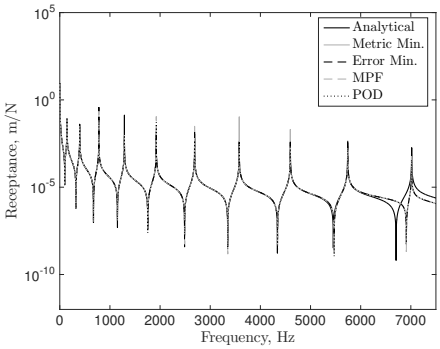

(e) Diagonal, FF

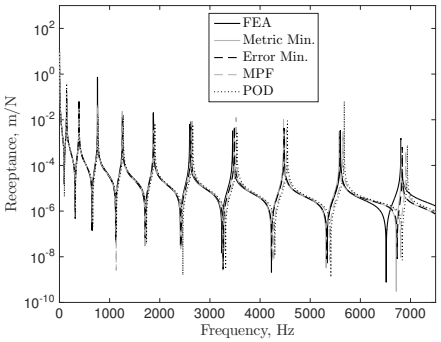

(f) Zigzag, FF

Figure 5.22: FRFs of exact solution and model approximations for variable wrapping angle patterns given various boundary conditions.

Figure 5.22 shows that the four approximation method FRFs provide a good match to the exact results in terms of location of resonances and antiresonance, as well as magnitude. In particular, the approximate model results for the diagonal pattern are all quite similar whereas the results for the zigzag wrapping pattern exhibit noticeable differences in the range of higher modes. Further, the location of the antiresonances become less accurate for higher modes, typically after from the seventh mode of the system.

The second non-periodic pattern considered involves the addition of a second string to a non-periodically wrapped string-harnessed system with a single string. The second string that is added begins from the left end of the system and follows that same wrapping pattern as the first string up to a specified point. This specified point, which will be called the switching location, is varied throughout the numerical simulations. The properties of the second string are identical to those previously listed with the exception of an increased modulus of $E_{s2} = 1.875 \times 10^{11}$ N/m^2 and an increased density of $\rho_{s2} = 8000$ kg/m^3.

The wrapping pattern the strings follow begins with the wrapping angle that would be required to periodically wrap the system with 10 fundamental elements, and then the wrapping angle is decrease a fixed percentage amount each time the string goes from one side to the next until there is a total of 3 wraps of the string around the system. Schematics for these wrapping patterns are presented in Fig. 5.23.

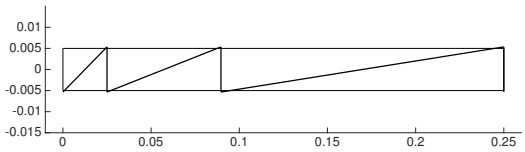

(a) Diagonal, -59.4%

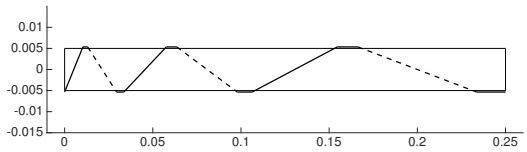

(b) Zigzag, -15.0%

Figure 5.23: Schematics of wrapping patterns for multiple strings numerical simulations.

Consider first the effect of variable switching location, the location where the system goes from two strings to one, on the frequency results. Figures 5.24 and 5.25 present the fundamental and tenth mode frequency results for the exact, perturbation theory, as well as the various proposed methods for model approximation results. Multiple boundary conditions are considered and the diagonal wrapping pattern is considered in Fig. 5.24, and the zigzag wrapping pattern is considered in Fig. 5.25.

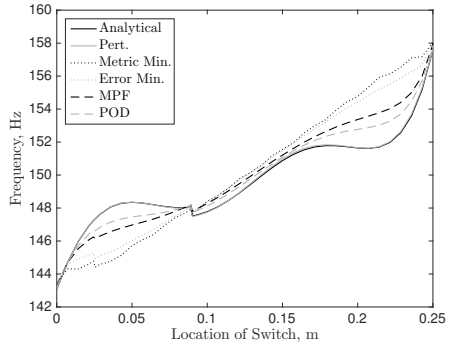

(a) CC, Mode 1

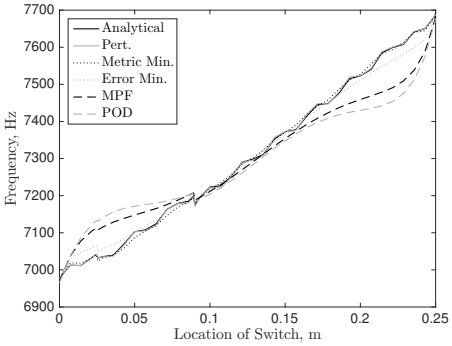

(b) CC, Mode 10

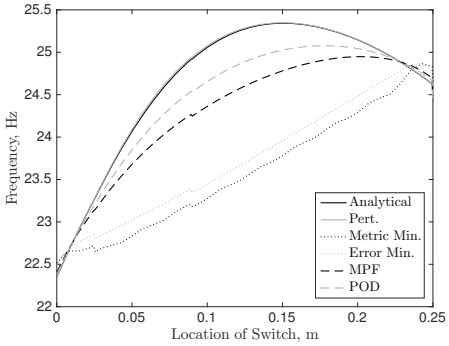

(c) CF, Mode 1

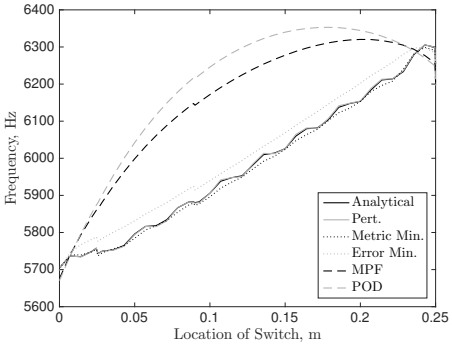

(d) CF, Mode 10

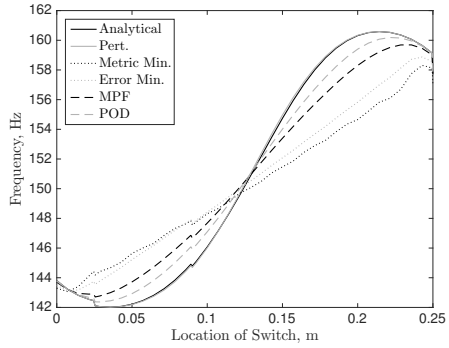

(e) FF, Mode 1

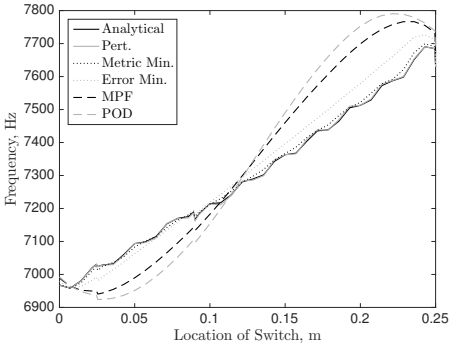

(f) FF, Mode 10

Figure 5.24: Frequency results for fundamental and tenth mode given variable switching location and diagonal wrapping pattern.

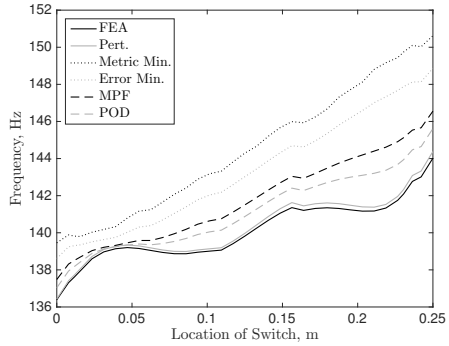

(a) CC, Mode 1

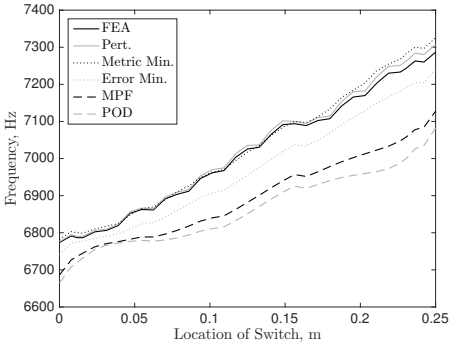

(b) CC, Mode 10

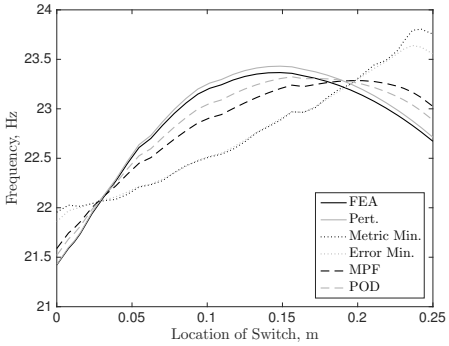

(c) CF, Mode 1

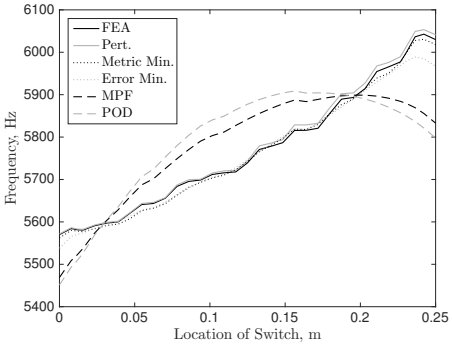

(d) CF, Mode 10

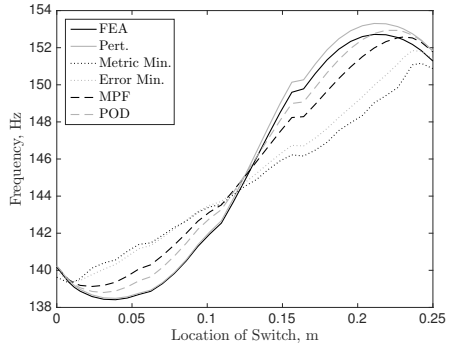

(e) FF, Mode 1

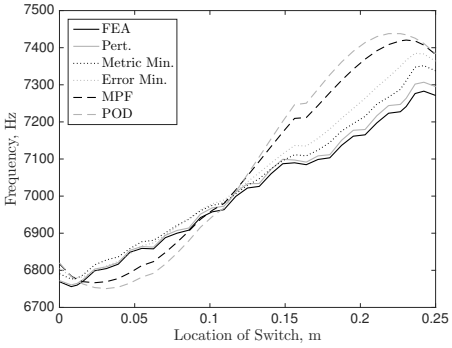

(f) FF, Mode 10

Figure 5.25: Frequency results for fundamental and tenth mode given variable switching location and zigzag wrapping pattern.

As discussed in Section 4.2.2, the behaviour of the frequencies in Figs. 5.24 and 5.25 is due to a small change in the switching location either adding more stiffness or mass. More stiffness is added to the system compared to the mass effect when a small increase in the switching location occurs near high curvature areas. More mass effect is added to the system compared to the stiffness effect when a small increase in the switching location occurs around high displacement areas of the mode shape. The locations where high curvature and large displacements occur will depend on the mode number in consideration, as well as the boundary conditions. The latter reason explains the difference in frequency behaviour for variable switching location for the various boundary conditions.

As previously discussed, the difference between the model and perturbation theory are of interest for the metric minimization and therefore there will be a tendency for the frequency results of the method to be more similar to the higher modes. The error between the model and perturbation theory frequencies are of interest for the error minimization. Therefore, the error minimization method tries to match the higher modes somewhat more accurately while keeping the error in the fundamental mode relatively small, thus creating more accurate frequency behaviour to the exact and perturbation theory results for the tenth mode when compared to the fundamental mode. The MPF and POD methods place higher importance on matching the fundamental mode. Due to this, it is observed in Figs. 5.24 and 5.25 that the MPF and POD methods more accurately match the exact and perturbation theory results for the fundamental mode and the metric and error minimization methods more accurately match the exact and perturbation theory results for the tenth mode.

Next, the results for the coefficients $\widehat{EI}$ and $\widehat{\rho A}$ from the various approximation methods and the HOM method are presented for variable switching location. The results for the diagonal wrapping pattern are presented in Fig. 5.26 and the results for the zigzag wrapping pattern are presented in Fig. 5.27.

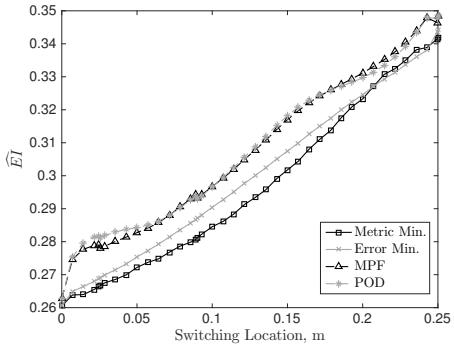

(a) $\widehat{EI}$, CC

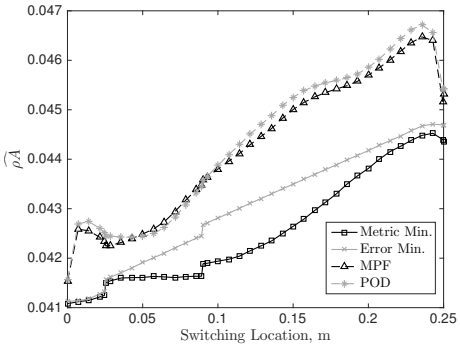

(b) $\widehat{\rho A}$, CC

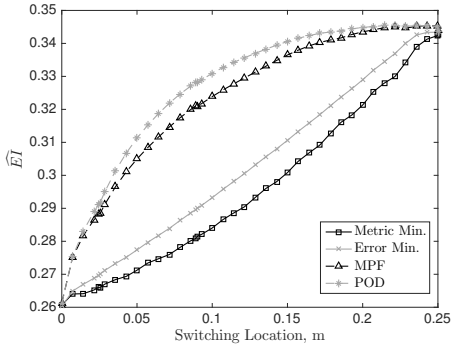

(c) $\widehat{EI}$, CF

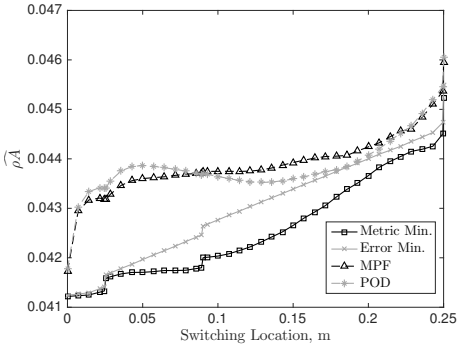

(d) $\widehat{\rho A}$, CF

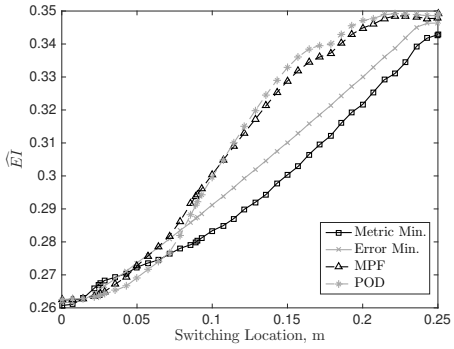

(e) $\widehat{EI}$, FF

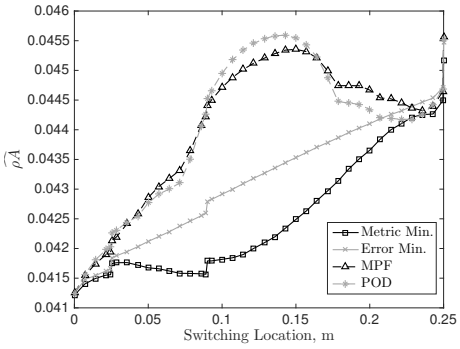

(f) $\widehat{\rho A}$, FF

Figure 5.26: Results for $\widehat{EI}$ and $\widehat{\rho A}$ coefficients for diagonal wrapping pattern with variable switching location.

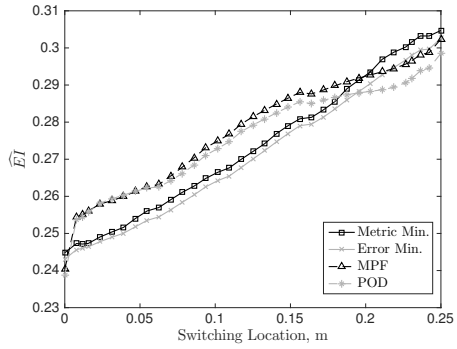

(a) $\widehat{EI}$, CC

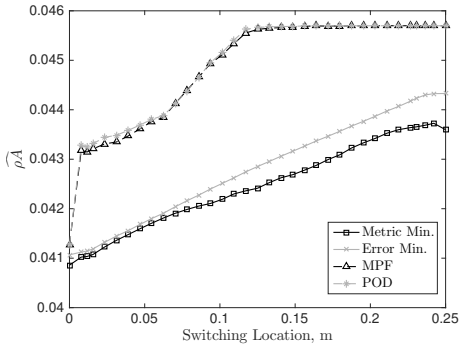

(b) $\widehat{\rho A}$, CC

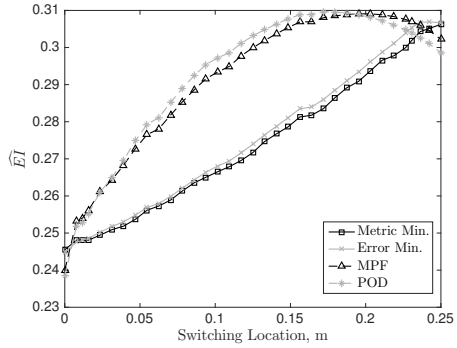

(c) $\widehat{EI}$, CF

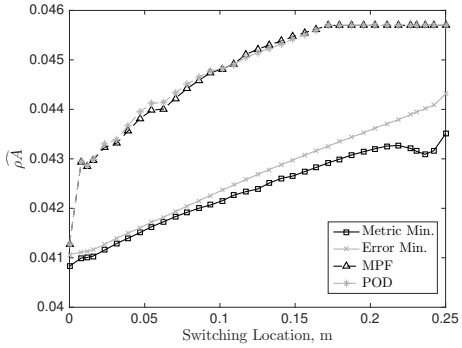

(d) $\widehat{\rho A}$, CF

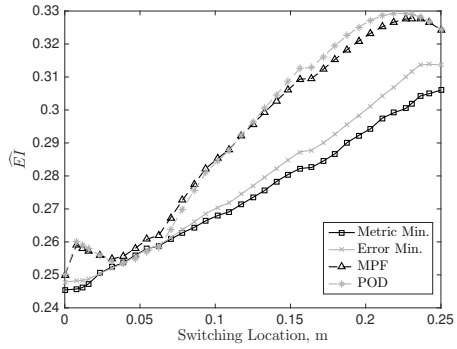

(e) $\widehat{EI}$, FF

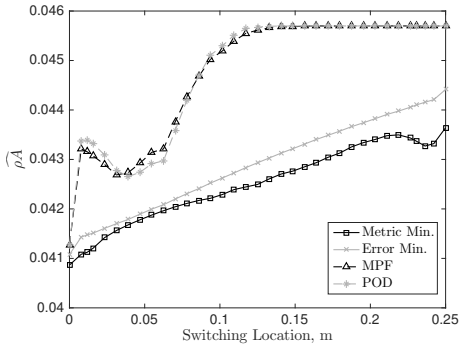

(f) $\widehat{\rho A}$, FF

Figure 5.27: Results for $\widehat{EI}$ and $\widehat{\rho A}$ coefficients for zigzag wrapping pattern with variable switching location.

For the diagonal wrapping pattern coefficients in Fig. 5.26, it is seen for the metric and error minimization methods that the pattern for the $\widehat{EI}$ coefficient is similar in behaviour to the tenth mode frequency results in Fig. 5.24. The MPF and POD methods predict a value for $\widehat{EI}$ that is similar to the behaviour of the fundamental mode results in Fig. 5.24. Overall there is an increase in the value of $\widehat{EI}$, as expected since adding a second string increases the bending stiffness of the system. With respect to the $\widehat{\rho A}$ variable, it is observed that all four of the proposed methods demonstrate a sudden increase in value when the switching location crosses over a lumped mass and the total mass suddenly increases. Overall it is also seen that the value of $\widehat{\rho A}$ increases as the switching location increases.

Consider the zigzag wrapping pattern $\widehat{EI}$ and $\widehat{\rho A}$ coefficients in Fig. 5.18. It is observed that, similar to the diagonal wrapping pattern case, the metric and error minimization methods predict values for $\widehat{EI}$ that are similar in behaviour to the frequency results for the tenth mode in Fig. 5.16 and for the MPF and POD methods the behaviour of $\widehat{EI}$ is similar to the behaviour of the frequency results for the fundamental mode in Fig. 5.16. Overall there is an increase in the value of $\widehat{EI}$, as expected since adding a second string increases the bending stiffness of the system. Considering the coefficient $\widehat{\rho A}$, there is an overall increase in the value as the second string is added to the system due to the increase in total mass.

As a second string is added into the system, there is both an increase in the bending stiffness as well as an increase in the mass per unit length. Depending on which of these effects is more dominant, the fundamental frequency may experience an increase or decrease in value. One important consideration for the approximation models is that they accurately capture these effects and do not, for example, associate an increase in frequency due to added stiffness as being caused by a reduction in mass. Considering the results in Figs. 5.26 and 5.27, it is seen that the MPF and POD methods demonstrate larger variations in the value of $\widehat{\rho A}$ when compared to the metric and error minimization methods. This is particularly evident for the diagonal wrapping pattern with FF boundary conditions. The more consistent increase in the value of $\widehat{\rho A}$ obtained for the metric and error minimization methods is a benefit to employing these models as the approximations.

The first step in quantifying the accuracy of each of the proposed approximation models given variable switching location is to examine the error between these and the perturbation theory results. Recall that the perturbation theory results were the results the approximate models attempted to match. The results for the diagonal wrapping pattern are presented in Fig. 5.28 and the zigzag pattern in Fig. 5.29.

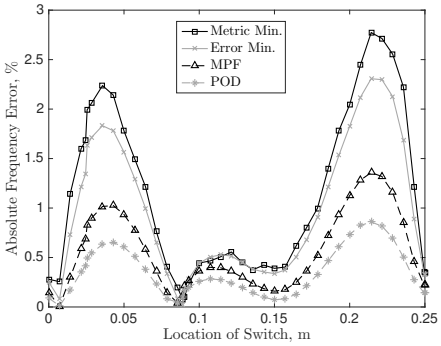

(a) Frequencies, CC

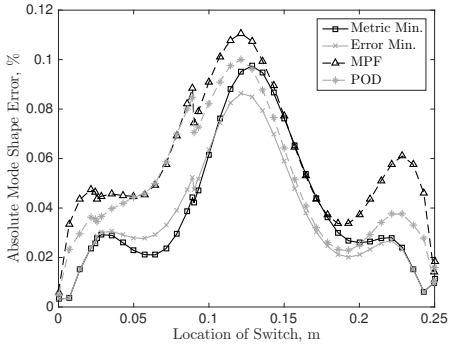

(b) Mode shapes, CC

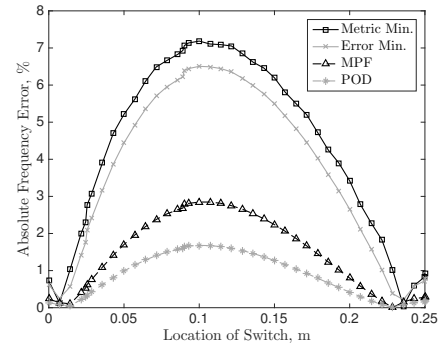

(c) Frequencies, CF

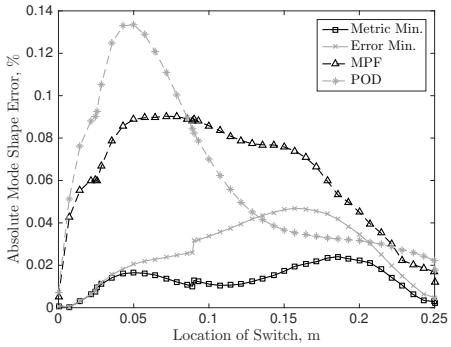

(d) Mode shapes, CF

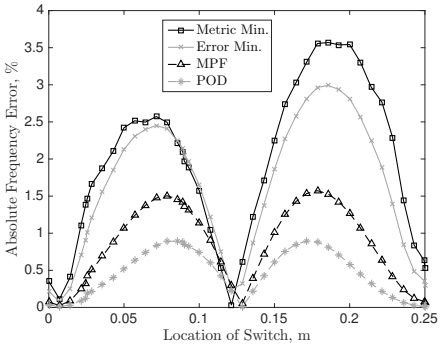

(e) Frequencies, FF

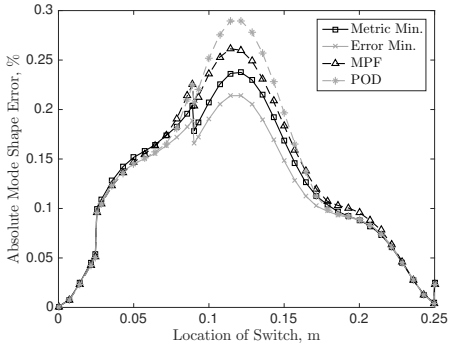

(f) Mode shapes, FF

Figure 5.28: Error in fundamental frequency and mode shape of approximate models to perturbation theory given variable switching location and diagonal wrapping pattern.

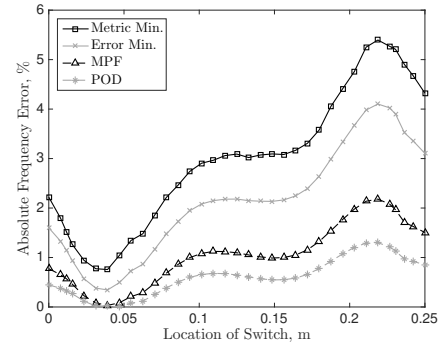

(a) Frequencies, CC

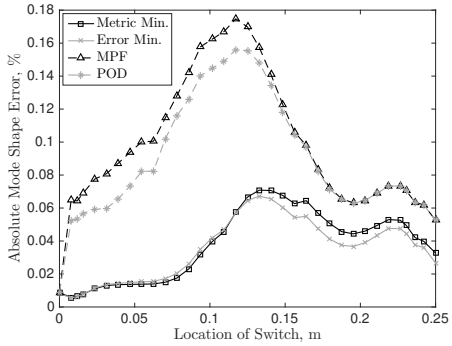

(b) Mode shapes, CC

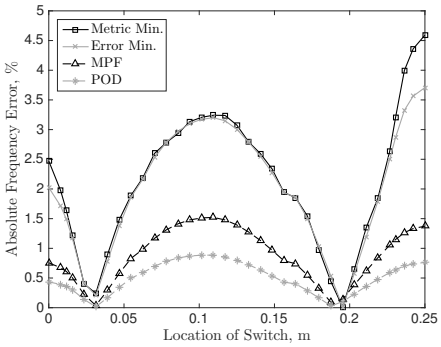

(c) Frequencies, CF

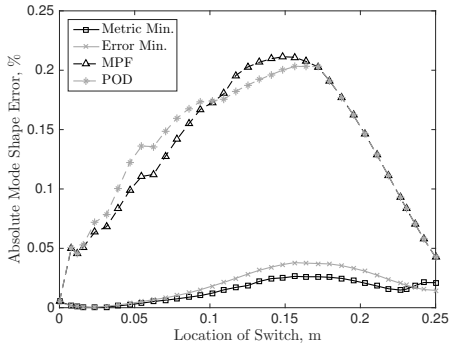

(d) Mode shapes, CF

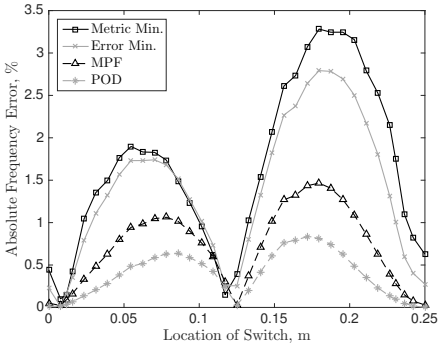

(e) Frequencies, FF

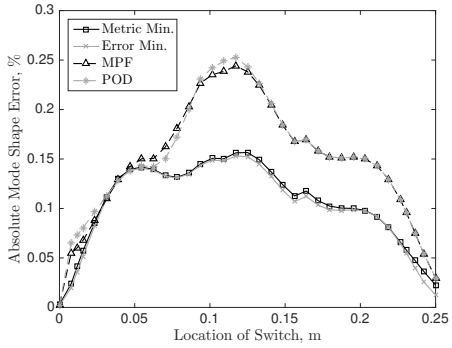

(f) Mode shapes, FF

Figure 5.29: Error in fundamental frequency and mode shape of approximate models to perturbation theory given variable switching location and zigzag wrapping pattern.

Figures 5.28 and 5.29 demonstrate a clear order for the errors in predicting the fundamental frequency. The POD is typically the most accurate approximation method, followed by the MPF method, next is the error minimization, and finally the metric minimization. With respect to the mode shape, the metric and error minimization methods consistently reported the smallest errors of the four methods, and the MPF and POD methods clearly produced the largest errors. Furthermore, it is interesting to note that the error for the fundamental frequency reaches minimal values for the four proposed methods at very similar switching locations. In other words, the locations where the fundamental frequency for the approximation methods are very similar to the perturbation theory results in Figs. 5.24 and 5.25 are quite similar across the various methods.

In addition to the accuracy of the proposed methods for the fundamental frequency and mode shape, the error with respect to the perturbation theory over multiple modes is considered. To this end, the sum of the absolute error of the first 10 modes of the system is considered and the average value of this sum for variable switching location is reported. The results for both wrapping patterns, each of the proposed approximation methods, and the various boundary conditions are presented in Table 5.7.

Table 5.7: Average sum of absolute percentage of error to perturbation theory for the first 10 natural frequencies and associated mode shapes for variable switching location with multiple strings

	Frequency Results			Mode Shape Results		
Result	CC	CF	FF	CC	CF	FF
	Diagonal Pattern			*Diagonal Pattern*		
Metric Min.	3.5194	8.3114	5.6082	5.95483934	5.20659034	7.56847098
Error Min.	3.5910	9.7016	5.5994	5.90541132	5.17041879	7.49053912
MPF	5.8793	27.3696	10.2917	6.11450350	5.32063127	7.66941008
POD	7.3924	32.8353	13.3433	6.00933435	5.37970274	7.70637068
	Zigzag Pattern			*Zigzag Pattern*		
Metric Min.	10.0852	7.0464	6.7883	4.10510995	3.71451015	4.56976302
Error Min.	9.1583	7.0315	6.5329	4.08478447	3.69486945	4.54498367
MPF	13.5540	13.5892	9.4947	4.69631091	4.34280229	5.05677107
POD	16.5124	16.4726	11.8699	4.61621719	4.36802364	5.06680108

It is seen in Table 5.7 that for the diagonal wrapping pattern the metric minimization method typically was the most accurate in predicting the frequencies, with the error minimization only being slightly more accurate in the case of FF boundary conditions.

Overall, the metric and error minimization methods both provide quite accurate methods for approximating the string-harnessed system, especially when compared to the large errors reported by the MPF and POD methods. With respect to the mode shapes, the error minimization method was the most accurate, followed by the metric minimization methods. The results for the zigzag wrapping pattern in Table 5.7 indicate that the error minimization method was the most accurate of the four methods for both frequency and mode shape results given all the boundary conditions. The metric minimization was the second most accurate method for the frequencies and mode shapes given all the boundary conditions. Overall, it is seen in Table 5.7 that the POD method was typically the least accurate method for both the frequencies and mode shapes, given both wrapping patterns and all the boundary conditions. The one exception was for the error in the mode shapes given CC boundary conditions. This indicates that when the behaviour of the frequencies given a variable parameter changes significantly between the various modes of interest, then an approximation methods that equally takes into account each of the modes is advantageous over methods that focus more strongly on approximating the fundamental modes.

Finally, the average sum of absolute error, given variable switching location, of the perturbation theory and the four proposed approximation methods to the exact solutions is presented in Table 5.8. The results for both wrapping patterns and the various boundary conditions are presented.

Table 5.8: Average sum of absolute percentage of error for the first 10 natural frequencies and associated mode shapes for variable switching location with multiple strings

	Frequency Results			Mode Shape Results		
Result	CC	CF	FF	CC	CF	FF
	Diagonal Pattern			*Diagonal Pattern*		
Perturbation	0.2605	0.2839	0.3188	0.10377754	0.08535005	0.13718868
Metric Min.	3.4900	8.1811	5.4228	6.16663218	5.49572167	8.01344090
Error Min.	3.4653	9.7025	5.5787	6.08734267	5.43816925	7.88174622
MPF	5.7017	27.4409	10.4197	6.24209527	5.56298963	7.97125086
POD	7.2204	32.9074	13.4921	6.28684039	5.58771879	7.99211329
	Zigzag Pattern			*Zigzag Pattern*		
Perturbation	1.1247	1.2999	1.4287	0.12759072	0.13578752	0.17124855
Metric Min.	10.7419	7.0535	6.5167	4.43607644	4.22983373	5.16244093
Error Min.	9.0534	6.9389	6.6661	4.40579896	4.19903920	5.12365073
MPF	12.9530	13.6748	9.9819	4.95712613	4.79735064	5.57070390
POD	15.7737	16.5756	12.3837	4.97561921	4.80800554	5.58070854

In Table 5.8, it is seen for the diagonal wrapping pattern that the error between the perturbation theory and the analytical results is not negligible for both the frequency and mode shapes, and for the zigzag wrapping pattern the error between perturbation theory and FEA is the largest of all the numerical simulations considered. Due to the size of the errors between the perturbation theory and exact solutions, it is expected that the errors in Table 5.8 will differ quite a bit from the errors in Table 5.7. For the case of variable switching location, it is seen that the order of the most to least accurate approximation method is changed when comparing the results in Table 5.8 to those of Table 5.7

With respect to the four approximation methods, it is seen in Table 5.8 that the most accurate method for predicting the frequencies is split between the metric minimization and the error minimization. The most accurate method for predicting the mode shapes is the error minimization method, regardless of wrapping pattern or boundary conditions. For the wrapping patterns considered and the various boundary conditions, the POD is consistently the least accurate method for both the frequencies and the mode shapes, and the MPF is consistently the second least accurate method for the frequencies and the mode shapes

Finally, the FRFs for the case of a switching location at $x = l/2$ are presented for the approximation methods and the exact solutions. Figure 5.30 presents driving point FRFs with an actuation and sensing location of $x = 0.025$ for CC boundary conditions and the

free end for CF and FF boundary conditions. In Fig. 5.30, both wrapping patterns are considered as well as the various boundary conditions. Note that since damping is not included in the models, the values of the resonant peaks are not relevant but rather their location is of interest.

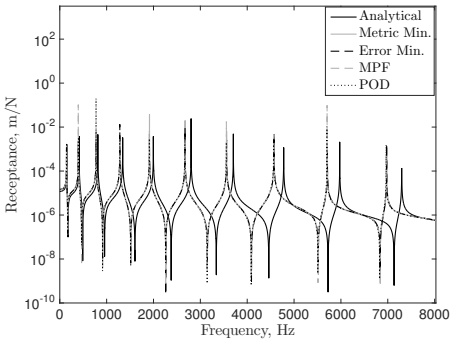

(a) Diagonal, CC

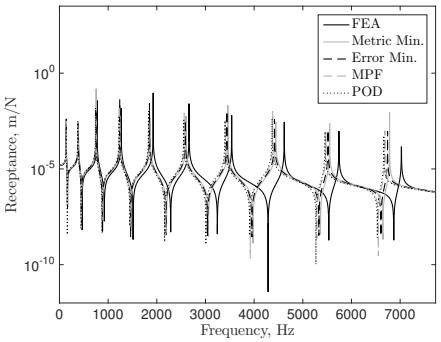

(b) Zigzag, CC

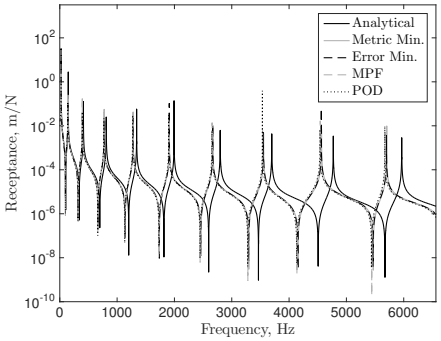

(c) Diagonal, CF

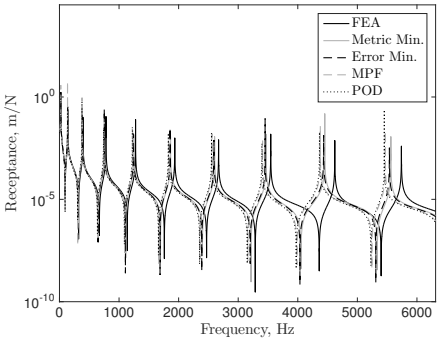

(d) Zigzag, CF

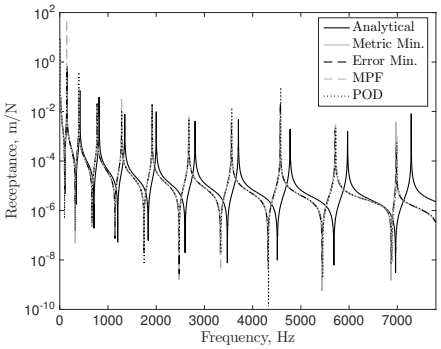

(e) Diagonal, FF

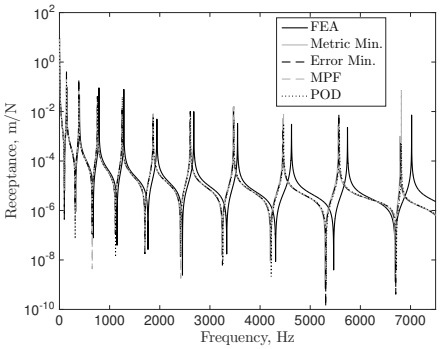

(f) Zigzag, FF

Figure 5.30: FRFs of exact solution and model approximations for variable switching location given various boundary conditions.

Overall in Fig. 5.30, it is seen that the FRFs of the approximate models are quite similar to the exact results for the lower modes with respect to location of resonances and antiresonances, as well as magnitude. For higher modes of the system, the approximate models become less accurate in predicting the resonant frequencies and antiresonances, however predict the magnitude quite well. The difficulty in predicting the FRF for the higher modes is a result of the original string-harnessed system being dissimilar to an constant coefficient beam due to variable wrapping angle and multiple strings. The approximate model FRF results for the diagonal wrapping pattern are seen to be very similar to one another. For the zigzag wrapping pattern it is seen, particularly in Figs. 5.30b and 5.30d, that the metric and error minimization methods predict FRFs that are a closer match to the FEA results than the MPF and POD methods. This is due to the metric and error minimization methods placing equal importance on matching all the modes of the system instead of a higher importance on the lower modes as in the MPF and POD methods.

In summary, non-periodic wrapping patterns with variable wrapping angle and variable number of strings were considered. In many of the numerical simulations performed, the difference in the bending stiffness and mass per unit length of the original string-harnessed system varied quite significantly across the length of the system. It has been shown that using a constant coefficient Euler-Bernoulli model and selecting the coefficients using the proposed methods provides quite accurate results for the frequencies and mode shapes, and hence FRFs, when compared to exact solutions. Through numerical simulations, it was seen that the MPF and POD methods excel at predicting the lower modes, in particular the fundamental mode, of the system while the metric and error minimization methods performed better over a larger number of modes. Of particular interest, the error minimization method is the only method of the four that had an average sum of absolute percentage error less than 10% for the various numerical simulations. Since the first ten modes were considered in the sum, this means that the error minimization method was the only method that predicted average error in each mode to be less than 1%.

5.2.3 Convergence of Approximate Models

In determining the results of the approximate models there are two key factors that can be varied, namely the number of modes in consideration and the value for sampling interval used in the POD method. To investigate the convergence of the results of the methods with respect to these parameters, the case of variable wrapping angle given a zigzag pattern is considered.

First consider the effect of increasing number of modes on the value predicted for $\widehat{EI}$ and $\widehat{\rho A}$. Figure 5.31 presents the results for the metric minimization method, Fig. 5.32

presents the results for the error minimization method, Fig. 5.33 presents the results for the MPF method, and Fig. 5.34 presents the results for the POD method. In each of these figures the results for CC, CF, and FF boundary conditions are given.

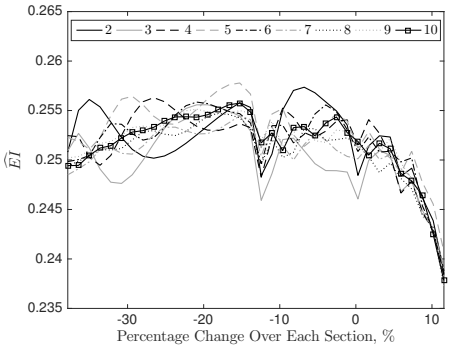

(a) $\widehat{EI}$, CC

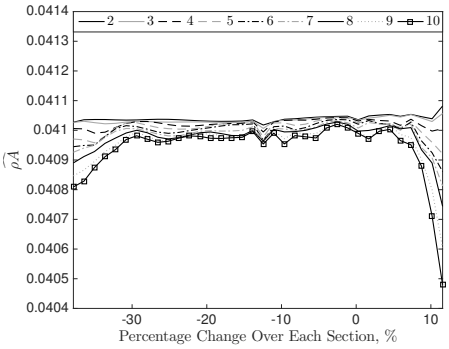

(b) $\widehat{\rho A}$, CC

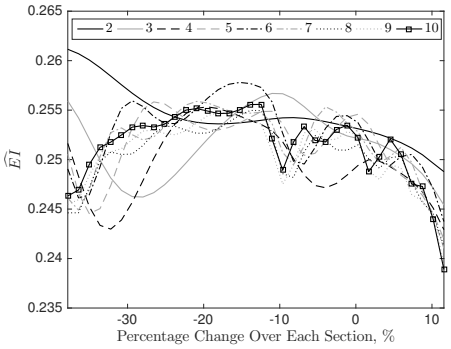

(c) $\widehat{EI}$, CF

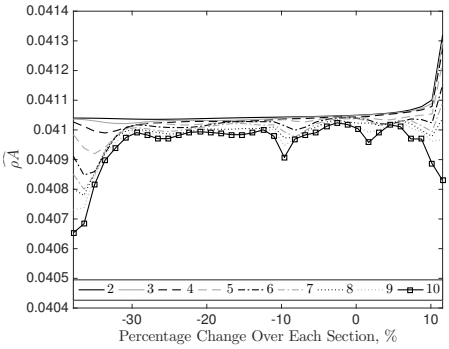

(d) $\widehat{\rho A}$, CF

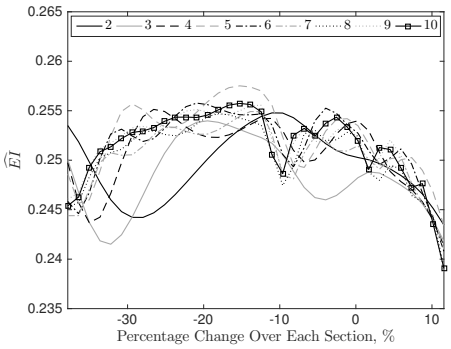

(e) $\widehat{EI}$, FF

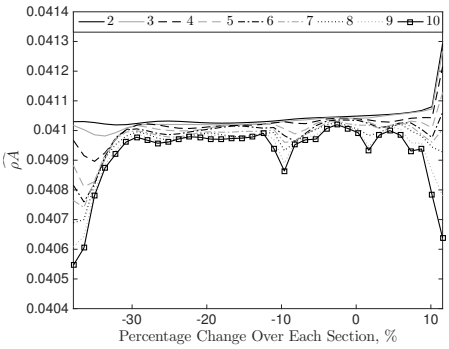

(f) $\widehat{\rho A}$, FF

Figure 5.31: Convergence of metric minimization method with respect to number of modes

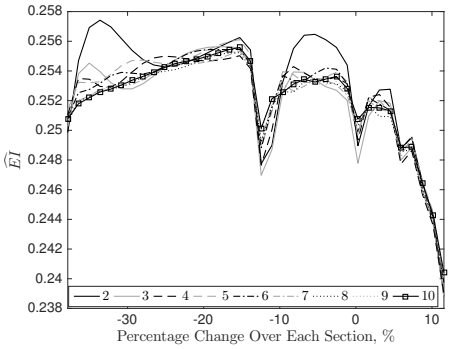

(a) $\widehat{EI}$, CC

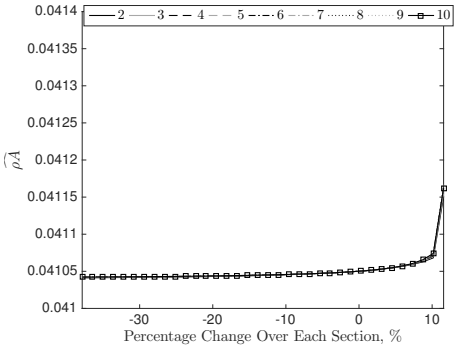

(b) $\widehat{\rho A}$, CC

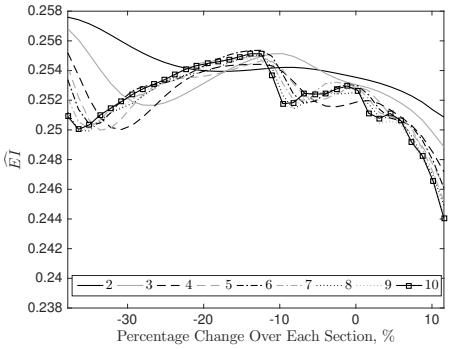

(c) $\widehat{EI}$, CF

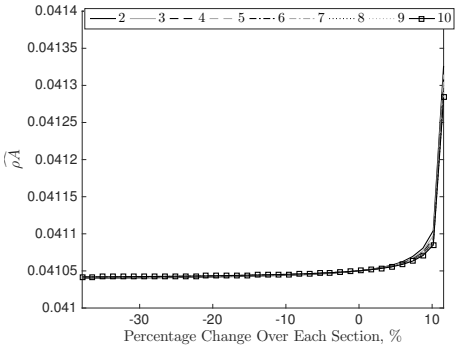

(d) $\widehat{\rho A}$, CF

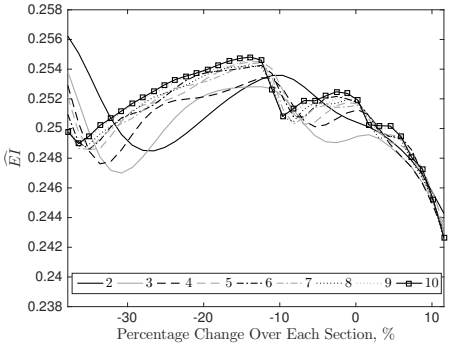

(e) $\widehat{EI}$, FF

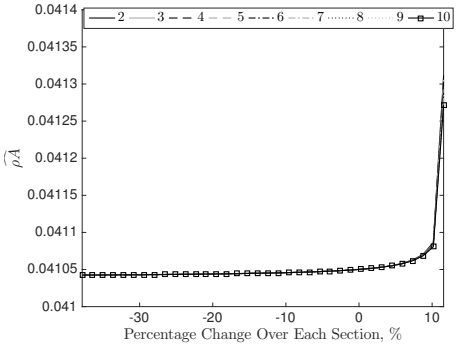

(f) $\widehat{\rho A}$, FF

Figure 5.32: Convergence of error minimization method with respect to number of modes

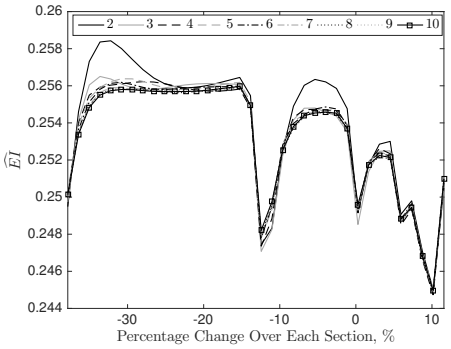

(a) $\widehat{EI}$, CC

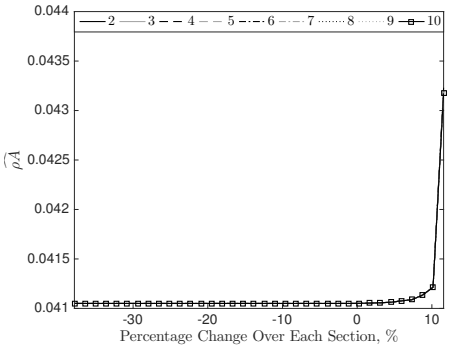

(b) $\widehat{\rho A}$, CC

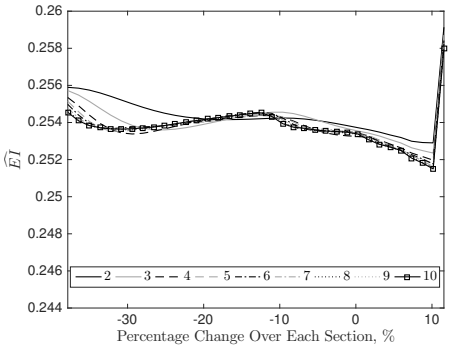

(c) $\widehat{EI}$, CF

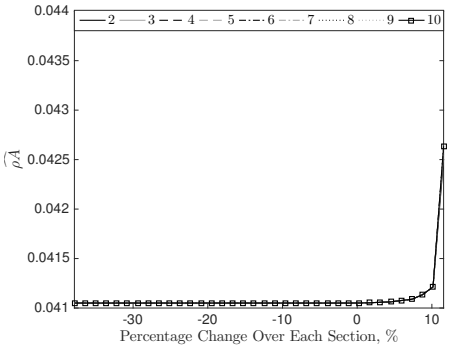

(d) $\widehat{\rho A}$, CF

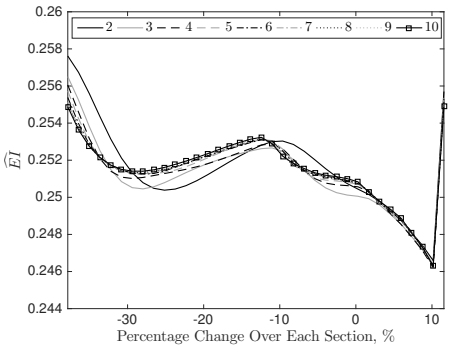

(e) $\widehat{EI}$, FF

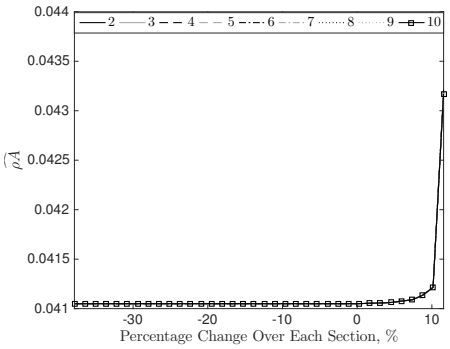

(f) $\widehat{\rho A}$, FF

Figure 5.33: Convergence of MPF method with respect to number of modes

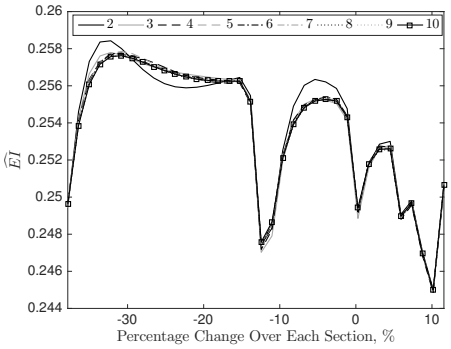

(a) $\widehat{EI}$, CC

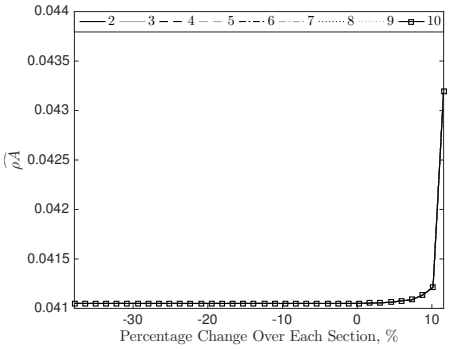

(b) $\widehat{\rho A}$, CC

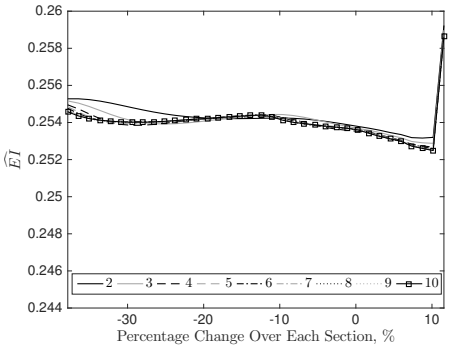

(c) $\widehat{EI}$, CF

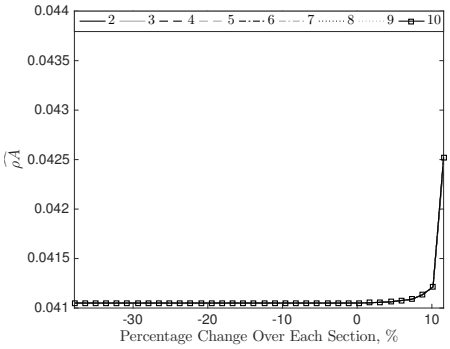

(d) $\widehat{\rho A}$, CF

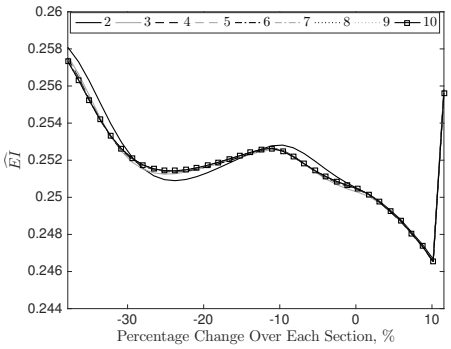

(e) $\widehat{EI}$, FF

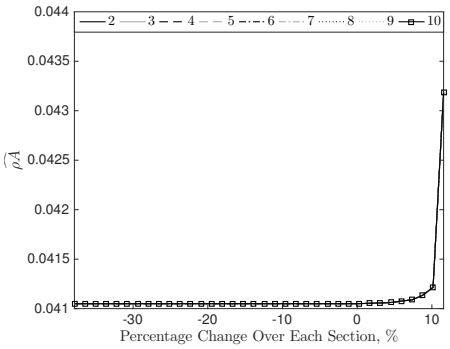

(f) $\widehat{\rho A}$, FF

Figure 5.34: Convergence of POD method with respect to number of modes

Overall, it is seen in Figs. 5.31 - 5.34 that for the cases of few number of modes in consideration, typically 2-5 modes, the behaviours of the $\widehat{EI}$ coefficient for variable percentage change in wrapping angle over each section are different from one another. This is also seen for the $\widehat{\rho A}$ coefficient when a metric minimization approach is employed. As the number of modes under consideration increases, the predicted values exhibit smaller variations and the results becomes quite similar for 8-10 modes. For the $\widehat{\rho A}$ coefficient predicted by the error minimization, the MPF method, and the POD method are almost identical regardless of the number of modes under consideration. Altogether, it is demonstrated that as the number of modes under consideration increases the results converge.

To explain the convergence with respect to number of modes under consideration, consider the following. If a large number of modes are used to determine the unknown coefficients $\widehat{EI}$ and $\widehat{\rho A}$, say for example 20 modes, then it is expected that the addition of a single mode will not have a great influence on the predicted values. For the results presented above, it appears as though once the approximation methods considered 7-8 modes, then the addition of one or two additional modes did not significantly impact the results.

POD Convergence with Respect to Sampling Interval

Next, consider the sampling interval, $\overline{T}$, used in the POD method. This sampling interval appears in the expression for the correlation function R in Eq. (5.17). It is expected that a sufficient number of periods of the fundamental mode will be related to the convergence of the POD method with respect to the sampling interval $\overline{T}$. Therefore, the convergence of the sampling interval will depend on the frequencies of the system, in particular the fundamental mode which has the longest period. Figure 5.35 considers the various boundary conditions and lists results for 4 distinct systems. The percentage change in the wrapping angle over each section for these systems are taken as equally spaced points from the range previously considered, including the left and rightmost points.

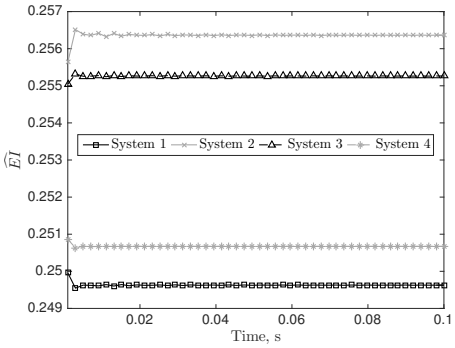

(a) $\widehat{EI}$, CC

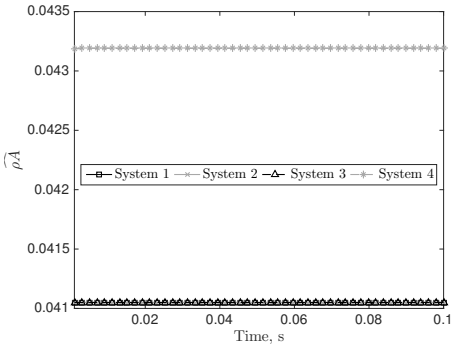

(b) $\widehat{\rho A}$, CC

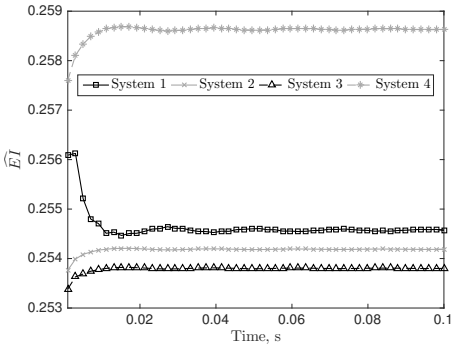

(c) $\widehat{EI}$, CF

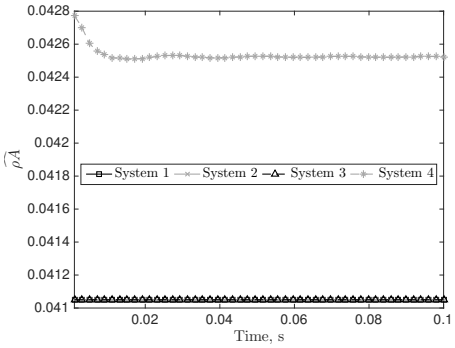

(d) $\widehat{\rho A}$, CF

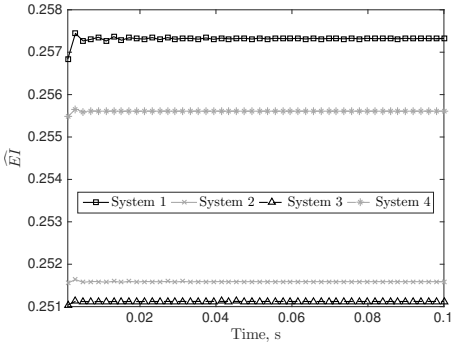

(e) $\widehat{EI}$, FF

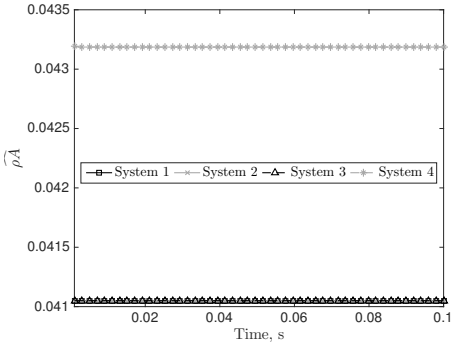

(f) $\widehat{\rho A}$, FF

Figure 5.35: Convergence of POD method with respect to the sampling interval

It is seen in Fig. 5.35 that the presented results all converge to a single value as the sampling interval increases. It is noted that the time for the predicted values of $\widehat{EI}$ and $\widehat{\rho A}$ is slower for CF boundary conditions when compared to CC and FF boundary conditions. This is due to a CF system having a smaller natural frequencies than when CC or FF boundary conditions are applied to the same system. A smaller natural frequency means that the time for the system to go through a single period of the fundamental mode is longer, thus increasing the time for convergence of the results.

For the results presented the smallest natural frequency occurred for System 4, corresponding to the right most point in the range considered for the percentage change in wrapping angle over each section. This natural frequency is also the smallest observed value over the entire range, as seen in Fig. 5.16. The smallest fundamental circular frequencies are 862.4 rad/s for CC boundary conditions, 138.7 rad/s for CF boundary conditions, and 870.9 rad/s for FF boundary conditions. These values correspond to a period of 0.0073 s, 0.0453 s, and 0.0072 s, respectively. In Fig. 5.35 it is observed that after one period of the fundamental mode the results for the coefficients begin to converge and after two full periods the results demonstrate very small differences as the sampling interval increases. For CC boundary conditions, after two full periods of the fundamental mode the variations in $\widehat{EI}$ and $\widehat{\rho A}$ were no larger than 0.0175% and 3.33×10^{-4}%, respectively. For CF boundary conditions, after two full periods of the fundamental mode the variations in $\widehat{EI}$ and $\widehat{\rho A}$ were no larger than 0.0073% and 0.0058%, respectively. For FF boundary conditions, after two full periods of the fundamental mode the variations in $\widehat{EI}$ and $\widehat{\rho A}$ were no larger than 0.0242% and 9.68×10^{-4}%, respectively. It is concluded that 2 full periods of the fundamental mode are sufficient to ensure that the coefficients in the POD method have converged with respect to time. The amount of time required to obtain a convergence can be determined from the perturbation theory results for the fundamental frequency of the system to be approximated.

5.3 Comparison of Approximate Models to Experimental Results

The accuracy of the proposed approximate models is further investigated with a comparison to experimental results. The experimental results considered for comparison are the results in Section 2.4 for periodic wrapping patterns and in Section 4.3 for non-periodic wrapping patterns. First, the FRFs of the system are compared in Figs. 5.36 - 5.38. In each of the figures, the results for the experimental test and the four approximation methods are presented. Furthermore, for the periodic wrapping pattern tests from Section 2.4 the

HOM model results are also included in Fig. 5.36. In this case, the HOM model results are equivalent to the STR model results presented in Chapter 2.

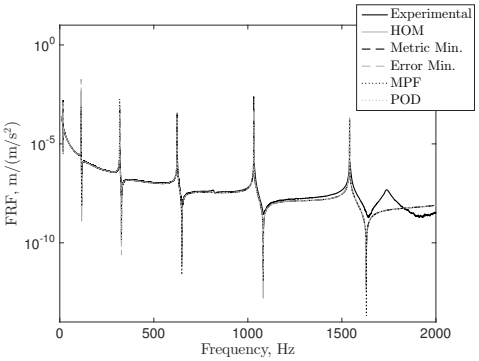

(a) Test 1

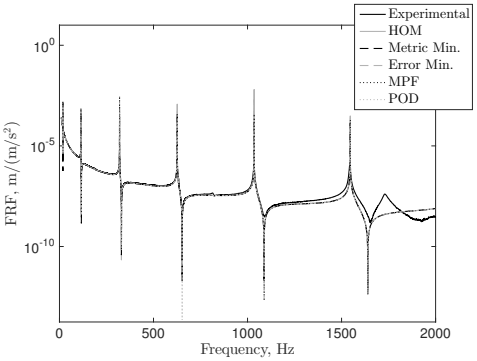

(b) Test 2

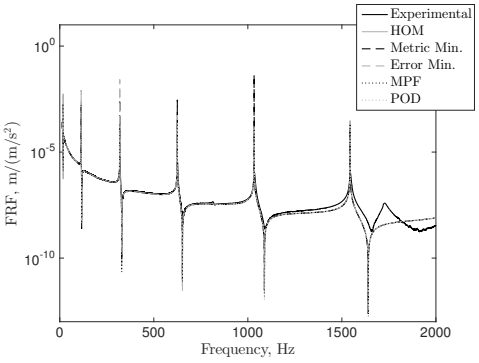

(c) Test 3

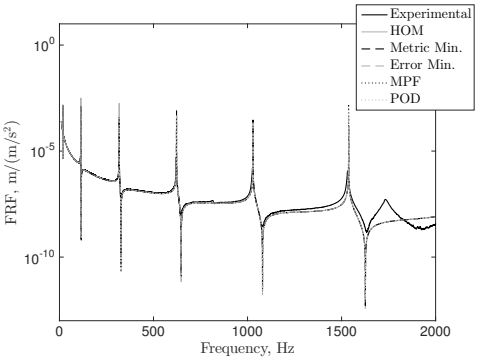

(d) Test 4

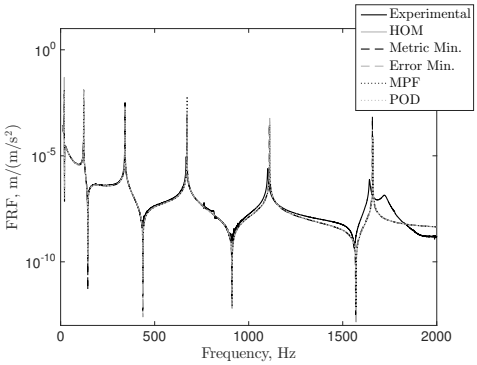

(e) Test 5

Figure 5.36: FRFs for experimental tests, HOM model, and approximation models given a periodic wrapping pattern

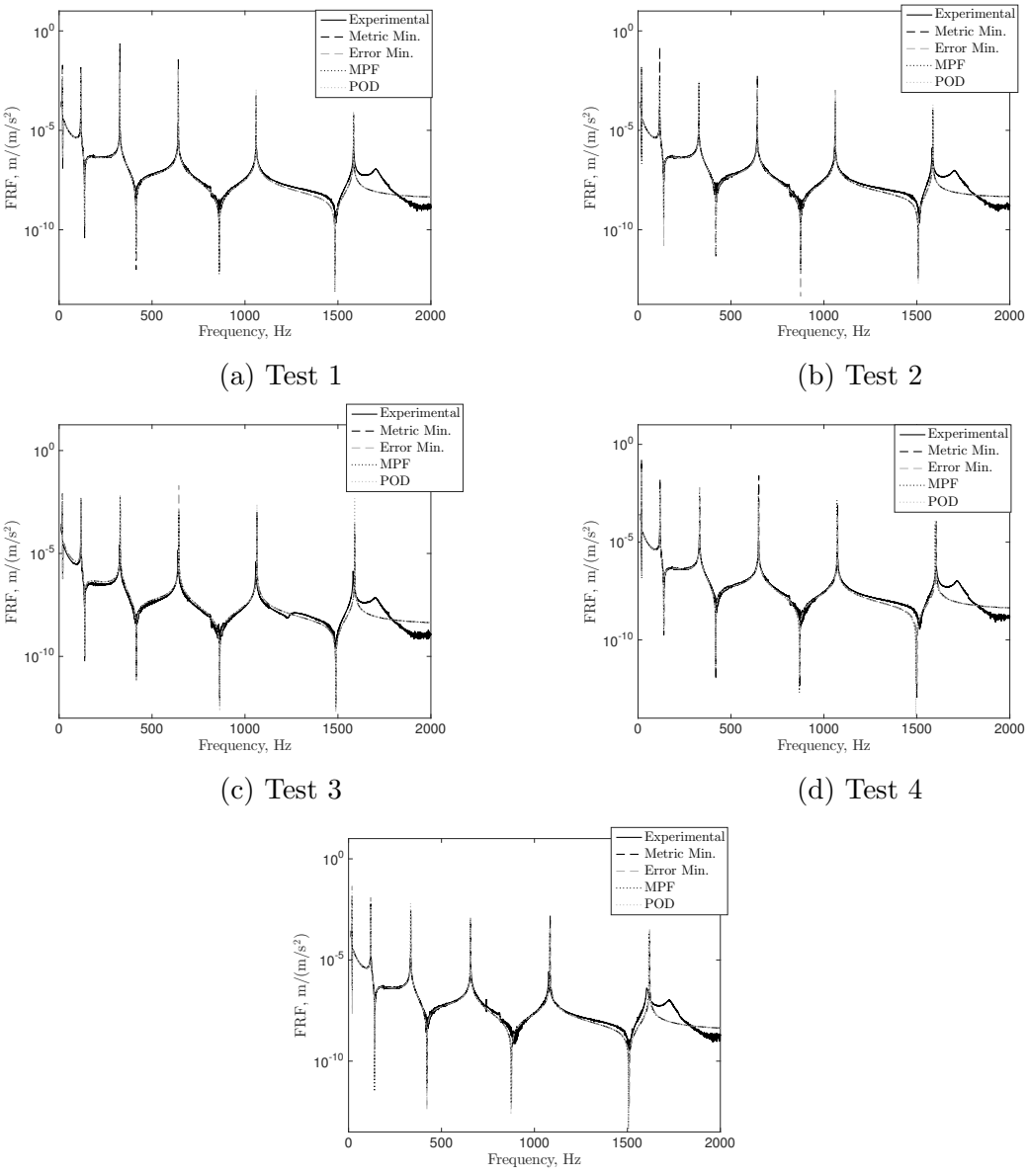

(a) Test 1

(b) Test 2

(c) Test 3

(d) Test 4

(e) Test 5

Figure 5.37: FRFs for experimental tests and approximation models given a non-periodic wrapping pattern and a single string

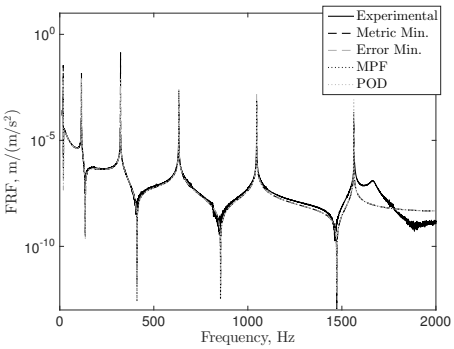

(a) Test 1

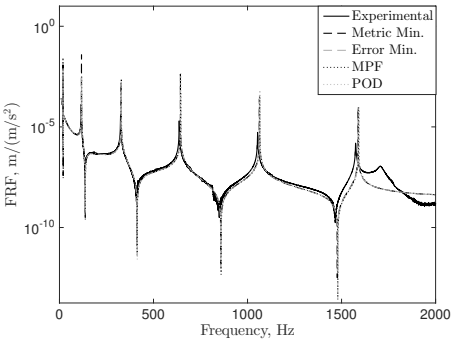

(b) Test 2

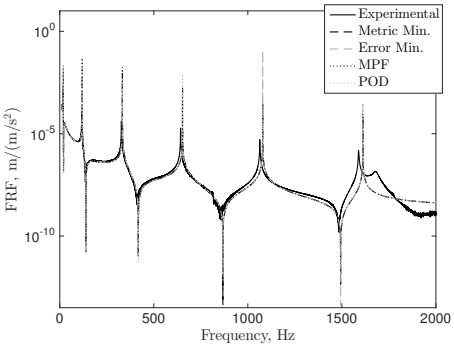

(c) Test 3

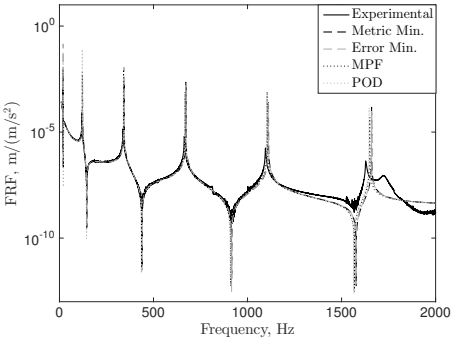

(d) Test 4

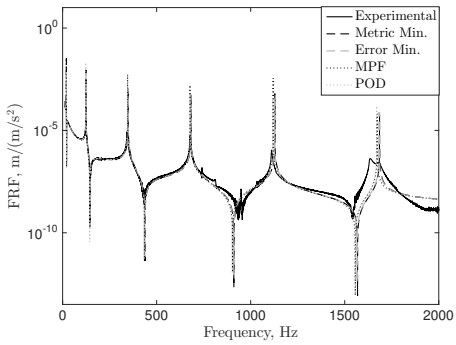

(e) Test 5

Figure 5.38: FRFs for experimental tests and approximation models given a non-periodic wrapping pattern and three strings

It should be noted that the magnitude of the resonant peaks in the FRFs are not expected to match between the experimental results and the HOM and approximate models in Figs. 5.36 - 5.38. This is due to the HOM and approximate models not including the effects of damping, hence the value of the peaks are meaningless. The important factors to consider when determining if the results are a good match are the locations of the resonant frequencies, the antiresonances, and the magnitude of the FRFs.

For the results using the periodic wrapping patterns in Fig. 5.36, it is seen that the results for the HOM and approximate models are very similar and only exhibit very small differences between them. For all of the presented results, the magnitude of the FRFs and the location of the antiresonances match quite well. Recall that the bump that is seen near 1,700 Hz is due to the section of beam that extends beyond the clamp and is not a frequency for the string-harnessed system. In terms of predicting the natural frequencies of the system, it is seen that there is a strong agreement from all the models. There is a slight amount of difference observed for the higher modes of the test with three strings in Fig. 5.36e. This is due to the method for modelling the string-harnessed system overpredicting the stiffness added due to one string, multiplied threefold for the three string test.

For the single string non-periodic wrapping pattern tests in Fig. 5.37, it is seen again that the results for the various proposed approximation models are very similar and only exhibit very small differences between them. For all of the presented results, the magnitude of the FRFs and the location of the antiresonances match quite well. With respect to the natural frequencies, the approximation models do a very good job of matching the experimental frequencies. It is observed that for test 5, the case where the system is the most loosely wrapped, there is an increase in the error when predicting the frequencies using the proposed models.

For the three string non-periodic wrapping pattern tests in Fig. 5.38, it is observed that as the test number increases, heading towards a more loosely wrapped system, the differences between the various proposed models become more noticeable. This is due to the fact that for the three string tests, as the test number increases the pattern of the experimental frequencies becomes less like an EB beam model. In these cases, the various manners in which the approximation models determine the unknown coefficients $\widehat{EI}$ and $\widehat{\rho A}$ will play a more significant role in predicting the frequencies. In the cases of tests 1 and 2, the frequencies of the string-harnessed system are similar in behaviour to those of an EB beam model. Therefore the various approximation methods tend to predict very similar results. For all the presented results, the magnitude of the FRFs and the location of the antiresonances match quite well. Regarding the natural frequencies, there is increasing error in the prediction of the frequencies as the wrapping pattern becomes more loosely

wrapped, from test 1 to test 5.

To quantify the errors in the FRF results, the values for the frequencies and the error compared to experimental results are presented. Table 5.9 lists the results for the periodic wrapping pattern tests, Table 5.10 lists the results for the single string non-periodic wrapping pattern tests, and Table 5.11 lists the results for the three string non-periodic wrapping pattern tests.

In Table 5.9 for the periodic wrapping patterns, it is observed that the HOM and the four proposed models agree quite well with the experimental results. The errors reported are typically less than 1% in each of the modes with the exceptions occurring for test 5, the case in which three strings are wrapped around the beam. In Table 5.9, the average sum of the absolute value of error in a given test is 2.58% for the HOM model, 2.4% for the metric minimization, 2.56% for the error minimization, and 2.64% for the MPF and POD methods. It is seen that on average each of the methods report similar accuracy, with the metric minimization producing the smallest average error.

In Table 5.10 for the single string non-periodic wrapping patterns, it is seen that the proposed approximate models all report errors of less than 1% when the system is more tightly wrapped, tests 1 through 3. As the string is more loosely wrapped the errors reported increase, with a maximum reported error of 1.50%. The average sum of the absolute value of error in a given test for Table 5.10 is 2.68% for the metric minimization, 2.51% for the error minimization, 2.22% for the MPF method, and 2.19% for the POD method. Again, it is seen that the average value for the error in a given test is fairly similar across the various proposed methods, with the POD method producing the smallest average error in this case.

Table 5.11 presents the results for the three string non-periodic wrapping patterns and it is seen that the errors reported are larger than for the single string test. This is due to the three strings producing a set of frequencies for the string-harnessed system that are less likely to follow the behaviour of the frequencies for an EB beam model. As the test number increases it is seen that the typical value for the error also increases, the largest error obtained was 4.13%. In Table 5.11, the average sum of the absolute value of error in a given test is 8.51% for the metric minimization, 8.22% for the error minimization, 7.00% or the MPF method, and 6.74% for the POD method. In the case of three strings harnessing the system it is observed that there is a larger difference between the accuracies of each of the models, with the POD method producing the smallest average error.

It is important to reiterate that the approximation models are attempting to match the frequencies predicted using a perturbation theory approach. Therefore any error between the perturbation theory results and the experimental results will introduce additional errors

Table 5.9: Experimental, HOM model, and proposed approximation models natural frequencies, in Hz, and percentage of error to experimental for periodically wrapped systems.

	Mode						Mode					
Result	1	2	3	4	5	6	1	2	3	4	5	6
	Test 1 Frequencies, Hz						*Test 1 Errors, %*					
Experimental	18.05	113.48	319.15	624.85	1033.0	1542.5	–	–	–	–	–	–
HOM	18.15	113.72	318.42	623.97	1031.5	1540.8	0.53	0.21	-0.23	-0.14	-0.15	-0.11
Metric Min.	18.14	113.71	318.39	623.92	1031.4	1540.7	0.5	0.20	-0.24	-0.15	-0.16	-0.12
Error Min.	18.15	113.72	318.42	623.98	1031.5	1540.8	0.53	0.21	-0.23	-0.14	-0.15	-0.11
MPF	18.15	113.73	318.43	624.00	1031.5	1540.9	0.54	0.22	-0.22	-0.14	-0.14	-0.10
POD	18.15	113.73	318.44	624.01	1031.5	1540.9	0.54	0.22	-0.22	-0.13	-0.14	-0.10
	Test 2 Frequencies, Hz						*Test 2 Errors, %*					
Experimental	18.05	113.44	319.35	625.05	1033.5	1542.5	–	–	–	–	–	–
HOM	18.21	114.12	319.55	626.19	1035.1	1546.3	0.89	0.60	0.063	0.183	0.16	0.25
Metric Min.	18.21	114.09	319.46	626.01	1034.8	1545.9	0.86	0.57	0.033	0.15	0.13	0.22
Error Min.	18.21	114.13	319.56	626.20	1035.2	1546.3	0.89	0.60	0.065	0.185	0.16	0.25
MPF	18.21	114.14	319.61	626.30	1035.3	1546.6	0.91	0.62	0.080	0.200	0.18	0.27
POD	18.21	114.15	319.61	626.31	1035.3	1546.6	0.91	0.62	0.082	0.202	0.18	0.27
	Test 3 Frequencies, Hz						*Test 3 Errors, %*					
Experimental	18.05	113.70	319.95	626.25	1035.5	1545.0	–	–	–	–	–	–
HOM	18.18	113.94	319.02	625.16	1033.4	1543.8	0.72	0.21	-0.29	-0.174	-0.20	-0.080
Metric Min.	18.18	113.90	318.93	624.98	1033.1	1543.3	0.69	0.18	-0.319	-0.204	-0.23	-0.11
Error Min.	18.18	113.94	319.03	625.17	1033.5	1543.8	0.73	0.21	-0.29	-0.172	-0.20	-0.078
MPF	18.18	113.96	319.08	625.27	1033.6	1544.0	0.74	0.23	-0.27	-0.16	-0.18	-0.062
POD	18.18	113.96	319.09	625.28	1033.6	1544.1	0.74	0.23	-0.27	-0.15	-0.18	-0.06
	Test 4 Frequencies, Hz						*Test 4 Errors, %*					
Experimental	17.95	112.79	317.10	620.90	1026.0	1532.0	–	–	–	–	–	–
HOM	18.11	113.46	317.7	622.56	1029.1	1537.4	0.86	0.60	0.19	0.268	0.31	0.35
Metric Min.	18.11	113.46	317.70	622.57	1029.2	1537.4	0.87	0.60	0.19	0.269	0.31	0.35
Error Min.	18.11	113.46	317.70	622.57	1029.2	1537.4	0.87	0.60	0.19	0.269	0.31	0.35
MPF	18.11	113.46	317.70	622.57	1029.2	1537.4	0.87	0.60	0.19	0.269	0.31	0.35
POD	18.11	113.46	317.70	622.57	1029.2	1537.4	0.87	0.60	0.19	0.269	0.31	0.35
	Test 5 Frequencies, Hz						*Test 5 Errors, %*					
Experimental	19.42	121.25	340.60	667.80	1101.1	1642.0	–	–	–	–	–	–
HOM	19.55	122.52	343.07	672.27	1111.3	1660.1	0.67	1.05	0.724	0.670	0.928	1.103
Metric Min.	19.52	122.35	342.60	671.35	1109.8	1657.8	0.54	0.911	0.586	0.532	0.79	0.964
Error Min.	19.55	122.49	342.99	672.11	1111.1	1659.7	0.65	1.03	0.700	0.646	0.904	1.08
MPF	19.56	122.56	343.18	672.50	1111.7	1660.7	0.71	1.08	0.758	0.704	0.962	1.14
POD	19.56	122.57	343.20	672.54	1111.8	1660.8	0.71	1.09	0.764	0.710	0.968	1.14

Table 5.10: Experimental and proposed approximation models natural frequencies, in Hz, and percentage of error to experimental for non-periodically wrapped systems with a single string.

	Mode						Mode					
Result	1	2	3	4	5	6	1	2	3	4	5	6
	Test 1 Frequencies, Hz						*Test 1 Errors, %*					
Experimental	18.535	116.25	326.65	640.30	1059.8	1583.2	–	–	–	–	–	–
Metric Min.	18.654	116.90	327.33	641.43	1060.3	1584.0	0.641	0.56	0.21	0.177	0.05	0.05
Error Min.	18.650	116.88	327.27	641.31	1060.1	1583.7	0.623	0.54	0.19	0.158	0.03	0.03
MPF	18.649	116.87	327.24	641.26	1060.0	1583.5	0.614	0.53	0.18	0.15	0.02	0.02
POD	18.649	116.87	327.24	641.26	1060.1	1583.5	0.615	0.53	0.18	0.15	0.02	0.02
	Test 2 Frequencies, Hz						*Test 2 Errors, %*					
Experimental	18.570	116.25	326.55	640.05	1058.9	1581.6	–	–	–	–	–	–
Metric Min.	18.670	117.00	327.61	641.99	1061.3	1585.3	0.539	0.65	0.326	0.303	0.22	0.24
Error Min.	18.672	117.01	327.64	642.05	1061.3	1585.5	0.548	0.66	0.334	0.312	0.23	0.24
MPF	18.681	117.07	327.81	642.38	1061.9	1586.3	0.600	0.71	0.386	0.364	0.28	0.30
POD	18.684	117.09	327.86	642.48	1062.1	1586.5	0.615	0.72	0.402	0.379	0.30	0.31
	Test 3 Frequencies, Hz						*Test 3 Errors, %*					
Experimental	18.610	116.70	327.75	642.80	1063.5	1588.8	–	–	–	–	–	–
Metric Min.	18.725	117.35	328.58	643.88	1064.4	1590.0	0.618	0.55	0.25	0.168	0.08	0.075
Error Min.	18.725	117.35	328.58	643.88	1064.4	1590.0	0.618	0.56	0.25	0.168	0.08	0.076
MPF	18.725	117.35	328.58	643.89	1064.4	1590.0	0.619	0.56	0.25	0.169	0.08	0.076
POD	18.725	117.35	328.58	643.89	1064.4	1590.0	0.619	0.56	0.25	0.169	0.08	0.077
	Test 4 Frequencies, Hz						*Test 4 Errors, %*					
Experimental	18.660	117.50	329.95	647.90	1071.4	1602.1	–	–	–	–	–	–
Metric Min.	18.896	118.42	331.57	649.75	1074.1	1604.5	1.26	0.78	0.492	0.286	0.25	0.15
Error Min.	18.877	118.30	331.25	649.12	1073.0	1602.9	1.17	0.68	0.394	0.188	0.15	0.05
MPF	18.831	118.01	330.44	647.52	1070.4	1599.0	0.916	0.44	0.15	-0.058	-0.093	-0.19
POD	18.818	117.93	330.21	647.07	1069.7	1597.9	0.846	0.37	0.078	-0.13	-0.16	-0.26
	Test 5 Frequencies, Hz						*Test 5 Errors, %*					
Experimental	18.800	119.15	332.40	656.45	1076.7	1603.3	–	–	–	–	–	–
Metric Min.	19.082	119.59	334.85	656.17	1084.7	1620.3	1.50	0.37	0.736	-0.043	0.74	1.06
Error Min.	19.073	119.53	334.68	655.85	1084.2	1619.5	1.45	0.32	0.687	-0.092	0.69	1.01
MPF	19.030	119.26	333.92	654.35	1081.7	1615.9	1.22	0.090	0.458	-0.319	0.46	0.784
POD	19.018	119.18	333.72	653.95	1081.0	1614.9	1.16	0.03	0.397	-0.380	0.40	0.722

Table 5.11: Experimental and proposed approximation models natural frequencies, in Hz, and percentage of error to experimental for non-periodically wrapped systems with three strings.

	Mode						Mode					
Result	1	2	3	4	5	6	1	2	3	4	5	6
	Test 1 Frequencies, Hz						*Test 1 Errors, %*					
Experimental	18.270	114.55	322.20	632.00	1046.3	1565.1	–	–	–	–	–	–
Metric Min.	18.416	115.41	323.15	633.24	1046.8	1563.7	0.798	0.75	0.29	0.197	0.05	-0.087
Error Min.	18.409	115.37	323.03	633.02	1046.4	1563.2	0.762	0.71	0.26	0.161	0.01	-0.12
MPF	18.407	115.36	323.00	632.96	1046.3	1563.0	0.752	0.70	0.25	0.15	0.002	-0.13
POD	18.409	115.37	323.03	633.01	1046.4	1563.2	0.760	0.71	0.26	0.159	0.01	-0.12
	Test 2 Frequencies, Hz						*Test 2 Errors, %*					
Experimental	18.450	115.65	324.90	636.65	1053.7	1574.4	–	–	–	–	–	–
Metric Min.	18.702	117.20	328.17	643.09	1063.1	1588.0	1.37	1.34	1.01	1.01	0.89	0.866
Error Min.	18.707	117.23	328.26	643.25	1063.3	1588.5	1.39	1.37	1.03	1.04	0.92	0.892
MPF	18.739	117.43	328.82	644.35	1065.2	1591.2	1.56	1.54	1.21	1.21	1.09	1.06
POD	18.748	117.49	328.97	644.66	1065.7	1591.9	1.61	1.59	1.25	1.26	1.14	1.11
	Test 3 Frequencies, Hz						*Test 3 Errors, %*					
Experimental	18.620	116.65	327.60	642.20	1063.6	1588.2	–	–	–	–	–	–
Metric Min.	18.984	118.97	333.12	652.78	1079.1	1612.0	1.95	1.99	1.68	1.647	1.46	1.50
Error Min.	18.978	118.94	333.02	652.59	1078.8	1611.5	1.92	1.96	1.66	1.618	1.43	1.47
MPF	18.978	118.93	333.02	652.59	1078.8	1611.5	1.92	1.96	1.65	1.617	1.43	1.47
POD	18.978	118.93	333.02	652.58	1078.8	1611.5	1.92	1.96	1.65	1.616	1.43	1.47
	Test 4 Frequencies, Hz						*Test 4 Errors, %*					
Experimental	18.770	120.00	337.55	663.65	1095.1	1628.2	–	–	–	–	–	–
Metric Min.	19.545	122.49	342.97	672.08	1111.0	1659.6	4.13	2.07	1.60	1.27	1.45	1.93
Error Min.	19.532	122.40	342.73	671.62	1110.2	1658.5	4.06	2.00	1.54	1.20	1.38	1.86
MPF	19.425	121.74	340.86	667.95	1104.2	1649.4	3.49	1.45	0.981	0.648	0.83	1.30
POD	19.391	121.52	340.26	666.77	1102.2	1646.5	3.31	1.27	0.803	0.471	0.65	1.13
	Test 5 Frequencies, Hz						*Test 5 Errors, %*					
Experimental	19.270	123.50	341.60	676.60	1110.7	1635.0	–	–	–	–	–	–
Metric Min.	19.849	124.39	348.29	682.52	1128.2	1685.4	3.00	0.72	1.96	0.874	1.58	3.08
Error Min.	19.820	124.21	347.80	681.54	1126.6	1683.0	2.86	0.58	1.81	0.730	1.43	2.94
MPF	19.694	123.42	345.58	677.20	1119.5	1672.3	2.20	-0.06	1.16	0.088	0.79	2.28
POD	19.661	123.21	344.99	676.05	1117.6	1669.4	2.03	-0.23	0.994	-0.081	0.62	2.11

for the approximate models when compared to the experimental results. For this reason it is seen in Figs. 5.9 - 5.11 that the POD method does not always predict the smallest error for the fundamental frequency as would be expected since it places the highest importance on matching the fundamental mode over the other methods. If the accuracy of the perturbation theory results compared to experimental was increased, then it would be expected that the POD method would be the most accurate in predicting the fundamental frequency and the average sum of error for a given test would be smallest for the error minimization method. This was seen in the previous section when comparing the approximate methods to the perturbation theory results for numerical simulations.

To summarize, in this chapter it is seen through numerical simulations that a constant coefficient EB model can accurately predict the frequencies of a string-harnessed system with both periodic and non-periodic wrapping patterns. This is quite advantageous in control applications as a simple model describing the dynamics of the system will result in quicker computational times. The strength of the proposed approximation model was shown by comparison to experimental results. In the case of a single string any of the approximation methods yield accurate predictions for the natural frequencies when compared to experimental results. For the three strings tests, larger errors are reported for all four proposed methods.

5.4 Chapter Summary

In this chapter, constant coefficient Euler-Bernoulli models were used to approximate the dynamic behaviour of string-harnessed systems. This was done for both periodic and non-periodic wrapping patterns, with the main motivation coming from the non-periodic case. Various approaches were considered to determine the coefficients in the approximate model. For the periodic wrapping pattern cases, it was shown that the model approximations were always more accurate the the homogenized model results. If only the fundamental or first couple of modes are of interest, a modal participation factor or proper orthogonal decomposition method are the best choices. This is due to these methods placing more emphasis on matching the lower modes of the system. If it is desired to match multiple modes in the system the error minimization approach should be used. The model approximation methods were then compared to the experimental results obtained for periodic and non-periodic wrapping patterns in Sections 2.4 and 4.3. It was seen that the model approximation methods? FRF results matched quite well with the experimental FRFs.

Chapter 6

Conclusion, Recommendations, and Future Work

6.1 Conclusion and Contributions

Motivated by the problem of harnessed signal and power cables greatly affecting the dynamics of the host structure, the presented work considers a simple initial step into this new area of research by developing and analyzing a string-harnessed model. First, after multiple efforts, an accurate method for modelling the string and beam system was developed. A homogenization technique was then applied to determine an equivalent continuum model for two types of periodic wrapping patterns, diagonal and zigzag. Numerical simulations were performed and it was shown that the homogenized model was quite accurate in predicting the natural frequencies of the system when compared to a fully coupled finite element analysis (FEA). Next the homogenized model was experimentally verified using various system setups and the results agreed quite strongly. This served to demonstrate the accuracy of the modelling technique used for the string-harnessed system.

A natural extension once an analysis is performed on periodic wrapping patterns is to consider non-periodic wrapping patterns. As the spatially dependent partial differential equation cannot be solved directly, a perturbation theory approach is employed. To be able to apply the perturbation theory to the wrapping patterns in consideration, the current literature on the topic had to be updated to include lumped masses. In addition, further corrections for the frequencies and the mode shapes of the system were determined to improve the accuracy of the perturbation theory. Once developed, the improved perturbation theory was applied to non-periodic string-harnessed systems. Numerical simulations

indicated that the perturbation theory was quite accurate in predicting the frequencies of the string-harnessed system when compared to a decoupled FEA. In particular, it was determined that using a gradient norm minimization approach to determine the reference values necessary to apply the perturbation theory was the most accurate. Another advantage of the gradient norm minimization approach is that the final result for the expression of the frequencies is simpler in form than when applying the other reference value selection methods. The perturbation theory results were then experimentally verified using multiple different non-periodic wrapping patterns. The results were in good agreement, particularly for the case of a single string in the harnessed system. This served to highlight the ability and accuracy of the perturbation theory, as well as the modelling technique developed earlier, for the more general case of non-periodic wrapping patterns.

Similar to the idea of a homogenized model accurately predicting the frequencies and mode shapes of a periodically wrapped system, constant coefficient Euler-Bernoulli models were used to predict the frequencies and mode shapes of periodically and non-periodically wrapped systems. To investigate the efficacy of these models to serve as an approximate model for the string-harnessed system, multiple methods for choosing the unknown constant coefficients were considered. Numerical simulations of periodic wrapping patterns indicated that all of the four proposed methods produced more accurate results for the frequencies and mode shapes when compared to the homogenization method. This highlights the value of using methods for determining an equivalent continuum model other than the homogenization technique. Numerical simulations of non-periodic wrapping patterns showed that typically the most accurate of the proposed approximation methods was the error minimization approach. This was with respect to the perturbation theory results, which were taking as accurate. When the approximation methods were compared to FEA results, it was found that either a metric or error minimization approach would produce results with similar levels of error for the frequencies and mode shapes. Finally, the model approximation methods were compared to all of the previously obtained experimental data. With the exception of somewhat higher errors occurring when then system is more loosely wrapped, it was shown that the frequency response functions matched quite well.

The contributions of the presented work can be summarized as follows:

1. *Modelling of string-harnessed systems*
2. *Applying homogenization technique for global dynamics behaviour of string-harnessed systems*
3. *Improvements to Lindstedt-Poincaré perturbation theory for Euler-Bernoulli model*

4. *Applying perturbation theory to string-harnessed systems*

5. *Experimental validation of string-harnessed system modelling*

6. *Transverse vibration model approximation of periodically and non-periodically wrapped string-harnessed systems*

6.2 Future Work and Recommendations

In terms of future work, the are a few ways in which the string-harnessed model could be further improved. First, the model used to describe the vibration of the system could be generalized. For instance, a shear or Timoshenko beam model could be employed. Another generalization that would be of great value is coupling between the various coordinates of vibration. It was seen in the presented work for a finite element analysis that coupling plays an important role in the prediction of the frequencies of the system when certain parameters, such as string radius and tension, play an important role. Following the development of a coupled string-harnessed model, applying the techniques of homogenization and perturbation theory would be useful for investigating the behaviour of the frequencies under parameter variations as well as periodic and non-periodic wrapping patterns.

Another interesting step for future research would be the inclusion of damping. Damping can be included in the model in two main ways: through the interaction between the string and the host structure, as well as damping within each of the components of the string-harnessed system. The latter would be particularly useful since once a damped model is developed, it could be combined with the results in the literature focused on the characterization of cables typically used in aerospace applications. This would allow for the development of an analytical model for a cable-harnessed structure.

Finally, the results for the model approximation using a constant coefficient Euler-Bernoulli beam are quite promising. To obtain further accuracy, the approach presented in the presented work could be extended for more generalized models. For example a generalized Euler-Bernoulli model with additional components, such as a constant compressive force, could be considered. By increasing the number of unknown coefficients in the model, the likelihood of obtaining smaller errors when predicting the frequencies is greater. In addition, by including additional coefficients into the approximate model that are physically motivated this will provide the researcher with an intuitive manner in which string-harnessed systems, and changes to their parameters and wrapping pattern, can be understood.

Letter of Copyright Permission

fashion.

3. Scope of License; Limitations and Obligations.

3.1 All Works and all rights therein, including copyright rights, remain the sole and exclusive property of the Rightsholder. The license created by the exchange of an Order Confirmation (and/or any invoice) and payment by User of the full amount set forth on that document includes only those rights expressly set forth in the Order Confirmation and in these terms and conditions, and conveys no other rights in the Work(s) to User. All rights not expressly granted are hereby reserved.

3.2 General Payment Terms: You may pay by credit card or through an account with us payable at the end of the month. If you and we agree that you may establish a standing account with CCC, then the following terms apply: Remit Payment to: Copyright Clearance Center, 29118 Network Place, Chicago, IL 60673-1291. Payments Due: Invoices are payable upon their delivery to you (or upon our notice to you that they are available to you for downloading). After 30 days, outstanding amounts will be subject to a service charge of 1-1/2% per month or, if less, the maximum rate allowed by applicable law. Unless otherwise specifically set forth in the Order Confirmation or in a separate written agreement signed by CCC, invoices are due and payable on "net 30" terms. While User may exercise the rights licensed immediately upon issuance of the Order Confirmation, the license is automatically revoked and is null and void, as if it had never been issued, if complete payment for the license is not received on a timely basis either from User directly or through a payment agent, such as a credit card company.

3.3 Unless otherwise provided in the Order Confirmation, any grant of rights to User (i) is "one-time" (including the editions and product family specified in the license), (ii) is non-exclusive and non-transferable and (iii) is subject to any and all limitations and restrictions (such as, but not limited to, limitations on duration of use or circulation) included in the Order Confirmation or invoice and/or in these terms and conditions. Upon completion of the licensed use, User shall either secure a new permission for further use of the Work(s) or immediately cease any new use of the Work(s) and shall render inaccessible (such as by deleting or by removing or severing links or other locators) any further copies of the Work (except for copies printed on paper in accordance with this license and still in User's stock at the end of such period).

3.4 In the event that the material for which a republication license is sought includes third party materials (such as photographs, illustrations, graphs, inserts and similar materials) which are identified in such material as having been used by permission, User is responsible for identifying, and seeking separate licenses (under this Service or otherwise) for, any of such third party materials; without a separate license, such third party materials may not be used.

3.5 Use of proper copyright notice for a Work is required as a condition of any license granted under the Service. Unless otherwise provided in the Order Confirmation, a proper copyright notice will read substantially as follows: "Republished with permission of [Rightsholder's name], from [Work's title, author, volume, edition number and year of copyright]; permission conveyed through Copyright Clearance Center, Inc. " Such notice must be provided in a reasonably legible font size and must be placed either immediately adjacent to the Work as used (for example, as part of a by-line or footnote but not as a separate electronic link) or in the place where substantially all other credits or notices for the new work containing the republished Work are located. Failure to include the required notice results in loss to the Rightsholder and CCC, and the User shall be liable to pay liquidated damages for each such failure equal to twice the use fee specified in the Order Confirmation, in addition to the use fee itself and any other fees and charges specified.

3.6 User may only make alterations to the Work if and as expressly set forth in the Order Confirmation. No Work may be used in any way that is defamatory, violates the rights of third parties (including such third parties' rights of copyright, privacy, publicity, or other tangible or intangible property), or is otherwise illegal, sexually explicit or obscene. In addition, User may not conjoin a Work with any other material that may result in damage to the reputation of the Rightsholder. User agrees to inform CCC if it becomes aware of any infringement of any rights in a Work and to cooperate with any reasonable request of CCC or the Rightsholder in connection therewith.

4. Indemnity. User hereby indemnifies and agrees to defend the Rightsholder and CCC, and their respective employees and directors, against all claims, liability, damages, costs and expenses, including legal fees and expenses, arising out of any use of a Work beyond the scope of the rights granted herein, or any use of a Work which has been altered in any unauthorized way by User, including claims of defamation or infringement of rights of copyright, publicity, privacy or other tangible or intangible property.

5. Limitation of Liability. UNDER NO CIRCUMSTANCES WILL CCC OR THE RIGHTSHOLDER BE LIABLE FOR ANY DIRECT, INDIRECT, CONSEQUENTIAL OR INCIDENTAL DAMAGES (INCLUDING WITHOUT LIMITATION DAMAGES FOR LOSS OF BUSINESS PROFITS OR INFORMATION, OR FOR BUSINESS INTERRUPTION) ARISING OUT OF THE USE OR INABILITY TO USE A WORK, EVEN IF ONE OF THEM HAS BEEN ADVISED OF THE POSSIBILITY OF SUCH DAMAGES. In any event, the total liability of the Rightsholder and CCC (including their respective employees and directors) shall not exceed the total amount actually paid by User for this license. User assumes full liability for the actions and omissions of its principals, employees, agents, affiliates, successors and assigns.

6. Limited Warranties. THE WORK(S) AND RIGHT(S) ARE PROVIDED "AS IS". CCC HAS THE RIGHT TO GRANT TO USER THE RIGHTS GRANTED IN THE ORDER CONFIRMATION DOCUMENT. CCC AND THE RIGHTSHOLDER DISCLAIM ALL OTHER WARRANTIES RELATING TO THE WORK(S) AND RIGHT(S), EITHER EXPRESS OR IMPLIED, INCLUDING WITHOUT LIMITATION IMPLIED WARRANTIES OF MERCHANTABILITY OR FITNESS FOR A PARTICULAR PURPOSE. ADDITIONAL RIGHTS MAY BE REQUIRED TO USE ILLUSTRATIONS, GRAPHS, PHOTOGRAPHS, ABSTRACTS, INSERTS OR OTHER PORTIONS OF THE WORK (AS OPPOSED TO THE ENTIRE WORK) IN A MANNER CONTEMPLATED BY USER; USER

UNDERSTANDS AND AGREES THAT NEITHER CCC NOR THE RIGHTSHOLDER MAY HAVE SUCH ADDITIONAL RIGHTS TO GRANT.

7. Effect of Breach. Any failure by User to pay any amount when due, or any use by User of a Work beyond the scope of the license set forth in the Order Confirmation and/or these terms and conditions, shall be a material breach of the license created by the Order Confirmation and these terms and conditions. Any breach not cured within 30 days of written notice thereof shall result in immediate termination of such license without further notice. Any unauthorized (but licensable) use of a Work that is terminated immediately upon notice thereof may be liquidated by payment of the Rightsholder's ordinary license price therefor; any unauthorized (and unlicensable) use that is not terminated immediately for any reason (including, for example, because materials containing the Work cannot reasonably be recalled) will be subject to all remedies available at law or in equity, but in no event to a payment of less than three times the Rightsholder's ordinary license price for the most closely analogous licensable use plus Rightsholder's and/or CCC's costs and expenses incurred in collecting such payment.

8. **Miscellaneous.**

8.1 User acknowledges that CCC may, from time to time, make changes or additions to the Service or to these terms and conditions, and CCC reserves the right to send notice to the User by electronic mail or otherwise for the purposes of notifying User of such changes or additions; provided that any such changes or additions shall not apply to permissions already secured and paid for.

8.2 Use of User-related information collected through the Service is governed by CCC's privacy policy, available online here: http://www.copyright.com/content/cc3/en/tools/footer/privacypolicy.html.

8.3 The licensing transaction described in the Order Confirmation is personal to User. Therefore, User may not assign or transfer to any other person (whether a natural person or an organization of any kind) the license created by the Order Confirmation and these terms and conditions or any rights granted hereunder; provided, however, that User may assign such license in its entirety on written notice to CCC in the event of a transfer of all or substantially all of User's rights in the new material which includes the Work(s) licensed under this Service.

8.4 No amendment or waiver of any terms is binding unless set forth in writing and signed by the parties. The Rightsholder and CCC hereby object to any terms contained in any writing prepared by the User or its principals, employees, agents or affiliates and purporting to govern or otherwise relate to the licensing transaction described in the Order Confirmation, which terms are in any way inconsistent with any terms set forth in the Order Confirmation and/or in these terms and conditions or CCC's standard operating procedures, whether such writing is prepared prior to, simultaneously with or subsequent to the Order Confirmation, and whether such writing appears on a copy of the Order Confirmation or in a separate instrument.

8.5 The licensing transaction described in the Order Confirmation document shall be governed by and construed under the law of the State of New York, USA, without regard to the principles thereof of conflicts of law. Any case, controversy, suit, action, or proceeding arising out of, in connection with, or related to such licensing transaction shall be brought, at CCC's sole discretion, in any federal or state court located in the County of New York, State of New York, USA, or in any federal or state court whose geographical jurisdiction covers the location of the Rightsholder set forth in the Order Confirmation. The parties expressly submit to the personal jurisdiction and venue of each such federal or state court.If you have any comments or questions about the Service or Copyright Clearance Center, please contact us at 978-750-8400 or send an e-mail to info@copyright.com.

v 1.1

AIAA journal
Permission type: Republish or display content
Type of use: Republish in a thesis/dissertation

TERMS AND CONDITIONS

The following terms are individual to this publisher:

Verification of copyright ownership is your responsibility. You should only submit requests for materials that are owned by AIAA. Please review the copyright statement for the source material before submitting a reprint permission request, to ensure that AIAA is the copyright owner:

- For AIAA meeting papers, journal papers, or books with independently authored chapters (e.g., many Progress Series volumes), look at the bottom of the first full-text page (not the cover page). There will be a footnote

indicating who holds copyright.

- For other books, look at the copyright statement on the back of the title page.

If the statement reads "Copyright by the American Institute of Aeronautics and Astronautics, Inc.," then AIAA is the copyright owner, and you may submit your request.

If the statement reads otherwise, AIAA does not hold copyright, and cannot grant permission to reprint. You must seek permission from the copyright owner rather than AIAA.

Preferred credit line for reprinted material: From [original title and authors]; reprinted by permission of the American Institute of Aeronautics and Astronautics, Inc. Note that the original source also should be cited in full in the reference list.

Other Terms and Conditions:

STANDARD TERMS AND CONDITIONS

1. Description of Service; Defined Terms. This Republication License enables the User to obtain licenses for republication of one or more copyrighted works as described in detail on the relevant Order Confirmation (the "Work(s)"). Copyright Clearance Center, Inc. ("CCC") grants licenses through the Service on behalf of the rightsholder identified on the Order Confirmation (the "Rightsholder"). "Republication", as used herein, generally means the inclusion of a Work, in whole or in part, in a new work or works, also as described on the Order Confirmation. "User", as used herein, means the person or entity making such republication.

2. The terms set forth in the relevant Order Confirmation, and any terms set by the Rightsholder with respect to a particular Work, govern the terms of use of Works in connection with the Service. By using the Service, the person transacting for a republication license on behalf of the User represents and warrants that he/she/it (a) has been duly authorized by the User to accept, and hereby does accept, all such terms and conditions on behalf of User, and (b) shall inform User of all such terms and conditions. In the event such person is a "freelancer" or other third party independent of User and CCC, such party shall be deemed jointly a "User" for purposes of these terms and conditions. In any event, User shall be deemed to have accepted and agreed to all such terms and conditions if User republishes the Work in any fashion.

3. Scope of License; Limitations and Obligations.

3.1 All Works and all rights therein, including copyright rights, remain the sole and exclusive property of the Rightsholder. The license created by the exchange of an Order Confirmation (and/or any invoice) and payment by User of the full amount set forth on that document includes only those rights expressly set forth in the Order Confirmation and in these terms and conditions, and conveys no other rights in the Work(s) to User. All rights not expressly granted are hereby reserved.

3.2 General Payment Terms: You may pay by credit card or through an account with us payable at the end of the month. If you and we agree that you may establish a standing account with CCC, then the following terms apply: Remit Payment to: Copyright Clearance Center, 29118 Network Place, Chicago, IL 60673-1291. Payments Due: Invoices are payable upon their delivery to you (or upon our notice to you that they are available to you for downloading). After 30 days, outstanding amounts will be subject to a service charge of 1-1/2% per month or, if less, the maximum rate allowed by applicable law. Unless otherwise specifically set forth in the Order Confirmation or in a separate written agreement signed by CCC, invoices are due and payable on "net 30" terms. While User may exercise the rights licensed immediately upon issuance of the Order Confirmation, the license is automatically revoked and is null and void, as if it had never been issued, if complete payment for the license is not received on a timely basis either from User directly or through a payment agent, such as a credit card company.

3.3 Unless otherwise provided in the Order Confirmation, any grant of rights to User (i) is "one-time" (including the editions and product family specified in the license), (ii) is non-exclusive and non-transferable and (iii) is subject to any and all limitations and restrictions (such as, but not limited to, limitations on duration of use or circulation) included in the Order Confirmation or invoice and/or in these terms and conditions. Upon completion of the licensed use, User shall either secure a new permission for further use of the Work(s) or immediately cease any new use of the Work(s) and shall render inaccessible (such as by deleting or by removing or severing links or other locators) any further copies of the Work (except for copies printed on paper in accordance with this license and still in User's stock at the end of such period).

3.4 In the event that the material for which a republication license is sought includes third party materials (such as photographs, illustrations, graphs, inserts and similar materials) which are identified in such material as having been used by permission, User is responsible for identifying, and seeking separate licenses (under this Service or otherwise) for, any of such third party materials; without a separate license, such third party materials may not be used.

3.5 Use of proper copyright notice for a Work is required as a condition of any license granted under the Service. Unless otherwise provided in the Order Confirmation, a proper copyright notice will read substantially as follows: "Republished with permission of [Rightsholder's name], from [Work's title, author, volume, edition number and year of copyright]; permission conveyed through Copyright Clearance Center, Inc. " Such notice must be provided in a reasonably legible font size and must be placed either immediately adjacent to the Work as used (for example, as part of a by-line or footnote but not as a separate electronic link) or in the place where substantially all other credits or notices for the new work containing the republished Work are located. Failure to include the required notice results in loss to the Rightsholder and CCC, and the User shall be liable to pay liquidated damages for each such failure equal to twice the use fee specified in the Order Confirmation, in addition to the use fee itself and any other fees and charges specified.

3.6 User may only make alterations to the Work if and as expressly set forth in the Order Confirmation. No Work may be used in any way that is defamatory, violates the rights of third parties (including such third parties' rights of copyright, privacy, publicity, or other tangible or intangible property), or is otherwise illegal, sexually explicit or obscene. In addition, User may not conjoin a Work with any other material that may result in damage to the reputation of the Rightsholder. User agrees to inform CCC if it becomes aware of any infringement of any rights in a Work and to cooperate with any reasonable request of CCC or the Rightsholder in connection therewith.

4. Indemnity. User hereby indemnifies and agrees to defend the Rightsholder and CCC, and their respective employees and directors, against all claims, liability, damages, costs and expenses, including legal fees and expenses, arising out of any use of a Work beyond the scope of the rights granted herein, or any use of a Work which has been altered in any unauthorized way by User, including claims of defamation or infringement of rights of copyright, publicity, privacy or other tangible or intangible property.

5. Limitation of Liability. UNDER NO CIRCUMSTANCES WILL CCC OR THE RIGHTSHOLDER BE LIABLE FOR ANY DIRECT, INDIRECT, CONSEQUENTIAL OR INCIDENTAL DAMAGES (INCLUDING WITHOUT LIMITATION DAMAGES FOR LOSS OF BUSINESS PROFITS OR INFORMATION, OR FOR BUSINESS INTERRUPTION) ARISING OUT OF THE USE OR INABILITY TO USE A WORK, EVEN IF ONE OF THEM HAS BEEN ADVISED OF THE POSSIBILITY OF SUCH DAMAGES. In any event, the total liability of the Rightsholder and CCC (including their respective employees and directors) shall not exceed the total amount actually paid by User for this license. User assumes full liability for the actions and omissions of its principals, employees, agents, affiliates, successors and assigns.

6. Limited Warranties. THE WORK(S) AND RIGHT(S) ARE PROVIDED "AS IS". CCC HAS THE RIGHT TO GRANT TO USER THE RIGHTS GRANTED IN THE ORDER CONFIRMATION DOCUMENT. CCC AND THE RIGHTSHOLDER DISCLAIM ALL OTHER WARRANTIES RELATING TO THE WORK(S) AND RIGHT(S), EITHER EXPRESS OR IMPLIED, INCLUDING WITHOUT LIMITATION IMPLIED WARRANTIES OF MERCHANTABILITY OR FITNESS FOR A PARTICULAR PURPOSE. ADDITIONAL RIGHTS MAY BE REQUIRED TO USE ILLUSTRATIONS, GRAPHS, PHOTOGRAPHS, ABSTRACTS, INSERTS OR OTHER PORTIONS OF THE WORK (AS OPPOSED TO THE ENTIRE WORK) IN A MANNER CONTEMPLATED BY USER; USER UNDERSTANDS AND AGREES THAT NEITHER CCC NOR THE RIGHTSHOLDER MAY HAVE SUCH ADDITIONAL RIGHTS TO GRANT.

7. Effect of Breach. Any failure by User to pay any amount when due, or any use by User of a Work beyond the scope of the license set forth in the Order Confirmation and/or these terms and conditions, shall be a material breach of the license created by the Order Confirmation and these terms and conditions. Any breach not cured within 30 days of written notice thereof shall result in immediate termination of such license without further notice. Any unauthorized (but licensable) use of a Work that is terminated immediately upon notice thereof may be liquidated by payment of the Rightsholder's ordinary license price therefor; any unauthorized (and unlicensable) use that is not terminated immediately for any reason (including, for example, because materials containing the Work cannot reasonably be recalled) will be subject to all remedies available at law or in equity, but in no event to a payment of less than three times the Rightsholder's ordinary license price for the most closely analogous licensable use plus Rightsholder's and/or CCC's costs and expenses incurred in collecting such payment.

8. **Miscellaneous.**

8.1 User acknowledges that CCC may, from time to time, make changes or additions to the Service or to these terms and conditions, and CCC reserves the right to send notice to the User by electronic mail or otherwise for the purposes of notifying User of such changes or additions; provided that any such changes or additions shall not apply to permissions already secured and paid for.

8.2 Use of User-related information collected through the Service is governed by CCC's privacy policy, available online here: http://www.copyright.com/content/cc3/en/tools/footer/privacypolicy.html.

8.3 The licensing transaction described in the Order Confirmation is personal to User. Therefore, User may not assign or transfer to any other person (whether a natural person or an organization of any kind) the license created by the Order Confirmation and these terms and conditions or any rights granted hereunder; provided, however, that User may assign such license in its entirety on written notice to CCC in the event of a transfer of all or substantially all of User's rights in the new material which includes the Work(s) licensed under this Service.

8.4 No amendment or waiver of any terms is binding unless set forth in writing and signed by the parties. The Rightsholder and CCC hereby object to any terms contained in any writing prepared by the User or its principals, employees, agents or affiliates and purporting to govern or otherwise relate to the licensing transaction described in the Order Confirmation, which terms are in any way inconsistent with any terms set forth in the Order Confirmation and/or in

References

[1] A. Abdulle and B. Engquist. Finite element heterogeneous multiscale methods with near optimal computational complexity. *Multiscale Modeling and Simulation*, 6(4):1059–1084, 2007.

[2] S. Abrate. Vibration of non-uniform rods and beams. *Journal of Sound and Vibration*, 185(4):703–716, 1995.

[3] B. Akgöz and Ö. Civalek. Free vibration analysis of axially functionally graded tapered bernoulli-euler microbeams based on the modified couple stress theory. *Composite Structures*, 98:314–322, 2013.

[4] T. Aktosun, D. Gintides, and V.G. Papanicolaou. The uniqueness in the inverse problem for transmission eigenvalues for the spherically symmetric variable-speed wave equation. *Inverse Problems*, 27(11), 2011. (article number 115004).

[5] A.L. Andrew. Computing Sturm-Liouville potentials from two spectra. *Inverse Problems*, 22(6):2069–2081, 2006.

[6] N.D. Ankit. Free transverse vibration of ocean tower. *Ocean Engineering*, 107:271–282, 2015.

[7] E.V. Ardelean, J.C. Goodding, D.M. Coombs, J.C. Griffee, V. Babuška, L.M. Robertson, and S.A. Lane. Cable effects study: Tangents, rat holes, dead ends, and valuable results. In *51st AIAA/ASME/ASCE/AHS/ASC Structures, Structural Dynamics, and Materials Conference*, Orlando, FL, United States, April 2010. AIAA. (AIAA 2010-2806).

[8] E.V. Ardelean, J.C. Goodding, G. Mehle, D.M. Coombs, V. Babuška, L.M. Robertson III, S.A. Lane, B.R. Ingram, and E.J. Hansen. Dynamics of cable harnesses on large precision structures. In *48th AIAA/ASME/ASCE/AHS/ASC Structures,*

Structural Dynamics, and Materials Conference, volume 8, pages 8225–8235, Waikiki, HI, United States, April 2007. AIAA.

[9] A. Askar and A.S Cakmak. A structural model of a micropolar continuum. *International Journal of Engineering Science*, 6(10):583–589, 1968.

[10] N.M. Auciello and G. Nolè. Vibrations of a cantilever tapered beam with varying section properties and carying a mass at the free end. *Journal of Sound and Vibration*, 214(1):105–119, 1998.

[11] V. Babuška, D.M. Coombs, J.C. Goodding, E.V. Ardelean, L.M. Robertson, and S.A. Lane. Modeling and experimental validation of space structures with wiring harnesses. *Journal of Spacecraft and Rockets*, 47(6):1038–1052, 2010.

[12] M. Balcı and Ö. Gündoğdu. Determination of physical properties of Euler Bernoulli beam via the method of inverse vibration problem. *Structural Longevity*, 6(3):115–126, 2011.

[13] V. Barcilon. On the solution of inverse eigenvalue problems of high orders. *Geophysical Journal of the Royal Astronomical Society*, 39(1):143–154, 1974.

[14] V. Barcilon. On the uniqueness of inverse eigenvalue problems. *Geophysical Journal of the Royal Astronomical Society*, 38(2):287–298, 1974.

[15] V. Barcilon. Inverse problem for a vibrating beam. *Journal of Applied Mathematics and Physics*, 27(3):347–358, 1976.

[16] V. Barcilon. Inverse problem for the vibrating beam in the free-clamped configuration. *Philosophical Transactions of the Royal Society of London. Series A, Mathematical and Physical Sciences*, 304(1483):211–251, 1982.

[17] S. Bashash, A. Salehi-Khojin, and N. Jalili. Forced vibration analysis of flexible Euler-Bernoulli beams with geometrical discontinuities. In *2008 American Control Conference*, pages 4029–4034, Seattle, Washington, June 2008.

[18] N. Buannic and P. Cartraud. Higher-order effective modeling of periodic heterogeneous beams. i. asymptotic expansion method. *International Journal of Solids and Structures*, 38(40–41):7139–7161, 2001.

[19] B. Burgardt and P. Cartraud. Continuum modeling of beamlike lattice trusses using averaging methods. *Computers and Structures*, 73(1–5):267–279, 1999.

[20] D. Caillerie. Thin elastic and periodic plates. *Mathematical Methods in the Applied Sciences*, 6(2):159–191, 1984.

[21] Y. Capdeville, L. Guillot, and J.-J. Marigo. Non-periodic homogenization of the elastic wave equation for wave propagations in complex media. In *3rd International Conference on Computational Methods in Structural Dynamics and Earthquake Engineering, COMPDYN 2011*, Corfu, Greece, May 2011. (Code 86982).

[22] D. Capecchi and F. Vestroni. Monitoring of structural systems by using frequency data. *Earthquake Engineering and Structural Dynamics*, 28(5):447–461, 1999.

[23] P. Cartraud and T. Messager. Computational homogenization of periodic beam-like structures. *International Journal of Solids and Structures*, 43(3–4):686–696, 2006.

[24] D.I. Caruntu. Dynamic modal characteristics of transverse vibrations of cantilevers of parabolic thickness. *Mechanics Research Communications*, 36(3):391–404, 2009.

[25] A. Chatterjee. An introduction to the proper orthogonal decomposition. *Current Science*, 78(7):808–817, 2000.

[26] G. Cheng and J.W. Zu. Dynamic analysis of an optical fiber coupler in telecommunications. *Journal of Sound and Vibration*, 268(1):15–31, 2003.

[27] L.D. Chiwiacowsky, H.F. De Campos Velho, and P. Gasbarri. A variational approach for solving an inverse vibration problem. *Inverse Problems in Science and Engineering*, 14(5):557–577, 2006.

[28] J. Choi and D.J. Inman. Development of modeling for cable harnessed structures. In *54th AIAA/ASME/ASCE/AHS/ASC Structures, Structural Dynamics, and Materials Conference*, Boston, MA, United States, April 2013. AIAA. (AIAA 2013-1888).

[29] J. Choi and D.J. Inman. Spectral element method for cable harnessed structure. In *31st International Modal Analysis Conference on Structural Dynamics*, volume 7, pages 377–387, Garden Grove, CA, United States, February 2013. SEM.

[30] J. Choi and D.J. Inman. Spectrally formulated modeling of a cable-harnessed structure. *Journal of Sound and Vibration*, 14:3286–3304, 2014.

[31] C.I. Christov. A method for identification of homoclinic trajectories. In *Proceedings of the Fourteenth Spring Conference of the Union of Bulgarian Mathematicians*, pages 571–577, Sunny Beach, April 1985.

[32] F. Clementi, L. Demeio, C.E.N. Mazzilli, and S. Lenci. Nonlinear vibrations of non-uniform beams by the mts asymptotic expansion method. *Continuum Mechanics and Thermodynamics*, 27(4–5):703–717, 2015.

[33] D.M. Coombs, J.C. Goodding, V. Babuška, E.V. Ardelean, L.M. Robertson, and S.A. Lane. Dynamic modeling and experimental validation of a cable-loaded panel. *Journal of Spacecraft and Rockets*, 48(6):958–973, 2011.

[34] H. Rezaei Da, M. Kadkhodaei, and H. Nahvi. Analysis of nonlinear free vibration and damping of a clamped-clamped beam with embedded prestrained shape memory alloy wires. *Journal of Intelligent Material Systems and Structures*, 23(10):1107–1117, 2012.

[35] A. Dall'asta and G. Leoni. Vibrations of beams prestressed by internal frictionless cables. *Journal of Sound and Vibration*, 222(1):1–18, 1999.

[36] Kenneth R. Davidson and Allan P. Donsig. *Real Analysis and Application Theory in Practice*. Undergraduate Texts in Mathematics. Springer, 2009.

[37] D.L. Dean and C.P. Ugarte. Field solutions for two-dimensional frameworks. *International Journal of Mechanical Sciences*, 10(4):315–339, 1968.

[38] M. Dilena and A. Morassi. Structural health monitoring of rods based on natural frequency and antiresonant frequency measurements. *Structural Health Monitoring*, 8(2):149–173, 2009.

[39] M. Dilena and A. Morassi. Reconstruction method for damage detection in beams based on natural frequency and antiresonant frequency measurements. *Journal of Engineering Mechanics*, 136(3):329–344, 2010.

[40] M.C. Ece, M. Aydogdu, and V. Taskin. Vibration of a variable cross-section beam. *Mechanics Research Communications*, 34(1):78–84, 2007.

[41] B.F. Feeny. On proper orthogonal co-ordinates as indicators of modal activity. *Journal of Sound and Vibration*, 255(5):805–817, 2002.

[42] B.F. Feeny. On the proper orthogonal modes and normal modes of continuous vibration systems. *Journal of Vibration and Acoustics*, 124(1):157–160, 2002.

[43] J. Franců. Outline of Nguetseng's approach to non-periodic homogenization. *Mathematics for Applications*, 1(2):117–128, 2012.

[44] A.R. Ghasemi, F. Taheri-Behrooz, S.M.N. Farahani, and M. Mohandes. Nonlinear free vibration of an euler-bernoulli composite beam undergoing finite strain subjected to different boundary conditions. *Journal of Vibration and Control*, page doi: 10.1177/1077546314528965, 2014.

[45] G.M.L. Gladwell. The inverse problem for the Euler-Bernoulli beam. *Proceedings of the Royal Society of London. Series A, Mathematical and Physical Sciences*, 407(1832):199–218, 1986.

[46] Graham M.L. Gladwell. *Inverse Problems in Vibration*, volume 119 of *Solid Mechanics and its Applications*. Kulwer Academic Publishers, 2nd edition, 2004.

[47] R.P. Goel. Transverse vibrations of tapered beams. *Journal of Sound and Vibration*, 47(1):1–7, 1976.

[48] J.C. Goodding. Spacecraft electrical cable harness structural test and analysis methods. In *26th IMAC: Conference and Exposition on Structural Dynamics*, pages 437–443, Orlando, FL, United States, 2008. SEM.

[49] J.C. Goodding, E.V. Ardelean, V. Babuška, L.M. Robertson, and S.A. Lane. Experimental techniques and structural parameter estimation studies of spacecraft cables. *Journal of Spacecraft and Rockets*, 48(6):942–957, 2011.

[50] J.C. Goodding, V. Babuška, D.T. Griffith, B.R. Ingram, and L.M. Robertson. Study of free-free beam structural dynamics perturbations due to mounted cable harnesses. In *48th AIAA/ASME/ASCE/AHS/ASC Structures, Structural Dynamics, and Materials Conference*, volume 8, pages 8242–8254, Waikiki, HI, United States, April 2007. AIAA.

[51] J.C. Goodding, J.C. Griffee, and E.V. Ardelean. Parameter estimation and structural dynamic modeling of electrical cable harnesses on precision structures. In *49th AIAA/ASME/ASCE/AHS/ASC Structures, Structural Dynamics, and Materials Conference*, Schaumburg, IL, United States, April 2008. AIAA. (AIAA 2008-1852).

[52] H.P.W. Gottlieb. Isospectral Euler-Bernoulli beams with continuous density and rigidity functions. *Proceedings of the Royal Society of London. Series A, Mathematical and Physical Sciences*, 413(1844):235–250, 1987.

[53] Y. Güldü. Inverse eigenvalue problems for a discontinuous Sturm-Liouville operator with two discontinuities. *Boundary Value Problems*, 2013, 2013. (article number 209).

[54] S. Guo and S. Yang. Transverse vibrations of arbitrary non-uniform beams. *Applied Mathematics and Mechanics (English Edition)*, 35(5):607–620, 2014.

[55] Y.S. Hamed, M. Sayed, D.X. Cao, and W. Zhang. Nonlinear study of the dynamic behavior of a string-beam coupled system under combined excitations. *Acta Mechanica Sinica/Lixue Xuebao*, 27(6):1034–1051, 2011.

[56] T.N. Harutyunyan. On a uniqueness theorem in the inverse Sturm-Liouville problem. *Matematicki Vesnik*, 61(2):139–147, 2009.

[57] R.C. Hibbeler. *Mechanics of Materials*. Pearson Prentice Hall, 8th edition, 2011.

[58] S.M. Hozhabrossadati. Exact solution for free vibration of elastically restrained cantilever non-uniform beams joined by a mass-spring system at the free end. *The IES Journal Part A: Civil & Structural Engineering*, 8(4):232–239, 2015.

[59] R.O. Hryniv and Ya.V. Mykytyuk. Inverse spectral problems for Sturm-Liouville operators with singular potentials. *Inverse Problems*, 19(3):665–684, 2003.

[60] C.-H. Huang, C.-C. Shih, and S. Kim. An inverse vibration problem in estimating the spatial and temporal-dependent external forces for cutting tools. *Applied Mathematical Modelling*, 33(6):2683–2698, 2009.

[61] L.M. Robertson III, S.A. Lane, B.R. Ingram, E.J. Hansen, V. Babuška, J. Goodding, M. Mimovich, G. Mehle, D. Coombs, and E.V. Ardelean. Cable effects on the dynamics of large precision structures. In *48th AIAA/ASME/ASCE/AHS/ASC Structures, Structural Dynamics, and Materials Conference*, volume 8, pages 8236–8241, Waikiki, HI, United States, April 2007. AIAA.

[62] D.J. Inman. *Engineering Vibration*. Pearson Education, New York, 3 edition, 2007.

[63] J.S. Issa and W.F. Habchi. Vibration suppression in a cantilever beam using a string-type vibration absorber. In *ASME 2010 International Mechanical Engineering Congress and Exposition*, pages 215–221, Vancouver, BC, Canada, November 2010. ASME.

[64] S.K. Jang and C.W. Bert. Free vibration of stepped beams: Exact and numerical solutions. *Journal of Sound and Vibration*, 130(2):342–346, 1989.

[65] S.K. Jang and C.W. Bert. Free vibration of stepped beams: Higher mode frequencies an effects of steps on frequency. *Journal of Sound and Vibration*, 132(1):164–168, 1989.

[66] R. Jategaonkar and D.S. Chehil. Natural frequencies of a beam with varying section properties. *Journal of Sound and Vibration*, 133(2):303–322, 1989.

[67] J.L. Kauffman and G.A. Lesieutre. Damping models for timoshenko beams with applications to spacecraft wiring harnesses. In *54th AIAA/ASME/ASCE/AHS/ASC Structures, Structural Dynamics, and Materials Conference*, Boston, MA, United States, April 2013. AIAA. (AIAA 2013-1890).

[68] J.L. Kauffman, G.A. Lesieutre, and V. Babuška. Damping models for shear beams with applications to spacecraft wiring harnesses. In *53rd AIAA/ASME/ASCE/AHS/ASC Structures, Structural Dynamics, and Materials Conference*, Honolulu, HI, United States, April 2012. AIAA. (AIAA 2012-1641).

[69] J.L. Kauffman, G.A. Lesieutre, and V. Babuška. Damping models for shear beams with applications to spacecraft wiring harnesses. *Journal of Spacecraft and Rockets*, 51(1):16–22, 2014.

[70] R.V. Kohn and M. Vogelius. A new model for thin plates with rapidly varying thickness. *International Journal of Solids and Structures*, 20(4):333–350, 1984.

[71] A.G. Kolpakov. Calculation of the characteristics of thin elastic rods with a periodic structure. *Journal of Applied Mathematics and Mechanics*, 55(3):358–365, 1991.

[72] H. Koyunbakan and E.S. Panakhov. A uniqueness theorem for inverse nodal problem. *Inverse Problems in Science and Engineering*, 15(6):517–524, 2007.

[73] S.K. Lai, J. Harrington, Y. Xiang, and K.W. Chow. Accurate analytical perturbation approach for large amplitude vibration of functionally graded beams. *International Journal of Non-Linear Mechanics*, 47(5):473–480, 2012.

[74] C.M. Leech. The modelling of net and cloth dynamics. *Journal of the Franklin Institute*, 307(6):361–378, 1979.

[75] S. Lenci, F. Clementi, and C.E.N. Mazzilli. Simple formulas for the natural frequencies of non-uniform cables and beams. *International Journal of Mechanical Sciences*, 77:155–163, 2013.

[76] G.A. Lesieutre. A viscous 'geometric' beam damping model that results in weak frequency dependence of modal damping. In *53rd AIAA/ASME/ASCE/AHS/ASC Structures, Structural Dynamics, and Materials Conference AIAA/ASME/ASCE/AHS/ASC Structures, Structural Dynamics, and Materials Conference*, 2012.

[77] G.A. Lesieutre and J.L. Kauffman. 'geometric' viscous damping model for nearly constant beam modal damping. *AIAA Journal*, 51(7):1688–1694, 2013.

[78] D. Lukkassen, G. Nguetseng, H. Nnang, and P. Wall. Reiterated homogenization of nonlinear monotone operators in a general deterministic setting. *Journal of Function Spaces and Applications*, 7(2):121–152, 2009.

[79] D. Manceau. Small amplitude homogenization applied to models of non-periodic fibrous materials. *Mathematical Modelling and Numerical Analysis*, 41(6):1061–1087, 2007.

[80] T.T. Marinov, R.S. Marinov, and C.I. Christov. Coefficient identification in elliptic partial differential equation. In I.Lirkov, S. Margenov, and J. Waśniewski, editors, *Large-Scale Scientific Computing*, volume 3743 of *Lecture Notes in Computer Science*, pages 450–459. Springer Berlin Heidelberg, 2006.

[81] T.T. Marinov and R.S. Marinova. Coefficient identification in Euler-Bernoulli equation from over-posed data. *Journal of Computational and Applied Mathematics*, 235(2):450–459, 2010.

[82] T.T. Marinov and A.S. Vatsala. Inverse problem for coefficient identification in the Euler-Bernoulli equation. *Computers and Mathematics with Applications*, 56(2):400–410, 2008.

[83] B. Martin and A. Salehian. Cable-harnessed space structures: A beam-cable approach. In *24th IASTED International Conference on Modelling and Simulation*, pages 280–284, Banff, AB, Canada, July 2013. ACTA Press.

[84] B. Martin and A. Salehian. Dynamic modelling of cable-harnessed beam structures with periodic wrapping patterns: A homogenization approach. *International Journal of Modelling and Simulation*, 33(4):185–202, 2013. (doi: 10.2316/Journal.205.2013.4.205-5981).

[85] B. Martin and A. Salehian. Vibration analysis of string-harnessed beam structures: A homogenization approach. In *54th AIAA/ASME/ASCE/AHS/ASC Structures,*

Structural Dynamics, and Materials Conference, Boston, MA, United States, April 2013. AIAA. (AIAA 2013-1892).

[86] B. Martin and A. Salehian. Vibration modelling of string-harnessed beam structures using homogenization techniques. In *Proceedings of the ASME 2014 International Mechanical Engineering Congress & Exposition*, Montreal, QC, Canada, November 2014. ASME. (IMECE2014-37039).

[87] B. Martin and A. Salehian. Homogenization modeling of periodically wrapped string-harnessed beam structures: Experimental validation. *AIAA Journal*, 54(12):3965–3980, 2016.

[88] B. Martin and A. Salehian. Mass and stiffness effects of harnessing cables on structural dynamics: Continuum modeling. *AIAA Journal*, 54(9):2881–2904, 2016.

[89] B. Martin and A. Salehian. String-harnessed beam structures: An inverse problem approach for model approximation. In *Proceedings of the 9th International Conference on Inverse Problems in Engineering*, 2017.

[90] B. Martin and A. Salehian. Approximating a string-harnessed system model using a constant coefficient euler-bernoulli model. *AIAA Journal*, (to be submitted).

[91] B. Martin and A. Salehian. Continuum modelling and vibration analysis of non-periodic string-harnessed structures: A perturbation theory approach. *AIAA Journal*, (to be submitted).

[92] B. Martin and A. Salehian. Perturbation theory results of non-periodically wrapped string-harnessed beam strcutures: Experimental validation. *AIAA Journal*, (to be submitted).

[93] B. Martin and A. Salehian. Reference value selection in a perturbation theory applied to non-uniform beams. *Journal of Sound and Vibration*, (to be submitted).

[94] J.R. McLaughlin. An inverse problem of order four. *SIAM Journal on Mathematical Analysis*, 7(5):646–661, 1976.

[95] J.R. McLaughlin. On constructing solutions to an inverse Euler-Bernoulli beam problem. In F. Santosa, Y.-H. Pap, W.W. Symes, and C. Holland, editors, *Inverse Problems of Acoustics and Elastic Waves*, pages 341–345. SIAM, 1984.

[96] J.R. McLaughlin. Analytical methods for recovering coefficients in differential equations from spectral data. *SIAM Review*, 28(1):53–72, 1986.

[97] T. Messager and P. Cartraud. Homogenization of helical beam-like structures: Application to single-walled carbon nanotubes. *Computational Mechanics*, 41(2):335–346, 2008.

[98] Ronald E. Miller. *Optimization: Foundations and Applications*. John Wiley and Sons, Inc., 2000.

[99] A. Morassi. Constructing rods with given natural frequencies. *Mechanical Systems and Signal Processing*, 40(1):288–300, 2013.

[100] D.J. More and S.B. Kumbhar. An experimental study on shift in natural frequency of sandwich beam with elastomeric core embedded with sma wires. In *2013 International Conference on Advanced Nanomaterials and Emerging Engineering Technologies*, pages 592–596, Chennai, India, July 2013. IEEE.

[101] S. Naguleswaran. Direct solution for the transverse vibration of euler-bernoulli wedge and cone beams. *Journal of Sound and Vibration*, 172(3):289–304, 1992.

[102] S. Naguleswaran. Vibration of an euler-bernoulli beam of constant depth and with linearly varying breadth. *Journal of Sound and Vibration*, 153(3):509–522, 1992.

[103] S. Naguleswaran. A direct solution for the transverse vibration of euler-bernoulli wedge and cone beams. *Journal of Sound and Vibration*, 172(3):289–304, 1994.

[104] Ali Hasan Nayfeh. *Perturbation Methods*. John Wiley & Sons, Inc., 1973.

[105] Arch W. Naylor and George R. Sell. *Linear Operator Theory in Engineering and Science*, volume 40 of *Applied Mathematical Sciences*. Springer-Verlag, 2nd edition, 1982.

[106] R. Nielsen and S. Sorokin. The wkb approximation for analysis of wave propagation in curved rods of slowly varying diameter. *Proceedings of the Royal Society of London. Series A, Mathematical and Physical Sciences*, 470(2167), 2014.

[107] A.K. Noor. Continuum modeling for repetitive lattice structures. *Applied Mechanics Review*, 41(7):285–296, 1988.

[108] A.K. Noor, M.S. Anderson, and W.H. Greene. Continuum models for beam- and platelike lattice structures. *AIAA Journal*, 16(12):1219–1228, 1978.

[109] A. Pankov. Periodic approximations of homogenization problems. *Mathematical Methods in the Applied Sciences*, 36(15):2018–2022, 2013.

[110] V.G. Papanicolaou. The spectral theory of the vibrating periodic beam. *Communications in Mathematical Physics*, 170(2):359–373, 1995.

[111] V.G. Papanicolaou. The periodic Euler-Bernoulli equation. *Transactions of the American Mathematical Society*, 355(9):3727–3759, 2003.

[112] V.G. Papanicolaou and D. Kravvaritis. An inverse spectral problem for the Euler-Bernoulli equation for the vibrating beam. *Inverse Problems*, 13(4):1083–1092, 1997.

[113] Donald A. Pierre. *Optimization Theory with Applications*. John Wiley and Sons, Inc., 1969.

[114] T. Pollock. Design, modelling, fabrication & testing of a miniature piezoelectric-based EMF energy harvester. Master's thesis, University of Waterloo, 2014.

[115] Jürgen Pöschel and Eugene Trubowitz. *Inverse Spectral Theory*, volume 130 of *Pure and Applied Mathematics*. Academic Press, Inc., 1987.

[116] Alexander G. Ramm. *Inverse Problems: Mathematical and Analytical Techniques with Applications to Engineering*. Springer Science+Business Media, Inc., 2005.

[117] J.N. Reddy. *Mechanics of Laminated Composite Plates and Shells: Theory and Analysis*. CRC Press LLC, Boca Raton, 2004.

[118] J.D. Renton. General properties of space grids. *International Journal of Mechanical Sciences*, 12(9):801–810, 1970.

[119] J.D. Renton. The beam-like behavior of space trusses. *AIAA Journal*, 22(2):273–280, 1984.

[120] R.D. Rirouz-Abadi, H. Haddadpour, and A.B. Novinzadeh. An asymptotic solution to transverse free vibrations of variable-section beams. *Journal of Sound and Vibration*, 204(3–5):530–540, 2007.

[121] M.A. De Rosa and N.M. Auciello. Free vibration of tapered beams with flexible ends. *Computers and Structures*, 60(2):197–202, 1996.

[122] W. Rundell and P. Sacks. Numerical technique for the inverse resonance problem. *Journal of Computational and Applied Mathematics*, 171(1–2):337–347, 2004.

[123] W. Rundell and P.E. Sacks. The reconstruction of Sturm-Liouville operators. *Inverse Problems*, 8(3):457–482, 1992.

[124] Hans Sagan. *Introduction to the Calculus of Variations*. Dover Publications, Inc., 1969.

[125] A. Salehian. Effects of strain rates on kinetics of elements of repeated pattern structures: A continuous modeling approach. *Shock and Vibration*, 19(4):545–554, 2012.

[126] A. Salehian and Y. Chen. On strain-rate dependence of kinetic energy in homogenization approach: Theory and experiment. *AIAA Journal*, 50(10):2029–2033, 2012.

[127] A. Salehian, E.M. Cliff, and D.J. Inman. Continuum modeling of an innovative space-based radar antenna truss. *Journal of Aerospace Engineering*, 19(4):227–240, 2006.

[128] A. Salehian, M. Ibrahim, and T.M. Seigler. Damping in periodic structures: A continuum modeling approach. *AIAA Journal*, 52(3):569–590, 2014.

[129] A. Salehian and D.J. Inman. Dynamic analysis of a lattice structure by homogenization: Experimental validation. *Journal of Sound and Vibration*, 316(1–5):180–197, 2008.

[130] A. Salehian and D.J. Inman. Micropolar continuous modeling and frequency response validation of a lattice structure. *Journal of Vibration and Acoustics*, 132(1):1–7, 2010.

[131] A. Salehian, T.M. Seigler, and D.J. Inman. Dynamic effects of a radar panel mounted on a truss satellite. *AIAA Journal*, 45(7):1642–1654, 2007.

[132] K. Sarkar and R. Ganguli. Closed-form solutions for non-uniform euler-bernoulli free-free beams. *Journal of Sound and Vibration*, 332(23):6078–6092, 2013.

[133] K. Sato. Transverse vibrations of linearly tapered beams with ends restrained elastically against rotation subjected to axial force. *International Journal of Mechanical Sciences*, 22(2):109–115, 1980.

[134] B. Schäfer. Free vibrations of a gravity-loaded clamped-free beam. *Ingenieur-Archiv*, 55(1):66–80, 1985.

[135] Irving H. Shames and Clive L. Dym. *Energy and Finite Element Methods in Structural Methods in Structural Mechanics*. Hemisphere Publishing Corporation, 1985.

[136] V.S. Sorokin and J.J. Thomsen. Eigenfrequencies and eigenmodes of a beam with periodically continuously varying spatial properties. *Journal of Sound and Vibration*, 347(7):14–16, 2015.

[137] K.S. Spak, G. Agnes, and D. Inman. Cable parameters for homogenous cable-beam models for space structures. In *Conference Proceedings of the Society for Experimental Mechanics Series*, volume 4, pages 7–18. 32nd IMAC Conference and Exposition on Structural Dynamics, 2014.

[138] K.S. Spak, G. Agnes, and D. Inman. Parameters for modeling stranded cables as structural beams. *Experimental Mechanics*, 54(9):1613–1626, 2014.

[139] K.S. Spak, G. Agnes, and D. Inman. Modeling vibration response and damping of cables and cabled structures. *Journal of Sound and Vibration*, 336:240–256, 2015.

[140] K.S. Spak, G.S. Agnes, and D.J. Inman. Cable modeling and internal damping developments. *Applied Mechanics Reviews*, 65(1), 2013. (article number: 010801).

[141] K.S. Spak, G.S. Agnes, and D.J. Inman. Comparison of damping models for space flight cables. In *31st International Modal Analysis Conference on Structural Dynamics*, volume 4, pages 183–194, Garden Grove, CA, United States, February 2013. SEM.

[142] K.S. Spak, G.S. Agnes, and D.J. Inman. Toward modeling of cable-harnessed structures: Cable damping experiments. In *54th AIAA/ASME/ASCE/AHS/ASC Structures, Structural Dynamics, and Materials Conference*, Boston, MA, United States, April 2013. AIAA. (AIAA 2013-1889).

[143] C.T. Sun and S.W. Liebbe. Global-local approach to solving vibration of large truss structures. *AIAA Journal*, 28(2):303–308, 1990.

[144] C.T. Sun and T.Y. Yang. A continuum approach toward dynamics of gridworks. *Journal of Applied Mechanics*, 40(1):186–192, 1973.

[145] A.-Y. Tang, J.-X. Wu, X.-F. Li, and K.Y. Lee. Exact frequency equations of free vibration of exponentially non-uniform functionally graded timoshenko beams. *International Journal of Mechanical Sciences*, 89:1–11, 2014.

[146] T. Wah and L.R. Calcote. *Structural Analysis by Finite Difference Calculus*. Van Nostrand Reinhold, New York, 1970.

[147] C.Y. Wang and C.M. Wang. Exact vibration solution for exponentially tapered cantilever with tip mass. *Journal of Vibration and Acoustics*, 134(4), 2012.

[148] B. Yang. Exact transient vibration of stepped bars, shafts and strings carrying lumped masses. *Journal of Sound and Vibration*, 329(8):1191–1207, 2010.

[149] W. Zhang and D.X. Cao. Studies on bifurcation and chaos of a string-beam coupled system with two degress-of-freedom. *Nonlinear Dynamics*, 45(1–2):131–147, 2006.

APPENDICES

Appendix A

Expressions for Coupled FEA

The Green-Lagrange strain tensor used for the FEA model that includes up to second-order terms is given by:

$$\begin{aligned}
\epsilon_{xx} &= \frac{\partial u}{\partial x} - y\frac{\partial^2 v}{\partial x^2} - z\frac{\partial^2 w}{\partial x^2} + \frac{1}{2}\left(\frac{\partial u}{\partial x} - y\frac{\partial^2 v}{\partial x^2} - z\frac{\partial^2 w}{\partial x^2}\right)^2 + \frac{1}{2}\left(\frac{\partial v}{\partial x} - z\frac{\partial \theta_x}{\partial x}\right)^2 + \frac{1}{2}\left(\frac{\partial w}{\partial x} + y\frac{\partial \theta_x}{\partial x}\right)^2 \\
\epsilon_{yy} &= 0 \\
\epsilon_{zz} &= 0 \\
\gamma_{xy} &= -z\frac{\partial \theta_x}{\partial x} - \frac{\partial u}{\partial x}\frac{\partial v}{\partial x} + \frac{\partial w}{\partial x}\theta_x + z\frac{\partial v}{\partial x}\frac{\partial^2 w}{\partial x^2} \\
\gamma_{xz} &= y\frac{\partial \theta_x}{\partial x} - \frac{\partial u}{\partial x}\frac{\partial w}{\partial x} - \frac{\partial v}{\partial x}\theta_x + y\frac{\partial w}{\partial x}\frac{\partial^2 v}{\partial^2 x} \\
\gamma_{yz} &= \frac{\partial w}{\partial x}\frac{\partial v}{\partial x}
\end{aligned} \tag{A.1}$$

The differential kinetic for the FEA model ignoring the rotatory inertia effect can be found as:

$$\begin{aligned}
\mathrm{d}T = \frac{1}{2}\Bigg[&\left(\rho_b A_b + \frac{\rho_s A_s}{\cos(\theta)}\right)\left(\frac{\partial u}{\partial t}\right)^2 + \left(\rho_b A_b + \frac{\rho_s A_s}{\cos(\theta)}\right)\left(\frac{\partial v}{\partial t}\right)^2 + \left(\rho_b A_b + \frac{\rho_s A_s}{\cos(\theta)}\right)\left(\frac{\partial w}{\partial t}\right)^2 \\
&+ \left(\rho_b I_{xx} + \frac{\rho_s A_s\left(y_s^2 + z_s^2\right)}{\cos(\theta)}\right)\left(\frac{\partial \theta_x}{\partial t}\right)^2 \Bigg] \mathrm{d}x
\end{aligned} \tag{A.2}$$

The differential strain energy for the FEA model will depend on the position of the string on that section of the beam. For parts where the string is located on the top or bottom of the beam, the differential strain energy can be found as:

$$
\begin{aligned}
\mathrm{d}U_{\mathrm{t/b}} =& \frac{1}{2}\Bigg[\left(E_b A_b + E_s A_s \cos^3(\theta)\right) \left(\frac{\partial u}{\partial x}\right)^2 + \Bigg(E_b I_{yy} \sin^2(\theta_0) + E_b I_{zz} \cos^2(\theta_0) + E_s A_s (y_s^*)^2 \cos^3(\theta) \\
&+ T (y_s^*)^2 \cos(\theta) - \frac{T\cos(\theta)\left(I_{yy}\sin^2(\theta_0) + I_{zz}\cos^2(\theta_0)\right)}{A_b} \Bigg) \left(\frac{\partial^2 v}{\partial x^2}\right)^2 + \Bigg(E_b I_{yy} \cos^2(\theta_0) + E_b I_{zz} \sin^2(\theta_0) \\
&+ E_s A_s (z_s^*)^2 \cos^3(\theta) + T (z_s^*)^2 \cos(\theta) - \frac{T\cos(\theta)\left(I_{yy}\cos^2(\theta_0) + I_{zz}\sin^2(\theta_0)\right)}{A_b} \Bigg) \left(\frac{\partial^2 w}{\partial x^2}\right)^2 \\
&+ \left(G_b J + E_s A_s \cos(\theta)\sin^2(\theta) z_s^2 + T\cos(\theta)\left((y_s^*)^2 + (z_s^*)^2\right) - \frac{T\cos(\theta) J}{A_b} \right) \left(\frac{\partial \theta_x}{\partial x}\right)^2 \\
&+ 2\Bigg(E_s A_s y_s^* z_s^* \cos^3(\theta) + T y_s^* z_s^* \cos(\theta) + \left(E_b I_{yy} - E_b I_{zz} - \frac{T\cos(\theta)\left(I_{yy} - I_{zz}\right)}{A_b} \right) \cos(\theta_0)\sin(\theta_0) \Bigg) \frac{\partial^2 v}{\partial x^2} \frac{\partial^2 w}{\partial x^2} \\
&\mp 2 E_s A_s \cos^2(\theta)\sin(\theta) z_s \left(\frac{\partial u}{\partial x}\frac{\partial \theta_x}{\partial x} - y_s^* \frac{\partial^2 v}{\partial x^2}\frac{\partial \theta_x}{\partial x} - z_s^* \frac{\partial^2 w}{\partial x^2}\frac{\partial \theta_x}{\partial x} \right) + 2\Big(E_s A_s \cos^3(\theta) \\
&+ T\cos(\theta) \Big) \left(-y_s^* \frac{\partial u}{\partial x}\frac{\partial^2 v}{\partial x^2} - z_s^* \frac{\partial u}{\partial x}\frac{\partial^2 w}{\partial x^2} \right) \pm 2T\sin(\theta_0)\sin(\theta) \left(-\frac{\partial u}{\partial x}\frac{\partial w}{\partial x} - \frac{\partial v}{\partial x}\theta_x + y_s^* \frac{\partial w}{\partial x}\frac{\partial^2 v}{\partial^2 x} \right) \\
&+ 2T\cos(\theta_0)\sin(\theta_0)\sin(\theta)\tan(\theta)\frac{\partial w}{\partial x}\frac{\partial v}{\partial x} + 2T\cos(\theta)\left(y_s^* \frac{\partial w}{\partial x}\frac{\partial \theta_x}{\partial x} - z_s^* \frac{\partial v}{\partial x}\frac{\partial \theta_x}{\partial x} \right) \\
&\mp 2T\sin(\theta)\Big(\cos(\theta_0) - 1\Big)\frac{\partial u}{\partial x}\frac{\partial v}{\partial x} \pm 2T\sin(\theta)\Big(\cos(\theta_0) - 1\Big)\frac{\partial w}{\partial x}\theta_x \pm 2T z_s^* \cos(\theta_0)\sin(\theta)\frac{\partial v}{\partial x}\frac{\partial^2 w}{\partial x^2} \\
&\mp 2T z_s \sin(\theta)\frac{\partial \theta_x}{\partial x} + 2T\cos(\theta)\left(-y_s^* \frac{\partial^2 v}{\partial x^2} - z_s^* \frac{\partial^2 w}{\partial x^2} \right) + \frac{T^2}{E_s A_s \cos(\theta)} + \frac{T^2 \cos^2(\theta)}{E_b A_b} + \frac{6T^2 \sin^2(\theta)}{5 G_b A_b} \Bigg] \mathrm{d}x
\end{aligned}
\tag{A.3}
$$

For the FEA differential strain energy of the parts where the string is located on the side

of the beam, we get:

$$
\begin{aligned}
\mathrm{d}U_{\text{side}} =& \frac{1}{2}\Bigg[\left(E_b A_b + E_s A_s \cos^3(\theta)\right) \left(\frac{\partial u}{\partial x}\right)^2 + \Bigg(E_b I_{yy} \sin^2(\theta_0) + E_b I_{zz} \cos^2(\theta_0) + E_s A_s (y_s^*)^2 \cos^3(\theta) \\
&+ T (y_s^*)^2 \cos(\theta) - \frac{T\cos(\theta)\left(I_{yy}\sin^2(\theta_0) + I_{zz}\cos^2(\theta_0)\right)}{A_b}\Bigg) \left(\frac{\partial^2 v}{\partial x^2}\right)^2 + \Bigg(E_b I_{yy} \cos^2(\theta_0) + E_b I_{zz} \sin^2(\theta_0) \\
&+ E_s A_s (z_s^*)^2 \cos^3(\theta) + T (z_s^*)^2 \cos(\theta) - \frac{T\cos(\theta)\left(I_{yy}\cos^2(\theta_0) + I_{zz}\sin^2(\theta_0)\right)}{A_b}\Bigg) \left(\frac{\partial^2 w}{\partial x^2}\right)^2 \\
&+ \left(G_b J + E_s A_s \cos(\theta)\sin^2(\theta) y_s^2 + T\cos(\theta)\left((y_s^*)^2 + (z_s^*)^2\right) - \frac{T\cos(\theta) J}{A_b}\right) \left(\frac{\partial \theta_x}{\partial x}\right)^2 \\
&+ 2\Bigg(E_s A_s y_s^* z_s^* \cos^3(\theta) + T y_s^* z_s^* \cos(\theta) + \left(E_b I_{yy} - E_b I_{zz} - \frac{T\cos(\theta)\left(I_{yy} - I_{zz}\right)}{A_b}\right)\cos(\theta_0)\sin(\theta_0)\Bigg) \frac{\partial^2 v}{\partial x^2}\frac{\partial^2 w}{\partial x^2} \\
&\mp 2 E_s A_s \cos^2(\theta)\sin(\theta) y_s \left(\frac{\partial u}{\partial x}\frac{\partial \theta_x}{\partial x} - y_s^* \frac{\partial^2 v}{\partial x^2}\frac{\partial \theta_x}{\partial x} - z_s^* \frac{\partial^2 w}{\partial x^2}\frac{\partial \theta_x}{\partial x}\right) + 2\Big(E_s A_s \cos^3(\theta) \\
&+ T\cos(\theta)\Big)\left(-y_s^* \frac{\partial u}{\partial x}\frac{\partial^2 v}{\partial x^2} - z_s^* \frac{\partial u}{\partial x}\frac{\partial^2 w}{\partial x^2}\right) \pm 2T\sin(\theta_0)\sin(\theta)\left(-\frac{\partial u}{\partial x}\frac{\partial v}{\partial x} + \frac{\partial w}{\partial x}\theta_x + z_s^* \frac{\partial v}{\partial x}\frac{\partial^2 w}{\partial x^2}\right) \\
&- 2T\cos(\theta_0)\sin(\theta_0)\sin(\theta)\tan(\theta)\frac{\partial w}{\partial x}\frac{\partial v}{\partial x} + 2T\cos(\theta)\left(y_s^* \frac{\partial w}{\partial x}\frac{\partial \theta_x}{\partial x} - z_s^* \frac{\partial v}{\partial x}\frac{\partial \theta_x}{\partial x}\right) \\
&\pm 2T\sin(\theta)\Big(\cos(\theta_0) - 1\Big)\frac{\partial u}{\partial x}\frac{\partial w}{\partial x} \pm 2T\sin(\theta)\Big(\cos(\theta_0) - 1\Big)\frac{\partial v}{\partial x}\theta_x \mp 2T y_s^* \cos(\theta_0)\sin(\theta)\frac{\partial w}{\partial x}\frac{\partial^2 v}{\partial^2 x} \\
&\mp 2T\sin(\theta) y_s \frac{\partial \theta_x}{\partial x} + 2T\cos(\theta)\left(-y_s^* \frac{\partial^2 v}{\partial x^2} - z_s^* \frac{\partial^2 w}{\partial x^2}\right) + \frac{T^2}{E_s A_s \cos(\theta)} + \frac{T^2\cos^2(\theta)}{E_b A_b} + \frac{6T^2\sin^2(\theta)}{5 G_b A_b}\Bigg] \mathrm{d}x
\end{aligned}
\tag{A.4}
$$

In the above expressions $\theta_0(x)$ denotes the initial twist in the system and $y_s(x)$ and $z_s(x)$ denote the y and z-coordinates of the centre of the string segment when the beam is not rotated. Therefore, the position of the string once the system undergoes the initial twist θ_0 can be found as:

$$
\begin{aligned}
y_s^*(x) &= y_s(x)\cos(\theta_0(x)) - z_s(x)\sin(\theta_0(x)) \\
z_s^*(x) &= y_s(x)\sin(\theta_0(x)) + z_s(x)\cos(\theta_0(x))
\end{aligned}
$$

Further, $J = bh^3\left(\frac{1}{3} - \frac{64h}{\pi^5 b}\left(1 - \frac{h^4}{12b^4}\right)\right)$ is the torsion constant for a beam with rectangular cross section when $h < b$.

Appendix B

Perturbation Theory Expressions

B.1 Euler-Bernoulli Model

The expression for the function $\widetilde{u}_{n1}^{(i)}(X)$, $1 \leq i \leq m$, is:

$$
\begin{aligned}
\widetilde{u}_{n1}^{(i)}(X) =& u_{n1,p}^{(i)}(X) + \widetilde{u}_{n1}^{(1)}(X) - u_{n1,p}^{(1)}(X) \\
&+ \frac{1}{2}\sum_{k=1}^{i-1}\Bigg\{\kappa_{n1}^{(k)}(X_k) - \kappa_{n1}^{(k+1)}(X_k) \\
&\qquad + \frac{1}{\omega_{n0}}\left(\widehat{EI}^{(k+1)}(X_k) - \widehat{EI}^{(k)}(X_k)\right)\frac{\mathrm{d}^2\phi_{n0}(X_k)}{\mathrm{d}X^2}\Bigg\}\cos(\sqrt{\omega_{n0}}(X_k - X)) \\
&+ \frac{1}{2}\sum_{k=1}^{i-1}\Bigg\{ - \kappa_{n2}^{(k)}(X_k) + \kappa_{n2}^{(k+1)}(X_k) \\
&\qquad - \frac{1}{\sqrt{\omega_{n0}^3}}\frac{\mathrm{d}}{\mathrm{d}X}\left[\left(\widehat{EI}^{(k+1)} - \widehat{EI}^{(k)}\right)\frac{\mathrm{d}^2\phi_{n0}}{\mathrm{d}X^2}\right]_{X=X_k}\Bigg\}\sin(\sqrt{\omega_{n0}}(X_k - X)) \\
&+ \frac{1}{2}\sum_{k=1}^{i-1}\Bigg\{\kappa_{n3}^{(k)}(X_k) - \kappa_{n3}^{(k+1)}(X_k) \\
&\qquad - \frac{1}{\omega_{n0}}\left(\widehat{EI}^{(k+1)}(X_k) - \widehat{EI}^{(k)}(X_k)\right)\frac{\mathrm{d}^2\phi_{n0}(X_k)}{\mathrm{d}X^2}\Bigg\}\cosh(\sqrt{\omega_{n0}}(X_k - X)) \\
&+ \frac{1}{2}\sum_{k=1}^{i-1}\Bigg\{ - \kappa_{n4}^{(k)}(X_k) + \kappa_{n4}^{(k+1)}(X_k) \\
&\qquad + \frac{1}{\sqrt{\omega_{n0}^3}}\frac{\mathrm{d}}{\mathrm{d}X}\left[\left(\widehat{EI}^{(k+1)} - \widehat{EI}^{(k)}\right)\frac{\mathrm{d}^2\phi_{n0}}{\mathrm{d}X^2}\right]_{X=X_k}\Bigg\}\sinh(\sqrt{\omega_{n0}}(X_k - X))
\end{aligned}
$$

with

$$\begin{aligned}
\kappa_{n1}^{(j)}(X) =& u_{n1,p}^{(j)}(X) - \frac{1}{\omega_{n0}} \frac{\mathrm{d}^2 u_{n1,p}^{(j)}(X)}{\mathrm{d}X^2} \\
\kappa_{n2}^{(j)}(X) =& \frac{1}{\sqrt{\omega_{n0}}} \frac{\mathrm{d}u_{n1,p}^{(j)}(X)}{\mathrm{d}X} - \frac{1}{\sqrt{\omega_{n0}^3}} \frac{\mathrm{d}^3 u_{n1,p}^{(j)}(X_k)}{\mathrm{d}X^3} \\
\kappa_{n3}^{(j)}(X) =& u_{n1,p}^{(j)}(X) + \frac{1}{\omega_{n0}} \frac{\mathrm{d}^2 u_{n1,p}^{(j)}(X)}{\mathrm{d}X^2} \\
\kappa_{n4}^{(j)}(X) =& \frac{1}{\sqrt{\omega_{n0}}} \frac{\mathrm{d}u_{n1,p}^{(j)}(X)}{\mathrm{d}X} + \frac{1}{\sqrt{\omega_{n0}^3}} \frac{\mathrm{d}^3 u_{n1,p}^{(j)}(X_k)}{\mathrm{d}X^3}
\end{aligned}$$

For a clamped left end:

$$\widetilde{u}_{n1}^{(1)}(X) - u_{n1}^{(1)}(X) = -u_{n1,p}^{(1)}(0) \cosh(\sqrt{\omega_{n0}} X) - \frac{1}{\sqrt{\omega_{n0}}} \frac{\mathrm{d}u_{n1,p}^{(1)}(0)}{\mathrm{d}X} \sinh(\sqrt{\omega_{n0}} X)$$

For a free left end:

$$\widetilde{u}_{n1}^{(1)}(X) - u_{n1}^{(1)}(X) = -\frac{1}{\omega_{n0}} \frac{\mathrm{d}^2 u_{n1,p}^{(1)}(0)}{\mathrm{d}X^2} \cosh(\sqrt{\omega_{n0}} X) - \frac{1}{\sqrt{\omega_{n0}^3}} \frac{\mathrm{d}^3 u_{n1,p}^{(1)}(0)}{\mathrm{d}X^3} \sinh(\sqrt{\omega_{n0}} X)$$

B.2 Inclusion of Lumped Masses

The expressions for $\widetilde{u}_{n1}^{(i)}(X)$ are the same as in Appendix B.1. The presence of lumped masses introduces an additional function $m_{n1}^{(i)}(X)$. For $1 \leq i \leq m$, the expression for $m_{n1}^{(i)}(X)$ is

$$\begin{aligned}
m_{n1}^{(i)}(X) =& m_{n1}^{(1)}(X) + \frac{1}{2}\sqrt{\omega_{n0}} \sum_{k=1}^{i-1} \widehat{M}_k \phi_{n0}(X_k) \sin(\sqrt{\omega_{n0}}(X_k - X)) \\
& - \frac{1}{2}\sqrt{\omega_{n0}} \sum_{k=1}^{i-1} \widehat{M}_k \phi_{n0}(X_k) \sinh(\sqrt{\omega_{n0}}(X_k - X))
\end{aligned}$$

For a system with a clamped left end $m_{n1}^{(1)}(X) = 0$, and for a system with a free left end $m_{n1}^{(1)}(X) = \sqrt{\omega_{n0}} \widehat{M}_0 \phi_{n0}(0) \sinh(\sqrt{\omega_{n0}} X)$.

Appendix C

Reference Value Dependence

C.1 Euler-Bernoulli Model

For the boundary conditions considered, the particular solution $u^{(i)}_{n1,p}(X)$, $1 \leq i \leq m$, is:

$$\begin{aligned}
\epsilon u^{(i)}_{n1,p}(X) = \frac{1}{\rho A^*}\Bigg\{ & \frac{\sqrt{\omega_{n0}}}{2}\Bigg[\cos\left(\sqrt{\omega_{n0}}\, X\right) \int \sin\left(\sqrt{\omega_{n0}}\, X\right) \rho A^{(i)} \phi_{n0}\, \mathrm{d}X \\
& - \sin\left(\sqrt{\omega_{n0}}\, X\right) \int \cos\left(\sqrt{\omega_{n0}}\, X\right) \rho A^{(i)} \phi_{n0}\, \mathrm{d}X \\
& - \cosh\left(\sqrt{\omega_{n0}}\, X\right) \int \sinh\left(\sqrt{\omega_{n0}}\, X\right) \rho A^{(i)} \phi_{n0}\, \mathrm{d}X \\
& + \sinh\left(\sqrt{\omega_{n0}}\, X\right) \int \cosh\left(\sqrt{\omega_{n0}}\, X\right) \rho A^{(i)} \phi_{n0}\, \mathrm{d}X \Bigg] \Bigg\} \\
- \frac{1}{EI^*}\Bigg\{ & \frac{1}{2\sqrt{\omega_{n0}^3}}\Bigg[\cos\left(\sqrt{\omega_{n0}}\, X\right) \int \sin\left(\sqrt{\omega_{n0}}\, X\right) \frac{\mathrm{d}^2}{\mathrm{d}X^2}\left[EI^{(i)} \frac{\mathrm{d}^2 \phi_{n0}}{\mathrm{d}X^2} \right] \mathrm{d}X \\
& - \sin\left(\sqrt{\omega_{n0}}\, X\right) \int \cos\left(\sqrt{\omega_{n0}}\, X\right) \frac{\mathrm{d}^2}{\mathrm{d}X^2}\left[EI^{(i)} \frac{\mathrm{d}^2 \phi_{n0}}{\mathrm{d}X^2} \right] \mathrm{d}X \\
& - \cosh\left(\sqrt{\omega_{n0}}\, X\right) \int \sinh\left(\sqrt{\omega_{n0}}\, X\right) \frac{\mathrm{d}^2}{\mathrm{d}X^2}\left[EI^{(i)} \frac{\mathrm{d}^2 \phi_{n0}}{\mathrm{d}X^2} \right] \mathrm{d}X \\
& + \sinh\left(\sqrt{\omega_{n0}}\, X\right) \int \cosh\left(\sqrt{\omega_{n0}}\, X\right) \frac{\mathrm{d}^2}{\mathrm{d}X^2}\left[EI^{(i)} \frac{\mathrm{d}^2 \phi_{n0}}{\mathrm{d}X^2} \right] \mathrm{d}X \Bigg] \Bigg\} \\
= & \frac{\lambda^{(i)}_n(X)}{\rho A^*} - \frac{\chi^{(i)}_n(X)}{EI^*}
\end{aligned}$$

For a clamped left end, $\widetilde{u}_{n1}^{(1)}(X)$ is:

$$\begin{aligned}\epsilon\widetilde{u}_{n1}^{(1)}(X) =&\frac{1}{\rho A^*}\left\{\lambda_n^{(1)}(X) - \lambda_n^{(1)}(0)\cosh\left(\sqrt{\omega_{n0}}\,X\right) - \frac{1}{\sqrt{\omega_{n0}}}\frac{\mathrm{d}\lambda_n^{(1)}}{\mathrm{d}X}(0)\sinh\left(\sqrt{\omega_{n0}}\,X\right)\right\}\\ &- \frac{1}{EI^*}\left\{\chi_n^{(1)}(X) - \chi_n^{(1)}(0)\cosh\left(\sqrt{\omega_{n0}}\,X\right) - \frac{1}{\sqrt{\omega_{n0}}}\frac{\mathrm{d}\chi_n^{(1)}}{\mathrm{d}X}(0)\sinh\left(\sqrt{\omega_{n0}}\,X\right)\right\}\\ =&\frac{\eta_n^{(1)}(X)}{\rho A^*} - \frac{\mu_n^{(1)}(X)}{EI^*}\end{aligned}$$

For a free left end, $\widetilde{u}_{n1}^{(1)}(X)$ is:

$$\begin{aligned}\epsilon\widetilde{u}_{n1}^{(1)}(X) =&\frac{1}{\rho A^*}\left\{\lambda_n^{(1)}(X) - \frac{1}{\omega_{n0}}\frac{\mathrm{d}^2\lambda_n^{(1)}}{\mathrm{d}X^2}(0)\cosh\left(\sqrt{\omega_{n0}}\,X\right) - \frac{1}{\sqrt{\omega_{n0}^3}}\frac{\mathrm{d}^3\lambda_n^{(1)}}{\mathrm{d}X^3}(0)\sinh\left(\sqrt{\omega_{n0}}\,X\right)\right\}\\ &- \frac{1}{EI^*}\left\{\chi_n^{(1)}(X) - \frac{1}{\omega_{n0}}\frac{\mathrm{d}^2\chi_n^{(1)}}{\mathrm{d}X^2}(0)\cosh\left(\sqrt{\omega_{n0}}\,X\right) - \frac{1}{\sqrt{\omega_{n0}^3}}\frac{\mathrm{d}^3\chi_n^{(1)}}{\mathrm{d}X^3}(0)\sinh\left(\sqrt{\omega_{n0}}\,X\right)\right\}\\ =&\frac{\eta_n^{(1)}(X)}{\rho A^*} - \frac{\mu_n^{(1)}(X)}{EI^*}\end{aligned}$$

In general, the expression for the i^{th} section of $\widetilde{u}_{n1}^{(i)}(X)$ is, for $1 < i \leq m$:

$$\epsilon\widetilde{u}_{n1}^{(i)}(X) = \frac{\eta_n^{(i)}(X)}{\rho A^*} - \frac{\mu_n^{(i)}(X)}{EI^*}$$

where:

$$\begin{aligned}\eta_n^{(i)}(X) =&\lambda_n^{(i)}(X) + \eta_n^{(1)}(X) - \lambda_n^{(1)}(X)\\ &+ \frac{1}{2}\sum_{k=1}^{i-1}\left\{\overline{\kappa}_{n1}^{(k)}(X_k) - \overline{\kappa}_{n1}^{(k+1)}(X_k)\right\}\cos(\sqrt{\omega_{n0}}(X_k - X))\\ &+ \frac{1}{2}\sum_{k=1}^{i-1}\left\{-\overline{\kappa}_{n2}^{(k)}(X_k) + \overline{\kappa}_{n2}^{(k+1)}(X_k)\right\}\sin(\sqrt{\omega_{n0}}(X_k - X))\\ &+ \frac{1}{2}\sum_{k=1}^{i-1}\left\{\overline{\kappa}_{n3}^{(k)}(X_k) - \overline{\kappa}_{n3}^{(k+1)}(X_k)\right\}\cosh(\sqrt{\omega_{n0}}(X_k - X))\\ &+ \frac{1}{2}\sum_{k=1}^{i-1}\left\{-\overline{\kappa}_{n4}^{(k)}(X_k) + \overline{\kappa}_{n4}^{(k+1)}(X_k)\right\}\sinh(\sqrt{\omega_{n0}}(X_k - X))\end{aligned}$$

with:

$$\begin{aligned}
\overline{\kappa}_{n1}^{(j)}(X) =& \lambda_n^{(j)}(X) - \frac{1}{\omega_{n0}} \frac{\mathrm{d}^2 \lambda_n^{(j)}(X)}{\mathrm{d}X^2} \\
\overline{\kappa}_{n2}^{(j)}(X) =& \frac{1}{\sqrt{\omega_{n0}}} \frac{\mathrm{d}\lambda_n^{(j)}(X)}{\mathrm{d}X} - \frac{1}{\sqrt{\omega_{n0}^3}} \frac{\mathrm{d}^3 \lambda_n^{(j)}(X_k)}{\mathrm{d}X^3} \\
\overline{\kappa}_{n3}^{(j)}(X) =& \lambda_n^{(j)}(X) + \frac{1}{\omega_{n0}} \frac{\mathrm{d}^2 \lambda_n^{(j)}(X)}{\mathrm{d}X^2} \\
\overline{\kappa}_{n4}^{(j)}(X) =& \frac{1}{\sqrt{\omega_{n0}}} \frac{\mathrm{d}u_{n1,p}^{(j)}(X)}{\mathrm{d}X} + \frac{1}{\sqrt{\omega_{n0}^3}} \frac{\mathrm{d}^3 u_{n1,p}^{(j)}(X_k)}{\mathrm{d}X^3}
\end{aligned}$$

and:

$$\begin{aligned}
\mu_n^{(i)}(X) =& \chi_n^{(i)}(X) + \mu_n^{(1)}(X) - \chi_n^{(1)}(X) \\
&+ \frac{1}{2} \sum_{k=1}^{i-1} \left\{ \widetilde{\kappa}_{n1}^{(k)}(X_k) - \widetilde{\kappa}_{n1}^{(k+1)}(X_k) \right. \\
&\qquad \left. - \frac{1}{\omega_{n0}} \left(EI^{(k+1)}(X_k) - EI^{(k)}(X_k) \right) \frac{\mathrm{d}^2 \phi_{n0}(X_k)}{\mathrm{d}X^2} \right\} \cos(\sqrt{\omega_{n0}}(X_k - X)) \\
&+ \frac{1}{2} \sum_{k=1}^{i-1} \left\{ - \widetilde{\kappa}_{n2}^{(k)}(X_k) + \widetilde{\kappa}_{n2}^{(k+1)}(X_k) \right. \\
&\qquad \left. + \frac{1}{\sqrt{\omega_{n0}^3}} \frac{\mathrm{d}}{\mathrm{d}X} \left[\left(EI^{(k+1)} - EI^{(k)} \right) \frac{\mathrm{d}^2 \phi_{n0}}{\mathrm{d}X^2} \right]_{X=X_k} \right\} \sin(\sqrt{\omega_{n0}}(X_k - X)) \\
&+ \frac{1}{2} \sum_{k=1}^{i-1} \left\{ \widetilde{\kappa}_{n3}^{(k)}(X_k) - \widetilde{\kappa}_{n3}^{(k+1)}(X_k) \right. \\
&\qquad \left. + \frac{1}{\omega_{n0}} \left(EI^{(k+1)}(X_k) - EI^{(k)}(X_k) \right) \frac{\mathrm{d}^2 \phi_{n0}(X_k)}{\mathrm{d}X^2} \right\} \cosh(\sqrt{\omega_{n0}}(X_k - X)) \\
&+ \frac{1}{2} \sum_{k=1}^{i-1} \left\{ - \widetilde{\kappa}_{n2}^{(k)}(X_k) + \widetilde{\kappa}_{n2}^{(k+1)}(X_k) \right. \\
&\qquad \left. - \frac{1}{\sqrt{\omega_{n0}^3}} \frac{\mathrm{d}}{\mathrm{d}X} \left[\left(EI^{(k+1)} - EI^{(k)} \right) \frac{\mathrm{d}^2 \phi_{n0}}{\mathrm{d}X^2} \right]_{X=X_k} \right\} \sinh(\sqrt{\omega_{n0}}(X_k - X))
\end{aligned}$$

with

$$\begin{aligned}
\widetilde{\kappa}_{n1}^{(j)}(X) =& \chi_n^{(j)}(X) - \frac{1}{\omega_{n0}} \frac{\mathrm{d}^2 \chi_n^{(j)}(X)}{\mathrm{d}X^2} \\
\widetilde{\kappa}_{n2}^{(j)}(X) =& \frac{1}{\sqrt{\omega_{n0}}} \frac{\mathrm{d}\chi_n^{(j)}(X)}{\mathrm{d}X} - \frac{1}{\sqrt{\omega_{n0}^3}} \frac{\mathrm{d}^3 \chi_n^{(j)}(X_k)}{\mathrm{d}X^3} \\
\widetilde{\kappa}_{n3}^{(j)}(X) =& \chi_n^{(j)}(X) + \frac{1}{\omega_{n0}} \frac{\mathrm{d}^2 \chi_n^{(j)}(X)}{\mathrm{d}X^2} \\
\widetilde{\kappa}_{n4}^{(j)}(X) =& \frac{1}{\sqrt{\omega_{n0}}} \frac{\mathrm{d}\chi_n^{(j)}(X)}{\mathrm{d}X} + \frac{1}{\sqrt{\omega_{n0}^3}} \frac{\mathrm{d}^3 \chi_n^{(j)}(X_k)}{\mathrm{d}X^3}
\end{aligned}$$

The final coefficient determined using mass normalization for a CC system is

$$\begin{aligned}
\epsilon A_{n1}^{(1)} =& \frac{1}{\rho A^*} \left\{ \frac{\alpha_{n2}}{2\omega_{n0}} \int_0^1 X \phi_{n0} \frac{\mathrm{d}\phi_{n0}}{\mathrm{d}X} \, \mathrm{d}X - \int_0^1 \phi_{n0} \eta_n \, \mathrm{d}X \right. \\
& \left. + \frac{\eta_n^{(m)}(1) \int_0^1 \phi_{n0} \left\{ \sin(\sqrt{\omega_{n0}} X) - \sinh(\sqrt{\omega_{n0}} X) \right\} \mathrm{d}X}{\left\{ \sin(\sqrt{\omega_{n0}}) - \sinh(\sqrt{\omega_{n0}}) \right\}} - \frac{\alpha_{n2}}{\omega_{n0}} \right\} \\
& - \frac{1}{EI^*} \left\{ \frac{\alpha_{n1}}{2\omega_{n0}} \int_0^1 X \phi_{n0} \frac{\mathrm{d}\phi_{n0}}{\mathrm{d}X} \, \mathrm{d}X - \int_0^1 \phi_{n0} \mu_n \, \mathrm{d}X \right. \\
& \left. + \frac{\mu_n^{(m)}(1) \int_0^1 \phi_{n0} \left\{ \sin(\sqrt{\omega_{n0}} X) - \sinh(\sqrt{\omega_{n0}} X) \right\} \mathrm{d}X}{\left\{ \sin(\sqrt{\omega_{n0}}) - \sinh(\sqrt{\omega_{n0}}) \right\}} \right\} + \frac{1}{2} \\
=& \frac{\widetilde{A}_{n1}}{\rho A^*} - \frac{\overline{A}_{n1}}{EI^*} + \frac{1}{2}
\end{aligned}$$

and the first correction to the mode shape, $1 \leq i \leq m$, is

$$\begin{aligned}
\epsilon \phi_{n1}^{(i)}(X) =& \frac{1}{\rho A^*} \left\{ \widetilde{A}_{n1} \phi_{n0}(X) - \frac{\alpha_{n2}}{2\omega_{n0}} X \frac{\mathrm{d}\phi_{n0}}{\mathrm{d}X} + \eta_n^{(i)}(X) - \frac{\eta_n^{(m)}(1) \left\{ \sin(\sqrt{\omega_{n0}} X) - \sinh(\sqrt{\omega_{n0}} X) \right\}}{\left\{ \sin(\sqrt{\omega_{n0}}) - \sinh(\sqrt{\omega_{n0}}) \right\}} \right\} \\
& - \frac{1}{EI^*} \left\{ \overline{A}_{n1} \phi_{n0}(X) - \frac{\alpha_{n1}}{2\omega_{n0}} X \frac{\mathrm{d}\phi_{n0}}{\mathrm{d}X} + \mu_n^{(i)}(X) - \frac{\mu_n^{(m)}(1) \left\{ \sin(\sqrt{\omega_{n0}} X) - \sinh(\sqrt{\omega_{n0}} X) \right\}}{\left\{ \sin(\sqrt{\omega_{n0}}) - \sinh(\sqrt{\omega_{n0}}) \right\}} \right\} \\
& + \frac{1}{2} \phi_{n0}(X) \\
=& \frac{f_{n1}(X)}{\rho A^*} - \frac{f_{n2}(X)}{EI^*} + \frac{\phi_{n0}(X)}{2}
\end{aligned}$$

The final coefficient determined using mass normalization for a CF system is

$$\begin{aligned}\epsilon A_{n1}^{(1)} =&\frac{1}{\rho A^*}\Bigg\{\frac{\alpha_{n2}}{2\omega_{n0}}\int_0^1 X\phi_{n0}\frac{\mathrm{d}\phi_{n0}}{\mathrm{d}X}\,\mathrm{d}X-\int_0^1\phi_{n0}\eta_n\,\mathrm{d}X\\&-\frac{\frac{\mathrm{d}\eta_n^{(m)}(1)}{\mathrm{d}X^2}\int_0^1\phi_{n0}\left\{\sin(\sqrt{\omega_{n0}}X)-\sinh(\sqrt{\omega_{n0}}X)\right\}\,\mathrm{d}X}{\omega_{n0}\left\{\sin(\sqrt{\omega_{n0}})+\sinh(\sqrt{\omega_{n0}})\right\}}-\frac{\alpha_{n2}}{\omega_{n0}}\Bigg\}\\&-\frac{1}{EI^*}\Bigg\{\frac{\alpha_{n1}}{2\omega_{n0}}\int_0^1 X\phi_{n0}\frac{\mathrm{d}\phi_{n0}}{\mathrm{d}X}\,\mathrm{d}X-\int_0^1\phi_{n0}\mu_n(X)\,\mathrm{d}X\\&-\frac{\frac{\mathrm{d}^2\mu_n^{(m)}(1)}{\mathrm{d}X^2}\int_0^1\phi_{n0}\left\{\sin(\sqrt{\omega_{n0}}X)-\sinh(\sqrt{\omega_{n0}}X)\right\}\,\mathrm{d}X}{\omega_{n0}\left\{\sin(\sqrt{\omega_{n0}})+\sinh(\sqrt{\omega_{n0}})\right\}}\Bigg\}+\frac{1}{2}\\=&\frac{\widetilde{A}_{n1}}{\rho A^*}-\frac{\overline{A}_{n1}}{EI^*}+\frac{1}{2}\end{aligned}$$

and the first correction to the mode shape, $1\le i\le m$, is

$$\begin{aligned}\epsilon u_{n1}^{(i)}(X) =&\frac{1}{\rho A^*}\Bigg\{\widetilde{A}_{n1}\phi_{n0}(X)-\frac{\alpha_{n2}}{2\omega_{n0}}X\frac{\mathrm{d}\phi_{n0}}{\mathrm{d}X}+\eta_n^{(i)}(X)\mu_n^{(i)}(X)+\frac{\frac{\mathrm{d}^2\eta_n^{(m)}(1)}{\mathrm{d}X^2}\left\{\sin(\sqrt{\omega_{n0}}X)-\sinh(\sqrt{\omega_{n0}}X)\right\}}{\omega_{n0}\left\{\sin(\sqrt{\omega_{n0}})+\sinh(\sqrt{\omega_{n0}})\right\}}\Bigg\}\\&-\frac{1}{EI^*}\Bigg\{\overline{A}_{n1}\phi_{n0}(X)-\frac{\alpha_{n1}}{2\omega_{n0}}X\frac{\mathrm{d}\phi_{n0}}{\mathrm{d}X}+\mu_n^{(i)}(X)+\frac{\frac{\mathrm{d}^2\mu_n^{(m)}(1)}{\mathrm{d}X}\left\{\sin(\sqrt{\omega_{n0}}X)-\sinh(\sqrt{\omega_{n0}}X)\right\}}{\omega_{n0}\left\{\sin(\sqrt{\omega_{n0}})+\sinh(\sqrt{\omega_{n0}})\right\}}\Bigg\}\\&+\frac{1}{2}\phi_{n0}(X)\\=&\frac{f_{n1}(X)}{\rho A^*}-\frac{f_{n2}(X)}{EI^*}+\frac{\phi_{n0}(X)}{2}\end{aligned}$$

The final coefficient determined using mass normalization for a FF system is

$$\begin{aligned}\epsilon A_{n1}^{(1)} =&\frac{1}{\rho A^*}\Bigg\{\frac{\alpha_{n2}}{2\omega_{n0}}\int_0^1 X\phi_{n0}\frac{\mathrm{d}\phi_{n0}}{\mathrm{d}X}\,\mathrm{d}X-\int_0^1\phi_{n0}\eta_n\,\mathrm{d}X\\&-\frac{\frac{\mathrm{d}\eta_n^{(m)}(1)}{\mathrm{d}X^2}\int_0^1\phi_{n0}\left\{\sin(\sqrt{\omega_{n0}}X)+\sinh(\sqrt{\omega_{n0}}X)\right\}\,\mathrm{d}X}{\omega_{n0}\left\{\sin(\sqrt{\omega_{n0}})-\sinh(\sqrt{\omega_{n0}})\right\}}-\frac{\alpha_{n2}}{\omega_{n0}}\Bigg\}\\&-\frac{1}{EI^*}\Bigg\{\frac{\alpha_{n1}}{2\omega_{n0}}\int_0^1 X\phi_{n0}\frac{\mathrm{d}\phi_{n0}}{\mathrm{d}X}\,\mathrm{d}X-\int_0^1\phi_{n0}\mu_n\,\mathrm{d}X\\&-\frac{\frac{\mathrm{d}^2\mu_n^{(m)}(1)}{\mathrm{d}X^2}\int_0^1\phi_{n0}\left\{\sin(\sqrt{\omega_{n0}}X)+\sinh(\sqrt{\omega_{n0}}X)\right\}\,\mathrm{d}X}{\omega_{n0}\left\{\sin(\sqrt{\omega_{n0}})-\sinh(\sqrt{\omega_{n0}})\right\}}\Bigg\}+\frac{1}{2}\\=&\frac{\widetilde{A}_{n1}}{\rho A^*}-\frac{\overline{A}_{n1}}{EI^*}+\frac{1}{2}\end{aligned}$$

and the first correction to the mode shape, $1 \leq i \leq m$, is

$$\begin{aligned}
\epsilon u_{n1}^{(i)}(X) =& \frac{1}{\rho A^*}\left\{ \widetilde{A}_{n1}\phi_{n0}(X) - \frac{\alpha_{n2}}{2\omega_{n0}} X \frac{\mathrm{d}\phi_{n0}}{\mathrm{d}X} + \eta_n^{(i)}(X) + \frac{\frac{\mathrm{d}^2\eta_n^{(m)}(1)}{\mathrm{d}X^2}\left\{\sin(\sqrt{\omega_{n0}}X) + \sinh(\sqrt{\omega_{n0}}X)\right\}}{\omega_{n0}\left\{\sin(\sqrt{\omega_{n0}}) - \sinh(\sqrt{\omega_{n0}})\right\}} \right\} \\
& - \frac{1}{EI^*}\left\{ \overline{A}_{n1}\phi_{n0}(X) - \frac{1}{2\omega_{n0}}\alpha_{n1} X \frac{\mathrm{d}\phi_{n0}}{\mathrm{d}X} + \mu_n^{(i)}(X) + \frac{\frac{\mathrm{d}^2\mu_n^{(m)}(1)}{\mathrm{d}X}\left\{\sin(\sqrt{\omega_{n0}}X) + \sinh(\sqrt{\omega_{n0}}X)\right\}}{\omega_{n0}\left\{\sin(\sqrt{\omega_{n0}}) - \sinh(\sqrt{\omega_{n0}})\right\}} \right\} \\
& + \frac{1}{2}\phi_{n0}(X) \\
=& \frac{f_{n1}(X)}{\rho A^*} - \frac{f_{n2}(X)}{EI^*} + \frac{\phi_{n0}(X)}{2}
\end{aligned}$$

C.2 Inclusion of Lumped Masses

For the boundary conditions considered, the particular solution $u_{n1,p}^{(i)}(X)$, $1 \leq i \leq m$, is:

$$\begin{aligned}
\epsilon u_{n1,p}^{(i)}(X) = \frac{1}{\rho A^*}\Bigg\{ & \frac{\sqrt{\omega_{n0}}}{2}\Bigg[\cos\left(\sqrt{\omega_{n0}}\,X\right) \int \sin\left(\sqrt{\omega_{n0}}\,X\right) \rho A^{(i)} \phi_{n0}\,\mathrm{d}X \\
& - \sin\left(\sqrt{\omega_{n0}}\,X\right) \int \cos\left(\sqrt{\omega_{n0}}\,X\right) \rho A^{(i)} \phi_{n0}\,\mathrm{d}X \\
& - \cosh\left(\sqrt{\omega_{n0}}\,X\right) \int \sinh\left(\sqrt{\omega_{n0}}\,X\right) \rho A^{(i)} \phi_{n0}\,\mathrm{d}X \\
& + \sinh\left(\sqrt{\omega_{n0}}\,X\right) \int \cosh\left(\sqrt{\omega_{n0}}\,X\right) \rho A^{(i)} \phi_{n0}\,\mathrm{d}X \Bigg]\Bigg\} \\
- \frac{1}{EI^*}\Bigg\{ & \frac{1}{2\sqrt{\omega_{n0}^3}}\Bigg[\cos\left(\sqrt{\omega_{n0}}\,X\right) \int \sin\left(\sqrt{\omega_{n0}}\,X\right) \frac{\mathrm{d}^2}{\mathrm{d}X^2}\left[EI^{(i)} \frac{\mathrm{d}^2\phi_{n0}}{\mathrm{d}X^2}\right] \mathrm{d}X \\
& - \sin\left(\sqrt{\omega_{n0}}\,X\right) \int \cos\left(\sqrt{\omega_{n0}}\,X\right) \frac{\mathrm{d}^2}{\mathrm{d}X^2}\left[EI^{(i)} \frac{\mathrm{d}^2\phi_{n0}}{\mathrm{d}X^2}\right] \mathrm{d}X \\
& - \cosh\left(\sqrt{\omega_{n0}}\,X\right) \int \sinh\left(\sqrt{\omega_{n0}}\,X\right) \frac{\mathrm{d}^2}{\mathrm{d}X^2}\left[EI^{(i)} \frac{\mathrm{d}^2\phi_{n0}}{\mathrm{d}X^2}\right] \mathrm{d}X \\
& + \sinh\left(\sqrt{\omega_{n0}}\,X\right) \int \cosh\left(\sqrt{\omega_{n0}}\,X\right) \frac{\mathrm{d}^2}{\mathrm{d}X^2}\left[EI^{(i)} \frac{\mathrm{d}^2\phi_{n0}}{\mathrm{d}X^2}\right] \mathrm{d}X \Bigg]\Bigg\} \\
= & \frac{\lambda_n^{(i)}(X)}{\rho A^*} - \frac{\chi_n^{(i)}(X)}{EI^*}
\end{aligned}$$

For a clamped left end, $\widetilde{u}_{n1}^{(1)}(X)$ is:

$$\begin{aligned}
\epsilon\widetilde{u}_{n1}^{(1)}(X) = & \frac{1}{\rho A^*}\left\{ \lambda_n^{(1)}(X) - \lambda_n^{(1)}(0)\cosh\left(\sqrt{\omega_{n0}}\,X\right) - \frac{1}{\sqrt{\omega_{n0}}}\frac{\mathrm{d}\lambda_n^{(1)}}{\mathrm{d}X}(0)\sinh\left(\sqrt{\omega_{n0}}\,X\right) \right\} \\
& - \frac{1}{EI^*}\left\{ \chi_n^{(1)}(X) - \chi_n^{(1)}(0)\cosh\left(\sqrt{\omega_{n0}}\,X\right) - \frac{1}{\sqrt{\omega_{n0}}}\frac{\mathrm{d}\chi_n^{(1)}}{\mathrm{d}X}(0)\sinh\left(\sqrt{\omega_{n0}}\,X\right) \right\} \\
= & \frac{\eta_n^{(1)}(X)}{\rho A^*} - \frac{\mu_n^{(1)}(X)}{EI^*}
\end{aligned}$$

and $\epsilon m_{n1}^{(1)}(X) = 0 = \frac{1}{\rho A^*}\widetilde{m}_n^{(1)}(X)$. That is to say $\widetilde{m}_n^{(1)}(X) = 0$. For a free left end, $\widetilde{u}_{n1}^{(1)}(X)$ is:

$$\begin{aligned}\epsilon\widetilde{u}_{n1}^{(1)}(X) =& \frac{1}{\rho A^*}\left\{\lambda_n^{(1)}(X) - \frac{1}{\omega_{n0}}\frac{\mathrm{d}^2\lambda_n^{(1)}}{\mathrm{d}X^2}(0)\cosh\left(\sqrt{\omega_{n0}}\,X\right) - \frac{1}{\sqrt{\omega_{n0}^3}}\frac{\mathrm{d}^3\lambda_n^{(1)}}{\mathrm{d}X^3}(0)\sinh\left(\sqrt{\omega_{n0}}\,X\right)\right\} \\ & - \frac{1}{EI^*}\left\{\chi_n^{(1)}(X) - \frac{1}{\omega_{n0}}\frac{\mathrm{d}^2\chi_n^{(1)}}{\mathrm{d}X^2}(0)\cosh\left(\sqrt{\omega_{n0}}\,X\right) - \frac{1}{\sqrt{\omega_{n0}^3}}\frac{\mathrm{d}^3\chi_n^{(1)}}{\mathrm{d}X^3}(0)\sinh\left(\sqrt{\omega_{n0}}\,X\right)\right\} \\ =& \frac{\eta_n^{(1)}(X)}{\rho A^*} - \frac{\mu_n^{(1)}(X)}{EI^*}\end{aligned}$$

and $\epsilon m_{n1}^{(1)}(X) = \frac{1}{\rho A^*}\left\{\sqrt{\omega_{n0}}\frac{M_0}{l}\phi_{n0}(0)\sinh(\sqrt{\omega_{n0}}X)\right\} = \frac{1}{\rho A^*}\widetilde{m}_n^{(1)}(X)$.

In general, the expression for the i^{th} section of $\widetilde{u}_{n1}^{(i)}(X)$ is, for $1 < i \leq m$:

$$\epsilon\widetilde{u}_{n1}^{(i)}(X) = \frac{\eta_n^{(i)}(X)}{\rho A^*} - \frac{\mu_n^{(i)}(X)}{EI^*}$$

where:

$$\begin{aligned}\eta_n^{(i)}(X) =& \lambda_n^{(i)}(X) + \eta_n^{(1)}(X) - \lambda_n^{(1)}(X) \\ & + \frac{1}{2}\sum_{k=1}^{i-1}\left\{\overline{\kappa}_{n1}^{(k)}(X_k) - \overline{\kappa}_{n1}^{(k+1)}(X_k)\right\}\cos(\sqrt{\omega_{n0}}(X_k - X)) \\ & + \frac{1}{2}\sum_{k=1}^{i-1}\left\{-\overline{\kappa}_{n2}^{(k)}(X_k) + \overline{\kappa}_{n2}^{(k+1)}(X_k)\right\}\sin(\sqrt{\omega_{n0}}(X_k - X)) \\ & + \frac{1}{2}\sum_{k=1}^{i-1}\left\{\overline{\kappa}_{n3}^{(k)}(X_k) - \overline{\kappa}_{n3}^{(k+1)}(X_k)\right\}\cosh(\sqrt{\omega_{n0}}(X_k - X)) \\ & + \frac{1}{2}\sum_{k=1}^{i-1}\left\{-\overline{\kappa}_{n4}^{(k)}(X_k) + \overline{\kappa}_{n4}^{(k+1)}(X_k)\right\}\sinh(\sqrt{\omega_{n0}}(X_k - X))\end{aligned}$$

with:

$$\begin{aligned}
\overline{\kappa}_{n1}^{(j)}(X) =& \lambda_n^{(j)}(X) - \frac{1}{\omega_{n0}} \frac{\mathrm{d}^2 \lambda_n^{(j)}(X)}{\mathrm{d}X^2} \\
\overline{\kappa}_{n2}^{(j)}(X) =& \frac{1}{\sqrt{\omega_{n0}}} \frac{\mathrm{d}\lambda_n^{(j)}(X)}{\mathrm{d}X} - \frac{1}{\sqrt{\omega_{n0}^3}} \frac{\mathrm{d}^3 \lambda_n^{(j)}(X_k)}{\mathrm{d}X^3} \\
\overline{\kappa}_{n3}^{(j)}(X) =& \lambda_n^{(j)}(X) + \frac{1}{\omega_{n0}} \frac{\mathrm{d}^2 \lambda_n^{(j)}(X)}{\mathrm{d}X^2} \\
\overline{\kappa}_{n4}^{(j)}(X) =& \frac{1}{\sqrt{\omega_{n0}}} \frac{\mathrm{d}u_{n1,p}^{(j)}(X)}{\mathrm{d}X} + \frac{1}{\sqrt{\omega_{n0}^3}} \frac{\mathrm{d}^3 u_{n1,p}^{(j)}(X_k)}{\mathrm{d}X^3}
\end{aligned}$$

and:

$$\begin{aligned}
\mu_n^{(i)}(X) =& \chi_n^{(i)}(X) + \mu_n^{(1)}(X) - \chi_n^{(1)}(X) \\
&+ \frac{1}{2} \sum_{k=1}^{i-1} \left\{ \widetilde{\kappa}_{n1}^{(k)}(X_k) - \widetilde{\kappa}_{n1}^{(k+1)}(X_k) \right. \\
&\qquad \left. - \frac{1}{\omega_{n0}} \left(EI^{(k+1)}(X_k) - EI^{(k)}(X_k) \right) \frac{\mathrm{d}^2 \phi_{n0}(X_k)}{\mathrm{d}X^2} \right\} \cos(\sqrt{\omega_{n0}}(X_k - X)) \\
&+ \frac{1}{2} \sum_{k=1}^{i-1} \left\{ - \widetilde{\kappa}_{n2}^{(k)}(X_k) + \widetilde{\kappa}_{n2}^{(k+1)}(X_k) \right. \\
&\qquad \left. + \frac{1}{\sqrt{\omega_{n0}^3}} \frac{\mathrm{d}}{\mathrm{d}X} \left[\left(EI^{(k+1)} - EI^{(k)} \right) \frac{\mathrm{d}^2 \phi_{n0}}{\mathrm{d}X^2} \right]_{X=X_k} \right\} \sin(\sqrt{\omega_{n0}}(X_k - X)) \\
&+ \frac{1}{2} \sum_{k=1}^{i-1} \left\{ \widetilde{\kappa}_{n3}^{(k)}(X_k) - \widetilde{\kappa}_{n3}^{(k+1)}(X_k) \right. \\
&\qquad \left. + \frac{1}{\omega_{n0}} \left(EI^{(k+1)}(X_k) - EI^{(k)}(X_k) \right) \frac{\mathrm{d}^2 \phi_{n0}(X_k)}{\mathrm{d}X^2} \right\} \cosh(\sqrt{\omega_{n0}}(X_k - X)) \\
&+ \frac{1}{2} \sum_{k=1}^{i-1} \left\{ - \widetilde{\kappa}_{n2}^{(k)}(X_k) + \widetilde{\kappa}_{n2}^{(k+1)}(X_k) \right. \\
&\qquad \left. - \frac{1}{\sqrt{\omega_{n0}^3}} \frac{\mathrm{d}}{\mathrm{d}X} \left[\left(EI^{(k+1)} - EI^{(k)} \right) \frac{\mathrm{d}^2 \phi_{n0}}{\mathrm{d}X^2} \right]_{X=X_k} \right\} \sinh(\sqrt{\omega_{n0}}(X_k - X))
\end{aligned}$$

with

$$\begin{aligned}
\widetilde{\kappa}_{n1}^{(j)}(X) =& \chi_n^{(j)}(X) - \frac{1}{\omega_{n0}} \frac{\mathrm{d}^2 \chi_n^{(j)}(X)}{\mathrm{d}X^2} \\
\widetilde{\kappa}_{n2}^{(j)}(X) =& \frac{1}{\sqrt{\omega_{n0}}} \frac{\mathrm{d}\chi_n^{(j)}(X)}{\mathrm{d}X} - \frac{1}{\sqrt{\omega_{n0}^3}} \frac{\mathrm{d}^3 \chi_n^{(j)}(X_k)}{\mathrm{d}X^3} \\
\widetilde{\kappa}_{n3}^{(j)}(X) =& \chi_n^{(j)}(X) + \frac{1}{\omega_{n0}} \frac{\mathrm{d}^2 \chi_n^{(j)}(X)}{\mathrm{d}X^2} \\
\widetilde{\kappa}_{n4}^{(j)}(X) =& \frac{1}{\sqrt{\omega_{n0}}} \frac{\mathrm{d}\chi_n^{(j)}(X)}{\mathrm{d}X} + \frac{1}{\sqrt{\omega_{n0}^3}} \frac{\mathrm{d}^3 \chi_n^{(j)}(X_k)}{\mathrm{d}X^3}
\end{aligned}$$

In general, the expression for the i^{th} section of $m_{n1}^{(i)}(X)$ is, for $1 < i \leq m$:

$$\begin{aligned}
\epsilon m_{n1}^{(i)}(X) =& \frac{1}{\rho A^*} \left\{ \widetilde{m}_{n1}^{(1)}(X) + \frac{1}{2}\sqrt{\omega_{n0}} \sum_{k=1}^{i-1} \frac{M_k}{l} \phi_{n0}(X_k) \sin(\sqrt{\omega_{n0}}(X_k - X)) \right. \\
& \left. - \frac{1}{2}\sqrt{\omega_{n0}} \sum_{k=1}^{i-1} \frac{M_k}{l} \phi_{n0}(X_k) \sinh(\sqrt{\omega_{n0}}(X_k - X)) \right\}
\end{aligned}$$

The final coefficient determined using mass normalization for a CC system is

$$\begin{aligned}
\epsilon A_{n1}^{(1)} =& \frac{1}{\rho A^*} \left\{ \frac{\alpha_{n2}}{2\omega_{n0}} \int_0^1 X \phi_{n0} \frac{\mathrm{d}\phi_{n0}}{\mathrm{d}X} \,\mathrm{d}X - \int_0^1 \phi_{n0} \eta_n \,\mathrm{d}X + \frac{\eta_n^{(m)}(1) \int_0^1 \phi_{n0} \{\sin(\sqrt{\omega_{n0}}X) - \sinh(\sqrt{\omega_{n0}}X)\} \,\mathrm{d}X}{\{\sin(\sqrt{\omega_{n0}}) - \sinh(\sqrt{\omega_{n0}})\}} \right. \\
& \left. - \int_0^1 \phi_{n0} \widetilde{m}_n \,\mathrm{d}X + \frac{\widetilde{m}_n^{(m)}(1) \int_0^1 \phi_{n0} \{\sin(\sqrt{\omega_{n0}}X) - \sinh(\sqrt{\omega_{n0}}X)\} \,\mathrm{d}X}{\{\sin(\sqrt{\omega_{n0}}) - \sinh(\sqrt{\omega_{n0}})\}} - \frac{\alpha_{n2}}{\omega_{n0}} \right\} \\
& - \frac{1}{EI^*} \left\{ \frac{\alpha_{n1}}{2\omega_{n0}} \int_0^1 X \phi_{n0} \frac{\mathrm{d}\phi_{n0}}{\mathrm{d}X} \,\mathrm{d}X - \int_0^1 \phi_{n0} \mu_n \,\mathrm{d}X + \frac{\mu_n^{(m)}(1) \int_0^1 \phi_{n0} \{\sin(\sqrt{\omega_{n0}}X) - \sinh(\sqrt{\omega_{n0}}X)\} \,\mathrm{d}X}{\{\sin(\sqrt{\omega_{n0}}) - \sinh(\sqrt{\omega_{n0}})\}} \right\} \\
& + \frac{1}{2} \\
=& \frac{\widetilde{A}_{n1}}{\rho A^*} - \frac{\overline{A}_{n1}}{EI^*} + \frac{1}{2}
\end{aligned}$$

and the first correction to the mode shape, $1 \leq i \leq m$, is

$$\begin{aligned}
\epsilon\phi_{n1}^{(i)}(X) =& \frac{1}{\rho A^*}\left\{ \widetilde{A}_{n1}\phi_{n0}(X) - \frac{\alpha_{n2}}{2\omega_{n0}} X \frac{\mathrm{d}\phi_{n0}}{\mathrm{d}X} + \eta_n^{(i)}(X) - \frac{\eta_n^{(m)}(1)\left\{\sin(\sqrt{\omega_{n0}}X) - \sinh(\sqrt{\omega_{n0}}X)\right\}}{\left\{\sin(\sqrt{\omega_{n0}}) - \sinh(\sqrt{\omega_{n0}})\right\}} \right. \\
& \left. + \widetilde{m}_{n1}^{(i)}(X) - \frac{\left\{\sin(\sqrt{\omega_{n0}}X) - \sinh(\sqrt{\omega_{n0}}X)\right\}}{\left\{\sin(\sqrt{\omega_{n0}}) - \sinh(\sqrt{\omega_{n0}})\right\}} \widetilde{m}_{n1}^{(m)}(1) \right\} \\
& - \frac{1}{EI^*}\left\{ \overline{A}_{n1}\phi_{n0}(X) - \frac{\alpha_{n1}}{2\omega_{n0}} X \frac{\mathrm{d}\phi_{n0}}{\mathrm{d}X} + \mu_n^{(i)}(X) - \frac{\mu_n^{(m)}(1)\left\{\sin(\sqrt{\omega_{n0}}X) - \sinh(\sqrt{\omega_{n0}}X)\right\}}{\left\{\sin(\sqrt{\omega_{n0}}) - \sinh(\sqrt{\omega_{n0}})\right\}} \right\} \\
& + \frac{1}{2}\phi_{n0}(X) \\
=& \frac{f_{n1}(X)}{\rho A^*} - \frac{f_{n2}(X)}{EI^*} + \frac{\phi_{n0}(X)}{2}
\end{aligned}$$

The final coefficient determined using mass normalization for a CF system is

$$\begin{aligned}
\epsilon A_{n1}^{(1)} =& \frac{1}{\rho A^*}\left\{ \frac{\alpha_{n2}}{2\omega_{n0}} \int_0^1 X\phi_{n0}\frac{\mathrm{d}\phi_{n0}}{\mathrm{d}X}\,\mathrm{d}X - \int_0^1 \phi_{n0}\eta_n\,\mathrm{d}X - \frac{\frac{\mathrm{d}\eta_n^{(m)}(1)}{\mathrm{d}X^2}\int_0^1 \phi_{n0}\,\left\{\sin(\sqrt{\omega_{n0}}X) - \sinh(\sqrt{\omega_{n0}}X)\right\}\,\mathrm{d}X}{\omega_{n0}\left\{\sin(\sqrt{\omega_{n0}}) + \sinh(\sqrt{\omega_{n0}})\right\}} \right. \\
& \left. - \int_0^1 \phi_{n0}\widetilde{m}_n\,\mathrm{d}X - \frac{\frac{\mathrm{d}^2\widetilde{m}_n(1)}{\mathrm{d}X^2}\int_0^1 \phi_{n0}\,\left\{\sin(\sqrt{\omega_{n0}}X) - \sinh(\sqrt{\omega_{n0}}X)\right\}\,\mathrm{d}X}{\omega_{n0}\left\{\sin(\sqrt{\omega_{n0}}) + \sinh(\sqrt{\omega_{n0}})\right\}} - \frac{\alpha_{n2}}{\omega_{n0}} \right\} \\
& - \frac{1}{EI^*}\left\{ \frac{\alpha_{n1}}{2\omega_{n0}} \int_0^1 X\phi_{n0}\frac{\mathrm{d}\phi_{n0}}{\mathrm{d}X}\,\mathrm{d}X - \int_0^1 \phi_{n0}\mu_n(X)\,\mathrm{d}X - \frac{\frac{\mathrm{d}^2\mu_n^{(m)}(1)}{\mathrm{d}X^2}\int_0^1 \phi_{n0}\,\left\{\sin(\sqrt{\omega_{n0}}X) - \sinh(\sqrt{\omega_{n0}}X)\right\}\,\mathrm{d}X}{\omega_{n0}\left\{\sin(\sqrt{\omega_{n0}}) + \sinh(\sqrt{\omega_{n0}})\right\}} \right\} \\
& + \frac{1}{2} \\
=& \frac{\widetilde{A}_{n1}}{\rho A^*} - \frac{\overline{A}_{n1}}{EI^*} + \frac{1}{2}
\end{aligned}$$

and the first correction to the mode shape, $1 \leq i \leq m$, is

$$\begin{aligned}
\epsilon u_{n1}^{(i)}(X) =& \frac{1}{\rho A^*}\left\{ \widetilde{A}_{n1}\phi_{n0}(X) - \frac{\alpha_{n2}}{2\omega_{n0}} X \frac{\mathrm{d}\phi_{n0}}{\mathrm{d}X} + \eta_n^{(i)}(X)\mu_n^{(i)}(X) + \frac{\frac{\mathrm{d}^2\eta_n^{(m)}(1)}{\mathrm{d}X^2}\left\{\sin(\sqrt{\omega_{n0}}X) - \sinh(\sqrt{\omega_{n0}}X)\right\}}{\omega_{n0}\left\{\sin(\sqrt{\omega_{n0}}) + \sinh(\sqrt{\omega_{n0}})\right\}} \right. \\
& \left. + \widetilde{m}_{n1}^{(i)}(X) + \frac{\frac{\mathrm{d}^2\widetilde{m}_{n1}^{(m)}(1)}{\mathrm{d}X^2}\left\{\sin(\sqrt{\omega_{n0}}X) - \sinh(\sqrt{\omega_{n0}}X)\right\}}{\omega_{n0}\left\{\sin(\sqrt{\omega_{n0}}) + \sinh(\sqrt{\omega_{n0}})\right\}} \right\} \\
& - \frac{1}{EI^*}\left\{ \overline{A}_{n1}\phi_{n0}(X) - \frac{\alpha_{n1}}{2\omega_{n0}} X \frac{\mathrm{d}\phi_{n0}}{\mathrm{d}X} + \mu_n^{(i)}(X) + \frac{\frac{\mathrm{d}^2\mu_n^{(m)}(1)}{\mathrm{d}X}\left\{\sin(\sqrt{\omega_{n0}}X) - \sinh(\sqrt{\omega_{n0}}X)\right\}}{\omega_{n0}\left\{\sin(\sqrt{\omega_{n0}}) + \sinh(\sqrt{\omega_{n0}})\right\}} \right\} \\
& + \frac{1}{2}\phi_{n0}(X) \\
=& \frac{f_{n1}(X)}{\rho A^*} - \frac{f_{n2}(X)}{EI^*} + \frac{\phi_{n0}(X)}{2}
\end{aligned}$$

The final coefficient determined using mass normalization for a FF system is

$$\begin{aligned}
\epsilon A_{n1}^{(1)} =& \frac{1}{\rho A^*}\left\{ \frac{\alpha_{n2}}{2\omega_{n0}} \int_0^1 X\phi_{n0} \frac{\mathrm{d}\phi_{n0}}{\mathrm{d}X}\,\mathrm{d}X - \int_0^1 \phi_{n0}\eta_n\,\mathrm{d}X - \frac{\frac{\mathrm{d}\eta_n^{(m)}(1)}{\mathrm{d}X^2}\int_0^1 \phi_{n0}\,\{\sin(\sqrt{\omega_{n0}}X)+\sinh(\sqrt{\omega_{n0}}X)\}\,\mathrm{d}X}{\omega_{n0}\{\sin(\sqrt{\omega_{n0}})-\sinh(\sqrt{\omega_{n0}})\}} \right. \\
& \left. - \int_0^1 \phi_{n0}\widetilde{m}_n\,\mathrm{d}X - \frac{\frac{\mathrm{d}^2\widetilde{m}_n(1)}{\mathrm{d}X^2}\int_0^1 \phi_{n0}\,\{\sin(\sqrt{\omega_{n0}}X)+\sinh(\sqrt{\omega_{n0}}X)\}\,\mathrm{d}X}{\omega_{n0}\{\sin(\sqrt{\omega_{n0}})-\sinh(\sqrt{\omega_{n0}})\}} - \frac{\alpha_{n2}}{\omega_{n0}} \right\} \\
& - \frac{1}{EI^*}\left\{ \frac{\alpha_{n1}}{2\omega_{n0}} \int_0^1 X\phi_{n0} \frac{\mathrm{d}\phi_{n0}}{\mathrm{d}X}\,\mathrm{d}X - \int_0^1 \phi_{n0}\mu_n\,\mathrm{d}X - \frac{\frac{\mathrm{d}^2\mu_n^{(m)}(1)}{\mathrm{d}X^2}\int_0^1 \phi_{n0}\,\{\sin(\sqrt{\omega_{n0}}X)+\sinh(\sqrt{\omega_{n0}}X)\}\,\mathrm{d}X}{\omega_{n0}\{\sin(\sqrt{\omega_{n0}})-\sinh(\sqrt{\omega_{n0}})\}} \right\} \\
& + \frac{1}{2} \\
=& \frac{\widetilde{A}_{n1}}{\rho A^*} - \frac{\overline{A}_{n1}}{EI^*} + \frac{1}{2}
\end{aligned}$$

and the first correction to the mode shape, $1 \le i \le m$, is

$$\begin{aligned}
\epsilon u_{n1}^{(i)}(X) =& \frac{1}{\rho A^*}\left\{ \widetilde{A}_{n1}\phi_{n0}(X) - \frac{\alpha_{n2}}{2\omega_{n0}} X\frac{\mathrm{d}\phi_{n0}}{\mathrm{d}X} + \eta_n^{(i)}(X) + \frac{\frac{\mathrm{d}^2\eta_n^{(m)}(1)}{\mathrm{d}X^2}\left\{\sin(\sqrt{\omega_{n0}}X)+\sinh(\sqrt{\omega_{n0}}X)\right\}}{\omega_{n0}\left\{\sin(\sqrt{\omega_{n0}})-\sinh(\sqrt{\omega_{n0}})\right\}} \right. \\
& \left. + \widetilde{m}_{n1}^{(i)}(X) + \frac{\frac{\mathrm{d}^2\widetilde{m}_{n1}^{(m)}(1)}{\mathrm{d}X^2}\left\{\sin(\sqrt{\omega_{n0}}X)+\sinh(\sqrt{\omega_{n0}}X)\right\}}{\omega_{n0}\left\{\sin(\sqrt{\omega_{n0}})-\sinh(\sqrt{\omega_{n0}})\right\}} \right\} \\
& - \frac{1}{EI^*}\left\{ \overline{A}_{n1}\phi_{n0}(X) - \frac{1}{2\omega_{n0}}\alpha_{n1}X\frac{\mathrm{d}\phi_{n0}}{\mathrm{d}X} + \mu_n^{(i)}(X) + \frac{\frac{\mathrm{d}^2\mu_n^{(m)}(1)}{\mathrm{d}X}\left\{\sin(\sqrt{\omega_{n0}}X)+\sinh(\sqrt{\omega_{n0}}X)\right\}}{\omega_{n0}\left\{\sin(\sqrt{\omega_{n0}})-\sinh(\sqrt{\omega_{n0}})\right\}} \right\} \\
& + \frac{1}{2}\phi_{n0}(X) \\
=& \frac{f_{n1}(X)}{\rho A^*} - \frac{f_{n2}(X)}{EI^*} + \frac{\phi_{n0}(X)}{2}
\end{aligned}$$

Appendix D

Stepped Beam Analytical Solution

Assuming a separable solution to the piecewise constant Euler-Bernoulli beam model, a general solution can be found over each constant valued section. Assume that there is a lumped mass at each interface between two constant valued sections. For the i^{th} constant valued section of the system

$$f_i(x) = A_i \cos(\beta_i x) + B_i \sin(\beta_i x) + C_i \cosh(\beta_i x) + D_i \sinh(\beta_i x)$$

with $\beta_i^4 = \omega^2 \frac{\rho A_i}{EI_i}$.

Assuming m constant valued sections exist, applying the necessary boundary and continuity conditions produces the characteristic equation

$$0 = \kappa_1^\top B_1^\top B_2^\top \dots B_{m-1}^\top A B_{m-1} \dots B_2 B_1 \kappa_2$$

where B_i is given by:

$$B_i = \begin{bmatrix} (1+r_{EI})\cos & (1+r_{EI})\sin & (1-r_{EI})\cosh & (1-r_{EI})\sinh \\ -r_\beta(1+r_{EI})\sin + r_M \cos & r_\beta(1+r_{EI})\cos + r_M \sin & r_\beta(1-r_{EI})\sinh + r_M \cosh & r_\beta(1-r_{EI})\cosh + r_M \sinh \\ (1-r_{EI})\cos & (1-r_{EI})\sin & (1+r_{EI})\cosh & (1+r_{EI})\sinh \\ -r_\beta(1-r_{EI})\sin - r_M \cos & r_\beta(1-r_{EI})\cos - r_M \sin & r_\beta(1+r_{EI})\sinh - r_M \cosh & r_\beta(1+r_{EI})\cosh - r_M \sinh \end{bmatrix}$$

and A, κ_1 and κ_2 depend on the boundary conditions. In the expression for B_i the argument of the trigonometric functions is $\beta_i (x_{i-1} - x_i)$. Furthermore define $r_{EI} = \frac{EI_i \beta_i^2}{EI_{i+1} \beta_{i+1}^2}$, $r_\beta = \frac{\beta_i}{\beta_{i+1}}$, and $r_M = \frac{\beta_{i+1} M_i}{\rho A_{i+1}}$.

For a clamped left end $\kappa_1 = [1 \;\; 0 \;\; -1 \;\; 0]^\top$, $\kappa_2 = [0 \;\; -1 \;\; 0 \;\; 1]^\top$, and for a free left end $\kappa_1 = [1 \;\; 0 \;\; 1 \;\; 0]^\top$ and $\kappa_2 = [0 \;\; 1 \;\; 0 \;\; 1]^\top$.

For a clamped right end

$$A = \begin{bmatrix} 0 & 1 & \cos\sinh + \sin\cosh & \cos\cosh + \sin\sinh \\ -1 & 0 & -\cos\cosh + \sin\sinh & -\cos\sinh + \sin\cosh \\ -\cos\sinh - \sin\cosh & \cos\cosh - \sin\sinh & 0 & 1 \\ -\cos\cosh - \sin\sinh & \cos\sinh - \sin\cosh & -1 & 0 \end{bmatrix}$$

and the trigonometric functions have $\beta_m\,(x_{m-1} - l)$ as their argument. For a free right end the first two columns of A are

$$A(:,[1,2]) = \begin{bmatrix} 0 & -1 \\ 1 & 0 \\ -\cos\sinh - \sin\cosh + r_M\cos\cosh & \cos\cosh - \sin\sinh + r_M\sin\cosh \\ -\cos\cosh - \sin\sinh + r_M\cos\sinh & \cos\sinh - \sin\cosh + r_M\sin\sinh \end{bmatrix}$$

and the third and fourth columns of A are

$$A(:,[3,4]) = \begin{bmatrix} \cos\sinh + \sin\cosh - r_M\cos\cosh & \cos\cosh + \sin\sinh - r_M\cos\sinh \\ -\cos\cosh + \sin\sinh - r_M\sin\cosh & -\cos\sinh + \sin\cosh - r_M\sin\sinh \\ 0 & -1 \\ 1 & 0 \end{bmatrix}$$

For the system with a free right end the trigonometric functions have $\beta_m\,(x_{m-1} - l)$ as their argument and $r_M = \frac{2\beta_m M_m}{\rho A_m}$.

Using the above defined quantities, the mode shapes for the n^{th} mode over the i^{th} section is given by

$$f_{ni}(x) = \frac{A_{n1}}{2^{i-1}}\left[\cos(\beta_{ni}(x_{i-1} - x)) \quad \sin(\beta_{ni}(x_{i-1} - x)) \quad \cosh(\beta_{ni}(x_{i-1} - x)) \quad \sinh(\beta_{ni}(x_{i-1} - x))\right] B_{i-1}\ldots B_1\,(\kappa_1 - k_n\kappa_2)$$

In the expression for the mode shape, A_{n1} is an unknown coefficient determined after applying mass normalization. The value for k_n for a clamped right end is

$$k_n = \left\{\left[\cos \;\; \sin \;\; \cosh \;\; \sinh\right] B_{m-1}\ldots B_1\kappa_1\right\}\left\{\left[\cos \;\; \sin \;\; \cosh \;\; \sinh\right] B_{m-1}\ldots B_1\kappa_2\right\}^{-1}$$

and the argument for the trigonometric functions is $(\beta_{nm}(x_{m-1} - l))$. The value for k_n for a free right end is

$$\begin{aligned} k_n = &\left\{\left[-\sin + r_M\cos \;\; \cos + r_M\sin \;\; -\sinh + r_M\cosh \;\; -\cosh + r_M\sinh\right] B_{m-1}\ldots B_1\kappa_1\right\} \\ &\left\{\left[-\sin + r_M\cos \;\; \cos + r_M\sin \;\; -\sinh + r_M\cosh \;\; -\cosh + r_M\sinh\right] B_{m-1}\ldots B_1\kappa_2\right\}^{-1} \end{aligned}$$

with $r_M = \frac{\beta_{nm} M_m}{\rho A_m}$ and the argument for the trigonometric functions is $(\beta_{nm}(x_{m-1} - l))$.

Appendix E

Decoupled Finite Element Analysis

In the decoupled finite element analysis (FEA) a polynomial form is assumed for the displacement between the nodes.

$$w(x,t) = a_0(t) + xa_1(t) + x^2a_2(t) + x^3a_3(t) = \begin{bmatrix} 1 & x & x^2 & x^3 \end{bmatrix} a = P^\top a$$

At an arbitrary node i the parameters of interest are the displacement $w_i(t)$ and the slope $\frac{\partial w_i}{\partial x}(t)$. Assuming an element of length L, the nodal parameters and the functions $a_j(t)$ can be related by

$$\begin{bmatrix} w_i(t) \\ \frac{\partial w_i}{\partial x}(t) \\ w_{i+1}(t) \\ \frac{\partial w_{i+1}}{\partial x}(t) \end{bmatrix} = \begin{bmatrix} 1 & 0 & 0 & 0 \\ 0 & 1 & 0 & 0 \\ 1 & L & L^2 & L^3 \\ 0 & 1 & 2L & 3L^2 \end{bmatrix} a$$

This relationship can be written in vector notation as $q_e^i = Ca$. Using this relationship the displacement between two nodes of the FEA can be expressed as $w(x,t) = P^\top C^{-1} q_e^i = N^\top q_e^i$ where $N = C^{-\top} P$ is a vector of the interpolating functions. This expression for the displacement is then used in the calculation of the strain and kinetic energy of the system.

For an Euler-Bernoulli system with bending stiffness $EI(x)$ and mass per unit length $\rho A(x)$, the mass and stiffness matrices for a single element of the FEA are

$$K_e^i = \int_0^L EI(x) \left(\frac{\mathrm{d}^2 N}{\mathrm{d}x^2} \otimes \frac{\mathrm{d}^2 N}{\mathrm{d}x^2} \right) \mathrm{d}x$$

$$M_e^i = \int_0^L \rho A(x) \left(N \otimes N \right) \mathrm{d}x$$